

SCIENCE AT THE ENVIRONMENTAL RESEARCH STATION SCHNEEFERNERHAUS/ ZUGSPITZE

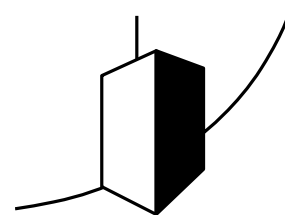
Prof. Dr. Michael Bittner; Ed.
(Coordinator Science Team UFS)



Umwelt
Forschungsstation
Schneefernerhaus

SCIENCE AT THE ENVIRONMENTAL RESEARCH STATION SCHNEEFERNERHAUS/ ZUGSPITZE

Prof. Dr. Michael Bittner; Ed.
(Coordinator Science Team UFS)



Umwelt
Forschungsstation
Schneefernerhaus

Table of contents

Preface: Thorsten Glauber, Bavarian Stateminister of the Environment und Consumer Protection	4
Preface: Prof. Dr. Michael Bittner, Editor	5
1. The environmental research station Schneefernerhaus	7
Siegfried Specht	
2. Studies on patients with atopic diseases at the Environmental Research Station Schneefernerhaus (UFS)	37
B. Eberlein, J. Huss-Marp, F. Pfab, R. Fischer, R. Franz, M. Schmitt, M. Leibl, V. Allertseder, J. Gloning, M. Kriegisch, R. Hennico, J. Latotski, C. Ebner von Eschenbach, U. Darsow, H. Behrendt, R. Huber and J. Ring	
3. Monitoring of persistent pollutants at the UFS	53
Korbinian P. Freier, Gabriela Ratz, Wolfgang Körner, Bernhard Henkelmann, Karl-Werner Schramm, Manfred Kirchner, Wolfgang Moche and Peter Weiss	
4. Observation and Modeling of Climate Driven Trends at the Zugspitze Summit	68
Thomas Gallemann, Michael Mahr, Andreas von Poschinger and Bernhard Wagner	
5. Cloud and Precipitation Observed with Radar	79
Martin Hagen, Axel Häring, Stefan Kneifel and Kersten Schmidt	
6. Environmental radionuclides as tracers for transport processes in snow	96
Kerstin Hürkamp and Jochen Tschiersch	
7. Temperature and Precipitation Anomalies at Mount Zugspitze in Relation to Large-scale Atmospheric Circulation Patterns and North-Atlantic European Modes of Variability	112
Jucundus Jacobeit and Markus Homann	
8. Solar UV-Radiation	130
P. Koepke, M. Garhammer, P. Hoeppe, B. Klotz, J. Reuder and M. Seefeldner	
9. Plant Life on Germany's highest Mountain – Vegetation and Vegetation Dynamics on the Zugspitzplatt	144
Oliver Korch and Arne Friedmann	
10. Large scale dynamics of the atmosphere: Planetary waves	158
Lisa Küchelbacher and Michael Bittner	
11. Statistical downscaling of future global climate scenarios for Alpine high mountain regions	176
Andreas Philipp, Christoph Beck, Severin Kaspar, Stefanie Seubert and Jucundus Jacobeit	

12. Evaluation of Measurement Series from high Mountain Stations	193
Ludwig Ries, Cedric Couret, Ye Yuan, Esther Giemsa, Jucundus Jacobeit and Stephan Hachinger	
13. Cosmic rays and the Earth	217
Vladimir Mares and Werner Rühm	
14. Observations of OH airglow at UFS "Schneefernerhaus"	232
Carsten Schmidt, Patrick Hannawald, René Sedlak, Stefan Noll, Sabine Wüst and Michael Bittner	
15. Passive sampling of POP and PAH with virtual organisms in alpine environments	245
Karl-Werner Schramm and Marchela Pandelova	
16. Introduction to solar FTIR spectrometry of the atmosphere and research highlights from the Zugspitze summit	260
Ralf Sussmann and Petra Hausmann	
17. Environmental medicine in the alpine region	277
Claudia Traidl-Hoffmann and Volker Schiller	
18. Lidar remote sensing of water vapor with DIAL	288
Hannes Vogelmann and Thomas Trickl	
19. Hydrological investigations in the Wetterstein Mountains at the UFS Schneefernerhaus (Bavarian Alps)	305
K.-F. Wetzel, M. Bernhardt, S. Weishaupt and M. Weber	
20. Gravity waves: A brief summary of theory and data analysis results in the alpine region	322
Sabine Wüst	
21. Simultaneous lidar measurements of ozone, water vapour, and particles: long-term investigation of atmospheric transport up to the hemispheric scale	333
Thomas Trickl and Hannes Vogelmann	
22. Impact of turbulence on cloud microphysics	353
Gholamhossein Bagheri, Eberhard Bodenschatz, John Lawson, Jan Moláček, Freja Nordsiek and Oliver Schlenczek	
List of Contributors	369
Impressum	372

Liebe Leserin, lieber Leser,



Forschung ist die Grundlage unseres Wissens und Handelns. Dies gilt besonders für den Klimawandel und seine dynamische Entwicklung. Eine der größten Herausforderungen der Zukunft weltweit, aber auch in Bayern, sind die durch den Klimawandel ausgelösten Veränderungen, die wir alle in vielen Bereichen spüren. Besonders plastisch wird uns das in der äußerst sensiblen Alpenregion vor Augen geführt. Die Gletscher – nicht nur die bayerischen – schmelzen, der Temperaturanstieg in den Alpen ist nahezu doppelt so hoch wie der globale Durchschnitt.

Es freut mich, dass wir in Bayern mit der Umweltforschungsstation Schneefernerhaus (UFS) auf 2.650 m Deutschlands höchst gelegene Forschungsstation betreiben können. Die UFS entstand durch den vollständigen Umbau eines 1931 errichteten Hotels als gemeinsame Initiative des Freistaats und des Bundes als Reaktion auf die Ergebnisse der Konferenz von Rio 1992. Seit 1999 bildet die UFS eine einzigartige Plattform für die kontinuierliche Beobachtung physikalischer und chemischer Eigenschaften der Atmosphäre sowie für die Analyse wetter- und klimawirksamer Prozesse. Sie trägt damit entscheidend zur Erforschung und Dokumentation des Klimawandels sowie zur Erarbeitung von Strategien und Lösungsvorschlägen zur Beherrschung der Klimafolgen bei.

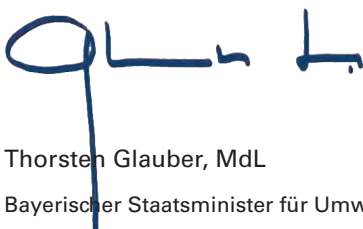
Die Station wird unter Federführung des Bayerischen Umweltministeriums als „Virtuelles Institut“ geführt, dem neben Einrichtungen des Freistaates Bayern weitere hochkarätige Institutionen angehören, wie Umweltbundesamt, Deutscher Wetterdienst, Deutsches Zentrum für Luft- und Raumfahrt, Karlsruher Institut für Technologie, Helmholtz-Zentrum München, Max-Planck-Gesellschaft, Ludwig-Maximilians-Universität München, Technische Universität München und Universität Augsburg.

Die vielfältige Forschung, die dort oben betrieben wird, umfasst ein weites Spektrum, das von regionalem Klima über Satellitenbeobachtung, kosmische Strahlung, Hydrologie, Umwelt- und Höhenmedizin bis hin zur globalen Atmosphärenbeobachtung und Wolkendynamik reicht.

Die Forscherinnen und Forscher arbeiten dabei eng zusammen und zeigen, dass gemeinsames Handeln einen großen Mehrwert bringt. Kooperation steht dabei im Mittelpunkt getreu dem Motto „Gemeinsam mehr sehen und mehr verstehen“.

Die Ergebnisse dieser Arbeit sind im vorliegenden Band zusammengefasst. Er gibt einen Überblick über aktuelle Forschung auf der UFS, bietet aber auch breites Grundlagenwissen für angehende Forscherinnen und Forscher. Ich wünsche viel Vergnügen bei der Lektüre.

Ihr

A handwritten signature in blue ink, appearing to read 'Glauber'.

Thorsten Glauber, MdL

Bayerischer Staatsminister für Umwelt und Verbraucherschutz

Foreword Prof. Bittner



The Alpine region is particularly sensitive to variations of the Earth's climate. Here, temperatures alter more strongly, the lengths of the seasons shift more noticeably, and changes in the water balance and the flow system of the atmosphere are more perceptible than in many other places on Earth. At the same time, the Alps are among the most densely populated mountain regions in the world. It is obvious: a sustainable development of this living and economic space for the people living there and the many tourists visiting this attractive region every year is important. This is also in line with internationally agreed environmental goals: at the European level with the Europe 2020 Strategy and the European Green Deal, and at the global level with the Kyoto Protocol, the Paris Agreement and

the UN Sustainable Development Goals (SDGs), countries are required to adopt environmentally friendly policies.

The magnitude of changes occurring in almost all parts of the alpine Earth system is composed of so-called "intrinsic" forcings of the climate system (natural forcings such as the El Niño or the Quasi Biennial Oscillation etc.), "extrinsic" influences (e.g., solar radiation, solar wind, or cosmic rays), and, increasingly, anthropogenic activities (e.g., pollutant emissions from transportation and industry). Research can help detect such changes, understand them, quantitatively describe the processes at work, and incorporate them into computer models of the Earth system that give us a glimpse into the future. After all, the ability to answer the question "What if?" has become relevant for society; it supports decision-making in politics, business and society. In this context, the more well-founded our knowledge, the more accurate the models and the more reliable the basis for decision-making are.

The Alps have a complex topography. This results in a particular diversity of quite different microclimates on comparatively small spatial scales, which cannot be well resolved by climate models to date. It should be stressed that this limitation of the spatiotemporal resolution of climate models is not solely due to a limited computing capacity. Increasing the spatiotemporal resolution in models also requires a corresponding understanding of processes on finer scales to ensure an adequate representation of the processes represented in the model. Previous research has shown that the processes at work in the alpine Earth system are complex: in order to reach the abovementioned goal it is not sufficient to study the respective processes in isolation from each other. The next step must be to better link the processes in the various disciplines of the alpine Earth system (geosphere, biosphere, hydrosphere, cryosphere, atmosphere and also medicine), i.e. to identify and precisely understand coupling processes between the areas of the alpine Earth system as comprehensively as possible. This underlines that the respective specialized research groups must exchange their results and jointly search their data for climate signals that are evident in the different areas of the alpine Earth system. On this basis, a quantitative process understanding for the alpine Earth system can then be developed. This approach is in line with the strategic plan of the World Climate Research Program for the period 2019 to 2028. Also, the European program Destination Earth (DestinE), which aims to contribute to the European Commission's Green Deal and Digital Strategy by developing a high-precision digital model of the Earth to monitor and simulate natural and human activities, will rely on the above coupling processes between the domains of the Earth system being correctly included in the model.

The Environmental Research Station Schneesfernerhaus, UFS, is a highly visible example of how the natural sciences are working to understand climate change. The research activities at the UFS are probably unique in the region in terms of their technical diversity and represent a "micro-lab" for the Alpine region – and comparable mountain regions – as a whole. It thus makes sense to bundle the expertise concentrated here in a way that opens the door to efficient interdisciplinary collaboration. In this way, an added value is created that clearly reaches beyond the sum of the individual contributions.

On behalf of the Science Team of the UFS, in which prominent research institutions (Karlsruhe Institute for Technology, Helmholtz-Zentrum Munich, German Aerospace Center, Max Planck

Society), universities (Technical University of Munich, Ludwig Maximilian University of Munich, University of Augsburg) and subordinate authorities of the Free State of Bavaria (The Bavarian Environment Agency, LfU) and the Federal Government of Germany (German Environment Agency, UBA, Germany's National Meteorological Service, DWD) have joined forces to form the "Virtual Institute Schneefernerhaus"; may I say: the researchers working here are proud of this institution. The UFS serves us as a platform for experimental instrumentation and experimental setups, much in the same way as satellites, research ships or research aircraft are used as "carriers" for scientific instrumentation. Depending on the scientific question, we make use of the laboratory facilities, measuring areas and building services provided for our investigations. In doing so, we receive the best possible support from our colleagues in the UFS operations team that a scientist or engineer could wish for. We greatly appreciate the fact that the Bavarian State Ministry for the Environment and Consumer Protection, BayStMUV, continuously and vigorously promotes and supports the maintenance and constant improvement of the station. I emphasize this because the UFS, as an efficient and modern research platform, is of outstanding importance for the competitiveness of our scientists in the field of environment-related research. It is indispensable for staying at the forefront of innovation, making significant technological advances and opening up new areas of research, which in turn can also serve as a driver for new areas of application. It should not stay unmentioned that networking with the Leibniz Supercomputing Center in Garching is also an important component of the UFS research platform. The Alpine Environmental Data and Analysis Center, AlpEnDAC, which is jointly operated here, facilitates access to computing capacity, to complex numerical computer models and to a wide range of data, thus helping to accelerate scientific progress. All this puts us in a position to make visible contributions to sharpen the forecasts of expected future developments. The final result is the best possible knowledge base on which to formulate more targeted environmental policy decisions.

This book is intended to provide an insight into the diversity of scientific work in the UFS and also to put the work carried out in the context of current international research. In particular, it should also be able to be used as a source for the teaching of young scientists at universities. For this reason, the respective chapters also contain an outline of the technical basis of the research work presented.

Speaking for the entire scientific community active in the UFS, I hope you enjoy reading this book.



Prof. Dr. Michael Bittner

Augsburg, March 2022

1 Environmental Research Station Schneefernerhaus

Location, History, Organisation

Prof. Dr. rer. nat. Siegfried Specht¹

Prologue

In recent decades, scientific progress has provided us with extensive knowledge about global warming and its immense, threatening consequences. Since the 1970s, these findings have been accompanied in the scientific community by a worldwide climate debate and an increased desire for supraregional cooperation. Efforts to further clarify the facts, to make the best possible predictions regarding the expected changes, and to develop goal-oriented strategies for effective mitigation and adaptation measures have been intensified.

For the balance of anthropogenic interventions in creation, the term “Anthropocene” (Paul J. Crutzen) has meanwhile become accepted for our age.

The growing importance of this global scientific dialogue manifested itself in such important conferences as the first World Climate Conference in Geneva in 1979 (WCC-1/COP-2), the historic “World Climate Summit” in Rio de Janeiro in 1992 (UNFCCC/Framework Convention on Climate Change), and the Climate Conference in Berlin in 1995 (COP-1/Berlin Mandate).

Now held annually, the UN Climate Change Conference is the formal meeting of the Parties to the UN Framework Convention on Climate Change (Conference of the Parties, COP). Since 2005, the conferences have also served as meetings of the Parties to the Kyoto Protocol (1997/COP-3/quantitative emissions limitation) and, since 2018, as meetings of the Parties to the Paris Agreement (COP-21/2015/2-/1.5-degree target).

Particularly with the Paris Agreement, a piece of history was written, because here the community of nations agreed to limit the global temperature increase caused by the greenhouse effect to “well below two degrees Celsius” compared to the pre-industrial age, “with the ambition” to limit it (if possible) to 1.5-degrees Celsius.”

Against this background, the results of the recent climate conference in Glasgow (COP-26), which was postponed to 2021 for pandemic reasons, can certainly be seen as a reaffirmation of the Paris agreements and also as another positive milestone on the road to climate-neutral economic and social systems. After all, around 200 signatory states have agreed on a final protocol, the implementation of which will have a strong, global orientation function.

Above all, agreements and concessions were reached on the acceptance of scientific findings by political decision-makers. And associated with this, a significantly stronger acceptance of scientific, model-based mitigation and adaptation strategies as a basis for future-oriented political action. The currently discernible progress of climate-neutral economic and social concepts is important evidence of this.

Notwithstanding this, there are still varying deadline commitments for achieving the interim targets considered necessary, as well as problem areas that could only be inadequately addressed or did not find sufficient entry into the final document.

Positive examples are the additions to the rules on the uniform recording of greenhouse gas emissions and on international trading in emission certificates, as well as the emphasis on the role of ecosystems as natural CO₂ sinks, the preservation or restoration of which has been clearly highlighted as important measures.

¹ Former head of department at the Bavarian State Ministry of the Environment and Consumer Protection (BayStMUV), Munich, and 2007–2016 Chairman of the Consortium of the “Virtual Institute” – Environmental Research Station Schneefernerhaus/Zugspitze (UFS)

Negative balance points are the too vague formulation of the coal phase-out (“phase down” instead of “phase out”), the insufficient consideration of the interactions between climate and biodiversity and, last but not least, the insufficient financial support from the perspective of the developing countries to compensate for the existing and foreseeable damages and losses caused by climate change (“LOSS and DAMAGE”).

It should be emphasized, however, that the conference in Glasgow sent a clear signal to the community of states to significantly increase their contributions to limiting CO₂-emissions with the goal of recognizably limiting the temperature increase caused by humans due to the greenhouse effect to 1.5 degrees Celsius. The calculations in this regard cover the beginning of industrialization in time up to the year 2100, using the average of the years 1850 to 1900 as the pre-industrial value.

This increased acceptance for a more targeted approach to the 1.5-degree target is reflected in the significantly improved climate protection programs of some countries, as expressed, for example, in more ambitious targets for achieving climate neutrality.

The Federal Republic of Germany is now aiming for climate neutrality by 2045. The United States, Japan, South Korea, the United Emirates, Australia, and probably also Brazil want to achieve this goal by 2050. Russia, Saudi Arabia, and China have pledged to achieve this goal by 2060, although China still insists on an emissions maximum in 2025 or 2030.

The EU Commission plans climate neutrality by 2050, but wants to reduce emissions by at least 55% by 2030 compared to 1990 ([Handelsblatt 2022/01](#)).

The Free State of Bavaria wants to achieve climate neutrality by 2040 ([Bayern 2021](#)), with the interim goal of ensuring a 65% reduction in greenhouse gas emissions by 2030 ([StMUV 2021](#)).

Important climate goals of the current federal government for 2030 are, among others: 80% of electricity from renewable sources, quadrupling of solar and wind power plants at sea, reservation of 2% of the federal area for wind power plants, solar obligation for new commercial buildings, natural gas as a transitional energy source, conversion of organic farming in agriculture to 30%, climate-neutral generation of heat at 50% and bringing forward the coal phase-out “ideally” to the year 2030 ([Franz 2021](#)).

A study conducted by the Berlin University of Applied Sciences (HTW) in 2021 shows that these reduction approaches can only be a start worldwide. Using a so-called “per capita budget approach,” the scientists calculated an upper limit for the CO₂-emissions still permissible worldwide for achieving the 1.5-degree target and derived the German per capita share from this. ([Quaschnig 2021](#)).

As a result of these model calculations, it is shown that the climate protection measures adopted by the governing “Ampel-Coalition” make carbon dioxide neutrality by 2045 seem possible, but not compliance with the Paris Agreement ([idw 2021](#)). To achieve the latter, climate neutrality would be required between 2030 and 2035 (equivalent to an emissions limit of only 6.7 billion t CO₂) ([SVR 2019](#)).

The aspect of the foreseeable exceeding of the emission budget to which the FRG is still arithmetically entitled ([Quaschnig 2021](#)) is the key point of the currently pending renewed constitutional complaint of January 26th 2022 against the amendment of the German Climate Protection Law of August 31th 2021 (see below).

All this is evidence that, despite all the difficulties and conflicts of interest, world politics has recognized that contractual agreements have become indispensable. In other words, it has been understood that humanity must protect itself from becoming a force of nature that Genesis did not intend for it. This is at the same time a historical-social mandate that must also be responsibly shared by science.

In order to fulfill this mandate in a socio-politically correct and credible manner, science must communicate its results in a fair and comprehensible manner. A clear distinction must be made between whether a statement is proven, whether it is merely based on a (plausible) assumption, or whether it is based on a (well-founded) hypothesis. For general usage, this means a strict separation of facts and opinions. This procedure is also indispensable against the background that statements in the media are often only possible in abbreviated form and there is too little

time to also name the “error bar” and explain the boundary conditions under which the statement alone is valid.

It is the author’s conviction that the boundaries between political and scientific competence should also be strictly observed. This is a proven rule of conduct in democratic societies, because democracy is per se committed to truth-orientation.

If this is the case, scientists can rely on their acceptance and, if necessary, demand the respect due to them for their work. However, just because they think they know something better and represent a good cause, they should not be tempted to take on the role of politicians and their media-savvy use of language.

The research findings on global warming clearly show that there will be winners and losers. In climate research in particular, this finding in no way releases scientists from their obligation to publicly point out the consequences of their research findings and to comprehensibly review the effects of measures taken by policymakers.

In short, scientists must strictly adhere to the communication rules of their profession, because laws of nature are not a matter of faith.

In this respect, the profession of scientist is also a privilege that must be justified again and again through honesty to the public.

In this context, the right to freedom of expression in public debate is indispensable. In our society, there is a guaranteed right to one’s own opinion. However, there is no right to one’s own facts. Therefore, a fair debate does not justify “alternative facts.”

Based on the results of COP-26 in Glasgow, it can now be seriously assumed that the available scientific facts have found general acceptance and that a global consensus on curbing anthropogenic global warming can be reached on this basis.

The existing legal requirements in the countries on the way to climate neutrality or to achieving the 1.5-degree target are currently accompanied in Europe by highly motivated constitutional lawsuits demanding further-reaching measures in a shorter time.

With regard to the Paris Agreement, for example, the German Federal Constitutional Court (BVerfG-2021/01), in its ruling of April 29th 2021, saw in the then applicable version of the Climate Protection Act (KSG) the unreasonable risk of a serious loss of freedom for the younger generation (this was the tenor of the decision). With reference to the results of Glasgow and the emission limits promised in the meantime to achieve the 1.5-degree path (see above), a new constitutional complaint was filed on January 26th 2022. This time against the climate protection law amendment of August 31th 2021. A decision is expected by February 2023 (BVerfG 2022/02). If one takes into account an existing ruling by the District Court of The Hague (Netherlands) of May 26th 2021 on the SHELL Group (SZ 2022/01), it will be interesting to see whether the upcoming ruling from Karlsruhe could possibly lead to a fundamental discussion between the judiciary and the legislature. in which the state of science would also be of importance (as of February 2022).

Another example of pending court decisions on climate issues is emerging with regard to the EU Commission’s current taxonomy proposals. On February 2th, 2022, the Commission decided by means of a delegated act to include nuclear power plants and gas-fired power plants (at least temporarily) in its taxonomy regulation. Provided they each meet a number of time, technical and licensing requirements, they would thus qualify as “sustainable”.

By awarding this “green” label, the applied classification system is intended to improve the market overview for authorities and investors and to increase the attractiveness for “green” investments. The Commission’s aim is to accelerate the transition to a climate-neutral European economy and to prevent so-called “greenwashing” through various reporting requirements. If the EU Parliament (with a qualified majority) and the EU Council of Ministers do not object within four to six months, the law will automatically enter into force.

In this case, some EU countries have already announced that they will file individual lawsuits against the inclusion of both or at least one of the two power plant systems (status February 2022).

As expected, opinions clash hard in the current political taxonomy debate, with conceptual distinctions between “sustainable,” “climate-friendly,” “environmentally friendly,” and “green” often not made. In line with the different meanings of the terms mentioned, different positions are quite likely to emerge on this issue, which is very significant for climate protection in general and for the upcoming industrial transformation of society. Be it for reasons of realistic feasibility, be it with regard to acceptance or be it from the point of view of political credibility.

Depending on the interests at stake, conflicting conclusions and positions are to be expected in the interpretation of the “bridge technology gas” alone, which is considered absolutely necessary in Germany. The already decided phase-out of nuclear energy (by the end of 2022) and of coal-fired power generation (by 2030?/2038), according to studies, requires 70 new gas-fired power plants in order to achieve the climate targets with security of supply ([Handelsblatt 2022/02](#)).

In order to ensure the targeted climate neutrality from 2045, the gas-fired power plants available by then would then have to be operated with hydrogen or biogas.

The French government argues similarly: With reference to the additional requirements of the EU taxonomy regulation, the construction of up to 14 new nuclear power plants is announced for the period up to 2050. Currently, 56 reactors are in operation, covering 70 % of the electricity demand. Two-thirds of French energy consumption is still based on fossil fuels such as oil and gas. This share would have to be completely replaced by regenerative sources by 2030. ([SZ 2022/02](#))

Without prejudging pending court decisions, reference is made to the following information:

- The 1987 Brundtland Report of the UN World Commission on Environment and Development states: *“Sustainable development is development that meets the needs of the present generation, without compromising the ability of future generations to meet their own needs.”* ([Brundtland 1987](#))
- In the Amsterdam EU Treaty of 1997 and in reports of the Enquete Commission of the German Bundestag “Schutz des Menschen und der Umwelt” (Protection of Man and the Environment), the so-called *“Three-Pillar-Model of sustainability”* as an important achievement of environmental protection in the economy, politics and society and as an important, future-oriented development of human existence in the economic, ecological and social dimension. According to this model, sustainable development is based on a balanced relationship between economy, ecology and social aspects. ([Stoll 2022](#)).

Of course, policymakers always have a duty to take appropriate and effective precautions against hazards. However, it must be borne in mind that statutory measures must be balanced in accordance with the constitutional principle of proportionality, with the consequence that they can generally only be aimed at *minimizing risk*, because 100% exclusion of many risks in a liberal social order would fail due to constitutional limits.

Analogously, it remains the task of science to develop methods and algorithms with which the effects of political decisions can be estimated as early and reliably as possible. In doing so, it is essential for all stakeholders to take into account the state of science as far as possible for the present and with regard to future generations.

In today’s society, the objection is often raised that the political value of knowledge is often overestimated and that we will never know enough to permanently avoid erroneous developments or even errors. Socrates is fondly quoted as saying in his defense speech before the Athenian court in 399 B.C.: “I know that I know nothing.” Contrary to the common translation, however, the correct quotation is “I know that I do not know.” So we can confidently assume that Socrates did not intend to negate all knowledge for himself, but merely to point out the limits of human knowledge in general.

Of course, we will never know “everything.” But future generations will certainly not accuse us of being knowledge-based, but of not paying enough attention to the knowledge we do have. We may not know everything when it comes to making decisions, but we know enough to act in a sustainable manner.

Quote: *“Whether humanity has the collective wisdom to navigate the Anthropocene to sustain a livable biosphere for humans and civilizations, and for the rest of the life with which we share the planet, is the most daunting challenge facing humanity”* ([Queally 2021](#)).

Having recognized this at an early stage is one of the merits of the research partners at the “Virtual Institute – Environmental Research Station Schneefernerhaus/Zugspitze (UFS)”. The pressing issues of climate change, which will dramatically affect our future, have been the focus here for about 25 years. It is significant that this research is conducted in an interdisciplinary, cross-border manner and in a constant collegial exchange of the knowledge gained. Fair information of the public while maintaining scientific principles is a matter of course. In the following, the history of the institute and its high alpine environment are presented in more detail.

1.1 Introduction – The UFS as a center for climate and high-altitude research in the Zugspitze region (“www.schneefernerhaus.de”)



Fig. 1: View to the east with the Schneefernerhaus and the Zugspitze summit

Germany’s highest research institute, the “Virtual Institute – Environmental Research Station Schneefernerhaus / Zugspitze (UFS)” is situated at an altitude of 2,560 m above sea level, and is built into the south wall of the Zugspitze mountain.

Standing nine storeys tall, and with two storeys, protrude into the deep rock, the main building is firmly embedded in this section of the Wetterstein mountain range.

It is named after the nearby glacier and was originally a hotel bearing the same name built in 1929. The conversion was funded by the Free State of Bavaria and the Federal Republic of Germany.

The UFS has a several outdoor platforms for observations, measurements and experiments, and also has access to a unique botanical garden on the nearby Schachen (1,870 m above sea level) with indigenous plants from the Alps. The UFS is operated in trans-border cooperation with key high-altitude research stations of the Alpine region within the framework of a scientific cooperation agreement (see chapter 8 and 10).

Now networked worldwide, the UFS is, today, a research platform, observatory and scientific communications center in one. It also provides the world's only education and training center for atmospheric scientists from developing countries.

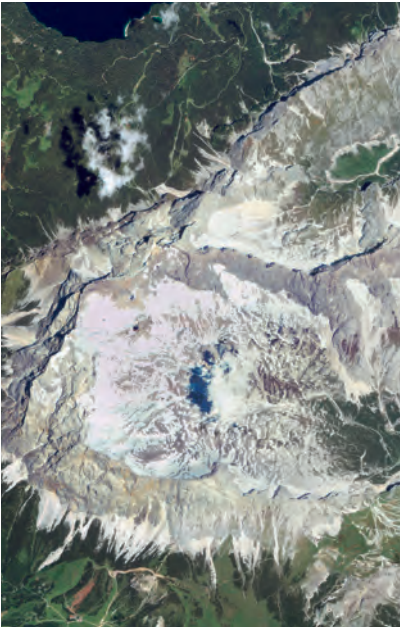


Fig. 2: IKONOS-Satellite photo of the Zugspitze massif



Fig. 3: The glacier "Northern Schneeferner (NSF)" in 2009



Fig. 4: Summit cross on the eastern summit of the Zugspitze

The UFS is surrounded by the Zugspitze massif (Fig. 2) where a section of the German-Austrian border stretches towards the west. The summit ridge has the shape of an eastwards-opening horseshoe and rises over 2000 m above the valley.

The longer side of the horseshoe is formed by the almost 20 km long east-west ridge of the Wetterstein mountain range, whereas its shorter side is formed by the massive side flanks of the so-called Riffelwände which extend as far as the two Waxenstein peaks and the Loisachtal valley beyond.

The horseshoe itself surrounds the so-called "Zugspitzplatt" (karst plateau) in its center, and to the west the (smaller) "Southern Schneeferner" and the (larger) "Northern Schneeferner" – two of today's three remaining Zugspitze glaciers (Fig. 3).

To the north west of this rugged mountain ridge rises the twin-peaked summit of the Zugspitze – Germany's highest mountain – reaching 2,962 m above sea level. The mountain was first mentioned in records in 1590 and for a long time bore the masculine name "der Zugspitz". Right up into the 19th century, it was regarded by locals as an untouched fortress of ice, and, with its dramatic avalanches, "absolutely unclimbable."

Looking out today onto the surrounding area of the Schneefernerhaus,, one can see tourists, restaurants, ski slopes extending between 2,000 m and 2,800 m, and the small chapel "*Mariä Heimsuchung*" (see chapter 06).

Towering above everything else is the western summit of the Zugspitze that now, since December 2017, bears the new high-tech cable car "*Seilbahn Zugspitze*" ("*Zugspitze Cable Car*," see chapter 06). Next to it, practically untouched, is the eastern summit with its distinctive golden summit cross (Fig. 4). The first summit cross was erected in 1851 at the initiative of the priest Christoph Ott, who was also a meteorological observer based at Hohenpeissenberg that is situated somewhat to the north of the mountain range. The summit cross was originally erected on the western summit, which at that time stood 2 meters higher than the eastern summit.

Due to increased development of the western summit for other purposes, the summit cross was restored in 1982 and then re-erected on the adjacent eastern summit. In 1993 it was replaced with a replica which was restored in 2009 and which had to be repaired again in 2017 after damage caused during the construction of the new Cable Car "*Seilbahn Zugspitze*".

It is to be noted, however, that although the tourist infrastructure on the Zugspitze massif was established at a very early date, it was not this which was directly responsible for the inception of the research station UFS which, size-wise, is unparalleled anywhere in the Alps. Well before this time, some 200 years ago in the Napoleonic era, interest in this area was triggered when the exact delineation of borders was required due to the frequent changes in land ownership. This was coupled with a growing scientific interest in this high altitude "terra incognita," this interest being predominantly focused on the flora and, most particularly, on the weather.

Despite the inadequate mountaineering equipment at the time, a kind of "Faustian urge" developed to venture into these seemingly inhospitable high alpine mountains with their mighty glaciers.

It is therefore exciting to tell, together with the history of the Schneefernerhaus, also about one of the most magnificent views in the entire northern ridge of the Limestone Alps, about the adventurousness and scientific curiosity of the locals, about the first technical achievements, about the rivalry of the neighboring countries, about

the impressive flora and fauna, about the carelessness in the course of the emerging mass tourism, and, also the ever-present risks and dangers that are encountered at high-altitudes – even today.

1.2 A brief historical account of the development of the Zugspitze region and the “Plattachferner” glacier

From a historical point of view, the regional upswing of the Zugspitze and its surroundings began at the beginning of the 19th century.

In 1802, the region “Werdenfelser Land” became part of the Electorate of Bavaria (“Kurbayern”), after having belonged to the Prince-Bishopric of Freising for over 500 years as Imperial County (“reichsunmittelbare Grafschaft”).

(The Greek letter “γ” in the name “Bavaria” was, however, only introduced bindingly in 1825 by the Bavarian King Ludwig I.).

In 1806, the Elector Maximilian I. Joseph (honorary member of the Bavarian Academy of Sciences since 1781) was appointed King of Bavaria by Napoleon.

This was reason enough for him, (once again) to accurately determine the borders between the new kingdom and the Austrian neighbor country for the “Werdenfels map” in the “Atlas of Bavaria”. This concerned, in particular, the boundary along the “Wetterstein ridge” (Wettersteinkamm) and around the rocky ridges surrounding the “Platt” (plateau).

Another survey campaign about ten years later became important for strategic reason in order to incorporate the geographical border changes that had resulted from the agreements of the Congress of Vienna.

The order for mapping this region was given by the “Royal Bavarian Topographical Institute” to the “Royal Bavarian Lieutenant Josef Naus” who was born in Reutte-Lechaschau, Tyrol and was a trained surveyor. The first attempt to reach the top of the “Zugspitze” failed, but the second one was successful. On 27th August 1820 he finally reached the western summit of the “Zugspitze” via “Platt” and “Schneeferner ... after overcoming several deadly perils and engaging in extreme efforts”. Lieutenant Naus was accompanied by his “surveying assistant Maier” and the guide Johann Georg Tauschl, and had already climbed several other mountains above the “Loisachtal” valley in preparation for this ascent.

Because of bad weather and a lack of time, they could only leave behind “a short climbing stick with a red cloth tied to it to mark their success” “to prove we were there”. Lieutenant Naus is documented as being the first person known to successfully climb the mountain. Whether he reached the Eastern Summit of the Zugspitze as well is not known.

Although not yet recognized as such, this marked an important step in the history of the “Scientific Location Zugspitze”. Scientifically motivated excursions were already taking place at this time. First meteorological data were being collected and spectacular first ascents of other high mountains were being accomplished. A prime example is the “Meteorological Observatory at Hohenpeissenberg” that, today, with its continuous meteorological record from 1781 onwards, and the psychrometric water vapor measurements that started in 1841, boasts two of the world’s longest measurement series in this field. Other examples of the “zeitgeist” are the first ascents in particular of Mont Blanc in 1786, Grossglockner in 1800, Ortler in 1804 and the Jungfrau-Massif in 1811.

Other early scientific high-altitude expeditions at this time are described in the landscape studies of diplomat and nature researcher Count Franz Gabriel von Bray, president of the Botanical Society in Regensburg from 1811. These studies were published in 1808 and again in 1825 (“Reise durch Tirols Alpen” / “Journey through Tyrol’s Alps”). In 1807 Gabriel von Bray had set off from Partenkirchen with other like-minded scientific colleagues and a dozen porters. He writes “.. the purpose of our journey was to follow the river Partnach to its source on the glacier between Zugspitze and Wetterstein, to measure its temperature at different altitudes and also to botanise the plants”. In the light of this, it is important to remember that the Alpine glaciers

– related to modern times – probably at their greatest expansion in the first half of 19th century and were particularly difficult to reach. Not least because of this situation, the first winter ascent of the Zugspitze did not take place until 1882. It is therefore useful to take a brief look at the development of the Alpine glaciers.

1.3 Notes on the Bavarian Alpine glaciers

Although our knowledge is far from complete, we do know a great deal about the history of Alpine glaciers. Not least thanks to the excellent research projects of the “Geodesy and Glaciology Team of the Bavarian Academy of Sciences and Humanities (BAdW)” as well as the “Photogrammetry and Remote Sensing Team of the Technical University of Munich (TUM)”. Reference is made here to the publication (Mayer et. al. 2021).

Their archives contain one of the longest data records of direct glacier mass balance observations at Vernagtferner glacier in the Ötztal / Tyrol. The regular glacier geometry surveys date right back to 1889, when the first accurate topographic map of an entire glacier was produced by Prof. S. Finsterwalder. These researchers also maintain a series of surface surveys for all Bavarian glaciers spanning more than 70 years. In particular, they have been monitoring the glaciers at the foot of the UFS, just south of the Zugspitze summit, for over 120 years. Series of measurements of this kind are a unique and irreplaceable source of information for scientific understanding of the history of glaciers and climate change.

Global climate variations modify the local meteorological conditions, which are the driver for glacial evolution. However, response times of glaciers are in the order of decades and thus in the same timescale as the definition of climate (the mean atmospheric situation, averaged over 30 years). The documentation of glacial variations (e. g. retreat and advance cycles) therefore allows inferences to be made concerning the local climate variations in the past.

Without going into great detail, the history of Alpine glaciers can today be summarized as follows (Mayer 2021/02):

- During the so-called “little ice age” (about 1570 to 1850) the Alpine glaciers showed a periodic fluctuation. Approximately every 35 years on average, expressed advance periods could be observed that were interrupted by periods of glacier retreat. It is assumed that this glacier reaction was triggered by periodic changes between cool and wet as well as hot and dry summers. The last major advance period lasted until 1850. At this time, the glaciers also reached their maximum size during the entire period. Their surface extent was about twice that in the late 20th century.
These characteristic cycles became less and less pronounced and were no longer perceptible after 1850, when an overriding trend toward warmer conditions slowly took control. In contemporary climate research, it is generally accepted that the increase in greenhouse gas imissions since the beginning of industrialization is responsible for this trend in global warming. Finally, after 1980 this development became the dominant factor and has been influencing glacier development ever since.
- At the end of the “little ice age”, after around 1850, a consistent and ongoing decline in the mass and surface area of Alpine glaciers was observed, corresponding to the upward trend of the global mean temperatures. This was interrupted by two minor phases of glacial growth before 1920 and during the 1960s and 1970s, which – just as during the little ice age – were most likely driven by periods of cool and wet summers. The drivers behind these deviations from the general trend were considered to be a combination of periodically decreased solar radiation, a denser cloud cover, and on short time scales greater turbidity in the stratosphere of the Earth’s atmosphere due to sulphate aerosols coming from massive volcanic eruptions (e. g. Agung / Bali) (Weber, Braun 2018).
- Other probable reasons for the short growth periods are the increase in air pollutant imissions as a consequence of increasing global industrialization after 1850 and, on the other hand, the counteracting effects of legal Measures to improve air quality at the administrative level. This is a physically coherent approach, known in the scientific community as “Global Dimming / Global Brightening”-Effect. Although it took years of research and scientific debate to con-

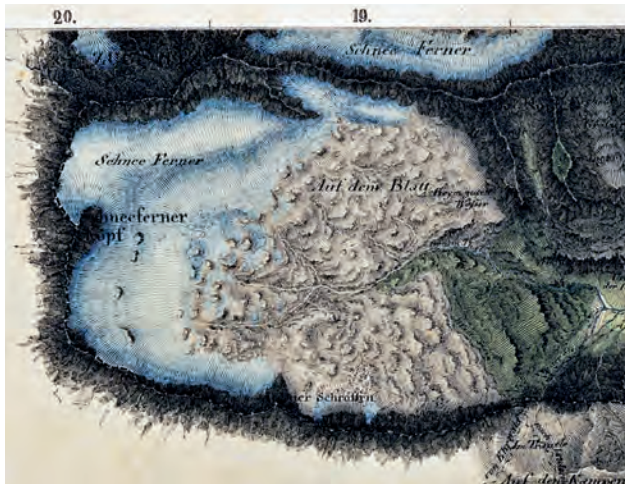


Fig. 5: Survey of the Zugspitzplatt by Josef Naus (1820)



Fig. 6: The "Plattachferner" glacier shortly before it split (1875)

solidate the general conclusion about the significance of this effect. However, a direct link between global brightening / dimming and the local glacier evolution is hard to prove.

- There are currently five glaciers in the Bavarian Alps:
 - „Nördlicher Schneeferner (NSF)“ (“Northern Schneeferner”);
 - „Südlicher Schneeferner (SSF)“ (“Southern Schneeferner”);
 - „Höllentalferner (HTF)“ (“Hell Valley Glacier”);
 - „Watzmanngletscher (WMG)“ (“Watzmann Glacier”);
 - „Blau eis (BEI)“ (“Blue Ice”).

The first three on this list are in the immediate vicinity of the Zugspitze and the remaining two are in the Bavarian Berchtesgaden region.

In 2018, they covered a total area of 44.6 ha with a volume of 3.95 million m³. In the last decade alone, they have lost a total of almost two-thirds of their volume. The “Nördlicher Schneeferner (NSF)” is the only one of them, to date, on which ski lifts are being operated. Due to its ice losses, however, it is now only the second largest of these glaciers, behind the HTF.

The story of the Bavarian glaciers fits nicely into these general historical observations, which can be especially well demonstrated using the two Schneeferner glaciers (NSF and SSF) as an example.

The map drawn by Josef Naus (Fig. 5) in 1820 shows, that the “Plattachferner”, with a surface area of about 300 hectares, still covered the entire karst plateau (“Platt”) of the Zugspitze massif.

In the subsequent survey in 1875 (Fig. 6) there are already indications of an upcoming separation of the glacier that led to the formation of the Northern Schneeferner and the Southern Schneeferner in 1900 (a small eastern one already disappeared at an early stage).

Whereas during the 20th century the development of the glaciers was still very much governed by the feedback between surface mass balance (snow accumulation and snow/ice melt) and ice dynamics (transport of ice towards the lower glacier regions), this situation very much changed at the beginning of the new millennium. During this period, the glaciers became so thin that ice transport became insignificant, while at the same time the anthropogenic induced climate change started to fully dominate the ice loss (Fig. 7).

In addition: Significant changes in the short wave and long wave radiation budget, in combination with other self-reinforcing factors, accelerate the process of deglaciation and will inevitably lead to the loss of the ice reserves in the Bavarian Alps.

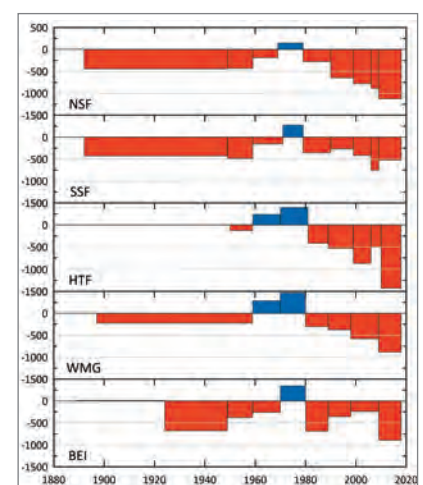


Fig. 7: Average changes in height (mass loss) of Bavarian glaciers since the start of the periodic observations by the glaciologists of BAdW in the middle of the 20th century

Expressed in numbers, this means that during the summer seasons the maximum ice thickness of the Northern Schneeferner (NSF), which was still 45 m in 2006, will continuously decrease, with average annual ice loss rates of up to 3 m in recent decades.

It is therefore expected that the Northern Snow Glacier will be completely melted in 5 to 10 years (Fig. 8), while the “Southern Snow Glacier (SSF)” is already in the final stage of decay (Marowsky 2010).

The results above indicate that in the field of glacier and climate research, striking findings have indeed been made. The verdict on which of the many hypotheses will hold up in the long term, however, requires further long-term research at the highest level.

A great deal more data from longer series of measurements and more precise methods are needed to fill the gaps from the past, to clarify feedback effects and to reduce some still significant error bars from proxy data and theoretical considerations.

Due to its location and infrastructure, but also due to its international networking, the Schneefernerhaus Environmental Research Station is an excellent location to make valuable contributions to this together with the glaciologists* of BAdW and TUM.

1.4 The “Munich House” (“Münchner Haus”)

While the development of the Zugspitze region at the beginning of the 19th century was mainly due to official requirements and curiosity about the largely unknown high-altitude landscape, over the years a lively interest in new experiences of nature and the associated sporting challenges developed.

This went hand-in-hand with a growing desire to collect scientific data – particularly concerning the weather – and a boom in high-altitude tourism. Ultimately, this increase in human activity caused a significant impact on the hitherto untouched natural environment.

A clear sign of this was the founding of the “Deutscher Alpenverein” (“German Alpine Club”) and the “Verschönerungsverein Garmisch” (“Beautification Society of Garmisch”) – both in 1869. The number of visiting members really took off after the arrival of the railway in 1889, which reduced the journey time from Munich to Garmisch from 10 to 3 hours. In 1883 a “lockable hut” with room for 12 persons was erected without much ado by the Munich section of the Alpine Club just beneath the western summit of the Zugspitze, the name having been changed from “Zugspitz” to the female noun “Zugspitze” in 1836.

On the other hand, there was considerable resistance to the construction of the “Münchner Haus” directly on the summit before permission was finally granted in 1886.

Some alpinists from the Munich section of the Alpine club still demanded at the general meeting in 1895: “... if you can't reach the summit without a hostel, you should stay at home!”. The Austrian alpinist and writer Eugen Guido Lammer, an early pioneer of adventure mountaineering, is quoted as saying: “... callous fools who now want to violently destroy this last asylum of wild nature, ...”.

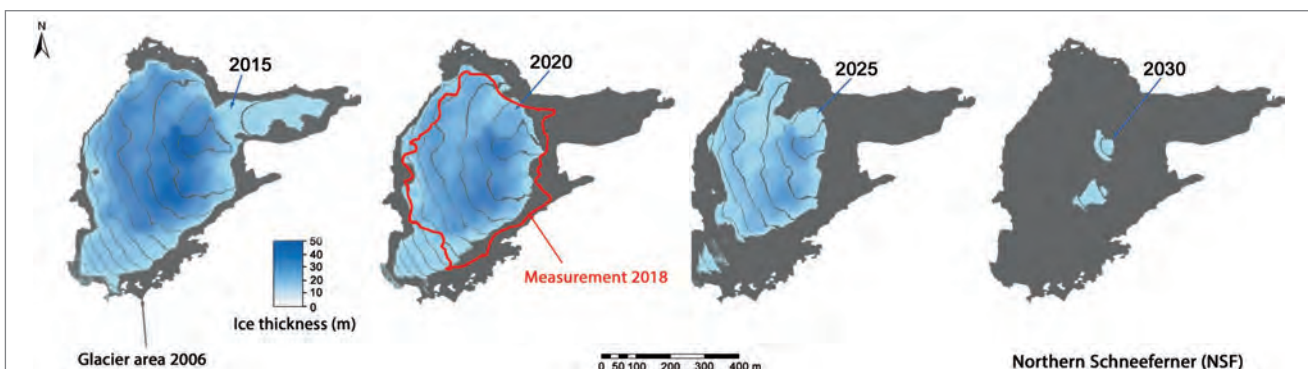


Fig. 8: Predicted mass loss of the “Northern Schneeferner (NSF)” (BAdW 2021)



Fig. 9: Oil painting "Zugspitze mit Münchner Haus" by Ernst Platz (1899)

Before the inauguration ceremony could take place on 19 September 1897 at an altitude of 2,959 m above sea level, a construction site of some 200 m² had to be blasted open, construction work lasting two summers had to be completed and 21 km of telephone wires as well as 5.5 km of lightning conductors had to be laid.

The addition of a 9 m high, 4×4 m wide tower on the western end of the building was of major scientific significance. This housed a meteorological station, which had been pushed for by the German and Austrian Alpine Clubs and was designed by Kommerzienrat (councillor of commerce) *Adolf Wenz*, the ambitious officer responsible for the Wetterstein mountain range (Fig. 9).

Handed over to the state administration as "Royal Bavarian Meteorological High Altitude Station Zugspitze" on 19 July 1900, this meteorological observatory has been a department of the German Meteorological Office ("Deutscher Wetterdienst" (DWD)) since 1952. The first meteorologist stationed on the Zugspitze was *Josef Enzensberger*, who went on to become famous as an Antarctic researcher. He was also the first to spend the winter alone on the mountain (7 months) in 1900/1901.

1.5 Development of the Zugspitze summit for the general public

Parallel to the scientific development, the Zugspitze gradually became a popular destination and center for winter sports activities. This was accompanied by a trans-regional discussion about the limits of tourism development, with the Bavarian and Austrian sides competing for visitors and guests from all over the world, as they are still doing today. Clearly inspired by the successful construction of a railway on the Swiss Jungfrauoch, which was built from 1896 to 1912, reaching an altitude of 3,454 m over sea level, the idea grew also the Zugspitze make accessible to non-experienced mountain hikers. However, the Prinz Regent Luitpold von Bayern rejected a license application for development of a cogwheel railway in 1899, citing a "non-existent transport need".

In the meantime, the Austrian Josef Cathrein, who was living in Munich, developed the concept of a Cable Car starting at the Eibsee and extending up to the summit on the North side of the Zugspitze.

It is interesting to note that it was not until 1962 that this concept was actually implemented as the “Eibsee Cable Car”. And in 2017, the new “Cable Car Zugspitze” was even built in its place (see chapter 06). In 2017 the new “Cable Car Zugspitze” was even built in its place. Cathrein was not going to give up, and soon presented his new proposal for a cogwheel railway on the south side of the Zugspitze, for which he received a permit in 1914. The project failed again, however, in 1925 and in 1927 due to lack of funding.

In 1928 a German consortium was more successful when it filed an application for the construction of a “mixed adhesion and rack railway” which was to run the entire stretch from Garmisch to the summit. After receiving the permit on 18th June 1928 the joint enterprise “Bayerische Zugspitzbahn AG” was founded.

The documents show that in 1924 the General Assembly of the German and Austrian Alpine Association still unanimously rejected such a project (“... *an attack upon the natural serenity of the mountains, ... a sin against nature, ... no public demand*”).

It was therefore a huge surprise that, on 5 July 1926, in a seemingly “clandestine operation” and after a construction period of just 14 months, the “Austrian Zugspitze Cable Car” opened on the Tyrolean side of the mountain. In contrast to the subsequent, technically optimized cable cars, it extended from the small town of Ehrwald (“only”) up to an altitude of just 2,805 m. It ended 160 m beneath the western summit at what was once the “Kammhotel” (“Ridge Hotel”).

Anyone wanting a panoramic view from the summit had to embark on a difficult hike. Secured with a rope, the tourist was led to the summit by a mountain guide. The annals further report that this resulted in a serious feud between the Tyrolean and the Bavarian mountain guides because they fought over the guests and could not agree on uniform rules.

Regarding the history of the Schneefernerhaus, (see chapter 06) it is important to realize that this was the reason for the decision to excavate a pedestrian tunnel from the upper station of the “Austrian Zugspitze Cable Car” (“Zugspitzkamm”) to the Zugspitze plateau (“Zugspitzplatt”) on the Bavarian side. This project was, however, temporarily stopped “half-way” at the so-called Zugspitzeck, due to objections from the Bavarians.

It did not get going again until 1937. This was the year in which the two railway companies merged as a result of shares of the Austrian Zugspitzbahn being sold to the Bavarian Zugspitzbahn AG. And it was the year in which construction of the cogwheel railway – approved in 1928 – was completed on the Bavarian side.

It remained clear that the Schneefernerhaus (among other things) should continue to serve both as a hotel and as the terminus for the (Tyrolean) Cable Car. Therefore, the somewhat outdated pedestrian tunnel was extended 720 meters into the hotel building. (Which, incidentally, also ended the aforementioned mountain guide dispute.) Between the former “Kammhotel” and the “Hotel Schneefernerhaus”, an underground border crossing with panoramic windows was thus created for tourists. Although this tunnel is no longer needed today, it is still an attractive sight for today’s visitors to the UFS research station.

Information about the alpine history in this period can also be found in the literature given below (BZB 2020/01, Hiebeler 1979, Schott 1987, Ritschel 2000).

1.6 The Hotel Schneefernerhaus (1930–1992)

The period around the turn of the year 1929/1930 was a complicated structural interplay for the Zugspitze summit between the construction of the cogwheel railway on the one side and the Schneefernerhaus Hotel on the other.

The hotel building was already the highest hotel in Germany at that time (2,650 m above sea level, about 300 m below the summit). It was envisaged from the outset that it would serve both as the terminus of the cogwheel railway and as the valley station of a separate summit railroad. Construction began in the fall of 1929, was completed on December 24, 1930, and officially opened as a hotel on January 20, 1931.

Because the Cogwheel railway project was to be completed by the time of the Passion Play in Oberammergau in 1930, only two years remained for its realization. Construction began under



Fig. 10: Tunnel course of the planned cogwheel railway in the interior of the Zugspitze



Fig. 11: Wooden shuttering in the tunnel during construction in 1929



Fig. 12: Workers during excavation work on the Zugspitze tunnel for the planned cogwheel railway

great time pressure as early as the fall of 1928 and was inaugurated on July 8, 1930. The technically most difficult part of the work was the construction of the tunnel inside the mountain massif, which has a length of 4,453 m with a height difference of 1,010 m (Fig. 10). A masterpiece of engineering that is still recognized today.

The journals report a particularly severe winter and accidents that unfortunately claimed 10 lives. In order to complete the construction in the planned time despite some interruptions, the tunnel was excavated by up to 2,500 workers simultaneously, at five different openings and also from above and below at the same time (Fig. 11 and 12). In total, 2,500 workers moved 85,000 cubic meters of earth and 160,000 cubic meters of rock. They used almost 200 tonnes of explosives to do so.

The final breakthrough took place on February 8, 1930 and showed a deviation from the planned projections of only 5 cm in width and 8 cm in height. **“Men make meters”** – this was the slogan in the local newspapers and the concept under which the project was successfully completed. The project cost 20 million Reichsmarks. (BZB 2020/01)

However, the hotel was not yet finished when the cogwheel railway, on July 8, 1930, was opened in its turn. Therefore, in 39 days (!) of all haste, an additional wooden building was erected by a specialized Saxon firm (Christoph & Unmack AG, Niesky) as a temporary solution. It could accommodate 400 day guests, but initially offered no overnight accommodations.

It should be noted that after the opening of the “Hotel Schneefernerhaus”, the wooden building was rebuilt to offer simple rooms for tourists, but it was also planned to replace it with a stone building. However, this did not happen. The wooden tourist hostel was severely damaged in an avalanche in 1965 and subsequently demolished (Fig. 10 and 14)

With the opening of the “Hotel Schneefernerhaus” and the connected Cable car, the summit of the Zugspitze was now accessible to tourists (Fig. 14 and 15). Guests came in droves and rode comfortably inside the mountain to the top station of the railroad at an altitude of 2,650 m (Fig. 16), which is still accessible today.

Germany’s highest hotel was originally designed as a luxury hotel, offering guests from all over the world a unique destination with extravagant attractions, including an exposed sun terrace with a unique mountain panorama. It was also a major attraction during the 1936 Winter Olympics, held in the twin town of Garmisch-Partenkirchen, which had merged only a year earlier. It was also a popular destination during the 1975 World Ski Championships (Fig. 15, 16 and 17).



Fig. 13: Hotel poster to attract ski tourists. In the background the “Hotel Schneefernerhaus” with the wooden tourist hostel around 1930/1936

Seized by the Americans at the end of World War II, the Schneefernerhaus was returned to its owners in the early 1950s. The following decades saw an extensive expansion of the ski lift infrastructure, from which the hotel initially benefited after its reopening on December 13, 1952.

In 1950, ski lifts and a small cable car ("alte Hangbahn") provided access to Schneefernerhaus; in 1954, the lift was equipped with modern light-weight cars that shortened the travel time up the mountain, and a new terrace café provided more comfort for day guests, who were able to reach Schneefernerhaus via the new "Eibseebahn" ("Eibsee Cable Car") from 1962. Skiing had now also become a popular sport for day guests.

The hotel then suffered a major setback on May 15, 1965, when the Sun Terrace was hit by a devastating avalanche that claimed ten lives and injured 24 people. As a result, extensive avalanche protection facilities were built. The event led to the introduction of a state avalanche warning service and the formation of local avalanche commissions. Substantial investments were required for avalanche barriers, for the construction of a single-track cable car between Schneefernerhaus and Zugspitzplatt (1978, "new slope cable car"), for further remodeling and expansion work inside the hotel, etc.

A notable event near the Schneefernerhaus was the consecration of the chapel "Mariä Heimsuchung" on the Zugspitzplatt (Fig.18) on October 11, 1981 by Joseph Cardinal Ratzinger, Pope Benedict XVI, who in the meantime was emiritated on February 28, 2013. The chapel is the highest place of worship in Germany. It is dedicated to all mountaineers and also bears a memorial plaque for the victims of the avalanche of 1965.

Regardless of this, winter tourism remained popular in the Zugspitze region, but at the end of the 1980s this necessitated a better infrastructure, in order to get the many skiers and tourists to the Zugspitzplatt more quickly and comfortably without the detour via Schneefernerhaus. As a solution, it was decided in 1985 to build an additional 975-meter tunnel branching off from the existing tunnel tube of the cogwheel railway and leading directly to the Zugspitz plateau. Today, this branch is known as the "Rosi-Tunnel," named after its namesake, local Olympic champion Rosi Mittermaier-Neureuther. It was completed on March 6, 1987.

Since then, the new tourist terminus of the cogwheel railway is the "SonnAlpin": At 2,521 m above sea level, the "SonnAlpin" is both the terminus of the cogwheel railway and the "Gletscherbahn". A restaurant complex is also attached. The "Gletscherbahn" runs between the Zugspitze plateau and the Zugspitze summit and has a transport capacity of 1,000 people per hour since its renovation in 1992.

However, the highlight of the expansion of the tourist infrastructure on the Zugspitze by the „Bayerische Zugspitzbahn Bergbahn AG (BZB)" is the northern connection between the Eibsee valley station and the Zugspitze summit. Here, the old cable car was replaced by a sensational new cable car (from 998 m to 2,944 m above sea level).

This new "Cable Car Zugspitze" offers space for 120 people per cabin and has a travel time of only 10 minutes. It can thus transport 580 people per hour in both directions. The spectacular structure at an altitude of almost 3,000 meters has caused a worldwide sensation not only with its enormous transport capacity, but also with three structural world records.

Built between 2015 and 2017 on Germany's highest mountain, this cable car has two floor-to-ceiling glazed cabins for 120 people each and provides a grandiose panoramic experience with maximum comfort. Visitors to Zugspitze cross the 127-meter steel pylon, the highest for a reversible aerial tramway in the world, they overcome the world's largest total height difference of 1,945 meters in one section and they experience the longest free span in the world at 3,213 meters. (BZB 2019/01)



Fig. 14: "Schneefernerhaus Station" at 2,650 m above sea level inside the hotel (2021).



Fig. 15: Dining room in Hotel Schneefernerhaus around 1936



Fig. 16: Ski tourists during the ascent to the Hotel around 1934



Fig. 17: Sun terrace of the Schneefernerhaus hotel around 1936



Fig. 18: View from the Schneefernerhaus onto the Zugspitzplatt with the chapel “Mariä Heimsuchung” (“Visitation of the Virgin Mary”)

For the Schneefernerhaus Research Station (UFS), the development of traffic in the Zugspitze region has important consequences. Since Schneefernerhaus has had its own cable car (“Research Cable Car”) since 2009 (see chapter 09), the research station can now be reached from the valley via three different routes:

1. “Southern route”: the scientists and visitors travel from Grainau/Eibsee with the regular service of the cogwheel railway through the “Rosi-Tunnel” to the “SonnAlpin” station and from there in a second step with their own “Research Cable Car” to the UFS building.
2. “Northern route”: Scientists and visitors use the scheduled service of the (new) “Cable Car Zugspitze” from the Eibsee station to the summit, then take the “Gletscherbahn” down to the “SonnAlpin” station in a second step, and from there take the UFS’s own “Research Cable Car” to the UFS building.
3. “VIP route”: On special occasions or for guests of honor, the BZB can arrange special trips with the cogwheel railway, which then (as in the past) lead on the originally route directly into the interior of the UFS building and stop at the still preserved platform of the original Schneefernerhaus station (see Fig. 14)

Note: This demand-driven third access is of particular importance for the high alpine research station because it allows large loads and heavy measuring equipment to be transported to the UFS laboratories and UFS measuring terraces regardless of the weather. This unique selling point distinguishes the UFS from other high alpine research stations in Europe.



Fig. 19: Construction site of the new summit station for BZB’s “Seilbahn Zugspitze” (“Cable Car Zugspitze”)



Fig. 20: Cabin of the new “Cable car Zugspitze”, as connection between the “Eibsee Station” and the summit on the north side of the mountain

1.7 From hotel to research station

But how did it come about that the “Hotel Schneefernerhaus” could become a research station at all?

As described in the previous chapter, alpine ski tourism experienced a dramatic upswing, especially in the second half of the 20th century, from which the Zuspitz region also profited considerably. The expansion of ski slopes, cable cars, hotels and restaurants was the result. At the same time, however, the competitive situation throughout the Alps intensified. The best possible comfort was in demand.

Parallel to this, however, the “Hotel Schneefernerhaus” lost more and more of its success with the public, so that in 1990 first the hotel operation and in 1992 also the entire gastronomy was discontinued. In addition – as described – the cogwheel railway access to the Schneefernerhaus was closed for tourism after 62 years. The Bayerische Zugspitzbahn Bergbahn AG, which still owned the building (and still does), immediately raised the question of a sensible and preferably future-proof subsequent use.

At the suggestion of scientists from the “Fraunhofer Institute for Atmospheric Environmental Research” in Garmisch-Partenkirchen (later “IMK-IFU Institute”), the Bavarian Ministry of Economic Affairs and Traffic began converting the hotel building in 1993 so that the first research organizations could rent space there.

According to later considerations, it was considered in different variants to merge the Schneefernerhaus with the IMK-IFU Institute (today’s “KIT-Campus Alpin”) and to link it organizationally to the Karlsruhe Research Center (today’s “Karlsruhe Institute of Technology / KIT”). It would thus have become a member of the Helmholtz Association. However, all such concepts ultimately failed the question of financing and the limited ability of non-governmental research institutions to bear the considerable risks inevitably associated with the operation of an alpine high-altitude research station.

For the Free State of Bavaria and the Federal Republic of Germany, the opportunity arose to realize a concept that had been discussed for a long time: *“The establishment of a center for environmental research and climate observation that is unique in Europe and the world.”* So said the then Bavarian State Minister for Economic Affairs and Traffic at the opening ceremony on May 12th 1999. An initial investment of round 8 million Euros was made. The minister emphasized that despite the proximity to tourist facilities, the size of the building, the year-round accessibility for people and heavy equipment, and the possibility of setting up further test platforms on neighboring peaks represented a unique combination of features. In addition, the Schneefernerhaus as a high-altitude research station closes an important gap in the scientific infrastructure in Germany.

1.8 Organisational structure of the “Virtual Institute UFS”

In order to do justice to the growing importance of a sustainable climate policy, the Bavarian Council of Ministers decided on 08.08.2005 to bundle the competences for climate research and climate policy more strongly. For this purpose, the responsibility for the Schneefernerhaus Environmental Research Station was transferred to the “Bavarian State Ministry for the Environment, Public Health and Consumer Protection (StMUGV, today StMUV)” – the first environmental ministry in the world, founded on December 8, 1970.

After the Bavarian Council of Ministers had decided on 08.08.2005 to bundle the competences and expertise for climate research and climate policy more strongly, the responsibility for the Schneefernerhaus Environmental Research Station was transferred on 07.11.2006 to the “Bavarian State Ministry for the Environment, Public Health and Consumer Protection (StMUGV, today StMUV)”; the world’s first Ministry for the Environment (founded on 08.12.1970).

This mandate included the task of submitting a concept proposal for a comprehensive organizational, scientific and personnel realignment of the station by the end of 2007. In response, the Council of Ministers, in a legendary meeting held in the “*Gletscherstube*” of the Schneefernerhaus on April 24, 2007 (Fig.30), adopted a fundamentally new concept for the future organizational structure, for funding and for a timely scientific strategy of Germany’s highest research station, and at the same time issued the negotiating mandate for its implementation.

The first high-profile event of this reorientation was the signing of a consortium agreement on July 16, 2007, in which initially four renowned research organizations agreed with the Free State of Bavaria on the conditions for cooperating in the long term within the framework of a “**Virtual Institute – Environmental Research Station Schneefernerhaus / Zugspitze UFS**”. Complementing this, in the same year the Council of Ministers decided on a “Climate Program for Bavaria 2020”, which already included concrete infrastructure measures for the UFS.

In § 01 of the UFS Consortium Agreement, the future task of the UFS was defined as follows: “*The purpose of the consortium agreement is to establish a Virtual Institute at the UFS and to develop it into an internationally networked center of excellence for altitude and climate research, focusing in particular on the development, demonstration, and operation of innovative technologies in the context of climate and atmospheric research, satellite data validation, and altitude medical early detection of natural hazards.*”

In addition, the contract contains the necessary specifications for the operation of the station, the conditions for its use, its financing, and information on the rights and obligations of the steering and control bodies.

First signatories of this scientific cooperation were the following world-renowned research organisations (current names of the organisations):

- Deutsches Zentrum für Luft- und Raumfahrt (DLR) / (*German Aerospace Center*), Köln and Oberpfaffenhofen;
- Deutscher Wetterdienst (DWD) / (*German Meteorological Office*), Offenbach, including the Meteorologisches Observatorium Hohenpeißenberg / (*Meteorological Observatory Hohenpeißenberg*); Karlsruher Institut für Technologie (KIT) / (*Karlsruhe Institute for Technology*);
- Deutsches Forschungszentrum für Gesundheit und Umwelt (HMGU) / Helmholtz-Zentrum München / (*Helmholtz Center Munich*);
- Umweltbundesamt Dessau-Roßlau (UBA) / (*Federal Environment Agency*), including Sonnenobservatorium Schauinsland (SBO) / Leibniz-Institut für Sonnenphysik, Freiburg / (*Sun Observatory Schauinsland*);

The initiator of the agreement:

- Freistaat Bayern / (*Free State of Bavaria*), represented by the Bayerisches Staatsministerium für Umwelt und Verbraucherschutz (StMUV) / (*Bavarian State Ministry of the Environment and Consumer Protection*) with its specialised departments, including the Bayerisches Landesamt für Umwelt (LfU) / (*Bavarian Environment Agency, Augsburg*).

Other cooperation partners that joined in the following years were:

- 2007 the Technische Universität München (TUM) / (*Technical University of Munich*),
- 2008 the Ludwig-Maximilians-Universität München (LMU) / (*Ludwig-Maximilian University of Munich*),
- 2009 the Universität Augsburg (UAU) / (*University of Augsburg*) as well as
- 2009 the Max-Planck-Gesellschaft zur Förderung der Wissenschaften (MPG), München / (*Max Planck Society for the Advancement of Science*).

All research partners agreed from the outset that the ambitious goal set out in the consortium agreement could only be achieved on the basis of a performance-oriented partnership and with an effective and efficient organization.

The following objectives were defined as guiding principles for the new concept:

- All research institutions in Germany or in the area of the Alps should be given to get uncomplicated access to the UFS if they need the environmental conditions of the high mountains for their scientific work.
- As far as possible, the organization should pursue a cooperative approach, i. e. interdisciplinary, with different methods and internationally networked.



Fig. 21: Logos of the participating UFS research partners (status: May 2021)

- On the one hand, internal UFS cooperation should be supported in the best possible way, on the other hand, each partner should be able to decide for itself whether and in which form it would like to participate in a UFS project.
- The organisation is to foster on a cooperation approach as far as possible, i. e. interdisciplinary, using different methods and internationally networked.
- On the one hand, UFS-internal cooperation should be given the best possible support, on the other hand, each partner should be allowed to decide whether and in which form it wishes to participate in a UFS project.
- A common data pool should be created that enables rapid exchange of data on the basis of common rules, regardless of location, allows.
- The service staff (staff) should provide neutral support to all UFS members and organize all operations with a minimum of bureaucracy.

The organisation chart given in Fig. 22 was developed on the basis of these guiding principles (compare www.schneefernerhaus.de). It is also in line with the proven administration model for large scientific equipment.

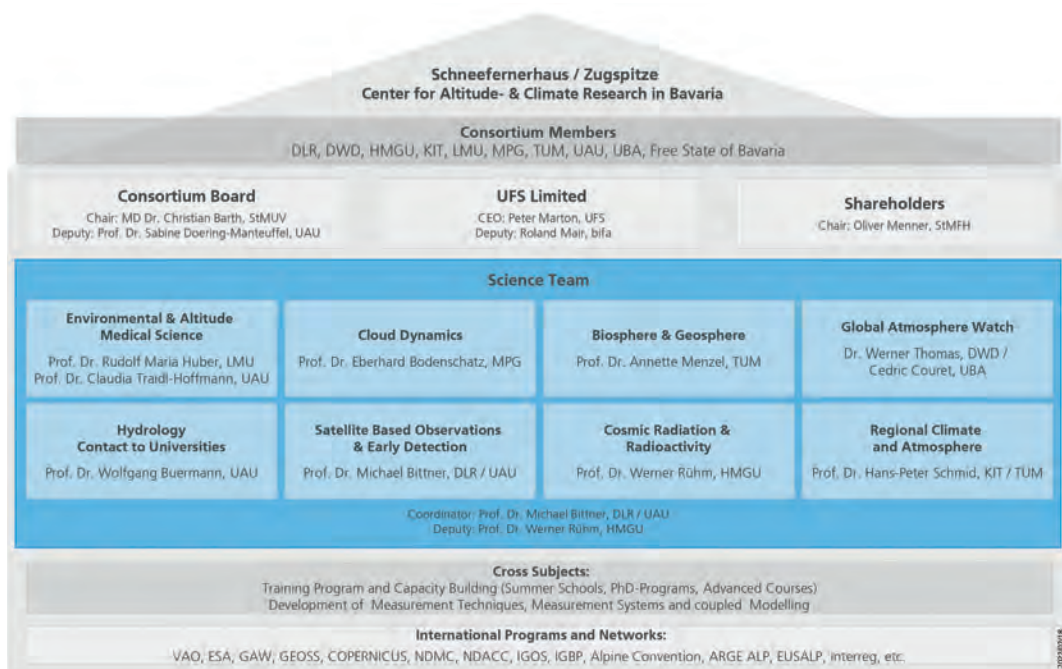


Fig. 22: Organisation chart with UFS-Consortium Board and UFS-Science Team (status: February 2022)

The there in accomplished distribution of tasks has proven its worth:

1. Die UFS is, in legal terms, a so called “internal company”:The operation, infrastructure, visitor service and public relations work of the UFS are warranted through the operating company “**Betriebsgesellschaft UFS GmbH (Operating Company UFS Limited)**”. This company is a neutral service partner for all scientists, visitors and guests alike. Obligations for the operation of the station shall only be undertaken by this operating company. To minimise costs it is (currently) supported by the company “*bifa-Umweltinstitut GmbH, Augsburg*” (*bifa-Environmental Institut Limited*), within the framework of an agency agreement .
2. The “**UFS-Gesellschafterversammlung**” (**UFS shareholders’ assembly**) includes the following members: the Free State of Bavaria (chair), the municipality and county of Garmisch-Partenkirchen as well as the municipality of Grainau. Its key task is the supervision and control of the UFS operating company. The Free State of Bavaria awards the UFS GmbH an annual allowance as institutional support that can be used for basic financial coverage and for infrastructural investments. Irrespective of this, the Free State of Bavaria or third parties may at any time introduce own research projects to the UFS-members or the UFS Operating Company, as required.
3. On the basis of the UFS Consortium Agreement the associated research partners go to the station with their research topics, with their teams and with their funds. Here they hire labs, measurement platforms or offices, as required, and pay a user fee that is primarily charged as a lump sum. This is based on an individual use agreement with the UFS Operating Company. Any exceptional requirements put to the infrastructure or services are charged for separately. In this way, the scientific teams remain associated with the delegating research institutions (thus *Virtual Institute*”).
4. In addition to the UFS shareholders’s assembly there are two other democratically organised supervisory and control committees: the “**UFS-Konsortialrat**” (**UFS-Consortium Board**) and the **Scientists organisation**, the “**UFS Science Team**”:
 On the **Consortium Board** each research partner is represented by a high-level delegate whose voting rights depend on the level of the annual use fees of the respective organisation. Long-term fundamental and strategy decisions are reserved for this body. Particularly important decisions require a 75% majority of the votes. The members of the Consortium Board elect a chairperson (external or internal) for a specific term of office. This chairperson has no voting right.
 The **Science Team** advises the Consortium Board and is the “science brain” of the research station. It is responsible for scientific quality, the smooth cooperation between the research groups, improvement suggestions regarding equipment facilities, the installation of external measurement platforms, joint programme targets, technical sessions and international cooperation. Other responsibilities are the development and supervision of the joint data storage centre (AlpEnDAC) and a joint report that is published every two years giving the scientific results of the Environmental Research Station UFS. The Science Team is made up of elected “speakers” (compare item 5 and Fig. 23) who all have equal voting rights.
 The body is chaired by the “**Scientific Coordinator of the UFS**” (**Wissenschaftlicher Koordinator der UFS**) who is proposed by the Team members and elected for a term of office by the Consortium Board. He/she also attends its meetings as a permanent reporter and advisory member. Meetings of the Science Team are partly held as internal meetings (only the speakers who are entitled to vote, and with the managing director of the operating company as guest) and partly as public meetings (where all scientists can attend). The scientific coordinator has the right to veto resolutions of the Science Team, the issue is then decided on by the Consortium Board.
5. As Fig. 22 shows, the UFS has **eight key topic pillars**, to which the Science Team assigns the research projects or new internal or external suggestions. At the Science Team meetings these projects are then subjected to a joint and interdisciplinary discussion among all scientific persons of the UFS community concerning their acceptance, implementation and results. Beyond this, one or two researcher colleagues are elected as scientific mentors for each of the eight topic blocks, and serve as the respective “**speaker**” both internally and externally. They attend Science Team meetings as coordinating reporter, where they exercise their right to vote. Their coordinating activity represents the respective specialised field and is therefore independent of the partner organisation handling the individual project in question.

1.9 Infrastructure expansion and safety

The extensive realignment of the Schneesfernerhaus Environmental Research Station that commenced in 2007 had to cover both the remaining interior conversion and refurbishment work, as well as the essential safety precautions for researchers, operating personnel and guests. This concerned the workstations, the conference and accommodation facilities as well as the access and transport by an existing but technically obsolete cable car.

Criteria for the required investment were, in addition to safety, the ecological role model expected from governmental institutions, the implementation of an optimal research infrastructure and also the minimiation of operating costs.



Fig. 23: View of the construction site for the integrated rockfall and avalanche protection system for the high-altitude research station UFS (see also Fig. 25)



Fig. 24: Permafrost measuring system, installed in the remaining summit tunnel between the UFS and the former terminus of the "Austrian Zugspitze Cable Car"



Fig. 25: New "Research Cable Car" for access from the Zugspitzplatt to the UFS building with the summit in the background

The extreme and ever-changing environmental conditions at the Schneesfernerhaus frequently ruled out routine construction methods. These conditions accelerate wear, demand technically more sophisticated solutions (rockfall, avalanche protection, heat recovery), make external services more expensive (access transport, helicopters) and, because they are so different to normal conditions, require extended approval procedures. On the other hand, many of the structural refurbishment measures or improvements to the equipment infrastructure were made easier due to the possibility of direct access to the UFS' own railway station by means of the very efficient rack railway. This applied, in particular, in difficult weather conditions or when heavy loads had to be moved.

The following gives an account of some of the refurbishment and investment steps:

- 2007/2016 Preparation of an "Innovative energy and waste/sewage concept" which included the installation of a 100 m² solar panel façade, 110 m³ fire-fighting water storage tanks as a buffer for heat storage, four heat pumps on propane gas basis, each with 20.44 KW capacity. This was supplemented in 2016 with an additional PV system with 4.8 kWh. All cooling systems were converted from CFC to propane gas. In 1996, before any of this took place, a 9.5 km sewage pipe from the Zugspitze summit and an 8 km long high-pressure drinking water pipeline from the Eibsee had already been built under extremely harsh conditions.
- 2007/2016/2020 Preparation of a new safety manual and preparation of a precautionary structural and organizational concept for eliminating the impact of the low-level radon-emissions from the bedrock.
- 2007/2008 Preparation of an avalanche protection concept by the "Swiss Federal Institute for Snow and Avalanche Research" in Davos for both the Schneesfernerhaus and the planned new access "Research Cable Car." 2008 Building authority approval and construction of the entire "Integrated Rockfall and Avalanche Protection System". The safety concept implemented was in response to the three avalanches that occurred in 1965, 2002 and 2008 had become imperative. It was "put to the test" in 2019 and has proven to be very effective.
- 2007 Installation of a long-term permafrost monitoring system in two new boreholes drilled beneath the Zugspitze summit at an altitude of 2.930 m, measuring 44 m and 58 m in length (125 mm diameter), carried out by the Bavarian Environment Agency on behalf of the Bavarian Ministry of the Environment (Fig. 24).
- 2008/2009 Approval for the construction and operation of the new "Research Cable Car" in accordance with Art. 21 BayESG (Bavarian Railway and Cable Car Act), planning permission and commencement of the construction of the lower and upper stations for the new cable car as well as approval for continued use of an access cable car in accordance with Article 33 BayESG for the Bayerische Zugspitzbahn Bergbahn AG (BZB).

2009 Official inauguration and commissioning of the new “Research Cable Car” having the following specifications: 326 m in length, 65 m difference in elevation, cabin size for 8 persons or for EU-Standard pallets, transport capacity of 80 persons per hour (Fig. 25).

- 2009 Certificate of TÜV SÜD Life Service GmbH awarded for exemplary health and safety protection to the UFS Operating Company.
- 2010 Installation of a second, larger laser dome on the UFS roof for an extreme RAMAN-LIDAR for producing profiles of water vapour and temperature in the atmosphere up to 24 km vertically (Fig. 26 and Fig. 27).
- 2011/2012 Energy-efficient refurbishment and provision of a canteen for the operating team and for conference guests (80 m²).
- 2012/2013 Commissioning of an electric snow blower (Specs: 375 kg, two rechargeable batteries, 400 Ah/29.7 V). Specially developed by the Institute of Automotive Technology of the TU Munich, to maintain the existing air quality.
- 2013/2018 Approval for renting the former ski-lift station “Schneefernerkopf” as an external measuring platform (2.875 m above sea level), as well as commencement of the development of an IT link between the Schneefernerkopf and the Schneefernerhaus, with webcam and weather station (Fig. 28 and 29).
- 2013/2015/2017/2020 Refurbishment of the panoramic conference room “Gletscherstube” (56 m²)/(Fig. 30) and conversion and complete refurbishment of the Large Conference Room “Prof. Siegfried Specht” (144 m²/ (Fig. 31).
Completion of the refurbishment of the accommodation facilities, which now comprise 45 beds in 15 rooms.
- 2015/2016 First field tests with drones (UAVs) for air quality measurements within the framework of a feasibility study.
- 2016/2017 Installation of ultrasonic anemometers and high-speed cameras mounted on a stainless steel-sled on the roof of the Schneefernerhaus (2,700 m above sea level).
Experiments performed with this arrangement aim to provide long-term measurements in the turbulent boundary layer and on in-situ observations of passing rain (or ice-containing) clouds.
- 2017/2018 Master thesis on the topic “Development of a CO₂-free energy system as stand-alone solution for a research station”
- 2018 Realization of a new concept for an energy-saving renovation of the entrance and reception hall, as well as the entire lower conference area. In addition, there are initial considerations for setting up a small museum on the history of the Schneefernerhaus.
- 2020/2021 Three projects, among others, are being planned for the near future, although due to the current (2020/21) corona pandemic, precise implementation dates cannot yet be specified:
 - Energetic and safety-related renovation of the access terrace between the UFS-owned “Research Cable Car” mountain station and the interior of the building. This project also requires a separate refurbishment of the surrounding rock walls;
 - Creation of a small external 360-degree measurement site (80 m²) on the “summit ridge” above the UFS Building, at a horizontal distance from the other buildings on the Zugspitze summit of about 300–400 m. In contrast to the measuring station on the measuring station on the Schneefernerkopf (Fig. 29), this facility offers easier access for research personnel.



Fig. 26: Installation of the large laser tower for the RAMAN-LIDAR on the roof platform of the UFS building (2010)



Fig. 27: Water vapour laser “DIAL-LASER” in operation



Fig. 28: View from a UFS measurement platform to the “Schneefernerkopf” with a small measurement hut on top (see also Fig. 29)



Fig. 29: Measurement hut on top of the “Schneefernerkopf” 2.875 m above sea level (see also Fig. 28)

1



Fig. 30: UFS Conference Room "Gletscherstube" with panoramic view



Fig. 31: UFS Large conference Room "Prof. Siegfried Specht"



Fig. 32: View of the UFS building and some measurement devices



Fig. 33: View from the Zugspitzplatt to the UF building with the rockfall and avalanche protection system

- In order to meet the wide-ranging interests of the scientifically diverse research groups, both within and outside the UFS, and to make the recent progress in measurement technology available to them, the construction of an airfield for drones – or "UAVs" ("Unmanned Aerial Vehicle") is being examined. This would be Germany's highest take-off and landing site of this kind.

Even without the expansion plans described above, the Environmental Research Station Schneefernerhaus is already one of the largest and best-equipped high-altitude research stations (Fig. 33). It is a member of the most important supra-regional research organizations in the sectors of weather, climate and the environment. (Bittner et. al. 2017/02)

Together with the Hohenpeißenberg observatory, it also has the status of a global station in the "Global Atmosphere Watch Programme (GAW)" of the "World Meteorological Organisation (WMO)": For this purpose, twice a year, the UFS runs "Global Education and Training Center (GAWTEC)" courses for the next generation of measurement technology professionals worldwide. It is also part of the international NDACC program and cooperates with the "ICSU/WMO World Data Center for Remote Sensing of the Atmosphere (WDC-RSAT)":

Some important characteristics of the existing infrastructure are listed below:

- Year-round access and year-round transportation of heavy loads independent of weather conditions (see chapter 07);
- 11 floors (nine storeys above ground and two storeys in the bedrock);
- 5,000 m² of usable space in total, for example:
 - 480 m² outdoor experiment platforms;
 - 750 m² laboratory and office space;
 - 82 m² new entrance and reception hall with direct access from the conference area;
 - 80 m² canteen for the operating team and conference guests;
 - 144 m² "Large Conference Room Prof. Siegfried Specht" for 80–90 persons;
 - 56 m² panoramic conference room "Gletscherstube" for up to 25 persons;
- Overnight facilities for 45 persons in 15 rooms;
- Special technical facilities, for example:
 - Emission-free concept and environmentally-friendly utility supply and disposal systems;
 - Ultra-pure water and liquid nitrogen available;
 - Electric, battery-powered snow-blower;
- High-speed internet connection to the Munich Scientific Network (operated by the "Leibniz Supercomputing Center (LRZ)," Garching, near Munich).

1.10 The new project "Virtual Alpine Observatory (VAO)" (www.vao.bayern.de)

1.10.1 Background

In 2016, after two years of discussion, an extension of the scientific UFS strategy was adopted, which provides for additional activities to further develop the UFS founding concept in the section "International Cooperation and Networking" (Bittner et. al. 2020/02)

The reason for this request was that since the 1990s at the latest, scientific findings from all areas of high mountain and climate research have been revealing the drastic consequences of global warming in the Alpine region

and signaled very early on that the Alpine ecosystem is one of the most sensitive regions on earth.

This has been evidenced, for example, by glacier mass loss, retreating permafrost, an increase in extreme weather, the shift in elevation of tree lines, longer growing seasons, an increase in geological hazards, and – most strikingly – a temperature increase of +2°C that is almost twice as high as in other regions of Europe.

Both “intrinsic” (i.e., natural) forcings of the climate system and “extrinsic” influences (e.g., solar radiation) are responsible for these threatening changes in all areas of the alpine Earth system. In addition, significant “anthropogenic” forcings, i.e. consequences of human activities, contribute quite substantially.

Issues of this kind are not only of scientific interest. The Alpine region, with its eight neighboring countries and around 14 million inhabitants, forms an important economic area in the heart of Europe. It is therefore necessary to quickly clarify the extent to which the effects of climate change pose a threat to the human habitat and nature. Far-reaching impacts on the economy, transport, human health and irreversible losses in biodiversity are to be expected.

Joint efforts are therefore essential to understand and monitor climate change and its impacts faster than before. On the basis of reliable results for the particularly sensitive Alpine region (or comparable high-mountain regions), forecasts must be made rapidly in order to be able to predict more quickly the effects of global warming on the bio- and geosphere, in particular on biodiversity, on weather systems, on human health, and on the economy and transport.

In alpine climate research, it was therefore recognized early on that research data should increasingly be collected in projects coordinated by the division of labor and according to uniform quality criteria. This would enable a faster cross-border exchange of data and lead to an accelerated gain of knowledge for all. In addition, the Alpine region could thus become a model case for other high mountain regions internationally.

In other words, it was recognized that the scientific monitoring of global warming in the Alpine region requires a transnational and interdisciplinary approach, given the scale and urgency of the task. Consequently, this complex problem was taken up about 10 years ago in a holistically networked project that led to a founding initiative primarily focused on the Alpine region, which began in the UFS. The following is therefore intended to report on it at this point.

1.10.2 On the beginnings of the “VAO” project

In 2012, the Scientific Coordinator of the UFS, Professor Michael Bittner, submitted a possible solution to the UFS-ScienceTeam and the UFS-Consortium Council.

Based on the good experiences with the organizational model “Virtual Institute”, he proposed the foundation of an analogously organized research network, which would initially address the existing Alpine observatories on a cross-border basis. The goal and mission of this “Virtual Alpine Observatory (VAO)” should be to create a voluntary network in the European Alps with the existing observatories, research institutions, data archives and supercomputing centers. Integrated into a networked infrastructure and, if possible, research topics coordinated on a division of labor basis.

Following a UFS-internal preparation phase that was supported by the Free State of Bavaria, the “**V**irtual **A**lpine **O**bservatory (**VAO**)” was officially launched in the Schneefernerhaus on 20th of September 2013 by the Bavarian State Minister of the Environment, Health and Consumer Protection. The founding motto, which is still adhered to today was: “*Scientific cooperation – joining forces instead of duplicating efforts*”. Founding members were, besides the UFS, representatives of the stations “Jungfrauoch & Gornergrad (HFSJG)” / Switzerland, “Sonnblick Observatorium” / Austria and „EURAC-LT(S)ER site Macia/Matsch“ / Italy.

The VAO has, in the meantime, become well established and the number of cooperation partners has expanded significantly. Fig. 34 and Fig. 35 show the list of participating observatories and associated partners (status: May 2021).

List of participating observatories and institutions:

Country:	VAO research stations/institutions	Altitude:
Germany	Environmental Research Station Schneefernerhaus (UFS)	2.650 m
	Schauinsland Observatory	1.284 m
	Hohenpeißenberg Observatory	975 m
France	Observatoire de Haute-Provence	650 m
	Station Alpine Joseph Fourier, Lautaret-Pass	2.058 m
	Vallot Observatory, Mont Blanc	4.362 m
Italy	Sentinel Alpine Observatory, Ritten	2.260 m
	Eurac-LT(S)ER site Macia/Matsch	2.700 m
Austria	Sonnblick Observatory	3.106 m
Switzerland	High Altitude Research Station Jungfrauoch (HFSJG)	3.580 m
	High Altitude Research Station Gornergrat (HFSJG)	3.135 m
Slovenia	Otlica Observatory	945 m
Supporting research infrastructures:		
Germany	Leibniz Supercomputing Centre (LRZ), Garching	
	World Data Centre for Remote Sensing of the Atmosphere (WDC-RSAT), Oberpfaffenhofen	
France	Observatoire des Sciences de l'Univers de Grenoble (OSUG)	
Italy	European Academy of Bolzano (EURAC Research)	
Country:	Associated VAO-Partners	Altitude:
Georgia	Abastumani Astrophysical Observatory	1.700 m
Norway	Alomar Observatory	380 m
Bulgaria	BEO Moussala	2.925 m
Supporting research infrastructures:		
Czech	Institute of Atmospheric Physics, Prague	
Observer		
	European Space Agency (ESA) Alpine Convention	

Fig. 34: Participating observatories and institutions of the VAO (status: May 2021)

In addition to the research institutions, the countries bordering the Alps have also supported the VAO project within the framework of the “European Alpine Convention” (European Convention on the Protection of the Alps of 1995) and the “EU Alpine Strategy” (“EUSALP”). In the provisional minutes of the decision of the 58th meeting of the Standing Committee of the Alpine Conference, Bolzano, 12–13 March 2015, it says in this regard under item B4a (freely translated):

“The Standing Committee ...

1. ... ,

2. notes that, against the background of progressive climate change and in view of and in accordance with the “Action Plan on Climate Change in the Alps”; increased cooperation between the Contracting Parties in the field of climate observation is necessary,

3. supports the intention of the High-Altitude Research Stations of Germany, France, Italy, Switzerland and Slovenia to deepen the already initiated cooperation for a Virtual Alpine Observatory and welcomes the intention to develop it into a center of climate and environmental research in the Alps,

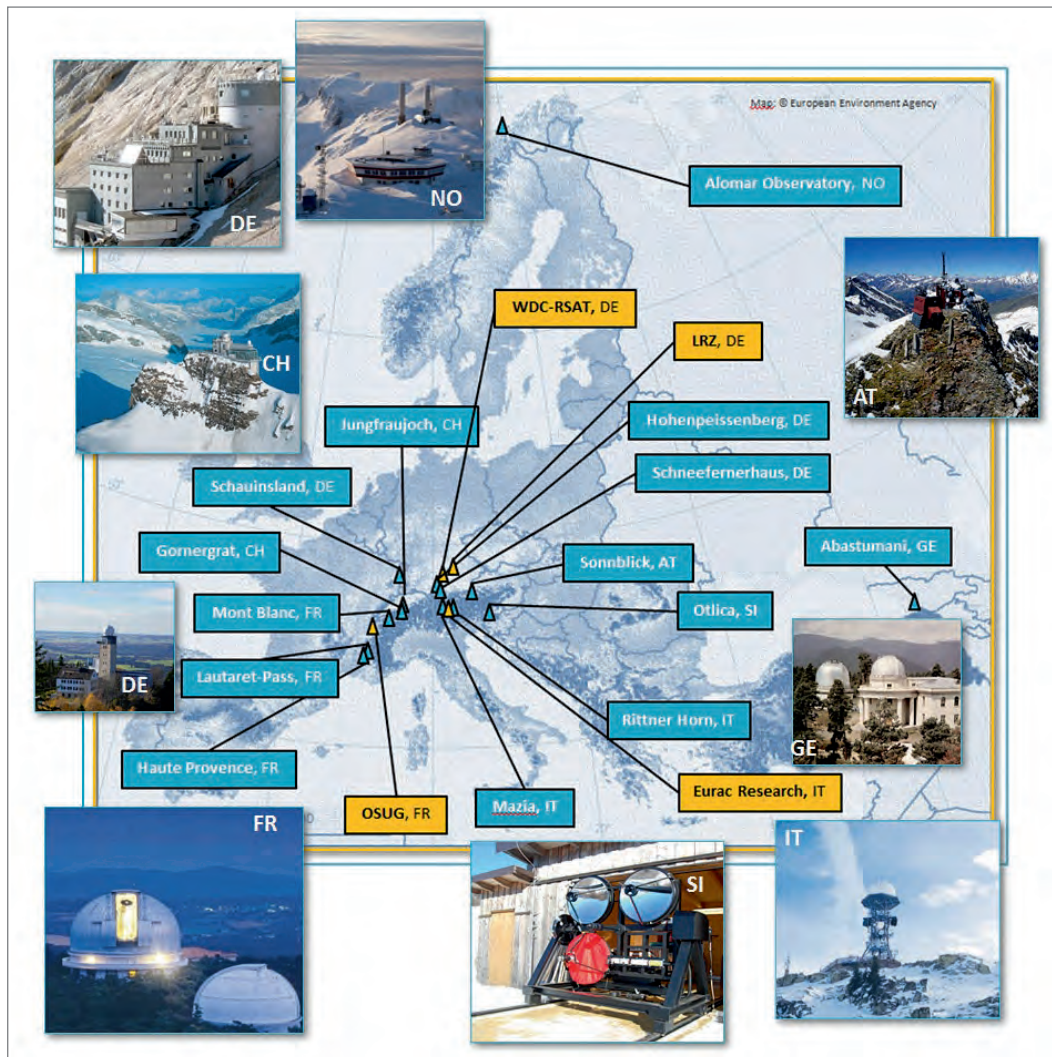


Fig. 35: Cartographic assignment of the VAO partners

4. invites the Contracting States within the scope of their possibilities to ensure that future collaborations between the partners of the Virtual Alpine Observatory are supported by EU funding programs, in particular "HORIZON 2020";
5. invites the Permanent Secretariat, in cooperation with the observatories participating in the Virtual Alpine Observatory, to identify possible interfaces with the Alpine Observation and Information System, thereby contributing to the governance of the Virtual Alpine Observatory and to the dissemination of relevant scientific knowledge gained in the Virtual Alpine Observatory,
6. invites the Contracting Parties to consider the possibility of integrating the Virtual Alpine Observatory into their national climate policies and taking into account its research results in the further development of EU climate and energy policies, ..."

1.10.3 About the "VAO" project itself

With the establishment of the "Virtual Alpine Observatory", some further essential goals were achieved (VAO 2020):

- VAO serves to give coherence – where appropriate – to the various research efforts and programs undertaken by the VAO partner organizations or within their infrastructures to try to maximize the scientific benefits. As an example, VAO gives the scientific community the flexibility to conduct highly specialized field measurements in very diverse scientific areas, through coordinated simultaneous campaigns at different sites, and also promotes an interdisciplinary approach, in order to more effectively address specific scientific questions.

- VAO further supports such activities by granting access to additional resources (additional data and information, computing power, numerical models, analysis tools etc.). Consequently, VAO helps to improve the understanding of the environment of the environment and thus contributes to the development of a consolidated basic knowledge. This can also help the (political) decision-makers to sustainably (political) decision-makers to balance economic, social and environmental interests in a sustainable way (see Fig. 37). In fact, the VAO is already part of the “European Alpine Convention” and the EU’s Alpine Strategy (see above).
- VAO brings together existing infrastructures (observatories, data centers, and high-performance computing centers), scientists, engineers, medical experts and technicians from various disciplines and facilities (universities, major research institutions and public authorities). This creates a synergy – a synergy from which results and new results can be achieved at ever shorter intervals and with comparatively little and with comparatively little effort, and new results can be achieved in ever time intervals and with comparatively fewer resources. “It is obvious, networking these capacities a higher result than just the sum of the individual parts”
- The cross-link to well-established WMO/ICSU World Data Centers and other data repositories (e.g., other data archives, the COPERNICUS Atmospheric Service CAMS) provides the scientific communities with a standardized (based on state-of-the-art Information Technology) access to additional data, information and services, for example, from satellite-based measurements (e.g. EU-COPERNICUS, other ESA-satellites) or from other ground-based observational networks (e.g. Long-Term Ecosystem Research network (LTER)). The cross-link to supercomputing centers not only facilitates the use of complex numerical models and advanced data analysis tools by the scientific communities, but also allows optimization of computational applications (e.g. parallelization of numerical codes, improved use of big data concepts through support from IT experts).
Scientists are thus empowered to improve the assessment of their own results and thereby enhance their scientific knowledge and turn this new knowledge into innovative services tailored to users’ needs (for example: new concepts for near real time (NRT) satellite validation in order to improve NRT-services such as improved forecasting of mesoscale phenomena, or the implementation of tailored health services for individual persons, etc.).
As a result, this concept strengthens the long term international competitiveness of European research and development.
- Where appropriate, cooperation with European industrial sectors could be advantageous for both parties, for example, with regard to technology development (e.g., improving the performance of instrumentation or adapting technologies to other fields of application). It is equally conceivable that parties may cooperate in the development of services tailored to users’ needs (so-called ‘downstream services’, such as the provision of information products).

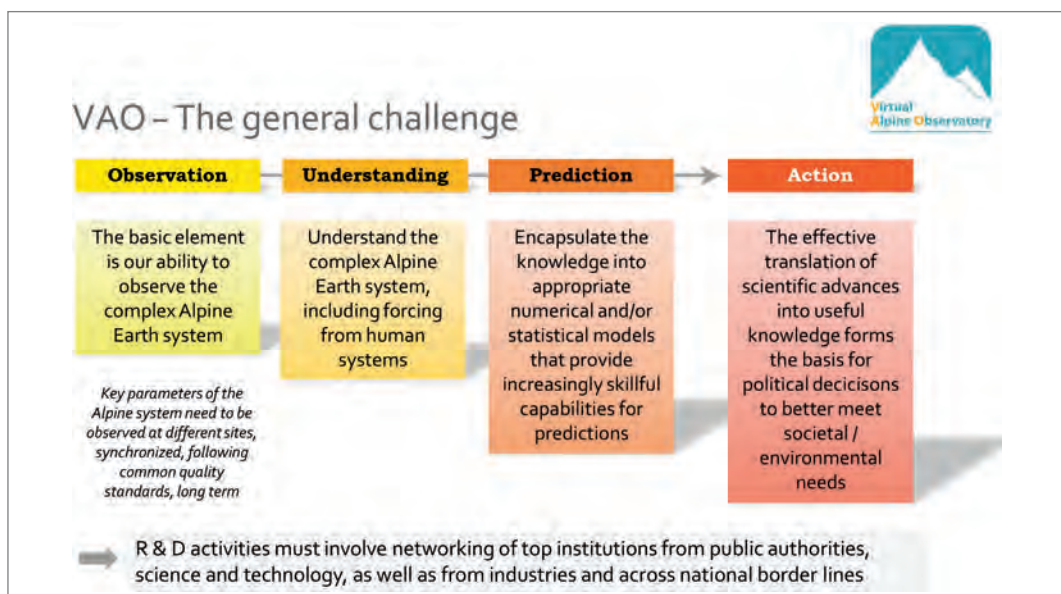


Fig. 36: VAO’s vision from data to understanding to action (Bittner 2020/01)

From what has been said above, it follows that the vision of the VAO can be characterized in at least five dimensions (Bittner 2020/01):

- (1) setting new standards in terms of the common development of new instrumentation ("**open hardware**"), often in cooperation with industry;
- (2) providing information products and data analysis tools tailored to the scientists' needs ("**computing-on-demand**");
- (3) scheduling measurement procedures harmonized between various measurement sites and customized to a specific application ("**operating-on-demand**");
- (4) archiving and delivering data (and meta-data), as well as value-added information, adjusted to specific requirements ("**data-on-demand**"), and
- (5) delivering services addressing especially – but not exclusively – public needs ("**service-on-demand**").

The VAO is already established and is becoming more and more visible and attractive. During the first VAO-Board Meeting, held in 2016 at the Bavarian State Ministry for the Environment and Consumer Protection in Munich, it became clear that a strategy was required for the upcoming decade, which will assist the further development of the VAO in a target-oriented way. The following VAO mission statement is based on broad discussions within the scientific communities and reads:

*"The overarching objective of the VAO is to bring together already existing infrastructures (observatories, data centers, and high-performance computing centers), scientists, engineers, medical experts and technicians from various disciplines and facilities (universities, large research institutes, and public authorities) to perform environment, climate and climate change research in the Alps. Cross-linking all these capacities therefore means a lot more than just the sum of it. The motto is and remains: "**Joining forces instead of duplicating efforts**".*

The consequence of this means that the future development of the VAO is to be pursued in two ways:

- (1) Deepened definition of the scientific core topics to be worked on jointly as VAO in the future scientific core topics (research strategy "VAO-II");
- (2) Strengthening the scientific competitiveness of the VAO research association by VAO through further development of its organizational structure ("VAO-III").

1.10.4 Core scientific topics

The implementation of the VAO strategy rests on four pillars (Bittner 2020/01):

- Pillar I: advancing the research infrastructures in the Alps, especially at high altitudes;
- Pillar II: enhancing the scientific and technological portfolio;
- Pillar III: advancing the services, and
- Pillar IV: strengthening public outreach.

VAO-internal discussion on the specification of these jointly-decided pillars resulted in a prioritization of the following research areas:

- Atmospheric and climatic variability;
- Climate impact on the Alpine environment, hazards and risks;
- Alpine water cycle; and
- Environment and human health.

The overarching scientific challenges that the VAO will address in the next years are part of the research fields, put together in Fig. 37.

1.10.5 Further organizational development:

- The research association VAO is currently striving to transform the VAO Network into a legally binding structure. The goal is the foundation of a "European Association for Territorial cooperation (EGTC)".

This organizational transformation should strengthen the alpine research of the high alpine research stations of the Alps and to make them scientifically more effective by coordinating and bundling their potentials in calls for proposals.

Scientific challenges: The overarching scientific challenges the VAO will address to in the upcoming decade are part of the following research fields:

<i>Challenge 1</i>	Understanding the coupling mechanisms among atmosphere, clouds and land surface and their changes in view of impact on the greenhouse effect
<i>Challenge 2</i>	Understanding the impact of the Alps (mountains) on atmospheric dynamics in the middle atmosphere (10–100 km height)
<i>Challenge 3</i>	Understanding if there is an impact of climate change on the characteristics of cosmic radiation in the atmosphere
<i>Challenge 4</i>	Monitoring and understanding of the contamination of the Alps
<i>Challenge 5</i>	Impact of meteorological extremes in the Alps and surrounding regions on natural hazards
I) Climate impact on Alpine environment, hazards and risks	
<i>Challenge 6</i>	Understanding the dynamics of the Alpine vegetation in response to climate (change)
<i>Challenge 7</i>	Interrelation of the environment with seismic activity
II) Alpine water cycle	
<i>Challenge 8</i>	Understanding the Alps as a water tower for the pre-Alpine regions under climate change conditions
III) Environment and human health	
<i>Challenge 9</i>	Understanding the impact of pollutants, radiation and meteorological stress on human health
IV) Improving the Infrastructure	
<i>Challenge 10</i>	Improving the validation of satellite-based measurements through in-situ and remote sensing measurements
<i>Challenge 11</i>	Establish a powerful IT-linkage between all observatories, high-performance computing centres and data repositories (e. g. further develop AlpEnDAC)

Fig. 37: Future research fields of the VAO-cooperation

- In a first step, the high alpine research stations in Germany (Environmental Research Station Schneesfernerhaus / UFS), Austria (Sonnblick Observatory / SBO) and Switzerland (High altitude research stations Jungfrauoch and Gornergrat / HFSJG) will join forces to form an “EGTC-VAO”
- With its foundation, this “EGTC-VAO” shall start a first research project. Its central research goal is the investigation of coupling processes in the different areas of the alpine climate system. Processes in different parts of the alpine climate system. The expected findings may contribute significantly to the optimization of climate simulations and show the effects on specific ecosystems and cycles.
- Within the VAO network, specialists from the fields of geosphere, biosphere, hydrosphere, cryosphere and atmosphere are working interdisciplinarily on important questions of the alpine earth system. With this professional diversity, the VAO stations already cover an research from the solid body of the earth to the edge of space. In this respect, the research activities at the above-mentioned observatories are unique in the entire Alpine region.

Epilogue

Climate change currently poses the greatest threat to life on our planet. Consistent and targeted action by policymakers is therefore imperative.

For political measures to be credible and democratically legitimate in the long term, it is essential that they are based on the current state of research. There is no room for “alternative facts.”

Scientific data must meet the recognized, subject-specific criteria without restriction, so that they are not communicated in an interest-driven manner.

Scientific knowledge is an essential prerequisite for respectful and successful treatment of the creation entrusted to us. Since its foundation, the “Virtual Institute – Environmental Research Station Schneesfernerhaus (UFS)/Zugspitze” has placed itself unreservedly at the service of this challenge.

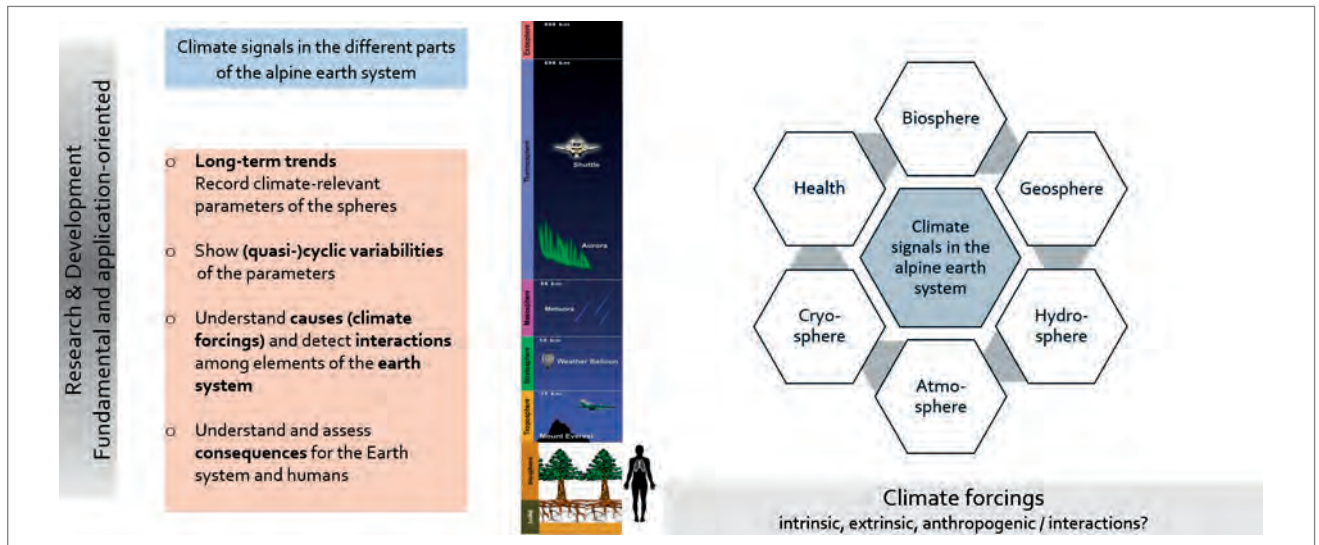


Fig. 38: The basic concept of the VAO-III-project (Bittner et. al. 2020/02)

This is evidenced by the cross-border climate research currently being carried out in the Alpine region at its suggestion under the title “Virtual Alpine Observatory (VAO)”. It is unique in its kind.

Acknowledgements

In this summarizing presentation of the development of the science location Zugspitze, many persons and institutions have supported me greatly in their proven willingness to cooperate. Be it through the provision of photos and diagrams, be it in the form of personal discussions or through important organizational assistance.

My very special thanks go to Prof. Dr. Michael Bittner, the scientific coordinator of the UFS, his colleagues Karla Wagner and Dr. Lisa Küchelbacher, as well as the former or current members of the UFS operating team, Dr. Christian Mikulla, Dr. Simone von Loewenstern, Markus Neumann (as well as his wife Fiona Neumann), Peter Marton, Roland Mair (bifa GmbH Augsburg), Dr. Till Rehm, Dr. Inga Beck and Hannes Hiergeist, who all always had “an open ear” for me.

Also important to me was the scientific advice from the Bavarian Academy of Sciences and Humanities on the subject of Geodesy and Glaciology. First and foremost the advice and the text contribution of Dr. Christoph Mayer as well as the publications of his colleagues Dr. Markus Weber and Dr. Ludwig Braun.

Indispensable and beyond that for the success of the entire present book project was also the competent, goal-oriented management and support on the part of the Bavarian State Ministry of the Environment and Consumer Protection, represented in the project by Dr. Martin Frede, Dr. Gerhard Drechsler, Dr. Helmut Theiler and Birgit Einhellinger.

Current and historical text and image material on the above chapter topic was also kindly provided by: Former UFS Managing Director and photographer Markus Neumann, the Austrian and German Alpine Associations, the Stiftung Deutsches Technik Museum Berlin, the Deutsches Museum Munich, and the Dr. Paul Wolff & Tritschler Bildarchiv in Offenburg. The contribution of the Bayerische Zugspitzbahn Bergbahn AG, Garmisch-Partenkirchen through Matthias Stauch and Verena Altenhofen was also particularly effective.

It is important for me to thank them all once again!



Fig. 39: “1999 a national opportunity – 2021 an international success”

References

- (Handelsblatt 2022/01): „... Welche Staaten bis wann klimaneutral werden wollen“ vom 18.02.2022;
- (Bayern 2021) „Klimaschutz in Bayern“ / Regierungserklärung Ministerpräsident Marcus Söder vom 21. Juli 2021“; Bayerisches Landesportal (www.bayern.de);
- (StMUV 2021): „Klimareport 2021“, Bayerisches Staatsministerium für Umwelt und Verbraucherschutz (StMUV), München, vom 24.02.2021);
- (Franz 2021): Nicole Franz „MDR-Klima-Update“ vom 26. November 2021 („www.mdr.de“);
- (Quaschnig 2021): Volker Quaschnig (Scientistes for Futur) „(Die) Ampel plant beim Klimaschutz zu wenig“; Resümee des SWR 2-Interviews am 22.10.2021 zu der hauseigenen HTW-Studie zur Klimaneutralität;
- (idw 2021): idw-Nachrichten vom 30.11.2021: „Studie der HTW Berlin: 1,5-Grad-Pfad mit Koalitionszielen für Solar und Wind nicht erreichbar“;
- (SVR 2019): Klimapolitik-Sondergutachten des Sachverständigenrates der Bundesregierung Deutschland von 2019;
- (BVerfG 2021/01): Entscheidung des Bundesverfassungsgerichts in Karlsruhe vom 29.04.2021 zur Verfassungsbeschwerde gegen das Bundes-Klimaschutzgesetz von 2019; / Pressemitteilung Nr. 31 / 2021 vom 29. April 2021;
- (BVerfG 2022/02): Verfassungsbeschwerde vom 26.01.2022 der DUH und neun Jugendlichen gegen die Novelle des Bundes-Klimaschutzgesetzes vom 31.08.2021;
- (SZ 2022/01): „Gerichtsurteil: SHELL muss das Klima schützen“; Süddeutsche Zeitung vom 26.05.2021;
- (Handelsblatt 2022/02): SIEMENS-Vorständin Maria Ferraro: „Die EU kann ihre Klimaziele nicht ohne grüne Gaskraftwerke erreichen“ Handelsblatt vom 18.02.2022;
- (SZ 2022/02): Thomas Kirchner: „Vive l'Atomkraft“; Süddeutsche Zeitung vom 10.02.2022;
- (Brundtland 1987): „Our Common Future“; Report of the “World Commission on Environment and Development (WCED) vom 20.03.1987 (“Brundtland-Report”);
- (Stoll 2022) Michael Stoll, REMEX GmbH, „Drei-Säulen-Modell der Nachhaltigkeit“ (www.michael-stoll.info/glossar-3-saeulen-modell);
- (Queally 2021): Jon Queally, Managing Editor, published at March 22, 2021, “Common Dreams.org”;
- (Mayer et. al. 2021): Christoph Mayer, Markus Weber, Anja Wendt und Wilfried Hagg, „Die bayerischen Gletscher, die verbliebenen Eisreserven Deutschlands“; Polarforschung, 91, 1-7, 2021;
- (Mayer 2021/02): Persönliche Zuarbeit von Dr. Christian Mayer, „Erdmessung und Glaziologie der Bayerische Akademie der Wissenschaften (BAW), München vom 7.06.2021;
- (Weber, Braun 2018): Markus Weber, Ludwig Braun „Die Gründe für den beschleunigten Gletscherschwund ab der Mitte des 19. Jhs. Bis zur Gegenwart“; Jahrbuch des Vereins zum Schutz der Bergwelt 2018 (München), S. 165 ff.
- (Marowsky 2010): K. Marowsky „Die Validierung des Gletschermodells SURGES am Beispiel von Vernagtgletscher sowie Nördlichem und Südlichem Schneeferner“, Diplomarbeit, Kath. Univ. Erlangen-Ingolstadt, 2010;
- (BAW 2021) Bayerische Akademie der Wissenschaften (BAW) und Bayerisches Staatsministerium für Umwelt und Verbraucherschutz (StMUV): „Zukunft ohne Eis“ – Zweiter Bayerischer Gletscherbericht vom 29.04.2021, Seite 45;
- (Hiebler 1979): Toni Hiebler „Zugspitze – Von der Erstbesteigung bis heute“, Mosaikverlag GmbH, München, 1979;
- (Schott 1987): Heinrich Schott „Die Zugspitze – Gipfel der Technik, Triumphe und Tragödien“, Süddeutscher Verlag GmbH, München, 1987;
- (Ritschel 2000): Bernd Ritschel, Tom Dauer, „Die Zugspitze-Menschen, Massen, Mythen“, Bruckmann Verlag GmbH, München, 2000;
- (BZB 2020/01): BAYERISCHE ZUGSPITZBAHN Bergbahn AG, Ausstellungsbooklet „90 Jahre Zahnradbahn“ vom 8. Juli 2020;
- (BZB 2019/01): BAYERISCHE ZUGSPITZBAHN Bergbahn AG, Zusammenstellung der Technischen Daten seiner Seil- und Bergbahnen in der Broschüre „Daten & Technik“ (Januar 2019);
- (Bittner 2017/02): Prof. Dr. Michael Bittner (Ed.) „UFS-Wissenschaftliche Resultate: 2009 / 2010–2011 / 2012–2013 / 2014–2015 / 2016 / 2017 / 2019 / 2020 / www.schneefernerhaus.de/downloads/zweijaehrige-wissenschaftliche-resultate.html;
- (Bittner 2020/01): Michael Bittner, et. al.: „Zukunftsplanung auf der Grundlage des UFS-Perspektivpapiers“, Internes UFS-Strategiepapier, Garmisch-Partenkirchen vom 31. Juli 2016 und „Strategy Virtual Alpine Observatory“, VAO-Paper at 2017 19th June;
- (VAO 2020): „VAO-Fact-Sheet“ (2020, contact: Birgit Einhellinger (info@vao.bayern.de));
- (Bittner et. al. 2020/02): Markus Leuenberger, Michael Bittner, Elke Ludewig, „Konzeptvorschlag: VAO-III: Beobachtung und Verständnis der komplexen Klimaantriebe und deren Auswirkungen auf das alpine Erdsystem vom Boden bis an den Rand zum Weltraum“ vom 28. April 2020.

2 Studies on patients with atopic diseases at the Environmental Research Station Schneefernerhaus (UFS)¹

Eberlein B.^{2,3}, Huss-Marp J.³, Pfab F.³, Fischer R.⁴, Franz R.², Schmitt M.², Leibl M.², Allertseder V.², Gloning J.², Kriegisch M.³, Hennico R.³, Latotski J.³, Ebner von Eschenbach C.³, Darsow U.², Behrendt H.³, Huber R.⁴, Ring J.²

Correspondence:

Prof. Dr. Bernadette Eberlein

Klinik und Poliklinik für Dermatologie und Allergologie am Biederstein, Technische Universität München, Biedersteiner Str. 29; D-80802 München, Germany

Tel. +49-89-4140-3191; Fax +49-89-4140-3145

E-mail: bernadette.eberlein@tum.de

Abstract

Mountain climate therapy takes advantage of specific climatic conditions to treat chronic allergic diseases. The aim of the study was to investigate effects of a 5-day observation period on atopic diseases at the Environmental Research Station Schneefernerhaus (UFS; Umweltforschungsstation).

18 patients with grass pollen-induced rhinoconjunctivitis, atopic eczema or asthma and 11 non-allergic controls were included in this study. Skin physiology parameters, changes of the respiratory and nasal functions, subjective symptoms and blood parameters were measured during a 5-day observation period in the Environmental Research Station Schneefernerhaus at the moderate altitude mountain region (Zugspitze; 2650 m alt.) compared to a low altitude area (Munich; 519 m alt.).

Histamine induced itch decreased significantly. Several of the skin physiology parameters changed significantly during the observation period (decrease of skin hydration, increase of skin smoothness, skin roughness, skin scaliness and pH-value). In patients with atopic eczema, the SCORAD (Severity Scoring of Atopic Dermatitis) and the scores of the DELH (Deutsches Instrument zur Erfassung der Lebensqualität bei Hauterkrankungen) did not change significantly. Parameters of nasal function (rhinomanometry, eosinophil cationic protein (ECP) in nasal secretions) did not change significantly. The vital capacity (VC) decreased significantly, several other parameters of lung function (FEV1/VC, PEF, MEF 50, MMFEF 25/75) showed a slight, but statistically significant improvement. ECP (eosinophil cationic protein) and IL-33 in the serum and parameters of blood count changed significantly.

In dependence on the atopic disease the benefit of a moderate altitude mountain climate sojourn over a period of 5 days differed – especially itching of the skin and asthma parameters improved. Assessing the parameters during a longer observation periods in alpine climate would be useful.

The methodology used can serve as a suitable template for qualified studies on the effect of climate therapy.

Key words: mountain climate therapy, atopic diseases, atopic eczema, asthma, rhinoconjunctivitis allergica, skin physiology parameters, rhinomanometry, parameters of lung function, Umweltforschungsstation Schneefernerhaus, Zugspitze

¹ This study was published as Brief Communication: Eberlein, B. et al. Influence of alpine mountain climate of Bavaria on patients with atopic diseases: studies at the Environmental Research Station Schneefernerhaus (UFS – Zugspitze) – a pilot study. *Clinical and Translational Allergy* 2014; 4: 17

² Department of Dermatology and Allergy Biederstein, Technical University Munich, Germany

³ Center of Allergy and Environment (ZAUM, Zentrum Allergie und Umwelt), Technische Universität München and Helmholtz Center Munich

⁴ Medizinische Klinik Innenstadt, Fachbereich Pneumologie, Ludwig-Maximilians-Universität München

2.1 Introduction

Allergies have increased in most countries of the world in recent decades. Prevalence rates of 20 to 30% of the total population are estimated today. Particularly common allergic diseases are allergic rhinoconjunctivitis (if seasonally occurring “hay fever”; allergic asthma bronchiale, atopic eczema (atopic dermatitis, anaphylaxis (maximum variant of an acute allergic reaction with life-threatening character, allergic contact dermatitis (one of the most common occupational diseases) and the manifold spectrum of food and drug intolerance reactions.

Allergies are typical environmental diseases; they are based on genetic susceptibility via a misdirected reaction of the effector organ immune system against natural and anthropogenic substances from the environment. Air pollutants and allergens can influence each other in many ways (1, 2).

Climate therapy comprises the use of certain climatic conditions in the treatment of chronic diseases. In allergy, maritime and moderate altitude mountain zones are of interest. Mountain climatotherapy can be performed in moderate altitude (relative height of > 2000 m) and low altitude (> 500–2000 m alt.) (3).

Increasing altitude implies climatic changes in the following factors: air pressure, oxygen partial pressure, temperature, water vapour pressure, UV radiation, global radiation and reduction of allergens such as house dust mite. Some of these factors are considered as “stimulating”; the relative purity of the air and low allergen content as protective factors (4).

From the experience of special rehabilitation clinics in the moderate high mountains, especially in Davos, Switzerland, we know since decades that the mountain climate exerts a favorable influence on numerous inflammatory diseases of the skin and respiratory system. Especially the climatic situation in moderate high mountains (5) has been proven in many studies to be particularly effective in the treatment of allergic respiratory and skin diseases, with most long-term studies in Davos (6,7). From patients with atopic eczema (AE) treated in the German Hospital for Dermatology and Allergy Davos (Switzerland) some 94% returned either completely free or with considerably improved symptoms (4). Also in patients with asthma mountain climate therapy is a well-established therapeutic option (5).

The effects of mountain climate include normalization of misguided immune responses (T cell responses, IgE levels, changes in cutaneous reactivity, histamine and allergen pricktest thresholds), influences on vegetative parameters such as sweating, and beneficial effects on the subjective symptom itching. The nature of these effects, especially with regards to the only more recently elucidated pathophysiological reactions of the allergic inflammatory cascade, is investigated only to a limited extent. Increased cortisol and catecholamine levels as well as modulation of lymphocyte regulatory functions might be mechanisms explaining the effects of climate therapy in these disorders (8, 9).

Many patients – especially those with severe forms of the above-mentioned diseases – cannot be subjected to allergological testing in the lowlands under the conditions of daily life at all. This is due to the fact that either the skin organ or the respiratory tract constantly show symptoms and must be treated, which prevents the patient from testing, or strong symptoms occur immediately when the medication is discontinued, which makes testing impossible. For such patients, moderate high mountain conditions are particularly valuable for providing them with a further treatment strategy. Compared to Davos (1.600 m) the altitude in Bavaria with Oberjoch (approx. 1200 m) and Berchtesgaden-Buchenhöhe (approx. 900 m) are still relatively low. With a height of 2650 m, the UFS offers a location comparable to that of the Jungfrauojoch in Europe.

It was the aim of this study to follow objective and subjective parameters in patients suffering from rhinoconjunctivitis and/or atopic eczema, asthma over a 5 days observation period in the Environmental Research Station Schneefernerhaus (UFS) at the Zugspitze (2650 m alt.) in the alpine mountain climate of Bavaria compared to lowland in Munich (518 m alt.). Clinical symptoms, skin and lung parameters, blood parameters and self-assessed health status were analyzed.

2.2 Materials and methods

2.2.1 Study Design

Five-day observation periods at the Environmental Research Station Schneesfernerhaus (UFS) were performed with groups up to 10 patients and/or controls in July/August 2008, March 2009 and July 2009. Skin physiology parameters, changes of the respiratory and nasal functions, subjective symptoms and blood parameters were measured 3 to 4 days in Munich before the sojourn at the UFS (t1), at the first and second day (t2) and at the fourth and fifth (t3) day during the sojourn at the UFS as well as about 4 weeks later in Munich (t4). All participants reached the UFS by railway within four hours. All study procedures were conducted according to the Declaration of Helsinki. The local Ethical Committee approved the study. Patients had given informed consent.

2.2.2 Patients

18 patients (6 males, 12 females; mean age: 30 years, range: 24–43 years) with grass-pollen induced rhinoconjunctivitis, atopic eczema or asthma and 11 non-allergic controls (4 males, 7 females; mean age: 26 years, range 18–32 years) were included in the study. Characteristics of patients are shown in Tab. 1.

2.2.3 Diagnostic criteria

Atopic eczema was diagnosed according to the criteria of Hanifin and Rajka, the UK working party and Ring et al. (10,11,12). Asthma in adults was diagnosed according to Global Strategy for Asthma Management and Prevention (13).

2.2.4 Blood tests

A maximum of 20 ml per blood sampling time (maximum 3 time points) was required. The total IgE, a spectrum of specific IgE antibodies (main focus on inhaled allergens), a complete blood count and parameters of inflammation of the skin and respiratory tract (eosinophilic cationic protein ECP and soluble receptors) were determined.

2.2.5 Measurements

2.2.5.1 Dermatological examination

The examination of the skin was carried out in a standardised manner by trained physicians. The focus of the study was set on the qualitative and quantitative description of atopic eczema. The severity of the atopic eczema was determined by the SCORAD (scoring index for atopic dermatitis). This is a standardised survey tool developed for this purpose, which records the parameters of extent, intensity (divided into the criteria erythema, edema/papules, wetness/crusts, excoriations, lichenification, dryness) and subjective symptoms (daytime pruritus and sleep loss). (14)

2.2.5.2 Skin prick test

The skin prick test was performed on the volar sides of the forearms. Commercial extracts of grass pollen allergens in various dilutions as well as saline and histamine solutions were used as controls. The reactions were evaluated after 15 minutes and categorized according to the diameter of the wheal and flare reaction. A wheal diameter of ≥ 3 mm was defined as positive. Tests in which the negative control was positive or in which there was no positive reaction (including positive control) were excluded from the final evaluation.

Itch intensity after prick testing of histamine was rated on a computerized visual analogue scale (VAS) ranging from 1 to 100, where 0 was defined as 'no itch' and 100 as 'maximum itch'. The scale was anchored at one-third of the VAS, defined to patients as the 'scratch threshold' (15).

Tab. 1: Clinical characteristics, skin tests, determination of total and specific IgE in the patient group (41)

Patient number	Age (years)	Sex	Atopic disease	Prick-test (positive)	Total IgE (IU/ml)	Specific IgE (CAP-class)
01	31	f	Asthma, AR	birch, grass, cat, celery	275	D. pter. 2, cat 2, dog 3, hazelnut 2, celery 1, grass 4, birch 4, hazel 3
02	25	f	AR	D. pter., birch, grass, mugwort	964	D. pter. 3, celery 3, grass 6, birch 4, hazel 5, wheat flour 3, rye 5, mugwort 3
03	25	f	AR	D. pter., cat, grass, mugwort	79.4	D. pter. 3, cat 1, grass 2, rye 2, mugwort 2
04	31	f	AR	hazel, celery, Alt. alternata	14.2	grass 2
05	23	f	Asthma, AR	D. pter., birch, dog, cat	134	D. pter. 4, cat 2, dog 2, grass 3
06	24	f	AE, Asthma, AR	grass	161	D. pter. 5, grass 2, mugwort 1, ambrosia 1
07	24	f	AE, Asthma	trees, mugwort, birch, D. pter., alder, grass, hazel	2248	D. pter. 4, cat 3, celery 3, grass 3, birch 5, wheat flour 3, mugwort 3, ambrosia 3, latex 2
08	30	m	AE, AR	trees, birch, D. pter., alder, grass, hazel, dog, cat	1822	D. pter. 6, cat 4, grass 5, birch 3, wheat flour 1, mugwort 1, milk 2
09	28	m	AR	trees, mugwort, birch, blatella, D. far., D. pter., alder, grass, hazel, dog, cat, ambrosia, herbage	226	D. pter. 4, cat 2, hazel nut 3, grass 2, birch 3, mugwort 2, ambrosia 1
10	25	f	AD	grass, cat, herbage	113	cat 3, grass 4
11	18	m	Asthma	D. far., D. pter., grass	493	D. pter. 2, grass 5, ambrosia 1
12	20	m	AE, Asthma, AR	trees, birch, D. far., D. pter., alder, hazel, aspergillus, ambrosia	56.2	D. pter., 3, birch 3
13	20	f	AE, Asthma	negative	136	negative
14	27	m	AE, Asthma, AR	trees, birch, D. pter., alder, grass, hazel, dog, cat, horse, Alternaria tenuis, ambrosia	1455	D. pter. 3, cat 5, grass 3, birch 6, wheat flour 2, mugwort 3, egg white 2, codfish 2, Cladosporium herbarum 3
15	24	f	AE, Asthma, AR	trees, birch, D. far., D. pter., alder, grass, hazel, dog, cat, herbage, horse	159	D. pter. 4, cat 2, grass 2, birch 3
16	26	f	AD	Mugwort, grass, herbage	8.7	grass 3
17	32	m	AR	trees, birch, alder, grass, herbage, ambrosia	142	D. pter. 1, cat 2, grass 4, birch 2, wheat flour 1, ambrosia 2
18	28	f	Asthma, AR	trees, birch, D. far., D. pter., alder, grass, hazel, herbage,	775	D. pter. 3, celery 1, grass 3, birch 4, ambrosia 2

Abbreviations: AD: atopic diathesis; AE: allergic rhinitis; D. far.: Dermatophagoides farinae; D. pter.: Dermatophagoides pteronissinus; f: female; m: male

2.2.5.3 Measurement of skin physiological parameters (Fig. 1)

Parameters of skin layers function, especially with regard to the barrier function of the upper skin layers (16), were investigated under the conditions of the altitude climate:

2.2.5.4 Sebum content

A sebumeter (SEBUMETER SM 810, Courage and Khazaka electronics GmbH, Köln, Germany) was used for the quantitative measurement of skin surface fat. The measurement was based on fat spot photometry. The mat tape of the sebumeter was brought into contact with skin (here forehead). It became transparent in relation to the sebum on the surface of the measurement area. Then the tape was inserted into the aperture of the device and the transparency was measured by a photocell. The light transmission represented the sebum content and the result was displayed in $\mu\text{g}/\text{cm}^2$.



Fig. 1: Measurement of skin physiology parameters

2.2.5.5 Skin hydration

To determine the skin hydration, a corneometer (CORNEOMETER CM825, Courage and Khazaka electronics GmbH, Köln, Germany) was used to determine the moisture content of the outer layer of the epidermis (stratum corneum) by means of a capacitive measuring method. Changes in the skin surface hydration resulted in a change in the capacitance of a precision capacitor due to the change of a dielectric medium. This was evaluated electronically and displayed as a corneometer value. The value scale ranged from 1–150 units. For measurement, the active front face of the probe head, coated with special glass, was placed on the flexor side of the forearm. The corneometer reading was displayed after 1 second.

2.2.5.6 PH-value

The pH-value of the skin surface provides important information about the condition of the skin and its protective acid mantle. Since the skin's surface with its excretions and high moisture content comes very close to the properties of an "aqueous solution", it is suitable for immediate pH measurement. The sensor for pH measurement on the skin surface of the skin-pH-meter (SKIN-pH-METER PH 900, Courage and Khazaka electronics GmbH, Köln, Germany) was characterised by the fact that its active part was designed as a flat surface in order to be able to measure on the skin (here: flexor side of the forearm). The measurement was based on a high quality combined electrode, where both glass H^+ ion sensitive electrode and additional reference electrode were placed in one housing. It was connected to a probe handle containing the measurement electronics. The result of the measurement within seconds was displayed with an accuracy of 0.1 pH.

2.2.5.7 Skin roughness (Fig. 2)

Skin roughness can be determined by means of an impression procedure to determine the skin surface texture. Replicas were taken from the flexor side of the forearm with a polyether impression material (Permadyne Garant 2:1, ESPE, Seefeld, Germany) according to a previous publication (16). Each skin print is measured with the aid of a commercially available surface measuring device (VisioScan VC98 with the software SELS 2000, Courage and Khazaka electronics GmbH, Köln, Germany). For the description of skin roughness, those parameters were chosen that have proven to be particularly meaningful for the description of the skin surface texture (skin scalliness, skin smoothness).



Fig. 2: Replica of the skin surface for measurement of skin roughness

2.2.5.8 Transepidermal water loss

A tewameter (Tewameter TM 300, Courage and Khazaka electronics GmbH, Köln, Germany) was used to determine the transepidermal water loss as a measure of the skin barrier function. The physical basis for measuring the evaporation of water on a surface is the diffusion law discovered by Adolf Fick:

$$\frac{dm}{dt} = -D \cdot A \cdot A \cdot \frac{dp}{dx}$$

(A = surface (m^2); m = water transported (g); t = time (h); D = diffusion constant (= 0.0877 g/m(h(mm Hg))); p = vapour pressure of the atmosphere (mm Hg); x = distance from skin surface to point of measurement (m))

The diffusion current dm/dt indicates how much mass is transported per time unit. The diffusion current is proportional to the surface A of the perpendicularly penetrating interface and the change in density per unit of displacement length dp/dx . D is the diffusion coefficient of water vapour in atmospheric air. This law is only valid within a homogeneous diffusion zone. This is approximately created by a hollow cylinder open on both sides, the shorter side of which is placed on the skin (open chamber measurement). The water evaporating from the surface of the skin evaporates through the cylinder on the opposite side. The resulting density gradient is indirectly measured and evaluated by two pairs of sensors (temperature and relative humidity) in the cylinder. The values are given in g/hm^2 . The transepidermal water loss was measured according to the guidelines of Pinnagoda et al. (17) on the flexor side of the forearm. This parameter is of particular importance as it can be used to detect very small disorders of the skin barrier function both in healthy skin and in patients with atopic eczema, which already show elevated levels of TEWL in non-affected areas.

2.2.5.9 Alkali resistance test

The alkali resistance test assesses the alkaline resistance of the skin. For this purpose, a skin area was moistened with 0.5 M NaOH solution for 2×10 minutes and covered with a small glass platelet. In between was a 10-minute drying and observation area. The control was 0.9% aqueous saline solution. The TEWL was then measured over both areas.

2.2.5.10 Laser Doppler flowmetry (Fig. 3)

By means of Laser-Doppler Imager (Moor Instruments, Axminster, England) it was possible to measure the skin blood circulation without contact. A low energy laser was guided over the surface of the skin (here both forearms) in a meandering manner by a mirror that can be rotated on two axes. The light was scattered through the static surface and the moving blood. The double shifted and unchanged light components were directed to two detectors via the movable scanning mirror and the incoming mixed signal was used to calculate the parameter Flux (proportional to the blood flow). The value was given in device-specific units.

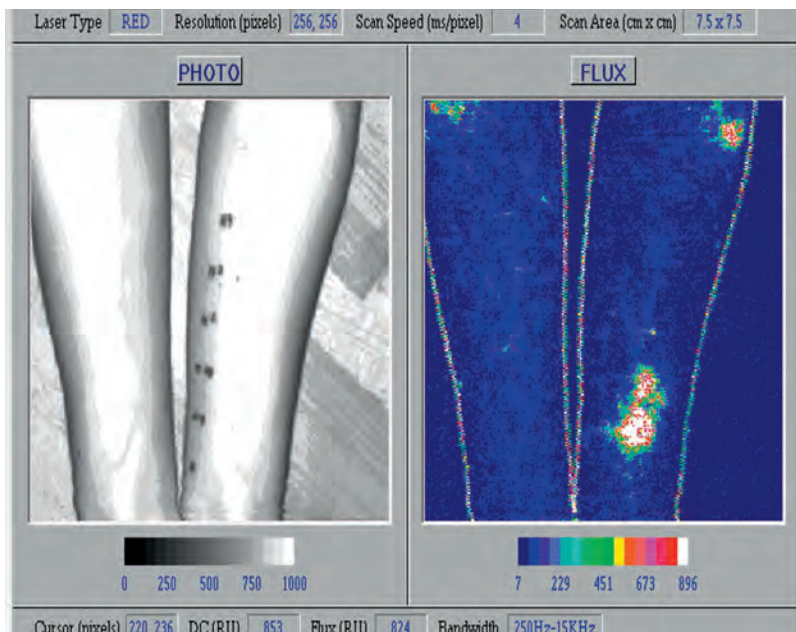


Fig. 3: Laser Doppler Flowmetry

2.2.6 Respiratory parameters

2.2.6.1 Peak flow measurement

The severity of a breathing disorder can be assessed by peak flow measurement. This method measured the maximum exhalation flow (peak flow) at forced expiration at the mouth in l/s or l/min. The mouthpiece of the peak flow meter (Mini-Wright-Peak-Flow-Meter, Clemente Clark, Essex, England) was attached to the mouth and the pointer is positioned at 0 l/min. The patient breathed deeply while standing, held the device horizontally, covered the mouthpiece with his or her lips and exhaled through the device as fast and powerfully as possible. The value was read above the pointer. In healthy subjects, the peak flow rate is usually between 400 and 700 l/min. In this study, the subjects were instructed to perform a peak flow measurement three times a day with the nose clamp attached while standing. The peak flow measurement was carried out three times at each measuring point and the best results were documented.

2.2.6.2 Rhinomanometry

In all subjects rhinomanometric function parameters were determined with a spirometer (Flowscreen Pro, Jaeger GmbH, Hoechberg, Germany). The measurement method was used to determine the airway resistance when inhaling through the nose. During inhalation and exhalation, a special respiratory mask was used to measure the differential pressure between the space in front of the nostril and the oral cavity. With the aid of nasal olives, the choke pressure and flow were determined and the measured value was graphically recorded in a nasal resistance curve. The value of the nostril was selected as the reference point showing the least resistance before exposure.

In the nasal provocation test, after adaptation to room temperature, the provocation was applied with NaCl 0.9% to the lower nasal concha on the mucous membrane and the flow was recorded. The usual provocation with pollen was avoided due to the risk of an asthma attack.

2.2.6.3 Extraction of nasal secretion

To obtain nasal secretion, we used the absorption method with small cotton wool pieces: These small cotton wool pieces were inserted into the middle nasal passage on both sides under anterior rhinoscopy with a bayonet forceps for 15 minutes. Subsequently, they were centrifuged at +8 °C and 3000 R for 20 min and the nasal secretion obtained was stored at -70 °C until further processing. In all samples the eosinophilic cationic protein (ECP) was analyzed (CAP ECP FEIA, Pharmacia, Uppsala, Sweden).

2.2.6.4 Pulmonary function parameters

In all subjects pulmonary function parameters were determined with a spirometer (Flowscreen Pro, Jaeger GmbH, Hoechberg, Germany). The pulmonary function test measured parameters for the characterisation of lung size, certain partial volumes and flow resistance. The measured values were assessed in relation to standard values, so that a normal or limited lung function could be detected in the individuals. The lung function, but especially the intensity of change over time, is currently the most significant non-invasive parameter for measuring the co-reaction of the lungs and bronchi.

The routine parameters VC max, FEV1, FEV1/VC max, ITGV, R tot, SR tot and the flow-volume curve were evaluated using bodyplethysmography (Master Screen Body, Jaeger GmbH, VIASYS Healthcare, Höchberg, Germany). (Fig. 4)

Under resting conditions and/or slow breathing conditions the vital capacity as well as its partial volumes (VCin, ERV, IRC) were determined and the forced expiratory volume in one second (FEV1) and other parameters (FVC, FEV1 % VC, PEF, MEF75, MEF50, MEF25, MMEF) were determined by forcing expiratory volume in one second from the flow-volume curve. Bodyplethysmographically, the airway resistances and the intrathoracic gas volume at the end of normal exhalation (FRC) were determined by means of short term occlusion at the mouthpiece (18).



Fig. 4: Bodyplethysmography

2.2.6.5 Methacholine provocation

The methacholine provocation (for subjects with normal lung function) is one of the pharmacological bronchial provocation tests that have a firm place in patient care as well as in scientific and expert questions. This challenge test was performed with a bodyplethysmograph (Master Screen Body, Jaeger GmbH, VIASYS Healthcare, Hoechberg, Germany). After inhalation of a control solution (physiological saline solution) the inhalative provocation with methacholine was carried out in different dose levels. Inhaled methacholine does not cause any reaction at all in healthy airways. If the airways are inflamed and therefore hypersensitive, there is a brief airway constriction, which can be detected very well and early in the lung function. Lung function examinations were performed prior to provocation and after control and individual dose levels.

2.2.6.6 Measurement of nitrogen oxide (NO) in the exhaled air (Fig. 5)

The measurement of nitric oxide in exhaled air serves as an objective and simple marker of respiratory inflammation. For NO measurement, the patient exhaled in a seated position, then NO-free air was inhaled via a mouthpiece. Finally, the patient breathed out slowly into the mouthpiece, with the results being visible directly on a screen. After 3 measurements the correct value was displayed. FE_{NO} measurements (NIOX MINO; Aerocrine, Solna, Sweden) were performed at the different time points (19).



Fig. 5: Measurement of nitrogen oxide (NO) in the exhaled air

2.2.6.7 Conjunctival provocation test

Five serial dilutions (1:10) of grass pollen extracts were created. The test was carried out gradually up to a clinical reaction with a score of at least 2+ for itching and redness. Conjunctival symptoms (itching, burning, foreign body sensation, tears, redness, chemosis, eyelid swelling) were evaluated according to a score of 0 (none) to 3 (heavy) for each eye prior to allergen provocation and 5, 10, 15, 20 minutes after challenge. A single drop (20 μ l) of the lowest concentration was placed in the conjunctival sac followed by the next concentration at 10-min intervals switching from one eye to the other until symptoms appeared. 0.1% saline was used as negative control.

2.2.7 Questionnaires

2.2.7.1 SF-36 Health Survey Test

The Short Form Health Survey is a 36-item, patient-reported survey of patient health. The SF-36 covers 8 different dimensions that can be classified in the areas of “physical health” and “mental health”: Physical functioning, physical role functioning, physical pain, general health perception, vitality, social function, emotional role functioning and mental health (20).

2.2.7.2 Eppendorf Itch Questionnaire (EIQ)

The Eppendorf itch questionnaire (21) is a validated instrument for qualitative and quantitative assessment of pruritus. It contains 80 items on itch sensation in blocks of ten. Each item is rated with regard to the itch sensation on a five-point scale from 0 (not applicable) to 4 (very applicable).

German Instrument for Measuring the Quality of Life in Skin Diseases – Deutsches Instrument zur Erfassung der Lebensqualität bei Hauterkrankungen (DIELH)

This questionnaire examines the quality of life for skin diseases in the areas of physical ailments, mental health, everyday life, leisure, job/school, personal environment and treatment on the basis of 36 questions (22).

2.2.7.3 Rhinoconjunctivitis Quality of Life Questionnaire (RQLQ)

The Rhinoconjunctivitis Quality of Life Questionnaire (RQLQ) measures the functional problems (physical, emotional, social and occupational) that are most troublesome to adults (17–70 years) with either seasonal or perennial rhinoconjunctivitis of either allergic or non-allergic origin. The RQLQ has 28 questions in 7 domains (activity limitation, sleep problems, nose symptoms, eye symptoms, non-nose/eye symptoms, practical problems and emotional function). There are 3 ‘patient-specific’ questions in the activity domain which allow patients to select 3 activities in which they are most limited by their rhinoconjunctivitis. Patients recall how bothered they have been by their rhinoconjunctivitis during the previous week and respond to each question on a 7-point scale (0 = not impaired at all –6 = severely impaired). The overall RQLQ score is the mean of all 28 responses and the individual domain scores are the means of the items in those domains (22).

2.2.7.4 Blood parameters

The following blood parameters were determined: complete blood count (Sysmex XT-2000 i/ XT-1800i; Sysmex Corporation, Japan), eosinophil cationic protein (CAP ECP FEIA, Pharmacia, Uppsala, Sweden), human IL-16 (DuoSet ELISA Development System, R&D Systems Europe, Abingdon, United Kingdom) and IL-33 (Human IL-33 ELISA Quantitation Kit, Gentaur, Brussels, Belgium).

2.2.7.5 Statistical analysis

Data were analyzed using SPSS. For statistical analysis the Friedman’s one-way analysis for variance by ranks was used for paired samples and the Wilcoxon test for unpaired samples. For the disease-related analysis the univariate analysis of Variance (ANOVA) was used. The critical value for significance was set at $P < 0.05$ for all analyses. Data are presented as mean (\pm SD).

2.3 Results

2.3.1 Patients

Out of the 18 patients 13 had rhinoconjunctivitis, 10 had asthma and 7 patients suffered from atopic eczema. 11 patients had positive prick tests to house dust mites, 14 to grass pollen and 12 to early flowering species (hazel, alder, birch). 14 patients had specific IgE antibodies to house dust mites, 16 to grass pollen and 10 to early flowering species. (Tab. 1)

Tab. 2: Significant results of skin, nasal, conjunctival and lung parameters, questionnaires and blood parameters at the beginning (t1) in Munich, at time point 2 (t2) and 3 (t3) in the UFS and time point 4 (T4) in Munich in the different groups: data are means \pm SD (41)

Parameter	t1 (pat.)	t1 (contr.)	t2 (pat.)	t2 (contr.)	t3 (pat.)	t3 (contr.)	t4 (pat.)	t4 (contr.)	Wilcoxon	ANOVA
Skin parameters										
Str. corneum hydration (arb. units)	46 \pm 10	48 \pm 7	36 \pm 8	39 \pm 6	38 \pm 7	39 \pm 5	44 \pm 14	47 \pm 4	**t1/t2 **t3/t4	
PH	4.9 \pm 1.3	5.2 \pm 1.2	5.9 \pm 1.3	5.4 \pm 1.2	5.9 \pm 1.3	5.4 \pm 1.2	5.2 \pm 1.3	4.5 \pm 1.2	**t1/t2 **t3/t4	
Skin roughness (arb. units)	0.6 \pm 0.3	0.5 \pm 0.2	1.0 \pm 0.3	0.6 \pm 0.2	0.6 \pm 0.4	0.5 \pm 0.2	0.6 \pm 0.4	0.5 \pm 0.2	*t1/t2 **t3/t2	
Skin scaliness (arb. units)	0.3 \pm 0.2	0.3 \pm 0.2	0.7 \pm 0.3	0.7 \pm 0.4	0.8 \pm 0.3	0.6 \pm 0.3	0.6 \pm 0.3	0.5 \pm 0.2	**t1/t2 **t3/t4	
Skin smoothness (arb. units)	18.2 \pm 2.0	18.2 \pm 3.8	21.0 \pm 3.8	18.8. \pm 4.4	22.3 \pm 4.3	18.5 \pm 4.3	19.0 \pm 2.9	15.1 \pm 0.5	**t1/t2 **t3/t4	\downarrow AE t1/t2
TEWL (g/(hm ²))	8.0 \pm 5.0	6.0 \pm 1.4	6.2 \pm 2.5	5.9 \pm 1.2	7.1 \pm 3.8	7.0 \pm 1.8	9.8 \pm 9.2	7.5 \pm 2.2		\uparrow AE t3/t4
Blood flow (right) (arb. units)	109 \pm 23	96 \pm 16	n.d.		121 \pm 49	97 \pm 19	108 \pm 15	98 \pm 16		\uparrow AE t1/t3
Blood flow (left) (arb. units)	115 \pm 28	98 \pm 15	n.d.		124 \pm 60	96 \pm 23	113 \pm 28	101 \pm 20		\uparrow AE t1/t3 \downarrow AE t3/t4
Wheal diluted 1:10 (mm)	6.2 \pm 2.9	n.d.	5.7 \pm 2.3	n.d.	6.1 \pm 2.6	n.d.	4.9 \pm 1.6	n.d.		
Wheal diluted 1:100 (mm)	2.9 \pm 1.1	n.d.	2.9 \pm 1.1	n.d.	3.6 \pm 1.2	n.d.	2.8 \pm 1.0	n.d.	*t2/t3	
Flare diluted 1:10 (mm)	31.3 \pm 10.1	n.d.	25.1 \pm 10.8	n.d.	23.4 \pm 8.5	n.d.	25.0 \pm 9.6	n.d.	**t1/t2	
Nasal and conjunctival parameters										
Resistance (after prov.) (ml/s)	1.1 \pm 1.8	1.3 \pm 2.1	0.7 \pm 0.6	0.6 \pm 0.6	0.5 \pm 0.3	0.6 \pm 0.5	0.5 \pm 0.5	0.7 \pm 0.6		\uparrow Asthma t2/t3
Conjunctival provocation (score) Allergen 1/100 (5 min)	0.7 \pm 0.5	n.d.	0.4 \pm 0.5	n.d.	0.5 \pm 0.5	n.d.	0.6 \pm 0.5	n.d.		\uparrow Asthma t1/t2 \downarrow Asthma t2/t3
Lung parameters										
FVC (l)	5.1 \pm 1.7	4.6 \pm 1.0	5.2 \pm 2.0	5.0 \pm 1.3	4.6 \pm 1.2	4.7 \pm 1.2	4.7 \pm 1.5	5.0 \pm 1.0	*t2/t3	
FEV1/MC (%)	78 \pm 15	88 \pm 12	80 \pm 17	89 \pm 8	85 \pm 11	90 \pm 7	81 \pm 14	89 \pm 9	*t1/t3	
PEF (l/s)	9.1 \pm 2.9	10.0 \pm 2.63	10.1 \pm 2.5	11.2 \pm 3.0	9.6 \pm 2.5	10.9 \pm 2.9	9.9 \pm 2.7	10.2 \pm 2.4	**t1/t2 **t2/t3 *t3/t4	

Parameter	t1 (pat.)	t1 (contr.)	t2 (pat.)	t2 (contr.)	t3 (pat.)	t3 (contr.)	t4 (pat.)	t4 (contr.)	Wilcoxon	ANOVA
MEF50 (l/s)	4.26 ± 1.7	5.35 ± 2.0	4.76 ± 2.0	5.84 ± 2.1	4.85 ± 1.9	5.60 ± 1.8	4.67 ± 1.5	5.5 ± 1.4	*t1/t2	
MMEF 25/75 (l/s)	3.75 ± 1.5	4.73 ± 1.6	4.23 ± 1.8	5.19 ± 1.8	4.22 ± 1.6	5.02 ± 1.6	4.25 ± 1.1	5.02 ± 1.1	**t1/t2	
Resistance after 0.1 % methacholine (kPA*s/l)	0.33 ± 0.1	0.23 ± 0.02	0.42 ± 0.2	0.31 ± 0.2	0.52 ± 0.2	0.24 ± 0.1	n.d.		**t1/t2 **t1/t3	↓Asthma t1/t2 ↑AE t1/t2
FeNO (ppb)	41.6 ± 34.6	17.6 ± 7.9	32.0 ± 24.9	12.8 ± 10.2	38.2 ± 34.3	20.0 ± 15.4	33.2 ± 26.5	16.2 ± 9.3		
Questionnaires										
DIELH (score)	30 ± 30	1 ± 1	27 ± 30	1 ± 1	29 ± 29	1 ± 2	24 ± 28	0 ± 1		↑AE t1/t2
ROLO (score)	5.6 ± 0.9	6.6 ± 0.3	5.6 ± 1.0	6.8 ± 0.2	5.8 ± 0.9	6.8 ± 0.2	5.7 ± 0.9	6.6 ± 0.3	*t1/t3	↓Asthma t2/t3 ↑AE t2/t3
SF-36 (score)	2.2 ± 0.4	2.0 ± 0.4	2.2 ± 0.4	2.0 ± 0.5	2.2 ± 0.4	2.0 ± 0.5	2.4 ± 0.2	2.2 ± 0.2		↓AR t2/t3
Blood parameters										
Erythrocytes (10 ⁶ /ml)	4.85 ± 0.4	4.85 ± 0.6	5.27 ± 0.5	5.09 ± 0.92	4.92 ± 0.42	4.86 ± 0.57	5.01 ± 0.37	4.79 ± 0.4	**t1/t2 **t2/t3	↓AR t2/t3
Hemoglobin (g/dl)	14.2 ± 1.5	14.1 ± 1.7	15.3 ± 1.8	14.9 ± 2.6	14.4 ± 1.5	14.0 ± 1.6	14.5 ± 1.4	13.8 ± 1.20	**t1/t2 *t2/t3 *t3/t4	
Hematocrit (%)	42.9 ± 3.7	42.3 ± 4.5	46.6 ± 4.6	44.3 ± 6.7	43.4 ± 3.6	42.6.0 ± 4.0	44.8 ± 3.2	43.0 ± 2.90	**t1/t2 *t2/t3	↓AR t2/t3
Eosinophils (%)	4.0 ± 3.1	1.9 ± 1.3	4.3 ± 2.9	2.0 ± 1.2	4.9 ± 3.1	3.1 ± 1.8	4.2 ± 3.1	2.3 ± 1.1	**t1/t3	
Basophils (%)	0.5 ± 0.2	0.4 ± 0.2	0.4 ± 0.2	0.3 ± 0.2	0.5 ± 0.2	0.5 ± 0.2	0.5 ± 0.2	0.3 ± 0.20	**t1/t3	
ECP (mg/ml)	16.0 ± 11.0	6.0 ± 4.0	5.0 ± 5.0	2.0 ± 2.0	11.0 ± 11.0	6.0 ± 6.0	14.0 ± 9.0	5.0 ± 3.0	**t1/t2 **t2/t3 **t3/t4	
IL-33 (ng/ml)	2.96 ± 4.04	4.16 ± 5.98	2.81 ± 4.1	4.0 ± 5.92	2.72 ± 3.91	3.72 ± 5.97	1.85 ± 2.45	5.16 ± 6.94	*t1/t2	↑Asthma t3/t4

Abbreviations: AE: atopic eczema; AR: allergic rhinitis; arb. units: arbitrary units; contr.: controls; DIELH: Deutsches Instrument zur Erfassung der Lebensqualität bei Hauterkrankungen; ECP: eosinophil cationic protein; FeNO: fractional exhaled nitric oxide; FEV1/Vc: forced expiratory volume in one second/volume capacity; FVC: forced volume capacity; MEF50: maximum expiratory flow at 50% of vital capacity; MMEF 25/75: maximal mid-expiratory flow between 25% and 75% of vital capacity; n.d.: not done; pat.: patients; PEF: peak expiratory flow; ppb: parts per billion; RQLO: Rhinitis Quality of Life Questionnaire; prov.: provocation; Str.: stratum; TEWL: transepidermal water loss; * $p < 0.05$; ** $p < 0.01$

2.3.2 Dermatological examination and skin function measurements (Tab. 2)

The severity of eczema as measured by SCORAD showed no significant changes (Fig. 6). Also the sebum concentrations did not change significantly over the study period. Stratum corneum hydration decreased significantly during the stay at the UFS (Fig. 7). Skin surface pH showed a significant increase at the UFS between time point 1 and time point 2 as well as between time point 3 and time point 4 (Fig. 8).

Skin roughness showed a significant increase ($p < 0.05$) at time point 2 (controls: 0.6 ± 0.2 ; patients: 1.0 ± 0.3) vs. 1 (controls: 0.5 ± 0.2 ; patients: 0.6 ± 0.3) as well as a significant decrease ($p < 0.01$) at time point 3 (controls: 0.5 ± 0.2 ; patients: 0.6 ± 0.4) vs. time point 2 (controls: 0.6 ± 0.2 ; patients: 1.0 ± 0.3). Skin scaliness and skin smoothness increased significantly during the stay at the UFS with significant differences ($p < 0.01$) between time point 1 (controls: 0.3 ± 0.2 ; patients: 0.3 ± 0.2 /controls: 18.2 ± 3.8 ; patients: 18.2 ± 2.0) vs. time point 2 (controls: 0.7 ± 0.4 ; patients: 0.7 ± 0.3 /controls: 18.8 ± 4.4 ; patients: 21.0 ± 3.8) and time point 3 (controls: 0.6 ± 0.3 ; patients: 0.8 ± 0.3 /controls: 18.5 ± 4.3 ; patients: 22.3 ± 4.3) to time point 4 (controls: 0.5 ± 0.2 ; patients: 0.6 ± 0.3 /controls: 15.1 ± 0.5 ; patients: 19.0 ± 2.9).

Transepidermal water loss (TEWL) did not show significant changes over the study period. Also TEWL measured during the alkali resistance test showed no significant change during the study period. The dermal blood flow did not show significant changes over the study period, but in patients with atopic eczema this parameter increased significantly ($p < 0.01$) between time point 3 vs. 1.

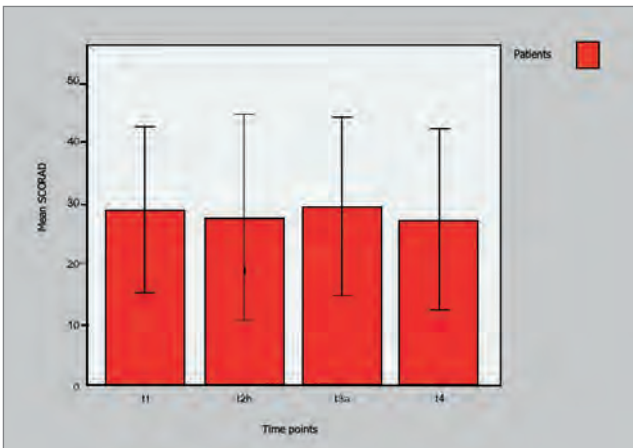


Fig. 6: SCORAD of patients with atopic eczema at the different time points (t1 and t4: Munich; t2 and t3: UFS)

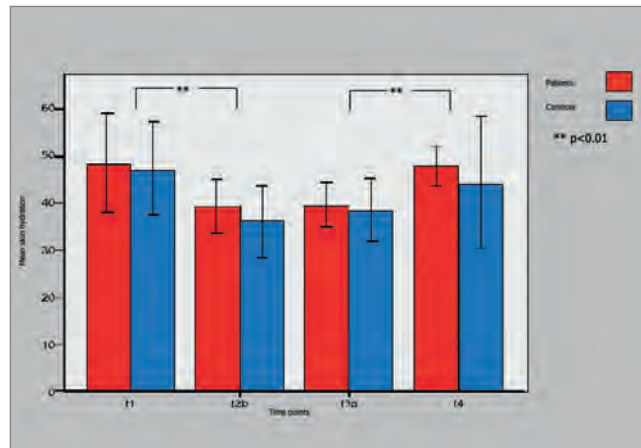


Fig. 7: Skin hydration of patients and controls at the different time points (t1 and t4: Munich; t2 and t3: UFS)

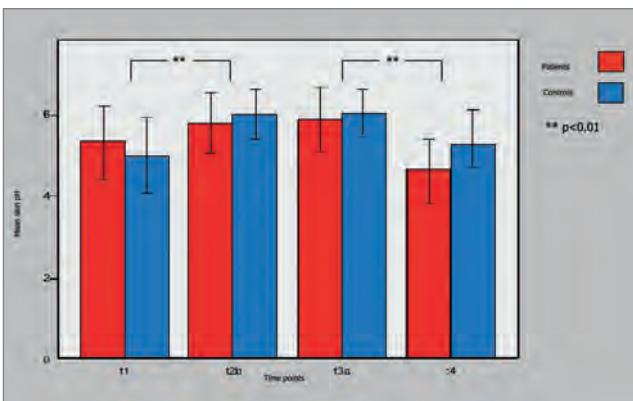


Fig. 8: PH-values of patients and controls at the different time points (t1 and t4: Munich; t2 and t3: UFS)

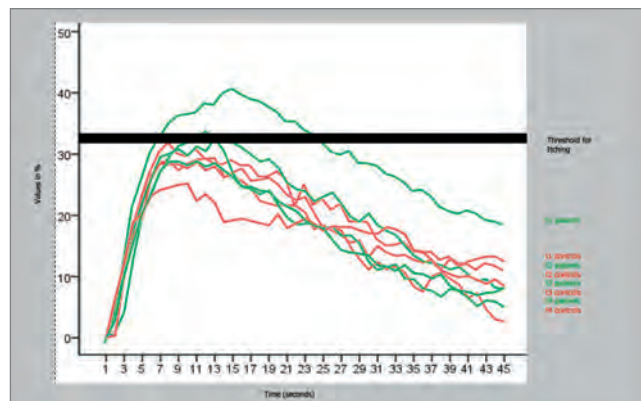


Fig. 9: Itch intensity after skin prick test with histamine of patients and controls at the different time points (t1 and t4: Munich; t2 and t3: UFS) (41)

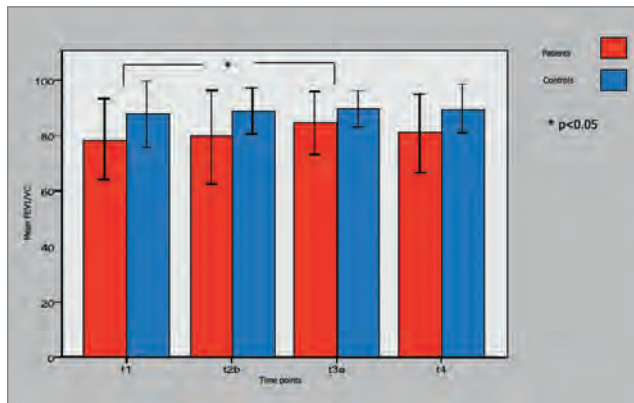


Fig. 10: FEV1/VC of patients and controls at the different time points (t1 and t4: Munich; t2 and t3: UFS)

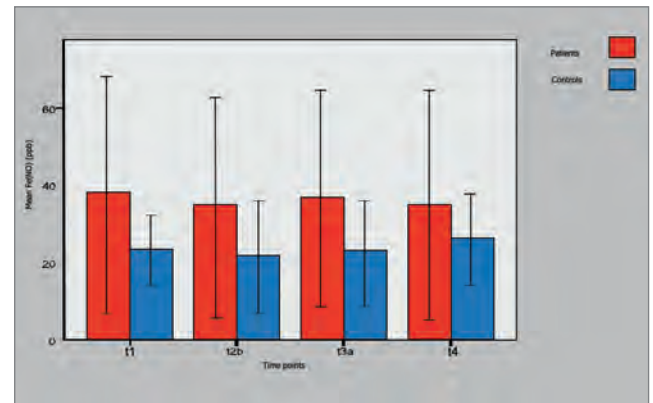


Fig. 11: FE(NO) of patients and controls at the different time points (t1 and t4: Munich; t2 and t3: UFS)

The size of the wheals and flares after a prick test with different concentrations of the grass pollen showed minor changes, namely an increase of the wheal size after prick test of the 1:100 solution at time point 3 vs. 2 and the decrease of the flare size of the 1:10 solution at time point 1 vs. 2 (data not shown). In patients with rhinoconjunctivitis the wheal size of the 1:10 solution increased significantly ($p < 0.05$) between time point 1 vs. 2.

Itch intensity after prick testing of histamine rated on a computerized visual analogue scale (VAS) decreased significantly between time point 2 vs. 1 and between time point 3 vs. 2 (Fig. 9). In patients with rhinoconjunctivitis itch intensity decreased significantly ($p < 0.05$) between time point 1 vs. time point 2.

2.3.2.1 Respiratory parameters (Tab. 2)

No significant changes in the rhinomanometric parameters (nasal flow and nasal resistance) were found before and after application of NaCl during the study.

The forced vital capacity (FVC) showed a significant decrease ($p < 0.05$) at time point 3 (controls: 4.7 ± 1.2 l; patients: 4.6 ± 1.2 l) vs. time point 2 (controls: 5.0 ± 1.3 l; patients: 5.2 ± 2.0 l). FEV1/VC (Fig. 10), PEF, MEF 50 and MMEF25/75 (data not shown) increased significantly ($p < 0.05$) at time point 3 or 2 vs. 1. The resistance during provocations tests with different concentrations of methacholinchloride, peak-flow values and values of the measurement of exhalative nitric oxide (NO) did not differ significantly at the different time points (Fig. 11).

2.3.2.2 Conjunctival provocation test (Tab. 2)

Conjunctival provocation with allergen solution in different concentrations did not differ significantly at the different time points. In patients with asthma there was a significant increase ($p < 0.05$) of this parameter at a concentration of 1:100 after 5 minutes at time point 1 vs. 2 and a significant decrease ($p < 0.05$) at time point 2 vs. 3 (ANOVA).

2.3.1.3 Quality of life – questionnaires (Tab. 2)

Statistical analysis of several questionnaires (SF-36 Questionnaire, Eppendorf Itch questionnaire, Deutsches Instrument zur Erfassung der Lebensqualität bei Hauterkrankungen [DIELH]) revealed no significant differences of the scores at all time points. The score of the Rhinoconjunctivitis Quality of Life Questionnaire [RQLQ]) increased significantly ($p < 0.05$) between time point 1 (controls: 6.6 ± 0.3 ; patients: 5.6 ± 0.9) vs. 3 (controls: 6.8 ± 0.2 ; patients: 5.8 ± 0.9). This increase reflects an improvement of symptoms.

2.3.2.4 Blood parameters (Tab. 2)

Erythrocytes, hemoglobin and hematocrit increased significantly ($p < 0.01$) at time point 2 vs. time point 1. In the serum a significant decrease ($p < 0.01/p < 0.05$) of the eosinophil cationic protein (ECP) and of interleukin-33 was found at the beginning of the stay at the UFS versus the first assessment in Munich (t2 vs. t1) and again a significant increase for ECP ($p < 0.01$) at the

last assessment in Munich versus the end of the stay at the UFS (t4 vs. t3). Interleukin-16 in the serum and ECP in the nasal secretions did not differ significantly during the different time points.

For the influence of the different atopic diseases (rhinoconjunctivitis, atopic eczema, asthma) on the above mentioned parameters (ANOVA) see Tab. 2.

2.4 Discussion

It was shown in this study, that a 5-day-sojourn at the Environmental Research Station Schneefernerhaus (UFS Zugspitze) at an altitude of 2650 m alt. exerts different effects on atopic diseases with amelioration of itching and some respiratory parameters.

A clinical improvement of atopic eczema skin lesions using the severity score SCORAD was not found. This was in contrast to reported benefits of climate therapy in patients with atopic eczema during treatment in specialized in-patient facilities in the alpine mountain climate of Bavaria (24, 25) or in mountain altitude conditions like Davos (4, 7, 26). Moreover a worsening of some skin physiology parameters (e.g. stratum corneum hydration, pH, skin roughness) was observed. One reason of this phenomenon might be the fact that topical glucocorticosteroids were withdrawn 1 week before time point 1, another reason could be the low air humidity at this altitude with negative influences on the skin. Only histamine-induced itching improved significantly during the observation period at the UFS. It is known that in the Swiss mountain area of Davos itch intensity was found to be correlated with some meteorological variables, especially air temperature (27).

Several lung parameters (FEV1/VC, PEF, MEF 50 and MMEF25/75) improved, only the forced vital capacity decreased. This is in accordance to previous studies with children and adolescents in in-patient rehabilitation programs (28, 29, 30, 31) in moderate high mountain climate showing an improvement of lung function disturbances. Decrease of exhaled NO as a parameter of lung inflammation was also seen in asthmatic patients under mountain climate therapy (5), but not in our study.

The SF-36 questionnaire was constructed to survey health status and designed for use in clinical practice and research, health policy evaluations and general population surveys (20). In our study at the UFS there were no significant differences of the score at the different time points. Furthermore the scores of the skin specific questionnaires emphasizing the pruritus (The Eppendorf Itch Questionnaire) and the quality of life (DIELH) did not differ significantly in our study. By contrast, in the AURA study we found a significant amelioration of the scores confirming the benefit of the therapy in Pfronten (25). Only the RQLQ showed a significant difference between time point 1 and time point 2 in our study with a negative influence of atopic eczema and a positive influence of asthma.

Exposure to the moderate altitude had significant effects on red blood cells (32) with an increase of eosinophils during the stay at the UFS. This is in contrast to other studies during hospital treatment of atopic eczema in the mountain climate (33) and the North Sea climate with decreased eosinophils (34).

Elevated ECP and IL-33 levels are regarded as markers of inflammation in asthma and atopic eczema (35, 36). In our patients with atopic diseases ECP together with IL-33 decreased significantly. Similar effects had been shown in the mountain climate of Davos for ECP (8).

It could be shown that circulating IL-16 levels are correlated with the SCORAD in adult patients with atopic eczema (37) and decreased significantly in these patients after successful treatment (38). We did not find a decrease in our patients with atopic diseases.

Despite the extensive and detailed measurements of characteristics of atopic diseases during a 5 day observation period in the mountain climate of the Zugspitze in Bavaria only a few parameters improved. The stay was helpful for patients with asthma, whereas patients with atopic eczema did not benefit from it and even their skin physiology parameters worsened. This might be due to the short duration of the sojourn and specific environmental factors at this altitude. It would be of interest assessing the skin parameters and characteristics of atopic eczema during observation periods lasting several weeks in the alps.

Since there is recently some criticism regarding validated data for the moderate altitude therapy for patients with allergic diseases (39, 40) the methodology presented can serve as a suitable template for qualified studies on the effect of climate therapy.

Acknowledgement

The statistical analysis was performed by the Institut für Medizinische Statistik und Epidemiologie, Technische Universität München (Bernhard Haller).

The authors also want to thank Free State of Bavaria (Bayerisches Staatsministerium für Umwelt und Gesundheit) for funding and the Christine Kühne Center for allergy research and education (CK – CARE) for support in data evaluation.

References

1. Ring J., Eberlein-König B., Behrendt H. Environmental pollution and allergy. *Ann Allergy Asthma Immunol* 2001; 87: 2–6
2. Behrendt H. Environmental factors as determinants of allergy development. *MMW Fortschr Med* 2006; 148: 32–33
3. Bärtsch P., Dvorak J., Saltin B. Football at high altitude. *Scand J. Med Sports* 2008; 28 Suppl I: iii–iv
4. Steiger T., Borelli S. Significance of climatic factors in the treatment of atopic eczema (Atopic Constitutional Neurodermitis). In: *Handbook of atopic eczema*. T. Ruzicka, J. Ring, B. Przybilla, eds. Springer, Berlin pp 1991; 420–428.
5. Schultze-Werninghaus G. Should asthma management include sojourns at high altitude. *Chem. Immunol Allergy* 2006; 91: 16–29.
6. Karagiannidis C., Hense G., Rueckert B., Mantel PY, Ichtors B., Blaser K., Menz G., Schmidt-Weber C. B. High-altitude climate therapy reduces local airway inflammation and modulates lymphocyte activation. *Scand J Immunol* 2006; 63: 304–310.
7. Guhring H. Complex high altitude climate therapy for children and adolescents with neurodermitis constitutionalis atopica. *Kinderärztl. Praxis* 1992; 60:150–155.
8. Engst R., Vocks E. High-mountain climate therapy for skin diseases and allergy: Mode of action, therapeutic results, and immunologic effects. *Rehabilitation (Stutg)* 2000; 39: 215–222.
9. Simon S., Weigl L., Disch R. Influence of high-altitude climate therapy on atopic eczema. *Allergologie* 1999 Suppl 1; S26–S28.
10. Hanifin JM, Rajka G. Diagnostic features of atopic dermatitis. *Acta Derm Venereol* 1980; Suppl 92: 44–47.
11. Williams H. C., Burney P. G., Hay R. J., Archer C. B., Shipley M. J., Hunter J. J., Bingham F. A., Finlay A. Y., Pembroke A. C., Graham-Brown R. A. The U. K. Working Party's Diagnostic Criteria for Atopic Dermatitis. I. Derivation of a minimum set of discriminators for atopic dermatitis. *Br J. Dermatol* 1994; 152: 735–741.
12. Ring J., Ruzicka T., Przybilla B. *Handbook of atopic eczema*. 2nd edition. 2006; Springer, Berlin, Germany
13. Global Strategy for Asthma Management and Prevention. updated December. Scientific information and recommendations for asthma programs. NIH Publication 2011; No. 02-3659
14. Kunz B., Oranje A. P., Labreze L., Stalder J. F., Ring J., Taieb A. Clinical validation and guidelines for the SCORAD index: consensus report of the European Task Force on Atopic Dermatitis. *Dermatology* 1997; 195: 10–19.
15. Pfab F., Valet M., Sprenger T., Toelle T. R., Athanasiadis G. I., Behrendt H., Ring J., Darsow U. Short-term alternating temperature enhances histamine-induced itch: a biphasic stimulus model. *J. Invest Dermatol* 2006; 126: 2673–2678.
16. Eberlein-König B., Schäfer T., Huss-Marp J., Darsow U., Möhrenschrager M., Herbert O., Abeck D., Krämer U., Behrendt H., Ring J. Skin surface pH, stratum corneum hydration, trans-epidermal water loss and skin roughness related to atopic eczema and skin dryness in a population of primary school children. *Acta Derm Venereol* 2000; 80: 188–191.
17. Pinnagoda J., Tupker R. A., Agner T., Serup J. Guidelines for transepidermal water loss (TEWL) measurement. A report from the Standardization Group of the European Society of Contact Dermatitis. *Contact Dermatitis* 1990; 22: 164–178
18. Fischer R., Lang S. M., Bergner A., Huber R. M. Monitoring of expiratory flow rates and lung volume during a high altitude expedition. *Eur J. Med Res* 2005; 10: 469–474

19. Huss-Marp J., Krämer U., Eberlein B., Pfab F., Ring J., Behrendt H., Gulyas A. F. Reduced exhaled oxide values in children with asthma after inpatient rehabilitation at high altitude. *J. Allergy Clin Immunol* 2007; 120: 471–472
20. Ware J. J., Snow K. K., Kosinski M., Gandek B. SF-36 Health Survey. Manual and interpretation guide. 1993; Boston, The Health Institute, New England Medical Center
21. Darsow U., Mautner V. F., Bromm B., Scharein E., Ring J. The Eppendorf Pruritus Questionnaire. *Hautarzt* 1997; 48: 730–733.
22. Schäfer T., Staudt A., Ring J. German instrument for the assessment of quality of life in skin diseases (DIELH). Internal consistency, reliability, convergent and discriminant validity and responsiveness. *Hautarzt* 2001; 52: 624–628.
23. Juniper EF, Guyatt GH. Development and testing of a new measure of health status for clinical trials in rhinoconjunctivitis. *Clin Exp Allergy* 1991; 21: 77–83
24. Eberlein B., Gulyas A., Schultz K., Lecheler J., Flögel S., Wolfmeyer C., Thiessen K., Gass S., Kroiss M., Huss-Marp J., Darsow U., Hollweck R., Schuster T., Behrendt H., Ring J. Benefits of alpine mountain climate of Bavaria in patients with allergic diseases and chronic obstructive pulmonary disease: results from the AURA study. *J. Investig Allergol Clin Immunol* 2009; 19: 159–161.
25. Eberlein B., Gulyas A., Schultz K., Lecheler J., Flögel S., Wolfmeyer C., Thiessen K., Jakob T., Hollweck R., Ring J., Behrendt H. Domestic allergens and endotoxin in three hospitals offering in-patient rehabilitation for allergic diseases in the alpine mountain climate of Bavaria – the AURA study. *Int J Environ Health* 2009; 212: 21–26.
26. Autio P, Komulainen P, Larni H. M. Heliotherapy in atopic dermatitis: a prospective study on climato-therapy using the SCORAD index. *Acta Derm Venereol* 2002; 82: 436–440.
27. Vocks E., Busch R., Fröhlich C., Borelli S., Mayer H., Ring J. Influence of weather and climate on subjective symptom intensity in atopic eczema. *Int J Biometeorol* 2001; 45: 27–33.
28. Petermann F., Gulyas A., Niebank K., Stübing K., Warschburger P. Rehabilitationserfolge bei Kindern und Jugendlichen mit Asthma und Neurodermitis. *Allergologie* 2000; 23: 492–502.
29. Grootendorst D. C., Dahlen S. E., van den Bos J. W., Duiverman E. J., Veselic-Charvat M., Vrijlandt E. J. L. E., O’Sullivan S., Kumlin M., Sterk P. J., Roldaan A. C. Benefits of high altitude allergen avoidance in atopic adolescents with moderate to severe asthma, over and above treatment with high dose inhaled steroids. *Clin Exp Allergy* 2001; 31: 400–408.
30. van Velzen E., van den Bos J. W., Benckhuijsen J. A., van Essel T., de Bruijn R., Aalbers R. Effect of allergen avoidance at high altitude on direct and indirect bronchial hyperresponsiveness and markers of inflammation in children with allergic asthma. *Thorax* 1996; 51: 582–584.
31. Rijssenbeek-Nouwens LH, Bel EH. High-altitude treatment: a therapeutic option for patients with severe, refractory asthma? *Clin Exp Allergy* 2011; 41: 775–782
32. Schmidt W. Effects of intermittent exposure to high altitude on blood volume and erythropoietic activity. *High Alt Med Biol* 2002; 3: 167–176
33. Simon H. U., Grotzer M., Nikolaizik K., Blaser M., Schöni H. High altitude climate therapy reduces peripheral blood T-lymphocyte activation, eosinophilia and bronchial obstruction in children with house-dust mite allergic asthma. *Pediatr Pulmonol* 1994; 17: 302–311.
34. Pürschel W., Pahl O. Behaviour of eosinophilic granulocytes, total IgE and allergen specific IgE antibodies in atopic neurodermitis during hospital treatment of the North Sea climate. *Z Hautkr* 1985; 60: 661–670.
35. Remes S., Korppi M., Remes K., Savolainen K., Mononen I., Pekkanen J. Serum eosinophil cationic protein (ECP) and eosinophil protein X (EPX) in childhood asthma: the influence of atopy. *Pediatr Pulmonol* 1998; 25: 167–174.
36. Kurowska-Stolarska M., Hueber A., Stolarski B., McInnes I. B. Interleukin-33: a novel mediator with a role in distinct disease pathologies. *J. Intern Med* 2011; 269: 29–35
37. Angelova-Fischer I., Hipler U. C., Bauer A., Fluhr J. W., Tsankov N., Fischer T. W., Elsner P. Significance of interleukin-16, macrophage-derived chemokine, eosinophil cationic protein and soluble E-selectin in reflecting disease activity of atopic dermatitis – from laboratory parameters to clinical score. *Br J Dermatol* 2006; 154: 1112–1117.
38. Masuda K., Katoh N., Okuda F., Kishimoto S. Increased levels of serum interleukin-16 in adult type atopic dermatitis. *Acta Derm Venereol* 2003; 83: 249–253.
39. Massimo T., Blank C., Strasser B., Schobersberger W. Does climate therapy at moderate altitudes improve pulmonary function in asthma patients? A systematic review. *Sleep Breath* 2014; 18: 195–206
40. Fieten K. B., Weststrate A. C., van Zuuren E. J., Bruijnzeel-Koomen C. A., Pasmans S. G. Alpine climate treatment of atopic dermatitis: a systematic review. *Allergy* 2015; 70: 12–2
41. Eberlein B., Huss-Marp J., Pfab F., Fischer R., Franz R., Schlich M., Leibl M., Allertseider V., Liptak J., Kriegisch M., Hennico R., Latotski J., Ebner von Eschenbach C., Darsow U., Buters J., Behrendt H., Huber R., Ring J. Influence of alpine mountain climate of Bavaria on patients with atopic diseases: studies at the Environmental Research station Schneesfernerhaus (UFS- Zugspitze) – a pilot study. *Clin Transl Allergy* 2014; 4: 17

3 Monitoring of persistent pollutants at the UFS

Korbinian P. Freier¹, Gabriela Ratz¹, Wolfgang Körner¹, Bernhard Henkelmann², Karl-Werner Schramm², Manfred Kirchner², Wolfgang Moche³, Peter Weiss³



Fig. 1: Measurement equipment at the UFS for sampling ambient air and deposition for the detection of persistent organic pollutants. Picture: KF, LfU

3.1 Summary

At the UFS, levels of persistent organic pollutants (POPs) in ambient air and deposition are determined since 2005. The results of these monitoring activities contribute to international control and regulation of such chemicals.

POP are emitted from anthropogenic burning, industrial processes or products, and are characterized by four properties: They are resistant to environmental degradation through chemical, biological, and photolytic processes, they are prone to bio-accumulate, and they are toxic to wildlife and humans. Moreover, most of these pollutants are semi-volatile and can be transported globally through the atmosphere in gaseous phase or attached to aerosols.

Monitoring devices are active air samplers characterized by low volume (30 L/min) and high volume (100 L/min) throughput and heated bulk deposition samplers. The samplers are equipped with filters and trapping cartridges, employing adsorbents which are conditioned to capture the target substances.

At intervals of three months, the sampling-cartridges are exchanged and analysed in laboratories. Gas chromatography coupled to mass spectrometry in combination with a stable isotope dilution analysis (SIDA) enables the accurate determination of the content of polychlorinated dibenzo-p-dioxins and dibenzofurans (PCDD/Fs), polychlorinated biphenyls (PCBs), organochlorine pesticides (OCPs), polycyclic aromatic hydrocarbons (PAHs) and halogenated flame retardants (HFRs).

¹ Bavarian Environment Agency, Augsburg, Germany

² Helmholtz Zentrum München – German Research Center for Environmental Health, Munich, Germany

³ Environment Agency Austria, Vienna, Austria

Results indicate the importance of cold-condensation effects. Even though air concentrations at the alpine summits are up to two orders of magnitude lower than in urbanized regions, deposition rates are similar or only slightly lower. Hence, to determine the impact of persistent chemicals into mountain-ecosystems the measurement of bulk deposition is essential. Source regions of the measured POPs can be identified as regional and global.

The monitoring enables a control of international chemical's legislation. It shows that concentrations in air for about 30% of OCP and several brominated flame retardants have been decreasing since 2005. However, for the majority of the pollutants significant reductions cannot be observed. For emerging compounds, the results proof the potential for persistency and long-range transport and show that regulation of individual chemicals often causes a substitution by chemicals which may have similar problematic properties.

3.2 The relevance of chemicals monitoring in the Alps

In an industrialized world, the unspoiled nature of the Alps and its sensitive ecosystems are no longer guaranteed. Air currents carry persistent organic pollutants (POPs) that originate from sources all over the globe into the Alpine region. Moreover, the Alps are located in the heart of Europe, one of the most industrialized and agriculturally active regions in the world. Due to the cooler temperatures in the Alps, pollutants can be deposited via condensation effects. In addition, the Alps act as a meteorological barrier: the accumulation of air masses causes the highest rainfall in Europe, which also scavenges pollutants from the air.

Especially for the Alps with unique ecosystems and a high biodiversity, the early detection of inputs of problematic substances is important. In addition, high-quality food and feed products originate from the Alps and a significant part of the regional and supra-regional water supply in Bavaria, Austria, Switzerland, northern Italy, Slovenia and the South of France relies on a high environmental quality in the Alps.

Substances that combine persistent, bioaccumulative and toxic properties (PBT) are particularly critical for humans and the environment:

Tab. 1: PBT-Characteristics

P	Persistency: The substance is persistent in the environment, so it is hardly degradable. Neither chemical-physical nor biological processes in water, soil or air are able to decompose the substance to any significant extent. The degradation is particularly difficult in cold climates.
B	Bioaccumulation: The substance is bioaccumulating. It prefers to concentrate in the tissue of living organisms. The reason for this is usually the solubility in fat of the substances and the lack of the possibility of excretion. Bioaccumulative substances accumulate strongly via the food chains, which also means that the pollutants occur in higher concentrations in particularly sensitive media, such as breast milk.
T	Toxicity: The substance is toxic to organisms. The toxicity of the substances depends mainly on their concentration and the duration of their action; in the case of carcinogenic or mutagenic substances, it is considered that a threshold cannot be established.

Into the environment, POP are emitted for example as active ingredients of pesticides or unintentionally, for example as by-products in combustion processes. Of all chemicals produced worldwide, more than 2,000 substances have the potential for PBT properties, which equates to several million tonnes per year of produced quantities (Schering et al., 2014).

Most of these chemicals remain where they are used as they have a low evaporation pressure and a low tendency to enter the atmosphere. However, the escape of very small amounts from products into the ambient air already leads to globally measurable contaminations. Contaminants from combustion processes, such as PCDD/Fs or PAHs, are directly emitted into the atmosphere.

The distribution of pollutants takes place via air currents and is coupled to the water cycle. Higher concentrations can be measured near the sources. However, because of their longevity and atmospheric long-range transport, pollutants reach remote areas. There, they can accumu-

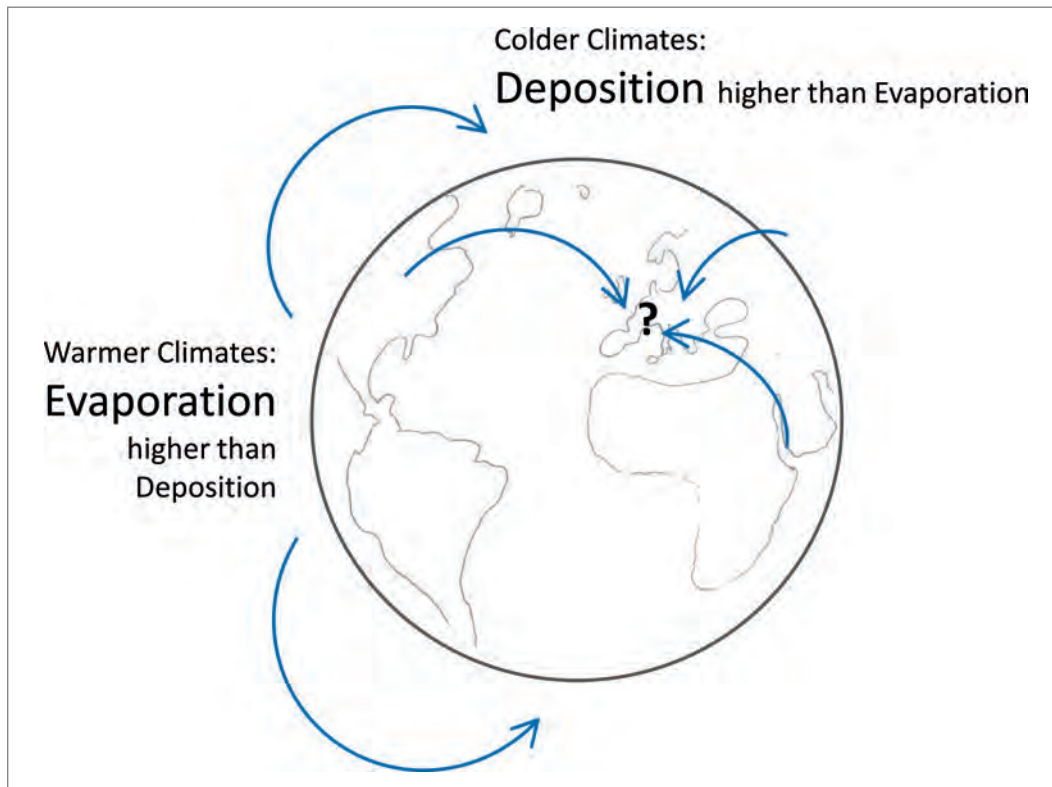


Fig. 2: Unevenly distributed temperatures over the globe lead to the phenomenon of “global distillation” (Wania and Mackay, 1996) at the poles and “cold trapping” in mountain areas such as the Alps. Source: KF, LfU

late through increased condensation, especially in cool regions such as the poles, where deposition is greater than evaporation (“global distillation”; see Fig. 2). Therefore, PBTs are detected even in areas where they have never been produced or used, such as in the Arctic or Antarctic.

Mountain ranges in the mid latitudes such as the Alps can be regarded as further hot-spots of deposition because they are located in the same latitudes as the sources but local temperatures are considerably lower and precipitation rates are in many cases higher. A comparison of the atmospheric loads of POPs in the Alps with those of the surrounding regions, shows that the alpine soils (see Fig. 3) are a considerable sink for POPs, which are mainly emitted from regions outside of the Alps (Belis et al., 2009). This indicates that the phenomenon of a cold trap is an underlying mechanism for the deposition in the Alps.

For most chemicals, the principle applies that a harmful effect begins at a certain concentration. However, if a pollutant does not degrade and additionally accumulates through the food chain, it is often only a matter of time before problematic concentrations in organisms are reached.

To cope with this risk on a precautionary basis, pollutants must already be recorded when entering ecosystems from the air. For this reason, to protect Alpine ecosystems, a monitoring of atmospheric concentrations and depositions rates of POPs was established in 2005 for the Alpine region under the project MONARPOP (Monitoring Network in the Alpine Region for Persistent and other Organic Pollutants, Federal Ministry of Agriculture, Forestry, Environment and Water Management, 2009). Up to date, this POPs monitoring is continued at the UFS and in parallel at the Sonnblick Observatory (SOB) in Austria within the projects called PureAlps (till 2015 also the monitoring station at Weissfluhjoch/Switzerland was part of the projects). Considering a mountain range in the mid latitudes, the gathered time series are worldwide unique in their duration and extent.



Fig. 3: The contents of POPs in the alpine soils indicate that from a global perspective the Alps are a sink of pollutants. Even if the concentration levels in the soils are at the lower range compared to other comparable soils in central Europe, the Alps cannot be regarded as uncontaminated. Picture: Robert Traidl, LfU

If new POPs are detected in the environment, only international measures are able to diminish concentration levels and deposition loads substantially. Additionally, regulated POPs need to be regularly monitored in order to evaluate if the applied measures are effective in reducing loads. With its results, the monitoring at the UFS delivers important data on emerging and well known POPs. This contributes to the further development and effectivity control of chemicals legislation such as REACH⁴ of the European Union and the international Stockholm Convention on POP.

3.3 Active sampling of persistent pollutants in ambient air

Ambient air samples are taken at the UFS in order to be analysed for a huge number of individual POPs (see Table 2). These include PCDD/Fs, PCBs, OCPs, PAHs and HFRs.

Tab. 2: Chemicals which are focus of the monitoring

Class of substances	Examples	Sources
Organochlorine pesticides (OCP)	DDT and derivatives Lindane Hexachlorobenzene Endosulfane	Insecticide Insecticide and wood preservatives Fungicide and combustion processes Insecticide
Polycyclic aromatic Hydrocarbons (PAH)*	Benzo [a] pyrene Phenanthrene	Combustion processes
Polychlorinated dibenzo-p-dioxins and dibenzo-furans (PCDD/F)	2,3,7,8-TCDD (Seveso dioxin)	Combustion processes and by-product of chemical syntheses
Polychlorinated biphenyls (PCB)	PCB 126 (dioxin-like PCB) Indicator PCB: PCB 28, 52, 101, 138, 153, 180	Plasticizer, flame retardant, insulating oil, combustion processes
Halogenated flame retardants (HFR)*	Polybrominated diphenyl ethers (PBDE), e.g. DecaBDE, Hexabromocyclododecane (HBCD), Decabromodiphenylethane (DBDPE)	Flame protection in plastics and textiles Flame protection in building-insulation Substitute for decabromodiphenyl ether
Perfluorinated surfactants*# and Fluorotelomer alcohols*	Perfluorooctanoic acid (PFOA)	Water-repellent coatings
Mercury*#		Chloralkali electrolysis, combustion of stone and Brown coal

* substances marked with an star have not been continuously measured since the beginning of the monitoring or are only part of focus projects such as POPAlp, EMPOP and PureAlps

substances marked with an hash are only measured in deposition

Most POPs are semivolatile organic compounds (SVOCs) with a vapour pressure between 10 Pa and 10^{-5} Pa at thermodynamic standard temperature (25 °C), representing a range of boiling temperatures from 240–260 °C to 380–400 °C, at standard atmospheric pressure. In spite of their low vapour pressures SVOCs occur in the atmosphere at least partially in the gaseous phase. Any distribution ratio from 100% in the gaseous phase to complete attachment to aerosols is possible depending on the vapour pressure of the compound, ambient air temperature and aerosol concentration. Therefore, any sampling method for the assessment of ambient air concentrations of POPs must collect total suspended aerosols as well as the POPs in the gaseous phase.

⁴ Registration, Evaluation, Authorisation and Restriction of Chemicals

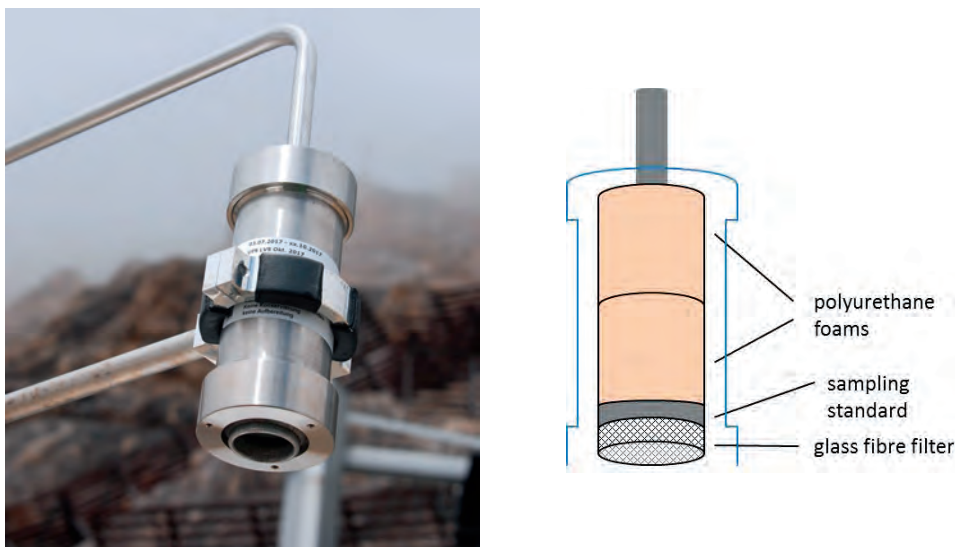


Fig. 4: Filter cartridge for sampling halogenated flame retardants (left) and sketch depicting the assembly. Picture: KF, LfU

For this purpose ambient air is continuously sucked by a pump unit through a sampling cartridge equipped with a glass fibre filter at the open side at the bottom to collect the particulate air components (Fig. 4). The used filter has a separation ratio of 99.8% for particles with aerodynamic diameters $> 0.3 \mu\text{m}$ (VDI 2464 part 2). After passing the glass fibre filter, gaseous air components of organic compounds boiling at high temperatures are adsorbed on the surface of a hydrophobic material. This adsorbent should have a large surface area and a high porosity with low resistance to the air flow and is packed in a sleeve made either of glass or stainless steel.

In the samplers at UFS, two different materials are used: In the cartridges for the OCP samples a granulate of styrene-divinylbenzene-copolymer (XAD-2 resin), packed into a glass sleeve, is used as described in detail in the German guideline VDI 2464 part 4.

For assessing ambient air concentrations of HFRs, PCDD/Fs and PCBs the sampling cartridge is equipped with a steel sleeve with two cylindrical polyurethane foams with open pores, according to the guideline VDI 2464 part 3 (see Fig. 1, foams: height: 50 mm, diameter: 60 mm) for HFRs and VDI 3498 part 1 for the PCDD/F and PCB. The PU foams are made of toluylenediisocyanate (TDI) and polyoxypropylentriol with a density of 25 kg/m^3 or TDI polyether soft foam with a density of 33 kg/m^3 .

Sampling of ambient air concentrations is done separately concerning the classes of substance (a) PCDD/Fs and PCBs, (b) OCPs and PAHs, and (c) HFRs. The measured volumes are all referred to standard conditions of 0°C and 1013.25 hPa .

For PCDD/Fs and PCBs, due to very low target concentrations of femtograms per cubic meter ambient air, a high volume sampler (HVS) is used, which is operated at a flow rate of 100 L min^{-1} ($6 \text{ m}^3 \text{ h}^{-1}$). Due to the pressure drop which is caused by the air drawn into the cartridge, under the high-alpine meteorological conditions at UFS, water vapour is condensating and immediately freezing. To prevent this effect, the filter cartridges are equipped with heated inlet tubes to avoid freezing (Fig. 5).

For OCPs/PAHs and HFRs low volume samplers (LVS) are used with a flow rate of 30 L min^{-1} ($1.8 \text{ m}^3 \text{ h}^{-1}$). The sampling is done separately for OCPs and HFRs in order to obtain two separated samples, because extraction, clean-up and measurement are performed separately for these two classes of POPs. The sampling of OCPs follows the guideline VDI 2464 part 4 and the sampling of HFRs is performed according to VDI 2464 part 3.



Fig. 5: In the front/top: Filter cartridges for sampling PCDD/Fs which are equipped with heated inlet tubes to avoid freezing (the mouth of the sampling system facing downward). Behind: Funnel adsorber deposition samplers. Picture: GR, LfU

Prior to use, all sampling materials must carefully be cleaned to avoid any contamination with the compounds to be determined: Glass fibre filters are heated for at least 5 h to 450 °C, then wrapped in aluminum foil and stored in a closed wide-neck flask until used for sampling. XAD-2 resin and PU foams are generally precleaned by extraction with those solvents which are used to extract the POPs of interest after sampling. Although it is strongly recommended to purchase high purity XAD-2 resin, precleaning of the whole glass sleeve filled with XAD-2 resin by Soxhlet extraction with acetone/n-hexane 1/3 (v/v) is necessary for the analysis of OCPs (VDI 2464 part 4).

Nevertheless, for each series of air samples or each single sample a corresponding field blank sample cartridge must be prepared in exactly the same way as the sample cartridge(s), transported to the sampling site, briefly opened to simulate the exchange of a cartridge, and stored closed in the darkness (e. g. wrapped in aluminum foil) either at the sampling site or in a refrigerator in the laboratory during the whole sampling period. Afterwards this field blank sample is processed and analysed in parallel to the corresponding air sample(s) in the same way to detect and quantify possible field blank values of the pollutants of interest.

If a field blank value is quantifiable, the limit of quantification (LOQ) is twice the field blank value referred to the sampling volume of each corresponding sample (VDI 2464 part 3). To be accepted as quantifiable, the value (absolute mass) of a compound in an air sample must be at least twice the corresponding field blank value.

By using automated control-units (DPA 96 MV, DIGITEL Elektronik GmbH, Austria) which are accessible via internet, the daily status of the HVS and LVS is controlled remotely. In the same way the throughput of air and additional metadata can be downloaded at the end of each sampling period.

In order to investigate the characteristics of different air masses, the HVS and LVS are equipped with a multi-channel system which can be used to sample four cartridges in one sampling period. For example, between 2006 and 2015 three predefined source regions have been investigated: northwest (NW), northeast/east (NE) and southwest/south/southeast (S). If the origin of the air masses was unspecified or was prevailing less than three days in one of the regions, it was classified as undefined and a fourth cartridge was used (UD) (Kirchner et al., 2016). The four available channels were selected on a daily basis after including the results of meteorological calculations using the FLEXPART model. The channel selection can be done automatically using computing-on-demand for the FLEXPART calculation and a subsequent upload of control commands to the automated control-units of the HVS and LVS.

3.4 Sampling of persistent pollutants in deposition

Deposition is the transfer of particles and molecules from the atmosphere to solid and liquid surfaces and thus a main pathway for the entrance of airborne persistent pollutants into terrestrial and aquatic ecosystems. Atmospheric deposition occurs predominantly in precipitation periods (wet deposition) but as well during dry weather conditions (dry deposition). In theory, atmospheric deposition is the sum of deposition consisting of gases which adsorb to surfaces, gases which are dissolved in precipitation, non-sedimenting particles which are scavenged by precipitation and sedimenting particles. In practice, a bulk deposition sampler does not completely cover the atmospheric deposition, but collects fractions of it, such as the gases which are dissolved in precipitation, the particles which are scavenged by precipitation and the major fraction of sedimenting particles.

One of three established sampling methods for bulk deposition of persistent organic pollutants is the funnel adsorber method which is standardized for PCDDs/PCDFs (VDI 2090-2) and low volatile PAHs (VDI 4320-4). These guidelines recommend an exposure period of 30 days.

To sample deposition of POPs under extreme climatically conditions, specially constructed funnel adsorber deposition samplers (Fa. Kroneis GmbH, Austria) are used (Fig. 6). These are standard funnel adsorber deposition samplers, following the guidelines DIN 19739-1, VDI 2090-2 and VDI 4320-4, with a circular area of 0.053 m² which are additionally equipped with isolation, heated glass funnels to melt snow, and a heated cartridge chamber to avoid freezing and frost shattering. The precipitation flows from the funnel through a glass cartridge equipped with a glass wool filter and a hydrophobic adsorbent (see Fig. 7), and ends up in a collecting tank in



Fig. 6: Heated funnel adsorber deposition samplers which are used at the UFS. Picture: KF, LfU

order to allow the quantification of precipitation. The adsorbent is the same material as used for active air sampling: A granulate of high purity, pre-cleaned XAD-2 resin.

As for ambient air sampling the parallel exposure and processing of field blank samples is mandatory to fulfil high quality demands of the analytical results. To quantify the transfer of persistent pollutants from the atmosphere into adjacent compartments the analytical data are expressed as deposition rates which is given in mass flow density (e. g. $\text{pg m}^{-2} \text{d}^{-1}$).

As sampling-period for active-air sampling and deposition sampling three months are chosen. This makes sure that enrichment of POPs in the adsorbents is sufficient to achieve measurements well above limits of quantification. After three months of exposure, filter cartridges are exchanged by hand and are transported into the laboratory for chemical analysis.

3.5 Chemical analysis

The chemical analysis of the various investigated compounds is principally based on gas chromatography coupled with mass spectrometry in combination with stable isotope dilution analysis (SIDA). In the following, the clean-up and analysis of OCPs is used as an example for the methodology. The analytical procedures for PCDD/Fs and HFRs are described in the respective VDI guidelines⁵.

Sampling and analytical method for quantitative determination of 31 OCPs in ambient air is performed according to VDI 2464 part 4⁶. Using a sampling system, the ambient air is passing through a filter and a glass cartridge filled with an Amberlite® XAD-2® adsorbent (poly-aromatic resin) adsorbing the hydrophobic compounds such as OCPs. Adding of sampling standards that are not expected to occur in ambient air and their recoveries allow to monitor the sampling process errors. Analytical procedure based on sample extraction and two clean-up steps using a stable isotope dilution assay (SIDA) enables the trace analysis of target compounds by gas-chromatography high resolution mass spectrometry (GC-HRMS).



Fig. 7: The interior of the funnel adsorber sampler: in the upper part of the cartridge there is included glass wool in order to collect particulate matter, the white material in the lower part is the adsorbent (XAD-2 resin). Picture: GR, LfU

⁵ PCDD/Fs: VDI 3498 part 1; HFRs: VDI 2464 part 3

⁶ VDI 2464 part 4 (draft): 2017-12, Ambient air measurement – Indoor air measurement – Measurement of persistent or organic pollutants (POPs) with GC/HRMS, Beuth Verlag GmbH, Berlin

Before exposure, the filter cartridges are carefully prepared to fulfil high quality standards for trace analyses. Prior to cartridge preparation, the entire glass equipment including glass wool and adsorbent is carefully cleaned by the specified purification process to ensure the prevention of contamination. 50 g of Amberlite® XAD® adsorbent are placed in the glass sampling cartridge equipped with a glass frit. After filling, a plug of glass wool was pressed on the top of the adsorbent. Three sampling standards ($^{13}\text{C}_{12}$ -PCB60, $^{13}\text{C}_{12}$ -PCB127, $^{13}\text{C}_{12}$ -PCB159) are added in an amount of 1000 pg for each at least three positions on the bed of the adsorbent. The filled glass cartridge is sealed with a glass stopper and a glass case (Fig. 8). The cartridge for field blanks is prepared in the same way.

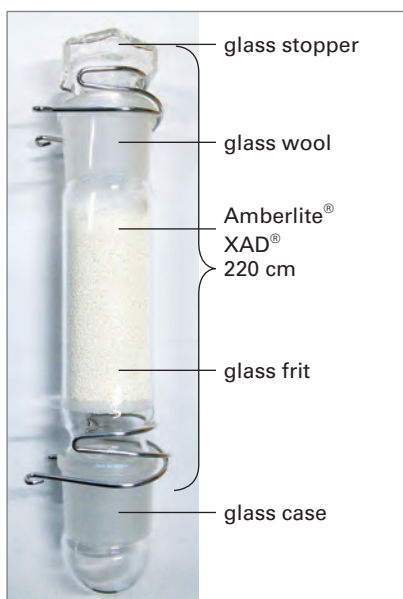


Fig. 8: Glass sampling cartridge filled with Amberlite® XAD® adsorbent.
Picture: GR, LfU

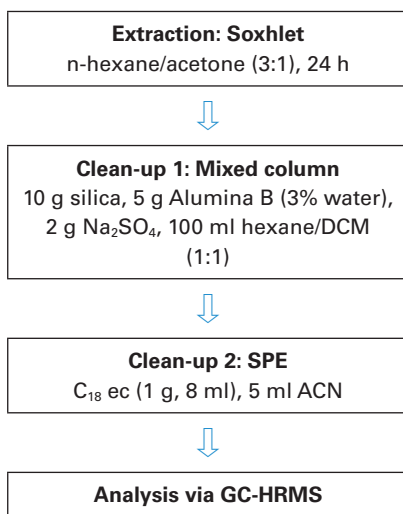


Fig. 9: Flow chart for OCP analysis.

After exposure of the cartridge in the field at the UFS, the outer wall of the exposed immission glass cartridge is cleaned with the extractant prior to extraction. After the spiking of the glass wool with stable isotopically labeled standards (^{13}C - and ^2H -), the cartridge containing filter, glass wool, and adsorbent is placed in a Soxhlet apparatus, and extracted with a mixture of 3 volumes of n-hexane and 1 volume of acetone for 24 hours at minimum rate of two cycles per hour. Sample extract is concentrated to 1 mL using a rotary evaporator and underwent two clean-up procedures (Fig. 9).

The first clean-up is performed using a multiple layer column containing 10 g neutral silica (treatment at 450 °C), 5 g Alumina B (deactivated with 3% water), 2 g anhydrous sodium sulphate and a mixture of 1 volume of n-hexane and 1 volume of dichloromethane as eluent. The column absorbents are conditioned with 60 mL eluent solvent prior to elution. The eluate is then solvent-exchanged to acetonitrile, concentrated to approx. 0.5 mL and further purified using a selective solid phase extraction (SPE) with octadecyl modified endcapped silica phase (C₁₈ec) (clean-up 2). The conditioning and elution is then conducted each with 5 mL acetonitrile. After concentration of the eluate to 0.5 mL, the sample is solvent-exchanged to 20 µL n-nonane in an inserted vial. The final concentration to 20 µL acetonitrile is performed under a nitrogen stream at 45 °C. Afterwards, the recovery standard is added to the sample for calculation of recovery of surrogate standards.

After the successful clean-up, the samples are transferred to a GC-HRMS system. Analysis of OCPs in ambient air samples is performed using a gas chromatograph equipped with a 30 m capillary column Rtx-CLPesticides2 (0.25 mm ID, 0.2 µm df, Restek GmbH, Bad Homburg). The sample volume of 0.5 µL is injected by means of GERSTEL cooled injection system (GERSTEL GmbH & Co. KG, Muelheim an der Ruhr) in splitless mode at 120 °C ramping with 12 °C/sec to 280 °C hold for 5 min. The following oven temperature was used: 60 °C/1.5 min, rate 12 °C/min up to 140 °C, rate 6 °C/min up to 300 °C/10 min. The GC to MS transfer line and ion source temperature was set at 300 °C and 260 °C, respectively. A total of 31 OCPs are quantified in electron impact ionization mode (EI+) at 47 eV operating in selective ion monitoring mode (SIM). Two or three exact masses (m/z) according to VDI 2464 part 4 are monitored for each target compound using a lock and cali-

bration mass obtained from perfluorophenanthrene (FC-5311). The instrumental method is calibrated using response factors for each analyte integrating sampling, surrogate and recovery standards.

3.6 Time series of persistent pollutants at the UFS

In general, several dozen individual compounds with PBT properties are measured above the analytical limit of quantification at the UFS. These include currently released flame retardants and combustion products. Also measured are OCPs, although these have not been allowed to be used in Europe for a long time.

Referring to the insecticide DDT and its transformation products as an example, we see that these substances can still be detected in every single sample, although their use in Europe has been prohibited since the 1990s. At the beginning of the monitoring in 2005, as part of the MONARPOP project (Federal Ministry of Agriculture, Forestry, Environment and Water Management, 2009), only 21 countries worldwide, mainly in tropical Africa and India, used DDT to combat malaria (UNEP, 2007). The ratio of DDT and its transformation products, as determined at the UFS, indicates that the substances are reaching the Alps from sources in Europe and in the tropics (Kirchner et al., 2016). This means that aged DDT still escapes from the former main European areas of application, for example from the soils of the Po Valley in northern Italy. Recently, “young” DDT is registered from tropical countries like India.

The measured substances are only detectable at low concentrations in the air on the Alpine summits. Values in urban or industrial air are three to a hundred times higher (Kirchner et al., 2018; Kirchner et al., 2016). Compared to Arctic regions, the concentrations at the Alpine peaks, with exceptions to substances such as pentachlorobenzene and BDE 209, are on a similar scale.

The pollutants reach the northern and central Alps to one third by air-masses from the Mediterranean region and another third from northwestern source regions with maritime background (Fig. 10). About 15 percent of the air masses reach the Alps from the northeast, the remaining air masses cannot be assigned to any exact source-region (Kirchner et al., 2016).

The northeast air masses are usually the most heavily contaminated with polychlorinated biphenyls (PCBs) and polychlorinated dioxins (PCDD/F) (Kirchner et al., 2018). However, this origin occurs less frequently, because the Alps are less influenced by air blowing from northeast.



Fig. 10: Origin of air-masses and source dependent differences in concentrations of persistent organic pollutants (2006–2015). Source: Mario Wilhelm, LfU

Therefore, about all of the source-regions, with the exception of UD (direct transport from the Atlantic), contribute approximately equally to the entry of these hardly degradable pollutants. Air masses from the Mediterranean and the NE are more heavily polluted with organochlorine pesticides, especially when compared to Atlantic air masses. These different concentrations with respect to the source-regions of flow confirm that some of the transported pollutants are residues from regional European sources.

Significant decreases in air concentrations for the period 2006 to 2015 can be reported for about one-third of organochlorine pesticides (see Table 3). This demonstrates the efficacy of the ban on the production and use of pollutants such as heptachlor and trans-chlordane (banned since 2004), lindane and pentachlorobenzene (since 2009) by the Stockholm Convention.

Tab. 3: Pollutants for which a reduction in concentrations can be demonstrated (statistically significant). „Current concentration level“ corresponds to the annual mean value of the 2015 measurements of Sonnblick, Weissfluhjoch and Zugspitze.

Substance/Class of substances	Decrease 2006–2015	Current concentration level in Alpine ambient air [picogram per cubic meter of air]
α -HCH	–55 %	5,51
Lindane (γ -HCH)	–68 %	4,92
Pentachlorobenzene	–24 %	39,31
Pentachloroanisole	–47 %	6,13
4,4'-DDT	–56 %	0,67
Chlordane (trans + cis)	–51 %	0,77
Heptachlor (+ cis-heptachlorepoxyde)	–45 to –50 %	0,97
Endosulfan-I + II	–93 %	3,41
2,4,4'-tribromodiphenyl ether (BDE 28)	–64%*	0,14

* For BDE 28, only measured values are available at the Zugspitze from 2012 on – therefore the percentage decrease refers to the years between the end of 2012 and mid-2016 (not yet statistically hedged).

Even the major component of DDT (4,4'-DDT) shows a decline in the period from 2006 to 2015, which is over 50 percent. Most notably, a decline of over 93 percent between 2006 and 2015 for the insecticide endosulfane was observed which has been included in the Stockholm Convention since 2011, but has been banned in the European Union since 2005 (Fig. 11). This decrease demonstrates that, even before the entry into force of the global ban, restrictions at the level of the European Union are able to reduce air concentrations to a relevant extent.

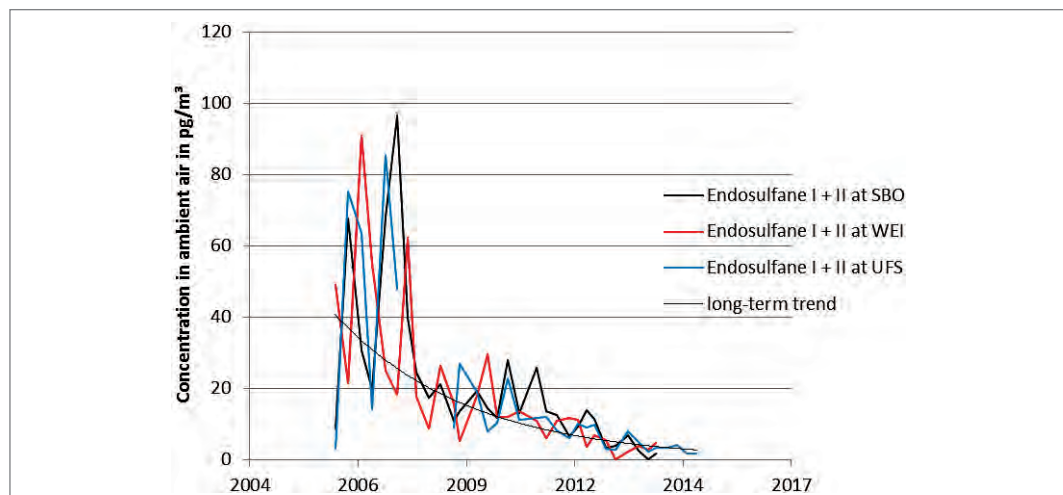


Fig. 11: Time series of ambient air-concentrations of endosulfane I and endosulfane II at Sonnblick Observatory (SBO), Weissfluhjoch (WEI) and UFS.

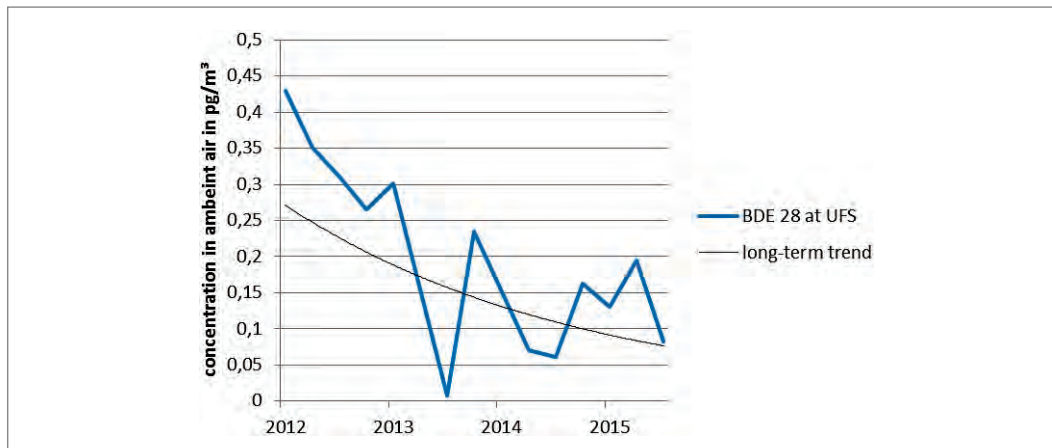


Fig. 12: Time series of ambient air-concentrations of BDE 28, a halogenated flame retardant of the first generation

A tendency for decreases in ambient air concentrations – probably due to EU legislation – is also visible for HFR of the first generation. For instance, 2,4,4'-tribromodiphenyl ether (BDE 28), most volatile component of the technical pentabromodiphenylether used as flame retardant, is very probably decreasing (see Fig. 12). Penta- and octabromodiphenyl ethers have been banned in new products in the EU since 2004. The use of decabromodiphenyl ether has been severely restricted in electrical and electronic equipment since 2006. However, the measurement series from 2013 is still too short to be able to derive statistically reliable statements.

The same can be stated for the deposition of BDE 209, the main component of decabromodiphenyl ether (DecaBDE), which was included by the European Union in the list of substances of very high concern under the REACH Regulation. Since May 2017, DecaBDE is also part of the Stockholm Convention. Between the first measurements of BDE 209 in the deposition at the Zugspitze 2008 and the last evaluated data from 2016 there is a decrease of about 90 percent (Freier K. P., Kirchner M., Denner M., Ratz G., Weiss P., Körner W., Moche W. (2019): Monitoring of Persistent Pollutants in the Alps, Bavarian Environment Agency & Environment Agency Austria; https://www.bestellen.bayern.de/shoplink/lfu_all_00161.htm).

More problematic are substances that are internationally regulated but do not decrease visibly in the past ten years referring to ambient air-concentrations and deposition, such as PCDD/Fs and PCBs.

With the beginning of the 1990s, the installation of appropriate exhaust gas filters in waste incineration and industrial plants reduced PCDD/F concentrations in metropolitan areas by about 80 percent (UBA, 2014). PCBs are also produced to a limited extent in combustion processes, but they were additionally used in large quantities as softeners and insulating oils until the end of the 1970s, so they still escape from buildings (joint sealants, paints) and improper disposal of transformers and capacitors. Since 2004, PCDD/Fs and PCBs are part of the Stockholm Convention.

From the beginning of the measurements in 2006, decreasing PCDD/F and PCB concentrations could be ascertained for the Alps, which until around 2010 proved the success of the mitigation measures. However, the concentration decrease stagnated after 2010 and in some cases substances even increased again from 2013 onwards. The same pattern is also shown for the input of PCDD/F by precipitation: Levels of deposited PCDD/Fs are similar to those deposited in 2006 (Fig. 13). There are also marked peaks visible that are four times higher than the usual deposition rates. The reasons of for these maxima could not be clarified so far.

Overall, PCDD/F and PCBs continue to enter the Alpine ecosystems, with a trend towards increasing levels of airborne concentrations in recent years. For this reason, it must be clarified on an international level, where similar effects can be observed, what causes the renewed increase in air concentrations, and whether further action is required. The extent to which living organisms in the Alps are burdened by these entries is investigated in the PureAlps projects 2016–2019 (Freier et al. 2019).

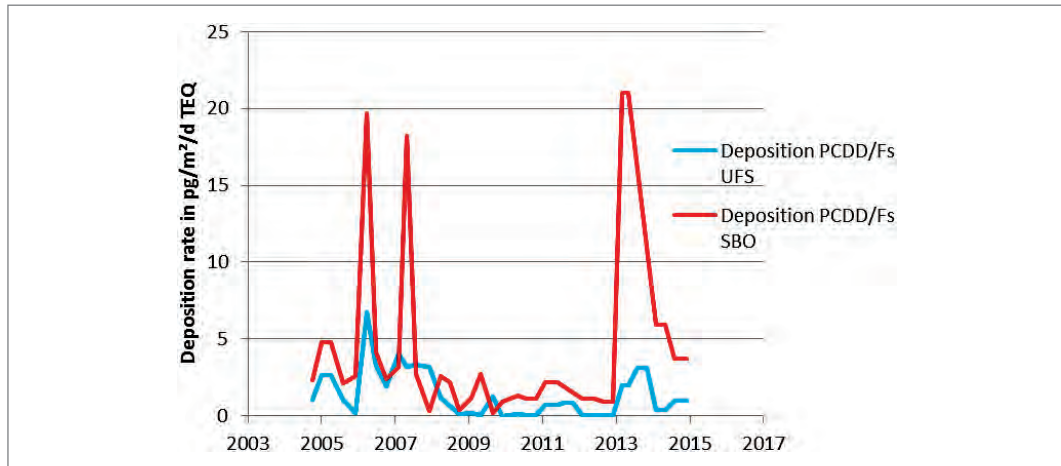


Fig. 13: Time-series of deposition of dioxins and furans (given as sum in toxicity-equivalents, TEQ)

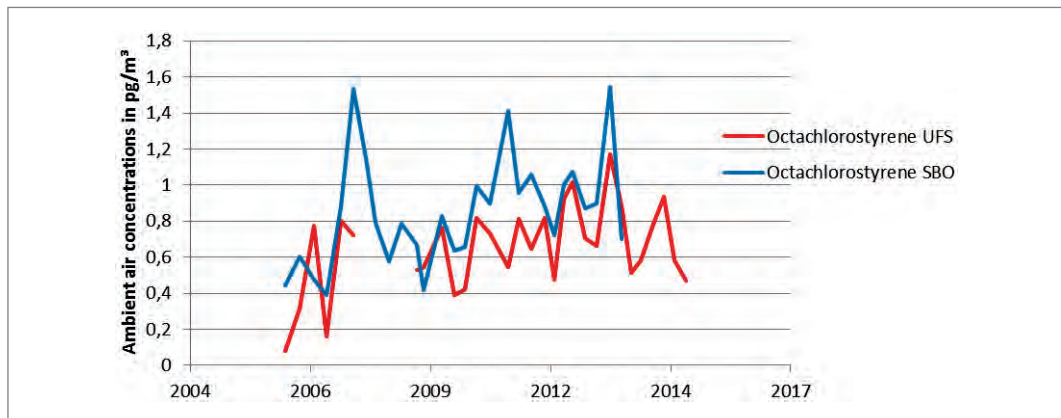


Fig. 14: Time series of Octachlorostyrene from UFS and Sonnblick Observatory (SBO)

From the group of OCP and related compounds, octachlorostyrene (OCS) can be identified as a possible problem case, a substance that has hitherto been neither nationally nor internationally regulated. Since the beginning of the program, ambient air concentrations of OCS have been steadily increasing at the alpine monitoring stations (see Fig. 14): The increase of 33% over the past ten years is statistically significant.

OCS is classified as a PBT substance (UBA, 2016) and it is also suspected that it acts as a hormone for certain organisms (WHO, 2013). OCS results from the extraction of aluminum and magnesium in chlorine chemistry and the combustion of plastics containing chlorine. Concerning the deposition in the alpine area, it is currently completely unclear, from which sources the OCS originates. The simultaneous measurement of high concentrations of penta- and hexachlorobenzene, however, suggests that the source of all three substances is the production of highly chlorinated solvents, such as perchloroethylene and carbon tetrachloride (Weber et al., 2011; Zhang et al., 2015). Therefore, it would be desirable for OCS to record internationally the main sources and quantities emitted in order to develop measures to prevent further increases in ambient air concentrations.

3.7 Detecting emerging pollutants

In the framework of chemical regulations, particular attention must be paid on risks due to irreversible pollutant inputs. Therefore, PBT substances that are considered novel pollutants, so-called emerging pollutants, are also being investigated within the chemicals monitoring at the UFS.

Emerging pollutants are only recently observed in the environment and are not or only partially regulated. The present monitoring should help to make the risk of these novel chemicals more manageable.

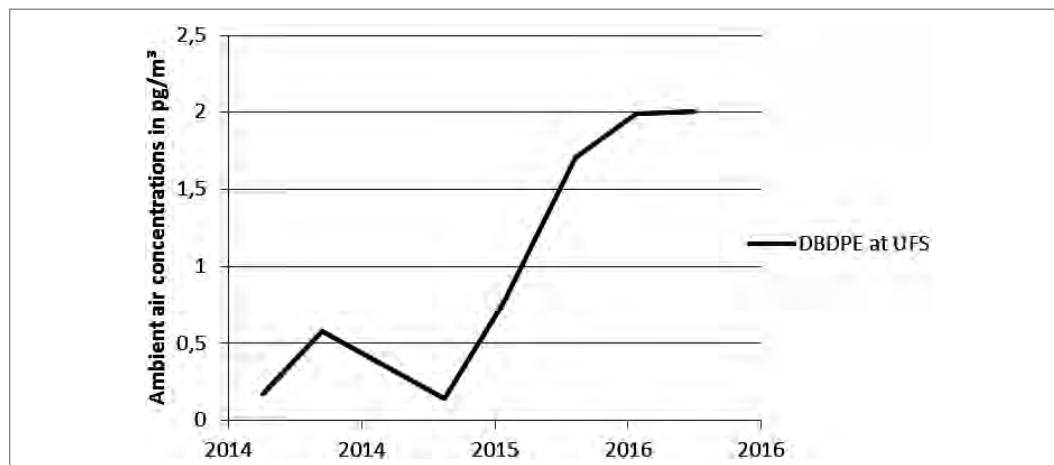


Fig. 15: Time-series of the halogenated flame retardant Decabromodiphenylethane (DBDPE)

Increasing demands on the fire protection of materials and at the same time increasing production volumes of plastics lead to a worldwide increasing use of novel flame retardants. Many of them are evaluated as PBT substances (Shaw et al., 2010), but so far are neither nationally nor internationally regulated. Therefore, new flame retardants are also monitored at the UFS. A total of eight of these novel substances have already been detected until 2017 in the air, seven also in precipitation.

Particularly noteworthy for the novel substances is decabromo-diphenyl-ethane (DBDPE). Several thousands of tons of this flame retardant were introduced into the EU back in 2001, and since the bans and restrictions on older flame retardants, such as DecaBDE, it has been increasingly used as a substitute. The reason for the use as a substitute lies in its similar properties compared to the previously used DecaBDE, which also suggests the similar chemical structure. This similarity extends to properties that affect the environmental risk. Despite already proven accumulation in seagulls and other animals (Betts, 2009), the decision on the final assessment of DBDPE has been postponed by the European Chemicals Agency (ECHA) to 2019 due to insufficient data (ECHA, 2016).

Ambient air concentrations at the UFS for DBDPE show strongly increasing tendencies (Fig. 15). In addition, in the deposition at the UFS DBDPE occurs in the highest concentrations of all flame retardants, the emerging pollutant has already overtaken the formerly dominant DecaBDE. The measurements at the UFS give evidence that DBDPE does not degrade appreciably in the atmosphere and undergoes long range transport.

The increase of DBDPE shows that effective restrictions for HFRs of the first generation such as BDE 28 (Fig. 12) have translated into a more intense use of non-regulated HFRs of a second generation with similarly problematic properties. This suggests that a successful chemicals regulation has to encompass both, the forcing of a phase-out of problematic substances and the promotion of alternatives which avoid an increased usage of substitutes which also reveal PBT-properties. In the best case, the promotion of alternatives not only covers a direct substitution by other chemicals but as well a technological shift, which makes the further demand of similar substances superfluous (Science for Environment Policy, 2017).

3.8 Perspectives of chemicals monitoring in the Alps

The results of the ten-year monitoring of PCDD/Fs, PCBs, and OCS show that there are currently higher levels of exposure to compounds, which are produced as undesirable by-products in the combustion of chlorine-containing materials and as well in chlorine-chemical industries. In order to determine whether the sources of these pollutants are located in Europe or in other areas, air masses must be sampled separately for their regional or global origin. Therefore, a pilot study at the UFS is testing whether it is possible to record air masses of the free troposphere separately from regional, ground-level air masses coming from nearby regions (Sig-



Fig. 16: Wintery atmospheric inversion indicated by the low-level clouds in the background. This represents a situation where the UFS is decoupled from lower atmospheric levels. Picture: KF, LfU

mund et al. 2019). The prerequisite for this is a procedure that automatically differentiates two cases: one case, where the atmosphere around UFS is definitely decoupled from the mixing-layer (see Fig. 16) and a second case, where the UFS is located inside the mixing-layer.

Climate change, as a core issue of the 21st century, is also relevant for the environmental risks due to chemicals: the question is to what extent changes in temperature and precipitation will affect the future input of pollutants in the Alpine region. It is also of concern that the use of pesticides in agriculture will likely increase as population in developing and emerging countries continues to grow, and climate conditions may deteriorate in Europe at the same time. In the case of persistent chemicals, this could also affect the cold trapping phenomenon in the Alps. Therefore, for this unique mountain range with its original ecosystems, a global, early commitment to a more environmentally sound economy would be desirable, which also takes into account the environmental and health risks of chemicals.

Another opportunity for the future of chemicals monitoring activities at the UFS may be the combination of continuous measurements of ambient air concentrations of emerging POPs and interval-monitoring of bioaccumulation in wildlife and humans of the surrounding areas. In this way, it would be possible to give evidence of two important characteristics of POPs at the same time: the monitoring at the UFS delivers insights on persistency and long-range transport of chemicals; the monitoring of wildlife and humans allows assessing the level of bioaccumulation under the given deposition rates. For instance, the Partnach-river below the UFS is characterized by karst hydrogeology and is well defined concerning its catchment where the UFS is situated within (Rappl et al., 2010). The accumulation of POPs in brown trout in the Partnach-river (Fig. 17) is therefore directly related to the deposition rates which are monitored at the UFS (Freier et al. 2019).



Fig. 17: Brown trout in a pristine alpine catchment is an indicator of background contamination with POP from atmospheric deposition. Picture: © Niklas Winter

Acknowledgements

The monitoring of persistent pollutants at the UFS has been financed by the European Union Alpine-Space Programme within the project MONARPOP and the Bavarian State Ministry for Environment and Consumer Protection within the projects POPAlp, EMPOP, VAO II and PureAlps.

The authors appreciate the irreplaceable and pleasant support of the personnel of the UFS and of all people which have been active in the aforementioned projects. Special thanks go also to the laboratory personnel of the Environment Agency Austria, the German Research Center for Environmental Health and the Bavarian Environment Agency for their reliable and high-qualitative work.

References

- Belis, C.A., Offenthaler, I., Uhl, M., Nurmi-Legat, J., Bassan, R., Jakobi, G., Kirchner, M., Knoth, W., Kräuchi, N., Levy, W., Magnani, T., Moche, W., Schramm, K.-W., Simončič, P., Weiss, P., 2009. A comparison of Alpine emissions to forest soil and spruce needle loads for persistent organic pollutants (POPs). *Environmental Pollution*. **157**, 3185–3191.
- Betts, K., 2009. Glut of data on “new” flame retardant documents its presence all over the world. *Environ. Sci. Technol.* **43**, 236–237.
- ECHA, 2016. Community rolling action plan (CoRAP). Case number A-009-2014. Accessed June 2017.
- Federal Ministry of Agriculture, Forestry, Environment and Water Management, 2009. MONARPOP Technical Report. Accessed May 2017.
- Freier, K.P., Kirchner, M., Denner, M., Ratz, G., Weiss, P., Körner, W., Moche, W., 2019. Monitoring of Persistent Pollutants in the Alps, Bavarian Environment Agency & Environment Agency Austria; https://www.bestellen.bayern.de/shoplink/lfu_all_00161.htm
- Kirchner, M., Jakobi, G., Körner, W., Levy, W., Moche, W., Niedermoser, B., Schaub, M., Ries, L., Weiss, P., Anritter, F., Fischer, N., Bernhard Henkelmann, B.H., Schramm, K.-W., 2016. Ambient Air Levels of Organochlorine Pesticides at Three High Alpine Monitoring Stations. Trends and Dependencies on Geographical Origin. *Aerosol Air Qual. Res.* **16**, 738–751.
- Kirchner, M., Moche, W., Jakobi, G., Körner, W., Freier, K.P., Ludewig, E., Schaub, M., Ries, L., Schramm, K.-W., Weiss, P., 2018. Air concentrations and deposition of dioxins and furans at three high Alpine monitoring stations: Trends and dependence on air masses. *submitted*.
- Rappl, A., Wetzel, K.-F., Buettner, G., Scholz, M., 2010. Dye tracer investigations at the Partnach Spring (German Alps). *Hydrologie und Wasserbewirtschaftung/Hydrology and Water Resources Management-Germany*. **54**.
- Scheringer, M., Fantke, P., Weber, R., 2014. How can we avoid the lock-in problem in the substitution of hazardous chemicals used in consumer products? *Organohalogen Compounds*. **76**, 914–917.
- Science for Environment Policy, 2017. Persistent organic pollutants: towards a POPs-free future; Future Brief 19. Brief produced for the European Commission DG Environment, Science Communication Unit, U.W.E., Bristol.
- Shaw, S., Blum, A., Weber, R., Kannan, K., Rich, D., Lucas, D., Koshland, C.P., Dobraca, D., Hanson, S., Birnbaum, L.S., 2010. Halogenated flame retardants: do the fire safety benefits justify the risks? *Reviews on environmental health*. **25**, 261–306.
- Sigmund, A., Freier, K.P., Rehm, T., Ries, L., Schunk, C., Menzel, A., Thomas, K., 2019. Multivariate statistical air mass classification for the high-alpine observatory at the Zugspitze Mountain, Germany. In *Atmospheric Chemistry and Physics* 19 (19), pp.12477–12494. DOI: 10.5194/acp-19-12477-2019.
- UBA, 2014. Dioxine und dioxinähnliche PCB in Umwelt und Nahrungsketten.
- UBA, 2016. Steckbrief Octachlorstyrol. Persistente, bioakkumulierende und toxische aromatische Organochlorverbindung.
- UNEP, 2007. *Report of the expert group on the assessment of the production and use of DDT and its alternatives for disease vector control*, Dakar.
- Wania, F., Mackay, D., 1996. Peer reviewed: tracking the distribution of persistent organic pollutants. *Environmental science & technology*. **30**, 390A–6A.
- Weber, R., Watson, A., Malkov, M., Costner, P., Vijgen, J., 2011. Unintentionally produced hexachlorobenzene and pentachlorobenzene POPs waste from solvent production—the need to establish emission factors and inventories. *Organohalogen Compd.* **73**, 2205–2208.
- WHO, 2013. State of the science of endocrine disrupting chemicals 2012.
- Zhang, L., Yang, W., Zhang, L., Li, X., 2015. Highly chlorinated unintentionally produced persistent organic pollutants generated during the methanol-based production of chlorinated methanes: A case study in China. *Chemosphere*. **133**, 1–5.

4 Observation and Modeling of Climate Driven Permafrost Trends at the Zugspitze Summit

Thomas Galleemann¹, Michael Mahr², Andreas von Poschinger¹, Bernhard Wagner¹

Abstract

Keywords: permafrost, climate change, rock temperature, modeling, Zugspitze, Northern Calcarous Alps

In 2007 the Bavarian Environment Agency (LfU) established a permanent measuring station for recording the permafrost temperatures at the Zugspitze mountain summit. A nearly horizontal, 44.5 m long, borehole was drilled through the peak and temperature sensors were installed inside.

A computer model, accounting for climatic atmosphere-rock interactions and rock temperatures including latent ice-water phase changes, was calibrated using the measured permafrost temperature data.

With the calibrated model past permafrost development, from 1915 until 2015, was calculated on basis of climate data, available since the year 1900. Future permafrost development, until the end of the 21st century, has been calculated on basis of an ambient temperature projection at the Zugspitze (WETTREG2010).

The mean ambient temperature at the Zugspitze increased by about 1.6 K over the last 100 years. Consequently, this resulted in a considerable reduction of the permafrost in the Zugspitze summit. According to the simulation, the permafrost has shrunk from a total length of 34 meters in 1915 to 24.5 meters in 2015. The projected ambient temperature increase indicates that the permafrost may disappear at the Zugspitze in the second half of the 21st century.

4.1 Introduction

The Zugspitze is the highest mountain in Germany, 2962 m above sea level. The summit is situated in the Northern Calcarous Alps, at the western rim of the Wetterstein mountain range. It consists of a sequence of more than 1200 m of limestones and secondary dolomites of the Alpine middle Triassic (HORNUNG & HAAS 2017a, b). Fig. 1 shows a view from the north with a schematic geology.

Because of its highest elevation, the largest permafrost occurrence in Germany is expected at the Zugspitze (NÖTZLI et al. 2006, BÖCKLI et al. 2011). The permafrost existence at the Zugspitze was first mentioned by KNAUER (1933). Then, KÖRNER & ULRICH (1965) and ULRICH & KING (1993) published more comprehensive data. At present, the average annual ambient air temperature at the Zugspitze is about -3°C , while in 1900, when the first regular weather records were collected, it was -5°C . This data indicates a clear upward temperature trend.

The amount of permanently frozen rock is very sensitive to the climate change; consequently, it is a significant climate change indicator. Therefore, longterm monitoring of the permafrost is essential for analysis of the climate change (BAYERISCHES STAATSMINISTERIUM FÜR UMWELT UND VERBRAUCHERSCHUTZ 2015). Another important issue is a stabilizing effect of the permafrost on rocks. Reduction of permafrost in high alpine regions, due to global warming, decreases the rock mechanical stability (KRAUTBLATTER et al. 2013). This, in turn, may lead to an increase of occurrence and intensity of mass movements (e. g. landslides and rockfalls) and influence the stability of building foundations (GRUBER et al. 2004, GUDE & BARSCH 2005, RAVANEL & DELINE 2011).

¹ Bayerisches Landesamt für Umwelt, Augsburg

² Dr. Mahr Ingenieurbüro, Wallgau



Fig. 1: The Zugspitze massif (north side) with indicated geological formations.

For these reasons, the Bavarian Environment Agency (Bayerisches Landesamt für Umwelt – LfU) installed in 2007 the permafrost measuring station. It is the only permafrost measuring station of that kind in the Bavarian Alps. However, similar stations do exist in Austria (Kitzsteinhorn, KEUSCHNIG et al. 2017), France (Aiguille du Midi, MAGNIN et al. 2015), Italy (Grawand, MAIR et al. 2011) and Switzerland (PERMOS 2013). The main reason for establishment of these stations was to gain a more wide-ranging knowledge about the influence of seasonal temperature variations and longterm climate changes on the permafrost condition.

First, a working platform was built on the southern side of the Zugspitze peak. Then, a nearly horizontal borehole (inclination 20°, diameter 125 mm, length 44.5 m) was drilled through the peak (Fig. 2) and a plastic tube was installed; the tube ends were tightly sealed in order to minimize thermal convection. Afterwards, 16 electronic temperature sensors were fixed to a fibre rod, for stabilization purposes. After that a cable loom was inserted in the tube without being filled by any medium except air. The technique of installing the sensors in air, without



Fig. 2: Platform with drill carriage, minicrane and dust protection filter.

any cementation, was already successfully applied by the Swiss Institute for Snow and Avalanche Research (SLF). This assembly approach allows an easy replacement of the sensors. Rock temperatures are being measured hourly and recorded by a data logger. The data can be retrieved by remote access. More information can be found on the internet: www.lfu.bayern.de ⇒ Geologie ⇒ Permafrost in Bayern ⇒ Permafrost an der Zugspitze ⇒ Messergebnisse

In order to analyse the permafrost condition for extended periods of time at the Zugspitze peak, a computer program has been developed and then it was calibrated using the measured data. The objective of this paper is to analyse the impact of climate trends on the permafrost condition using a mathematical model especially developed for this purpose. More details about the model can be found in GALLEMANN et al. (2017).

4.2 Modeling

4.2.1 Thermal atmosphere/rock interactions under frost conditions

For modeling the permafrost in rocks, the following transient thermal processes are taken into account:

- heat conduction in rocks
- heat convection at rock surfaces
- shortwave solar radiation on rock surfaces
- longwave radiation between rock surface and ambient environment
- ice/water phase changes

4.2.1.1 Heat conduction in rock

A transient model of heat conduction in solids (e.g. GRÖBER et al. 1988, BAEHR & STEPHAN 2013) is applied to rocks. Generally, for the three dimensional case, the Fourier equation has the following form:

$$c \cdot \rho \cdot \frac{dT}{dt} = \lambda \left(\frac{d^2T}{dx^2} + \frac{d^2T}{dy^2} + \frac{d^2T}{dz^2} \right)$$

with

- c = heat capacity of the (porous) rock
- ρ = rock density
- x = distance x
- y = distance y
- z = distance z
- T = rock temperature
- t = time
- λ = thermal conductivity of (porous) rock

With the thermal diffusivity $a = \lambda/(c \cdot \rho)$ and for one-dimensional heat transport, the above equation simplifies to:

$$\frac{dT}{dt} = a \cdot \frac{d^2T}{dx^2}$$

The values for density, heat capacity and thermal conductivity of the porous rock are calculated from the weighted volumetric contents of the respective rock fractions, water/ice contents and air filled pores. Additionally, varying rock thermal conductivities can also be taken into account. When modeling latent water/ice phase changes, the temperature in the respective node is being kept constant at phase change temperature, while any heat fluxes only cause freezing or thawing of the water/ice. Then, when the phase-change process is fully completed, temperatures will change again. The fraction of time dependent water/ice phase changes φ_{fi} during freezing/thawing processes can be calculated as follows:

$$\frac{d\varphi_{fl}}{dt} = \frac{\lambda}{h \cdot \rho \cdot \Phi} \cdot \frac{d^2T}{dx^2}$$

with

φ_{fl} = fraction of liquid phase

h = melting enthalpy ice/water

Φ = rock porosity

The complex equations applied for thermal interactions between atmosphere and rock, including solar and ambient short and long wave radiation, can be found in GALLEMANN et al. (2017).

4.2.2 Model calibration and numerical simulation

4.2.2.1 Numerical model

Rock temperatures are calculated based on the one-dimensional finite difference method using the Crank-Nicholson scheme. Temperatures along the permafrost borehole are calculated in a regular grid of 0.5 m length for the total length of 44.5 m; time steps for the simulation runs are 60 minutes.

Climate input data consists of global radiation, ambient air temperature, cloud cover and snow depth, which are available starting August 1900 by German Weather Service (DEUTSCHER WETTERDIENST 2015), except for global radiation, where measurements started in 2003. The rock thermal parameters follow data published by NÖTZLI et al. 2010 (thermal conductivity of rock $\lambda = 2.5 \text{ W/m K}$, volumetric heat capacity $c \cdot \rho = 2 \cdot 10^6 \text{ J/m}^3 \text{ K}$, porosity of rock $\Phi = 5\%$, where the pores are assumed to be filled 50% with air and 50% water resp. ice). The phase-change temperature (water/ice) in the Wetterstein limestone was assumed to be $-0.5 \text{ }^\circ\text{C}$ (KRAUTBLATTER et al. 2010).

4.2.2.2 Model calibration

Heat flow in rocks is influenced by several variables, whose exact values are largely unknown, such as spatial variability of the thermal rock parameters, convective heat flows due to precipitation and heat flows transversal to the direction of the measurements. Therefore, the model was calibrated by fitting obtained data to measured records. For this purpose, the two calibration factors $z1$ and $z2$ were introduced in the conduction heat transfer equation:

$$\frac{dT}{dt} = z1 + z2 \cdot a \cdot \frac{d^2T}{dx^2}$$

In the first step, $z1$ and $z2$ are determined for each of the nodes (i. e. about 170 fitting factors) by the least squares method for the calibration period of the two years (i. e. 2013 and 2014). This way the information from the measured data is implemented in the model in the form of a "thermal fingerprint". In the second step, the heat transfer parameters between rock surfaces and the ambient environment were also optimized by a least squares approach based on a comparison of measured and calculated temperatures. A special attention was paid to the insulating effect of snow cover (more details in GALLEMANN et al. 2017) that plays an important role at the southern surface, where snow may accumulate due to the less steeper terrain. On the northern side, the rock surface is more or less vertical, so that snow cover is not relevant there.

Calibration transferability was tested by a comparison of measured and calculated temperatures for the year 2015, after the calibration period (2013 and 2014). Obtained results were found to be in good agreement with measured data. As a result, it is concluded that the calibrated model produces valid projections for extended time periods, when no measured data is available. Fig. 3 shows measured and calculated temperatures for the last day of the year 2015.

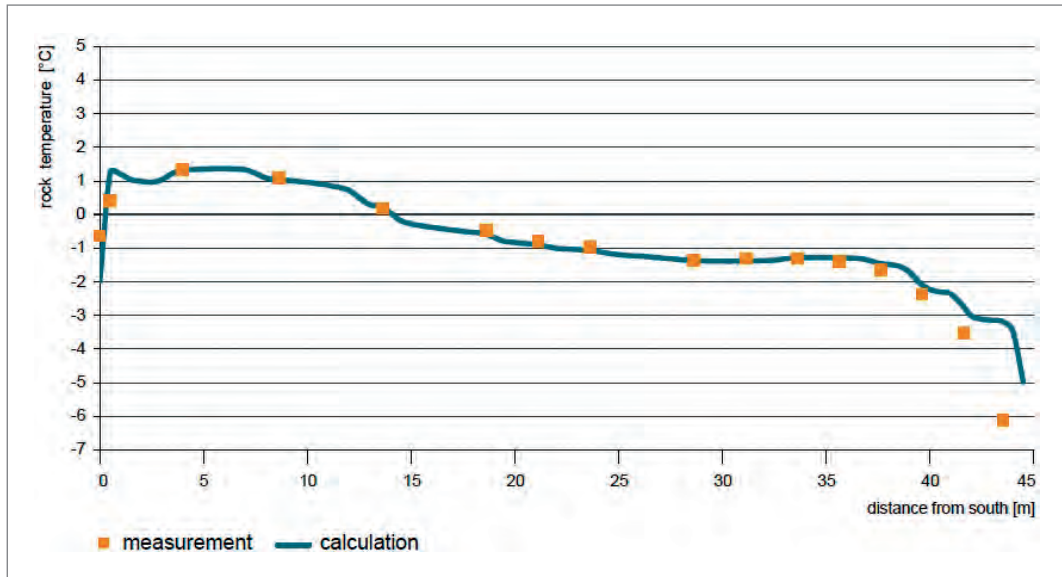


Fig. 3: Measured and calculated rock temperatures (daily average of December 31st, 2015) along the permafrost borehole.

4.3 Results

4.3.1 Temperature data from 2010 to 2016 at the Zugspitze summit

The measured rock temperatures, along the borehole cross section, from 2010 until 2016, are displayed in Fig. 4. Due to a slow transmission of heat inside the mountaintop, the highest temperatures at the borehole centre are recorded in winter and lowest in summer. The tendency of temperature development during the measurement period indicates a warming trend that corresponds to a general rise in ambient air temperature during that time span (see Fig. 5).

4.3.2 Computer simulation

In order to assess the impact of past ambient air temperature changes at the Zugspitze summit on the permafrost, the model calculations were performed, based on weather data starting in August 1900. To allow for equilibrium, temperatures are only visualized after 1915.

Potential future temperature changes inside the mountain, after 2015, were obtained from model calculations based on ambient temperature data generated by the regional climate model (RCM) WETTREG2010 (Climate & Environment Consulting Potsdam GmbH) that is based on the emission scenario SRES A1B of the 4th IPCC-assessment report. The WETTREG2010 uses statistical relations between large scale atmospheric patterns and the climate data from available weather stations to derive the future projection for regional climate (BAYERISCHES LANDESAMT FÜR UMWELT 2012). The climate input data for the model simulations is taken from one of the RCM scenarios of the WETTREG10 simulation. In order to assess the model sensitivity, a larger number of different simulations have to be used. However, this is a computationally very intensive process; so, only one representative model simulation was applied for the future projection of the permafrost.

Fig. 5 shows the moving averages of ambient air temperature over 1, 10 and 30 years for the simulation period of 185 years, i. e. between 1915 and 2100. Data until the end of 2015 was obtained from the Zugspitze weather station. After 2016 the data is taken from the regional climate model of the WETTREG2010 scenario.

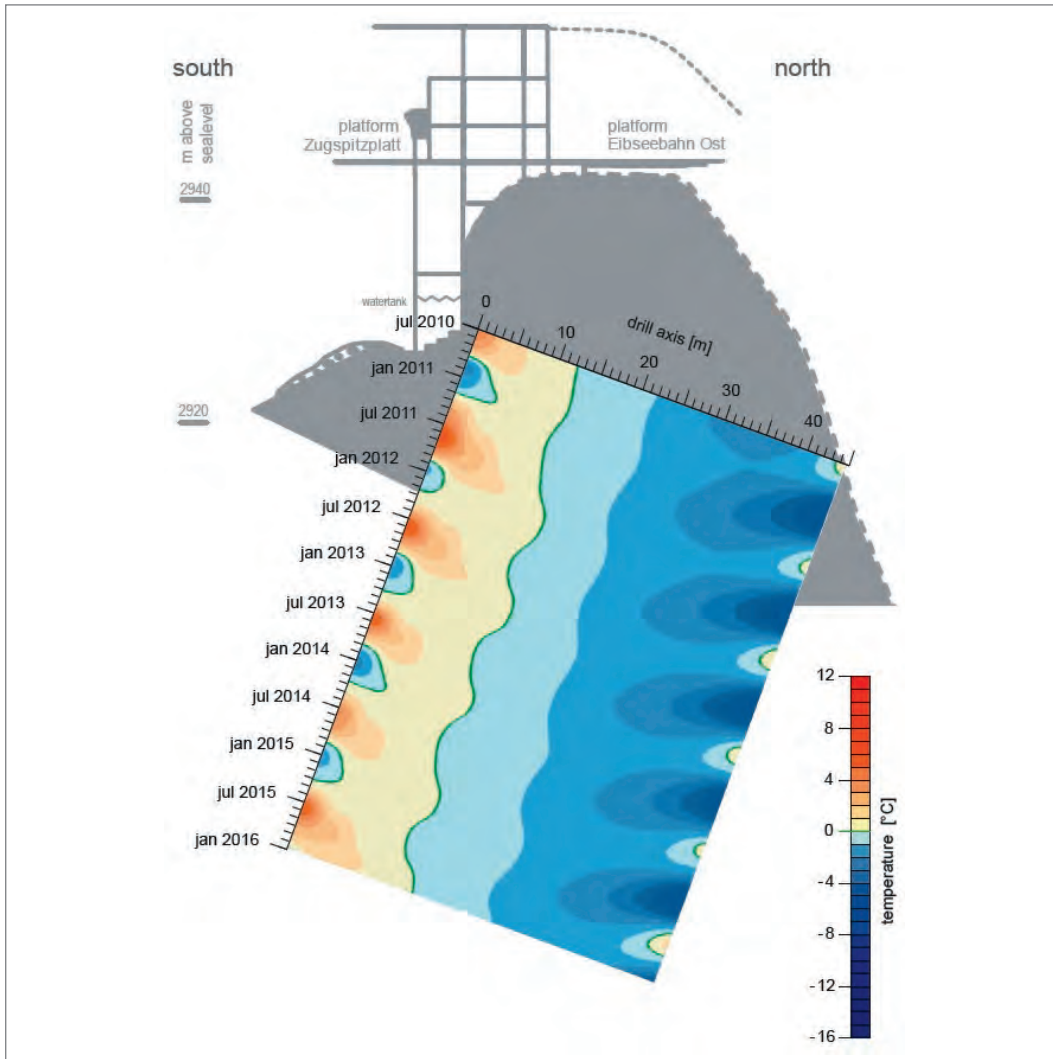


Fig. 4: Measured rock temperature from 2010 to 2016 along the permafrost borehole.

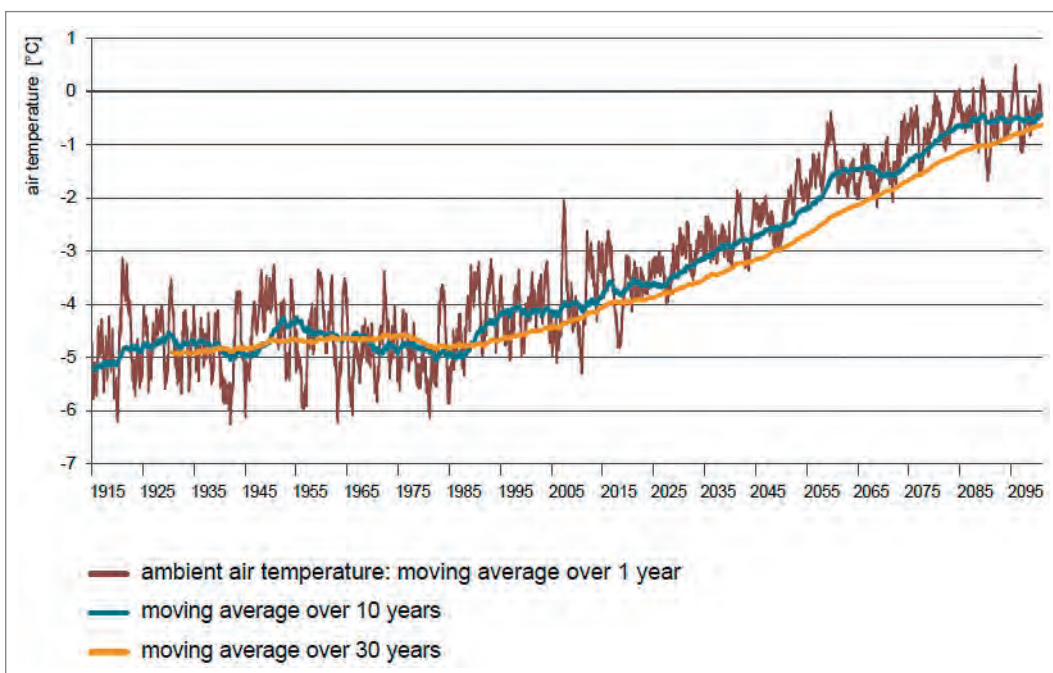


Fig. 5: Moving average of ambient air temperature over 1, 10 and 30 years (measured data until end of 2015, model data from 2016).

4.3.2.1 Past permafrost conditions from 1915 to 2015

Meteorological data, such as ambient air temperature, cloud cover and snow depth are available for the Zugspitze summit since August 1900. Data of global radiation is available from 2013 onward, so that recent measurements are used for global radiation of the simulation period.

For visualization of the longterm temperature projection, the calculated temperature distribution along the borehole on October 1st for the period of 100 years, from 1915 until 2015, is shown in Fig. 6. It has to be noted that not a seasonal temperature trend is shown in the Fig. 6, but the temperature projection along the borehole axis for the chosen date of October 1st. The rise of ambient air temperature during the simulation period is about 1.6 °C (moving average over 10 years). This increase is clearly reflected by the trend of rock temperature isolines indicating an increase of temperatures throughout the simulation period.

4.3.2.2 Future permafrost development from 2016 to 2100

For possible future condition of the permafrost, calculations were carried out until 2100, using the calibrated model. Calculated temperature distribution, along the permafrost borehole length, is shown in Fig. 7, on October 1st for the period of 85 years from 2016 until 2100. The warming trend, displayed in Fig. 6 for the past period 1915 until 2015, increases sharply due to projected additional increase of ambient air temperatures. This potentially may lead to a disappearance of the permafrost in the seventies of the 21st century, with the last permafrost on hand within a distance of about 30 m from the south (i. e. 14.5 m from the north).

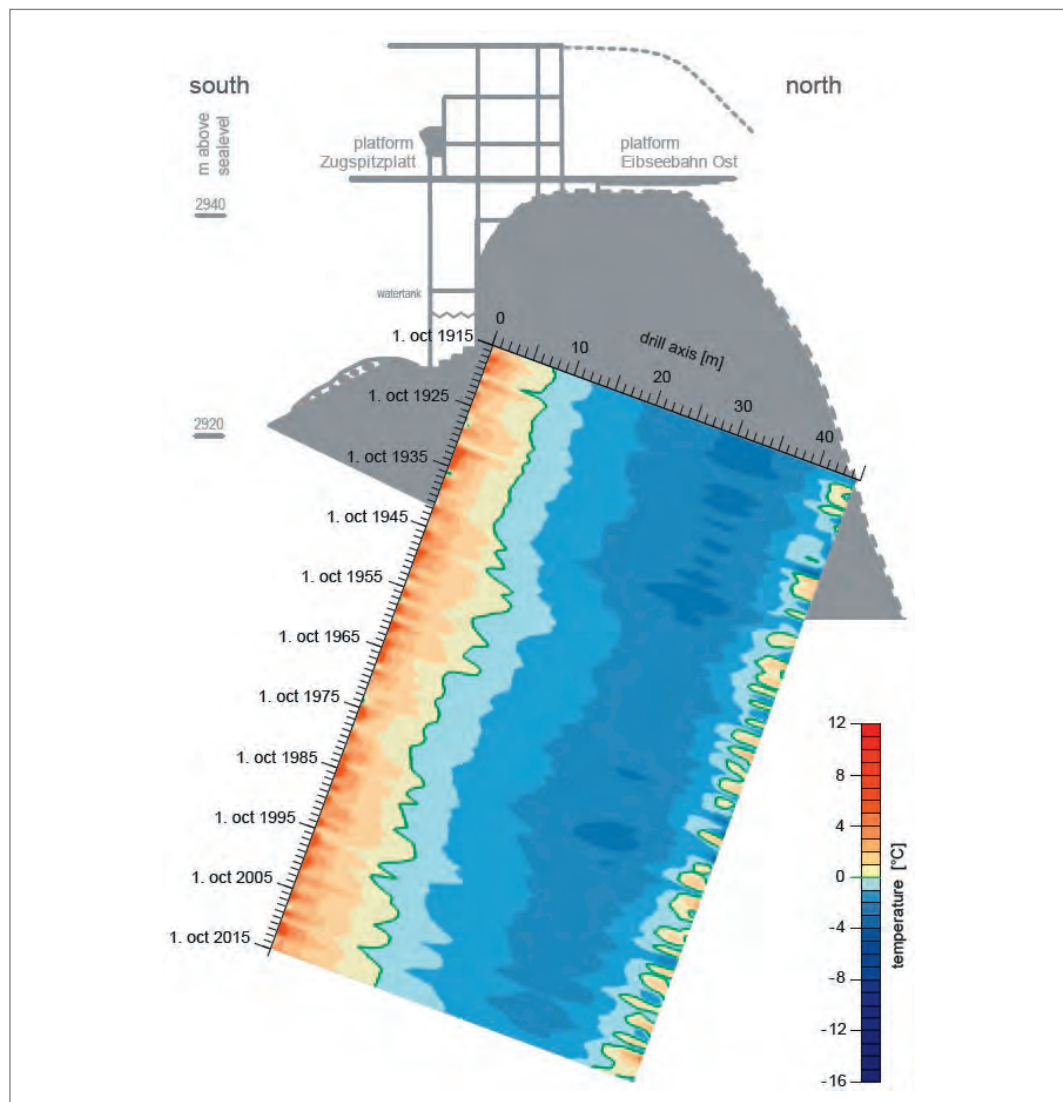


Fig. 6: Projected temperature distribution at October 1st for the years 1915–2015.

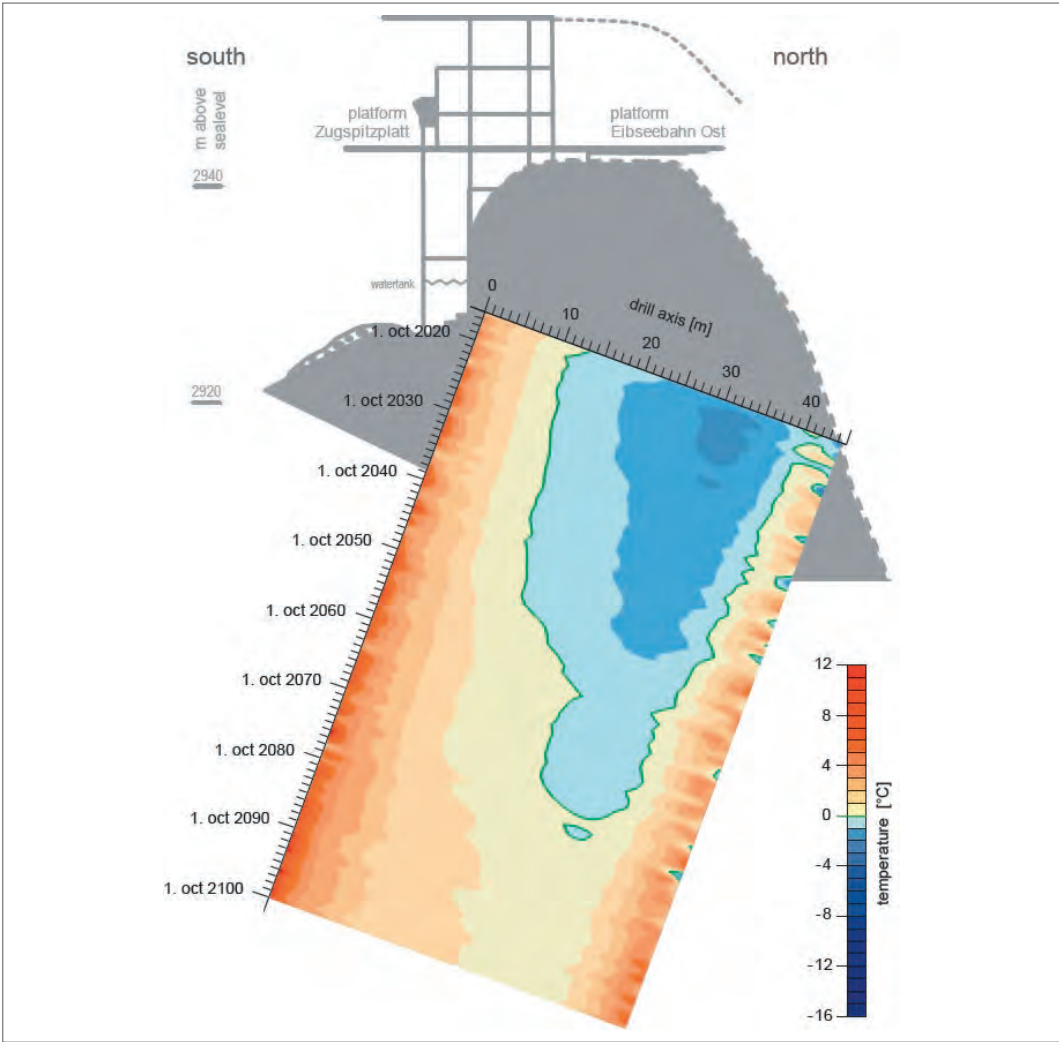


Fig. 7: Modeled temperature distribution at October 1st for the years 2016–2100.

The number of days per year with calculated average temperature above 0 °C along the borehole cross section, for selected years between 1915 and 2100, is shown in Fig. 8. The permafrost resides in the section, where no temperatures above 0 °C are measured during the year (zero values on y-axis). The figure illustrates that the sections with temperatures above 0 °C (i. e. areas with no permafrost) are proceeding from the north and from the south into the center of the mountain. In 2100 no more permafrost can be found in the borehole.

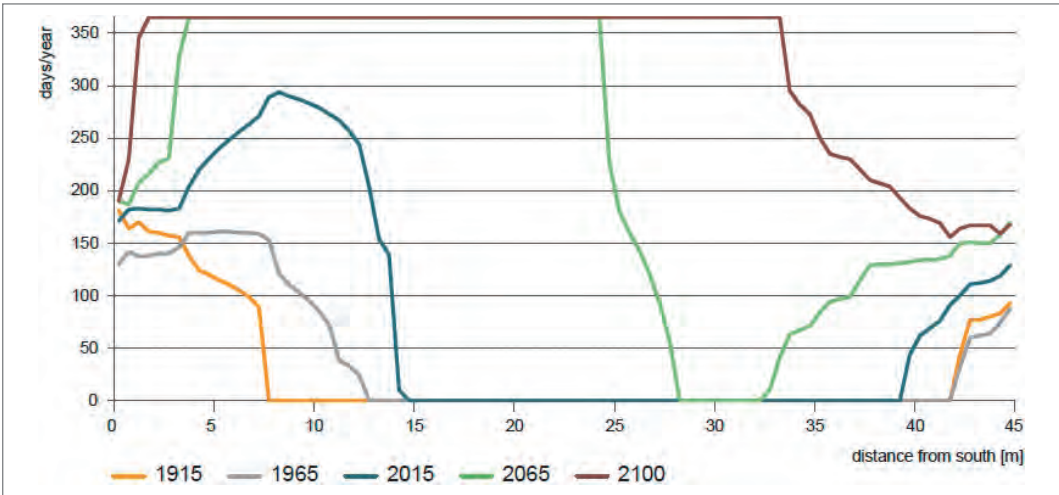


Fig. 8: Calculated number of days per year with rock temperatures above 0 °C along the permafrost borehole.

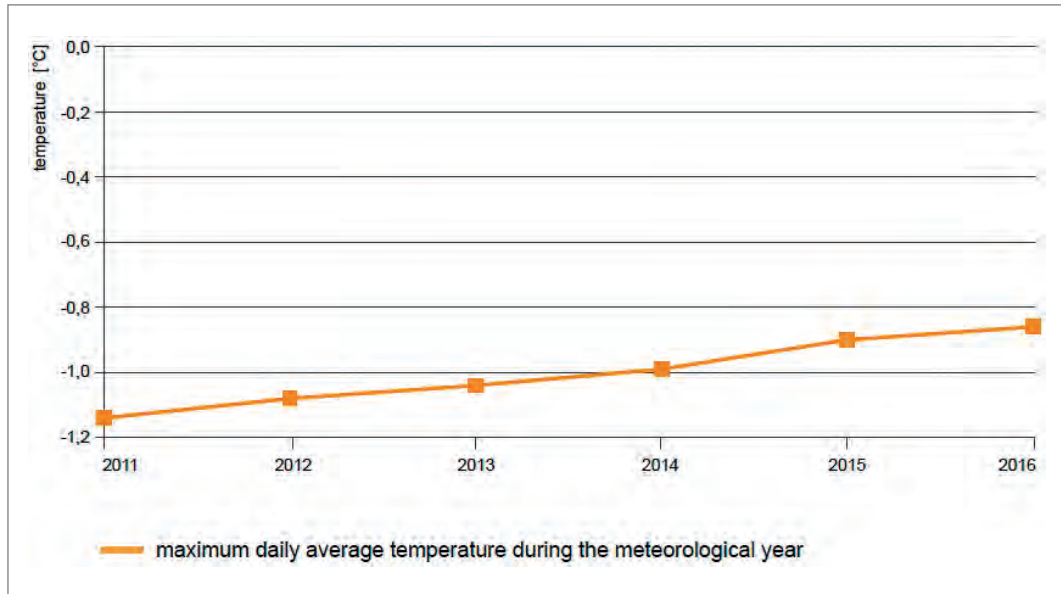


Fig. 9: Maximum of the daily average temperature during the meteorological year, 23.65 m distant from the south.

Due to the permafrost sensitivity to climate change, permafrost measuring data was added to the list of climate change indicators of the Bavarian climate impact monitoring program (BAYERISCHES LANDESAMT FÜR UMWELT 2018: I-BO-5 Decrease of Permafrost). The relevant parameter, highest daily temperature average during the meteorological year of the temperature sensor in 23.65 m distance from the south, is shown in Fig. 9. The temperature sensor was used, as it is located in the center of the borehole and hence it shows the lowest seasonal temperature variation. Nearly linear temperature increase was observed during the measurement period (2011 to 2016).

4.4 Conclusions

The transient temperature profile data, observed at the Zugspitze permafrost measuring station, could be successfully simulated using a numerical finite difference model. Due to the model calibration, the temperatures along the permafrost borehole could be calculated with a relatively high accuracy, within the measurement uncertainty. The calibrated model allows estimation of the past permafrost conditions with available climate data and to project potential permafrost conditions, based on climate future projections reaching until the end of the 21st century.

The 10 year moving average of the ambient air temperature at Zugspitze summit increased by 1.6 K within hundred years (1915: -5.2 °C, 2015: -3.6 °C). According to the model calculations, this significant increase of temperature had a considerable impact on the permafrost condition: according to the calculations the permafrost retreated by about 7 meters in the south and 2 meters on the north side of the borehole. The higher gradient of temperature increase during the 25 years after 1990 (KRAUTBLATTER et al. 2010) resulted in an accelerated permafrost shrinkage: during these 25 years permafrost retreated by 2 m from the north, while in the 75 years before reduction was only 0.5 m. Mean permafrost temperature rose to a value of -1 °C, that is not far from the ice melting temperature in the Wetterstein rock (-0.5 °C).

The increase of moving average of temperatures over 10 years, for the future climate scenario, amounted to 3.15 K (2015: -3.6 °C, 2100: -0.45 °C). This value is almost twice as high as the rise observed during the past 100 years. Following this scenario, no permafrost will be found in the borehole of the permafrost measuring station after 2080. Disappearance of the permafrost in the Bavarian Alps, and for this reason reduced stability of the mountain ranges, can be expected. This may lead to a potential increase of mass movements, like rock fall and landslides.

Acknowledgements

The permafrost measuring station construction and maintenance has been financed by the Bavarian State Ministry of the Environment and Consumer Protection (Bayerisches Staatsministerium für Umwelt und Verbraucherschutz). The authors are grateful to Prof. Dr. Krautblatter (Technical University Munich) for assistance and discussions on permafrost rock parameters and to Prof. Dr. Tarnawski (St. Marys University Halifax, Canada) for the manuscript review and valuable comments.

References

- Baehr, H.D. & Stephan, K. (2013): Wärme- und Stoffübertragung. – 804 p., Springer Vieweg.
- Bayerisches Landesamt für Umwelt (2012): Der Klimawandel in Bayern. Auswertung regionaler Klimaprojektionen; Klimabericht Bayern. – 22 p., Internet: http://www.bestellen.bayern.de/shoplink/lfu_klima_00082.htm (23.02.2018).
- Bayerisches Landesamt für Umwelt (2018): Indikatoren zu Klimafolgen und Klimaanpassung in Bayern – Machbarkeitsstudie. – 66 p., Internet: http://www.bestellen.bayern.de/shoplink/lfu_klima_00151.htm (14.03.2018).
- Bayerisches Staatsministerium für Umwelt und Verbraucherschutz (2015): Klima-Report Bayern 2015 – Klimawandel, Auswirkungen, Anpassungs- und Forschungsaktivitäten. – 199 p., München.
- Böckli, L., Nötzli, J. & Gruber, S. (2011): PermaNET-BY, Untersuchungen des Permafrosts in den Bayerischen Alpen, Final Report Project PermaNET in the AlpineSpace Program. – 60 p., Internet: https://www.lfu.bayern.de/geologie/permafrost/permanetby/doc/permanet_by_schlussbericht_v2komprimiert.pdf (23.02.2018).
- Deutscher Wetterdienst (2015): online published weather data Zugspitze (www.dwd.de).
- Galleman, T., Haas, U., Teipel, U., von Poschinger, A., Wagner, B., Mahr, M., & Bäse, F. (2017): Permafrost-Messstation am Zugspitzgipfel: Ergebnisse und Modellberechnungen. – *Geologica Bavarica*, 115: 77 p.
- Gröber, H., Erk, S. & Grigull, U. (1988): Die Grundgesetze der Wärmeübertragung. – 436 p., Springer.
- Gruber, S., Hoelzle, M. & Haeberli, W. (2004): Permafrost thaw and destabilization of Alpine rock walls in the hot summer of 2003. – *Geophys. Res. Lett.*, **31**: L13504, DOI: 10.1029/2004GL020051.
- Gude, M. & Barsch, D. (2005): Assessment of the geomorphic hazards in connection with permafrost occurrence in the Zugspitze area (Bavarian Alps, Germany). – *Geomorphology*, **66**(1–4): pp. 85–93.
- Hornung, T. & Haas, U. (2017a): Geologische Karte von Bayern 1 : 25 000 – Erläuterungen zum Blatt 8531 Zugspitze und 8532 Garmisch-Partenkirchen. – 96 p., Augsburg (Bayerisches Landesamt für Umwelt).
- Hornung, T. & Haas, U. (2017b): Geologische Karte von Bayern 1 : 25 000 Blatt Nr. 8531 Zugspitze & 8532 Garmisch-Partenkirchen. – Augsburg (Bayerisches Landesamt für Umwelt).
- Keuschnig, M., Krautblatter, M., Hartmeyer, I., Fuss, C. & Schrott, L. (2017): Automated Electrical Resistivity Tomography Testing for Early Warning in Unstable Permafrost Rock Walls Around Alpine Infrastructure. – *Permafrost and periglacial processes*, **28**: 158–171. DOI: 10.1002/ppp.1916.
- Knauer, J. (1933): Die geologischen Ergebnisse beim Bau der Bayerischen Zugspitzbahn. – Sonderdruck „Abhandlungen der Geologischen Landesuntersuchung am Bayerischen Oberbergamt“, **10**: pp. 23–50.
- Körner, H. & Ulrich, R. (1965): Geologische und felsmechanische Untersuchungen für die Gipfelstation der Seilbahn Eibsee-Zugspitze. – *Geol. Bavarica*, **55**: pp. 404–421, München (Bayerisches Geologisches Landesamt).
- Krautblatter, M., Funk, D. & Günzel, F.K. (2013): Why permafrost rocks become unstable: a rock-ice-mechanical model in time and space. – *Earth Surface Processes and Landforms*, **38**: pp. 876–887.
- Krautblatter, M., Verleysdonk, S., Flores-Orozco, A. & Kemna, A. (2010): Temperature-calibrated imaging of seasonal changes in permafrost rock walls by quantitative electrical resistivity tomography (Zugspitze, German/Austrian Alps)“. – *Journal of Geophysical Research – Earth Surface*, **115**: pp. 1–15, DOI: 10.1029/2008JF001209.
- Magnin, F., Brenning, A., Bodin, X., Deline, P. & Ravel, L. (2015): Modélisation statistique de la distribution du permafrost de paroi: application au massif du Mont Blanc. – *Géomorphologie: Relief, Processus, Environnement*, **21/2**: pp. 145–162, DOI: 10.4000/geomorphologie.10965.
- Mair, V., Zischg, A., Lang, K., Tonidandel, D., Krainer, K., Kellerer-Pirklbauer, A., Deline, P., Schoeneich, P., Cremonese, E., Pogliotti, P., Gruber, S. & Böckli, L. (2011): PermaNET – Permafrost Long-term Monitoring Network. Synthesebericht. – INTERPRAEVENT Schriftenreihe 1, Report 3, Klagenfurt.
- Nötzli, J., Gruber, S. & Haeberli, W. (2006): 3D-Modellierung der thermischen Bedingungen im Bereich des Gipfelgrates der Zugspitze. – Forschungsbericht der Glaciology and Geomorphodynamics Group, 17 p., Department of Geography, University of Zurich, Internet: https://www.lfu.bayern.de/geologie/permafrost/zugspitze/doc/modellierung_permafrost_zugspitze.pdf (23.02.2018).

- Nötzli, J., Gruber, S. & Poschinger, A. von (2010): Modellierung und Messung von Permafrosttemperaturen im Gipfelgrat der Zugspitze, Deutschland. – *Geographica Helvetica*, **65/2**: pp. 113–123. DOI: 10.5194/gh-65-113-2010.
- PERMOS (2013): Permafrost in Switzerland 2008/2009 and 2009/2010. – Nötzli, J. (ed.) Glaciological Report (Permafrost), Cryospheric Commission (CC) of the Swiss Academy of Sciences (SCNAT) **10/11**: 80 p.
- Ravanel, L. & Deline, P. (2011): Climate influence on rockfalls in high-Alpine steep rockwalls: The north side of the Aiguilles de Chamonix (Mont Blanc massif) since the end of the 'Little Ice Age'. – *The Holocene*, **21/2**: pp. 357–365, DOI: 10.1177/095968361037887.
- Ulrich, R. & King, L. (1993): Influence of mountain permafrost on construction in the Zugspitze mountains, Bavarian Alps, Germany. – 6th Int. Conf. on Permafrost, Beijing: pp. 625–630.

5 Cloud and Precipitation Observed with Radar

Martin Hagen¹, Axel Häring¹, Stefan Kneifel², Kersten Schmidt³

Abstract

Meteorological radar is an essential tool for research, diagnosis, and nowcasting of clouds and precipitation. Cloud radars use short wavelengths to enable detection of small ice particles or cloud droplets. The cloud radar at UFS Schneefernerhaus is operated since end of 2011. It has been used for a number of studies related to clouds and precipitation. In a synergistic combination with additional remote sensing instruments, a large variety of cloud and precipitation properties can be retrieved. The measurements at UFS Schneefernerhaus can be used for the evaluation of numerical weather prediction models and satellite measurements. The long-term observations allow assessing the seasonal and long-term evolution of cloud properties above the UFS in a warming climate.

Key words: radar, clouds, precipitation

5.1 Introduction

Clouds and precipitation play an important role in the atmosphere. Clouds do contribute considerable to the uncertainty of future climate predictions. Depending on the height and vertical extent, they contribute differently on the warming or cooling of the Earth surface. Clouds have also an essential impact on the local radiation budget and thus controlling the local climate. Cloud particles can grow to precipitation in the form of rain, snow, graupel, or hail. This has a direct impact on the local water budget.

While in-situ measurements (c.f. Chapter 22: Impact of turbulence on cloud microphysics) can describe the internal structure of clouds at a specific point in great detail, remote sensing techniques give more insights into the two- or three-dimensional variability. Optical methods (c.f. Chapter 18 and 21) are very suitable for optically thin clouds; however, radar is able to penetrate also clouds and even strong precipitation and thus, complements the optical observations in an optimal way.

Different types of meteorological radar systems are available and used for various purposes. Weather radars are mainly used by meteorological services for identification, monitoring and tracking of precipitation systems like frontal systems or thunderstorms. Short-term weather forecast is often done by tracking radar echoes and extrapolating their motion. The surveillance range is a few hundred kilometers. Fast scanning antennas and powerful signal processing allows high temporal (2–10 minutes) and spatial (50–1000 m) resolution of the volumetric measurement of precipitation systems. Weather radars use centimeter wavelengths because the signal is only weakly attenuated by even heavy precipitation, thus, allowing to receive information up to 300 km away from the radar. For the detection of non-precipitating clouds – where the typical particle size is in the order of 10 to 100 μm – cloud radars with a wavelength in the millimeter range are used. Those systems have limited measurement range up to 10 or 30 km, their antennas are either pointing vertically only, or able to scan but with a much slower scanning rate than what is used for weather radar.

At Umweltforschungsstation Schneefernerhaus (UFS), two vertically looking radar systems are permanently installed: a cloud radar and a micro rain radar with a wavelength of 0.8 cm and 1.2 cm, respectively. This contribution mainly focuses on cloud radars and their application with emphasis on the system operated at UFS.

¹ Deutsches Zentrum für Luft- und Raumfahrt, Institut für Physik der Atmosphäre

² Universität zu Köln, Institut für Geophysik und Meteorologie

³ Deutsches Zentrum für Luft- und Raumfahrt, Institut für Hochfrequenztechnik und Radarsysteme

5.2 Radar Principles

5.2.1 Radar Techniques

A radar transmits a short electromagnetic pulse with high power through a directional antenna. This pulse is reflected by an object and received by the radar receiver (c. f. Fig. 1). The direction in which the antenna is pointed and the round-trip time of the pulse are used to locate the object which is scattering the pulse. The principal components of a weather radar are the transmitter, the antenna, the receiver, the signal processor, and the product and image generator. The transmit/receive switch and/or limiter is needed to protect the sensitive receiver from the high power transmit pulse. Radar operation control, signal processing, and image generation is accomplished with powerful standard computers. Here, only a basic overview of radar systems can be provided. More details on meteorological radars can be found in textbooks like Fabry (2015) or Bringi and Chandrasekar (2001). Radar techniques are described in detail in Skolnik (2008).

In the following, some technical aspects of meteorological radars will be described. The weather radar is mentioned for completeness, the focus will be on the two radar systems – namely a cloud radar and a micro-rain-radar – operated for research at the Umweltforschungsstation Schneefernerhaus. Table 1 summarizes some technical characteristics of typical weather radar used in Europe and the two systems operated at UFS.

5.2.1.1 Weather Radar

Weather radars are used for a wide spectrum of operational applications such as:

- identifying precipitation systems (like fronts or thunderstorms) for weather prediction,
- detailed analysis of dynamical and microphysical structures in thunderstorms,
- monitoring thunderstorm motion for nowcasting,
- estimating precipitation amount for hydrological applications like flood forecasting for river catchments,
- identifying of thunderstorm or hail swaths,
- long term observations for precipitation climatologies.

The main focus of weather radar is on precipitating particles like rain, snow, graupel or hail, for this purpose long wavelengths are suited best. A total number of about 200 weather radars are operated by meteorological services in Europe today. Most weather radars in Europe are C-band radars (frequency 5.6 GHz, wavelength 5.4 cm); only some radars in the Mediterranean area are S-band radars (frequency 2.8 GHz, wavelength 10.7 cm). X-band radars (9.4 GHz, wavelength 3.2 cm) are used for research applications and short range observations like cities or river catchments, but also in mountainous regions to cover valleys which are shielded from the long-range radars located outside the mountains or on mountain peaks.

Besides measuring the strength of the backscattered signal (termed as reflectivity; c. f. section 5.2.2.1), weather radars can measure the motion of the scattering particles (c. f. section 5.2.2.2). Dual-polarization capabilities enable the estimation of the particle properties and the classification of hydrometeors (c. f. section 5.2.2.4, 5.2.2.5, and Bringi and Chandrasekar (2001)).

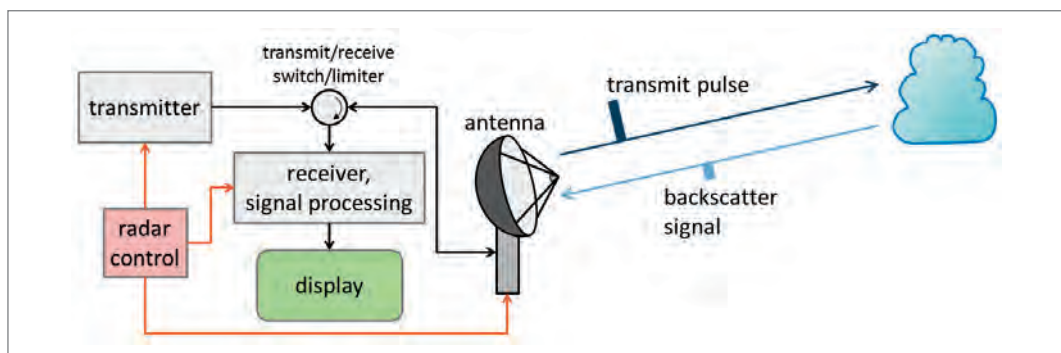


Fig. 1: Principle of meteorological radar.

Tab. 1: Characteristics of typical European weather radar, as well as of the cloud radar and the micro-rain-radar installed at Umweltforschungsstation Schneefernerhaus.

Parameter	Typical weather radar	MIRA36 cloud radar	MRR micro rain radar
Frequency band	C-band	Ka-band	K-band
Frequency/wavelength	5.6 GHz / 5.4 cm	35.5 GHz / 0.8 cm	24.1 GHz / 1.2 cm
Transmit power	500 kW (pulse peak)	25 kW (pulse peak)	50 mW (continuous wave)
Pulse duration	0.6–2 μ s	0.2 μ s	frequency modulated – continuous wave
Pulse repetition frequency	500–1200 Hz	5000 Hz	frequency modulated – continuous wave
Integration time per sample	0.02–0.1 s	10 s	60 s
Depth of measurement volume	90–300 m	30 m	50–100 m
Maximum range	100–300 km	15 km	1.5–3 km
Antenna diameter	4 m	1 m	0.6 m
Antenna rotation speed	2–6 rpm	fixed vertical pointing	fixed vertical pointing
Half-power beam width	1°	0.6°	2°

5.2.1.2 Cloud Radar

Cloud radars are designed for the observation of small cloud particles. For that purpose, radars with short wavelengths are used (Ka- or W-band; frequency 35 or 95 GHz; wavelength 8 or 3 mm, respectively). By using shorter wavelengths, the sensitivity to smaller particles, such as cloud droplets or tiny ice particles, increases. However, the backscattered signal also gets increasingly attenuated by hydrometeors and atmospheric gases which limits the maximum range that can be probed with the radar. Most of the cloud radars use vertically pointing antennas, only a few cloud radars are able to scan the hemisphere. Even though a variety of cloud radars does exist, this chapter is focused on the vertical pointing MIRA36 cloud radar installed at UFS and manufactured by METEK GmbH (e.g. Görsdorf et al., 2015). This radar system is characterized by high transmit power and its sensitivity to low backscatter signals. A number of MIRA36 systems are available worldwide. At the Meteorological Institute of Ludwig-Maximilians-Universität at Munich a MIRA36 radar with scanning capabilities is installed. A downward looking MIRA36 (Mech et al., 2014) is available to be flown onboard the German research aircraft HALO (High Altitude and Long-range) during specific campaigns.



Fig. 2: Installation of the MIRA36 cloud radar at Umweltforschungsstation Schneefernerhaus. Left: antenna of Casagrain type during the installation phase with parabolic dish, feed horn in the center and sub-reflector at the top. Center: antenna with clutter fence. Right: radar transmitter and receiver within the suspended ceiling of Wechselnutzlerlabor. Photos by M. Hagen.



Fig. 3: Installation of the PARSIVEL-2 disdrometer (left) and MRR micro rain radar (right) at the top terrace of the Umweltforschungsstation Schneefernerhaus. Photo by M. Hagen.

During the TOSCA campaign (c. f. section 5.3.3 and Löhnert et al., 2011) in 2008/2009 a MIRA36 cloud radar was temporarily installed at the terrace at UFS. With the experience collected during TOSCA and the added value generated by its combination with other remote sensing instrumentation at UFS, a permanent installation of a MIRA36 cloud radar was planned and realized in the end of 2011. The antenna of the cloud radar is mounted at the roof of the 5th floor (Fig. 2, left), the radar electronics and computers are installed within the suspended ceiling of the *Wechselnutzerlabor* at the 5th floor (Fig. 2, right). Radar control and support (uninterrupted power supply and dry air compressor) are installed in a computer rack at the *Wechselnutzerlabor*. The antenna is surrounded by a clutter fence (Fig. 2, middle) to prevent interference of the radar beam with the building and the mountains of the Zugspitzgrad. The radar has been operated continuously since December 2011. Due to maintenances and other technical issues, occasionally interruptions of the operation do occur.

The primary measurement quantity of the MIRA36 cloud radar is the Doppler spectrum (c. f. section 5.2.2.3), from which common moments or radar parameters such as reflectivity or Doppler velocity can be derived (c. f. section 5.2.2). Both, the Doppler spectra themselves and the moments, are stored for long-term access. Doppler spectra provide detailed information on the vertical motion of the particles. Under the assumption that there is no vertical air motion, information on the particle habit can be retrieved (e. g. Kollias et al., 2011). More detailed analysis of the spectra also allow to separate different hydrometeor classes (e. g. Melchionna et al., 2008). The polarization capabilities allow for the discrimination of spherical water drops, irregular shaped ice crystals, melting particles, as well as insects.

5.2.1.3 Micro Rain Radar

The micro rain radar (MRR) manufactured by METEK GmbH (e. g. Peters et al., 2002) is a low-cost radar designed for the estimation of vertical profiles of raindrop size distributions. Since the radar is using low-power electronics and is using the frequency-modulated continuous-wave (FM-CW) principle, it is a very robust system. A MRR is operated at the Umweltforschungsstation Schneefernerhaus since January 2008 on top of the building (Fig. 3). For the estimation of the in-situ raindrop size distribution, it is accompanied by an optical disdrometer PARSIVEL-2 (Löffler-Mang and Joss, 2000) manufactured by OTT-Hydromet GmbH. The disdrometer provides spectral particle size distribution and spectral fall-velocity distribution which can be used to classify the kind of precipitation (e. g., snow, rain, hail). Both instruments, the MRR and PARSIVEL-2, are designed for the observation of precipitating particles (raindrops, snowflakes or aggregates, graupel, hail); their sensitivity is not sufficient to observe cloud particles like cloud droplets or ice needles, plates, or dendrites.

The standard retrieval of raindrop size distributions provided by the manufacturer assumes a stagnant vertical air motion. The basic principle of this raindrop size distribution retrieval is shortly summarized in the following: within the Doppler spectra, each velocity bin (i. e. fall speed of raindrops) can be related to the associated raindrop size via known fall speed – drop size relations (e. g. Atlas et al., 1973). In a next step, the backscatter cross section for a single

drop of this size is estimated using Mie scattering theory. The measured spectral power at the relevant velocity bin is then simply divided by the known backscatter power for a single drop in order to obtain the number of drops for that size.

Even though the MRR has a lower sensitivity compared to the high power and high sensitive cloud radar, both instruments show good agreement over a wide range of precipitation intensity and with appropriate processing snow parameters can be derived (Kneifel et al., 2011). Due to the parallel operation of MIRA and MRR at UFS, the retrieval algorithms have been further developed to also enable the remote sensing community to measure snowfall with the MRR (Maahn and Kollias, 2012). Further evaluation of precipitation measurements by MRR are shown in Kneifel et al. 2022.

5.2.2 Radar Parameters

Air traffic control, military radars or ship radars aim detecting point targets. With meteorological radars, multiple targets filling the radar volume, such as rain or snow, shall not only be detected but also quantified. While conventional weather radars measure only the intensity of the returned signal, a Doppler radar additionally estimates the motion of the target. This provides for example information about the wind field but also allows to precisely monitor the motion of a thunderstorm. A further extension of Doppler radars is the addition of polarization which allows to derive a number of valuable additional radar parameters. Since dual-polarization radar use electromagnetic waves with two orthogonal polarizations, the derived radar parameters allow a characterization of the shape and orientation of the target. More details about the various radar parameters can be found in text books like Fabry (2015) or Bringi and Chandrasekar (2001).

5.2.2.1 Radar Reflectivity Factor

Radar reflectivity is a synonym for the magnitude of the reflected radar pulse. The radar equation for volume targets gives the relationship between the received signal P_r and the scattering cross section σ of the target

$$P_r = \frac{P_t g^2 \lambda^2 \pi r^2 \theta_0^2 h}{64 \pi^3 r^4} \frac{1}{8} \frac{1}{2 \ln(2)} \sum_{i=1}^n \sigma_i \quad (1)$$

with P_t the transmitted power, g the antenna gain, λ the wavelength, θ_0 the beam width, h the pulse length, r the distance to the targets, and σ_i the scattering cross section of the individual targets within volume. It is assumed that the measurement volume is uniformly filled with scattering targets. The first term describes the received power for a single point target, the second term the measurement volume, and the third term accounts for the fact that only part of the transmitted power is within the measurement volume bounded by the half-power beam width θ_0 .

For particles which are large compared to the wavelength (diameter $D > 10 \lambda$), the scattering cross section σ of a target is similar to its geometric cross section. For particles much smaller than the wavelength ($D < 1/10 \lambda$), the scattering cross section can be approximated by Rayleigh scattering

$$\sigma = \frac{\pi^5}{\lambda^4} |K|^2 D^6 \quad (2)$$

with $K = (m^2 - 1)/(m^2 + 2)$ representing the complex refractive index m of the scattering particle ($|K|^2 \approx 0.93$ for water and $|K|^2 \approx 0.2$ for ice). With the assumption that the targets are liquid water particles and much smaller than the wavelength, the radar reflectivity factor⁴ z is defined as the sum of D^6 of all particles within the unit volume V

$$z = \frac{1}{V} \sum_{i=1}^n D_i^6 \quad (3)$$

The common unit of z is mm^6/m^3 . Electrical engineers usually express a ratio R of two powers (p_1 and p_2) in a logarithmic notation $R = 10 \log_{10}(p_1/p_2)$. The “unit” of such a ratio is the decibel (dB). It is common in radar meteorology to express the reflectivity factor as a logarithmic ratio with respect to the reflectivity factor of a raindrop with a diameter of 1 mm.

⁴ Informally, but also in a large number of publications, the term “reflectivity” is used instead of “reflectivity factor.”

$$Z = 10 \log \left(\frac{Z}{1 \text{ mm}^6 \text{ m}^{-3}} \right) \quad (4)$$

The unit of the logarithmic quantity Z is termed dBz (decibel z).

5.2.2.2 Doppler Velocity and Spectral Width

If a relative motion does exist between the radar and the target, a frequency shift of the reflected wave can be observed by the radar. This effect was first described by the Austrian astronomer Christian Doppler in 1842. The resulting frequency is given by $f = f_0 (1 \pm v/c)$ with f_0 the transmitted frequency, v the relative speed and c the propagation speed of the wave (speed of light). The difference ($f - f_0$) is defined as the Doppler frequency f_D . In the case of radar the frequency shift is doubled, since the Doppler Effect occurs twice, once on the way to the target and once on the way back to the radar

$$f_D = \pm \frac{2v}{\lambda} \quad (5)$$

Due to technical limitations, the radar cannot measure the Doppler frequency directly; instead the radar detects phase differences between a number (~20 to ~250) of radar pulses and determines the Doppler frequency and its standard deviation from a time series of phase measurements. Even though radar doesn't measure the frequency shift directly, in radar meteorology the term Doppler velocity⁵ is widely used. Only a motion towards or away from the radar (the radial or line-of-sight component) can be detected by the Doppler Effect. By convention, a motion towards the radar introduces a negative Doppler velocity and a motion away from the radar a positive Doppler velocity. In general, it is assumed that precipitation particles move with the wind; however, their fall speed has to be taken into account. For vertical pointing radars, the observed Doppler velocity is the superposition of vertical air motion and fall speed of the particles.

The standard deviation of the phase measurements is termed spectral width because it describes the width of the Doppler velocity spectrum. Spectral width is a measure of the turbulence within the measurement volume – or – in the case of vertical pointing radar a measure of the diverse fall speed of different particle types and sizes.

5.2.2.3 Doppler Spectrum

Besides the technique described above, the phase measurements can be transferred by a Fourier transformation into frequency domain. Frequency is equivalent to Doppler velocity in this case (c. f. Eq. 5). The Doppler spectrum gives the backscattered power or reflectivity for each Doppler velocity bin. Fig. 4 shows an example of a Doppler spectrum from the vertical pointing MIRA36 cloud radar at UFS. The green area is the signal-to-noise ratio (SNR) of this spectrum

⁵ In radar meteorology the term "radial" component or velocity is preferred; scientists working with lidar prefer the term "line-of-sight" component or velocity.

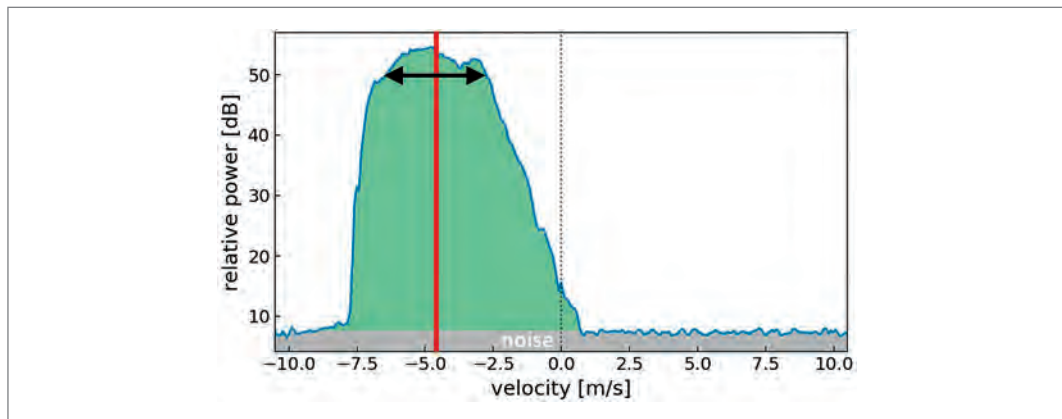


Fig. 4: Doppler spectrum (blue line) measured with MIRA36 at UFS (21 July 2018, 05:24 UTC, 300 m AGL). Grey area indicates noise level, green area is signal-to-noise power, red line is mean Doppler velocity, and black line with arrows indicates spectral width.

after the noise has been subtracted (in dB). With appropriate radar calibration constants, reflectivity can be derived from the measured SNR. Mean Doppler velocity is indicated by the red vertical line and the horizontal line with arrows indicate the estimation of the spectral width.

For the microphysical retrieval of observed clouds, several methods for evaluating Doppler spectra were developed, e.g. fitting of multi-modal Gauss curves (Melchionna et al., 2008) or determining of third (skewness) and fourth (kurtosis) moment of the spectrum to predict the onset of drizzle inside liquid clouds (Kollias et al., 2011; or Acquistapace et al., 2017).

5.2.2.4 Differential Reflectivity

Common dual-polarization weather radars use linear polarization with horizontal and vertical polarization planes. Differential reflectivity (Z_{DR}) is the ratio between the reflectivity factor measured at horizontal and vertical polarization

$$Z_{DR} = 10 \log \left(\frac{z_H}{z_V} \right) \quad (6)$$

with z_H the reflectivity factor at horizontal polarization and z_V the reflectivity factor at vertical polarization (both in mm^6/m^3). The unit of Z_{DR} is dB. Z_{DR} is the standard radar parameter, which can be measured with dual-polarization radar. Positive Z_{DR} is observed when particles are flat and fall more horizontally aligned. This is the case for raindrops larger than 1 mm in diameter and for ice needles or plates. Z_{DR} is used to improve the rainfall rate estimation and to identify hydrometeors. For measurements at low elevation angles, the range of Z_{DR} in rain is 0–5 dB. Particles like graupel or hail have an irregular shape and tumble and rotate during descent. Their Z_{DR} is typically around zero. For vertically pointing cloud radars this parameter is normally not used since particles fall horizontal aligned and due to their random horizontal orientation, no difference between the two orthogonal polarizations is observed.

5.2.2.5 Linear Depolarization Ratio

The linear depolarization ratio (LDR) describes how much energy of the transmitted horizontal polarized wave is scattered back vertically polarized

$$LDR = 10 \log \left(\frac{z_{VH}}{z_H} \right) \quad (7)$$

with z_{VH} the reflectivity factor (in mm^6/m^3) received with vertical polarization while transmitted with horizontal polarization. The unit of LDR is dB. LDR is caused by particles which are canted during falling or tumble and rotate heavily while falling. These are usually particles which have an irregular shape and/or are water coated ice particles like melting snowflakes or wet graupel or hail. LDR is about –35 dB in weak rain, –25 dB for graupel and –15 dB or higher for melting hail. LDR is also used to classify hydrometeors and to detect the presence of insects (frequently observed also at UFS). The lower limit of LDR is given by technical constraints like the isolation between the two receiver channels and the purity of the antenna shape and the feed horn.

5.3 Observations and Measurements at UFS

5.3.1 Clouds and Precipitation

5.3.1.1 Cloud Statistics

The continuous operation of the cloud radar since December 2011 allows for the evaluation of statistical properties of clouds and precipitation in the Alpine region above the Schneefernerhaus. An exemplary analysis is shown in Fig. 5, more detailed analysis can be found in Häring (2016). Kneifel et al., 2022 present a statistical analysis of clouds and precipitation at UFS by combining radar with other long-term remote sensing observations available at UFS.

Fig. 5 shows the frequency distribution of reflectivity and Doppler velocity as well as the normalized number of observations with height for the year 2014. The radar is located at 2671 m above sea level. For the first 150 or 180 m above the radar, no radar measurements are available since the radar has to switch from transmit to receive which requires a finite amount of time.

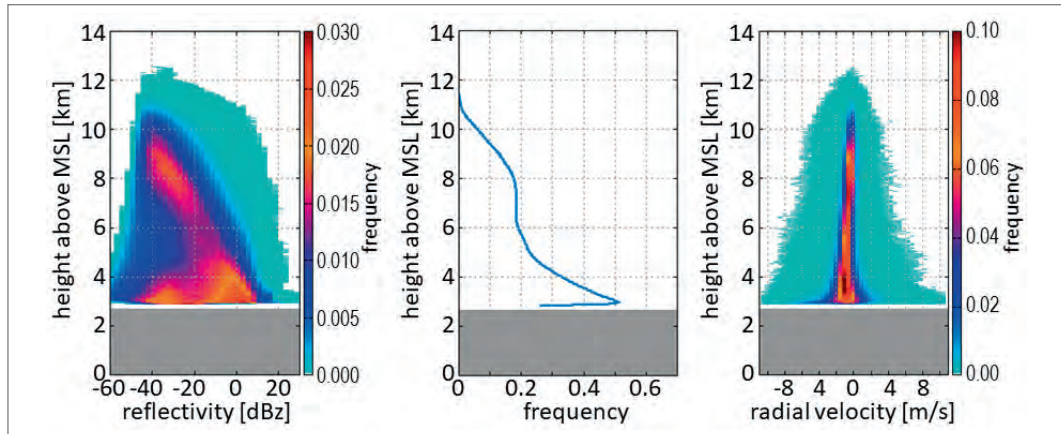


Fig. 5: Frequency distribution of reflectivity as a function of height (left), normalized number of reflectivity observations (center), and frequency distribution of Doppler velocity (right) for the year 2014.

An automatic quality control and hydrometeor classification was used to filter meteorological echoes from non-meteorological echoes like ground targets, birds, insects, or the gondola of the *Gletscherbahn*.

Fig. 5 (center) shows that about half of the time there are low clouds above Schneefernerhaus or the site itself is within clouds. The fraction is decreasing with height due to the variation in thickness of clouds. At about 20% of the time there are clouds in the height band 6 to 8 km above sea level. These are cirrus clouds with varying thickness. Clouds reach up to 12.5 km MSL.

The frequency of reflectivity measurements (Fig. 5, left) shows a wide range reaching from about 20 dBz down to the minimum sensitivity of the radar which is about -50 dBz at a range of 5 km from the radar. Three distinct maxima can be identified in the reflectivity distribution: The maximum around 8 km height indicates reflectivity values of cirrus clouds, the rare occurrence of high values at that height are related to deep convection. At low levels two maxima can be identified. The one at high reflectivity values is related to precipitation, the other at low reflectivity values is related to clouds. The high reflectivity values below 3.5 km indicate the occurrence of rain during summer. The growths of particles from cloud to precipitation can be seen with the increase of the reflectivity center with decreasing height.

The frequency distribution of Doppler velocity (Fig. 5, right) shows a wide range of observed velocities. While the fall speed (i. e. negative Doppler velocity) of cloud particles is in the order of 0.1 m/s, the typical fall velocity of snow is 1 m/s, and of rain is about 5 m/s; the observations show a broad distribution around the expected values. The reason for this is vertical air motion caused by the flow over the Alps and leading to strong up- and downdrafts. An example is shown in the next section.

5.3.1.2 Case Studies

Three exemplary observations typical for the cloud radar measurements at Schneefernerhaus will be shown in this section.

The first example contains observations of contrail cirrus. Fig. 6 shows the visual impression taken with a vertical looking camera and the associated reflectivity observations with the cloud radar. The reflectivity time-height display shows at least three structures which can be attributed to contrail cirrus, namely at 15:05, 15:20 and 15:30 UTC on March 3rd, 2015. The contrail cirrus forms first at about 3.9 km above the radar and then descent during about 3–4 minutes down to 3.3 km. Below that height, obviously ambient humidity is too low and the contrails dissolve rapidly. The cloud layer at about the same height later on indicates that the atmosphere was sufficiently humid for contrail formation. The very thin cloud layer between 15:15 and 15:30 is hardly to be seen in the photo.

Fig. 7 shows time-height cross-sections of reflectivity and Doppler velocity of a breaking wave event on September 30th, 2012. The velocity shows comb-like structures (7:10 to 7:40) a downward motion of about 3 m/s and next to it an updraft of about 4 m/s. The fall speed of the small

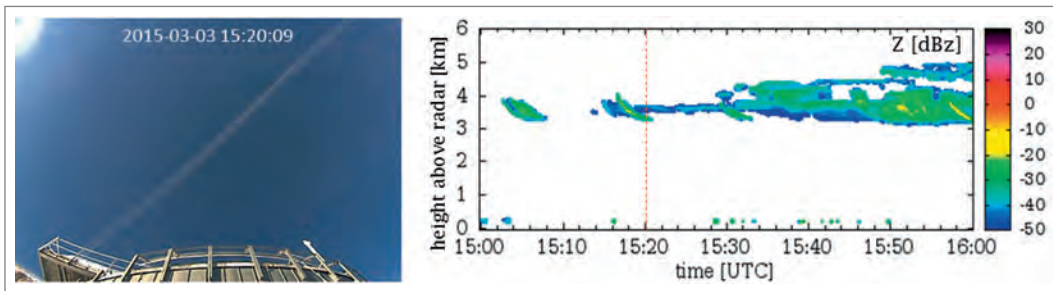


Fig. 6: Observation of a contrail by vertical looking camera (left) and cloud radar with a time-height display of reflectivity (right) on 3rd March 2015; the dashed orange line indicates the time of the photo by the automatic camera.

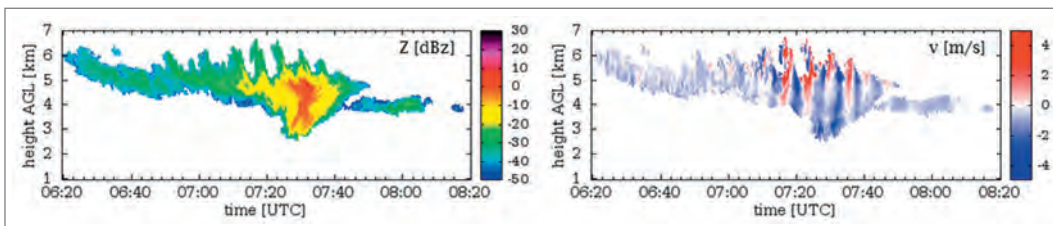


Fig. 7: Time-height cross-sections of reflectivity (left) and Doppler velocity (right) of a breaking wave event on 30th September 2012.

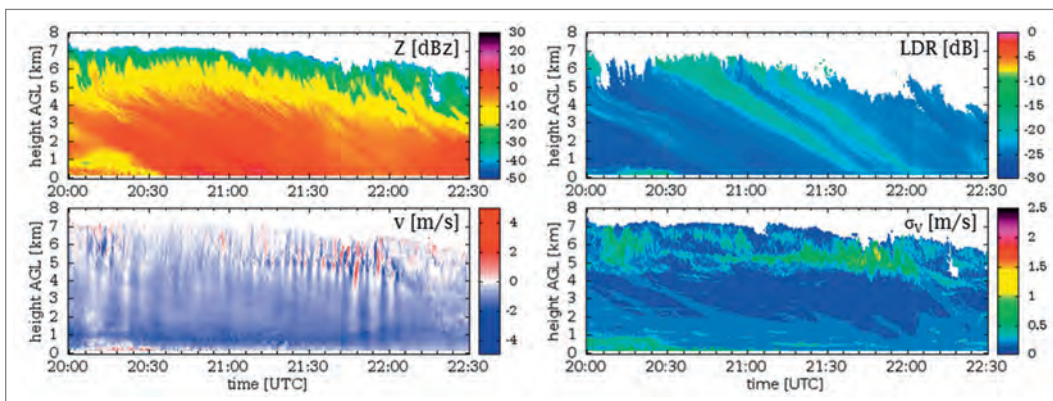


Fig. 8: Time-height cross-sections of reflectivity (upper left), linear depolarization ratio (upper right), Doppler velocity (lower left), and spectral width (lower right) of a fall streak event on 28th November 2012.

ice particles at that height is negligible (< 0.5 m/s). The breaking of waves is probably caused by strong wind shear at an inversion layer at about 9.5 km MSL (≈ 6.8 km above radar). The Innsbruck radio sounding from 3 UTC indicates horizontal winds with 21 m/s at 5 km and 39 m/s at 8 km above radar. Wind direction was 244° and 220°, respectively.

The third example is an event with fall streaks observed in snow. On November 28th, 2012 a homogeneous, about 7 km deep cloud layer with snowfall at ground was observed (Fig. 8). The time-height cross-section of reflectivity shows some diagonal structures which are related to fall streaks, when parcels of hydrometeors with enhanced reflectivity are falling down. At a time-height cross-section, the parcels can be seen first at cloud top and then later at the bottom. The signature of the fall streaks is more dominant in the linear depolarization ratio LDR (see Fig. 8, upper right). While LDR is about -25 dB outside the streaks it is about -15 dB within the streaks. This indicates larger and more irregular shaped particles with an unstable falling behavior. The main reason for the initiation of the streaks with enhanced LDR remains unclear. Doppler velocity shows up- and down-drafts at cloud top, there might be wind shear at that height. The enhanced turbulence in this upper region of the cloud is also seen in the spectral width (Fig. 8, lower left). Another possible explanation is the disturbances by aircraft, causing additional turbulence, humidity, and aerosol particles which in turn will initiate a different kind of ice particles.

5.3.1.3 Retrieval of Cloud Properties

Cloud physicists do prefer quantities which are related to cloud microphysics. Here we will show how radar parameters can be used to derive quantities like mean diameter of the particles and the ice water content.

A procedure to retrieve mean diameter from vertical pointing cloud radar was proposed by Matrosov et al. (2002). They use an empirical relation between mean diameter D_0 and fall velocity V_t

$$D_0 = 9 \cdot 10^{-4} V_t^3 - 6.6 \cdot 10^{-2} V_t^2 + 6.2 V_t - 9.7 \quad (8)$$

with $V_t \geq 0.06 \text{ m s}^{-1}$. From D_0 the ice water content IWC can be retrieved using a relation suggested by Atlas et al. (1995)

$$IWC = \frac{Z}{G \cdot D_0^3} \quad (9)$$

with Z in $\text{mm}^6 \text{ m}^{-3}$, IWC in g m^{-3} , and D_0 in μm . G is a coefficient which depends on the bulk density, the shape and the particle size distribution.

The disadvantage using this approach at Schneefernerhaus is the occurrence of large vertical air motions which can be hardly corrected with the required precision. An alternative approach was suggested by Protat et al. (2007). They suggest using reflectivity and ambient temperature

$$\log(IWC) = 0.000372 Z_{\text{dBz}} T + 0.0782 Z_{\text{dBz}} - 0.0153 T - 1.54 \quad (10)$$

with Z_{dBz} in dBz and temperature T in $^\circ\text{C}$; or alternatively using only reflectivity if temperature is not available

$$IWC = 0.082 z^{0.554} \quad (11)$$

Examples of the retrieval will be shown in section 5.3.2.2.

5.3.1.4 Retrieval of Vertical Velocity in Rain

As mentioned above in section 5.2.1.3 and 5.2.2.2, the measured Doppler velocity of a vertically pointing radar is the sum of the terminal fall velocity of the particles and the vertical air motion. Hauser and Amayenc (1981) suggested a method to retrieve rain drop size parameterization and vertical air motion. Assuming an exponential rain drop size distribution $n(D) = N_0 e^{-\lambda D}$, the parameters N_0 as the hypothetical number of drops with diameter 0, the slope λ of the distribution, and the vertical air motion will iteratively be estimated until the difference between measured and estimated reflectivity (from N_0 and λ) is minimized.

The number of cases where this algorithm can be applied to MRR observations at Schneefernerhaus is limited since a sufficient thick rain layer ($> 300 \text{ m}$) is fairly rare at the site. Fig. 9 shows two examples for the retrieval of the vertical air motion using a similar method proposed by Rogers (1964). On August 20th, 2016 mainly updrafts are observed, while on August 5th, 2016

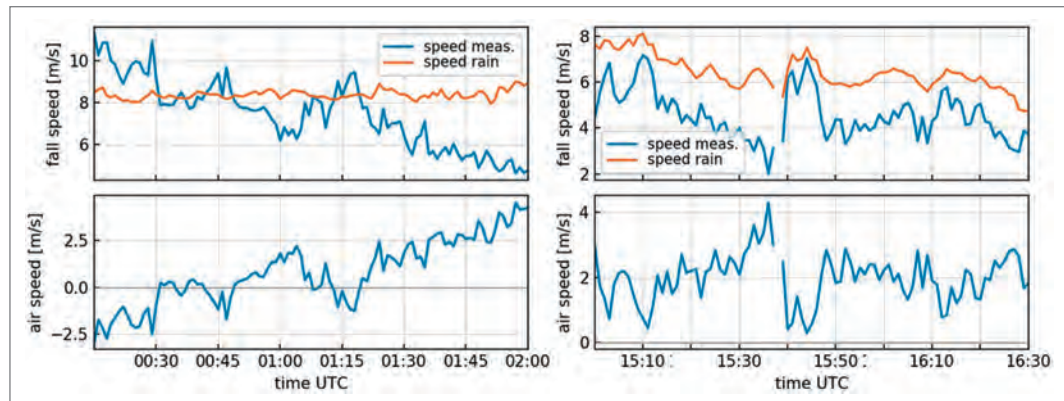


Fig. 9: Measured Doppler velocity (blue line – top figure) and retrieved vertical air motion (blue line – bottom figure) as well as fall velocity of the rain drop size distribution (orange line – top figure) for two events. Left: 5th August 2016; right: 20th August 2016. After Stucke (2017).

up- and downdrafts can be seen. The observations seem plausible considering the airflow on those days. Unfortunately, no independent verification for the retrieval of vertical air motion above UFS is available for these cases.

5.3.2 Evaluation of Satellite Observations with Radar at UFS

While the cloud radar and the micro rain radar provide high resolution data on a local vertical profile, satellite observations are used to provide information on a global or hemispheric scale. Satellites often only observe the top of the clouds and depending on the observation technique, the structure of the clouds and precipitation information can only be partly retrieved. Here we will show two examples, one using the polar orbiting cloud radar onboard CloudSat (Stephens et al., 2002), and a second example using the geostationary Meteosat Second Generation SEVIRI imager (Schmetz et al., 2002).

5.3.2.1 CloudSat Observations

Polar orbiting satellites like CloudSat, equipped with a nadir pointing W-band (wavelength 3.2 mm) cloud radar, or Calipso (equipped with lidar) very seldom pass directly over a specific site like the Schneefernerhaus. In addition, for the evaluation of cloud measurements, clouds have to be present during the short visiting time. To increase the sample number, all passes within 15 km have been used for the evaluation presented here. However, it has to be considered that due to the large inhomogeneity of the terrain, different types of clouds might be compared within the CloudSat footprint (diameter 1.2 km) and by the MIRA36 radar measuring only directly above UFS.

Fig. 10 shows a comparison of cloud properties and averaged reflectivity profiles for both cloud radars observed from 2012 to 2015. Only measurements above 3 km MSL have been considered for both systems in order to avoid disturbances due to surface reflections in the CloudSat data. The CloudSat radar is less sensitive compared to the MIRA36 radar. The reflectivity distribution and the averaged profiles agree very well, the difference is only 0.8 dB. The CloudSat radar is highly accurately calibrated using the well-known sea surface reflection (Kollias et al., 2019). The MIRA36 is calibrated by the manufacturer, a continuous independent calibration at the site is challenging because the radar beam cannot be directed towards a target whose scattering

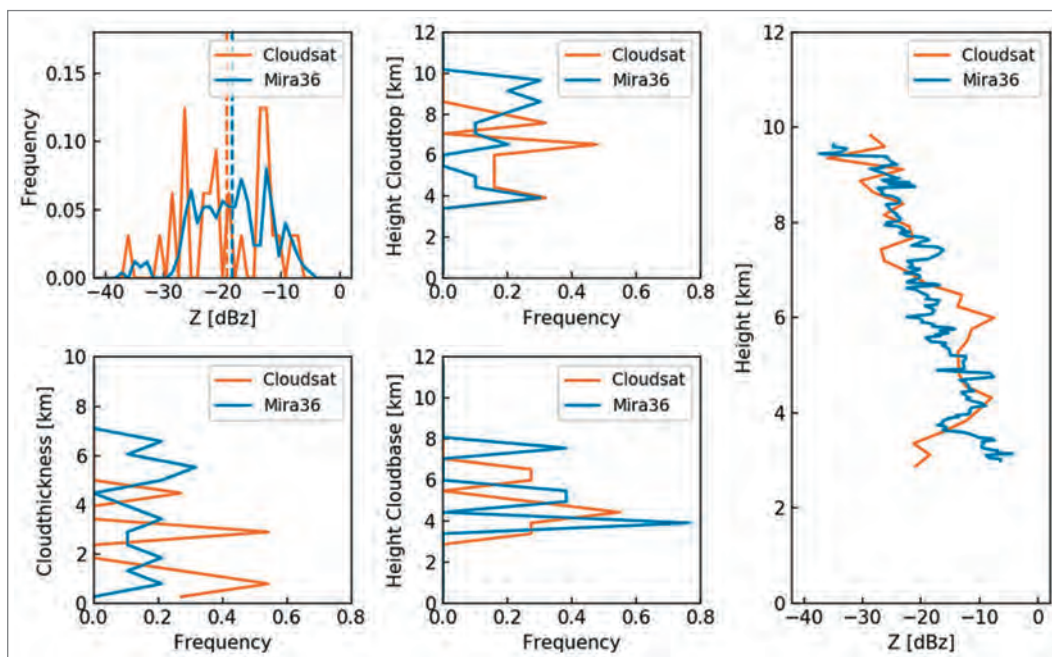


Fig. 10: CloudSat (orange) and UFS-MIRA (blue) observations of cloud properties for the years 2012–2015. Top left: frequency distribution of reflectivities; Top center: frequency distribution of cloud top height; bottom left: frequency distribution of cloud thickness; bottom center: frequency distribution of cloud base height. Right: averaged reflectivity profiles.

properties are well known. The lower reflectivity values for the CloudSat radar profile between 3 and 3.7 km are most likely caused by attenuation in thick clouds. The cloud properties show that the lower sensitivity of the CloudSat radar has limitations observing high thin cirrus clouds.

5.3.2.2 Meteosat SEVIRI Observations

The geostationary observations of SEVIRI allow for a continuous observation of cloud properties. For a comparison we select the ice water path (*IWP*) which is the vertical integral of *IWC*. SEVIRI resolution is about $3.2 \times 5.5 \text{ km}^2$ over the Schneefernerhaus. Nine values of *IWP* over an area of 3 by 3 pixels (app. $10 \times 16 \text{ km}^2$) were estimated using the APICS algorithm (Bugliaro et al., 2011). The *IWP* was then compared to the vertically integrated *IWC* derived from the MIRA36 measurements. The algorithms described by equations (9) to (11) were applied for the MIRA36 measurements.

Fig. 11 shows the comparison for two events, one in June 2014 and one in January 2015. In general, there is an agreement between the radar algorithms using reflectivity only (*IWP-Z*; Eq. 11) and temperature and reflectivity (*IWP-Z-T*; Eq. 10), whereas the algorithm using vertical velocity (*IWP-Z-VEL*; Eq. 9) shows a large scatter. This is attributed to the unknown vertical air motion over the site. Obviously, during times where the vertical air motion was small, the *IWP-Z-VEL* algorithm agrees well with the other two algorithms. The comparison to the APICS algorithm shows varying agreement. This mainly depends on the structure of the clouds and precipitation. The SEVIRI retrieval is dominated by information originating from the cloud top area due its limited capability to penetrate thicker clouds. The lower part of thick clouds or precipitation is not seen by SEVIRI.

The measurements on June 29th, 2014 show a nearly homogeneous cloud layer with precipitation, the *IWP* is overestimated by SEVIRI, especially during the time when rain was observed at Schneefernerhaus (approximately until 12:30). Only minor horizontal variation is visible within the 3×3 SEVIRI pixels. On January 16th, 2015 a deep cirrus layer was observed. The 3×3 SEVIRI pixels show large variation, this is an indication that there was high spatial variation in the cloud layer and the measurements by the radar might not be representative for the area seen by SEVIRI.

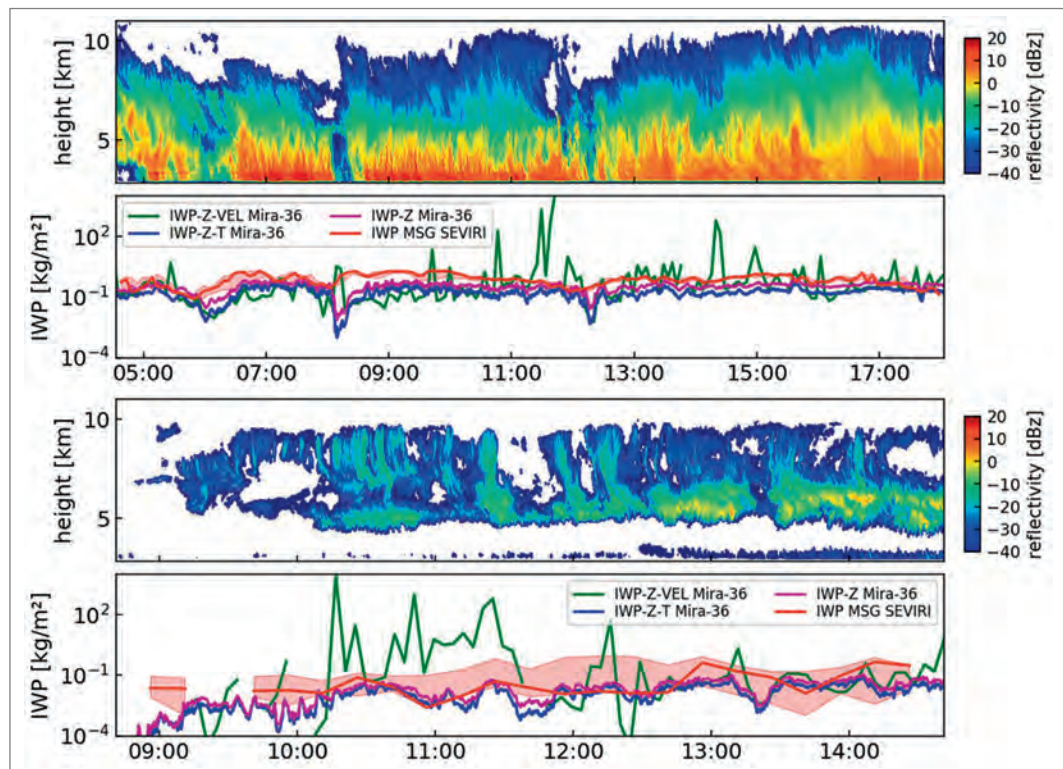


Fig. 11: Reflectivity observations by MIRA36 and retrieved ice-water-path (*IWP*) for 29 June 2014 (top 2 rows) and 16 January 2015 (bottom 2 rows). *IWP* estimated from MIRA by 3 techniques (see text) and from Meteosat SEVIRI. Red line is pixel over Schneefernerhaus; shaded area is range of *IWP* over 3×3 pixels.

5.3.3 The TOSCA Campaign

The TOSCA campaign (**T**owards an **O**ptimal estimation-based **S**now **C**haracterization **A**lgorithm) took place at Schneefernerhaus during the winter 2007/2008 and 2008/2009. Details can be found in Löhnert et al. (2011). The motivation for the campaign was a synergistic combination of state-of-the-art remote sensing instruments with the goal to develop a modular optimal-estimation algorithm and to evaluate the potential for deriving columnar snow microphysics. The success of running the first cloud radar at the UFS was the main motivation to permanently install such a radar at UFS. During TOSCA, the cloud radar data were combined with ceilometer and the two permanently installed microwave radiometers (Humidity and Temperature Profiler HATPRO and Dual Polarization Radiometer DPR) providing observations in the frequency range from 22 up to 150 GHz, which is similar to space-borne microwave sensors. In addition, in-situ sensor for the size, fall velocity and shape of the snowflakes were installed at the UFS. Radar and radiometer are often combined because the radar provides profile information while the radiometer is able to better quantify the integrated quantities in the atmospheric column (e.g., ice water path, liquid water path, water vapor integral). For snow and ice processes, the presence of supercooled liquid water (liquid water can be found down to -38 °C in the atmosphere) plays a central role. While it is very hard to detect it in radar observations, the radiometers are extremely sensitive to it, especially at the higher frequencies provided at the UFS. In general, the radiometers are only sensitive to scattering by ice and snow particles at frequencies larger than 90 GHz, which makes them well suited to constrain the amount of liquid water in comparison to ice.

One main outcome of TOSCA was that supercooled liquid water is almost always present in snowfall at UFS and its amounts could be quantified and linked to other parameters such as temperature, for the first time (Löhnert et al., 2011). The unique DPR radiometer, further provided the first observations of snow scattering signals in ground-based radiometers – an effect, which was so far only been known for space-borne radiometers. This confirmed the principal potential of ground-based radiometers to constrain snowfall properties (Kneifel et al., 2010). The polarimetric observations of the DPR further confirmed that snowflakes fall with a preferential orientation – a question which was debated for a long time in the snowfall remote sensing community (Xie et al., 2012).

The long-term combined radar-radiometer measurements also provided valuable data to develop new absorption models for supercooled liquid water (Kneifel et al., 2014; Turner et al., 2016), which are key components for global satellite retrievals. The parallel observations of the MIRA36 cloud radar and the MRR also provided a dataset to develop a new algorithm to measure snowfall with the MRR (Kneifel et al., 2011; Maahn and Kollias, 2012). These studies triggered the use of MRRs in other remote areas such as the Arctic and Antarctic for the so far very difficult estimation of snowfall – the main source term for the polar ice sheet mass balance.

An interesting feature found in the in-situ measurements (2D-video disdrometer; c.f. Fig. 7 in Löhnert et al., 2011) during TOSCA was that maximum snow particle size D_{\max} seems to be temperature independent – except for the temperature range between -10 and -15 °C where large snow crystals occur more frequent. In this temperature range, the super saturation over ice with respect to liquid water reaches its maximum value so that the Wegener-Bergeron-Findeisen process, i.e. the transformation of liquid drops to ice crystals via gas phase, will be more effective. Also, snow crystals are mostly of dendritic structure in this temperature range. Both conditions are preferable for the fast and effective growth by aggregation of snow crystals in this “secondary growth region.”

5.3.4 Cloudnet

Cloudnet is an European initiative (Illingworth et al., 2007) to provide a systematic evaluation of clouds and precipitation in numerical weather prediction models. The efforts to improve the representation of clouds and precipitation in forecast models have been limited by the difficulty to make appropriate and accurate observations. Cloud parameters used in models differ from the parameters which are available from observations; thus, a common basis needs to be defined for comparison and evaluation. Another fact is that often evaluations are performed based on case studies; however, to improve forecast models a long-term evaluation is needed. To achieve a suitable evaluation, the Cloudnet project was established. It involves instrument

operators as well as developers of forecast models all across Europe. A number of already existing ground based remote sensing sites were brought together for this purpose. These sites are operated now since many years in order to gain statistics unaffected by seasonality. Moreover, the Cloudnet community was able to develop robust algorithms for quality control and retrieval of microphysical quantities of clouds and precipitation.

Cloudnet is embedded in the European ACTRIS (Aerosols, Clouds and Trace gases Research Infrastructure) project and in Germany supported by the HD(CP)² (High Definition Clouds and Precipitation for advancing Climate Prediction) project. Currently, about 10 sites contribute to Cloudnet together with additional non-European sites equipped with similar instrumentation. The Meteorological Institute (MIM) at Munich University (LMU) and the UFS Schneefernerhaus are members of Cloudnet since 2018. Processing of UFS data is performed at MIM. Real-time observations and model forecasts together with daily and monthly quicklooks and statistics of model performance are provided at the Cloudnet web site (<http://cloudnet.fmi.fi/>).

The core instruments at MIM and UFS are the high power and sensitive MIRA36 cloud radar, a low-power lidar – the ceilometer, and the multi-wavelength microwave radiometer HATPRO. The radar provides detailed information on the vertical structure of the clouds. The ceilometer is used to identify the cloud base – mainly of water clouds – more accurately. If attenuation by cloud particles is not too strong, profiles of the lidar backscatter signal are available in the cloud. The microwave radiometer provides vertical profiles of temperature and humidity, and integrated quantities like liquid water path (LWP) and vertical integrated water vapor (I WV).

The Cloudnet processing chain includes in a first step a target classification using the fact that the radar is sensitive to large particles like rain, drizzle, ice particles, while the lidar is sensitive to smaller particles like cloud droplets and aerosols. Quality control of the radar data includes an attenuation correction for gaseous attenuation (water vapor and oxygen) as well as for liquid water using information from the microwave radiometer. Doppler velocity helps to distinguish between snow and rain. Higher level Cloudnet products comprise liquid water content (LWC), ice water content (IWC), and drizzle parameters. Fig. 12 shows a sample of the input measure-

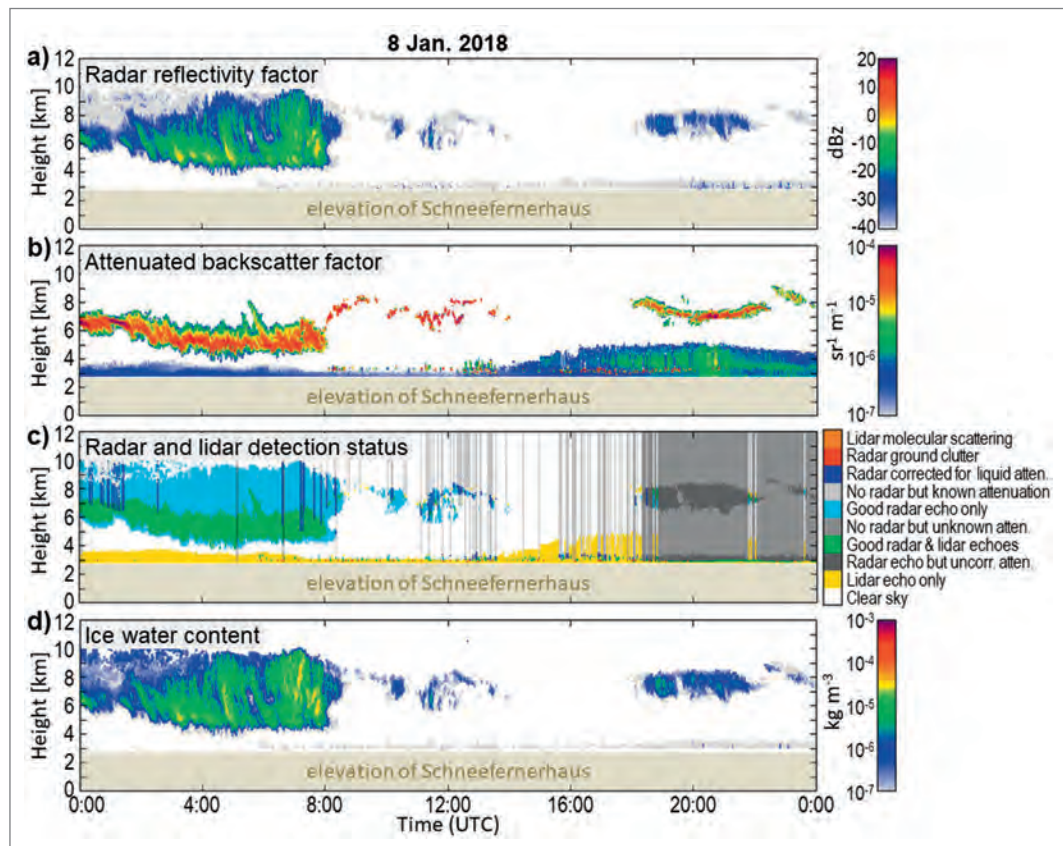


Fig. 12: Cloudnet products: Measurements with cloud radar (a) and ceilometer (b) at UFS Schneefernerhaus on 8th January 2018. The radar and lidar status is shown in c), the retrieved ice water content (IWC) in d).

ments and the retrieved quantities. It can be clearly observed that the lidar partly penetrates into the cloud and there is an overlap between both instruments. Future activities will also include the evaluation of satellite observations of clouds and precipitation.

5.4 Summary and Conclusions

Meteorological radar is an essential tool for research, diagnostic, and nowcasting of clouds and precipitation. Modern radar systems provide a number of parameters like reflectivity, Doppler velocity, or dual-polarization products. The parameters can be used to study intensity, motion, or habits of cloud and precipitation particles.

At UFS Schneefernerhaus a MIRA36 cloud radar (wavelength 8 mm) and a micro-rain-radar (MRR, wavelength 12 mm) have been installed. The cloud radar has been operated since the end of 2011, a similar system was installed already 2008–2009 during the TOSCA campaign; the MRR has been operated since the beginning of 2008. The long-term operation of the radars allows for deriving detailed statistics of clouds and precipitation above UFS Schneefernerhaus. Clouds cover the sky over Schneefernerhaus about half of the time and are observed up to 12.5 km above sea-level. Some examples of measurements of contrail cirrus or fall streaks were given to show the benefit from radar observations.

Both radar systems operate in a vertical pointing mode and provide cloud and precipitation structures above Schneefernerhaus. The cloud radar provides data with high temporal (10 seconds) and spatial (30 m) resolution at a beam width of 0.6° (e. g. diameter of 50 m at a distance of 5 km). Both systems provide in real-time the Doppler spectra, a quantity which can be used to study the falling behavior and thus the habit of cloud and precipitation particles. One of the major challenges in the data evaluation is the high variability of the surrounding wind field, especially the vertical air motion. Fall speed of cloud particles is superimposed to the vertical air motion and turbulence. Algorithms have been developed which are able to account for these effects; however, they require prior knowledge of terminal fall speed and the particle size distribution.

The long-term operation of the radars and the synergy with lidar and microwave radiometer gives a unique possibility for the evaluation of cloud and precipitation microphysics in numerical weather prediction models or of satellite measurements of clouds and precipitation. The UFS is worldwide the only mountain site which provides now a decade-long remote sensing observations of clouds and precipitation using this comprehensive instrument combination. This allows for monitoring potential changes in clouds and precipitation in a warming climate which is expected to be particularly pronounced at higher altitudes. The European project Cloudnet is designed for the evaluation of several weather forecast models by long-term observations at a number of sites with similar instrumentation like the Schneefernerhaus. Together with a ceilometer as low-cost and robust lidar system and the microwave radiometer, the cloud radar is contributing to Cloudnet. The same constellation together with the algorithms provided by Cloudnet can also be used for the evaluation of satellite measurements. Polar orbiting satellites like CloudSat, Calipso, GPM, or the upcoming EarthCARE satellite provide measurements with radar and lidar which are comparable to the observations at Schneefernerhaus. Geostationary satellites like Meteosat provide a set of additional cloud parameters which can be used for further evaluations. Even though the spatial resolution of geostationary satellites is not sufficient to describe clouds in the complex orography of the Wetterstein massif, they help in understanding the temporal evolution and regional distribution of the cloud systems observed above Schneefernerhaus.

Acknowledgement

The MIRA36 cloud radar was provided through the funds of the developing project plan (EPP) 2008–2012 of the Bavarian State Ministry of the Environment. The support from the UFS team – especially Markus Neumann and Till Rehm – is greatly acknowledged, without their help and support the installation and operation of the instruments would be much more challenging and the long time series of continuous operation would not be possible. We also have to thank Matthias Bauer-Pfundstein from METEK GmbH for the support during the installation and operation of the cloud radar.

References

- Acquistapace, C., S. Kneifel, U. Löhnert, P. Kollias, M. Maahn, and M. Bauer-Pfundstein, 2017: Optimizing observations of drizzle onset with millimeter-wavelength radars, *Atmos. Meas. Tech.*, **10**, 1783–1802, <https://doi.org/10.5194/amt-10-1783-2017>.
- Atlas, D., S.Y. Matrosov, A.J. Heymsfield, M. Chou, and D.B. Wolff, 1995: Radar and radiation properties of clouds. *J. Appl. Meteor.*, **34**, 2329–2345, [https://doi.org/10.1175/1520-0450\(1995\)034<2329:RARPOI>2.0.CO;2](https://doi.org/10.1175/1520-0450(1995)034<2329:RARPOI>2.0.CO;2).
- Atlas, D., R. Srivastava, and R. Sekhon, 1973: Doppler radar characteristics of precipitation at vertical incidence. *Rev. Geophys. Space Phys.*, **11**, 1–35, <https://doi.org/10.1029/RG011i001p00001>.
- Bringi, V.N., and V. Chandrasekar, 2001: *Polarimetric Doppler Weather Radar: Principles and Applications*. Cambridge University Press, 648 pp, <https://doi.org/10.1017/CBO9780511541094>.
- Bugliaro, L., T. Zinner, C. Keil, B. Mayer, R. Hollmann, M. Reuter, and W. Thomas, 2011: Validation of cloud property retrievals with simulated satellite radiances: a case study for SEVIRI. *Atmos. Chem. Phys.*, **11**, 5603–5624, <https://doi.org/10.5194/acp-11-5603-2011>.
- Fabry, F. (2015). *Radar Meteorology: Principles and Practice*. Cambridge: Cambridge University Press. <https://doi.org/10.1017/CBO9781107707405>.
- Görsdorf, U., V. Lehmann, M. Bauer-Pfundstein, G. Peters, D. Vavriv, V. Vinogradov, and V. Volkov, 2015: A 35-GHz polarimetric Doppler radar for long-term observations of cloud parameters – description of system and data processing. *J. Atmos. Oceanic Technol.*, **32**, 675–690, <https://doi.org/10.1175/JTECH-D-14-00066.1>.
- Häring, A., 2016: *Synergetic cloud observations with cloud radar and satellite instruments*. Master Thesis, Ludwig-Maximilians-Universität München, 69 pp. Available at <https://elib.dlr.de/107232>.
- Illingworth, A. J., R. J. Hogan, E. O’Connor, D. Bouniol, M. E. Brooks, J. Delanoé, D. P. Donovan, J. D. Eastment, N. Gaussiat, J. W. Goddard, M. Haefelin, H. K. Baltink, O. A. Krasnov, J. Pelon, J. Piriou, A. Protat, H. W. Russchenberg, A. Seifert, A. M. Tompkins, G. van Zadelhoff, F. Vinit, U. Willén, D. R. Wilson, and C. L. Wrench, 2007: Cloudnet: Continuous evaluation of cloud profiles in seven operational models using ground-based observations. *Bull. Amer. Meteor. Soc.*, **88**, 883–898, <https://doi.org/10.1175/BAMS-88-6-883>.
- Illingworth, A. J., H. W. Barker, A. Beljaars, M. Ceccaldi, H. Chepfer, N. Clerbaux, J. Cole, J. Delanoë, C. Domenech, D. P. Donovan, S. Fukuda, M. Hiraoka, R. J. Hogan, A. Huenerbein, P. Kollias, T. Kubota, T. Nakajima, T. Y. Nakajima, T. Nishizawa, Y. Ohno, H. Okamoto, R. Oki, K. Sato, M. Satoh, M. W. Shephard, A. Velázquez-Blázquez, U. Wandinger, T. Wehr, and G. van Zadelhoff, 2015: The EarthCARE satellite: The next step forward in global measurements of clouds, aerosols, precipitation, and radiation. *Bull. Amer. Meteor. Soc.*, **96**, 1311–1332, <https://doi.org/10.1175/BAMS-D-12-00227.1>.
- Kneifel, S., U. Löhnert, A. Battaglia, S. Crewell, and D. Siebler, 2010: Snow scattering signals in ground-based passive microwave measurements. *J. Geophys. Res.*, **115**, D16214, <https://doi.org/10.1029/2010JD013856>.
- Kneifel, S., M. Maahn, G. Peters, and C. Simmer, 2011: Observation of snowfall with a low-power FM-CW K-band radar (Micro Rain Radar). *Meteorol. Atmos. Phys.*, **113**, 75–87, <https://doi.org/10.1007/s00703-011-0142-z>.
- Kneifel, S., B. Pospichal, L. von Terzi, T. Zinner, M. Puh, M. Hagen, B. Mayer, U. Löhnert, S. Crewell, 2021: Multi-year cloud and precipitation statistics observed with remote sensors at the high-altitude Environmental Research Station Schneefernerhaus in the German Alps. *Meteorologische Zeitschrift*, **31**, 69–86. <https://doi.org/10.1127/metz/2021/1099>.
- Kneifel, S., S. Redl, E. Orlandi, U. Löhnert, M. P. Cadeddu, D. D. Turner, and M.-T. Chen, 2014: Absorption properties of supercooled liquid water between 31 and 225 GHz: Evaluation of absorption models using ground-based observations. *J. Appl. Meteor. Climatol.*, **53**, 1028–1045, <https://doi.org/10.1175/JAMC-D-13-0214.1>.
- Kollias, P., B. Puigdomènech Treserras, and A. Protat, 2019: Calibration of the 2007–2017 record of ARM Cloud Radar Observations using CloudSat, *Atmos. Meas. Tech.*, **12**, 4949–4964, <https://doi.org/10.5194/amt-12-4949-2019>.
- Kollias, P., J. Rémillard, E. Luke, and W. Szyrmer, 2011: Cloud radar Doppler spectra in drizzling stratiform clouds: 1. Forward modeling and remote sensing applications, *J. Geophys. Res.*, **116**, D13201, <https://doi.org/10.1029/2010JD015237>.
- Löffler-Mang, M. and J. Joss, 2000: An optical disdrometer for measuring size and velocity of hydrometeors. *J. Atmos. Ocean. Tech.*, **17**, 130–139, [https://doi.org/10.1175/1520-0426\(2000\)017<0130:AODFMS>2.0.CO;2](https://doi.org/10.1175/1520-0426(2000)017<0130:AODFMS>2.0.CO;2).
- Löhnert, U., S. Kneifel, A. Battaglia, M. Hagen, L. Hirsch, and S. Crewell, 2011: A multisensor approach toward a better understanding of snowfall microphysics: The TOSCA project. *Bull. Amer. Meteorol. Soc.*, **92**, 613–628, <https://doi.org/10.1175/2010bams2909.1>.
- Maahn, M. and P. Kollias, 2012: Improved Micro Rain Radar snow measurements using Doppler spectra post-processing, *Atmos. Meas. Tech.*, **5**, 2661–2673, <https://doi.org/10.5194/amt-5-2661-2012>.

- Matrosov, S.Y., A.V. Korolev, and A. J. Heymsfield, 2002: profiling cloud ice mass and particle characteristic size from Doppler radar measurements. *J. Atmos. Oceanic Technol.*, **19**, 1003–1018, [https://doi.org/10.1175/1520-0426\(2002\)019<1003:PCIMAP>2.0.CO;2](https://doi.org/10.1175/1520-0426(2002)019<1003:PCIMAP>2.0.CO;2).
- Mech, M., E. Orlandi, S. Crewell, F. Ament, L. Hirsch, M. Hagen, G. Peters, and B. Stevens, 2014: HAMP – the microwave package on the High Altitude and LOng range research aircraft (HALO), *Atmos. Meas. Tech.*, **7**, 4539–4553, <https://doi.org/10.5194/amt-7-4539-2014>.
- Melchionna, S., M. Bauer, and G. Peters, 2008: A new algorithm for the extraction of cloud parameters using multipeak analysis of cloud radar data – first application and preliminary results. *Meteorol. Z.*, **17**, 613–620, <https://doi.org/10.1127/0941-2948/2008/0322>.
- Peters, G., B. Fischer, T. Andersson, 2002: Rain observations with a vertically looking Micro Rain Radar (MRR). *Boreal Environ. Res.*, **7**, 353–362.
- Protat, A., J. Delanoë, D. Bouniol, A. J. Heymsfield, A. Bansemer, and P. Brown, 2007: evaluation of ice water content retrievals from cloud radar reflectivity and temperature using a large airborne in situ microphysical database. *J. Appl. Meteor. Climatol.*, **46**, 557–572, <https://doi.org/10.1175/JAM2488.1>.
- Rogers, R.R., 1964: An extension of the Z-R relationship for Doppler radar. *Proc. 11 Weather Radar Conf.*, Boulder, Amer. Meteor. Soc., 158–169.
- Schmetz, J., P. Pili, S. Tjemkes, D. Just, J. Kerkmann, S. Rota, and A. Ratier, 2002: An Introduction to Meteosat Second Generation (MSG). *Bull. Amer. Meteor. Soc.*, **83**, 977–992, [https://doi.org/10.1175/1520-0477\(2002\)083%3C0977:AITMSG%3E2.3.CO;2](https://doi.org/10.1175/1520-0477(2002)083%3C0977:AITMSG%3E2.3.CO;2).
- Skolnik, M.I., 2008: *Radar Handbook*. 3rd ed. McGraw-Hill Professional, 1350 pp.
- Stephens, G.L., D.G. Vane, R.J. Boain, G.G. Mace, K. Sassen, Z.Wang, A.J. Illingworth, E.J. O’Connor, W.B. Rossow, S.L. Durden, S.D. Miller, R.T. Austin, A. Benedetti, C. Mitrescu, and the CloudSat Science Team, 2002: The CloudSat mission and the A-Train. *Bull. Amer. Meteor. Soc.*, **83**, 1771–1790, <https://doi.org/10.1175/BAMS-83-12-1771>.
- Stucke, I., 2017: *Bestimmung der Vertikalgeschwindigkeit und des Tropfenspektrums aus Dopplermessungen mit einem vertikal gerichteten Mikro-Regen-Radar*. Bachelor Thesis, Leopold-Franzens-Universität Innsbruck, 61 pp.
- Turner, D.D., S. Kneifel, and M.P. Cadetdu, 2016: An improved liquid water absorption model in the microwave for supercooled liquid water clouds, *J. Atmos. Oceanic Tech.*, **33**, 33–44, <https://doi.org/10.1175/JTECH-D-15-0074.1>.
- Xie, X., U. Löhnert, S. Kneifel, and S. Crewell, 2012: Snow particle orientation observed by ground-based microwave radiometry, *J. Geophys. Res.*, **117**, D02206, <https://doi.org/10.1029/2011JD016369>.

6 Environmental radionuclides as tracers for transport processes in snow

Kerstin Hürkamp & Jochen Tschiersch

Helmholtz Zentrum München, German Research Center for Environmental Health,
Institute of Radiation Medicine,
Ingolstädter Landstraße 1, 85764 Neuherberg, GERMANY

kerstin.huerkamp@helmholtz-muenchen.de
tschiersch@helmholtz-muenchen.de

Abstract

Radionuclides are useful tracers for the determination of transport processes from the atmosphere to the hydrosphere by snowfall. Particularly in high altitudinal regions radionuclides released to the environment are efficiently removed from the atmosphere by snow. Once deposited, they will be concentrated in the snow cover due to evaporation and sublimation as long as ambient temperature stays low and no melt water runoff occurs. Short-term releases to surface waters after snowmelt initiation in spring may lead to high concentrations having an impact on water quality.

To trace radionuclide transport in the aquatic environments related to snow on Mt. Zugspitze, in addition to their concentrations, comprehensive knowledge about the type of precipitation and the size of the aerosols, they are bound at, the snow cover development, the influence of meteorological conditions on snow alteration and melt water runoff are necessary. A brief description of methods for the investigation of the transport of ubiquitously distributed environmental radionuclides from their atmospheric deposition over their behaviour in the snow cover at Zugspitzplatt to the recovery in the surface water at Partnach spring is given. Applications performed in research projects of the authors' work group since 2011 on Mt. Zugspitze are introduced and highlight the advantages of the location for studying water and radionuclide budgets related to snow. The results help to trace the pathways of radioactive particles from the atmosphere to aquatic environments. Consequently, in cases of extensive radionuclide releases to snow covered environments, peak discharges and the scope of action for countermeasures can be predicted to mitigate the impact on water quality and human radiation exposure.

Keywords: radionuclide tracer, snowmelt, wet deposition, radionuclide transport, snow characterisation, scavenging coefficient, meltwater runoff, gamma spectrometry

6.1 Introduction

Ionising radiation originates from decay of unstable nuclei, either in primordial, natural or man-made radioactive material, e.g. in nuclear reactors and accelerators for energy production or radiotherapy. In general, the exposure of human beings to ionising radiation released to the environment in high concentrations has negative effects on human health. Radiation exposure may damage or modify living cells leading to harm to organs or cancer (UNSCEAR 2000). The release of radioactivity after the nuclear accident of Chernobyl and Fukushima showed that trace contaminants can be rapidly transported world-wide within a few days. Once released to the atmosphere, radionuclides will be rapidly attached to aerosol particles. These are most effectively removed from the atmosphere by wet deposition. For snow, the collection efficiency is strongly influenced by the crystal type and the surface structure of the hydrometeors (Tschiersch et al. 2000, Kyrö et al. 2009, Paramonov et al. 2011). The more complex the crystals and the larger the surface area related to their volumes, the more efficient is the washout (Bernauer 2015).

Once deposited with (wet deposition) and onto (wet or dry deposition) snow, radionuclides are continuously concentrated during the winter due to evaporation and sublimation as long as no

meltwater runoff at the snow base occurs (Hürkamp et al. 2017, Marin et al. 2020). In high-altitudinal regions, soils that generally act as filters or sinks for contaminants are missing. Consequently, stored amounts of radionuclides can be directly released into surface and drinking water reservoirs shortly after snowmelt initiation in spring (Fig. 1). They are able to cause severe impacts on the water quality and provide a risk for radiation exposure to humans.

The wet deposition of aerosol-bound radionuclides is dominated by capture processes of falling hydrometeors, called below-cloud scavenging. The major contributors for the collection efficiency are the mechanisms of Brownian diffusion (~ 10 nm), interception and impaction (~ 1 μ m), depending on the aerosol size. Aerosol particles with sizes inbetween are less efficiently scavenged (Sportisse 2007).

The transport through the snow cover is highly dependent on its thickness, snow texture and density and still to a higher degree on meteorological conditions. Radionuclide transport is associated with the percolation of liquid water in the snowpack (Hürkamp et al. 2017). Consequently, as long as ambient temperature stays below the freezing point, no meltwater flow will occur. After snow ripening, radionuclides follow the downward penetration of water front through the snowpack. Inhomogeneities in snow densities, ice lenses or rain-on-snow events could lead to the formation of preferential flow paths, which favour the transport in some areas. Still, meltwater runoff and radionuclide release to soils and surface waters is delayed as long as the snow base layer is not fully water saturated.

Depending on the subsurface composition below the snow cover, radionuclide transport to surface or ground waters is highly variable. It can be rapidly stopped when meltwater is drained by soils or sediments. In many substrates, dissolved or particulate-bound radionuclides are immediately fixed to the grain surfaces. In the case of solid bedrock or frozen ground, meltwater discharge is constrained and turns into surface water. On Mt. Zugspitze, the snowpack covers "Wettersteinkalk" limestones at the so-called Zugspitzplatt. Due to the absence of soil covers, meltwater directly enters a karstic aquifer and is drained subsurface until it flows out again at the Partnach spring. Therefore, Mt. Zugspitze and the adjacent Zugspitzplatt are outstanding locations to study mass transport in snow and surface waters. In chapter 2, the advantages of the study site are discussed. Chapter 3 describes the applied methods for the investigation of the deposition and transport of environmental radionuclides from the atmosphere via snow to melt and surface water. In chapter 4 exemplary applications from research projects of the Institute of Radiation Medicine, Helmholtz Zentrum München since 2011 concerning radionuclide deposition, their behaviour in the snowpack, transport and release to surface water are introduced.

The environmental radionuclides, which are omnipresent in surface air and precipitation on Mt. Zugspitze, albeit in very low concentrations, are of natural and artificial origin. The highest activities in air and fresh precipitation can be measured for Be-7. Be-7 is a cosmogenic isotope with a half-life of 53.2 d. Its production mainly takes place in the upper troposphere and lower stratosphere by interactions of cosmic rays with atmospheric nitrogen and oxygen. Be-7 atoms are attached to atmospheric aerosol particles soon after their formation. With the advantage of the short half-life and relatively easy determination by gamma-spectrometry, Be-7 has been widely used as a tracer in atmospheric science (e.g. Winkler et al. 1998, Ioannidou and Paatero 2014).

The terrestrial radionuclide Pb-210 is a progeny of Rn-222. The main source of atmospheric Pb-210 is the emanation of short lived Rn-222 from rocks and sediments. Pb-210 atoms become quickly attached to aerosol particles after their formation in the planetary boundary layer. Therefore, they are associated with the aerosol population and allow the investigation of tropospheric transport and removal processes. Pb-210 is widely used in atmospheric modeling and sediment dating (e.g. Winkler et al. 1998, Putyrskaya et al. 2015). It has a half-life of 22.2 a.

Cs-137 has a half-life of 30.1 a and is produced anthropogenically by several types of nuclear activities including past testing of nuclear weapons, accidents in nuclear facilities, reprocessing

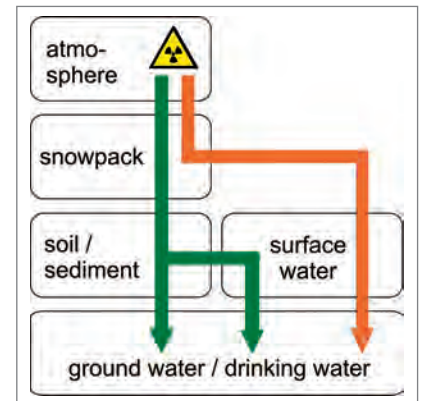


Fig. 1: Pathways of radionuclide transport from the atmosphere to the hydrosphere. Green arrows trace common lowland paths. In high altitudinal or permafrost regions, these are redirected in a way (orange arrow) that surface waters may be directly contaminated due to absence of soils that could act as filters or sinks.

of spent nuclear fuel and nuclear power plants. Recently measured activities of Cs-137 in central and northern Europe in air and precipitation are mainly ascribed to the fallout of the Chernobyl nuclear accident in April 1986 (Kulan 2006) and related subsequent resuspension processes (Garger et al. 1998). The forest topsoils in the Bavarian Alps and in the surrounding valleys of Mt. Zugspitze are still highly contaminated (Winkelbauer et al. 2012).

6.2 Study Site

The investigations on snow deposition and newly fallen snow were carried out on the terrace of the Environmental Research Station (UFS) Schneefernerhaus (2650 m a.s.l.) (Bernauer 2015, Bernauer et al. 2015, 2016). It is situated at the steep southern slope of Germany's highest mountain Mt. Zugspitze (2962 m a.s.l.). The devices for continuous measurement of aerosol concentration, airborne radionuclide concentration and characterisation of precipitation events were deployed here.

The adjacent Zugspitzplatt is a karstic plateau at 1500–2800 m of altitude (mean 2229 m a.s.l.). The snow measuring field (47°24'22.75"N, 11°59'00.39"E) with instrumentation for meteorological and snow parameters is situated at this plateau; where the the annual snow profiles are taken. It is composed of 600–800 m thick bedded limestones ('Wettersteinkalk', Ladin) with a slightly undulating relief. It is horse-shoe shaped surrounded by several summits and inclined to the east (Miller 1962). The underlying aquiclude consists of marly claystone ('Partnach-Schichten').

At the eastern margin of the 11.4 km² catchment, surface water that usually instantaneously infiltrates and drains through the karst aquifer, discharges at the Partnach spring (1440 m a.s.l.). At the Partnach gauge (1365 m a.s.l., 47°24'18.75"N, 11°02'03.07"E) 200 m downstream, discharge is continuously recorded (Fig. 2). Rappl et al. (2010) showed that the basin is almost hydrologically enclosed. No discharge occurs except for the leakage at Partnach spring. This emphasizes the suitability of the catchment for balancing water and radionuclide budgets, since it can be seen as a large natural lysimeter. Discharge velocities for the Zugspitzplatt karst were estimated with 130–170 m s⁻¹, even though during a summer storm event (Rappl et al. 2010).



Fig. 2: Study area at Zugspitzplatt with the location of the measuring sites (© OpenStreetMap, Licence CC-BY-SA 2.0, photos: K. Hürkamp).

Wetzel (2004) analysed hydrographs of Partnach spring in 1996 and 1997, and found a diurnal cycle of snowmelt water dominating the runoff during the ablation period and glacier melt influences after the ablation period, both superposed by storm events.

Average annual temperature on Mt. Zugspitze summit (2962 m a.s.l.) is -4.3 °C (1981–2010). The average annual precipitation is 2071 mm, mainly snow at 58 % of all days and 90 % of the precipitation days per year (DWD 2017). Continuous snow coverage exists at 150–300 d a year on Zugspitzplatt, depending on the altitude that increases to the northern and southern margins and to the west (Weber et al. 2016). The region is strongly wind exposed and experiences intensive solar radiation.

6.3 Materials and Methods

Specific methods and procedures were applied for sampling, analysis and parameterisation in the studies of transport processes of environmental radionuclides with snow. They were adapted to the unique high alpine measurement situation.

6.3.1 Snow sampling: fresh snow and annual profiles

Deposited amounts of radionuclides on and with snow can be determined by the analysis of integrated depth snow samples. For this, a continuously accumulating snow cover during the winter months without meltwater runoff at the snow base at the upper Zugspitzplatt offers best possibilities. Either the frequent sampling of fresh snow or the excavation and sampling of snow profiles at the end of the accumulation period in order to determine the total accumulated radionuclide inventory of the entire season are adequate methods.

An approximately 25 × 25 m wide area at the measuring field on central Zugspitzplatt surrounding the meteorological station is fenced each year to protect the natural snow cover against ski tourism. The area is used by the staff of the Bavarian Avalanche Warning Service to dig bimonthly snow profiles in order to generate parameters used for their daily avalanche warning reports. During the winters 2014/2015 and 2015/2016 also monthly fresh snow and seasonal accumulated samples from profiles over the total snow depth for the determination of the environmental radionuclide inventory were taken.

For the monthly fresh snow samples, the freshly fallen snow since the last sampling campaign was taken. The snow surface was therefore marked with a mesh after each sampling day. The samples were taken from an area of a pre-defined size (activity referred to area) over the total depth of the newly accumulated snow cover since the last sampling date.

At the end of the snow accumulation periods 2015 and 2016, integrated depth snow samples of each snow layer were taken horizontally from the profiles. For the gamma-spectrometric determination of the radionuclide activities of Be-7, Pb-210 and Cs-137 at existing environmental concentrations on Mt. Zugspitze, at least 5 L of SWE are necessary to reach the detection limits. Depending on the snow density, canisters with volumes of 20 L and 60 L barrels were filled with snow and used for the transport of the samples to the laboratory at Helmholtz Zentrum München. Preconditioned plastic containers and shovel were used for sampling: They were acidified with HNO_3 (5 mL HNO_3 conc. per L) to avoid radionuclide fixation to the walls of the barrels, canisters or glass beakers during pre-treatment. In addition, the acid prevents the growth of microorganisms, which could lead to radionuclide sorption and inhomogeneous mass distributions in the sample causing higher uncertainties in the measurement.

The seasonal profiles were excavated up to the depth of the solid bedrock and snow characteristics described in detail according to Fierz et al. (2009). Snow layers were distinguished due to differences in snow texture, grain size and roundness, hardness and water content of the layers (Fig. 3). Snow densities of each layer were determined *in situ* by use of a metal tube of known volume and a spring scale to measure the sample weight. Snow water equivalents (SWE) were calculated by multiplication of the density with the snow height. SWE are necessary to determine the activities of radionuclides deposited in the area of the total catchment of the Zugspitzplatt (11.4 km², Wetzel 2004). To trace the contents of radioactivity in the snow profiles



Fig. 3: Snow profile description and sampling at the end of the snow accumulation periods 2015 and 2016. In the profile of June 2016 (right figure) a prominent Saharan dust layer is visible, which allows dating the snow layer to an event that occurred on April, 5th/6th and which could be traced in the snow alpine-wide (Photos: E.-M. Schiestl, 2015-05-13 and K. Hürkamp, 2016-06-01).

over time, SWE are additionally needed to relocate snow layers of the same age. Due to evaporation, melt and compaction processes, snow height cannot be used to correlate coeval snow layers over the total season.

6.3.2 Surface water sampling at Partnach spring

About 200 m downstream the Partnach spring (1440 m a.s.l.) an automatic gauge and water sampling station is installed (Fig. 4). Precipitation, fluvial discharge, water temperature and electric conductivity are continuously recorded (Wetzel et al. this issue).

Samples of the Partnach surface water were taken irregularly between May and October 2015 and 2016 as grab samples of 20 L volume or as bulk samples from an automatic sampler which is operated in cooperation with the work group of Wetzel et al. (this issue). The automatic sampler is equipped with 24 × 1 L bottles and is programmable for the sampling period and amount of water pumped per sample. During the sampling campaigns in 2015/2016 the programmes were changed related to the expected time interval between the sampling days, ranging from three-hourly to daily sampling intervals for aliquots of 500 mL surface water each. At the sampling days, always all 24 bottles were merged to one bulk sample and transported in canisters to the laboratory.



Fig. 4: Partnach gauge 200 m downstream the Partnach spring. The station is equipped with sensors for the determination of surface water discharge parameters (left) and an automatic water sampler (right). In addition grab surface water samples were taken (middle) during the summers 2015 and 2016 (Photos: K. Hürkamp, 2016-07-12).

6.3.3 Gamma-spectrometry for radionuclide quantification

The snow and water samples are transported in barrels or canisters to the laboratory at Helmholtz Zentrum München, where they are weighted, and if necessary melted at room temperature. To concentrate the rather low environmental radionuclide concentrations in the snow and surface water of Mt. Zugspitze, and to reduce the sample volumes to measurable amounts, the liquid samples are evaporated by use of a rotational evaporator. Residual samples, that contain the total radionuclide inventory of non-volatile elements, are subsequently evaporated to about 100–200 mL on a heating plate at maximum temperatures of 80 °C and transferred to 250 ml polyethylene containers. The containers have defined geometries which are calibrated for the subsequent gamma-spectrometry measurements. Therefore, a defined filling level must be achieved to reproduce the same geometry as in the calibrated standard. To reach this level, samples will be filled up with deionised water.

Samples are measured by gamma spectrometry with high purity germanium detectors (HPGe, Gilmore 2008). Gamma radiation is an electromagnetic radiation consisting of gamma quanta (= photons). Gamma quanta do not carry an electric charge. Therefore, the interaction of gamma radiation with matter differs from that of charged particles with matter. The energy absorption is possible by the photo effect, the Compton effect, and pair production. All these effects cause the production of secondary electrons that are detected (as charged particles) in appropriate measurement devices. The operation of germanium detectors follows the interaction of gamma rays with a semi-conductor. Entered photons interact with the germanium crystal and excite electrons to the conduction band causing formation of electron-hole pairs. The number of electron-hole pairs is directly proportional to the energy absorbed in the material. The electric signal is amplified, sorted by height and energy and displayed in a typical gamma-spectrum (Fig. 5). The charges are collected to electrodes. Thermal electrons mask all weak signals. Therefore, germanium detectors have to be cooled down by liquid nitrogen or electronic cooling systems (Fig. 6).

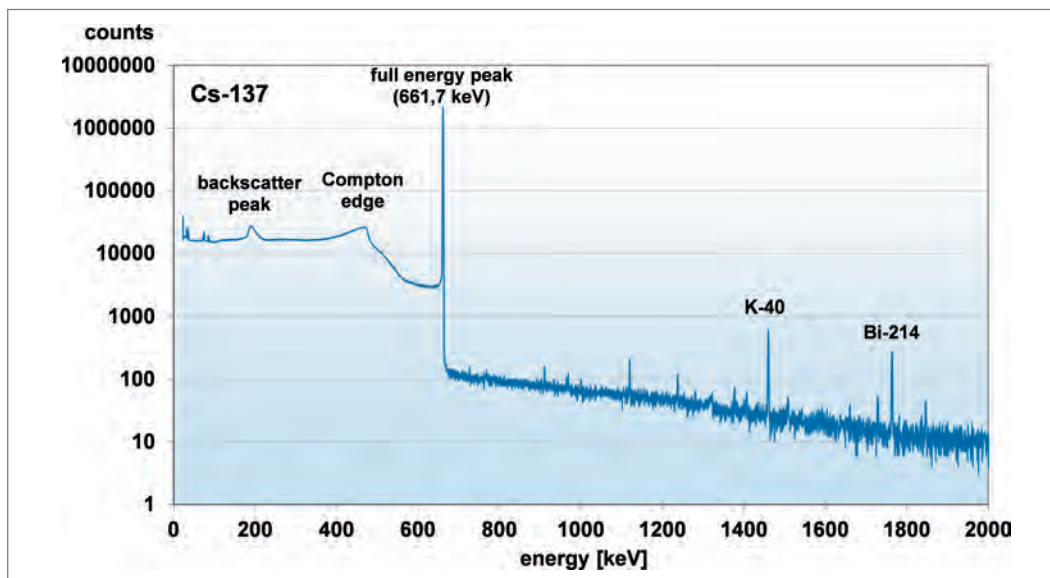


Fig. 5: Pulse-height gamma-spectrum for the discrete gamma energy of Cs-137, measured on a HPGe coaxial detector (rel. efficiency 40 %, resolution 1.9 keV (FWHM) at 1332 keV) in the radioanalytical laboratory at Helmholtz Zentrum München. At the full photon energy of 661.7 keV, the photopeak appears. The gamma quant is completely absorbed by a shell electron of the detector material. The photon vanishes and a free electron that carries the same energy is released. If the photon does not lose its entire energy, only an elastic collision with a shell electron of the detector material occurs (Compton effect) and the photon is scattered carrying still a reduced energy. The maximum energy of the Compton effect corresponds to the Compton edge in the pulse height spectrum. At lower energies, the spectrum continues with a plateau, the so-called Compton continuum. Photons may also pass the detector without any interaction and re-enter the detector with reduced energy after being backscattered in the surrounding material. The primordial K-40 and other radionuclides originating from the natural terrestrial decay chains (e. g., Bi-214, Pb-214) are ubiquitously distributed in the air and contribute to the background radiation.

Activities for the environmental radionuclides Be-7, Pb-210 and Cs-137 are calculated integrating the areas of the full energy peaks in the gamma spectra at energies of 477.6 keV for Be-7, at 46.5 keV for Pb-210 and at 661.7 keV for Cs-137. The net area of the peak is directly related to the intensity, but it is also necessary to correct for the efficiency of the detector (efficiency calibration is needed for each geometry and detector), the half-life of the nuclide and the respected background. The background mainly consists of natural radiation (e.g. cosmic and terrestrial radiation). The component is minimised by using 10 cm lead shielding enclosing the detector at all sides.

Still some samples are analysed by a low-level background gamma detector located at the Environmental Research Station Schneefernerhaus (Fig. 7). It is equipped with an active veto shield (Burnett and Davies 2012) placed on top of the lead shielding. It consists of plastic scintillators which detect and eliminate any signal of the strong (due to high altitude) incoming cosmic radiation and therefore additionally reduces the background by a factor of 1.9–2.2. A background correction due to additional contribution of terrestrial radiation from the radon decay chain has to be applied for the determination of Pb-210 in the snow and surface water samples. For this, a measurement in an empty lead shielding chamber is carried out bimonthly. The resulting peak areas of the radionuclides of interest are subtracted from the photopeak areas for each subsequent sample measurement.

Mean detection limits for the gamma-spectrometric activity determination depend on the measurement times and were about 30 mBq L⁻¹ for Be-7, 50–100 mBq L⁻¹ for Pb-210 and 2 mBq L⁻¹ for Cs-137 in snow and surface water at maximum acceptable measurement times of 14 d. Measurement uncertainties of ≤ 5% for Be-7, ~20% for Pb-210 in snow and ~20% for Cs-137 are achieved in surface water, even though they are much higher for Be-7 and Pb-210 in surface water and for Cs-137 in snow. Additional overall analytical errors sum up to 3%. To drop the uncertainties and detection limits, higher initial amounts of SWE or longer measurement times would be necessary. Quality assurance measurements concerning energy calibration, accuracy and reproducibility are monthly carried out with certified liquid multi-nuclide standard materials or calibration point sources of selected radionuclides (Cs-137, Co-60, Am-241) with known activities. The liquid standard, especially used for efficiency and energy calibration, contains eleven different radionuclides in the energy range of 40 keV to 2000 keV to cover the whole range of interest.

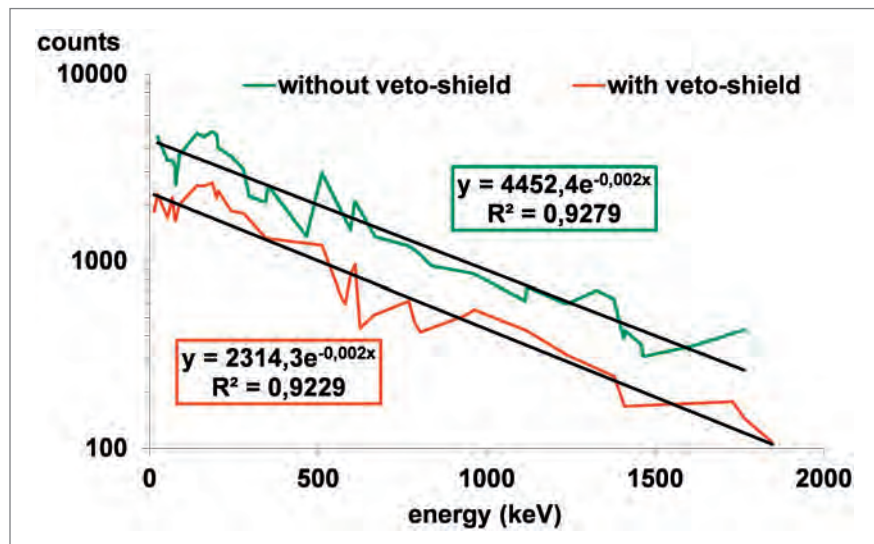


Fig. 6: HPGe broad energy gamma spectrometer system (left) at the Environmental Research Station Schneefernerhaus (Photo: K. Hürkamp, 2011-10-19). Detector cooling is performed with an electronically powered cryostat. An active veto shield (plastic scintillators) on top of the lead shielding provides additional reduction of the background due to elimination of altitude-induced enhanced cosmic radiation by a factor of 1.9 to 2.2. The right figure shows the measured background spectra with and without active veto-shield.

6.3.4 Snow Characterisation

6.3.4.1 Characterisation of hydrometeors

For the determination of washout efficiencies for aerosol-bound radionuclides with different precipitation events, the type of precipitation can be characterised by use of a 2D video disdrometer (2DVD, Fig. 7a). It consists of two line scan cameras that are aligned in a 90° angle to each other and a height difference of 6 mm (Fig. 7b). The cameras scan every hydrometeor falling through the sensitive area. From the shaded images that are matched for both cameras for each snowflake or raindrop (Bernauer 2015, Bernauer et al. 2015), crystal sizes and shapes are derived. The height difference of the cameras gives evidence about fall velocities. From typical distributions in size-fall velocity diagrams (Fig. 7c), falling hydrometeors can be classified into rain, snow and mixed events due to the fact that raindrops fall faster than snow and snowflakes have bigger sizes. Considering the shape of the hydrometeors, additionally three snow crystal classes, single crystals (needles, dendrites, plates), complex crystals (wet flakes and aggregates) and pellets (graupel, densely rimed rounded crystals) are distinguishable (Fig. 7d, Bernauer et al. 2016).

6.3.4.2 Scavenging coefficients

The characteristic measure for the efficiency of wet deposition is the scavenging coefficient. It can be determined from the decreasing aerosol particle concentration during precipitation. The particle concentration $c(d_p, t)$ is a function of its diameter d_p and time t . Under the assumption that precipitation scavenging is a dominant sink for $c(d_p, t)$ a first order decay equation can be set up:

$$\frac{\partial c(d_p, t)}{\partial t} = -\Lambda(d_p) c(d_p, t)$$

Integration yields the scavenging coefficient $\Lambda(d_p)$:

$$\Lambda(d_p) = -\frac{1}{t_1 - t_0} \ln \left(\frac{c(d_p, t_1)}{c(d_p, t_0)} \right)$$

for measurements at t_0 and t_1 (Laakso et al. 2003, Kyrö et al. 2009). Another possibility is to rearrange the equation to

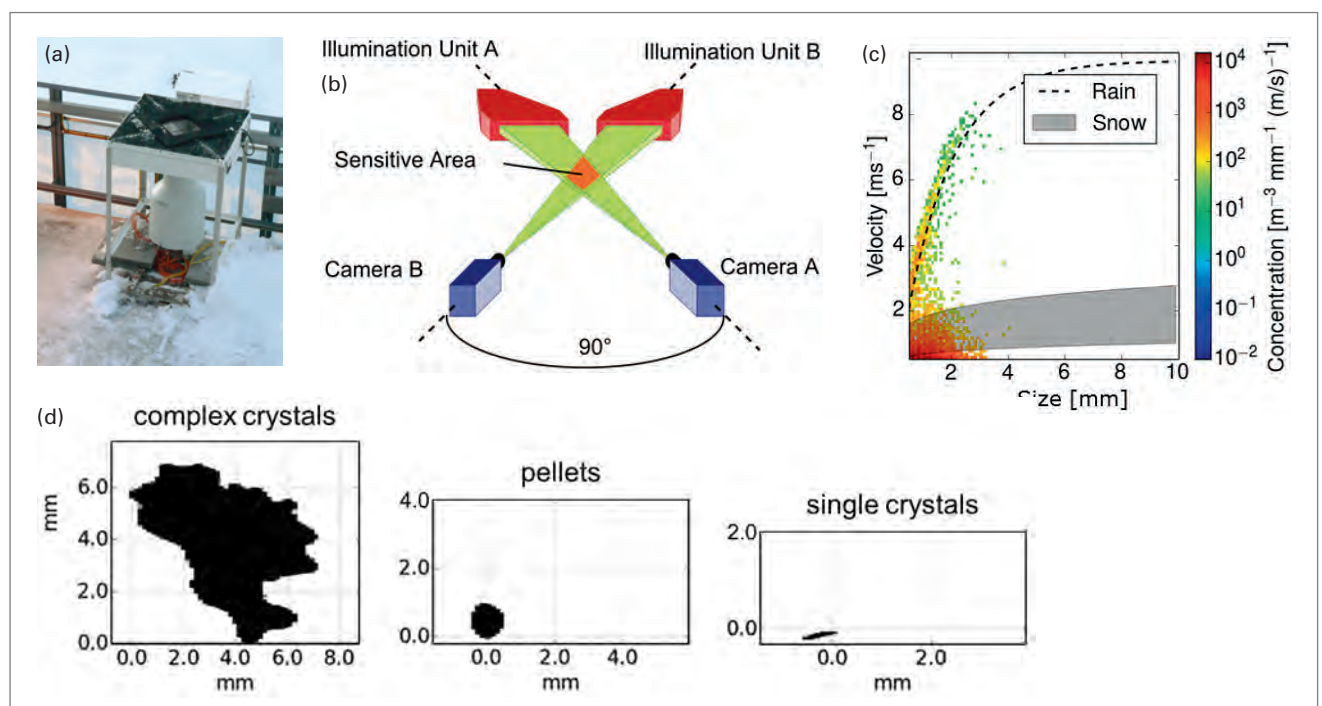


Fig. 7: (a) 2D video disdrometer (2DVD) for the characterisation of precipitation events (Photo: K. Hürkamp, 2013-11-14). (b) Measurement principle. (c) Particle size-fall velocity diagram for the differentiation between rain and snow events. (d) Scanned images of the 2DVD with examples for the three distinguishable snow crystal classes (Fig. c-d modified according to Bernauer 2015).

$$\ln(c(d_p, t)) = -\lambda(d_p) t + \ln(c(d_p, 0)).$$

It shows that $\lambda(d_p)$ is the slope of a linear fit to the logarithm of the aerosol particle concentration.

For the calculation of scavenging coefficients the aerosol particle concentration in the atmosphere is measured by a Scanning Mobility Particle Sizer (Birmili et al. 2016) before and during a precipitation event. Concentrations are subdivided into 14 size classes from 10–510 nm to cover the whole range of ultrafine aerosol particles that are predominantly absorbed in human lungs and may cause adverse health effects. From three consecutive 10 min-measurements of the size-related aerosol particle concentrations, their decrease is determined and expressed as washout or scavenging coefficient. The scavenging coefficients, calculated for snow events are useful input parameters to improve and regionalise atmospheric radionuclide distribution models in European decision support systems for the emergency management after nuclear or radiological accidents, in which only rain is considered so far.

6.3.4.3 Snow parameters for the observation of the snow cover development at Zugspitzplatt

Snow parameters are continuously recorded since 11/2012 at the central Zugspitzplatt (2420 m a.s.l.), where a meteorological station is additionally equipped with an ultrasonic snow depth sensor, a snow scale and a Snow Pack Analyser (SPA) for the determination of snow water equivalents (SWE), snow density, liquid water and ice contents in different heights of the snowpack (10 cm, 30 cm and 50 cm above rock 11/2012-09/ 2017, 10 cm, 20 cm and 30 cm height since 12/2017, Fig. 8). The sensors record and transmit (wireless transmission to a data storage server) data for each parameter every 10 min.

The snow scale measures the SWE for solid precipitation more precisely than precipitation gauges (Błaś et al. 2010, Lundberg et al. 2016). The measurement is carried out on a centre aluminium plate, surrounded by stabilising plates (on an area of 2.4×2.8 m) in order to compensate stress in the snowpack as well as to counteract the problem of ice bridges through the large surface area. Perforation of the plates prevents water accumulation, minimises the difference in temperature between the scale and the ground and promotes uniform melting.

The SPA (Stähli et al. 2004) measures the volumetric contents of ice, water and air and calculates the SWE and snow density when combined with a snow depth sensor. It consists of three 5 m weather and UV-resistant sensor bands that penetrate the snow in 10 cm, 30 cm and 50 cm above ground measuring the complex impedance. Snow consists of ice, air and water. They have different dielectric constants. Each band sends out measuring frequencies and is able to calculate the percentage of liquid water, ice and the remaining value as air from the returned value. The dielectric constant of ice has a strong frequency variation, which enables determination of the volumetric content of both frozen and liquid water. The band installed horizontal at 10 cm above the ground gives valuable information about beginning meltwater runoff.



Fig. 8: Meteorological station at central Zugspitzplatt (2420 m a.s.l.), operated by the Bavarian Avalanche Warning Service and the authors on behalf of the Environmental Research Station Schneefernerhaus. It is equipped with sensors for the determination of standard meteorological and snow parameters. The measurement data is recorded and transferred to the Alpine Environmental Data Analysis Center (AlpEnDAC, www.alpendac.eu), where it is publicly available (Photo: F. Bernauer, 2012-11-08).

Percentages of about 3–4%, up to 7–8% liquid water content indicate full water saturation of the basal snow layer (Denoth 2003, Heggli 2013). Generally, the increase of liquid water contents in the snowpack coincides with an increase in density and a decrease of snow heights due to snow compaction. When the threshold for irreducible water saturation of the snowpack is reached and amounts of SWE stagnate, runoff will start as indicated by mass loss on the snow scale and decreasing SWE. Therefore, the initiation of runoff and associated mass transport in the snowpack can be predicted by continuous observation of the measurement data.

6.4 Applications

Radioecological transport processes associated with snow and their consequences on human radiation exposure have been investigated in field studies and associated laboratory experiments at Helmholtz Zentrum München since 2011. The environmental radionuclides Be-7, Pb-210 and Cs-137 were used as tracers for transport processes from the atmosphere to the hydrosphere, including deposition, storage in the snowpack, release to melt water, karst aquifer and discharge at the Partnach spring. Monthly total deposition of radionuclides at the Zugspitzplatt and release to surface waters at Partnach spring was balanced for two hydrological years. The snow cover development was observed by use of the installed snow sensors at the central plateau. Residence times in the snowpack and timing of radionuclide release to melt water and recovery at Partnach spring were determined. The results help to trace the pathways of radioactive particles from the atmosphere to aquatic environments. Consequently, in cases of extensive radionuclide releases to snow covered environments, peak discharges and the scope of action for countermeasures can be predicted to mitigate the impact on water quality and human radiation exposure.

6.4.1 Scavenging coefficients for the washout of aerosol-bound radionuclides

Scavenging coefficients for the washout of aerosol-bound radionuclides with different precipitation events at the Environmental Research Station Schneefernerhaus were calculated. From 4800 h of precipitation events between November 2012 and December 2014 580 h met the criteria of meteorological stability (Bernauer 2015). These were classified as rain (7%), snow (74%) and mixed (19%) events as well as into three snow crystal classes considering their sizes, shapes and fall velocities (Fig. 7d, Bernauer et al. 2015, 2016). For every class the mean scavenging coefficients were calculated related to the aerosol particle sizes. Rain is comparably efficient to remove small particles (diffusion driven, Fig. 9a). However, the presence of snow significantly increases scavenging in the intermediate (interception) and large particle range (impaction). Fine single crystals, often in the shape of needles, plates or dendrites, very efficiently remove particles (Fig. 9b). Graupel-like pellets behave similar to rain. Complex crystals like wet snowflakes or aggregates of crystals are a bit less effective compared to single crystals. The larger the surface and the more complex the hydrometeors are, the higher is the washout efficiency for ultrafine aerosol particles.

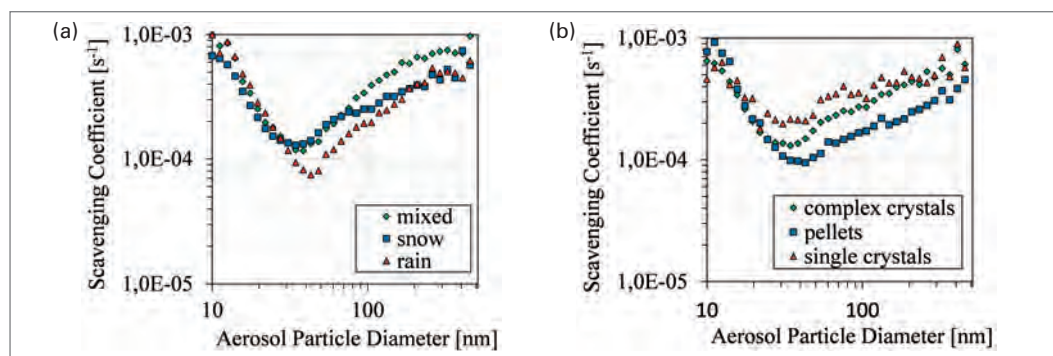


Fig. 9: Calculated scavenging coefficients for the washout of aerosol-bound radionuclides with different precipitation events (a) and differences between three snow crystal classes (b) related to the aerosol particle size. Shown are mean values of 580 h of precipitation at the Environmental Research Station Schneefernerhaus between 2012 and 2014.

6.4.2 Deposition of environmental radionuclides with snow

In addition to the calculated scavenging coefficients, *in situ* total deposition of the environmental radionuclides Be-7, Pb-210 and Cs-137 was determined in monthly fresh snow samples and in seasonal snow profiles at the end of the snow accumulation periods in May in 2015 and 2016 at central Zugspitzplatt.

Monthly radionuclide activity concentrations, determined in fresh snow at Zugspitzplatt, were quite low and range between 530–1770 mBq L⁻¹ for Be-7, 10–127 mBq L⁻¹ for Pb-210 and 0.2–3.2 mBq L⁻¹ for Cs-137 during the snow accumulation periods of October 2014 to May 2015 and November 2015 to May 2016. Radionuclide deposition activity notation is always given as activity referred to the sampled area. Therefore, monthly samples were taken from size-defined areas or otherwise (for samples from deeper seasonal profiles) activity concentrations were multiplied with the snow water equivalents (SWE) for the related snow samples. Resulting deposited mean activities in the fresh snow are calculated with 143 Bq m⁻² for Be-7, 7 Bq m⁻² for Pb-210 and 0.16 Bq m⁻² for Cs-137. The sums for both winters 2014/2015 and 2015/2016 for fresh snow samples, accumulated in the seasonal profiles at the end of the snow accumulation period in May each year and in precipitation samples (mainly rain) from the campus of Helmholtz Zentrum München in Neuherberg (500 m a.s.l.) during the same period for comparison are given in Tab. 1.

Tab. 1: Sums of mean deposited activities of the environmental radionuclides in snow samples at Zugspitzplatt and in fresh precipitation at the campus of Helmholtz Zentrum München in Munich-Neuherberg for comparison.

	Be-7 (Bq m ⁻²)	Pb-210 (Bq m ⁻²)	Cs-137 (Bq m ⁻²)
Sum of mean deposited activities in fresh snow of the winter seasons 2014/2015 and 2015/2016 at Zugspitzplatt	1005	46	0.8
Sum of mean deposited activities in accumulated snow at the end of the snow accumulation periods 2015 and 2016 at Zugspitzplatt	724	88	1.4
Sum of mean deposited activities in precipitation of the same period in Munich-Neuherberg	530	65	0.3

Higher concentrations of Cs-137 on Mt. Zugspitze compared to Munich can be explained by higher resuspension of Chernobyl fallout radiocaesium from the soils in the surrounding forested valleys, where concentrations are still high due to limited post-accidental distribution. In addition, the use of contaminated local wood for domestic heating in the surrounding towns and villages contributes to increased Cs-137 activities in the atmosphere in winters. Pb-210 activities are expected to be higher in the valleys due to its terrestrial origin. Similar to Cs-137, Pb-210 is progressively accumulated in altered snow due to the strong fixation to dust particles. The Be-7 activities of cosmic origin generally increase with altitude. Due to its short half-life of 53 d, the concentrations in the accumulated snow samples at the end of the winter season are much lower.

6.4.3 Snow cover development at Zugspitzplatt

A persistent snow cover with varying thickness of maximum 150–400 cm was existent at Zugspitzplatt since 2012 each year and always lasted from November to at least June/July. The measured snow parameters at the central Zugspitzplatt show that there is almost no mass loss of snow between November and April each year, except for some wind-drift of fresh powder snow during periods of high wind intensity and low temperature. This means, the altitude and recent meteorological conditions at this site induce a continuous accumulation of snow and prevent melt water runoff at the snow base during the winters. Still, partial melting at the snow surface and related snowpack compaction occur. Laboratory experiments with snow columns and applied artificial radionuclide tracers under controlled ambient conditions, adjusted in melt-freeze-cycles to real conditions of a typical spring day with snowmelt on Mt. Zugspitze,

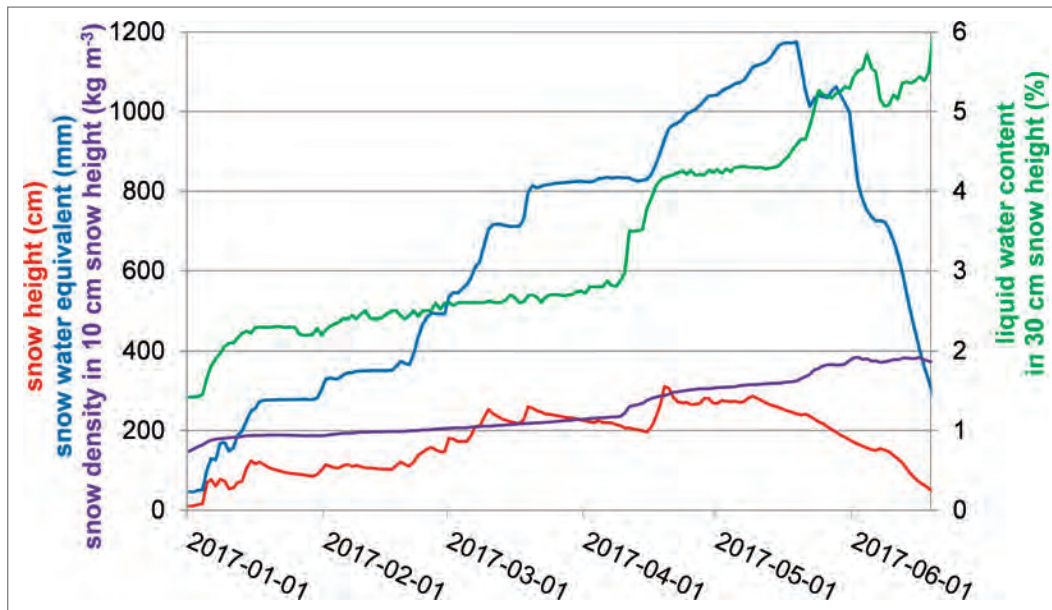


Fig. 10: Snow cover development during the winter season 2016/2017.

showed that radionuclide transport in a snowpack is associated with the percolation of liquid water in a snowpack (Hürkamp et al. 2017). Similar values were found for the release of other ions from snowpack (Cadle et al. 1984, Bales et al. 1989). As long as temperature stays below 0 °C radionuclide transport is almost disabled. It was shown that 80 % of the radionuclides were released within the first 20 % of melt water (> 50 % in first 10 %) in short time periods after snowmelt runoff started. This means, in case of a radioactive contamination on Mt. Zugspitze, the transport of a possible contamination in melt and surface water would be delayed until first melt water runoff in April or May, but will continue in a highly concentrated contamination plume in the melt and surface water.

Using the snow sensors installed at the central Zugspitzplatt, snowmelt runoff initiation and associated mass transport and release from snowpack can retrospectively be determined. By combination of information about air and snow temperature, snow water equivalent (SWE), liquid water contents and snow density, the time of first snowmelt runoff can be predicted. Measurement data of the winter season 2016/2017, plotted in Fig. 10, gives an adequate example.

Despite fluctuations of the snow height due to evaporation, surface snowmelt and related snow compaction, almost no mass loss/melt water runoff was recognised on the snow scale, indicated by a continuously accumulating SWE until 2017-05-19. Nevertheless, density and liquid water contents of the snowpack increased since the beginning of the year due to ablation and progressive snowpack compaction. When the snowpack got isothermal at 0 °C snow temperature (not continuously measured at the station) after several days of air temperatures > 0 °C, a wetting front could be traced by the increase of liquid water contents in different heights of the snowpack and finally at the snow base. A distinct increase was observed after 2017-04-07 and again after 2017-05-15 in 30 cm snow height, indicating full melt water saturation of the basal snow layers and imminent runoff initiation. After the first snowmelt release, liquid water contents generally further increase due to persistent melt water fluxes from upper snow layers.

The period of first melt water runoff in May is relatively constant since 2012. It varied between mid of April and mid of May, independent of the thickness of the snowpack. Assuming a potential radioactive contamination of the snowpack during the winter months of 2016/2017, its first release with snowmelt runoff would have occurred on 2017-05-19. If according to Hürkamp et al. (2017) a release of > 50 % of the radionuclides within the first 10 % of melt water is assumed, it would have taken only 11 h for their release to the surface water and karst aquifer respectively. This time interval strongly depends on the duration and intensity of the first melt-cycle and varied on Mt. Zugspitze between 15.5 d and 11 h since 2012. It also defines the scope of action to mitigate human radiation exposure by means of finding strategies for countermeasures, as

for example snow removal as an option for sealed urban regions. A prediction of a possible temporal and spatial distribution of the contamination plume in surface and ground water is feasible. It gives the chance to at least inform the population to be aware of an expected contamination plume in provided drinking water reservoirs.

6.4.4 Water and radionuclide budget for the catchment of the Partnach spring

Continuous measurements of the water discharge at Partnach spring (Wetzel et al. this issue) supplemented by the analysis of environmental radionuclides in grab samples of the Partnach surface water between May and September 2015 and 2016 were used to calculate a water and radionuclide budget for the catchment of the Zugspitzplatt for two hydrological years. Using the modelled area-weighted means for the snow water equivalents (SWE) according to Weber et al. (2016), the data represents the snow mass of the total catchment to 87.8% compared to the determined SWE on the snow scale at central Zugspitzplatt. Therefore, a factor of 0.878 was applied to calculate SWE for the entire catchment of the Partnach spring of 11.4 km² on the basis of the measured values. The comparison of SWE stored in the accumulated snowpacks in the seasons 2014/2015 and 2015/2016 until May with summed melt water discharges at Partnach spring between May and September each year provided a recovery of > 90% (Tab. 2). Each year, about 12 million m³ SWE were accumulated and discharged. This corresponded to a total discharge at Partnach spring until almost drying up by the end of October of 44% and 39%, respectively.

Mean activities of the environmental radionuclides deposited in the total area of the catchment summed up to 10 GBq Be-7, 500 MBq Pb-210 and 8 MBq Cs-137 each year. Fallout from the atomic bomb test can be detected in the snow of the catchment as well. The annual inventory is small in comparison: 20 kBq Pu-239, 15 kBq Pu-240 and 95 kBq Am-241 (Gückel et al. 2017).

The activity concentrations of the environmental radionuclides detected in the Partnach surface water samples were quite low and even below detection limits in many samples, especially for Be-7 and Pb-210. Besides the short half-life of Be-7 of 53.2 d, this explains the limited recovery of these radionuclides in the Partnach surface water (Tab. 2). Long residence times of precipitation-borne Be-7 in the snowpack as well as in the karst aquifer led to its almost complete decay when discharged at Partnach spring. Additional supply by fresh precipitation only occurred periodically and carried no weight. However, Cs-137 was well recovered in the Partnach water, and in 2016 even in higher concentrations than determined in the integrated amounts in the fresh snow during the preceding winter season. An accumulation of radiocaesium in long-term stored altered water in the karst aquifer that was replaced by the first fresh melt water fluxes was assumed. In addition, uptake of Cs-contaminated mineral or organic particles on its way to Partnach gauge seemed to have been possible.

The water stable isotopes $\delta^{18}\text{O}$ and $\delta^2\text{H}$ were used as additional conservative tracers for water discharge and mass transport processes associated with snow. Since their isotopic ratio alters due to fractionation they provide further information about snow alteration and melt processes (Hürkamp et al. 2019). Their distribution in fresh precipitation or deposited snow as input parameters and the isotopic composition of the Partnach surface water as output were applied

Tab. 2: Water and environmental radionuclide budget for the catchment of the Zugspitzplatt (11.4 km²) for two hydrological years 2014/2015 and 2015/2016.

	2014/2015				2015/2016			
	SWE (L)	Be-7 (Bq)	Pb-210 (Bq)	Cs-137 (Bq)	SWE (L)	Be-7 (Bq)	Pb-210 (Bq)	Cs-137 (Bq)
Input (snow)	1.21E+10	1.06E+10	5.42E+08	7.39E+06	1.22E+10	1.23E+10	4.94E+08	9.14E+06
Output (surface water)	1.10E+10	9.48E+07	5.30E+07	5.37E+06	1.13E+10	1.02E+09	< LOD	1.80E+07
Difference	1.05E+09	1.05E+10	4.89E+08	2.03E+06	9.22E+08	1.13E+10	4.94E+08	-8.82E+06
Recovery	91%	1%	10%	73%	92%	8%	0%	197%

to model the water transit times in the discharge at Zugspitzplatt (lumped-parameter exponential model according to Maloszewski and Zuber 1982). Residence times of about ten weeks were determined for the direct discharge considering a groundwater contribution of 50 %.

In collaboration with partners from EURAC research Bolzano, Italy within the framework of the Virtual Alpine Observatory (VAO), developments of snow coverage, liquid water contents of the snowpack and expected snowmelt could also be observed in remote sensing SAR Sentinel-1 data (Marin et al. 2020). We found that the multi-temporal SAR measurements allow the identification of the three melting phases that characterize the melting process i. e., moistening, ripening and runoff. In detail, we found that the C-band SAR backscattering decreases as soon as the snow starts containing water, and that the backscattering increases as soon as SWE starts decreasing, which corresponds to the release of meltwater from the snowpack. We show a spatially-distributed application of the identification of the runoff onset from SAR images for the Zugspitzplatt catchment. Results allow to better understand the spatial and temporal evolution of melting dynamics in mountain regions. The presented investigation could have relevant applications for monitoring and predicting the snowmelt progress over large-scaled regions.

6.5 Conclusions

Environmental radionuclides are useful tracers for the comprehension of mass transport pathways and processes concerning snow. In various applications since 2011, radionuclide deposition, snow cover development on Mt. Zugspitze and contained amounts of environmental radionuclides, as well as their transport and release to melt and surface waters, were investigated. It was proven that radionuclides are very efficiently removed from the atmosphere by snow. They are stored and accumulated in snowpack as long as temperatures remain below 0 °C, which is the case on Zugspitzplatt between November and April each year under current meteorological conditions. After initiation of snowmelt, a rapid transport through the snowpack starts until the base layer is fully water saturated. Radionuclides can then be short-term released to surface water. Laboratory experiments showed that > 50 % of the radionuclide inventory of a snowpack will be released within the first 10% of melt water runoff. In minimum it took 11 h at central Zugspitzplatt in May 2017. Depending on the duration and intensity of the first melt-cycle, variable radionuclide concentrations have to be expected in the surface water and are further distributed into soils, ground – or drinking water reservoirs. It was shown that their spatial and temporal release on Mt. Zugspitze can be predicted in order to improve radionuclide distribution models or to derive strategies and scope of action for countermeasures in case of a potential nuclear or radiological accident. The overall goal is to mitigate impact on water quality and human radiation exposure.

Acknowledgements

Parts of the applications in chapter 4 and the installation of the snow sensors at Zugspitzplatt were performed within the framework of the research project “Virtual Alpine Observatory (VAO)”, funded by the Bavarian State Ministry of Environment and Consumer Protection, Germany (71_1d-U8729-2013/193-24). Some parts were financed by the German Federal Ministry of Education and Research in the joint research projects “Radiation and Environment II” (02NUK015B) and “TransAqua” (02NUK030A). We thank numerous (former) colleagues of the Institute of Radiation Protection and Institute of Groundwater Ecology at Helmholtz Zentrum München for their collaboration concerning sampling, measurement and research data evaluation. We gratefully acknowledge the support by the staff and consortium of the Environmental Research Station Schneefernerhaus, the Bavarian Avalanche Warning Service and by all project partners of VAO. The contents are solely the responsibility of the authors.

References

- Bales, R.C., Davis, R.E., Stanley, D.A., 1989. Ion elution through shallow homogeneous snow. *Water Resour. Res.* 25, 1869–1877.
- Beniston, M., Keller, F., Goyette, S., 2003. Snow pack in the Swiss Alps under changing climatic conditions: an empirical approach for climate impacts studies. *Theor. Appl. Climatol.* 74, 19–31.
- Bernauer, F., 2015. Atmospheric washout of radioactive aerosol for different types of precipitation events. PhD thesis, Helmholtz Zentrum München, Institut für Strahlenschutz und Ludwig-Maximilians-Universität München (https://edoc.ub.uni-muenchen.de/20221/1/Bernauer_Felix.pdf).
- Bernauer, F., Hürkamp, K., Rühm, W., Tschiersch, J., 2015. On the consistency of 2-D video disdrometers in measuring microphysical parameters of solid precipitation. *Atmos. Meas. Tech.* 8, 3251–3261.
- Bernauer, F., Hürkamp, K., Rühm, W., Tschiersch, J., 2016. Snow event classification with a 2D video disdrometer – a decision tree approach. *Atmos. Res.* 172–173, 186–195.
- Birmili, W., Weinhold, K., Rasch, F., Sonntag, A., Sun, J., Merkel, M., Wiedensohler, A., Bastian, S., Schladitz, A., Löschau, G., Cyrus, J., Pitz, M., Gu, J., Kusch, T., Flentje, H., Quass, U., Kaminski, H., Kuhlbusch, Meinhardt, F., Schwerin, A., Bath, O., Ries, L., Gerwig, H., Wirtz, K., Fiebig, M., 2016. Long-term observations of tropospheric particle number size distributions and equivalent black carbon mass concentrations in the German Ultrafine Aerosol Network (GUAN). *Earth Syst. Sci. Data* 8, 355–382.
- Błaś, M., Cichała-Kamrowska, K., Sobik, M., Polkowska, Ż., Namieśnik, J., 2010. Conditions controlling atmospheric pollutant deposition via snowpack. *Environ. Rev.* 18, 87–114.
- Burnett, J.L., Davies, A.V., 2012. Development of a cosmic veto gamma-spectrometer. *J. Radioanal. Nucl. Chem.* 292, 1007–1010.
- Cadle, S.H., Muhlbaier Dasch, J., Grossnickle, N.E., 1984. Retention and release of chemical species by a Northern Michigan snowpack. *Water Air Soil Poll.* 22, 303–319.
- Denoth, A., 2003. Structural phase changes of the liquid water component in Alpine snow. *Cold Reg. Sci. Technol.* 37, 227–232.
- DWD, 2017. Deutscher Wetterdienst, Wetter und Klima vor Ort: Zugspitze, http://www.dwd.de/DE/wetter/wetterundklima_vorort/bayern/zugspitze/_node.html, status of 22.11.2017.
- Fierz, C., Armstrong, R.L., Durand, Y., Etchevers, P., Greene, E., McClung, D.M., Nishimura, K., Satyawali, P.K., Sokratov, S.A., 2009. The International Classification for Seasonal Snow on the Ground. IHP-VII Technical Documents in Hydrology N°83, IACS Contribution N°1, UNESCO-IHP, Paris.
- Garger, E.K., Paretzke, H.G., Tschiersch, J., 1998. Measurement of resuspended aerosol in the Chernobyl area – Part III. Size distribution and dry deposition velocity of radioactive particles during anthropogenic enhanced resuspension. *Radiat. Environ. Biophys.* 37, 201–208.
- Gilmore, G., 2008. Practical gamma-ray spectrometry. 2nd ed., John Wiley & Sons Ltd, Chichester.
- Gückel, K., Shinonaga, T., Christl, M., Tschiersch, J., 2017. Scavenged ²³⁹Pu, ²⁴⁰Pu, and ²⁴¹Am from snowfalls in the atmosphere settling on Mt. Zugspitze in 2014, 2015 and 2016. *Sci. Rep.* 7, 11848.
- Heggli, A., 2013. Data Analysis of the Snow Pack Analyzing System Tested by UCAR. Proceedings of the 81st Annual Western Snow Conference, Jackson Hole, Wyoming, 59–66.
- Hürkamp, K., Tafelmeier, S., Tschiersch, J., 2017. Influence of melt-freeze-cycles on the radionuclide transport in homogeneous laboratory snowpack. *Hydrol. Process.* 31, 1360–1370.
- Hürkamp, K., Zentner, N., Reckerth, A., Weishaupt, S., Wetzels, K.-F., Tschiersch, J., Stumpp, C., 2019. Spatial and temporal variability of snow isotopic composition on Mt. Zugspitze, Bavarian Alps, Germany. *J. Hydrol. Hydromech.* 67, 49–58.
- Ioannidou, A., Paatero, J., 2014. Activity size distribution and residence time of ⁷Be aerosols in the Arctic atmosphere. *Atmos. Environ.* 88, 99–106.
- Kyrö, E.-M., Grönholm, T., Vuollekoski, H., Virkkula, A., Kulmala, M., Laakso, L., 2009. Snow scavenging of ultrafine particles: field measurements and parameterization. *Boreal Environ. Res.* 14, 527–538.
- Kulan, A., 2006. Seasonal ⁷Be and ¹³⁷Cs activities in surface air before and after the Chernobyl event. *J. Environ. Radioactiv.* 90, 140–150.
- Laakso, Grönholm, T., Rannik, U., Kosmale, M., Fiedler, V., Vehkamäri, H., Kulmala, M., 2003. Ultrafine particle scavenging coefficients calculated from 6 years field measurements. *Atmos. Environ.* 37, 3605–3613.
- Lundberg, A., Gustafsson, D., Stumpp, C., Kløve, B., Feicabrino, J., 2016. Spatiotemporal Variations in Snow and Soil Frost – A Review of Measurement Techniques. *J. Hydrol.* 3, 1–28.
- Maloszewski, P., Zuber, A., 1982. Determining the turnover time of groundwater systems with the aid of environmental tracers: 1. Models and their applicability. *J. Hydrol.* 57, 207–231.
- Marin, C., Bertoldi, G., Premier, V., Callegari, M., Brida, C., Hürkamp, K., Tschiersch, J., Zebisch, M., Notarnicola, C., 2020. Use of Sentinel-1 radar observations to evaluate snowmelt dynamics in alpine regions. *Cryosphere* 14, 935–956.
- Miller, H., 1962. Zur Geologie des westlichen Wetterstein und Mieminger Gebirges. Dissertation, Ludwig-Maximilians-Universität München.
- Paramonov, M., Grönholm, T., Virkkula, A., 2011. Below-cloud scavenging of aerosol particles by snow at an urban site in Finland. *Boreal Environ. Res.* 16, 304–320.

- Putyrskaya, V., Klemm, E., Röllin, S., Astner, M., Sahli, H., 2015. Dating of sediments from four Swiss prealpine lakes with ^{210}Pb determined by gamma-spectrometry: progress and problems. *J. Environ. Radioactiv.* 145, 78–94.
- Rappl, A., Wetzler, K.-F., Büttner, G., Scholz, M., 2010. Tracerhydrologische Untersuchungen am Partnach-Ursprung – Dye tracer investigation at the Partnach Spring (German Alps). *Hydrol. Wasserbewirts.* 54, 220–230.
- Sportisse, B., 2007. A review of parameterizations for modelling dry deposition and scavenging of radionuclides. *Atmos. Environ.* 41, 2683–2698.
- Stähli, M., Stacheder, M., Gustafsson, D., Schläeger, S., Schneebeli, M., Brandelik, A., 2004. A new in situ sensor for large-scale snow-cover monitoring. *Ann. Glaciol.* 38, 273–278.
- Tschiersch, J., Frank, G., Winkler, R., 2000. Scavenging of aerosol-fixed radionuclides with rain and snow. Tech. Rep. BMU-2001–564, Bundesministerium für Umwelt, Naturschutz und Reaktorsicherheit.
- UNSCEAR, 2000. Sources and effects of ionizing radiation – United Nations Scientific Committee on the Effects of Atomic Radiation, Report to the General Assembly, with Scientific Annexes, Volume 1: Sources. United Nations, New York, 654 pp.
- Weber, M., Bernhardt, M., Pomeroy, J.W., Fang, X., Härer, S., Schulz, K., 2016. Description of current and future snow processes in a small basin in the Bavarian Alps. *Environ. Earth Sci.* 75, 1223.
- Wetzler, K.-F., 2004. On the hydrology of the Partnach area in the Wetterstein mountains (Bavarian Alps). *Erdkunde* 58, 172–186.
- Wetzler, K.-F. et al., 2018. Hydrological investigations in the Wetterstein Mountains at the UFS Schneefernerhaus. This issue.
- Winkelbauer, J., Völkel, J., Leopold, M., Hürkamp, K., Dehos, R., 2012. The vertical distribution of Cs-137 in Bavarian forest soils. *Eur. J. Forest Res.* 131, 1585–1599.
- Winkler, R., Dietl, F., Frank, G., Tschiersch, J., 1998. Temporal variation of ^7Be and ^{210}Pb size distributions in ambient aerosols. *Atmos. Environ.* 32, 983–991.

7 Temperature and Precipitation Anomalies at Mount Zugspitze in Relation to Large-scale Atmospheric Circulation Patterns and North-Atlantic European Modes of Variability

Jucundus Jacobeit and Markus Homann
Institute of Geography, University of Augsburg

Abstract

Relationships between the large-scale atmospheric circulation at the 500 hPa level and anomalies of temperature and precipitation at Mount Zugspitze are studied on monthly to seasonal time scales for the 1950–2015 period by two different approaches which are described in an extended methods section: firstly, T-mode principal component analysis (PCA) is used to determine basic circulation patterns during warm and cold months (winter, summer) and during wet and dry months (spring, autumn). Besides patterns with clear-cut association to one of these anomalies, other patterns exist with no distinct preference pointing to substantial internal variabilities (e.g. due to varying wave amplitudes and axis positions). Secondly, S-mode PCA derived modes of variability operating in context of teleconnection patterns like NAO (North Atlantic Oscillation), EA (East Atlantic Pattern), EAWR (East Atlantic West Russia Pattern) and SCAND (Scandinavian Pattern) are analyzed with respect to temperature or precipitation signals at Mount Zugspitze for pronounced positive and negative phases of these patterns. EA and EAWR turned out to show most often significant influence on seasonal climate anomalies at Mount Zugspitze.

Keywords: Mount Zugspitze, temperature, precipitation, circulation patterns, modes of variability, PCA, T-mode, S-mode

7.1 Introduction

Climate variability is closely linked to variations in the atmospheric circulation, and this relationship includes impacts from the large-scale dynamics of the atmosphere down to regional or even local climate conditions. In the present contribution, we will not use extended climate data sets for the whole Alpine region (Auer et al. 2007), but focus on Mount Zugspitze and its basic variables temperature and precipitation. Links to the large-scale atmospheric circulation are not analyzed with respect to weather types on a daily scale, but derived on climatic time scales (monthly to seasonal). This will be done not in terms of transfer functions in a classical downscaling context, but by means of two different approaches:

- at first basic circulation patterns (referring to the mid-tropospheric 500 hPa level) will be determined for those months with substantial deviations in temperature or precipitation from long-term mean conditions; these anomalies are defined by departures of more than one standard deviation above or below the corresponding mean values (cp. Jacobeit et al. 1998, p. 65).
- Secondly, we look at large-scale modes of variability (500 hPa level) in the North-Atlantic European area operating in context of particular teleconnection patterns according to the NOAA Climate Prediction Center (CPC). The most important ones – with respect to the target location – will be considered: North Atlantic Oscillation (NAO), East Atlantic Pattern (EA), East Atlantic West Russia Pattern (EAWR), and Scandinavian Pattern (SCAND). Since complete correlations with temperature or precipitation time series mostly do not yield convincing amounts of explained variance (see section 4.2), we focus on those months with pronounced anomalies in the time coefficients of these modes of variability (more than one standard deviation above or below the corresponding mean values) and analyze the associated temperature or precipitation signals at Mount Zugspitze.

Circulation patterns and modes of variability have to be determined by different variants of a powerful multivariate technique which will be explained and discussed in a separate section on basic approaches (section 3) before providing results with respect to the target location Mount Zugspitze (section 4).

7.2 Data

Daily temperature and precipitation time series are taken from the DWD (German Weather Service) measuring station Zugspitze, they are used for this contribution during the 1950–2015 period. This corresponds to the period of better quality in re-analysis data (NCAR/NCEP in this case, see Kalnay et al. 1996) from which the gridded geopotential height data (2.5° horizontal resolution) of the 500 hPa level have been extracted. Monthly time coefficients of the mid-tropospheric teleconnection patterns (NAO, EA, EAWR, SCAND) are taken from CPC's web site.

7.3 EOF/PCA techniques and their different modes of analysis

7.3.1 Some fundamentals

Before specifying the particular differences in analyzing data sets for circulation patterns or modes of variability, the general fundamentals of the underlying techniques should be elaborated. We try to give a condensed overview of what is explained in detail for example in the textbook of Jolliffe (2002). The principle aim of these techniques consists in replacing a large set of original variables V_i ($i = 1, \dots, n$) given for a certain number of cases k by a set of new quantities Q_j ($j = 1, \dots, m$) for the same cases k in such a way that their relation is described by the following set of equations

$$V_i = \sum_{j=1}^m l_{ij} \cdot Q_j + R_i \quad (1)$$

with $m \leq n$, l_{ij} as so-called *loadings* which constitute the linear combinations for V_i , and R_i as the remaining residuals in the set of equations. This transformation will be effective if the number of new quantities Q is considerably lower than the number of original variables V and if, at the same time, the residuals remain as small as possible: this would maintain the largest amount of information and allow a simplified representation which not only reduces the dimensionality of the data set, but also condenses the information to basic quantities with noise being filtered out. If Q_j are determined in context of empirical orthogonal function (EOF) or principal component analysis (PCA), they are even orthogonal (uncorrelated) to each other and constitute linear combinations for V_i by mutually independent basic quantities. The loadings provide the varying weights of these basic quantities in composing the different original variables.

As a first step for deriving these loadings, a correlation or a covariance matrix C is calculated from the original variables quantifying the degree of relationship for all pairs V_i, V_j ($i, j = 1, \dots, n$). Correlation coefficients reflect standardized relationships without physical units whereas the latter are maintained in case of calculating covariances. From matrix C a characteristic polynomial is generated by the determinant

$$\det(C - \lambda \cdot U), (U: \text{unit matrix})$$

whose zero positions λ_j ($j = 1, \dots, m$) are called Eigen-values. They allow to calculate orthogonal Eigen-vectors EV_j by means of the linear equation system

$$(C - \lambda_j \cdot U) \cdot EV_j = 0$$

The components ev_{ij} of Eigen-vector EV_j ($i = 1, \dots, n$) correspond to the loadings l_{ij} in EOF analysis, whereas in PCA the loadings are given by

$$l_{ij} = \sqrt{\lambda_j} \cdot ev_{ij}$$

Weighting the Eigen-vector components by the square root of the corresponding Eigen-value implies that these PCA loadings represent the correlation coefficients between the original variables V_i and the principal components PC_j (as far as C has been calculated as correlation matrix). They indicate the degree of relationship for all pairs of V_i and PC_j and thus allow to interpret the PCs in terms of properties characterizing sub-groups of variables with higher loadings on the same PCs.

Since squared correlation coefficients provide explained variances between the correlated quantities, statements on V_i and PC_j in terms of explained variances are possible by means of squared loadings l_{ij}^2 : summing them up for a particular PC_j for $i = 1, \dots, n$ – this gives the Eigen-value λ_j – and dividing it by the number of variables n , provides the amount of total variance in the data set explained by PC_j indicating its relative importance among all PCs in composing the original variables according to the set of equations (1). These explained variances λ_j/n decrease from $j = 1$ to $j = m$, since the Eigen-values λ_j constitute a descending sequence. Summing up the squared loadings for a particular variable V_i for $j = 1, \dots, m$ yields the so-called communalities indicating to which degree V_i is represented by all the included PCs (on the decision of their number m see later on).

Besides the loadings l_{ij} , EOF and PC analyses provide a second part of results, the so-called *scores* (or sometimes *amplitudes*) giving the values of the new quantities Q for all cases k covered by the original variables V . They can directly be calculated as

$$Q = (L^T \cdot L)^{-1} \cdot L^T \cdot V$$

with L as loadings matrix and L^T as its transposed variant (exchange between rows and columns). Thus, the scores specify the behavior of the EOFs or PCs across all cases k , whereas the loadings indicate their relationships to the original variables V .

It should be mentioned that the term “principal components” is sometimes used in another way (especially in Meteorology and Climate Research) reducing it to what we have called scores (or amplitudes), whereas in our context PCs include both parts of results (loadings as well as scores) motivated by the fact that these analyses can be run in different modes with different meanings of loadings and scores (see 3.2).

If C has been calculated as covariance matrix, one part of the results maintains the physical units (the other part being dimensionless). If the units shall be linked with the loadings l_{ij} , the operation mode PCA is necessary (i. e. weighting Eigen-vector components by the square root of the corresponding Eigen-value) with scores being divided by this λ square root (von Storch and Zwiers 1999).

In many cases EOFs or PCs are rotated in such a way that the assignment of original variables to EOFs or PCs is optimized. Rotation is especially reasonable if EOFs or PCs represent different regional domains, whereas no rotation should be applied if the focus is only on some few of the leading modes. As a result of rotation, explained variances are re-distributed among the EOFs or PCs with decreasing amounts for the leading ones and increasing amounts for the subordinated ones. Rotation can be done in different ways: maintaining orthogonality between the EOFs or PCs, but also running oblique rotations with PCs being no longer uncorrelated and the loadings l_{ij} being no longer identical with the correlations/covariances between V_i and PC_j .

A crucial point is the decision for an appropriate number of EOFs or PCs influencing the results especially if rotation is applied. There is a lot of criteria starting from simple ones (extracting only EOFs or PCs with $\lambda \geq 1$ according to *Kaiser* or using particular minimum thresholds for (individual or total) explained variances) to standard ones (like the ‘elbow criterion’ looking for distinct jumps in the sequence of Eigen-values) to more sophisticated ones (e. g. extracting only EOFs or PCs whose time coefficients significantly differ from white noise). Quite often some kind of a dominance criterion (Jacobeit 1993) can effectively be used considering only those EOFs or PCs which dominate at least one input variable (in terms of above-average (by more than one standard deviation) rotated loadings with respect to those of all other variables and EOFs/PCs, respectively). Thus, meaningless candidates which do not reflect real conditions but only represent background noise will not be extracted. For distinctly complex data sets, a further extension of this dominance criterion might be necessary, e. g. with respect to significant field correlations between input variables and EOF/PC scores (Philipp et al. 2007). Finally, be-

yond any statistical criteria, it might be reasonable to use only those EOFs/PCs which can be seen as manifestations of real processes or conditions and can be interpreted in a sound scientific manner.

It should additionally be mentioned that EOF and PC analyses can also be applied to a set of temporal sequences of spatial fields (extended analysis or principal sequence pattern analysis, see Compagnucci et al. 2001, Jacobeit et al. 2006) as well as to several fields (combined analysis) referring for example to different atmospheric levels or to different wind components (e. g. Jacobeit 1992). Furthermore, coupled pairs of patterns from two fields of related variables can be derived by canonical correlation analysis (CCA, e. g. Dünkeloh and Jacobeit 2003), and principal oscillation pattern (POP) analysis refers to patterns evolving in time (e. g. Schnur et al. 1993).

7.3.2 Different modes of analysis

Richman (1986) has made a distinction into six different modes of EOF/PC analysis depending on what kind of quantities is processed as input variables and on the nature of the cases for which values of these variables are included. Table 1 summarizes these six modes which imply different meanings of loadings and scores, respectively:

Tab. 1: Different modes of EOF/PC analysis in Meteorology and Climate Research (according to Richman 1986) defined by different settings of variables and cases

Mode	variables	cases
R-mode	meteorological parameters	spatial units
P-mode	meteorological parameters	temporal units
Q-mode	spatial units	met. parameters
O-mode	temporal units	met. parameters
S-mode	spatial units	temporal units
T-mode	temporal units	spatial units

- With R-mode (in our context meteorological parameters as variables, spatial units like stations or grid points as cases) the scores yield spatial patterns and the loadings reveal their meteorological meaning.
- With P-mode (once more meteorological parameters as variables, but now temporal units (days or months or years ...) as cases) the scores yield characteristic time series whose meteorological meaning is revealed by the loadings.
- With Q-mode (spatial units as variables, meteorological parameters as cases) a spatial composition (with spatial coherence even a regionalization) in terms of a set of characterizing parameters is achieved.
- With O-mode (temporal units as variables, meteorological parameters as cases) a temporal distinction in terms of a set of characterizing parameters is achieved.
- With S-mode (spatial units as variables, temporal units as cases) the loadings provide spatial patterns and the scores their time coefficients with respect to the included parameters (e. g. air pressure or temperature or precipitation ...).
- With T-mode (temporal units as variables, spatial units as cases) the scores provide spatial patterns and the loadings their time coefficients with respect to the included parameters.

In Meteorology and Climate Research, mostly S- and T-modes (including both spatial and temporal resolutions) are applied, and they directly lead to our objectives, modes of variability and basic circulation patterns, respectively. Starting with the latter, the fundamental idea consists in generating some few patterns which represent basic states of the atmospheric circulation in the study domain (e. g. a zonal pattern, a trough-like pattern, a ridge-like pattern etc.) from which all original fields (SLP or geopotential height fields for a number of temporal units like days or months) can be reproduced by linear combinations with varying time coefficients. The latter correspond to the T-mode loadings which specify the particular weight of the basic patterns (given by the T-mode scores) within the original fields reflecting their degree of similarity to the

basic patterns (Jacobeit et al. 2001). For example, a westerly flow at a particular date would have a dominant loading on a basic zonal circulation pattern. Thus, each individual field can be characterized by dominating and receding basic patterns allowing to group the original fields according to their different affinity to the basic patterns.

It has to be stressed that this procedure is not an usual classification since the attribution of original fields to basic patterns is not an unequivocal one (like in disjunctive classifications where each variable belongs to one and only one of the classified types). The EOF/PC loadings, however, also include non-zero values for those patterns which are not the leading ones thereby accounting for the fact that most variables contain elements from more than one basic pattern. Therefore, the correct view of (squared) loadings is a representation of varying amounts of explained variance with increasing and decreasing values for a particular pattern from one variable to the next. Comparing these values among all basic patterns allows to characterize the atmospheric circulation of the original fields with respect to these basic patterns. In T-mode, they have furthermore to be distinguished from centroid patterns resulting from classifications of circulation types: the latter result from averaging all the individual members of a classified type, whereas the T-mode scores are not averaged from individual objects, they represent a generic circulation pattern (Jacobeit 2010), some kind of a prototype with varying degrees of similarity to the original fields (expressed by the T-mode loadings). Thus, the individual objects are reproduced as superimpositions of prototype patterns with varying weights according to equation (1), and these prototype patterns reflect basic states of the atmospheric circulation as far as they prove to be no artefacts but manifestations of well-known patterns from the real dynamical system.

The other approach linked with S-mode circulation analyses intends to identify characteristic time series of SLP or geopotential height data being representative for a certain number of grid-points in the study domain (Jacobeit et al. 1998, p. 55). Therefore, these grid-points define the input variables which are replaced by EOFs/PCs constituting spatial centres of variation with corresponding S-mode scores providing these characteristic time series. The S-mode loadings reflect the degree of similarity between these scores and the original grid-point time series. High loadings indicate such a centre of variation which is characterized by a particular mode of temporal variability in SLP or geopotential heights. If the study domain is large enough, further loading maxima (positive or negative) may occur outside the primary centre of variation; in this case the field of loadings even provides teleconnection patterns indicating which regions are connected to each other in terms of same or opposite directions in temporal variability. For example, in the North-Atlantic European area the first winter-time S-mode EOF/PC mostly reflects the North-Atlantic Oscillation (NAO) with opposite loadings in the regions around Iceland and the Azores (other teleconnection patterns will be addressed in the next section). However, S-mode loading patterns cannot be interpreted as circulation patterns (like T-mode scores), since the maxima and minima do not represent high and low pressure centres, but locations with highest similarity (positive or negative) to the corresponding mode of temporal variability. Thus, in S-mode, scores describe the varying phases of teleconnections whose spatial patterns are specified by the loadings.

Summing up, S- and T-modes not only differ in the attributes of loadings and scores – the former giving spatial (temporal) information, the latter temporal (spatial) information in S-(T)-mode – but also in the meaning with respect to atmospheric circulation dynamics (see also Compagnucci and Richman 2008). S-mode analysis provides teleconnection patterns (if we focus on the spatial dimension) or modes of variability (if we focus on the temporal dimension), whereas T-mode analysis provides basic circulation patterns into which original fields can be decomposed. Especially the T-mode scores have great importance as generic circulation patterns whose superimpositions with varying weights reproduce the original fields and condense their information to a few decisive patterns. If we combine both modes of analysis, a comprehensive picture of atmospheric circulation dynamics can be initiated.

7.4 Results with respect to Mount Zugspitze

In this section we focus on relationships between the atmospheric circulation and both temperature and precipitation anomalies at Mount Zugspitze, and this will be done by using basic circulation patterns (derived from T-mode PCA, section 4.1) as well as modes of variability/teleconnection patterns (based on S-mode PCA, section 4.2).

7.4.1 Atmospheric circulation patterns

To identify relationships between temperature or precipitation and basic circulation patterns, we focus (as input variables for T-mode analysis) only on those months which differ (with positive or negative sign) by more than one standard deviation from the corresponding long-term mean value thus excluding all months near to average climate conditions. Based on these substantial anomalies which in most cases amount to seasonal numbers between 55 and 71 for the 1950–2015 period (only for wet and dry winter months a lower number of 44 is reached), distinct signals in the large-scale mid-tropospheric circulation (500 hPa level) can be expected.

From the eight analyses (temperature and precipitation anomalies separately for the meteorological seasons) we select in this chapter those referring to warm and cold anomalies during winter and summer as well as wet and dry anomalies during spring and autumn. The remaining analyses include some overlapping results and therefore can be left out.

7.4.1.1 Warm and cold anomalies during winter (DJF)

During the 1950–2015 period, 36 warm (more than one standard deviation above the long-term mean value) and 35 cold months (more than one standard deviation below the long-term mean value) occurred at Mount Zugspitze. With the monthly mean geopotential height fields (500 hPa level) of these 71 months as input variables, we get four (according to the dominance criterion) rotated T-mode principal components each explaining more than 10% of the original variance (all together nearly 97%). Fig. 1 displays the corresponding basic circulation patterns (T-mode scores), Fig. 2 is based on the time coefficients (T-mode loadings) indicating in squared terms the variances explained by each PC split up into warm and cold months. If there is a significant difference between these sub-samples (95% level according to Mann-Whitney's U-test), the corresponding circulation pattern is associated either to warm or to cold anomalies, the above-average value in Fig. 2 being averaged from those months with dominance of the corresponding PC (greatest loading among all PCs). If there is no significant loading difference between warm and cold sub-samples, the corresponding circulation pattern proves as a mixed one with alternating predominance during both thermal anomalies.

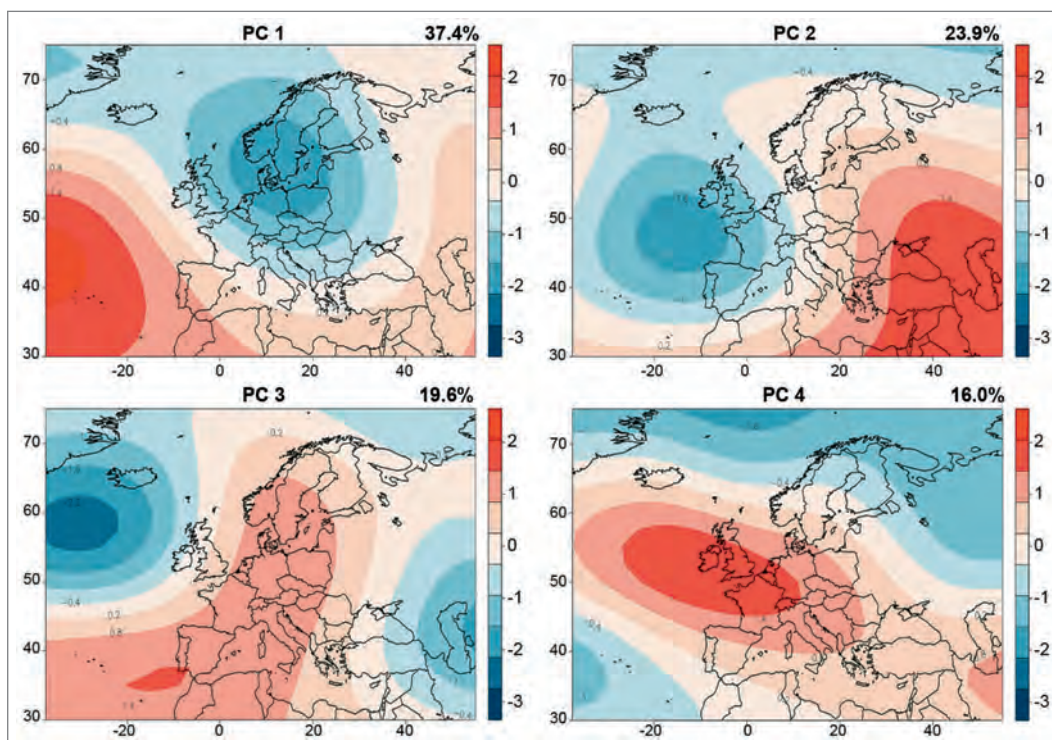


Fig. 1: Basic circulation patterns for warm and cold months (more than one standard deviation above or below the corresponding mean values) at Mount Zugspitze during winter (DJF) 1950–2015 derived from T-mode PCA of monthly mean geopotential height grids at the 500 hPa level (explained variances in %).

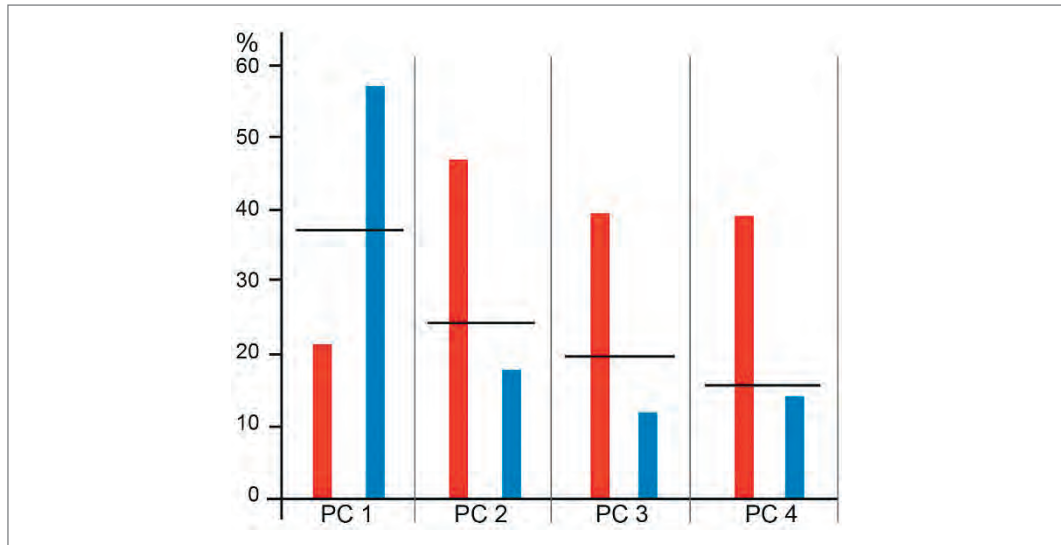


Fig. 2: Mean squared T-mode loadings (corresponding to explained variances in %) of PCs 1–4 from the geopotential height analysis for warm and cold months (red and blue color, respectively) during winter (DJF) 1950–2015. Black lines represent the mean values for each PC, red and blue values above this reference are averaged from those months with dominance of the corresponding PC (greatest loading among all PCs), red and blue values below this reference are averaged from all warm or cold winter months indicating systematic loading differences between them.

PC 1 clearly prevails during cold winter months, it represents a trough pattern with the cyclonic centre above southern Scandinavia and Mount Zugspitze at the rear of the cyclonic wave where (sub-)polar cold air is advected towards lower latitudes. This well-known pattern for strong winter conditions in large parts of the western and central European mid-latitudes (e. g. Jacobeit et al. 1998, p.125) even accounts for nearly all cold winter months at Mount Zugspitze. Since it is linked with northerly to north-westerly wind directions, one might ask for another well-known ‘cold’ pattern characterized by a strong and westward extended Russian high with easterly components in Central Europe (Jacobeit et al. 2009, p. 41). Indeed, such patterns prevail (with varying high pressure positions) during nearly the half of all cold winter months, however, the Russian high as a thermal pressure system with only limited vertical extension merely is present at lower atmospheric levels and cannot be identified any more at 500 hPa. Thus, PC 1 remains as the only mid-tropospheric pattern with a distinct linkage to cold winter months.

The other three circulation patterns of Fig. 1 are primarily related to warm winter months (see Fig. 2) and therefore might gain increased importance with enhanced global warming. PC 2 represents a pattern dominated by a low pressure system above the mid-latitudinal eastern Atlantic (high pressure only further to the east) with the Zugspitze region in front of it being located in the large-scale flow from southerly to south-westerly directions. PC 3 looks like a PC-2 pattern shifted towards the north-west, thus the Zugspitze region is included into the warm core of the anticyclonic ridge above continental Europe. The PC-4 pattern – already with insignificant loading differences, but mainly dominating during warm months – still displays another high-pressure centre now extending more in a zonal direction. Altogether, warm winter months are linked either to warm cores of meridional or zonal high pressure ridges or to wave patterns with warm air advection between the cyclonic phase to the west and the anticyclonic one to the east (PC 2).

It should furthermore be mentioned that particular shifts within the patterns of Fig. 1 are able to lead to opposite temperature effects: for example, if the wave pattern of PC 2 is shifted sufficiently to the east, the Zugspitze region might get into the cold core of the cyclonic wave (as in three cases of cold winter months). Another within-pattern change can take place if the high-pressure centre of PC 4 is sufficiently shifted to the west so that the Zugspitze region in front of it gets into the cold north-westerly flow (one case during the study period). Apart from these internal changes, however, the basic circulation patterns of Fig. 1 have a clear preponderance to either warm or cold anomalies during winter time.

7.4.1.2 Warm and cold anomalies during summer (JJA)

During the 1950–2015 period, 38 warm and 27 cold months occurred at Mount Zugspitze. Submitting the monthly mean geopotential height fields (500 hPa level) of these 65 months to a rotated T-mode PCA results in four PCs each explaining more than 20% of the original variance (all together more than 96%). Like in the preceding section, Figs. 3 and 4 reproduce the basic circulation patterns and their differences between warm and cold months.

According to Fig. 4, PC 1 is clearly linked to warm summer months, the corresponding circulation pattern (Fig. 3) is well-known from other studies (e.g. Jacobeit et al. 2003) and represents an anticyclonic ridge from the Azores region towards southern Scandinavia with the Zugspitze region being included in the warm core of this ridge. In contrast to that, PC 2 shows a trough pattern in this longitudinal section, high pressure influence is located upstream above the central North Atlantic. Accordingly, the Zugspitze region is exposed to cold advection from northerly to north-westerly directions, PC 2 proves to be a cold-anomaly pattern.

The remaining two PCs do not have a significant relationship to a particular temperature anomaly at Mount Zugspitze, warm as well as cold summer months may occur with them (Fig. 4).

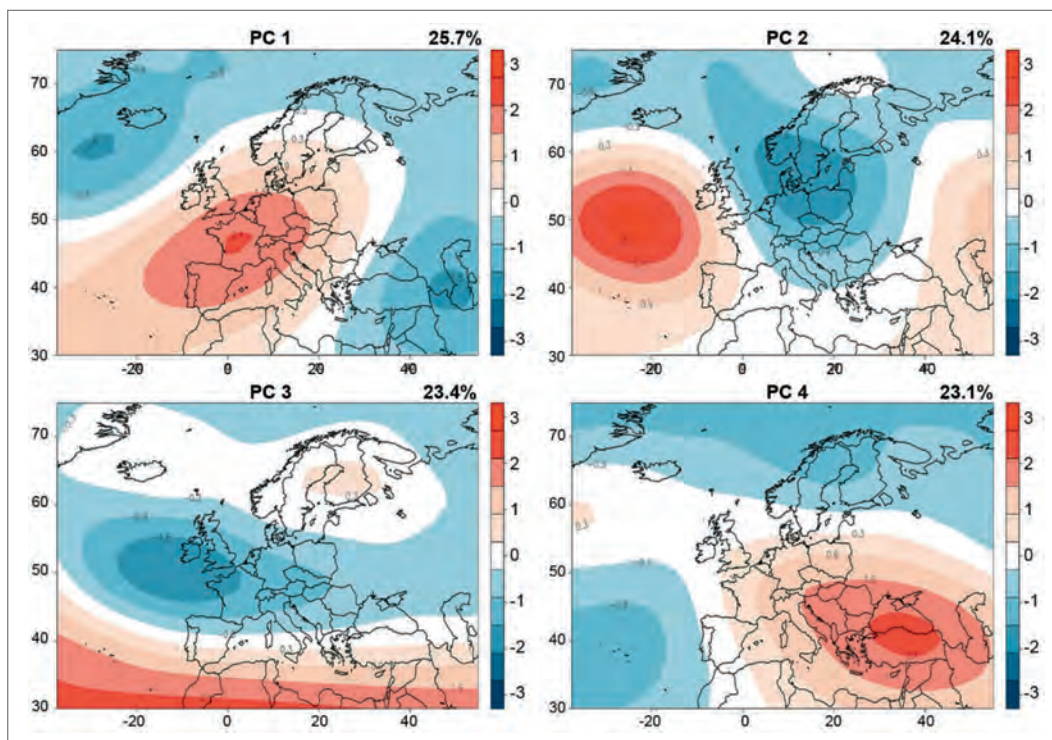


Fig. 3: As Fig. 1 but for warm and cold months during summer (JJA)

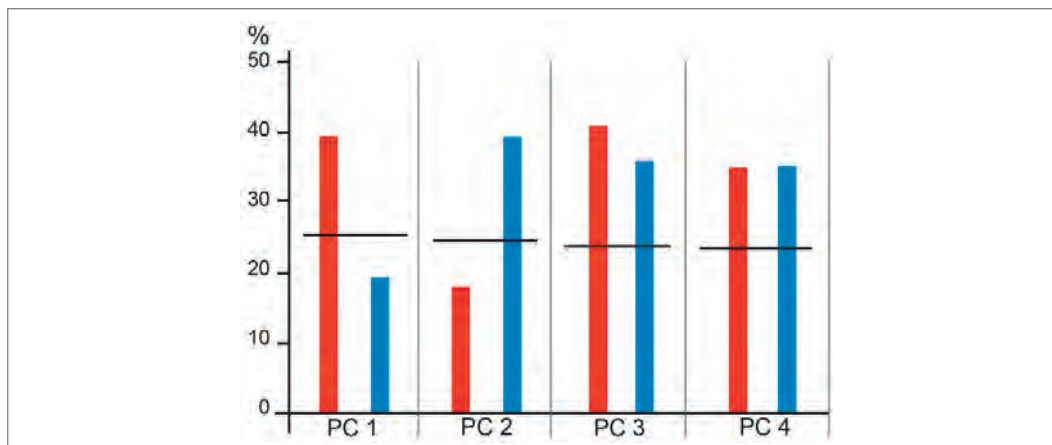


Fig. 4: As Fig. 2 but for warm and cold months during summer (JJA)

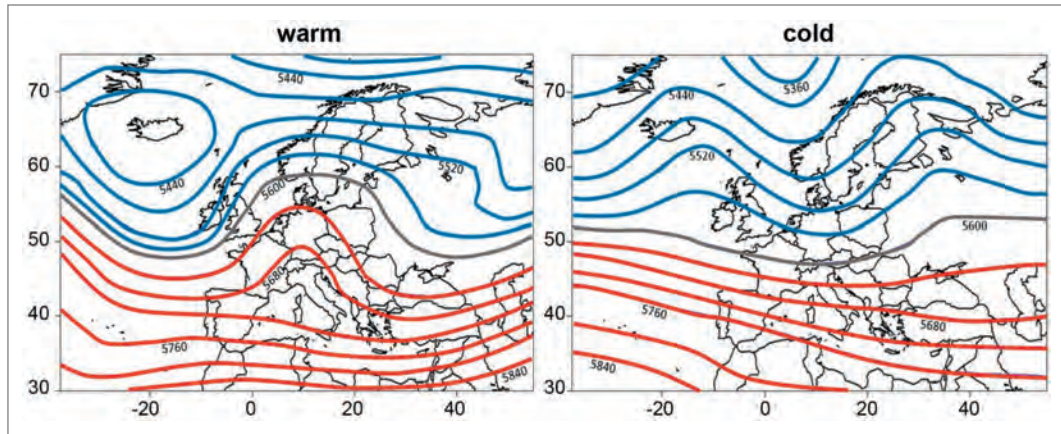


Fig. 5: Composites of monthly mean 500 hPa geopotential heights (gpm) for those warm or cold summer months having the highest loading on PC 3 from Fig. 3

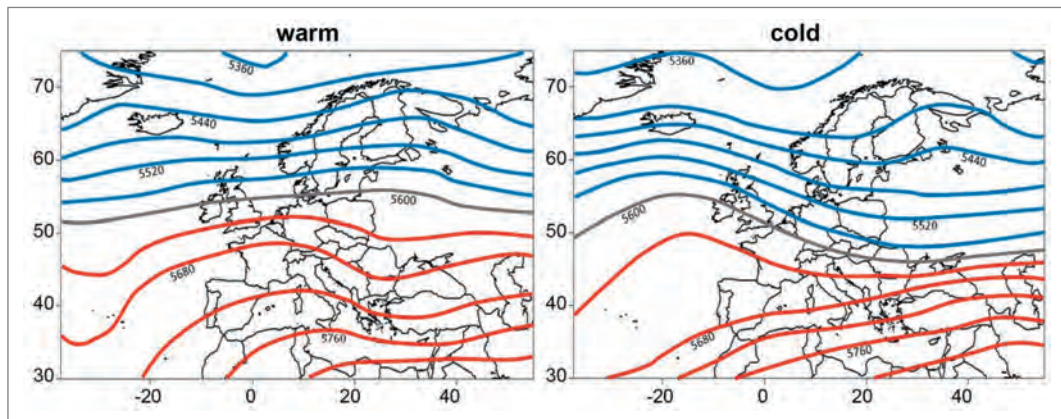


Fig. 6: As Fig. 5 but for PC 4 from Fig. 3

PC 3 depicts a cyclonic centre towards the west, PC 4 an anticyclonic one towards the south-east. Figs. 5 and 6 reveal the background of their thermal ambiguity: comparing the PC composites for the opposite thermal anomalies (i. e. the loading-weighted mean geopotential height fields for all warm or cold months linked to a particular PC) indicates in case of PC 3 that the cyclonic phase of the wave pattern is located considerably further west (further east) during warm (cold) summer months. In case of PC 4, an anticyclonic wave is developed around the Zugspitze region during warm months instead of north-westerly components during cold months. Thus, internal variations within these PC patterns imply the occurrence of different temperature anomalies, depending for example on varying wave lengths and phase positions like for PC 3 and PC 4.

7.4.1.3 Wet and dry anomalies during spring (MAM)

During the 1950–2015 period, 29 wet and 32 dry months occurred at Mount Zugspitze. Submitting the monthly mean geopotential height fields (500 hPa level) of these 61 months to a rotated-T-mode PCA results in four PCs each explaining more than 15% of the original variance (all together 97%). Like in the preceding sections, Figs. 7 and 8 reproduce the basic circulation patterns and their differences now between wet and dry months.

A clear link to wet (dry) conditions exists for PC 4 (PC 2) with the Zugspitze region in the core of a central low (high) pressure system. For PC 1 and PC 3, however, the circulation-precipitation link is ambiguous (Fig. 8) due to pressure centres located more westward with varying extensions towards the Zugspitze region. For the wet version of PC 1 (see Fig. 9), the cyclonic wave amplitude reaches more than 5° of latitude further south than for the dry version of the same PC. For PC 3 (see Fig. 10), the position of the anticyclonic wave axis differs by some 10° of longitude between wet and dry conditions, and this is decisive whether or not the Zugspitze region is included in its spatial domain. Thus, once more internal variations within particular PC patterns may influence the sign of a local climate anomaly.

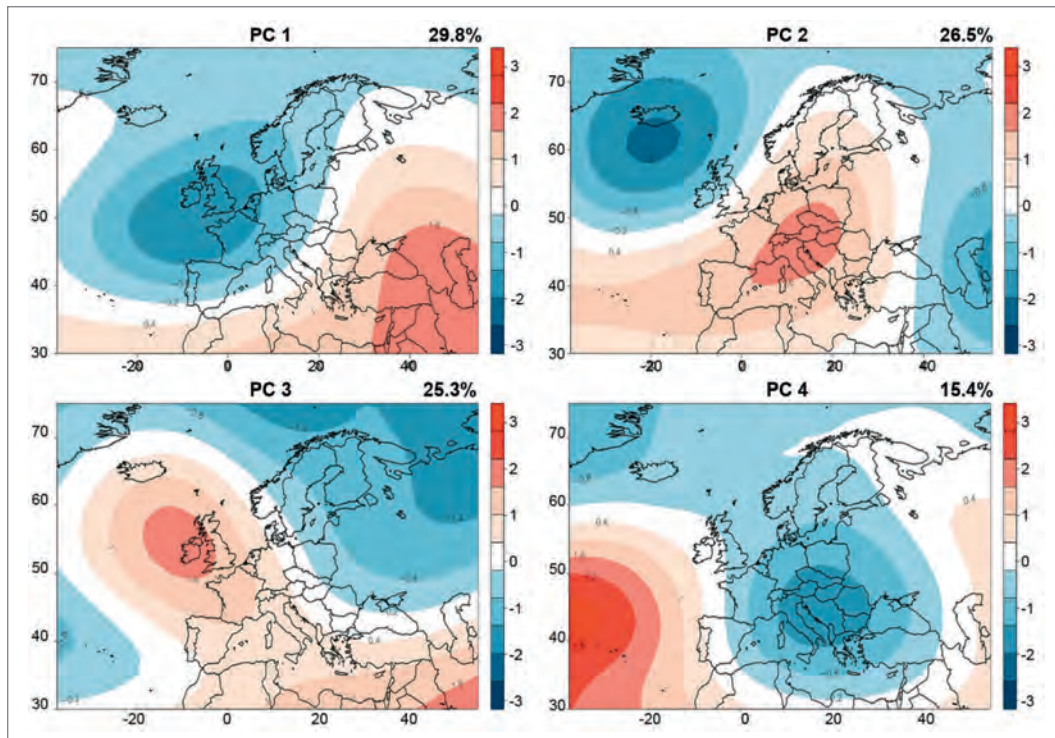


Fig. 7: As Fig. 1 but for wet and dry months during spring (MAM)

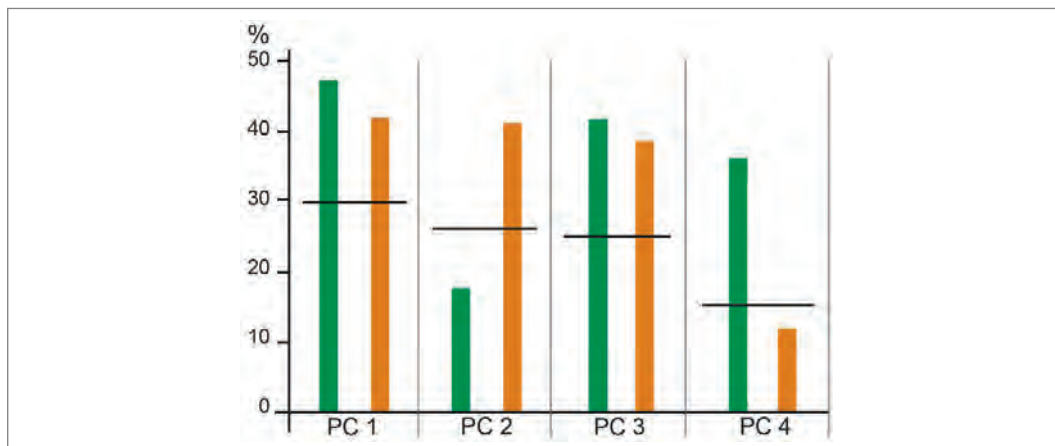


Fig. 8: As Fig. 2 but for wet and dry months (green and brown color, respectively) during spring (MAM)

7.4.1.4 Wet and dry anomalies during autumn (SON)

During the 1950–2015 period, 25 wet and 30 dry months occurred at Mount Zugspitze. Submitting the monthly mean geopotential height fields (500 hPa level) of these 55 months to a rotated-T-mode PCA results in four PCs each explaining more than nearly 10% of the original variance (all together 97%). Like in the preceding section, Figs. 11 and 12 reproduce the basic circulation patterns and their differences between wet and dry months.

PC 1 represents an anticyclonic ridge pattern from the Azores towards central Europe and is clearly linked to dry autumn months at Mount Zugspitze. Most of the wet months are related to PC 2 representing a central European trough pattern. The remaining PCs show some similarity to spring patterns and therefore are not specified by further composites: PC 3 generally resembles the first spring pattern concerning the wave phase positions and may likewise be linked to both wet and dry autumn months depending on varying amplitudes of the cyclonic wave to the west of Mount Zugspitze. Similar internal variations as for spring pattern 3 apply to PC 4 which, however, is realized in autumn 1950–2015 only in the dry version concerning Mount Zugspitze; therefore, no above-average value occurs for ‘wet’ in Fig. 12, but the loading difference between wet and dry remains insignificant.

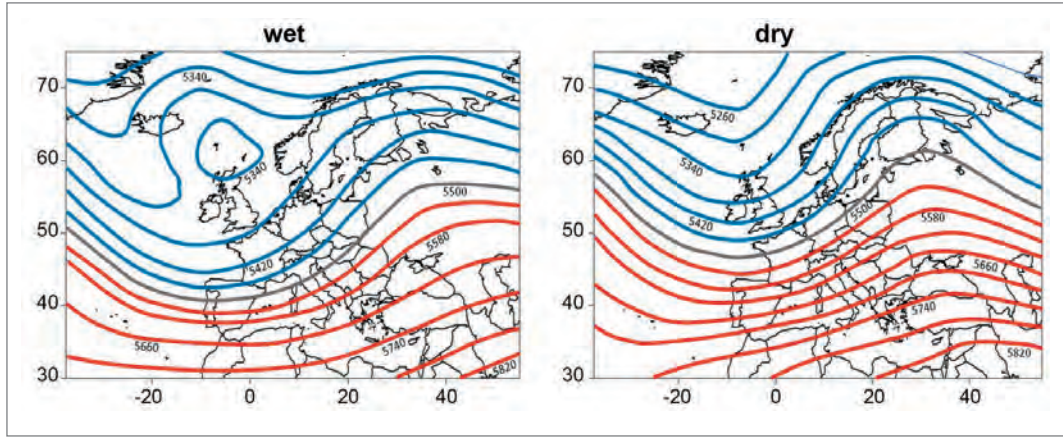


Fig. 9: Composites of monthly mean 500 hPa geopotential heights (gpm) for those wet or dry spring months having the highest loading on PC 1 from Fig. 7

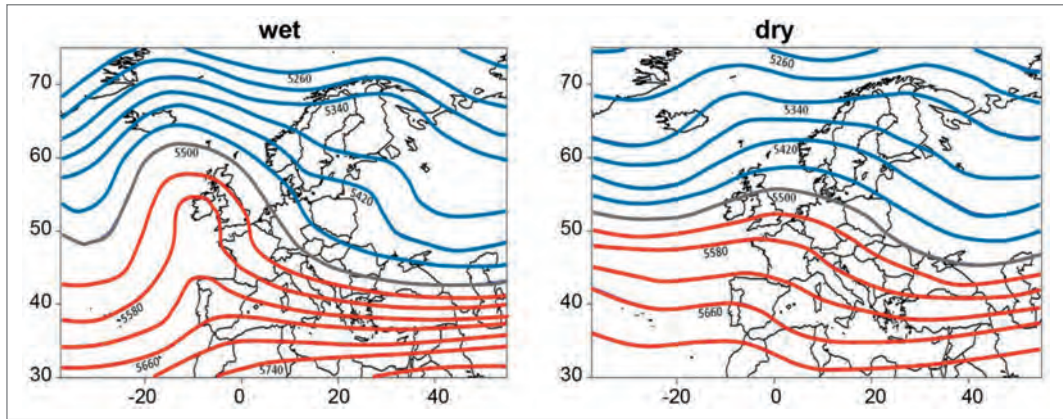


Fig. 10: As Fig. 9 but for PC 3 from Fig. 7

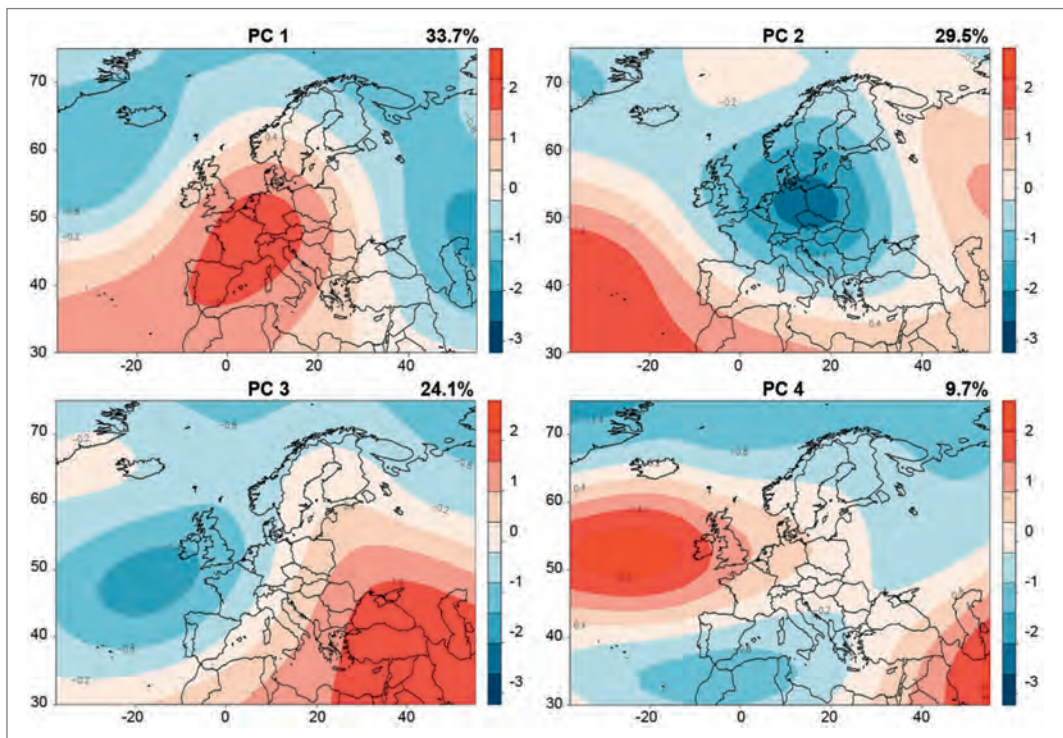


Fig. 11: As Fig. 1 but for wet and dry months during autumn (SON)

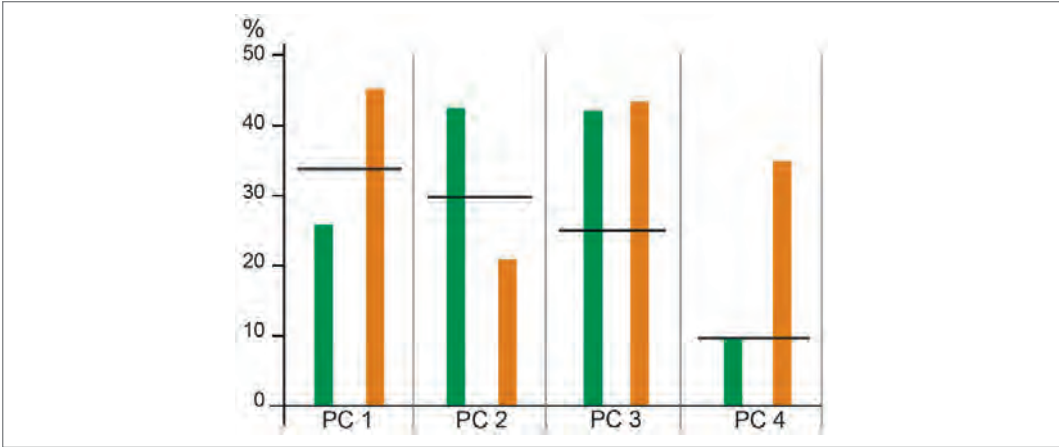


Fig. 12: As Fig. 8 but for wet and dry months during autumn (SON)

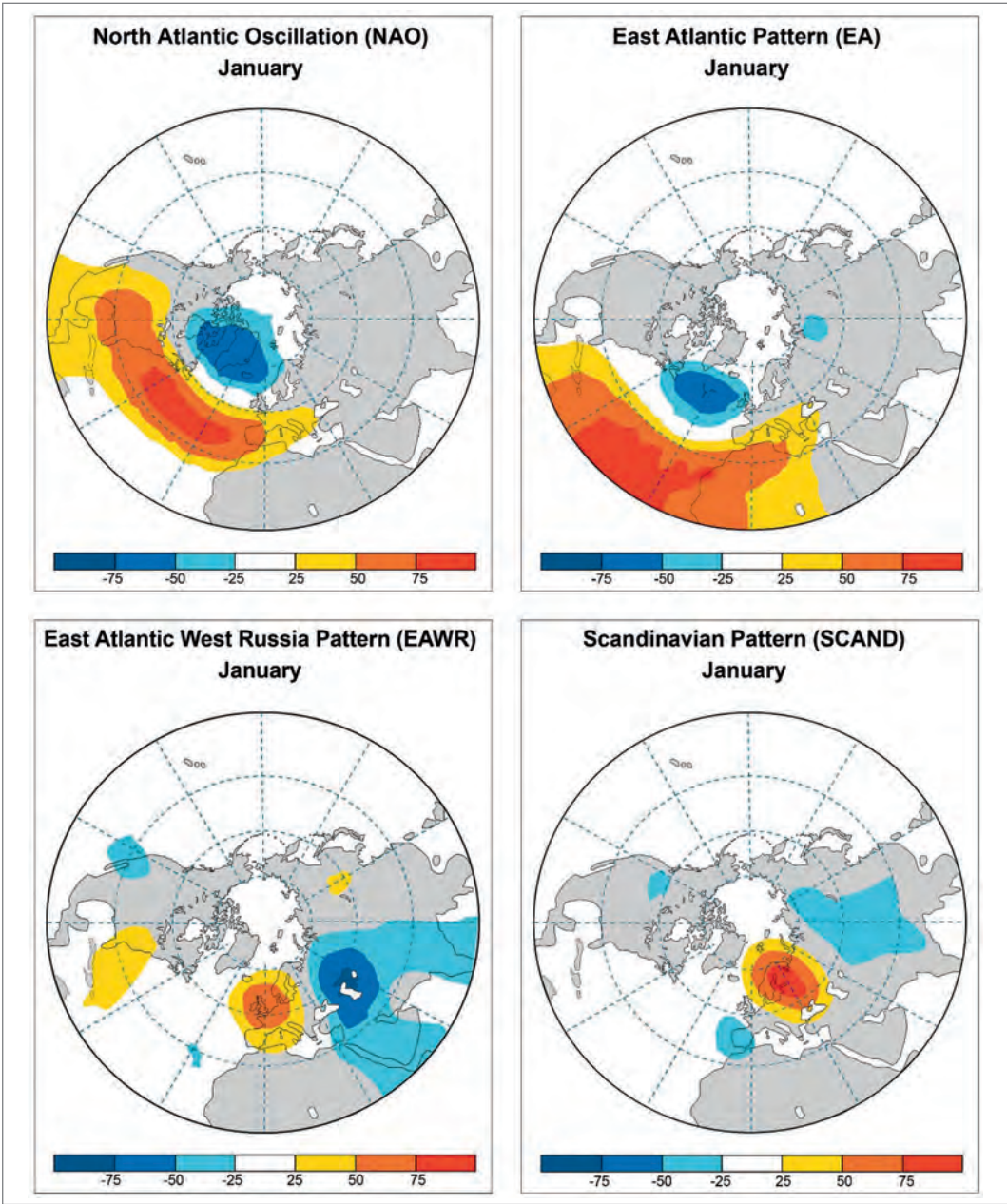


Fig. 13: The S-mode loading patterns for NAO, EA, EAWR and SCAND for the selected month of January in terms of the temporal correlation coefficients between the monthly normalized geopotential height anomalies (500 hPa level) at each grid point and the S-mode score time series for the corresponding teleconnection patterns (modified after Climate Prediction Center CPC).

7.4.2 Modes of variability / teleconnection patterns

In contrast to basic circulation patterns discussed in the previous sections, we now focus on possible impacts of large-scale modes of variability (referring again to the 500 hPa level) on monthly temperature and precipitation conditions at Mount Zugspitze. These modes of variability are provided by characteristic time series of well-known teleconnection patterns derived by S-mode EOF/PC analysis. In our context we focus on the most important teleconnection patterns in the North-Atlantic European region (NAO, EA, EAWR, SCAND, see Fig. 13) using their monthly time coefficients 1950–2015 as provided by the Climate Prediction Center (CPC).

Direct correlations between these time coefficients and the Zugspitze temperature or precipitation time series mostly yield small absolute values (lower than 0.4 corresponding to explained variances of distinctly less than 20%), only for the EA pattern and Zugspitze temperature there are slightly higher values (with maxima of 0.52 and 0.51 for autumn and winter, respectively). Considering time lags – as might be reasonable in teleconnective relationships – does not increase the correlation coefficients, they further drop down to even smaller values (maximum 0.21), probably arising from the monthly time scale of these analyses. In view of that, we prefer another ‘anomaly approach’, focusing on those months with deviations in the time coefficients for the teleconnection patterns of more than one standard deviation above or below the long-term mean values. For these anomaly months, the associated seasonal temperature and precipitation signals at Mount Zugspitze are quantified in two different ways: at first, providing the percentage frequencies of positive and negative deviations in temperature and precipitation for both anomaly phases of the teleconnection patterns; secondly, specifying for these opposite teleconnection phases the mean values of normalized temperature and precipitation, separately for positive and negative deviations. Thereby, possible impacts of pronounced teleconnection pattern anomalies on temperature and precipitation conditions at Mount Zugspitze will be identified on a seasonal basis.

7.4.2.1 North Atlantic Oscillation (NAO)

The well-known impacts of the NAO on the European climate (e. g. Appenzeller et al. 2000) are confirmed for the Zugspitze region (Tab. 2): the strongest signal (significant at the 99% level according to a two-tailed χ^2 -test) can be achieved for winter temperature with 75% (59%) of the pronounced NAO+ (NAO-) cases showing positive (negative) deviations at Mount Zugspitze with normalized mean values of +0.91 (-1.10). The same relationship – higher temperatures with strong mid-latitude westerlies and lower temperatures with decreased westerlies or more meridional circulation patterns – can still be seen for autumn though less pronounced (Tab. 2). During spring and summer, significance cannot be reached any more. Similar seasonal differences exist for precipitation with one important exception, however: NAO+ during autumn tends to be accompanied with below-average precipitation (75% of all cases) in contrast to winter with the majority (67%) pointing to above-average precipitation. This opposition is based on the fact that during the warmer half of the year the NAO+ does not represent a westerly but rather an anticyclonic ridge pattern from the Azores towards southern Scandinavia in prolongation of the high-summer NAO according to Folland et al. (2009). Altogether, NAO- does not include distinct signals in monthly Zugspitze precipitation, whereas NAO+ often leads to more (less) precipitation in winter (autumn).

7.4.2.2 East Atlantic Pattern (EA)

This pattern is similar to a southward shifted NAO pattern (see Fig. 13), its major centre of variation (implying negative geopotential height anomalies in the positive phase EA+) is located in the eastern mid-latitude Atlantic (west of the British Isles). There is a highly significant (99% level, see Tab. 3) temperature signal at Mount Zugspitze during all seasons with clearly dominating positive deviations during EA+ (with frequencies between 76 and 95% and mean normalized anomalies mostly greater than 1) and prevailing negative deviations during EA- (with frequencies between 68 and 80% and mean normalized anomalies near -1). In terms of circulation dynamics this is due to a large-scale south-westerly (north-westerly) flow in front of an eastern Atlantic low (high) pressure system.

The signals in Zugspitze precipitation are less distinct (Tab. 3) attaining significance only in summer (99% level) and autumn (95% level), and this is mainly due to EA+ with dominating

Tab. 2: Frequency (a) and intensity (b) of positive and negative deviations from the long-term mean in monthly temperature and precipitation at Mount Zugspitze for NAO+ and NAO- during the meteorological seasons (DJF, MAM, JJA, SON). Percentage frequencies refer to all months with deviations in the seasonal NAO time coefficient of more than one standard deviation above or below the long-term mean value. 2x2 sub-tables for a particular season and variable providing a significant two-tailed χ^2 -test are highlighted in dark and light color for the 99% and 95% level, respectively. Intensity is indicated by the mean value of the normalized monthly temperature or precipitation anomalies during those months counted in the frequency table.

a)

Frequency	Temperature ↑	Temperature ↓	Precipitation ↑	Precipitation ↓
Winter NAO+	75%	25%	67%	33%
Winter NAO-	41%	59%	49%	51%
Spring NAO+	59%	41%	52%	48%
Spring NAO-	49%	51%	49%	51%
Summer NAO+	53%	47%	37%	63%
Summer NAO-	49%	51%	44%	56%
Autumn NAO+	65%	35%	25%	75%
Autumn NAO-	39%	61%	48%	52%

b)

Intensity	Temperature ↑	Temperature ↓	Precipitation ↑	Precipitation ↓
Winter NAO+	0.91	-0.53	0.64	-0.61
Winter NAO-	0.64	-1.1	0.24	-0.56
Spring NAO+	0.79	-0.64	0.97	-0.59
Spring NAO-	0.71	-0.90	0.61	-0.66
Summer NAO+	0.65	-0.63	0.68	-0.77
Summer NAO-	0.89	-0.89	0.98	-0.58
Autumn NAO+	0.86	-0.79	1.05	-0.81
Autumn NAO-	0.85	-0.80	0.79	-0.58

Tab. 3: As Tab. 2 but for the East Atlantic Pattern (EA)

a)

Frequency	Temperature ↑	Temperature ↓	Precipitation ↑	Precipitation ↓
Winter EA+	81%	19%	59%	41%
Winter EA-	29%	71%	62%	38%
Spring EA+	76%	24%	41%	59%
Spring EA-	32%	68%	48%	52%
Summer EA+	83%	17%	22%	78%
Summer EA-	27%	73%	50%	50%
Autumn EA+	95%	5%	37%	63%
Autumn EA-	20%	80%	55%	45%

b)

Intensity	Temperature ↑	Temperature ↓	Precipitation ↑	Precipitation ↓
Winter EA+	1.01	-0.32	0.22	-1.03
Winter EA-	0.46	-0.96	0.82	-0.96
Spring EA+	0.89	-0.56	0.62	-0.57
Spring EA-	0.59	-1.07	1.15	-0.72
Summer EA+	1.28	-1.04	1.12	-0.58
Summer EA-	0.63	-0.84	0.69	-0.64
Autumn EA+	1.01	-0.61	0.35	-0.62
Autumn EA-	0.68	-1.04	0.92	-0.76

negative deviations in precipitation linked with the large-scale south-westerly flow. Otherwise, internal variations within the EA pattern concerning position and strength of the driving centre seem to prevent further significant signals in precipitation.

7.4.2.3 East Atlantic West Russia Pattern (EAWR)

This pattern includes two opposing centres of variation above Western Europe (centered around the North-Sea) and in the Caspian Sea region (Fig. 13). Its positive phase EAWR+ is defined for an anticyclonic system to the west and a cyclonic one further east. Temperature signals at Mount Zugspitze are highly significant (99% level) for three seasons (Tab. 4), only in summer no clear distinction between the opposite EAWR phases is present. Their contrast is most pronounced during winter with 82% positive temperature deviations (68% negative ones) for EAWR+ (EAWR-). This linkage indicates that the West European teleconnection centre determines the temperature response at Mount Zugspitze (positive with an anticyclonic, negative with a cyclonic system).

EAWR is the only of the four analyzed teleconnection patterns with significant phase distinctions for precipitation during all seasons (yet least pronounced in summer). This is in general accordance to findings of Qian et al. (2000) who identified a partly similar pattern (so-called 'North-Sea Pattern') as the most important one for precipitation in Europe. Mostly the impact of EAWR+ on decreased precipitation is dominating (see Tab. 4), however, during winter this changes to a distinct preference for increased precipitation with EAWR-. Thus, in the cold season the efficiency of the cyclonic phase around the North Sea seems to be more pronounced than that of its anticyclonic counterpart.

7.4.2.4 Scandinavian Pattern (SCAND)

This pattern includes two opposing centres of variation above Scandinavia (anticyclonic system in the positive phase) and above the Iberian peninsula (Fig. 13). It has been identified in several studies (e.g. Wibig 1999; Quadrelli et al. 2001; Efthymiadis et al. 2007), but nevertheless, it has the lowest number of significant signals in Zugspitze temperature and precipitation (Tab. 5) among the teleconnection patterns discussed in this contribution. During spring, a distinct preference for below-average precipitation is indicated for SCAND+, but during summer some

Tab. 4: As Tab. 2 but for the East Atlantic West Russia Pattern (EAWR)

a)

Frequency	Temperature ↑	Temperature ↓	Precipitation ↑	Precipitation ↓
Winter EAWR+	82%	18%	50%	50%
Winter EAWR-	32%	68%	79%	21%
Spring EAWR+	73%	27%	21%	79%
Spring EAWR-	30%	70%	46%	54%
Summer EAWR+	55%	45%	39%	61%
Summer EAWR-	45%	55%	55%	45%
Autumn EAWR+	69%	31%	31%	69%
Autumn EAWR-	26%	74%	58%	42%

b)

Intensity	Temperature ↑	Temperature ↓	Precipitation ↑	Precipitation ↓
Winter EAWR+	1.17	-0.72	0.51	-0.81
Winter EAWR-	0.53	-0.92	0.44	-0.71
Spring EAWR+	0.91	-0.95	1.13	-0.85
Spring EAWR-	0.66	-0.71	1.16	-0.52
Summer EAWR+	0.91	-0.85	0.75	-0.76
Summer EAWR-	0.76	-1.06	1.10	-0.70
Autumn EAWR+	0.98	-0.97	0.55	-0.91
Autumn EAWR-	0.46	-1.10	0.95	-0.54

Tab. 5: As Tab. 2 but for the Scandinavian Pattern (SCAND)

a)

Frequency	Temperature ↑	Temperature ↓	Precipitation ↑	Precipitation ↓
Winter SCAND+	53%	47%	44%	56%
Winter SCAND-	64%	36%	59%	41%
Spring SCAND+	53%	47%	20%	80%
Spring SCAND-	58%	42%	54%	46%
Summer SCAND+	31%	69%	50%	50%
Summer SCAND-	69%	31%	30%	70%
Autumn SCAND+	58%	42%	27%	73%
Autumn SCAND-	50%	50%	42%	58%

b)

Intensity	Temperature ↑	Temperature ↓	Precipitation ↑	Precipitation ↓
Winter SCAND+	0.62	-0.73	0.48	-0.60
Winter SCAND-	1.01	-0.84	0.97	-0.62
Spring SCAND+	0.66	-0.92	0.37	-0.68
Spring SCAND-	0.86	-1.39	1.32	-0.81
Summer SCAND+	0.40	-0.86	0.94	-0.65
Summer SCAND-	0.90	-0.67	0.52	-0.68
Autumn SCAND+	0.85	-0.87	1.03	-0.72
Autumn SCAND-	0.79	-0.62	0.86	-0.68

changes in the relationships can be observed: now the negative phase is decisive but once more in favor of below-average precipitation (Tab. 5). This is due to a much more widespread southern centre of variation during summer (not shown in Fig. 13) including in particular the Alpine region. For SCAND- this means anticyclonic influence (reduced precipitation as well as increased temperatures), and for SCAND+ this implies cyclonic influence which, however, is clearly reflected only in reduced temperatures, whereas for precipitation no frequency distinction but only slightly greater amounts in the mean normalized anomalies for positive deviations (Tab. 5) can be observed. Generally, the SCAND pattern seems to be characterized by a high level of internal variability thus confining the frequency of associated climate anomalies.

7.5 Conclusions

Among the teleconnection patterns discussed in section 4.2, a very remote one has not been considered: the ENSO teleconnection. This may be justified in view of results by Efthymiadis et al. (2007) indicating that its impact on the climate of the Greater Alpine Region is generally weak and non-stationary (even in sign). Therefore our focus was on patterns well-known within the North-Atlantic European area, looking at conditions with pronounced positive or negative phases of these patterns (beyond one standard deviation from long-term mean values in the corresponding time coefficients). Remarkably, it was not the NAO among these patterns showing the strongest or most frequent impacts on temperature and precipitation anomalies at Mount Zugspitze, only in autumn and winter significant relationships could be confirmed, positive for temperature and winter precipitation (Atlantic influence with NAO+), but negative for autumn precipitation (i. e. increased frequencies of negative anomalies during NAO+ due to anticyclonic influence). EA and EAWR proved to have more often significant influence on seasonal anomalies at Mount Zugspitze. EA, some kind of a southward shifted NAO pattern, reveals positive relationships with temperature throughout the whole year, whereas Zugspitze precipitation is driven significantly only in summer and autumn (with EA+ favoring dry anomalies). EAWR, a dipole pattern with a zonal axis, impacts on Zugspitze conditions via its western centre around the North Sea, leading to positive relationships with temperature (except of summer) and seasonally varying influence on precipitation (mostly with EAWR+ favoring dry

anomalies, but in winter with EAWR- favoring wet anomalies). The lowest number of significant signals occurs with SCAND, a dipole pattern with meridional axis. During spring, SCAND+ favors dry anomalies, however, during summer the extended domain of the southern centre leads to inverted relationships (SCAND- favoring dry and warm anomalies, SCAND+ mainly cold anomalies).

Generally, the impact of characteristic modes of variability included in large-scale teleconnection patterns of the atmosphere, can be identified down to even local scales as shown for the example of Mount Zugspitze. Sometimes, however, these relationships may change their sign between different seasons or lose statistical significance. This indicates a high level of internal variability within one or both phases of the corresponding teleconnection patterns, for example with respect to position, extension or strength of the driving centres of variation which constitute the affected teleconnection pattern. Such 'within-type changes' are obviously quite common phenomena, as shown repeatedly in context of circulation dynamics (e.g. Jacobeit et al. 2001, 2003; Beck et al. 2007).

The other approach for identifying circulation-climate relationships presented in section 4.1 refers to basic circulation patterns (500 hPa level) which have been derived for months with temperature or precipitation anomalies (beyond one standard deviation from long-term mean values) at Mount Zugspitze. Large-scale trough patterns are primarily important for cold anomalies during both summer and winter, especially during the latter season since the influence of cold Russian high pressure systems does not extend up to mid-tropospheric levels. In contrast, various types of anticyclonic ridges induce warm anomalies, during summer mainly as ridges from the Azores towards southern Scandinavia (corresponding to the summer NAO+), during winter in terms of ridges with more meridional or zonal axis orientation. Additionally, during winter, an eastern Atlantic low pressure system (corresponding to the EA+ pattern) is linked with warm anomalies. During summer, this pattern is part of particular wave patterns which may be associated with both warm and cold anomalies depending on varying wave lengths and phase positions in context of pronounced within-type variability.

Basic circulation patterns for wet and dry anomalies have been presented for the transitional seasons. They include central low or high pressure systems and trough or ridge patterns towards Central Europe with clear-cut attribution to wet or dry anomalies, respectively. Furthermore, various wave patterns do occur with mixed anomaly attribution depending on varying amplitudes and axis positions.

Concerning results from both S-mode and T-mode analyses with respect to climate conditions at Mount Zugspitze, we may generally conclude that some modes or patterns of the large-scale atmospheric circulation include a definite link with local anomalies in temperature or precipitation on a monthly scale, whereas some other modes or patterns are characterized by an elevated level of internal variability leading to ambiguous impacts on local climate anomalies.

References

- Appenzeller, C., T.F. Stocker and A. Schmittner (2000): Natural climate variability and climate change in the North-Atlantic European region: chance for surprise? *Integrated Assessment* 1, 301–306.
- Auer I., R. Böhm, A. Jurkovic et al. (2007): HISTALP — historical instrumental climatological surface time series of the Greater Alpine Region. *Int. J. Climatol.* 27, 17–46.
- Beck, C., J. Jacobeit and P.D. Jones (2007): Frequency and within-type variations of large scale circulation types and their effects on low-frequency climate variability in Central Europe since 1780. *International Journal of Climatology* 27, 473–491.
- Climate Prediction Center (CPC): <http://www.cpc.ncep.noaa.gov/data/teledoc/telecontents.shtml>
- Compagnucci, R.H., D. Araneo and P.O. Canziani (2001): Principal sequence pattern analysis: a new approach to classifying the evolution of atmospheric systems. *Int. J. Climatol.* 21, 197–217.
- Compagnucci, R.H. and M.B. Richman (2008): Can principal component analysis provide atmospheric circulation or teleconnection patterns? *Int. J. Climatol.* 28, 703–726.
- Dünkeloh, A. and J. Jacobeit (2003): Circulation dynamics of Mediterranean precipitation variability 1948–1998. *Int. J. Climatol.* 23, 1843–1866.
- Efthymiadis, D., P.D. Jones, K.R. Briffa, R. Böhm and M. Maugeri (2007): Influence of large-scale atmospheric circulation on climate variability in the Greater Alpine Region of Europe. *Journal of Geophysical Research* 112, D12104, doi:10.1029/2006JD008021.

- Folland, C.K, J. Knight, H.W. Linderholm, D. Fereday, S. Ineson and J.W. Hurrell (2009): The summer North Atlantic Oscillation: Past, Present, and Future. *Journal of Climate* 22, 1082–1103.
- Jacobeit, J. (1992): Die großräumige Höhenströmung in der Hauptregenzeit feuchter und trockener Jahre über dem südamerikanischen Altiplano (Large-scale upper flow in the main rainy season of wet and dry years above the South-American Altiplano). *Meteorologische Zeitschrift*, N. F. 1, 276–284.
- Jacobeit, J. (1993): Regionale Unterschiede im atmosphärischen Zirkulationsgeschehen bei globalen Klimaveränderungen (Regional differences of the atmospheric circulation under conditions of global climate change). *Die Erde* 124, 63–77.
- Jacobeit, J. (2010): Classifications in Climate Research. *Physics and Chemistry of the Earth* 35, 411–421.
- Jacobeit, J., C. Beck and A. Philipp (1998): Annual to Decadal Variability in Climate in Europe: Objectives and Results of the German Contribution to the European Climate Research Project ADVICE. *Würzburger Geographische Manuskripte* 43, 163 pp.
- Jacobeit, J., P.D. Jones, T. Davies and C. Beck (2001): Circulation changes in Europe since the 1780s. In: Jones, P.D., A.E. Ogilvie, T. Davies and K.R. Briffa (Eds.): *History and Climate: Memories of the Future*. Kluwer Academic/Plenum Publishers, New York et al., pp. 79–100.
- Jacobeit, J., H. Wanner, J. Luterbacher, C. Beck, A. Philipp, and K. Sturm (2003): Atmospheric circulation variability in the North-Atlantic-European area since the mid-seventeenth century. *Climate Dynamics* 20, 341–352.
- Jacobeit, J., A. Philipp and M. Nonnenmacher (2006): Atmospheric circulation dynamics linked with prominent discharge events in Central Europe. *Hydrological Sciences Journal* 51, 946–965.
- Jacobeit, J., A. Philipp, J. Rathmann and A. Walther (2009): European and North Atlantic daily to multidecadal climate variability: General Overview and Final Reports for the German Contribution to the European Climate Research Project EMULATE. *Geographica Augustana* 7, 65 pp.
- Jolliffe, I.T (2002): *Principal Component Analysis*. Springer, New York et al., 487 pp.
- Kalnay, E. et al. (1996): The NCEP/NCAR 40-year reanalysis project. *Bull. Amer. Meteor. Soc.* 77, 437–471.
- Philipp, A., P.M. Della-Marta, J. Jacobeit, D.R. Fereday, P.D. Jones, A. Moberg, and H. Wanner (2007): Long term variability of daily North Atlantic-European pressure patterns since 1850 classified by simulated annealing clustering. *Journal of Climate* 20, 4065–4095.
- Qian, B., J. Corte-Real and H. Xu (2000): Is the North Atlantic Oscillation the most important atmospheric pattern for precipitation in Europe? *Journal of Geophysical Research* 105 (D9), 11901–11910.
- Quadrelli, R., M. Lazzeri, C. Cacciamani and S. Tibaldi (2001): Observed winter Alpine precipitation variability and links with large-scale circulation patterns. *Climate Research* 17, 275–284.
- Richman, M.B. (1986): Rotation of principal components. *Journal of Climatology* 6, 293–335.
- Schnur, R., G. Schmitz, N. Grieger and H. von Storch (1993): Normal modes of the atmosphere as estimated by principal oscillation patterns and derived from quasi-geostrophic theory. *J. Atmos. Sci.* 50, 2386–2400.
- Von Storch, H. and F.W. Zwiers (1999): *Statistical Analysis in Climate Research*. Cambridge University Press, 484 pp.
- Wibig, J. (1999): Precipitation in Europe in Relation to Circulation Patterns at the 500 hPa level. *International Journal of Climatology* 19, 253–269.

8 Solar UV-Radiation

P. Koepke¹, M. Garhammer¹, P. Hoeppe¹, B. Klotz², J. Reuder^{1, 3}, M. Seefeldner¹

Keywords: UV irradiance, UVI, altitude effect, tilted receivers, human skin, solar radiation

Abstract

Solar UV-radiation on a horizontally oriented receiver, erythemally weighted as it is necessary to determine possible effects on humans, has been measured with high temporal resolution at the UFS for many years. Moreover, for a wide range of solar zenith angles and meteorological conditions, the UV-flux has been measured for a complete set of tilted surfaces. This provides information on the UV-exposure of the different parts of the human body, which in general are tilted. The data have been compiled with regard to the climatological changes of UV-radiation, to the variation of solar-UV with weather, and in order to check UV-radiation models. Actual values of solar UV are essential to inform the tourists at Zugspitze. At UFS the UV radiation reaches UVI > 11 (extreme), the highest values in Germany. The longtime variation of the solar UV radiation at the UFS does not show a significant trend.

8.1 Introduction

In the ultraviolet (UV) spectral range of electromagnetic radiation, i. e. wavelengths below 400 nm, the energy of a single photon may be able to break up the chemical bonds of various molecules. Thus, although UV radiation represents only a few percent of the total solar flux reaching the Earth's surface, it has significant impact on living organisms (Caldwell et al., 1998; Nolan and Häder, 1998) and is one of the key factors controlling the atmospheric chemistry (Blume and Güsten, 1976). For humans, the UV-radiation has both, positive effects like improvement of vitamin D status (Wacker and Holick, 2013) and negative effects like sunburn and skin cancer (e. g., Longstreth et al., 1998). Thus, it is important to quantify the amount of solar UV reaching the surface and to analyze how it varies with atmospheric composition, surface albedo and solar zenith angle. Long-term measurements of solar UV are required to get information on its climatological development and its short-term variability.

The reason for the investigation of solar UV in the last decade of the 20th century worldwide was its expected increase due to the observed depletion of the stratospheric ozone layer (e. g., Herman et al., 1996; WMO, 2007). The UFS represents, due to its position and environment, a particular interesting place for solar UV monitoring, with moreover very good measuring conditions. Thus, UV measurements started here at its beginning. In addition to the classical monitoring of the UV irradiance on a horizontal surface, we investigated the effect of the receiver orientation, since the affected human skin mostly is not oriented horizontally. Finally, actual UV-values are necessary for the information of the large number of tourists at Zugspitze, the highest mountain in Germany, which is easily accessible by cable cars.

8.2 UV radiation properties

Solar irradiance at the Earth's surface is composed by the direct solar beam and the diffuse sky radiation. It is given by spectral radiances $L(\lambda, \mu, \varphi)$ ($W \cdot m^{-2} \cdot sr^{-1} \cdot nm^{-1}$), with λ the wavelength, μ the cosine of the zenith angle and φ the azimuth angle. To obtain the total spectral irradiance on a flat receiver, the radiances have to be integrated over the upper half sphere, weighted with the cosine of the zenith angle.

$$E(\lambda) = \iint L(\lambda, \mu, \varphi) \cdot \mu \cdot d\mu \cdot d\varphi \quad (1)$$

¹ Meteorological Institute, L-M-University, Munich, Germany

² Biomedical Physics, Medical University Innsbruck, Austria

³ Geophysical Institute, University of Bergen, and Bjerknes Centre for Climate Research, Bergen, Norway

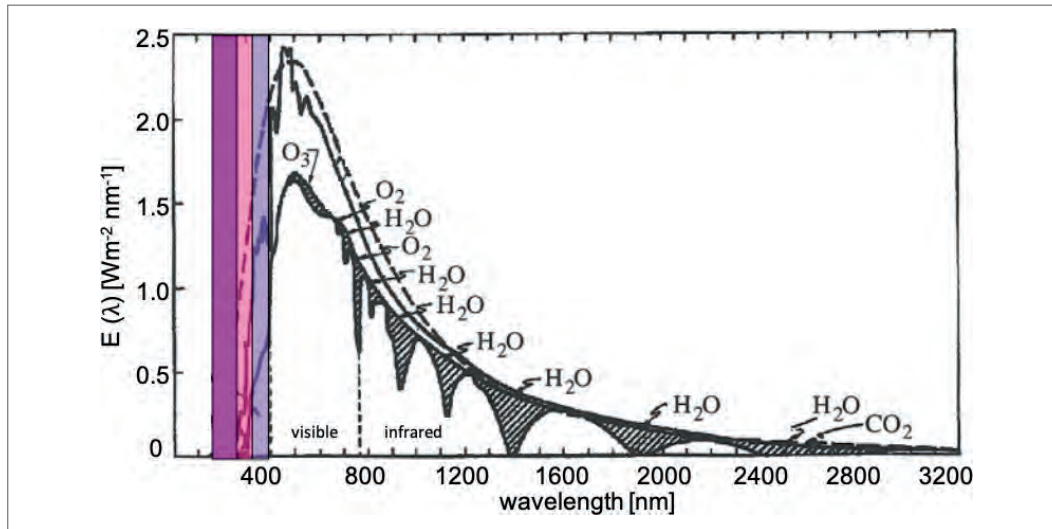


Fig. 1: Shown is the spectral solar irradiance outside the atmosphere (upper curve) and, for comparison, the irradiance of a blackbody with 6000 K (broken line). The lower curve shows the irradiance at sea level for cloud free mean atmospheric conditions and the dashed areas the reduction due to absorption by atmospheric gases.

Additionally given, are the spectral ranges, as explained in the text, of
 ■ UV-A (315–400 nm), ■ UV-B (280–315 nm), ■ and UV-C (< 280 nm)

For a flat and horizontally oriented surface, like the routinely used receivers for measuring solar UV irradiance, and thus generally applied for the UVI (see below), the zenith angle of the measurement is referred to the zenith of the sky. For these conditions only radiances from the upper half sphere contribute to the irradiance, i. e. radiation reflected at the surface has only an effect via backscattering at atmospheric molecules towards the receiver.

For the irradiance on a flat, but not horizontally oriented surface, as it is the case for most parts of the human skin, Eq. 1 is valid, as well. However, in this case the relevant zenith angle of the measurement refers to the local zenith, i. e. the direction perpendicular to the tilted surface. Under such condition, the radiation reflected at the ground also contributes directly to the irradiance.

The UV spectral region (Fig. 1) is divided into UV-A (315 to 400 nm), UV-B (280 to 315 nm) and UV-C (200 to 280 nm). For basic information on UV see e. g., Kiefer, 1976; WHO, 2002; Koepke et al., 2002; Vitt et al., 2020. Solar UV-C does not reach the ground, since it is totally absorbed by ozone and other gases on its way through the atmosphere. Solar UV-B is strongly affected by ozone, aerosol particles, and altitude, but is reaching the ground, at least for high sun. For UV-A the attenuation on its way through the atmosphere is lowest. Clouds reflect the radiation from the sun at all UV-wavelengths, in all spectral regions. UV-B is mainly responsible for sunburn, but also UV-A has biological effects.

The simplified A-B-C classification has historical reasons, but further is used to give information on cosmetic sun protection products applied to the skin. For any photo-biological or photo-chemical process, the absorption properties of the irradiated material have to be taken into account, since only the energy from the absorbed radiation has the potential to trigger a biological or chemical reaction. This has to be done on a spectral basis, with a spectral effectivity that depends on the process in question, resulting in specific weighting functions or action spectra, $s(\lambda)$, which often overlap the UV-A and UV-B regions.

For negative UV-effects on humans, generally the erythema action spectrum, $s_{\text{ery}}(\lambda)$, is used (McKinley and Diffey, 1987; Webb et al., 2011), which originally is derived from the UV effectivity for sunburn, but is also considered valid for the induction of skin cancer. The action spectrum $s_{\text{ery}}(\lambda)$ is normalized to 1 as maximum (see Fig. 2), and is not varied for different human skin types. To take into account the variable sensitivity of the different skin types, the concept of the minimal erythema dose, MED, is used. It specifies the minimum dose of erythemally weighted radiation that produces a faint but perceptible reddening of the skin 24 hours after irradiation. The MED is a personal measure of susceptibility to sunburn, but given for different skin types with standardized values (DIN, 2000).

As mentioned, UV irradiance also has positive effects for humans, by triggering the previtamin-D-production-rate. These effects are described by a previtamin-D action spectrum (Webb and Engelsen, 2006), which is similar to s_{ery} , but for longer wavelengths less sensitive (not discussed in this paper).

Solar irradiance is always a combination of photons of all wavelengths, however with variable spectral composition, depending on solar zenith angle, SZA, and atmospheric properties. Thus, to get the actual total erythemally weighted irradiance, E_{ery} , which is the relevant quantity for a process in the human skin, the incoming spectral radiation $E(\lambda)$ has to be weighted with the corresponding action spectrum $s_{\text{ery}}(\lambda)$ and integrated over all wavelengths.

$$E_{\text{ery}} = \int E(\lambda) \cdot s_{\text{ery}}(\lambda) \cdot d\lambda \quad (2)$$

Fig. 2 shows in logarithmic scale an example of spectral solar irradiance (green) and the action spectrum for erythema (red). Both spectral variations cover a range of 10^4 , however, their behavior is reverse: $s_{\text{ery}}(\lambda)$ has high values in the region around 300 nm, strongly decreasing with increasing wavelength, due to Einstein's radiation law and the spectral absorption properties of the molecules in the skin. In contrast, $E(\lambda)$ is decreasing with decreasing wavelength, as consequence of the solar spectrum and the radiation processes in the atmosphere. Due to these facts, the significant sensitivity combined with the low radiation at short wavelengths and the low sensitivity but high values of radiation at longer wavelengths, the erythemally weighted spectral irradiance (blue) is highest in the range around 310 nm. This is even clearer to be seen in Fig. 3, which shows $E_{\text{ery}}(\lambda)$ in a linear scale. In this figure, the boundary between UV-A and UV-B is given to show that both ranges contribute to the UV-radiation, which is of relevance for the human skin. As mentioned, the spectral composition of the incoming solar irradiance strongly varies with zenith angle and atmospheric conditions, and so consequently does $E(\lambda)$ and thus $E_{\text{ery}}(\lambda)$. For example, with increasing SZA the maximum is shifted to longer wavelengths and is reduced in its absolute value (not shown in a figure).

To inform the public, the quantity "UV-index" (UVI) has been introduced (WMO, 1995), simply by conversion of the erythemally effective solar UV irradiance into a dimensionless number. Of course, the UVI must be zero for dark conditions, with no solar UV-irradiance at all, i. e., thus the lowest value is UVI = 0. For conditions with high UV, it has been decided that the result should be handy numbers, up to 12 under normal conditions (and more in extreme cases). Thus, the conversion factor has been set to 40 ($1/(W \cdot m^{-2})$) if E_{ery} is given in $W \cdot m^{-2}$ (WMO, 1998; CIE,

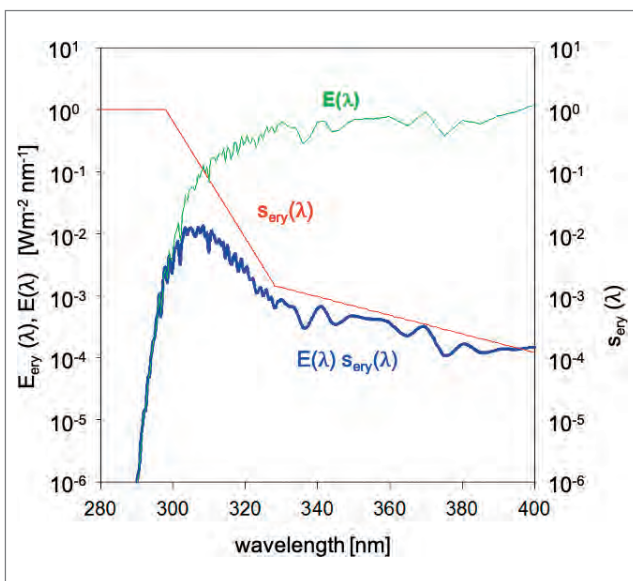


Fig. 2: Shown, in log scale, is the erythema action spectrum, $s_{\text{ery}}(\lambda)$, (red curve) (ISO/CIE, 1999; Webb et al., 2011). Additionally, given is an example for the spectral solar irradiance at the surface, $E(\lambda)$, (green), and the resulting erythema weighted solar irradiance $E_{\text{ery}}(\lambda) = E(\lambda) \cdot s_{\text{ery}}(\lambda)$ (blue).

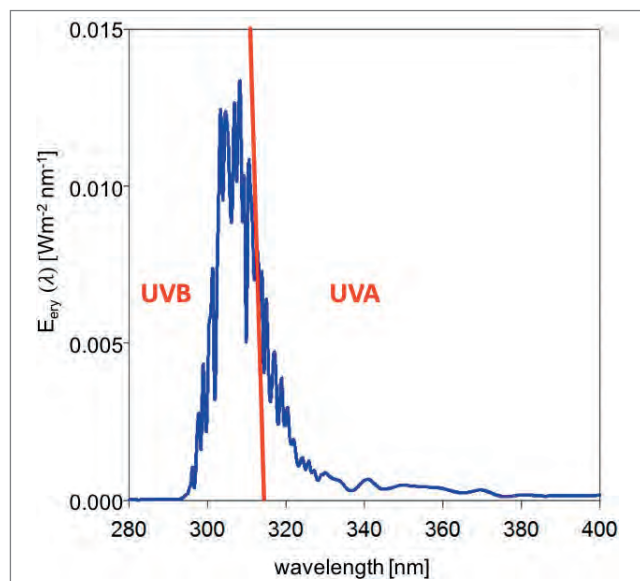


Fig. 3: Spectral erythemally weighted irradiance (values from Fig. 2) in linear scale. The area below the curve gives the spectrally integrated irradiance E_{ery} and shows the contributions of radiation from the spectral ranges UV-B and UV-A.

Tab. 1: To make the UVI-information easily usable, the related international organizations WHO, WMO, and UNEP decided for the shown quantification of the effects of solar UV for humans of skin type I and II, because they are the most sensitive (see Tab.2). (after COST-713, 2000)

UVI Range	UV effects for humans
< 2	LOW
3 to 5	MODERATE
6 to 7	HIGH
8 to 10	VERY HIGH
11 +	EXTREME

Tab. 2: Humans have different sensitivity to UV radiation, depending on the skin type. The properties of the types I to IV are described in the table. Additionally given, is the related MED, the minimal dose of erythemally weighted UV radiation that is resulting in an erythema. (COST, 2000; MED after DIN, 1992)

skin type	tan	sun burn	hair colour	eye color	1 MED
I	never	always	red	blue	200 J/m ²
II	sometimes	sometimes	blond	blue/green	250 J/m ²
III	always	rarely	brown	gray/brown	350 J/m ²
IV	always	rarely	black	brown	450 J/m ²

2003). Since the UVI is, by definition, a dimensionless number, the conversion factor depends on the dimension that is used for E_{ery} :

$$\text{UVI} = 40 \text{ (m}^2/\text{W)} \cdot E_{\text{ery}} \text{ (W/m}^2\text{)} = 400 \text{ (cm}^2/\text{mW)} \cdot E_{\text{ery}} \text{ (mW/cm}^2\text{)} = 1/25 \text{ (m}^2/\text{mW)} \cdot E_{\text{ery}} \text{ (mW/m}^2\text{)}$$

In the first time, the UVI was used only to give the UV-level as mean value for the hour around local noon. Meanwhile the UVI is determined to give a value for the erythemally weighted irradiance, for all conditions, even for that on tilted surfaces. It should be emphasized that the UVI is a physical quantity (irradiance) however weighted by a biological process (erythema).

The solar UV radiation is of interest for humans, because it has both: positive effects, like vitamin-D synthesis and treatment for psoriasis, and negative effects, like sunburn, skin cancer, immune depression, and eye diseases. At the UFS, solar UV also is of interest for atmospheric chemistry and its influence on plants and pollen. Since the human vitamin-D status can be supported by dietary supplements, the interest in negative UV-effects clearly dominates. Thus, education and warning against high UV levels is necessary. Because of the high variability of solar UV, due to meteorological and stratospheric conditions, prompt information of the public, based on measurements or forecast, is desired and required.

Since even the UVI seemed to be too complex to inform the general public, WMO decided for simple rating words (Tab. 1) to describe the UV conditions by its relevance for skin damages and thus for protection (WMO, 1998). These warnings for UV danger are already strong at relatively low UVIs, much lower than values, which occur in equatorial regions, because they are primarily essential for white people (skin type I and II). For these skin types the Minimal Erythema Doses (MEDs) are rather low (Tab. 2), and thus the danger of sunburn is high, while other skin types may tolerate more UV irradiance.

As mentioned, the effects of UV radiation on humans depend, besides repair mechanisms in the cell, on the dose of the erythemally weighted UV that has been absorbed by the skin. This dose, H_{ery} , is the product of irradiance and time:

$$H_{\text{ery}} \text{ (J/m}^2\text{)} = W \cdot s/\text{m}^2 = E_{\text{ery}} \text{ (W/m}^2\text{)} \cdot t \text{ (s)} \quad (3)$$

Thus, the general protection against too much solar UV is, on the one hand, to reduce the irradiance at the skin, e. g., by shadow, clothing, cosmetics and considering times with low sun, and, on the other hand, to reduce the time of exposure.

8.3 Measurements

Measurements of solar UV irradiance always have the problem of the low relative energy density values in the UV spectral range in comparison to high values in the visible, with its peak around 550 nm (Fig. 1). The irradiance for wavelengths below 400 nm is about 5% of the global radiation, i. e., the total solar spectral range. The considered erythemally weighted irradiance is even less than 0.2% of solar radiation. In Fig. 2 the decrease in the order of 10^5 between 400 nm and 290 nm can be seen. Thus, in the measurement process stray radiation from longer wavelengths has to be suppressed. This can be done by double-monochromators, which are precise, but expensive and often need too much time for recording a complete spectrum during a period with unchanged meteorological conditions. Radiometers with filters or array detectors avoid the problem of temporal resolution, have the advantage of spectral resolution, but have to meet challenges concerning spectral width and solarization (i. e., the destruction of components by the high energetic solar radiation). The development of appropriate array systems has made huge progress over the last years, but even now suffer from the stray light at wavelengths shorter than 310 nm (Egli et al., 2016). An array-based UV spectrometer, optimized for outdoor solar measurements with an out-of-band suppression of four orders of magnitude, is installed at UFS since summer 2017, measuring the spectral irradiance used to get the UVI (Bundesamt für Strahlenschutz, 2017).

The simplest and cheapest way to measure UVI are broadband radiometers, directly using an internal weighting that mimics the erythema action spectrum (Fig. 4). They have the advantage to be small, low in weight and thus suitable for measurements under tilted conditions. These radiometers are produced by different manufacturers (Eppley, Kipp & Zonen, Scintec, Solar Light, and YES), are thermostatised and thus can be used at a mountainous position like UFS. Of course, the radiometers must be calibrated to obtain the calibration factor between measured voltage and irradiance. The spectral weightings of these radiometers are similar to the erythema weighting, but individual for each radiometer, always with certain wavelength dependent differences referred to the official erythema weighting curve. Thus, the spectral composition of the actually measured UV-irradiance, which depends on SZA and meteorological conditions, has influence on its conversion into UVI. This is taken into account by using a calibration matrix that has been determined once a year for each radiometer in use, considering SZA and ozone amount (Bodhaine et al., 1998; Oppenrieder et al., 2003), resulting in a measurement uncertainty of less than 5%. Besides, comparison of different radiometers is used to ensure the stability of the instruments (e. g., PMOD, 2017).



Fig. 4: UVI measurement at UFS with calibrated broadband radiometer. (Koepke)

At the UFS the UV-radiometers were always installed at one of the southern balconies, for the most time close to the other radiation measurement devices. Here the northern half of the skyline is dominated by parts of the building and the top of the Zugspitze, up to an elevation of about 45° .

However, with regard to the skiers on the glacier, the measured UV values are suitable, since the skyline at the glacier is similar. However, to compare the measured UVI with data from other places, with an ideal horizon, the horizon-effect should be considered, taking into account cosine-weighted radiances that are reflected at the building and the mountain. For conditions without snow the albedo in the UV is only a few percent, resulting in a certain reduction of the measured UV irradiance referred to that of the free horizon. This reduction is for conditions with higher sun, resulting in an UVI higher than 2, less than 5%. For conditions with snow, with an albedo of 80%, it has been modeled (Hess and Koepke, 2008) that the UVI measured at UFS is higher than for conditions with free horizon. This result from the fact that the radiation reflected at the snow covered slope of the mountain facing south is higher than it would be coming from the sky, which would be dark blue in this altitude. This increase is up to 10% for conditions around noon, but lower for lower Sun. Since during winter the UVI generally is rather low, the absolute increase however is small.

It is a matter of fact that most of the human skin is not oriented horizontally. Thus, it is of interest how the UV-irradiance on surfaces with different

orientation change under different conditions. To enable such measurements, ASCARATIS (**A**nge **SC**Anning **RA**diometer for determination of erythemally weighted irradiance on **T**ilted **S**urfaces) has been developed (Seefeldner et al., 2004). With a combination of a horizontally and a vertically oriented positioning drive, an erythema broadband radiometer could be positioned to any direction in the sky, and towards the earth. To get meaningful measurements always 27 directions have been investigated in one scan: towards the actual direct Sun, to the zenith, vertical down (for albedo) and in circles with azimuth steps of 30° for the zenith angles 45° and 90° . These scans have been performed automatically during the whole day and at all weather conditions (Oppenrieder et al., 2004). Measuring the complete set took about 2 min. To be sure that the conditions (clouds) did not change during this time, continuous measurements were made with a second, horizontally fixed, radiometer (Fig. 5). If those values changed by more than 5% during the scanning period, the conditions have been classified to be not constant and the measurements of the tilted radiometer were ignored.

8.4 Results

The UVIs measured by the horizontally fixed radiometer (Fig. 6 and Fig. 8) show the typical behavior generally known for solar UV (e. g., Ambach and Blumthaler, 1994; Koepke et al., 2002; Douglass et al., 2011).

First, there is the strong increase of the UVI with decreasing solar zenith angle, which for cloud-free conditions leads to maximum values at noon and to the seasonal cycle. Fig. 6 shows daily courses the UVI monthly means for cloud free conditions. These maximum values at noon, i.e. sun in the south, solar azimuth 180° , are in winter less than 1 and up to 10 for the months with low SZA, i.e. May, June, and July (and even higher UVI on single days; Fig. 8).

The attenuation of the direct sun increases exponentially with the optical depth of the atmosphere, multiplied with the relative air mass, a quantity used for the length of the path through the atmosphere. Thus, the decrease of the spectral irradiance due to increasing SZA strongly increases with increasing spectral attenuation coefficients of the atmospheric components.



Fig. 5: Measurement of the UVI on tilted surfaces in the skiing area at Zugspitze-glacier with the system ASCARATIS, described in the text. Shown are the moving radiometer, which needs some time to observe all directions, and the radiometer that is permanently in horizontal position to check for unchanged illumination during the observation time. (Oppenrieder et al., 2004)

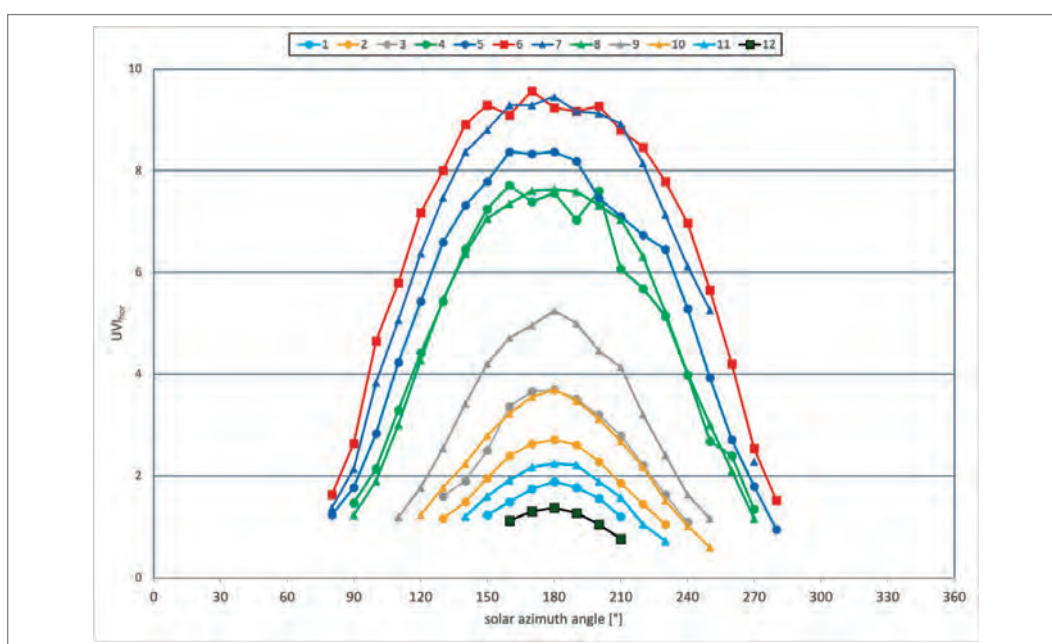


Fig. 6: Daily courses of the UVI on a horizontally oriented receiver, measured at UFS for conditions not disturbed by clouds. Given are monthly mean values. The month is indicated by color and symbol, shown in the top line. (Oppenrieder et al., 2005)

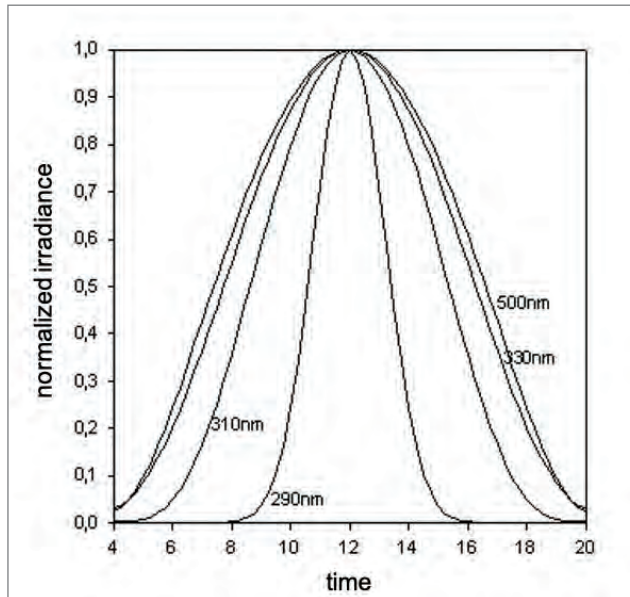


Fig. 7: Modeled values of the daily course of solar irradiance at different wavelengths. To show the effect of increased reduction with decreasing wavelength, due to the increased optical depth of the atmosphere in combination with time dependent SZA, the values are normalized to 1. The irradiance values are an example for a cloud free summer day at sea level, with low turbidity and 330 DU ozone. The (local) time gives the used SZA for 50° north at summer solstice.

The essential components attenuating the solar UV radiation on its way through the atmosphere are (besides clouds) ozone, air molecules, and aerosol particles. Since the attenuation of these three parameters increases with decreasing wavelength (see the difference between solar radiation outside the atmosphere and at sea level in Fig. 1), their effect is especially high for the erythemally weighted radiation (e.g., Koepke et al., 2002), much higher than at longer wavelengths of the solar spectral range.

To show the attenuation effect of both, increased spectral optical depth and decreased SZA, in Fig. 7 daily courses of the solar irradiance are presented for different wavelengths. To accentuate the effects, the values are normalized to 1. The irradiance values are modelled (with STAR; Ruggaber et al., 1994) as an example for a cloud free summer day at sea level with low turbidity and 330 DU ozone. The time, which is given in the figure, stands for the used SZA, valid for 50° north at summer solstice. The time as variable in the figure allows one to see the reduction of the time interval between “sun rise” and “sun set” for decreasing wavelengths, due to the increasing attenuation and the general effect of the SZA variation.

The spectral absorption properties of ozone in the UV range are well known (Molina and Molina, 1986; Burrows et al., 1999). They show a strong increase towards shorter wavelengths, resulting in an especially strong influence regarding UVI. This clear dependency of UV radiation on ozone amount is, on the one hand, used to determine the actual total ozone from UV measurement at the ground (Komhyr and Grass, 1989) and satellite (Herman et al., 1999; Wang et al., 2000) and, on the other hand, to model UVI at the surface, using ozone amount determined by satellite (Vitt et al., 2020). The ozone effect, of course, has influence on the UVI measured at UFS, as to be seen in Fig. 8 by its day-to-day variation, in combination with the also shown daily total ozone values. The total ozone amount in central Europe varies between mini holes with 250 DU and regions with high ozone, 450 DU, which both may pass a fixed location during one or two days.

Also shown in Fig. 8 are the reductions of the UVI by a cloud in front of the Sun, which may be more than 90% for a thick thunder storm cloud, but only a few percent for thin cirrus (e.g., Josefson and Landelius, 2000). For special cases, with free sun and a reflecting cloud nearby, the UVI even can be increased by clouds (Mims and Frederick, 1994). This effect is not shown here, but often occurs in the daily course of the UVI under conditions with scattered clouds. However, during such conditions the clouds usually are moving, resulting always in time intervals with shadow. Therefore, the UV-dose, which is relevant for biological processes, generally is reduced for cloudy conditions.

The optical depth of typical aerosols increases with decreasing wavelength in the UV spectral range. At the UFS the aerosol effect is low, because of the generally clean conditions. For regions with high turbidity, however, both the aerosol amount and the aerosol optical properties

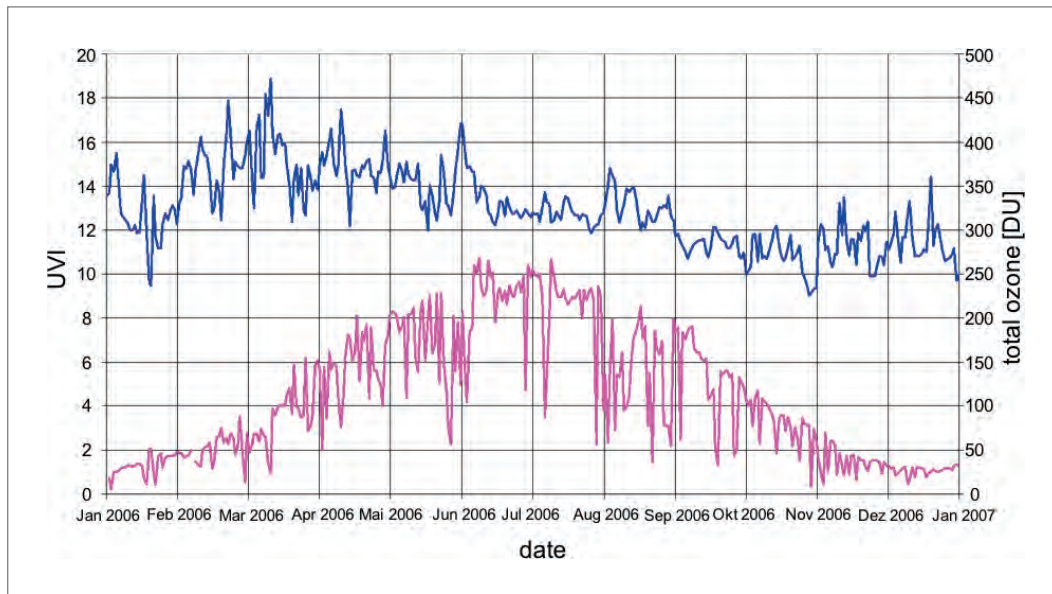


Fig. 8: Daily maximum UVI 10-min-averages measured at UFS in 2006 (violet). To be seen is the effect of solar elevation in the yearly course and the day-by-day variations due to cloudiness. Lower effects result from the variation of ozone (values in DU shown as blue curve with its typical yearly course; Koehler, 2007), aerosol and surface albedo (snow).

(scattering and absorption) must be considered, since they have different effects on the irradiance (Hess et al., 1998; Kylling et al., 1998).

The air molecules induce a radiation attenuation that is increasing with decreasing wavelength with a power of about 4, and therefore is strong in the UV, especially for erythemally weighted UV radiation. This effect, of course, depends on the amount of air molecules above the measuring site and thus on altitude. The variation of the attenuation with changing air pressure in a fixed height, however, is very low and thus is nearly negligible for the measured UVI at the UFS.

Contrariwise, the increase of UVI with altitude is remarkable (Blumthaler et al., 1997) and of interest for any stay of people at higher mountains. This increase is called altitude effect, AE, which gives the increase of UVI with increasing altitude for cloud free conditions in %/km (Schmucki and Philipona, 2002). In practice, the AE results not only from the reduced amount of air molecules, but also from the reduced ozone and aerosol amount above the measuring site, and often, from the increased albedo. Values of AE are one result of our UVI measurements at UFS (and other places). For cloud free conditions the UVI increases about 10% per 1 km increase in altitude (Pfeifer et al., 2006). Thus, the UVI at UFS (2700 m) in average is about 20% higher than in the flat region in front of the Alps (700 m). In the case of clouds between two nearby sites with different altitude, the difference between the UVIs, of course, is much bigger, resulting from the opposite effects of bright reflection above and strong reduction below the cloud deck.

The results of the UVI on inclined surfaces looking into different directions (Fig. 9) are of interest for human health, i. e. sunburn (Hoeppe et al., 2004). Moreover, the results have been used to check a model (Koepke and Mech, 2005), which allows one to make sensitivity studies, e. g. on the effects of sun protection by plants, umbrella or walls.

The ratio between the UVI on a tilted surface and that on the horizontal receiver (for the same atmospheric conditions) is given as tilt modification factor, TMF (Koepke and Mech, 2005). For fixed radiation from the hemisphere, the UVI on a tilted surface depends primarily on the relative contribution of the direct sun, including its weighting with cosine of the actual zenith angle, i. e. against the direction perpendicular to the receiver. Moreover, the tilted receivers are illuminated by radiation that has been directly reflected at the ground, i. e. the TMF depends on the albedo of the surrounding surface. For nearly all surface types, except of snow, the albedo in the UV is low, in the order of a few percent. Thus, under cloud free conditions, the TMF-values are lower than 1 in the shadow regions and higher than 1 only in directions towards the sun.

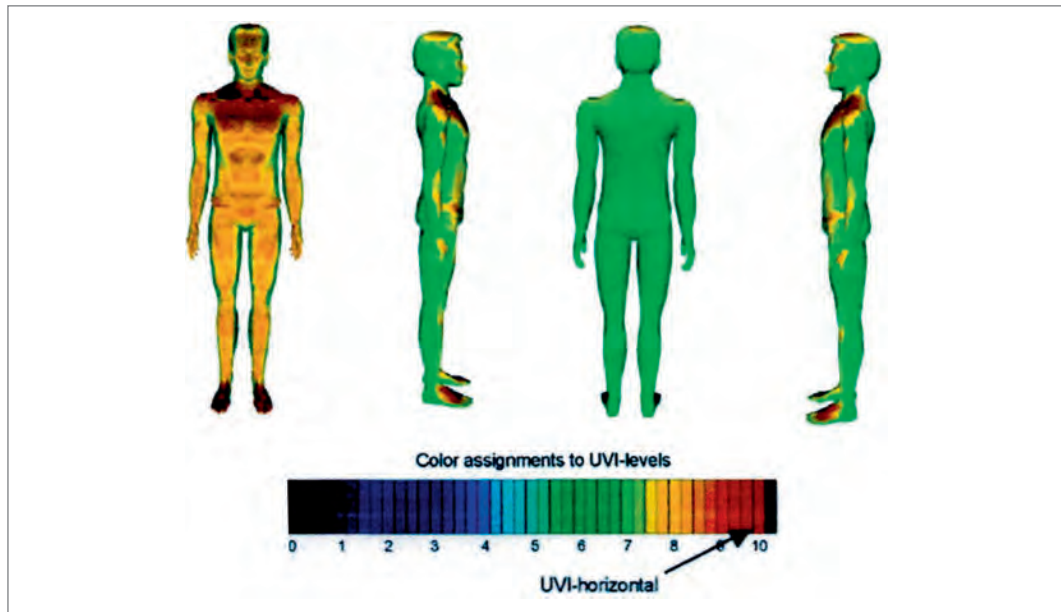


Fig. 9: UVI distribution on the body of a standing man facing to the south, based on UVI measured at UFS at noon 12th June 2001 (SZA 24,3°). (Hoeppel et al., 2004)

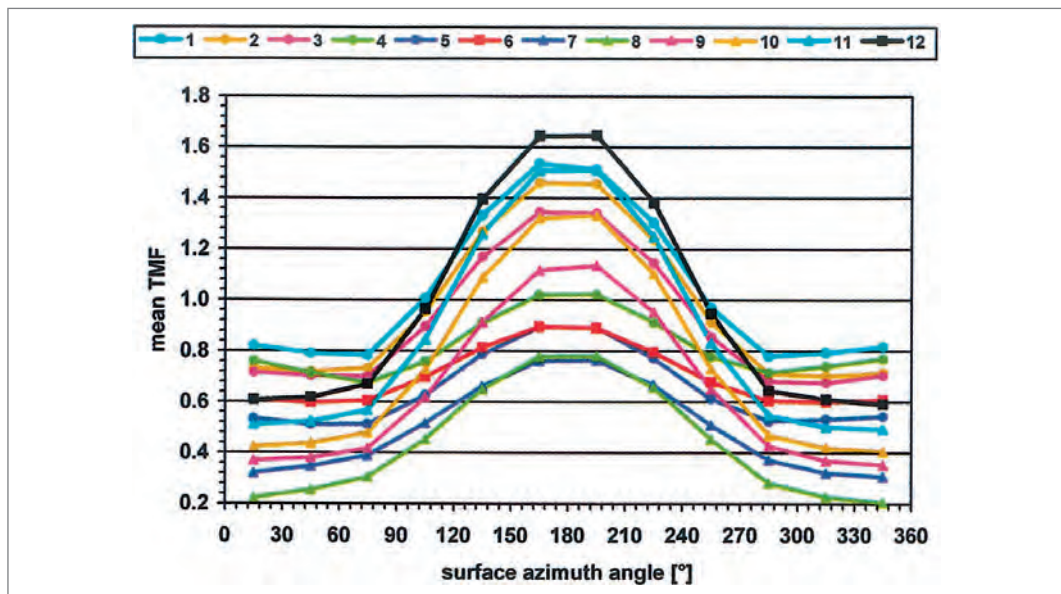


Fig. 10: Examples of tilt modification factors, TMF, (see text). The shown values are derived from monthly means of UVI, measured at UFS for conditions not disturbed by clouds, with solar azimuth 180°. The receiver has a tilt angle of 90°, the azimuth is varied in steps of 30°, The month is given by symbol and color in the top line. (after Koepke and Mech, 2005)

Fig. 10 shows, as an example, measured TMFs for a vertically oriented receiver, depending on azimuth, with monthly mean values of cloud free conditions for noon, i. e., solar azimuth 180° (Oppenrieder et al., 2005). As the TMF increases with the relative contribution of the direct sun in comparison to the total irradiance on the irradiated surface, it always is maximal for the highest sun, for sun in the south, in Fig. 10 given as azimuth of the sun 180°. With reduced sun height, increasing SZA, from summer to winter, the UVI on the horizontally oriented receiver decreases, however, the UVI on the vertical surface oriented towards the sun increases due to the reduced receiver oriented zenith angle. Generally, half of the radiances on the vertical surface are radiation reflected at the ground. This result in a reduction of the UVI on vertical surfaces for low values of ground albedo, but this reduction is less important for snow, with albedo values up to 99% (Grenfell et al., 1994). This explains the increase of the maximum TMF from summer to winter for the conditions shown in Fig. 10.

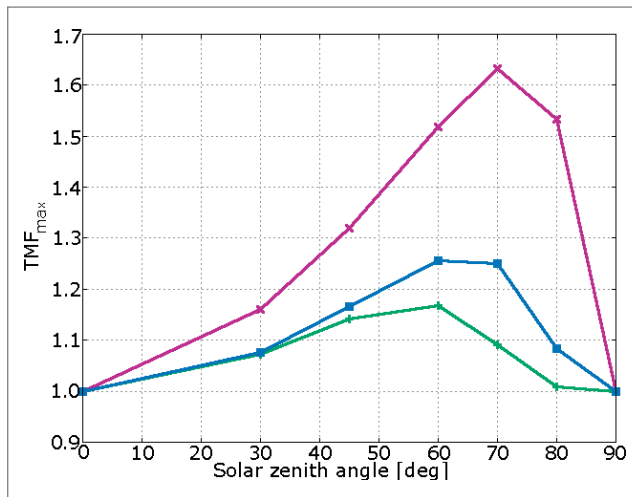


Fig. 11: Values of maximum TMFs, i. e., the receiver is always looking towards the sun, modelled for different atmosphere and surface conditions (without clouds):

Green: turbid atmosphere, pastureland, sea level

Blue: clear atmosphere, sandy beach, sea level

Violet: fresh snow, clear atmosphere, mountain (3000 m altitude)

(Köpke and Mech, 2006)

It should be mentioned that for the irradiance on a tilted receiver, i. e. also for the TMF, only the albedo of the nearby ground surface is responsible. This is different to the effect of the albedo on the irradiance on a horizontally oriented receiver, where photons reflected at the surface only can contribute via back-scattering and thus an area of more than 10 km width is of relevance (Deguenther et al., 1998). Moreover, for such a large area, the albedo may change with place and with time, even if the surface properties are described as “snow”, due to local differences in melting and getting dirty (Schwander et al., 1999).

Fig. 11 shows the variation of the maximum TMF, i. e. always the value for the receiver looking directly towards the Sun, for different conditions as function of the SZA and for different atmospheric and surface conditions. Here the strongest increase is resulting for the conditions on a high mountain, with the combination of clear atmosphere (dark sky and bright Sun) and fresh snow.

For overcast conditions, the dependency of the TMF on the orientation of the tilted surface is nearly negligible (Oppenrieder et al., 2004) and thus the irradiance on a tilted surface may be similar for all directions. Therefore, the vertically oriented face of a skier at the Zugspitze glacier can get sunburn even on a day with the sun permanently hidden behind thin clouds, at conditions with fresh snow in spring.

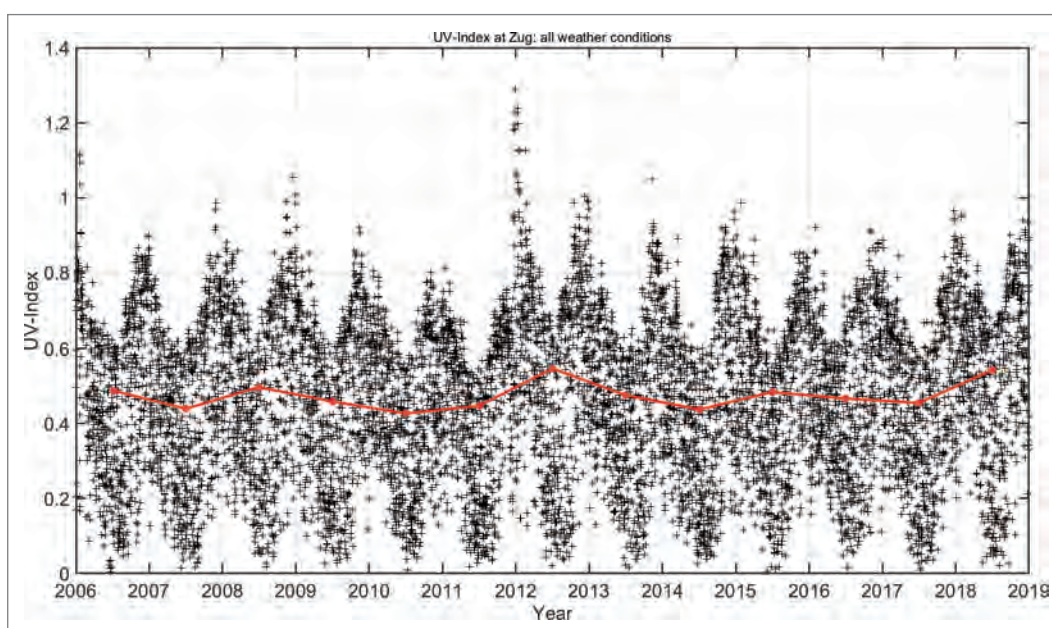


Fig. 12: Time series 2006–2018 of UVI, measured at UFS at all weather conditions. Shown are day-by-day values, but only for one solar zenith angle, SZA = 73°, not to analyze the variations of UVI due to changing solar elevation in the seasonal cycle. Annual means are shown in red.

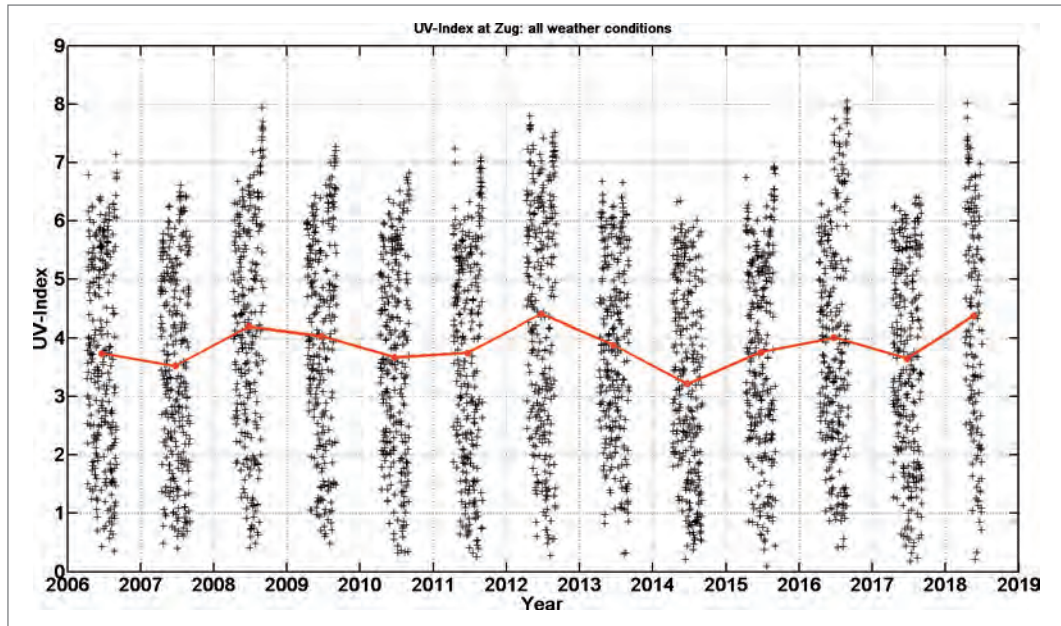


Fig. 13: Time series 2006–2018 of UVI measured at UFS at all weather conditions. Shown are only the values for $\text{SZA} = 40^\circ$. If the maximum solar elevation at UFS does not reach 50° , winter season, no data exist, resulting in gaps in the graph. Annual means are shown in red.

What about the long-term development of the UV-radiation at the UFS? Not to analyze the variation of UVI in the seasonal cycle due to changing of solar elevation, in Fig. 12 UVI values are shown only for one solar zenith angle, $\text{SZA} = 73^\circ$. The UVI were measured at all weather conditions, day by day from 2006 to 2018. Fig. 13 also shows the daily measured UVI, but for $\text{SZA} = 40^\circ$. Thus, no data are available for the winter months, resulting in gaps in the figure. In both figures, the annual means are shown in red.

The strong variations in both figures result from variable clouds that attenuate the sun, with more thick clouds in summer. The contribution of the direct sun to the UVI at UFS is high, since the radiation from the sky is rather low due to the usually clean atmosphere at the high altitude, with only small amount of scattered photons, and the reduced horizon at the UFS. In Fig. 12, the higher values during winter can mainly be explained by snow-albedo, and snow on the mountain area, which is seen by the radiometer. Another effect is the earth-sun distance, which in winter is up to 7% higher than in summer, and the ozone variability (see Fig. 8). It is to point out that for every day two values (AM and PM) are presented in the figures. Thus, since outliers are not suppressed, only three days with no clouds, low ozone and low aerosol amount already result in 6 especially high UVIs.

The annual means (red lines) show no trend for the all-sky UVI at the UFS during the last decade. This is in agreement with other data (Douglass et al., 2011). However, in cases of a strong change in the aerosol burden also the UVI may change significantly (Blumthaler et al, 2017). For northern mid-latitudes a small increase in UV radiation has been observed since the mid-1990s (Vitt et al., 2020), but they were mainly affected by changes in aerosols and cloud cover, while changes in ozone had a smaller impact (Fountoulakis et al., 2020).

With respect to solar UV radiation for human health, we want remind to the rule that humans with sensitive skin should avoid sun during situations with high sun, low SZA , i.e. time around noon in equatorial regions and during summer months in mid latitudes (Europe). We also reminded to the fact that the season with high UVI, which is resulting from high sun, is earlier in the year than the meteorological summer, due to the phase-shifted increase of temperatures. This has consequences with respect to the danger of sunburn, because humans may not realize that the solar UV is already high although the temperature is still low.

Due to the spectral properties of the atmospheric components, the SZA dependence of the attenuation in the UV is much stronger than for the total solar spectral range. In Germany, for cloud-free conditions, the variation for noon maximum and minimum is in the order of 3 for

visible solar radiation, but in the order of 10 for erythemally weighted UV. Thus, during winter the solar UVI often is much lower than considered by the visible impression, with consequences regarding vitamin-D synthesis. So, enjoy the solar radiation during winter, but be careful in summer, in equatorial regions and at skiing in high mountains.

For the future additional aspects have to be considered. Which weather conditions do people prefer to go skiing or to stay at the mountains? Do they prefer cloud free conditions or is their behavior independent of cloudiness? Do people change the length of their stay outside, with the air temperature, with information on the actual UVI, or not at all? What is their behavior with clothes, i. e. uncovered skin, during summer days? For these questions, it is clear that no trend can be found from UVI measurements. Here human behavior must be analyzed. However, for the information of the tourists at Zugspitze, an actually measured UVI is essential.

8.5 Conclusion

The UVI-measurements at UFS support the general knowledge on UVI, regarding solar position, atmospheric parameters and albedo. The UVI on tilted surfaces, which is essential for human health, has been determined for solar elevation angles up to 70° for different atmospheric and surface conditions. It shows a strong variability, depending on orientation towards the Sun, and thus consequences for Sun protection. Clearly found was the increase of UVI with altitude, with about 10 % per km. Thus, for Germany the UVI is highest at Zugspitze. In combination with the high albedo of snow, here the danger of sunburn is especially great for skiers, but holds for all people who stay outdoors (hiker, lumberjacks). Thus, UVI measurements at UFS are of interest for the direct information of the tourists at Zugspitze.

Independent of the development of the UVI in the future, the effects of solar UV on humans result from their exposure to solar UV. For the UFS, and the tourist area Zugspitze, even the summer temperatures during the next decades probably will not be so high that the visitors are looking for shadow. Thus, here also in the future the chance to get sunburn will be high, even if the ozone layer further recovers to their values before the ozone destruction.

Acknowledgements

We say thank you for funding the UVI research at UFS to:
Bavarian State Ministry of the Environment, Public Health and Consumer Protection,
Bavarian Research Network on Climate change (BayFORKLIM),
Bavarian Research Network on Elevated UV Radiation (BayFORUV), and
Umwelt Bundesamt (UBA).

References

- Ambach, W., M. Blumthaler (1994) Characteristics of solar UV irradiance, *Meteorolog. Zeitschrift*, N. F.3, 211–220.
- Bundesamt für Strahlenschutz (2017) Lückenschluss für UV-Messnetz in über 2600 Metern Höhe; available at: <http://www.bfs.de/SharedDocs/Pressemitteilungen/BfS/DE/2017/008.html>.
- Blume, H., H. Güsten (1976) Chemische Wirkung ultravioletter Strahlen. In: *Ultraviolette Strahlen*, J. Kiefer (Edt.) Walter de Gruyter, Berlin, 349–436.
- Blumthaler, M., W. Ambach, R. Ellinger (1997) Increase in solar UV radiation with altitude. *J. Photochem. Photobiol.* 39(2), 130–134.
- Blumthaler, M., B. Klotz, M. Schwarzmann, J. Schreder (2017) Austrian UV monitoring network. In: *AIP Conf. Proc.1810, Radiation Processes in the Atmosphere and Ocean (IRS2016)*, doi:10.1063/1.4975563, 110001-1–110001-4.
- Bodhaine, B.A., E.g. Dutton, R.L. McKenzie, P.V. Jonston (1998) Calibrating broadband UV instruments: ozone and solar zenith angle dependence. *J. Atmos. Oceanic. Technol.*, 15, 916–925.
- Burrows, J.P., A. Richter, A. Dehn, B. Deters, S. Himmelmann, S. Voigt, J. Orphal (1999) Atmospheric remote-sensing reference data from GOME-2. Temperature-dependent absorption cross sections of O₃ in the 231–794 nm range. *J. Quant. Spectrosc. Radiat. Transfer*, 61(4) 509–517.

- Caldwell, M. M., L. O. Björn, J. F. Bornman, S. D. Flint, G. Kulandaivelu, A. H. Teramura, M. Tevini (1998) Effects of increased solar ultraviolet radiation on terrestrial ecosystems. *J. Photochem. Photobiol. B*, 46, 40–52.
- CIE (2003) International Standard Global UV Index, CIE Standard S 013:2003, CIE Central Bureau, Vienna, Austria.
- COST (2000) UV-Index for the Public, Working Group 4 of the COST-713 Action "UVB Forecasting", Brussels, Belgium, ISBN 92-828-8142-3, 27 pp.
- Deguenther, M., R. Meerkötter, A. Albold, G. Seckmeyer (1998) Case study on the influence of inhomogeneous surface albedo on UV-irradiance. *Geophys. Res. Letters*, 25, 3587–3590.
- Douglass, A., V. Fioletov, S. Godin-Beekmann, R. Müller, R. S. Stolarski, A. Webb (Lead authors) (2011) Chapter 2: Stratospheric ozone and surface ultraviolet radiation in: Scientific Assessment of ozone depletion: 2010, Global ozone Research and Monitoring Project – Report No 52 516 pp.
- DIN (1992) DIN 5050, Solarien und Heimsonnen. Deutsches Inst. f. Normung, Beuth-Verlag, Berlin.
- DIN (2000) DIN 5031-10, Strahlungsphysik im optischen Bereich und Lichttechnik. Deutsches Inst. f. Normung, Beuth-Verlag, Berlin.
- Egli, L., J. Gröbner, G. Hülsen, L. Bachmann, M. Blumthaler, J. Dubard, M. Khazova, R. Kift, K. Hoogendijk, A. Serrno, A. Smedley, J.-M. Vilaplana (2016) Quality assessment of solar UV irradiance measured with array spectroradiometers. *Atmos. Meas. Tech.*, 9, 1553–1567.
- Fountoulakis, I., H. Diemoz, A.-M. Siani, G. Laschewski, G. Filippa, A. Arola, A. F. Bais, H. de Backer, K. Lakka, A. R. Webb et al. (2020) Solar UV irradiance in a changing climate: trends in Europe and the significance of spectral monitoring in Italy. *Environments*, 7, 1.
- Grenfell, T. C., S. G. Warren, P. C. Mullen (1994) Reflection of solar radiation by the Antarctic snow surface at ultraviolet, visible, and near-infrared wavelengths. *J. Geophys. Res.*, 99 (D1) 18669–18684.
- Herman, J. R., P. K. Bhartia, J. Ziemke, Z. Ahmad, D. Larko (1996) UV-B increases (1979–1992) from decreases in total ozone. *Geophys. Res. Letters*, 23, 2117–2120.
- Herman, J. R., N. Krotkov, E. Celarier, D. Larko, G. Labow (1999) Distribution of UV radiation at the Earth surface from TOMS measured UV-backscattered radiances. *J. Geophys. Res.*, 104, 12059–12076.
- Hess, M., P. Koepke, I. Schult (1998) Optical properties of aerosols and clouds: The software package OPAC. *Bul. American Met. Soc.*, 79 (5) 831–844.
- Hoeppe, P., A. Oppenrieder, C. Erianto, P. Koepke, J. Reuder, M. Seefeldner, D. Nowak (2004) Visualization of UV exposure of the human body based on data from a scanning UV-measuring system. *Int. J. Biometeorol.* 49, 18–25.
- ISO/CIE (1999) Joint ISO/CIE Standard: Erythema Reference action Spectrum and Standard Erythema Dose, ISO 17166 Geneva, CIE S 007/E Vienna.
- Josefson, W. and T. Landelius (2000) Effect of clouds on UV irradiance: As estimated from cloud amount, cloud type, precipitation, global radiation, and sunshine duration. *J. Geophys. Res.* 105 (D4), 4927–4935.
- Kiefer, J. (1976) Ultraviolette Strahlen, Walter de Gruyter, Berlin, 661 pp.
- Koehler, U. (2007) Ozone values measured at Met. Obs. Hohenpeißenberg, private communication
- Koepke, P., J. Reuder, H. Schwander (2002) Solar UV radiation and its variability due to the atmospheric components. ISBN: 81-7895-053-7, Recent Res. Devel. Photochem. Photobiol, 6, 11–34.
- Koepke, P., M. Mech (2005) UV radiation on arbitrarily oriented surfaces: Variation with atmospheric and ground properties, *Theor. Appl. Climatol.*, 81, 25–32.
- Köpke, P. and M. Mech (2006) Orientierungsabhängige UV-Bestrahlung des menschlichen Körpers. *Ozonbulletin des Deutschen Wetterdienstes*, 111.
- Komhyr, W. D. and R. D. Grass (1989) Dobson spectrophotometer 83: A standard for total ozone measurements 1962–1987. *J. Geophys. Res.* 94(D7), 9847–9861.
- Kylling, A., A. F. Bais, M. Blumthaler, J. Schreder, C. S. Zerefos, E. Kosmidis (1998) Effect of aerosols on solar UV irradiances during the Photochemical Activity and Solar Ultraviolet Radiation Campaign. *J. Geophys. Res.*, 103(D20), 26051–26060.
- Longstreth, J., F. R. d. Gruijl, M. L. Kripke, S. Abseck, F. Arnold, H. J. Slaper, G. Velders, Y. Takizawa, J. C. v. d. Leun (1998) Health risks. *J. Photochem. Photobiol. B: Biology*, 46, 20–39.
- Mc Kinlay, A. F., B. L. Diffey (1987) A reference action spectrum for ultraviolet induced erythema in human skin. *CIE J.*, 6, 17–22.
- Mims, F. M. and J. E. Frederick (1994) Cumulus clouds and UV-B. *Nature*, 371, 291.
- Molina, L. T., and M. J. Molina (1986) Absolute absorption cross sections of ozone in the 185–350 nm wavelength range. *J. Geophys. Res.*, 91 (D13), 14501–14508.
- Nolan, C. V., D.-P. Häder (1998) Role of solar UV-B radiation on ecosystems. *Europ. Comm., Ecosys. Res. Report No.30*, 174 pp.
- Oppenrieder, A., P. Hoeppe, P. Koepke, J. Reuder, J. Schween, J. Schreder (2003) Simplified calibration for broadband solar ultraviolet radiation measurements. *Photochem. Photobiol.*, 78(6), 603–606.
- Oppenrieder, A., P. Hoeppe, P. Koepke (2004) Routine measurement of erythemally effective UV irradiance on inclined surfaces, *J. Photochem. Photobiol., B: Biology*, 74, 85–94.

- Oppenrieder, A., P. Höpfe, P. Köpke, J. Reuder (2005) Long-term measurements of the UV irradiance of inclined surfaces and visualization of UV exposure of the human body. *Meteorolog. Zeitschrift*, 14 (2), 285–290.
- Pfeifer, M., P. Koepke, J. Reuder (2006) Effects of altitude and aerosol on UV radiation, *J. Geophys. Res.*, 111, DO1203, doi: 10.1029/2005JD006444, 11pp.
- PMOD (2017) International UV Filter radiometer comparison, *Phys. Meteorol. Obs. Davos, Davos, Switzerland*.
- Ruggaber, A., R. Dlugi, and T. Nakajima (1994) Modelling of radiation quantities and photolysis frequencies in the troposphere. *J. Atmos. Chem.* 18, 171–210.
- Schmucki, D.A. and R. Philipona (2002) UV radiation in the Alps: The altitude effect, *Opt. Eng.* 4 (12), 3090–3095.
- Schwander, H., B. Mayer, A. Ruggaber, A. Abold, G. Seckmeyer, P. Koepke (1999) Method to determine snow albedo values in the ultraviolet for radiative transfer modelling, *Appl. Opt.*, 38(18) 3869–3875.
- Seefeldner, M., A. Oppenrieder, D. Rabus, J. Reuder, M. Schreier, P. Hoeppe, P. Koepke (2004) A two-axis tracking system with data logger, *J. Atmos. Ocean. Tech.*, 21(6), 975–979.
- Vitt, R., G. Laschewski, A.F. Bais, H. Diemoz, I. Fountoulakis, A.-M. Siani, A. Matzarakis (2020) UV-Index climatology for Europe based on satellite data. *Atmosphere*, 11,727; doi:10.3390/atmos11070727.
- Wacker, M. and M.F. Holick (2013) Sunlight and vitamin D: A global perspective for health, *Dermato-Endocrinology*, 5(1), 51–108.
- Wang, P., Z. Li, J. Cihlar, D.I. Wardle, J. Kerr (2000) Validation of an UV inversion algorithm using satellite and surface measurements. *J. Geophys. Res.*, 105, 5037–5048.
- Webb, A.R. and Engelsen, O. (2006) Calculated ultraviolet exposure levels for a healthy vitamin D status. *Photochem. Photobiol.*, 82, 1697–1703.
- Webb, A.R., H. Slaper, P. Koepke, A. W. Schmalwieser (2011) Know your standard: Clarifying the CIE Erythema action spectrum. *Photochem. Photobiol.*, 87, 483–486.
- WHO (2002) Global solar UV index: a practical guide. A joint recommendation of the World Health Organization, World Meteorological Organization, United Nation Environmental Program, and International Commission on Non- Ionizing Radiation Protection. World Health Organization, Geneva, Switzerland.
- WMO (1995) Report of the WMO Meeting of Experts on UV-B Measurements, Data Quality and Standardization of UV Indices. WMO/GAW Report No. 95, Geneva, Switzerland.
- WMO (1998) Report of the WMO-WHO Meeting of Experts on Standardization of UV Indices and their Dissemination to the Public, WMO/GAW Report No. 127, Geneva, Switzerland.
- WMO (2007) Scientific assessment of ozone depletion: 2006. World Meteorolog. Org., Global ozone research and monitoring project – Rep No.50, 572 pp. Geneva; Switzerland.

9 Plant Life on Germany's highest Mountain – Vegetation and Vegetation Dynamics on the Zugspitzplatt

Oliver Korch & Arne Friedmann
Arbeitsgruppe Biogeographie, Institut für Geographie, Universität Augsburg,
Alter Postweg 118, D-86135 Augsburg

Abstract

Since 2009 the Working Group on Biogeography at the University of Augsburg is investigating the flora and vegetation on the Zugspitzplatt. This research is done within the two collaborative projects Klimagrad and Klimagrad 2. The Zugspitzplatt is Germany's highest investigation site with the longest altitudinal gradient providing excellent conditions for research. The first goal was to record all current plant species and plant communities. Based on this a long-term monitoring program on permanent sample plots has been established to record and identify long-range changes in flora and vegetation composition. This dynamic process is driven by a series of factors such as site characteristics and the geomorphologic processes influencing it. Along with the specific site climate, pedogenetic processes and soil conditions show considerable variation in the investigation area. Furthermore the vegetation on these sites is alternated by human impact as well as anthropo-zoogenic impact.

In the following book chapter some basic information on the alpine flora and vegetation is given, then research methods of the presented study are explained, and a summary of current results is provided.

9.1 Plant life in the Bavarian Alps

The flora of the European Alps originated from tertiary elements, immigrants from several different areas and new evolutions. Decisive selective events were geographical fragmentation, tectonic uplift and the quaternary glaciations (KÖRNER 2003).

Due to widespread site-heterogeneity the number of recorded species is high. A total of about 4500 species of vascular plants in the entire Alps (AESCHIMANN et al. 2004) justifies the status of a Hotspot in terms of phytodiversity. Among these about 650 species can be found between the alpine and nival vegetation belt thus representing the characteristic alpine flora. It consists of about 15% species from glacial refugia, 35% from mountainous regions of Central- and Southern Europe and a small portion of arcto-tertiary species. The remaining species are late- and postglacial immigrants (i. e. species from the tundra and the cold steppe). Furthermore a high proportion of endemic taxa is distinctive. Species richness diminishes towards the Central Alps and towards higher elevation. This decrease is about 40 species per 100 m (KÖRNER 2003).

The flora and vegetation of the Alps is characterized by an adaptation to altitude and extreme environmental conditions. This implies:

- a high proportion of evergreen species and early bloomers,
- only a few annual species,
- vegetative propagation (stolons, bulbs),
- wind- and self-pollination,
- slow growth and dwarfism,
- well developed root system,
- cushion- and rosette-growth,
- a dominance of hemicryptophytes, cryptophytes and chamaephytes,
- frequent occurrence of vicarious species (e. g. on silicate and calcareous rock),
- adaption of photosynthesis to high light intensity, low temperatures and lower atmospheric CO₂-concentrations.

The vegetation of the Alps can be divided along an altitudinal gradient with decreasing temperature into different belts (e. g. REISIGL & KELLER 1994). Each one having a different manifestation of site conditions (Tab. 1). Above 2500 m the Zugspitze-Range in the Wetterstein Mountains includes the subnival belt whilst the nival belt is currently not found in the Bavarian Alps.

Tab. 1: Generalized vegetation belts in the Bavarian Alps (adapted and modified after RINGLER 2009, WALENTOWSKI et al. 2006).

Vegetation belt	Elevation (m a.s.l.)	natural vegetation	Position	Growing Season (days)
submontane	500–800	beech forest with firs and deciduous trees	valleys and hillsides	130–160
montane	800–1500	mountain forest with beeches, firs, spruces	lower mountainous region	90–130
high montane	1500–1700	sparse spruce forest; in parts larch- or stone pine forest.	middle mountainous region	70–90
subalpine	1700–2000	krummholz dominated by dwarf mountain pine or green alder	high mountainous region	60–70
alpine	2000–2500	alpine meadows	upper mountainous region	30–60
subnival	2500–3000	single plants, mosses, lichens, algae	high altitude sites	< 30
nival	> 3000	isolated plants on favored sites	zone of snow and ice*	–

(*this zone currently does not exist in Bavaria).

During the past, the Bavarian Alps were almost completely covered with forests up to the tree line. Only flood plains, bogs, rocky terrain, avalanche tracks and the areas beyond the tree limit were naturally treeless. The original natural vegetation has been substantially altered and modified by human impact (alpine dairy and forestry) since thousands of years thus leading to anthropogenic substitutional communities (current actual vegetation, managed forests).

Parts of the Wetterstein Mountains belong to the nature reserve “Schachen und Reintal” (39,65 km²), the protected area “Wettersteingebiet einschließlich Latschengürtel bei Mittenwald” (85,89 km²), the FFH site “Wettersteingebirge” (42,57 km²) and the forest reserves “Schrofen” (87,1 ha), “Oberreintal” (7,1 ha) as well as “Wettersteinwald” (42,6 ha).

9.2 Methods

In order to identify and classify the plant communities of the Zugspitzplatt the well-established and table-based phytosociological approach of BRAUN-BLANQUET (1964) was used (DIERSCHKE 1994). According to this method, the sample plots on which the relevés were recorded should be chosen following subjective criteria, this guaranteeing homogenous vegetation and abiotic conditions on each site. The vegetation data were recorded from sample plots of varying size in order to record all species growing on each specific community. To determine the species magnitude the scale of REICHEL and WILMANN (1973) was applied combining abundance and dominance. In addition data to elevation, exposition, inclination, height and coverage of shrub-, herb- and moss-layer were recorded as well as the size and location of each sample plot. For further ecological analyses, Ellenberg indicator values (ELLENBERG et al. 2001) were added for all recorded taxa. The denominations of individual plant communities follow RENNWALD (2000). Information about the ecology of associations as well as characteristic species combinations is based on OBERDORFER (1992a, 1992b, 1993a, 1993b, 1998), GRABHERR and MUCINA (1993), MUCINA et al. (1993a, 1993b) and POTT (1995). The nomenclature of vascular plants follows WISSKIRCHEN and HAEUPLER (1998). The reconstruction of possible past shifts of the krummholz-line was realized by radiocarbon dating and the evaluation of historical sources e. g. historical maps (KORCH et al. 2013). 38 permanent sample plots (DIERSCHKE 1994; FISCHER and KLOTZ 1999) were estab-

lished along the altitudinal gradient of the study area to allow a long-term monitoring of vegetation dynamics (Fig. 1). Here, special focus was given to the two ecotones between the sub-alpine and the alpine as well as the alpine and subnival vegetation belt. GPS-data of all plots were recorded and borders were marked with aerosol paint on boulders. All sample plots have been recorded at least twice, some seven times between 2010 and 2017. The statistical analyses were performed using the proprietary software EXCEL[®] and the free statistical software PAST 3.0 (HAMMER et al. 2001; HAMMER 2013).

Soil analyses and mapping based upon 80 soil plots were carried out by GRASHEY-JANSEN et al. (2014) and ensure a further understanding of the heterogeneous site conditions and their interactions with the vegetation.

Boundary layer climate data (temperature and relative humidity) were collected on selected sites using Onset's HOBO Pro v2 data loggers and radiation shields. The equipment was placed directly on the ground in order to obtain realistic values for the dominating herbal layer.

9.3 Study area

Being a part of the Wetterstein Mountains in southern Bavaria the study area covers almost the entire Zugspitzplatt between 2000 m a.s.l. and 2700 m a.s.l. excluding only the steep faces of the so called Plattumrahmung (Fig. 1) which culminates in peaks like the inner Höllentalspitze (2741 m a.s.l.), the Zugspitze (2962 m a.s.l.), the Zugspitzeck (2818 m a.s.l.), the Schneefernerkopf (2875 m a.s.l.), the Wetterspitzen (2746 m a.s.l.), the Wetterwandeck (2698 m a.s.l.), the Plattspitzen (2680 m a.s.l.) and the Gatterlköpfe (2474 m a.s.l.). The whole area consists of the ladinian Wettersteinkalk, a Triassic limestone containing an average of 95,6% CaCO₃ and 2,4% MgCO₃ (HÜTTL 1999) and being about 800 m thick (MILLER, 1962, KÖRNER and ULRICH 1965). As a consequence many karst features can be found within the area and the nearly complete absence of surface runoff can even lead to edaphic aridity. Mainly on the foot of the Plattumrahmung there are vast areas covered with debris. On the upper part of the Zugspitzplatt there are two small retreating glaciers, the Nördlicher Schneeferner with 27.8 ha and the Südlicher Schneeferner with 4.8 ha (HAGG et al. 2012). Based upon data (1983–2012) from the DEUTSCHER WETTERDIENST (2013) for the nearby stations Zugspitze (2964 m a.s.l.) and Garmisch-Partenkirchen (719 m a.s.l.) the annual

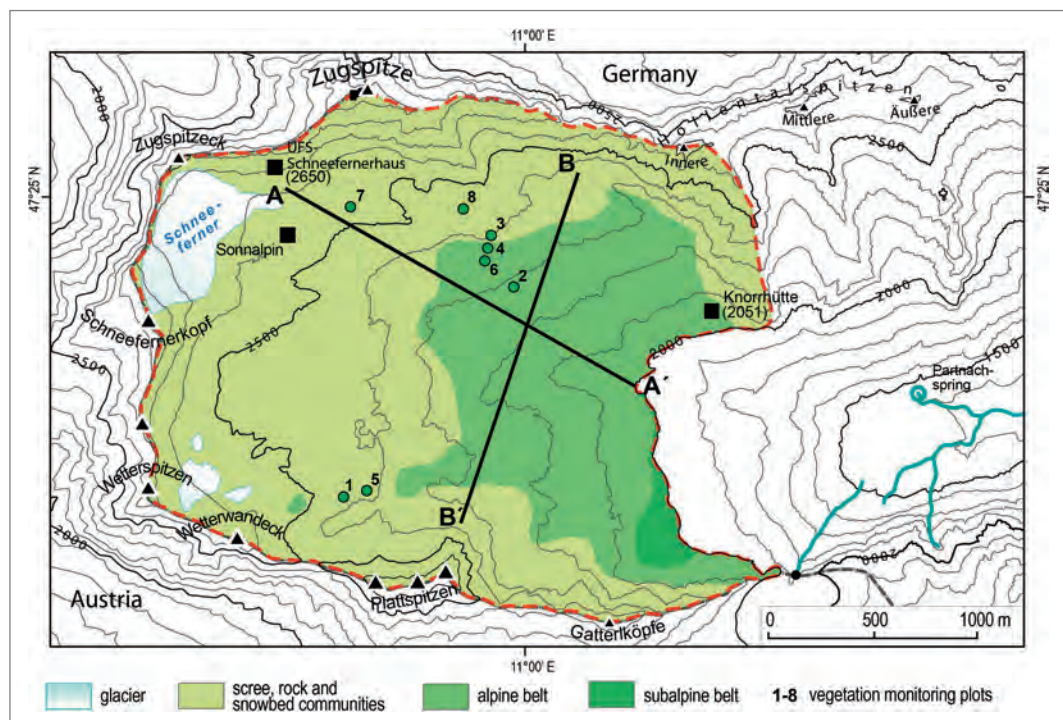


Fig. 1: Principal vegetation zones of the Zugspitzplatt, vegetation monitoring sites and transects shown in Fig. 8: a-b.

ferruginei (Rübel 1911). The latter one can be found on sites where the accumulation of folic Histosols has advanced to a point, where the roots of the plants have lost contact to the carbonate bedrock (SEIBERT 1992) and *Rhododendron hirsutum* is replaced by *Rhododendron ferrugineum*.

Most of the krummholz forms isolated patches and is often surrounded by larger areas of dwarf-shrub heath. Within these, acidophilic species like *Rhododendron hirsutum*, *Dryas octopetala* and *Carex sempervirens* dominate. The absence of species indicating acidity differ them from similar formations in the neighboring regions of the Ammergauer Alps and the Karwendel Alps (EGGENSBERGER 1993; DÜRING and WIERER 1995).

Species-rich grasslands mark the ecotone between the subalpine and the alpine belt (Fig. 2). These areas share many elements with the Seslerio-Caricetum sempervirentis (Br.-Bl. in Br.-Bl. et Jenny 1926), a community that has been well described for the neighboring regions of the Karwendel- and the Ammergauer Alps (Saitner and Pfadenhauer 1992; Eggensberger 1993). Growing on slopes with E to S exposition these communities are a slightly more imposing appearance than the dominating Caricetum firmae (Rübel 1911) of the alpine zone. Nevertheless, the presence of only one of the character species (*Nigritella nigra*) and just some differential species (*Dryas octopetala*, *Daphne striata*, *Erica carnea*, *Polygala chamaebuxus*) according to OBERDORFER (1974/1976), EGGENSBERGER (1993) and GRABHERR and MUCINA (1993) make it obvious, that these grasslands cannot be regarded as a fully developed Seslerio-Caricetum sempervirentis. Highly frequent species like *Androsace chamaejasme* and the name giving *Carex firma* in the relevées may support the characterization as a species-rich variation of the Caricetum firmae.

9.4.2 Alpine belt

As reported, the Caricetum firmae represents the most common grassland-community within the investigation area. It is the typical association of the alpine belt reaching an altitude of > 2500 m a.s.l. on climatically favored slopes on the southwestern Zugspitzplatt. It prevails also on consolidated scree as on karst-bedrock. Overall species-richness decreases with increasing altitude if you consider the 67 relevées in Fig. 3. The slightly higher number of species among relevées > 2400 m a.s.l. can be explained with locally favorable site conditions as well as a rising number of taxa originating from subnival scree or snowbed communities (ecotonal character).

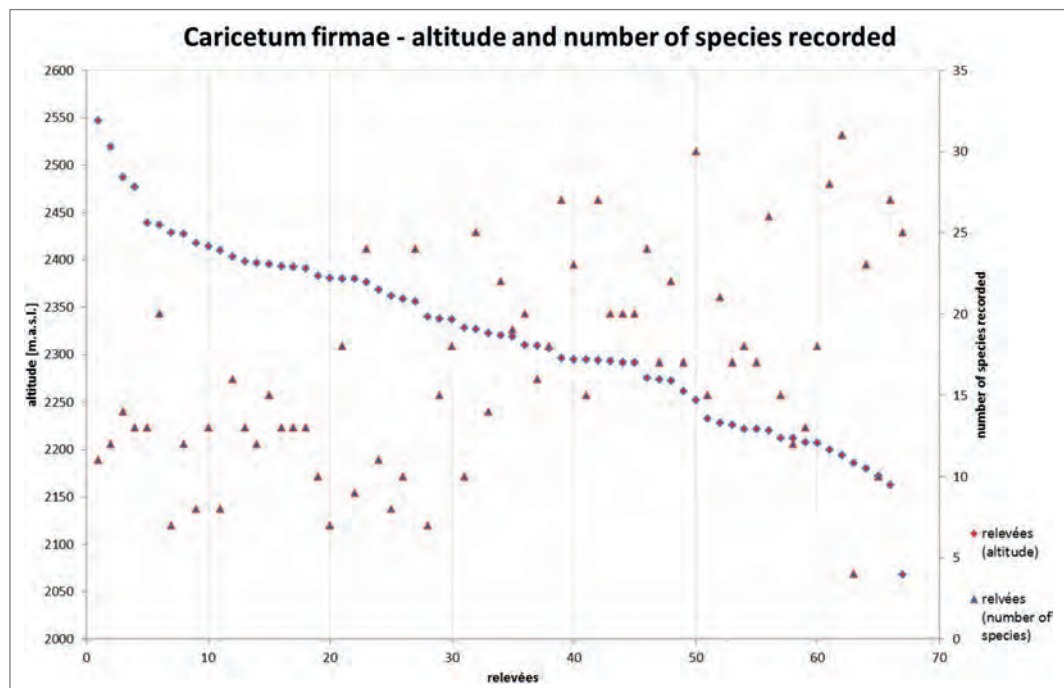


Fig. 3. Altitude and species-richness of recorded Caricetum firmae sites.

Four types of the Caricetum firmae were identified on the Zugspitzplatt: the largest group (41 relevées) with a total ≥ 10 species and implying two or more differential species according to GRABHERR and MUCINA (1993) can be regarded as the characteristic representative. The second group (13 relevées) is closely related but shows no or only one differential species with low cover-abundance. The third group (8 relevées) shares in addition a low number of species (≤ 10) and the absence of all class/order character species. The last group (5 relevées) shows a transitional character towards subnival communities of the Thlaspietea rotundifolii with several character- and differential species originating from these.

While the Caricetum firmae must be considered as a mostly stable community in the upper part of the alpine belt, further development leading to more complex associations like the Seslerio-Caricetum sempervirentis is possible in the lower parts.

Directly linked to acidified slopes, either by advancing pedogenetic development or on former krummholz sites, the Geo montani-Nardetum strictae (LÜDI 1928 nom. mutat. propos.) is the first of two plant communities within the investigation area of anthropogenic-zoogenic origin (KORCH 2014; KORCH and FRIEDMANN 2012, 2016). Promoted by grazing sheep *Nardus stricta* invades other communities with suitable conditions gaining more and more dominance as the animals avoid feeding on this species which in addition shows big tolerance to trampling (AICHINGER 1933; ELLENBERG and LEUSCHNER 2010). The community is restricted to Cambisols and former *Pinus mugo*-krummholz on the lower part of the Zugspitzplatt.

Likewise of anthropogenic-zoogenic origin is the Alchemillo-Poetum supinae (AICHINGER 1933) with a spotty distribution all over the alpine belt. It is the typical community found on places where grazing livestock stays over longer periods. Of low diversity and dominated by graminoids and other species with a high nutrient requirement (e.g. *Taraxacum alpinum*, *Urtica dioica*), it is adapted to herbivory and trampling.

9.4.3 Scree, rock and snowbed communities

Above the 2400 m contour line the general vegetation cover rapidly diminishes giving way to associations adapted to the harsh climatic conditions as well as to scree slopes, unprotected bedrock and snowbeds.

Among these the Salicetum retuso-reticulatae (Br.-Bl. in Br.-Bl. et Jenny 1926) takes an interim position between alpine meadows and scree communities (ZÖTTL 1950). On the Zugspitzplatt it has only a small distribution and is dominated by the dwarf willows *Salix retusa* and *Salix serpillifolia* whereas the name giving *Salix reticulata* is hardly found within the area.

The typical association of the study sites' snowbeds is the Arabidetum caeruleae (Br.-Bl. 1918). It shows not only an adaptation to a long snow cover (on the Zugspitzplatt > 10 months were observed during our investigations) but also to an excess supply of melting water during the short vegetation period (ENGLISCH et al. 1993). Soil profiles influenced by redox processes found at different locations on the Zugspitzplatt prove this. This is remarkable considering the general edaphic aridity of the area.

Beyond the snowbeds the Arabidetum caeruleae is widely found on the ski slopes of the upper Zugspitzplatt. Due to slope preparation it comes to an artificial accumulation and compacting of snow so these sites become snow-free significantly later than the surrounding environment. Although species of the Thlaspietum rotundifolii and the Leontodontetum montani also occur there, a classification as Arabidetum caeruleae can be justified due to the characteristic of *Arabis caerulea* as a very strong character species (ENGLISCH et al. 1993; OBERDORFER 1973).

9.5 Long-term monitoring

The data visualized in the figures 5 a–h show the development of recorded species on 8 permanent sample plots within the alpine and subnival belts during the period 2010 to 2016. The sample plots 1–2 can be assigned to the Caricetum firmae, the sample plots 3–6 to the Arabidetum caeruleae and the sample plots 7–8 to the Thlaspietum rotundifolii. The figures 4 a and b show a summarized biennial change of species richness and species magnitude of all 8

sample plots. In contrast the figures 5 a–h show the difference of species magnitude for each recorded species on each sample plot in 2010 and 2016 organizing them into herbaceous, dwarf shrub and graminoid taxa.

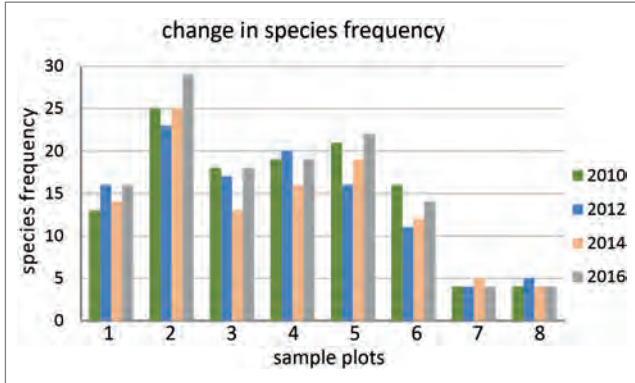


Fig. 4a: Species frequency for 8 sample plots over the period 2010–2016.

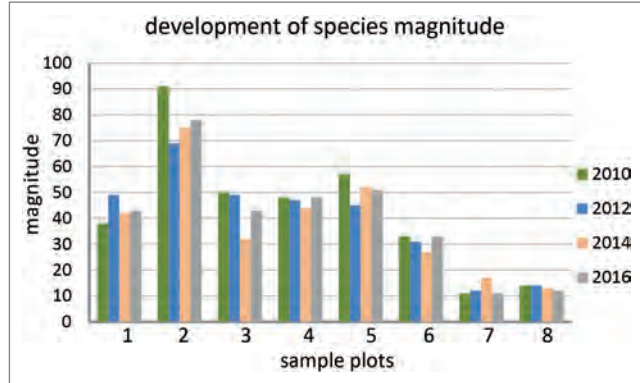


Fig. 4b: Species magnitude for 8 sample plots over the period 2010–2016.

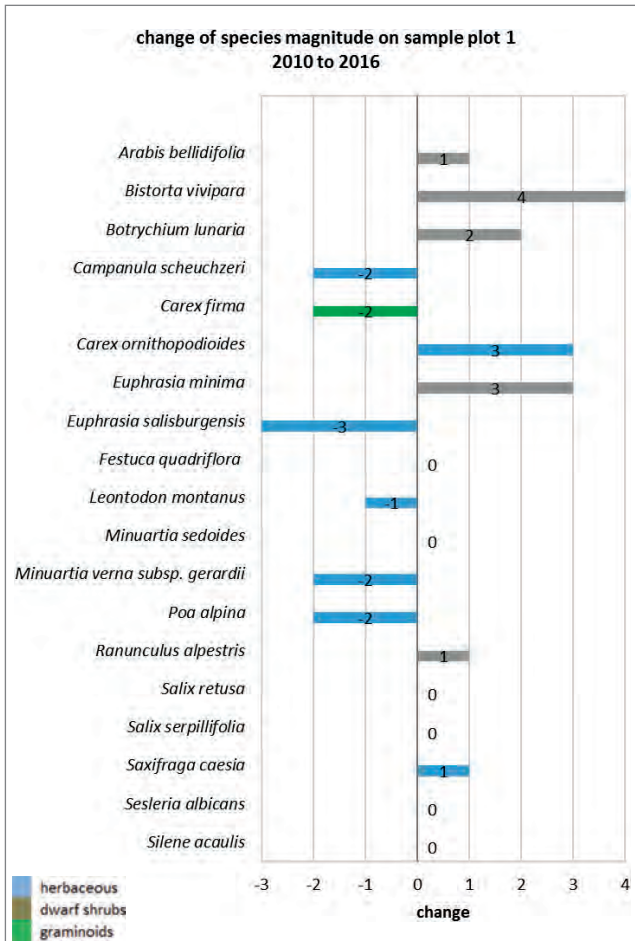


Fig. 5a: Sample Plot 1 (*Caricetum firmae*).

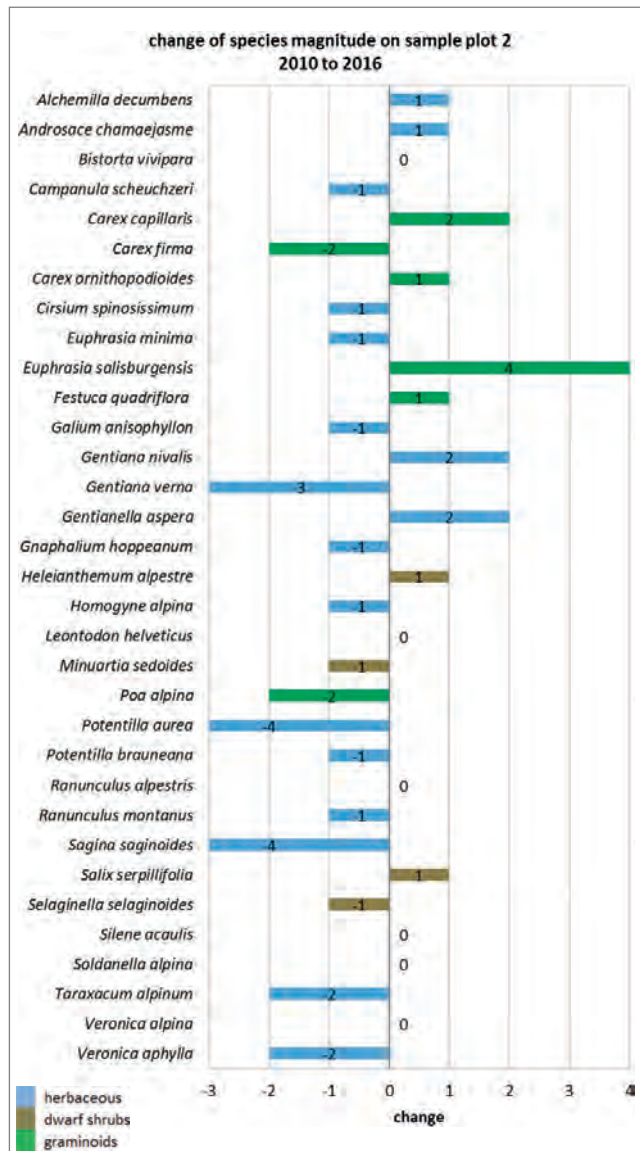


Fig. 5b: Sample Plot 2 (*Caricetum firmae*).

Regarding the comprehensive development on the sample plots, a positive development can be concluded for species richness as well as species magnitude for the sample plots 1–4 and 6 in 2016. On sample plot 6 species richness increased as well while species magnitude slightly decreased. This development was preceded by inconsistent development of both parameters in 2012 and 2014. By contrast the sample plots 7 and 8 show no or little negative development in 2016 and apparently also inconsistent development regarding the previous periods.

Analyzing the development of species magnitude of each species on each sample plot recorded in 2010 and in 2016 the development is apparently not very homogenous too. “Winners” and “losers” can be found within all three plant groups.

This inhomogeneity of the presented long-term monitoring provisional results shows the difficulty in obtaining significant unambiguous results within a short period of time. The recorded and described developments on the sample plots may be either the result of area-wide alterations of growing factors such as climate or changing grazing patterns. Analogue developments on a larger group of sample plots as the overall increase of species richness and species magnitude in 2016 may support this. The opposite development on the other plots together with a widely inconsistent development in all plots during the other years renders this result ambiguous.

In order to verify the provisional results and to finally eliminate the effect of the short monitoring time, single events and obtain reliable trends of future vegetation developments on the Zugspitzplatt, it is essential to continue with the monitoring program into the future.

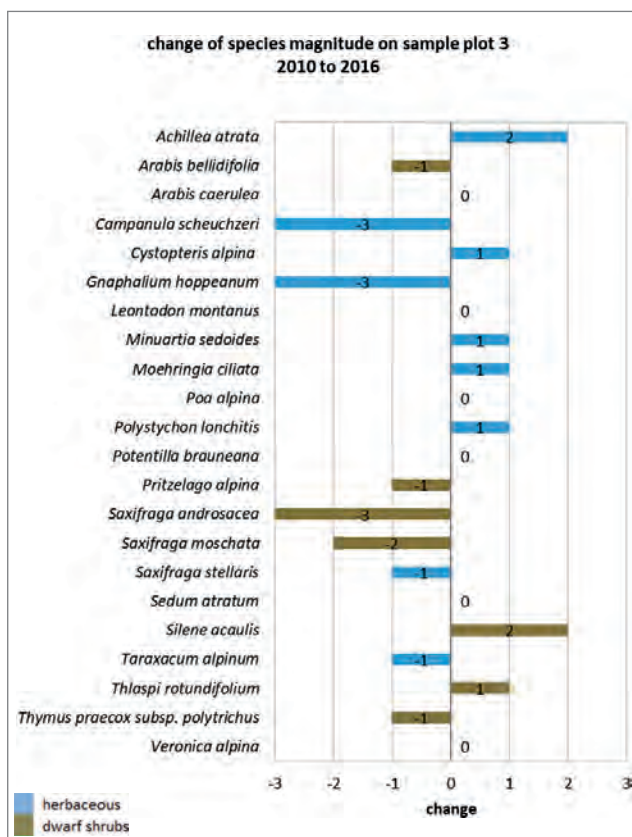


Fig. 5c: Sample Plot 3 (*Arabidetum caeruleae*).

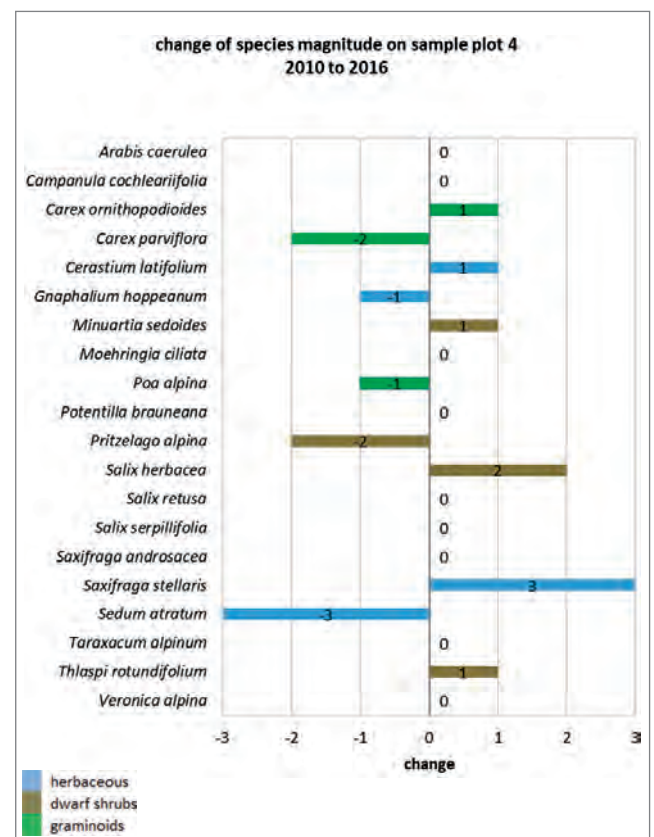


Fig. 5d: Sample Plot 4 (*Arabidetum caeruleae*).

9

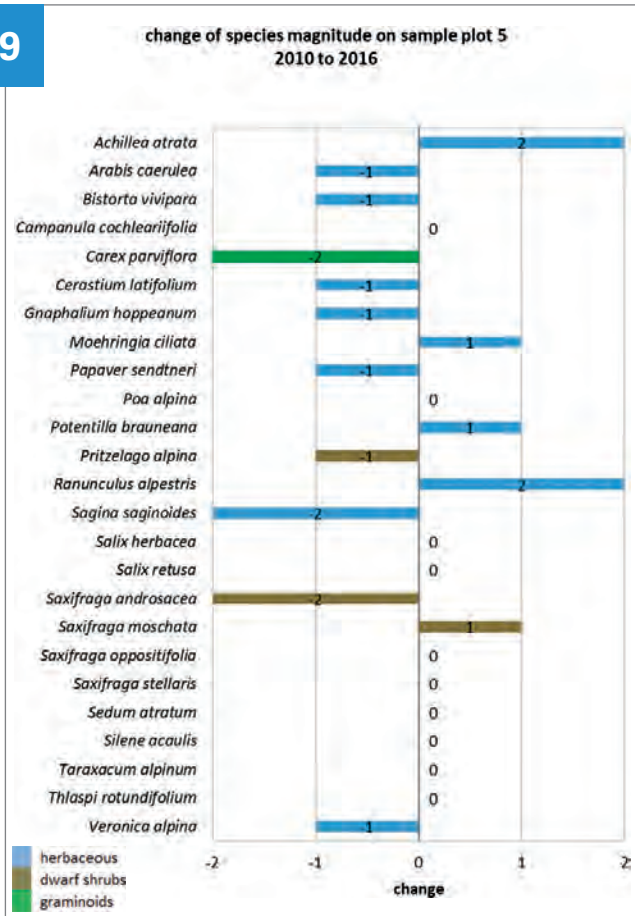


Fig. 5e: Sample Plot 5 (*Arabidetum caeruleae*).

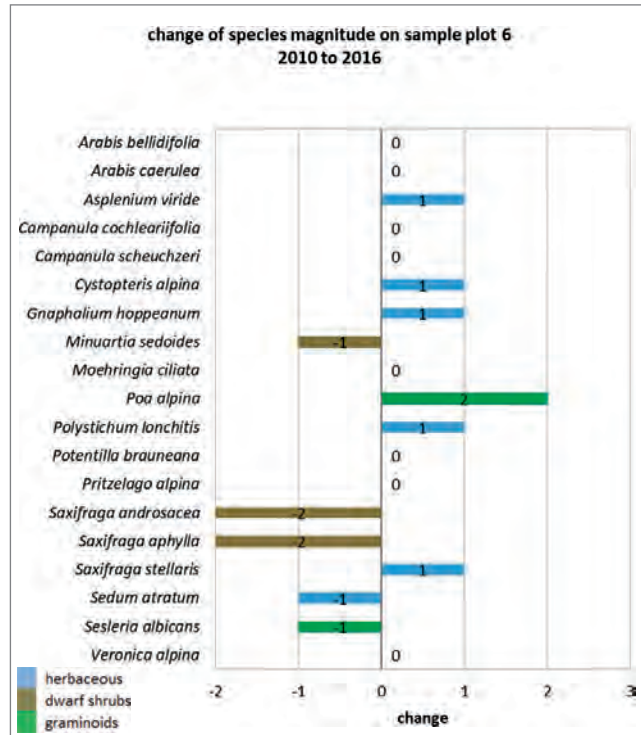


Fig. 5f: Sample Plot 6 (*Arabidetum caeruleae*).

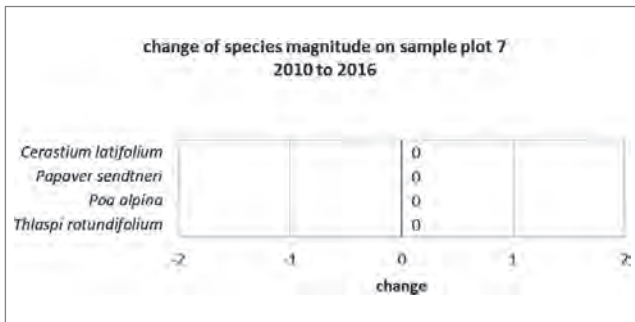


Fig. 5g: Sample Plot 7 (*Thlaspietum rotundifolii*).

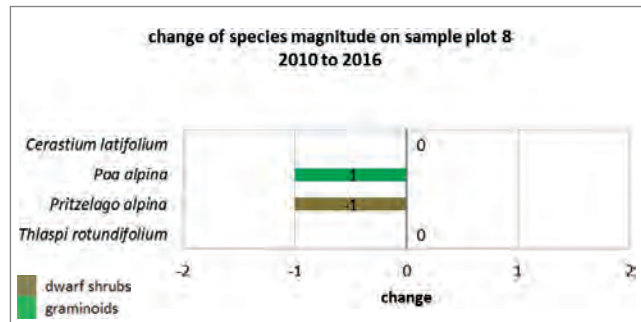


Fig. 5h: Sample Plot 8 (*Thlaspietum rotundifolii*).

9.6 Vegetation Dynamics

The current spatial vegetation patterns reflect the sum of all dynamic factors influencing flora and vegetation on the Zugspitzplatt. Therefore the ratio in which these factors influence every point of the investigation site is always different.

Firstly a location is influenced by geomorphologic processes such as rock fall or avalanches. These processes also influence the soil dynamics. The autochthonous Wetterstein-limestone strongly influences soil developing processes leading to carbonatic soil types. On the eastern Part of the Zugspitzplatt some sites show signs of soil acidification due to late glacial and actual aeolian deposition of mica from the Central Alps (KÜFMANN 2003, GRASHEY-JANSEN et al. 2014). Azonal acidophilic plant communities as the Geo-montani *Nardetum strictae* on cambisols are directly linked to this phenomenon.

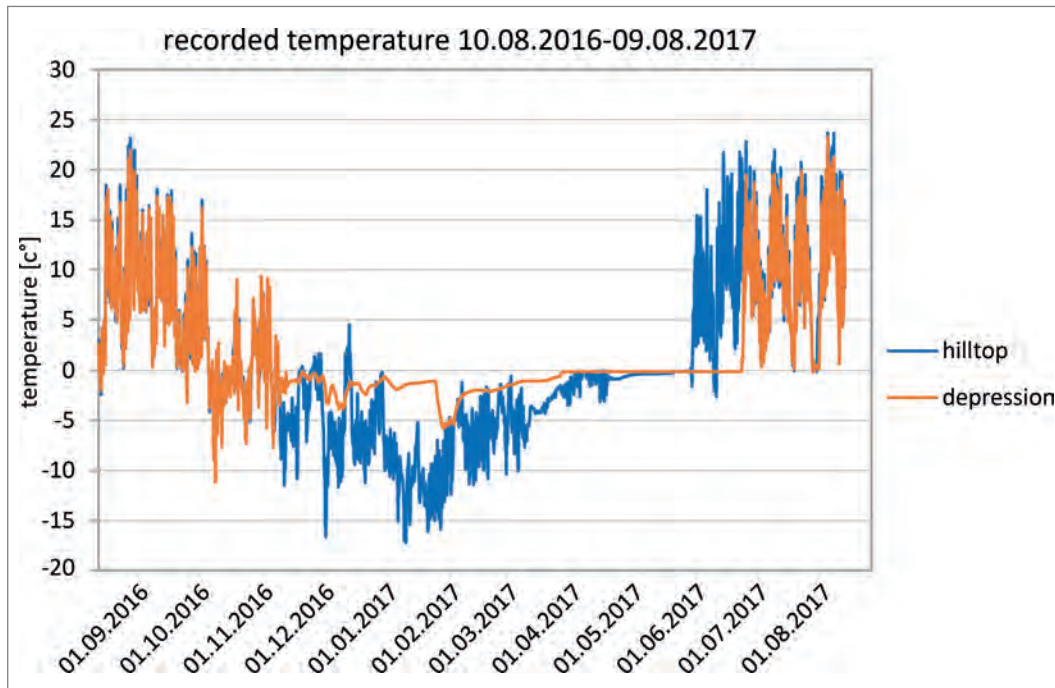


Fig. 6: Recorded temperature on two neighbouring sites (~ 2400 m a.s.l.) over the period 10.08.2016–09.08.2017. The *Caricetum firmae* on the hilltop-site shows a much shorter period of snow cover and thus harsher winter temperatures. At the same time, it benefits from an extended growing season compared to the *Arabidetum caeruleae* growing in the nearby depression.

In addition to geomorphological processes and soil conditions the vegetation dynamics of the Zugspitzplatt are mainly influenced by the local microclimate. Different solar exposition and dominating wind directions as well as the differing periods of annual snow cover directly influence the occurrence of plant communities. Boundary layer climate investigations on the Zugspitzplatt have shown that neighbouring sites often strongly differ in their site climate leading to completely altered vegetation. For example the *Arabidetum caeruleae*, which is linked to snowbeds with an annual snow cover up to ten months, can be found immediately next to *Caricetum firmae*-meadows indicating stronger insolation and thus a shorter snow cover (Fig. 6).

Although meteorological records show increasing temperatures and precipitation for the whole Zugspitzplatt, long-term changes of vegetation patterns such as an upward shifting of vegetation belts will not be possible to confirm until longer monitoring results are available.

Anthropogenic and anthropo-zoogenic alterations occurs by trampling mainly along the hiking trails and area-wide by the grazing sheep. Dating back to at least the 16th century within the alpine belt, the latter has without doubt the biggest impact on the natural vegetation leading to a partly of fully altered vegetation such as the acidified *Geo montani-Nardetum strictae* or the eutrophicated pastures of the *Alchemillo-Poetum supinae* (Fig. 7) Without grazing and eutrophication it is likely, that instead of the anthropogenic and zoogenic communities the zonal *Caricetum firmae* would prevail on more basophilic sites of the alpine belt. The occurrence of many species of the *Caricetum firmae* within the zoogenic communities (e.g. *Carex firma*, *Festuca quadriflora* and *Euphrasia salisburgensis*) evidences this. On the sites with more acidified soil conditions it is probable that with the absence of grazing the *Seslerio-Caricetum sempervirentis* or even krummholz communities would prevail on the sites actually occupied by the *Geo montani-Nardetum strictae*.

Finally, the previously mentioned factors and processes happen at different time scales, so time must be considered as a superordinate factor linking them. In the course of time, different connections, intensifications and interactions between the site conditions, site climate, grazing and anthropogenic disturbance can be observed and assumed.

To conclude, the described heterogeneous vegetation dynamics within the investigation area lead to the patchy mosaic of different plant communities found today (Figs. 2 and 7).

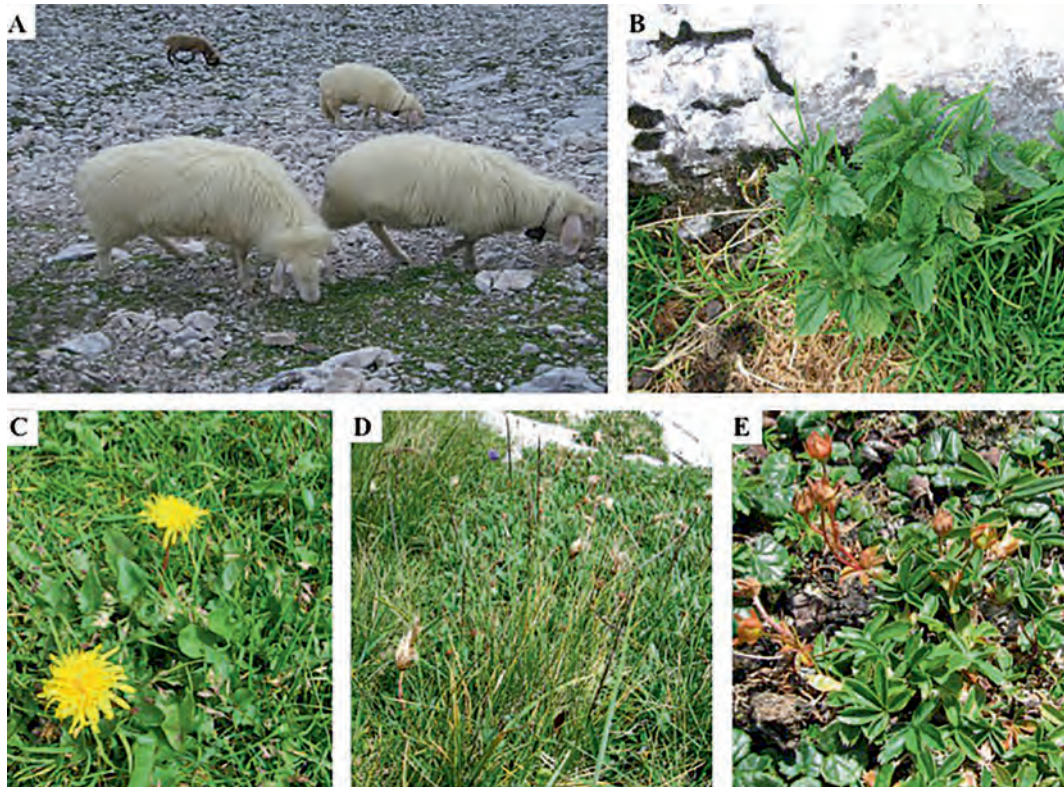


Fig. 7. Alteration of the vegetation due to anthropo-zoogenic nitrification and acidification. (A) Grazing sheep on the Zugspitzplatt (B) Nitrophilic *Urtica dioica*. (C) Nitrophilic *Taraxacum alpinum*. (D) Acidophilic and zoogenic *Nardus stricta*. (E) Acidophilic *Potentilla aurea*. All fotos: Oliver Korch.

9.7 Current vegetation patterns on the Zugspitzplatt as a result of heterogeneous site conditions and anthropo-zoogenic influences

Transect A-A' (Figs. 1, 8a) stretches from the UFS Schneefernerhaus (approx. 2700 m) in SSW-direction to the lower beginning of the Brunntal (approx. 2000 m). Above the 2500 m contour line the terrain is dominated by scree slopes. Together with the severe climatic conditions dominating these heights their vegetation is mainly limited to hardy *Thlaspietum rotundifolii* communities. Below 2500 m scree dynamics become less intense allowing other subnival communities to establish on favored sites between the still dominating *Thlaspietum rotundifolii*. Gentler climatic conditions below 2400 m allow the development of alpine meadows linked to the *Caricetum firmae*. Further downhill this typical plant community of the alpine zone within the northern Calcareous Alps becomes more and more dominant and well developed. Grazing sheep in the alpine zone prefer the numerous roches moutonnées for resting and ruminating. This leads to local eutrophication and the development of the *Alchemillo-Poetum supinae* on these hilltops. Further climatic improvement along with better conditions for soil development below 2200 m mark the beginning of the species rich *Seslerio-Caricetum sempervirentis* sites on the lower Zugspitzplatt. Where these communities grow on acidified Cambisols and especially where they are additionally influenced by grazing, the *Seslerio-Caricetum sempervirentis* is replaced by the anthropo-zoogenic *Geo montani-Nardetum strictae*. Eventually these meadows are more and more replaced by the krummholz of the *Rhododendro hirsuti-Pinetum mugo* marking the lowest point of the research area.

Transect B-B' (Figs. 1, 8b) crosses the Zugspitzplatt in transverse direction. Starting and ending in approx. 2400 m and with its lowest point just below 2200 m it is largely within the alpine vegetation belt. Nevertheless, scree, frost weathering along with cold site climate at the foot of the walls of the Plattumrahmung suppress alpine communities and give way to the subnival *Thlaspietum rotundifolii*. In depressions with an extremely long annual period of snow cover

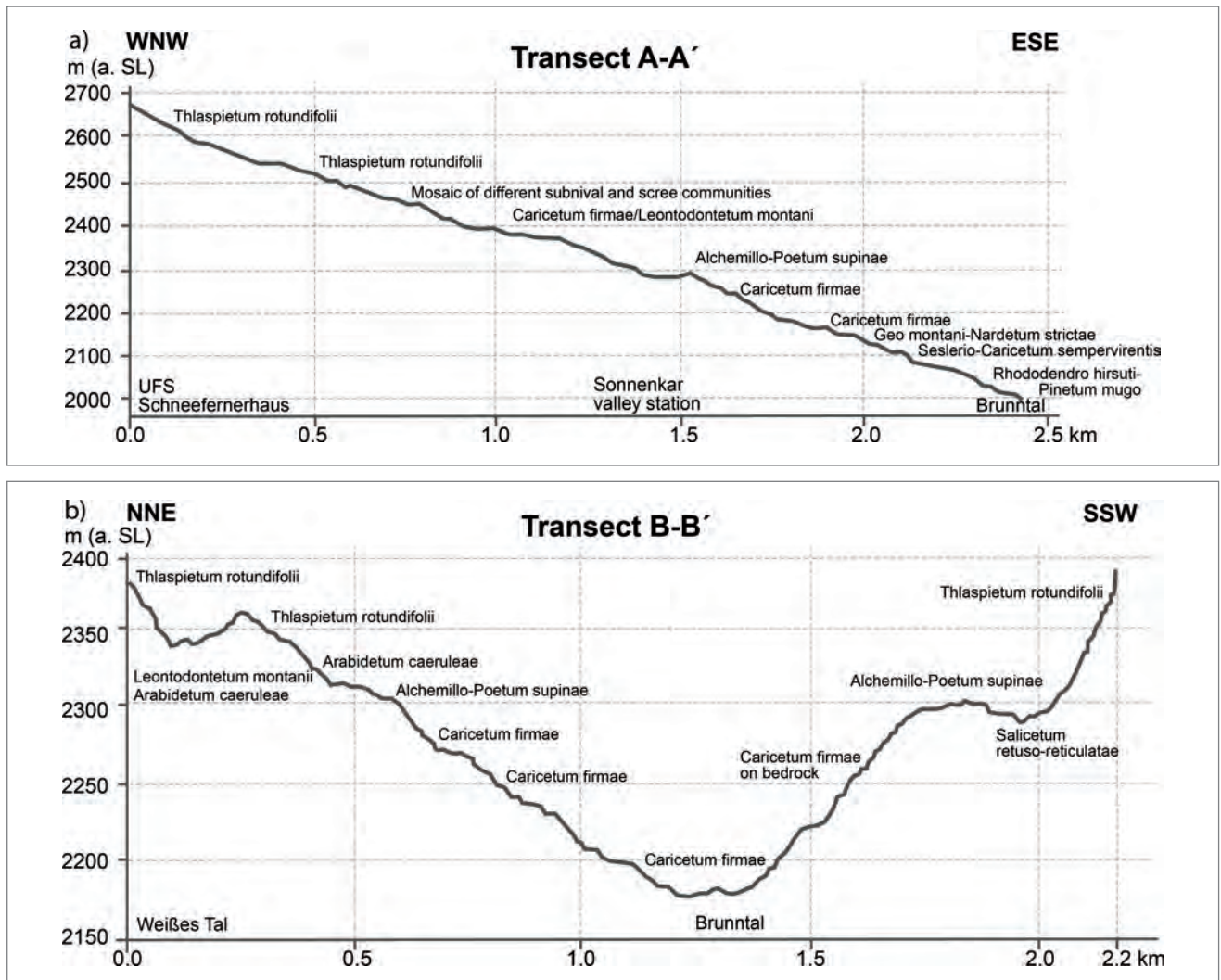


Fig. 8a and 8b: Transects A-A' and B-B' showing the heterogeneity of plant communities on the Zugspitzplatt.

especially adapted snowbed communities of the *Arabidetum caeruleae* are common. The related *Salicetum retuso-reticulatae*, a community dominated by dwarf willows can be found on snowbeds with more favourable climatic conditions and linking them to initial forms of the *Caricetum firmae*. In analogy to transect A-A' the latter community dominates vast parts of the lower parts of the transect, growing on consolidated scree as well as directly on bedrock. On roches moutonnées frequently visited by grazing sheep it is replaced by the *Alchemillo-Poetum supinae*.

9.8 Outlook

The reported research work has shown that the flora and vegetation dynamics on the Zugspitzplatt are the result of the interaction of several parameters. The vast impact of anthropogenic and zoogenic disturbance turns the study site largely into a cultural landscape with natural vegetation reduced only to the most remote and inaccessible sites.

Future research must focus on collecting further data from the long-term vegetation monitoring in order to better understand the involved factors and processes and their interactions. Additional data especially from site climate, grazing and anthropogenic impact would further improve the accuracy of predicting future changes of the flora and vegetation on Germany's highest research site.

Acknowledgements

We would like to thank the Bavarian State Ministry of the Environment and Consumer Protection (former Bavarian State Ministry of the Environment and Public Health) for funding the projects “Ecological analysis of the subalpine to subnival vegetation zones on the Zugspitzplatt (HÖHENZUG)” and “Vegetation dynamics on the Zugspitzplatt” which are part of the collaborative projects “Consequences of climatic change in the Alps – analysis by altitudinal gradients” Klimagrad (2009–2013) and Klimagrad 2 (2015–2018). We also would like to thank the Environmental Research Station Schneefernerhaus (UFS) for the logistic support, the Bayerische Zugspitzbahn Bergbahn AG (BZB) for providing free cable car access to the Zugspitzplatt 2010–2017 and the Weidegenossenschaft Partenkirchen for the support of the grazing pattern investigations.

References

- Aeschimann, D., Lauber, K., Moser, D.M. & Theurillat, J.-P. (2004): Flora alpina: Ein Atlas sämtlicher 4500 Gefäßpflanzen der Alpen. 3 Bde., Haupt Verlag, Bern, 2670 pp.
- Aichinger, E. (1933): Vegetationskunde der Karawanken. – Pflanzensoziologie, 2: 329 pp.
- Braun-Blanquet, J. (1964): Pflanzensoziologie. Grundzüge der Vegetationskunde. Wien, New York. 865 pp.
- Dierschke, H. (1994): Pflanzensoziologie. E. Ulmer Verlag, Stuttgart, 683 pp.
- Düring, C. & Wierer, U. (1995): Die subalpine und alpine Vegetation der Soierngruppe im Naturschutzgebiet Karwendelgebirge. *Hoppea* 56: 343–452.
- Deutscher Wetterdienst (2013): Weather Request and Distribution System. URL: <https://www.dwd.de>
- Ellenberg, H., Weber, H.E., Düll, R., Wirth, V. & Werner, W. (2001): Zeigerwerte von Pflanzen in Mitteleuropa. *Scripta Geobotanica* 18, 3rd edn. Göttingen. 262 pp
- Ellenberg, H. & Leuschner, C. (2010): Vegetation Mitteleuropas mit den Alpen. 6th edn. Stuttgart. 1333 pp.
- Eggensberger, P. (1993): Die Pflanzengesellschaften der subalpinen und alpinen Stufe der Ammergauer Alpen und ihre Stellung in den Ostalpen. PhD-Thesis, University of Regensburg, Regensburg. 232 pp.
- Englisch, T., Valahovič, M., Mucina, L., Grabherr, G. & Ellmauer, T. (1993): *Thlaspietea rotundifolii*. In: Grabherr, G. & Mucina, L. (1993): Die Pflanzengesellschaften Österreichs. Teil II: Natürliche und waldfreie Vegetation: 276–346.
- Fischer, A. & Klotz, S. (1999): Zusammenstellung von Begriffen, die in der Vegetations-Dauerbeobachtung eine zentrale Rolle spielen. – *Tuexenia*, 19: 3–11.
- Friedmann, A. & Korch, O. (2010): Die Vegetation des Zugspitzplatts (Wettersteingebirge, Bayerische Alpen): Aktueller Zustand und Dynamik. – *Berichte der Reinhold-Tüxen-Gesellschaft*. 22: 114–128.
- Grabherr, G. & Mucina, L. (1993): Die Pflanzengesellschaften Österreichs. Teil II: Natürliche und waldfreie Vegetation. Jena. 523 pp.
- Grashey-Jansen, S., Korch, O., Beck, C., Friedmann, A., Bernhard, R., Dubitzky, C. (2014): Aeolian influenced soil sites in consideration of atmospheric circulation types – a case study in the alpine zone of the Zugspitzplatt (Northern Calcareous Alps, Germany). *Journal of Geology, Agriculture and Environmental sciences* 2 (4): 11–19.
- Hagg, W., Mayer, C., Mayr, E. & Heilig, A. (2012): Climate and glacier fluctuations in the Bavarian Alps in the last 120 years. – *Erdkunde*, 66: 121–142.
- Hammer, Ø., Harper, D.A.T. & Ryan P.D. (2001): PAST: Paleontological statistics software package for data analysis. – *Paleontologica Electronica* 4: 9 pp.
- Hammer, Ø. (2013): *Paleontological Statistics – Version 3.0 – Reference manual*. Oslo. 221 pp.
- Hüttl, C. (1999): Steuerungsfaktoren und Quantifizierung der chemischen Verwitterung auf dem Zugspitzplatt (Wettersteingebirge, Deutschland). *Münch. Geogr. Abh., Reihe B* 30. München.
- Korch, O. & Friedmann, A. (2012): Phytodiversität und Dynamik der Flora und Vegetation des Zugspitzplatts. – *Jahrbuch Verein Schutz der Bergwelt* 76/77: 217–234.
- Korch, O., Friedmann, A., Grashey-Jansen, S. & Seipp, C. (2013): Vegetation und Böden oberhalb der Waldgrenze des Zugspitzplatts. – *Allgemeine Forstzeitschrift für Waldwirtschaft und Umweltvorsorge* 3: 36–38.
- Korch, O. (2014): Untersuchungen zu Flora und Vegetation des Zugspitzplatts (Wettersteingebirge, Bayerische Alpen) – Rezente Vegetationsdynamik unter besonderer Berücksichtigung klimatischer und anthropo-zoogener Prozesse. – PhD-Thesis, University of Augsburg, 187 pp.
- Korch, O. & Friedmann, A. (2016): Vegetation und Vegetationsdynamik auf dem Zugspitzplatt (Bayerische Alpen): Natur- und Kulturlandschaft im hochalpinen Raum als Produkt natürlicher, anthropogener und zoogener Einflüsse. – *Polarforschung* 86(1): 35–45.
- Körner, C. (2003): *Alpine plant life*. Springer, Berlin, 349 pp.

- Körner, H., Ulrich, R. (1965): Geologische und felsmechanische Untersuchungen für die Gipfelstation der Seilbahn Eibsee-Zugspitze. – *Geologica Bavarica* 55: 404–421.
- Küfmann, C. (2003): Soil types and eolian dust in high-mountainous karst of the Northern Calcareous Alps (Zugspitzplatt, Wetterstein Mountains, Germany). – *Catena* 53: 211–227.
- Küfmann, C. (2006): Quantifizierung und klimatische Steuerung von rezenten Flugstaubeinträgen auf Schneesoberflächen in den Nördlichen Kalkalpen (Wetterstein-, Karwendelgebirge, Berchtesgadener Alpen, Deutschland). – *Zeitschrift für Geomorphologie* 50: 245–268.
- Küfmann, C. (2008): Are Cambisols in Alpine Karst Autochthonous or Eolian in Origin? – *Arctic, Antarctic, and Alpine Research* 40 (3): 506–518.
- Hagg, W., Mayer, C., Mayr, E. & Heilig, A. (2012): Climate and glacier fluctuations in the Bavarian Alps in the last 120 years. *Erdkunde* 66: 121–142.
- Miller, H. (1962): Zur Geologie des westlichen Wetterstein- und Mieminger Gebirges. Ph.D. Thesis, Department of Geology, Ludwig-Maximilian University, Munich. 238 pp.
- Mucina, L., Grabherr, G. & Ellmauer, T. (1993a): Die Pflanzengesellschaften Österreichs. Teil I: Anthropogene Vegetation. Jena. 578 pp.
- Mucina, L., Grabherr G & Wallnöfer, S. (1993b): Die Pflanzengesellschaften Österreichs. Teil III: Wälder und Gebüsche. Jena. 353 pp.
- Oberdorfer, E. (1973): *Salicetea herbaceae* Br.-Bl. et al. 47. In: OBERDORFER, E. (ed.) (1998): Süddeutsche Pflanzengesellschaften. – Teil I: Fels- und Mauergesellschaften, alpine Fluren, Wasser-, Verlandungs-, und Moorgesellschaften. 4th ed. Jena. Pp 214–220.
- Oberdorfer, E. (1974/1976): *Seslerietea variaea* clas. nov. In: Oberdorfer, E. (ed.) Süddeutsche Pflanzengesellschaften. – Teil II: Sand- und Trockenrasen, Heide- und Borstgrasgesellschaften, alpine Magerrasen, Saum-Gesellschaften, Schlag- und Hochstauden-Fluren. 3rd ed. Jena, pp 194–203.
- Oberdorfer, E. (1992a): Süddeutsche Pflanzengesellschaften. – Teil IV: Wälder und Gebüsche – Textband. – 2nd edn. Jena. 282 pp.
- Oberdorfer, E. (1992b): Süddeutsche Pflanzengesellschaften. – Teil IV: Wälder und Gebüsche – Tabellenband. 2nd edn. Jena. 580 pp.
- Oberdorfer, E. (1993a): Süddeutsche Pflanzengesellschaften. – Teil II: Sand- und Trockenrasen, Heide- und Borstgrasgesellschaften, alpine Magerrasen, Saum-Gesellschaften, Schlag- und Hochstauden-Fluren. 3rd edn. Jena. 355 pp.
- Oberdorfer, E. (1993b): Süddeutsche Pflanzengesellschaften. – Teil III: Wirtschaftswiesen und Unkrautgesellschaften. 3rd edn., Jena. 455 pp.
- Oberdorfer, E. (1998): Süddeutsche Pflanzengesellschaften. – Teil I: Fels- und Mauergesellschaften, alpine Fluren, Wasser-, Verlandungs-, und Moorgesellschaften. 4th edn. Jena. 314 pp.
- Pott, R. (1995): Die Pflanzengesellschaften Deutschlands. Stuttgart. p 622.
- Reichelt, G. & Willmanns, O. (1973) *Praktische Arbeitsweisen Vegetationsgeographie*. Braunschweig. 210 pp.
- Reisigl, H. & Keller, R. (1994): *Alpenpflanzen im Lebensraum*. G. Fischer Verlag, Stuttgart, 149 pp.
- Rennwald, E. (2000): Verzeichnis und Rote Liste der Pflanzengesellschaften Deutschlands. – *Schriftenreihe für Vegetationskunde* 35: 800 pp.
- Ringler, A. (2009): *Almen und Alpen. Höhenkulturlandschaft der Alpen. Ökologie, Nutzung, Perspektiven*. Hrsg. vom Verein zum Schutz der Bergwelt, München. Langfassung, 1.448 pp.
- Saitner, A. & Pfadenhauer, J. (1992): Die Vegetation im Bereich des Dammkars bei Mittelwald und ihre Beeinflussung durch den Tourismus. – *Jahrbuch des Vereins zum Schutz der Bergwelt*, 57: 11–89.
- Seibert, P. (1992): Klasse *Vaccinio-Piceetea* Br.-Bl. In Br.-Bl. Et al. 39. In: Oberdorfer E (ed) Süddeutsche Pflanzengesellschaften. – Teil IV: Wälder und Gebüsche – Textband. 2nd ed. Jena, pp 53–80.
- Walentowski, H., Ewald, J., Fischer, A., Kölling, Ch. & Türk, W. (2006): *Handbuch der natürlichen Waldgesellschaften Bayerns*. – LWF Bayern. Verlag Geobotanica, Freising, 441 pp.
- Wetzel, K. F. (2004): On the hydrology of the Partnach area in the Wetterstein mountains (Bavarian Alps). *Erdkunde* 58: 172–186.
- Wisskirchen, R. & Haeupler, H. (1998): *Standardliste der Farn- und Blütenpflanzen Deutschlands*. Stuttgart. 765 pp.
- Zöttl, H. (1950): Die Vegetationsentwicklung auf Felsschutt in der alpinen und subalpinen Stufe des Wettersteingebirges. Ph.D-Thesis, LMU München, Munich. 201 pp.

10 Large scale dynamics of the atmosphere: Planetary waves

Theoretical overview, climate change, trends and variability

Lisa Küchelbacher, Michael Bittner

German Aerospace Center, DLR, German Remote Sensing Data Center, Oberpfaffenhofen

Abstract

Planetary waves (PW) are global scale waves in the atmosphere, which are known to considerably impact weather patterns in the mid-latitudes in the troposphere and the ozone distribution in the stratosphere. PW play an important role in coupling middle atmosphere dynamics. Due to the fact that climate change causes a decrease of the meridional temperature gradient, the strength of the zonal wind might decrease. This should, in turn, change the planetary wave activity (PWA). This chapter is based on Küchelbacher (2021, 2016) and references therein.

In order to quantify possible changes of the PWA we analyze ERA-Interim temperature data (10 m to approx. 65 km height) on the Northern Hemisphere and calculate the so-called dynamical activity index (DAI) as measure for the PWA. We analyze the PWA to find indications for PWA changes and variability. We also use rotational temperature data from hydroxyl airglow measurements at UFS Schneefernerhaus (Germany) embedded in the international Network for the Detection of Mesospheric Change (NDMC) in the upper mesosphere/lower thermosphere (UMLT).

We find an indication for a significant increase of the PWA in the stratosphere. The change of the PWA with higher zonal wavenumbers turns out to be strongest. This finding is in agreement with the expectation that a weakening of the meridional temperature gradient leads to improved vertical propagation conditions for planetary waves. With the empirical mode decomposition (EMD) we are able to extract non-stationary signals of the PWA time series. We further find that longer-term oscillations (QBO, ENSO and solar cycles) have a noticeable impact on the PW variability in all considered heights. Next to the 11-year cycle that is related to the sunspot-cycle in many studies, we also find a pronounced quasi-22-year signal. We tentatively interpret this signal as being due to the solar-magnetic-field ("Hale-cycle").

10.1 Fundamentals of PW

PW can be described as a periodic deviation from the mean state of a meteorological parameter, such as temperature or pressure, along one circle of latitude (Schöberl & Geller 1976). They arise from conservation of potential vorticity on the sphere and are therefore a direct consequence of the Earth's rotation. Compared to other atmospheric waves, like infrasound or gravity waves, the spatial- and temporal scale of PW is large. Their zonal wavelength is in the order of the Earth's radius and the period of traveling PW varies between several days up to one month. Due to their spatio-temporal size, they transport comparatively large amounts of energy. Thus, they significantly impact atmospheric circulation. Detailed descriptions of the theory of PW can be found for example in the text books written by Holton (1979), Andrews (2010), Pichler (1997) and Brasseur & Solomon (2005).

The troposphere is characterized by a pronounced pressure gradient between the polar regions and the equator: as the Earth is a sphere the incoming solar radiation intensity on the surface decreases towards the poles according to the cosine of latitude. This leads to a meridional pressure force gradient. Therefore, air parcels flow meridional towards higher latitudes to compensate this pressure gradient. Due to the rotation of the Earth the air parcels are deflected to the east on both Hemispheres until an equilibrium state between pressure and Coriolis force is achieved. A circumpolar westerly wind flow establishes at the mid-latitudes, known as the geostrophic wind. The geostrophic wind inhibits the exchange of air masses between lower and higher latitudes.

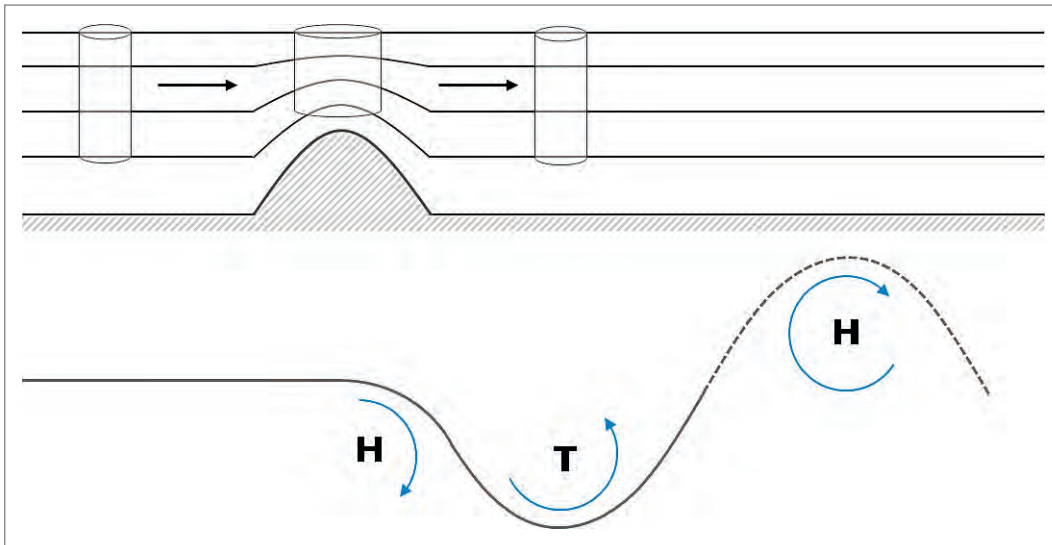


Fig. 1: Deviation of an air parcel while flowing over a mountain ridge. The upper image illustrates the vertical, the bottom image the horizontal view. As it is shifted vertically, it reduces its local angular momentum. As a result, it rotates anticyclonic and therefore flows southward. At a certain horizontal scale the increasing Coriolis force has to be considered. As the sum of local and global angular momentum is conservative, the local angular momentum must decrease. The air parcel rotates cyclonic and flows northward again. Due to the inertia of mass it overpasses its initial state. As the Coriolis force decreases, it leads again to an anticyclonic rotation. A PW is described.

In reality such an ideal zonal circumpolar current does not exist. It is disturbed by planetary scale wave motions causing pronounced meridional deviations. Rossby et al. (1939) described these waves using the principle of conservation of absolute vorticity for a barotropic, non-divergent atmosphere. Although Rossby (1939) made some significant simplifications in describing PW he was already able to explain many fundamental properties of the structure of PW.

Land-sea transitions or mountain ridges induce large scale vertical movements of air parcels in the atmosphere. The vertical displacement of the current causes a change in the air parcels angular momentum. This becomes clear when assuming that the isentropes are parallel to the ground. As an air parcel flows towards a mountain ridge, the distance between the isentropes narrows. This leads to a compression of the air parcel that flows over a mountain ridge and slows down the local angular momentum of the air parcel. Of distinct interest is the vertical component of the rotational vector of velocity $\vec{u} = (u, v, w)$, known as **relative vorticity** ζ :

$$\zeta = \frac{\partial v}{\partial x} - \frac{\partial u}{\partial y} \quad (1)$$

With u and v giving the zonal and meridional wind component. The meridional and vertical component of the rotation ($\vec{\nabla} \times \vec{u}$) can be neglected as long as only horizontal motions are considered. This assumption is well valid especially for the stratosphere, where static stability of the atmosphere is usually well established due to the temperature increase with height.

The so-called **Ertel potential vorticity** Z_E

$$Z_E = -\eta \cdot \frac{d\theta}{dp} = \text{const.} \quad (2)$$

with the **absolute vorticity** η

$$\eta = \zeta + f = \text{const.} \quad (3)$$

is given by the sum of the relative vorticity and the planetary vorticity, which is represented by the Coriolis parameter. The Ertel potential vorticity says that the change of the relative vorticity must be balanced. Within the Ertel potential vorticity the potential temperature θ describes the temperature an air parcel would take if it is adiabatically brought to 1013 hPa pressure level. p represents the pressure. If an air parcel moves upward, $\frac{d\theta}{dp}$ will increase.

As the air parcel flows parallel to a certain latitude the absolute vorticity simplifies to ζ . As Z_E is conserved, the local rotation of the air parcel ζ must decrease. The air parcel then turns towards the equator. On the Northern Hemisphere, as an example, the Rocky Mountains represent a meridional mountain ridge that is large enough (Godske et al. 1957) to generate a southward oriented air flow in the lee.

When the air parcel flows over a larger distance towards the south, the global angular momentum due to Earth's rotation, the Coriolis parameter f , has to be taken into account. As the air parcel moves towards lower latitudes the Coriolis parameter f decreases. This means that the local rotation of the air parcel ζ must increase, forcing the air parcel to rotate cyclonic. The air parcel then flows towards higher latitudes. Due to the inertia of mass the air parcel overflows its initial latitudinal position. The Coriolis parameter f then increases, the air parcel gets an anticyclonic rotation and is deviated southward again. The result is a sinusoidal oscillation of the air parcel around a certain center latitude while travelling zonally. This sequence describes an oscillation in space and time: a planetary wave (PW).

When regarding the distribution of land and sea masses in the Northern Hemisphere from Fig. 2 it becomes clear that especially Eurasia induces a PW with zonal wavenumber one (PW1) on the atmospheric circulation. Taking Northern America into account, a wave with zonal wave number (PW2) two is expected. These orographic induced PW1 and PW2 are indeed observed and represent the most dominant PW structures within the atmosphere. Besides these two wave components, a whole spectrum of PW is usually generated in the atmosphere. The PW described so far are obviously linked to topography. Consequently, these PW do not significantly change their phase in relation to the Earth's surface. Therefore, they are often called quasi-stationary waves.

In contrast to the Northern Hemisphere, land-sea-transitions on the Southern Hemisphere are much less pronounced. The shape of continent Antarctica is almost circumpolar and it is completely surrounded by oceans, as can be seen also from Fig. 2 right. It therefore becomes clear, why the geostrophic wind on the Southern Hemisphere is less disturbed. This difference in the PWA of the two hemispheres explains the finding that the ozone hole in the Southern Hemisphere can develop so strongly compared to the Northern Hemisphere. Stationary PW are frequently observed to interact and superimpose with each other and with travelling PW leading to strong increases of their amplitudes. When the amplitude of PW reaches a critical level they break and deposit their energy and momentum irreversibly into the surrounding atmosphere. This happens mostly in the stratosphere, as their amplitude is largest there. As a consequence the polar vortex weakens or even breaks down and comparatively warm temperatures are observed over the polar region. Such warmings effectively impede the development of an ozone hole in the Antarctic region where the polar vortex traps ozone-poor air masses. As

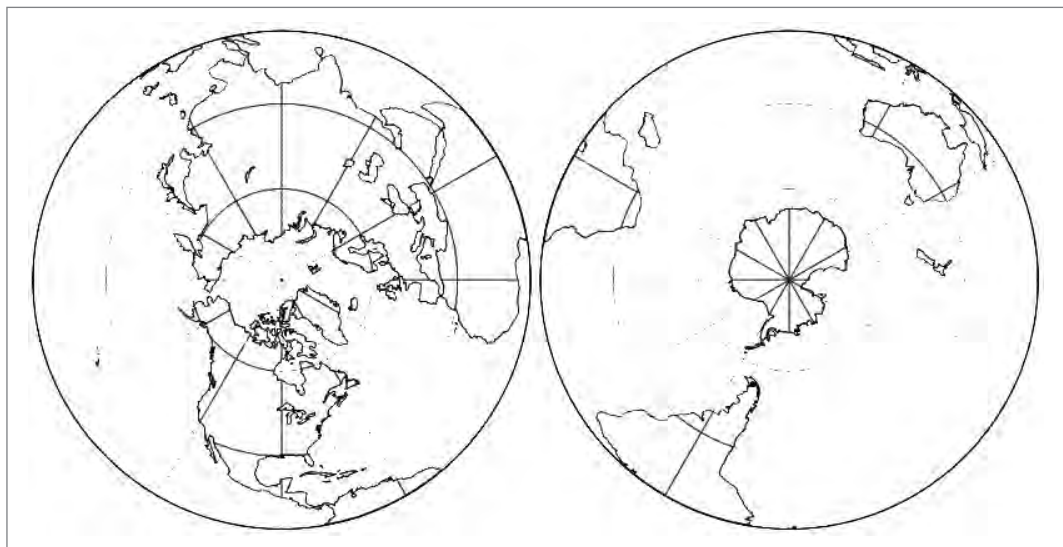


Fig. 2: Differences in distribution of land masses on northern (left) and southern hemisphere (right) lead to systematic differences in the excitation of PW. Map created with panoply by NASA <https://www.giss.nasa.gov/tools/panoply/credits.html>.

Scherhag (1958) discovered this phenomenon in 1952 above Berlin, it first was called “Berliner Phänomen”. Later, as it became clear, that the whole northern high latitudes are impacted, it was called “sudden stratospheric warming events” (SSW).

The basic concepts of PW can already be introduced by using strongly simplifying concepts such as considering an incompressible atmosphere, neglecting divergence and non-linear processes. PW can be described more realistic when the atmosphere is allowed to be baroclinic. In this case, isobars and isotherms are no longer parallel and the atmosphere is not free of divergence anymore. If the isobars are narrowing (widening), the flow must then accelerate (decelerate). Otherwise convergence (divergence) is observed.

In the mid-latitudes the meridional gradient of temperature is steepest. As a rule of thumb the atmosphere becomes baroclinic at a critical level of about 6 K per 1000 km, under dry adiabatic conditions (3.5 K per 1000 km humid adiabatic conditions) (Fortrak 1971). As already mentioned, the area of the isobars intersects the area of the isothermals. At the intersection, where pressure equals density, a rotating compensation current establishes. Due to these large-scale rotating currents so-called baroclinic PW can be generated. The disturbance originates spontaneously and does not require a vertical movement as described by barotropic waves. The description of PW within a baroclinic atmosphere considers also waves that are likely to travel along the circles of latitude. That means they change their phase in relation to the surface. Their amplitudes are generally smaller compared to the stationary waves and they usually have higher wavenumbers.

As mentioned above the mean flow is usually disturbed by a whole spectrum of PW. However, all waves superimpose and interact. The sum of all these PW describes the state of the atmosphere at mid-latitudes very well.

Atmospheric dynamics can be described by the fundamental equations of fluid-dynamics. The so-called “primitive equations” describe the complex motions in the atmosphere over a large spatio-temporal range of scales and include PW. The solution of the equations of motions leads to the dispersion relation which allows insight into the characteristic features of PW.

In the following PW are described in a barotropic, divergence-free atmosphere. Despite these restrictive assumptions many basic features of PW can be described quite well.

Newton’s second law, applied to a continuous fluid, results in the Navier-Stokes-Equation (Andrews 2010). This equation describes the conservation of momentum. The Navier-Stokes-Equation in its simplest form is described in the inertial frame of reference. This is a coordinate system at rest. Here, Newton’s law of inertia, $F = m \cdot a$ holds, giving:

$$\frac{d\vec{u}}{dt} = \underbrace{-\frac{1}{\rho}\vec{\nabla}p}_1 + \underbrace{\frac{\eta}{\rho}\left[\vec{\nabla}^2\vec{u} + \frac{1}{3}\vec{\nabla}(\vec{\nabla}\cdot\vec{u})\right]}_2 - \underbrace{g\hat{k}}_3 \quad (4)$$

Whereas \vec{u} describes the wind velocity, p the pressure, ρ the density, η the viscosity, g the acceleration of gravity and t the time. External forcings on the fluid, such as the pressure gradient force (1), the frictional force (2) and the gravitational acceleration (3) are considered therein over time.

For convenience, the equations are usually adapted to a reference system fixed to the rotating Earth. Frictional forcings are neglected in the following as large-scale motions are considered.

$$\frac{d\vec{u}}{dt} = -\frac{1}{\rho}\vec{\nabla}p - g\hat{k} - \underbrace{\vec{\Omega} \times (\vec{\Omega} \times \vec{r})}_4 - \underbrace{2\vec{\Omega} \times \vec{u}}_5 \quad (5)$$

Due to the rotation of the reference system pseudo forces such as the centrifugal force (4) and the Coriolis force (5) do now appear. $\vec{\Omega}$ represents the Earth’s angular velocity.

The Navier-Stokes-Equation in three dimensions contains five unknown quantities (zonal, meridional and vertical wind component, pressure and density). The system of equations is under-determined. Therefore, mass and energy conservation are taken into account.

As we assume the atmosphere being non-divergent the inflow must equal the outflow. The mass balance of inflow and outflow can be described by the continuity equation:

$$\frac{\partial\rho}{\partial t} + \vec{u}(\vec{\nabla}\rho) + \rho(\vec{\nabla}\cdot\vec{u}) = 0 \quad (6)$$

The first law of thermodynamics is an alternative formulation of the conservation of energy.

$$\frac{\partial p}{\partial t} + \vec{u} \cdot (\vec{\nabla} p) = \frac{c_p}{c_v} RT \left[\frac{\partial \rho}{\partial t} + \vec{u} \cdot (\vec{\nabla} \rho) \right] \quad (7)$$

R describes the universal gas constant, T temperature and c_v (c_p) the specific heat capacity at constant volume (pressure).

The abovementioned system of differential equations (5–7) is non-linear. No analytical solution can be given. Following Laplace, the system of differential equations can be linearized with the perturbation theorem after Laplace assuming that a slowly varying background is superimposed by comparatively small perturbations.

$$\vec{u} = \vec{u}_0 + \vec{u}'; \quad p = p_0 + p'; \quad \rho = \rho_0 + \rho' \quad (8)$$

The variables indicated with the index zero describe the background state, and those with the apostrophe describe the perturbation. As the perturbation is assumed to be very small in relation to the ground state the products of the non-linear perturbations become negligible. As a result the following linear differential system of equations is achieved:

$$\text{Navier-Stokes equation} \quad \frac{\partial \vec{u}'}{\partial t} + (\vec{u}_0 \vec{\nabla}) \vec{u}' = -\frac{1}{\rho_0} \vec{\nabla} p' - \frac{\rho'}{\rho_0} g \hat{k} - 2(\vec{\Omega} \times \vec{u}') \quad (9)$$

$$\text{Mass conservation} \quad \frac{\partial \rho'}{\partial t} + (\vec{u}_0 \vec{\nabla}) \rho' + \rho_0 (\vec{\nabla} \cdot \vec{u}') + w' \frac{\partial \rho_0}{\partial z} = 0 \quad (10)$$

$$\text{Energy conservation} \quad \frac{\partial p'}{\partial t} + (\vec{u}_0 \vec{\nabla}) p' + w' \frac{\partial p_0}{\partial z} = \frac{c_p}{c_v} RT_0 \left[\frac{\partial \rho'}{\partial t} + (\vec{u}_0 \vec{\nabla}) \rho' + w' \frac{\partial \rho_0}{\partial z} \right] \quad (11)$$

These equations form the basis of atmospheric circulation motions. After introducing some further assumptions, as for example an isothermal atmosphere, it can be shown that the equation system then can be solved for the variables Φ with the approach of a plane wave

$$\Phi = \Phi_0 e^{i(\mu_1 x + \mu_2 y + \mu_3 z - \omega t)} \quad (12)$$

Introducing this solution into the equation system yields a rather complex “dispersion relation”. Neglecting smaller scale dynamics such as atmospheric sound waves or gravity waves finally leads to the dispersion relation of PW (see Andrews 2010 for a more detailed description):

$$\frac{\sigma}{\mu_1} = - \frac{\beta}{\mu_1^2 + \mu_2^2 + \frac{f_0^2}{N^2} (\mu_3^2 + E^2)} \quad (13)$$

It is: $\beta = \frac{\partial f}{\partial y}$ the rate at which the Coriolis parameter f increases northward with $f = f_0 + \beta y$ (“Beta-plane-approximation”)

σ is the “intrinsic frequency”: The frequency $\sigma = \omega - u_0 \mu_1$ (14). Therein, σ is thus the frequency observed when moving with the zonal mean flow. It is called “intrinsic frequency”. If the zonal mean flow u_0 vanishes, σ equals ω .

μ_i is the wavenumber in zonal ($i = 1$), meridional ($i = 2$) and vertical ($i = 3$) direction

N means the “Brunt-Väisälä frequency”:

$$N^2 = -g \left(\frac{1}{\rho_0} \frac{\partial \rho_0}{\partial z} + \frac{g}{c_s^2} \right) \quad (15)$$

E represents the Eckard coefficient which is $E = \frac{g}{c_s^2} + \frac{1}{2} \frac{1}{\rho_0} \frac{\partial \rho_0}{\partial z}$ with c_s , the speed of sound.

Equation (13) already describes fundamental characteristics of large-scale PW in the atmosphere as it combines their temporal and spatial dimensions.

The zonal phase velocity is given by

$$c = \frac{\omega}{\mu_1} \quad (16)$$

Considering the definition of the intrinsic frequency (14) and considering only two dimensional horizontal waves the phase velocity of PW can be approximated from equation (13) by

$$c = u_0 - \frac{\beta}{\mu_1^2 + \mu_2^2} \quad (17)$$

It becomes clear, that the phase velocity of PW is dependent from β . As the Coriolis parameter increases with latitude, the phase velocity of PW increases accordingly.

Restricted to one dimension, equation (17) simplifies into

$$\begin{aligned} c &= u_0 - \frac{\beta}{\mu_1^2} & (18) \\ \Leftrightarrow u_0 - c &> 0 \\ \Leftrightarrow c &< u_0 \end{aligned}$$

first given by Rossby et al. (1939), clearly revealing some further basic features of PW:

PW obviously propagate westward in relation to the mean flow u_0 . Assuming a stationary planetary wave, $c = 0$, yields from equation (18):

$$u_0 = \frac{\beta}{\mu_1^2} = \frac{\beta \lambda_1^2}{4\pi^2} \quad (20)$$

The wavelength of stationary waves can be written as

$$\lambda_1 = 2\pi \sqrt{\frac{u_0}{\beta}} \quad (21)$$

If we consider the zonal mean flow being $10 \frac{\text{m}}{\text{s}}$, the wavelength of a stationary planetary wave at 45°N ($\beta = 1,6 \cdot 10^{-11}$) for westward propagating waves must be larger than 4980 km. Waves with shorter wavelengths then propagate eastward. In the mid-latitudes the mean phase velocity of non-stationary, travelling waves varies around six degrees in longitude per day to the east. A wave with exactly this wavelength does neither propagate westward nor eastward. This wavelength so describes stationary waves at 45° .

If PW propagate vertically, their amplitude will increase exponentially as long as energy is conserved. The reason is the exponential decrease of density with height. PW are likely to break in the stratosphere due to the strong amplification of the amplitude. As a consequence, energy and momentum is dissipated into the surrounding atmosphere. This leads to increasing temperatures, modulation of the mean current and in extreme, a reverse of the circulation (SSW). Therefore, PW play the mayor role in the circulation of the stratosphere.

It follows from equation (20) that stationary waves can only propagate vertically under westerly wind conditions. These propagation conditions were first described by Charney & Drazin (1961).

$$0 < u_0 < u_{\text{crit}} \quad \text{within} \quad u_{\text{crit}} = \frac{\beta}{\mu_1^2 + \mu_2^2} \quad (21)$$

In the troposphere westerlies are dominant during the whole year. Wave propagation up to the stratosphere is dependent from the season. The prevailing easterlies in the stratosphere summer inhibit the vertical propagation of stationary PW. During winter PW can propagate under westerly wind conditions. This annual difference leads to a strong yearly cycle in the wave activity. Moreover, the vertical propagation is restricted dependent from the wavenumbers, if the wind reaches the critical wind velocity. Considering horizontal motions under barotropic and divergence free conditions ($\mu_2^2 = 0$), the indirect dependence of the zonal wavenumber with the critical wind velocity becomes clear. The higher the zonal wavenumber, the smaller the restricting wind velocity. Considering higher altitudes the wind velocity increases steadily up to ~ 15 km in the mid-latitudes. The Jetstream inhibits waves with high wavenumbers from propagating into the stratosphere. Therefore, the wavenumbers most dominant in the stratosphere are one, two and three (see Fig. 3).

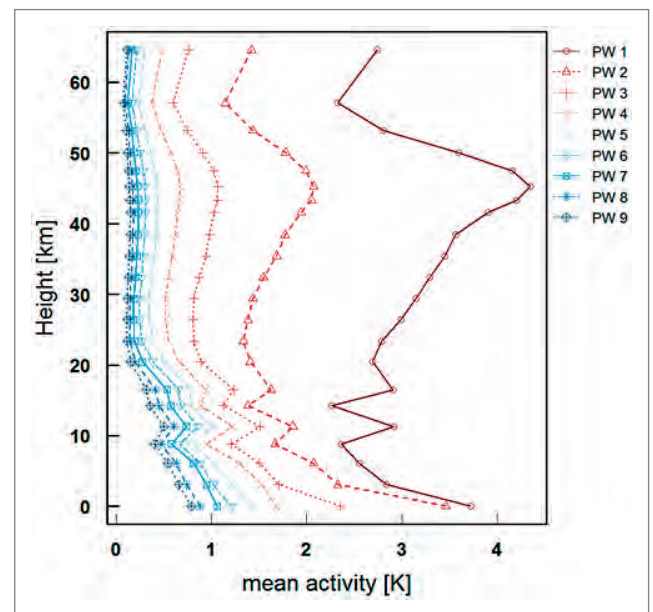


Fig. 3: The yearly mean PWA (DAI) for PW1 to PW9 from 10 m up to 65 km height derived of ERA-Interim temperature from 1979 until 2018 between 0° and 90°N . For the description of the calculation of the DAI see details in text.

10.2 Long-term changes of PW

10.2.1 Possible impacts of Arctic amplification to atmospheric circulation

The temperature at the Arctic increases twice as much as the global mean (Serreze et al. 2009) leading to a weakening of the meridional temperature gradient between the equator and the North Pole. This phenomenon is known as „Arctic amplification“ and is observed since the 90s during all seasons, but strongest in winter (Cohen et al. 2014). Following Cohen et al. (2014) and references therein, there are several processes induced by climate change that contribute to warming of the Arctic. One major contribution are radiative effects due to greenhouse gas forcing. An additional forcing effect is caused by the deposition of black carbon on snow and ice surfaces which leads to a reduction of the albedo. This, in turn, changes cryosphere, cloud cover, and water vapor. As a result, all such effects, which cause a stronger absorption of radiation induce positive feedbacks, amplifying the Arctic warming.

Arctic amplification is often associated with mid-latitude extreme weather events. The mechanism Francis & Vavrus (2012) propose can briefly be described as follows: The meridional temperature gradient between the North Pole and the equator weakens due to the abovementioned processes. Following the thermal wind equation (eq. 22) a change in the meridional temperature gradient results in a change of the vertical wind shear:

$$-f \frac{\partial u}{\partial z} = -\frac{g}{T} \frac{\partial T}{\partial y} \quad (22)$$

where u is the zonal mean flow, T is temperature and f the Coriolis parameter, g is the gravitational acceleration. In the troposphere where $\frac{\partial T}{\partial y} < 0$, the zonal mean flow, known as geostrophic wind, is hence accelerating in general with height. If the meridional temperature gradient weakens, the mean wind velocity of the zonal mean flow will be reduced. As a result of equation 21 the PWA may increase. The slower Jet stream is expected to meander stronger; meridional air flow components with cooler temperatures from the north and warmer temperatures from the south into the mid-latitudes, should be established more often. However, Barnes & Screen (2015) indicate, that the underlying processes are rather complex and not fully understood, yet. The question to what extent Arctic warming can impact midlatitude weather patterns is therefore subject to current research.

Francis and Vavrus (2012) showed that the zonal mean wind in the troposphere at 500 hPa height decelerated for about 4 m/s in winter (December, January, February) in a selected region (40°–60° N, 140°–0° W). As the change of the wind velocity of a specific region might be induced by a systematic change of pressure cells, the observed change of the wind velocity has to be regarded with caution in this context. Up to now, observational data cannot clearly confirm a weakening of the zonal component of the Jet in the upper troposphere (Cohen et al 2014). Moreover, Allen & Sherwood (2008) showed that the meridional temperature gradient actually has strengthened in the upper troposphere / lower stratosphere. In this altitude this would lead to an acceleration of the mean current and stands in direct contrast to considerations of the lower troposphere. Kozubek et al (2017) analysed zonal wind trends for the winter season (October–March) at 10 hPa from MERRA, ERA-Interim, NCEP/NCAR and JRA-55 reanalyses and found that there is no clear systematic trend in northern mid-latitudes. They find that trends can be positive or negative, depending on longitude along one latitude circle. They indicate that especially the change of ozone also has a clear impact on trends. This is because ozone strongly contributes to atmospheric heating and cooling rates. Overall, it turns out that the effects of the Arctic warming on the zonal wind component are still not fully understood and the stratosphere has to be taken into account as well.

As Arctic Amplification is often linked to an increase of extreme weather events, their occurrence frequency and / or intensity should have changed. An important point, that makes an objective trend analysis of extreme weather difficult is, that there does not exist a general definition of extreme weather events. Grotjahn et al. 2016 give an overview of different definitions taking into account aspects like the spatial extend of the region impacted as well as the

duration of each event in various ways. Comparisons between single studies of extreme weather events therefore have to be regarded with respect of the underlying definition of extreme events. Nevertheless, it is generally conceivable that the probability of extreme weather events is enhanced due to Arctic warming, as it is discussed by Screen and Simmonds (2014) or Francis and Vavrus (2012). As a conceivable mechanism they propose PW as the “missing link” between extreme weather events and Arctic amplification. There are numerous articles showing that high amplitudes of PW in the troposphere can induce extreme weather events (Mann et al. 2017, Kornhuber et al 2017, Kidston et al. 2015, Coumou et al. 2014, Pethoukov et al. 2013). In general it is concluded that high amplitudes are the result of resonant amplification. If so, this means: if extreme weather events had increased, the mean PWA should then have also increased. Screen & Simmonds (2013), however, stress that the PWA of waves six to eight derived by ERA-Interim in 500 hPa does not increase significant within 1979 until 2011. Also Barnes (2013) revisits the evidence of linking stronger meanders of the Jet due to enhanced PWA to extreme events. She shows that trends cannot properly be discriminated from artifact due to the analysis methodology and are therefore regarded to be inconclusive. Obviously, detecting trends of PWA in the troposphere seems to be a challenge so far.

In addition to the possible changes in atmospheric dynamics in the troposphere, it is becoming increasingly clear that consideration of the processes in the stratosphere is very important. Especially during winter, when PW can propagate up to the stratosphere, the stratospheric polar night Jet can sustainably be strengthened or weakened due to wave dissipation. Kidston et al (2015) introduce a possible mechanism for the downward influence from the stratosphere into the troposphere. At least, a strengthening of the Jet stream in the stratosphere leads to a poleward shift of the tropospheric Jet and therewith a change of storm tracks. A weakening of the stratospheric Jet leads to a higher probability of cold air outbreaks in northern Europe and North America, as also observed by Mitchell et al. (2013). Nakamura et al (2016) confirm that weak stratospheric vortex events lead to severe winter weather events in the Northern Hemisphere. Weak vortex events are often related to stratospheric warming events (described above). There are numerous studies dealing with the relation of stratospheric warming events and related changes in tropospheric weather, as for example Runde et al (2016), Mitchell et al (2013), Kodera et al. (2011) or Julian & Labitzke (1965).

There is obviously broad agreement, that the Arctic amplification might sustainably change atmospheric dynamic of the mid-latitudes. Nevertheless, the question about the details of the physical mechanism linking the Arctic amplification, changes of PWA and at least their impact on the extent of extreme weather events is yet under debate.

10.2.2 Trends of PW

Although there are various open questions, if and how Arctic amplification induces a change in atmospheric dynamics in the mid-latitudes, the question remains the same: has the atmospheric dynamic already changed?

There are various indices representing the PWA. A very common used diagnostic is for example the so called “eliassen-palm flux (EP flux)” introduced by Edmon et al (1980). In our work we use the so called “Dynamical Activity Index” (DAI) first introduced by Bittner et al. (1997) as a rather simple proxy for PWA. The data we used is based on temperatures from ERA-Interim Reanalysis and hydroxyl (OH) rotational temperatures derived from atmospheric airglow emissions originated at about 87 km height. The airglow measurements are described in detail by Schmidt et al. 2013 and Schmidt et al (Chapter 14).

ERA-Interim is a global database of meteorological parameters (see chapter 12) provided by the European Centre for Medium Range Weather Forecasts (ECMWF). The temperature dataset is equidistantly gridded with 0.75° spatial resolution. Four time steps (0, 6, 12, 18 UTC) are available for one day. Detailed information about ERA-Interim is given by Dee et al. (2011). The dataset covers the period from 1st January 1979 onwards. In this work we consider the time period from 1st January 1979 until 31st December 2018. The DAI is derived for 22 height levels of the ERA-Interim data set, which are separated from one another by about 3 km intervals. The DAI thus covers an altitude range between ground level and about 65 km height.

Rotational temperatures of upper mesosphere OH*(3,1) Meinel-band-emissions are near to the kinetic temperature of the atmosphere and are used in this study to cover higher altitudes in the atmosphere. The measurements by GRIPS represent the height regime at about 85–87 km with a full width at half maximum of ca. 6–9 km (e. g., Wüst et al. 2017). They are conducted by means of ground-based observations as they are part of the Network for the Detection of Mesospheric Change (NDMC). Nocturnal mean temperatures obtained above Wuppertal (51.52°N, 7.51°E), Oberpfaffenhofen (48.09°N, 11.28°E) and Schneefernerhaus (47.42°N, 10.8°E) are used from 1987–2018. A detailed description of these measurements is available in this book by Schmidt et al. and will therefore not be given here.

The calculation of the DAI is based on a well-established least-square approach, called harmonic analysis which is described in detail in Bittner et al. (1994, 2000). In order to estimate PW signatures the reanalysis temperature data, the zonally mean temperature at each circle of latitude is formed and then subtracted from the temperatures at each longitude. A linear combination of nine sinusoidals is then fitted consecutively to the temperature residuals along each circle of latitude Φ separately:

$$T'(\lambda)_{|\Phi,t} = \left[\sum_{i=1}^n A_i \sin\left(\frac{2\pi}{\lambda_i} \lambda + \varphi_i\right) \right]_{|\Phi,t} \quad (23)$$

$T'(\lambda)_{|\Phi}$ is the value of the temperature fluctuation at a specific geographical longitude λ for a fixed latitude Φ . A_i is the amplitude and φ_i is the phase of the i^{th} sinusoidal. In order to fit PW with zonal wave numbers 1 to 9 (planetary wave 1 to 9), the sinusoidal of $\lambda_1 = 360^\circ$, $\lambda_2 = 180^\circ$, $\lambda_3 = 120^\circ$, $\lambda_4 = 90^\circ$, $\lambda_5 = 72^\circ$, $\lambda_6 = 60^\circ$, $\lambda_7 = 51.5^\circ$, $\lambda_8 = 45^\circ$, $\lambda_9 = 40^\circ$ are consecutively fitted to temperature data.

As the sinusoidals are fitted consecutively to the data series the fit is equal, from a mathematical point of view, to a consecutive deconvolution of the spectrum. In order to achieve the best approximation in a least squares sense, it turned out that the approximation can be improved when all fitted sinusoidals are re-adjusted simultaneously in each step to provide the best fit. In other words: when the i^{th} sinusoidal is being fitted to the data series the preceding sinusoidals are re-adjusted simultaneously. This procedure is performed for each circle of latitude and has proven to perform very good and rather stable.

The amplitudes of the individual sinusoidals λ_i are then interpreted as being a good proxy for the planetary wave zonal numbers “ i ”. The mean amplitude of each zonal wave mode taken for all northern hemispheric latitudes serves as a measure for the integrated PWA (DAI). The DAI has proven to be useful and was therefore adapted as a key diagnostic in order to compare hemispheric ozone variability indices derived from satellite observations to a coupled chemistry-climate model (Erbertseder et al., 2006).

The time series of the monthly DAI of the zonal wave number one to nine is calculated for all available height levels from ground up to about 65 km for the time period from 1st January 1979 until 31st December 2018.

Figure 4 shows exemplarily the comparison between the global ERA-Interim temperature in 45 km height 2nd December 2014 and the reconstruction from nine zonal sinusoidals. Figure 5 gives the difference between the underlying ERA-Interim temperature field and the reconstruction, taking into account only zonal wave number one (Fig. 5, top), taking into account zonal wavenumbers 1–5 (Fig. 5, middle) or taking into account zonal wavenumbers 1–9 (Fig. 5, bottom). As expected, we find the low zonal wavenumbers (typically 1–5) as the dominant disturbances.

The approach described above holds for spatio-temporal data, that is the ERA-Interim data set. In order to estimate the PWA from the abovementioned airglow observations, that is data obtained at a single location only, we used another index, calculated following the approach described by Höppner & Bittner 2007. We updated the time series given in Höppner & Bittner (2007) with measurements at Schneefernerhaus (see Fig. 7, top). It becomes clear, that the PWA is modulated on different time scales. The variability of the PWA will be discussed later in greater detail.

To analyze changes in the DAI, it is helpful to distinguish between variability and trend. We consider variability as being a variation around a certain mean state of the atmosphere. Whereas a trend is then the long-term change that cannot be explained by a periodic oscillation – at least on the regarded temporal time scales. The simplest approach to estimate a trend is to fit

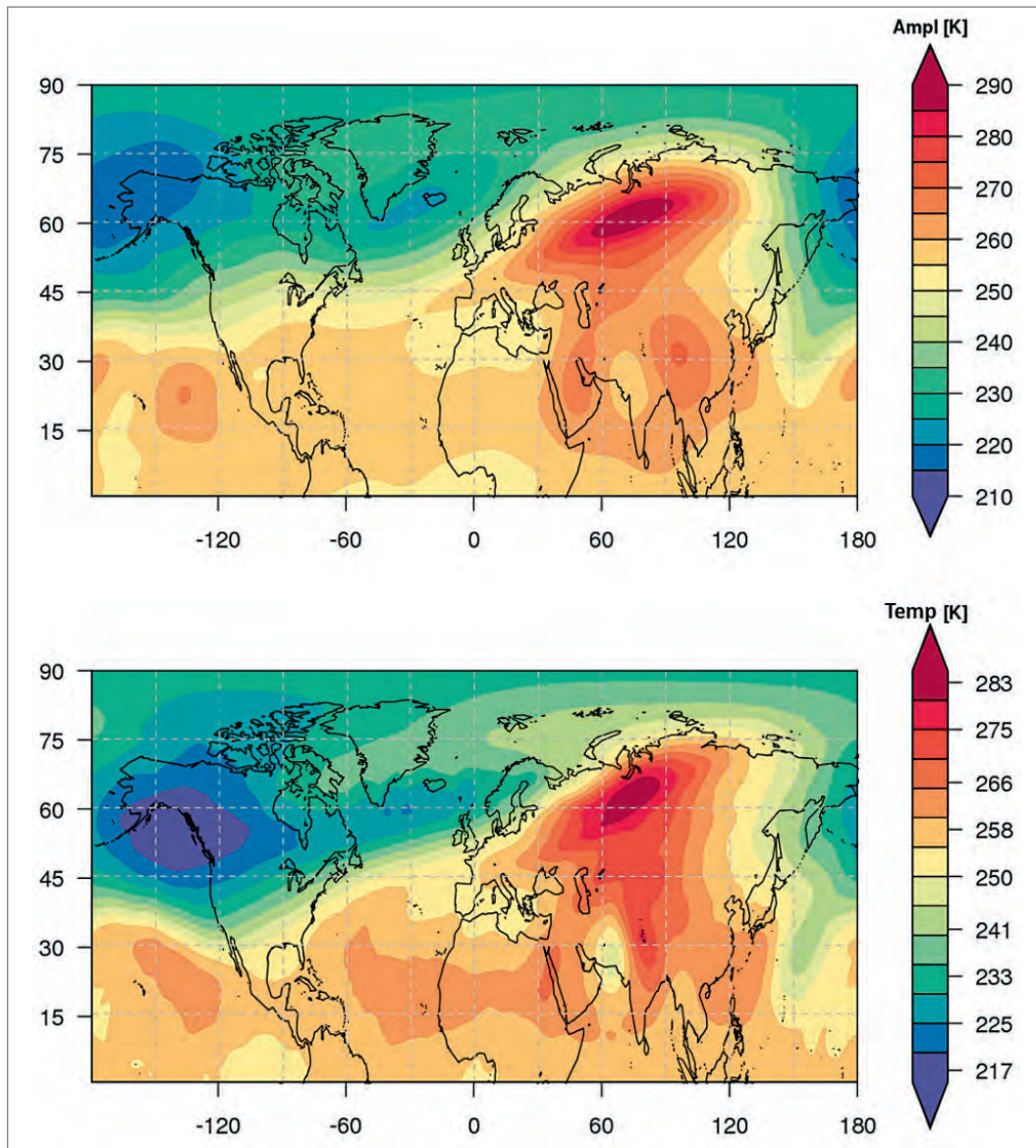


Fig. 4: The linear combination of the fitted sinusoids (PW 1 to 9) (top) represent the large-scale temperature pattern (bottom) on 2nd December 2014 in 45 km height quite reasonable.

a straight line to the time series. The slope m of the linear regression gives the rate of increase or decrease of the considered parameter.

The temporal evolution of the PWA can then be split into the following terms:

$$DAI(t) = \overline{DAI} + m \cdot t + \sum_{i=1}^n A_i \cdot \sin\left(\frac{2\pi}{T_i} \cdot t - \varphi_i\right) + \varepsilon(t) \quad (24)$$

\overline{DAI} represents the mean PWA

$$\overline{DAI} = \frac{1}{n} \sum_{i=1}^n DAI_i \quad (25)$$

onto which the linear trend, various periodic variabilities and a noise term $\varepsilon(t)$, considering for example effects due to volcanic eruptions, are added.

Analyzing the yearly mean of the DAI with a linear trend analysis for all available heights indicates significant increases of the PWA in the stratosphere. In contrast to this we do not find any significant trends of the DAI at lower altitudes (below about 25 km). The strongest increases are found in the upper stratosphere around 45 km. At all heights, PW 1 shows the largest absolute increase, PW 9 the smallest.

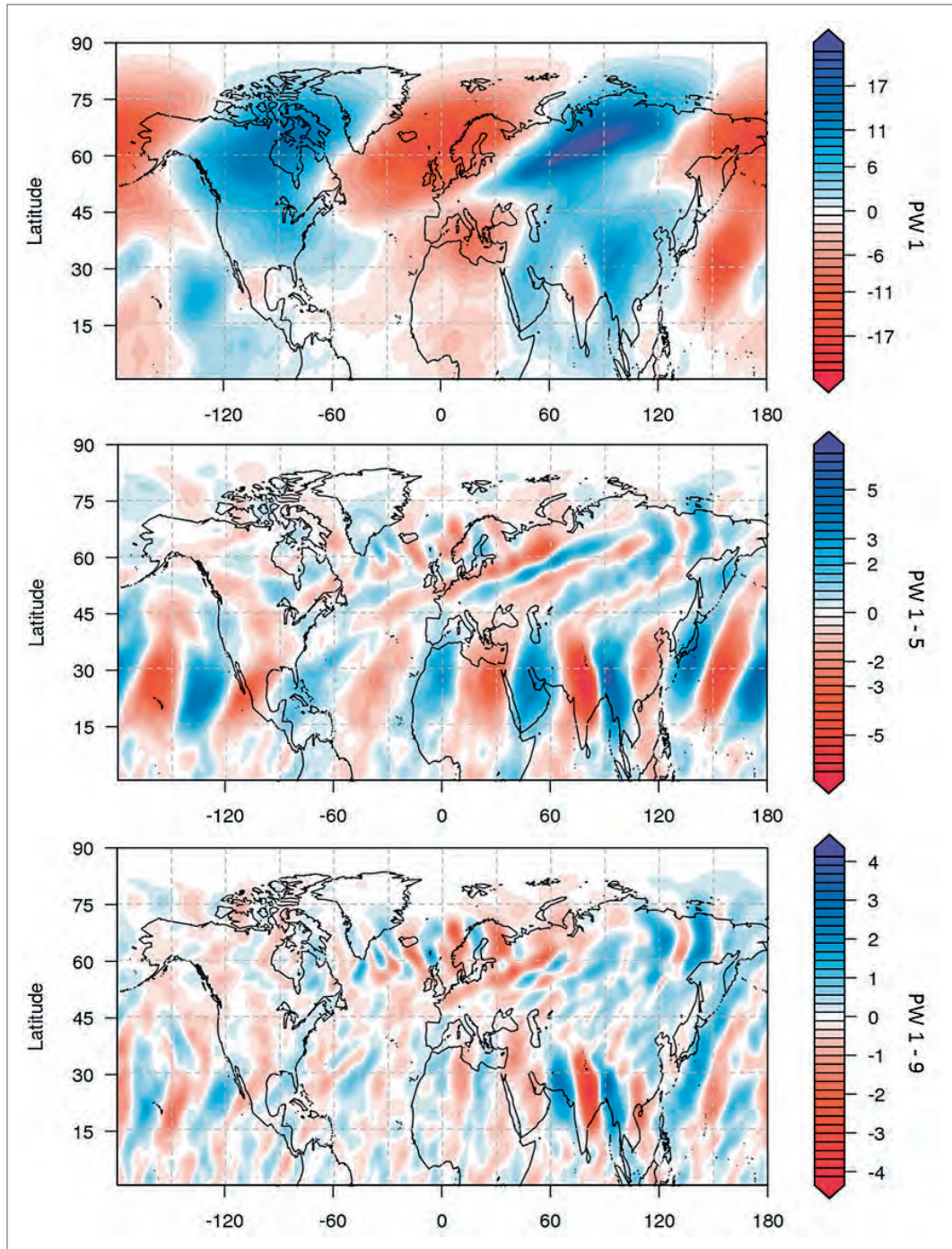


Fig. 5: Difference of ERA-Interim temperature at 45 km height for 2nd December 2014 and the respective temperatures derived from the linear combination of the fitted sinusoidals. The figure on top takes into account the fit of PW 1 only, the figure in the middle PW 1 to 5, the figure at the bottom PW 1 to 9. At most days and heights the superposition of PW 1 to 5 can be regarded as a good proxy for the dynamics in the Northern Hemisphere.

Considering the relative trend, the DAI also does not show any changes below about 25 km (see Fig. 6). Above 15 km the PWA of PW 1 to 9 strongly increases up to 30% in 40–50 km. Here, PW 9 increases most (30%), PW 1 and 2 (20%) least in their activity. The PWA of PW with higher wavenumbers obviously changes stronger in the stratosphere than the PWA of PW with lower wave numbers. Above ca. 45 km height the increase of PWA slightly weakens for all waves.

We estimated the statistical significance by the signal-to-noise ratio (S/N). It gives the deviations of the data to the calculated trend in comparison to the standard deviation of the dataset.

$$S/N = \frac{\text{trend}_n - \text{trend}_1}{\sigma} \quad (26)$$

The variable trend represents the fitted regression function of the time series. Here, trend_1 is the value of the regression for the first data point, trend_n is the value of the regression for the last data point. The standard deviation σ is given by:

$$\sigma = \sqrt{\frac{\sum_{i=1}^n (\text{DAI}_i - \overline{\text{DAI}})^2}{n-1}} \quad (27)$$

Up to an altitude of about 25 km the PWA does not change significantly with respect to the signal-to-noise ratio (see Fig. 7). At a height of about 30 km the change of PW 1 and PW 2 becomes significant at a confidence level of 85%. All waves with higher wavenumber even exceed a confidence level of 95%. Above 40 km the change of PW 4 to 9 becomes very significant (> 99%), whereas the relative change of PW with highest wavenumbers is most significant.

According to these results, we can conclude that the yearly PWA obviously has changed during the last 37 years. This is in agreement with what we would expect when the zonal wind changes due to a change of the meridional temperature gradient, as discussed above. If we assume that PW are generated in the troposphere, a reduced tropospheric wind velocity shall affect PW with high wavenumbers most, because they are already filtered by the wind. If the wind decelerates, the propagation conditions for these waves will improve. Such a change does not affect the waves with smaller zonal wavenumbers in the same extent, because they can propagate even if wind velocities are stronger.

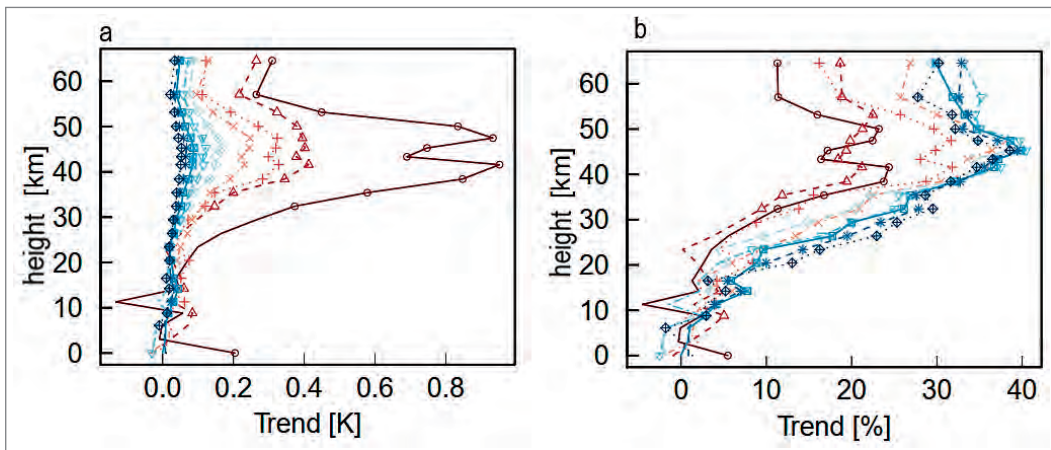


Fig. 6: Linear change in the PWA of PW1 to 9 in Kelvin from 10 m to 65 km in the northern hemisphere. The absolute change in Kelvin for the entire period 1979–2018 (left), the relative change based on the mean of the time series of each wavenumber and height (right). Legend as Fig. 3.

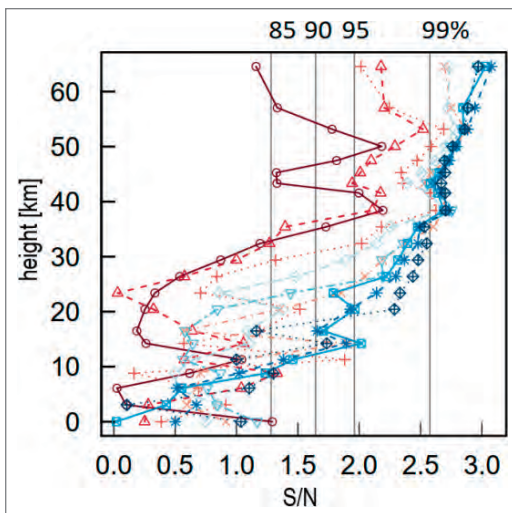


Fig. 7: Signal-to-noise ratio of the linear trend of the yearly PWA (PW 1 to 9) based on ERA-Interim data DAI for the temporal period from 1st January 1979 until 31st December 2018. Vertical lines indicate the confidence levels of 85%, 90%, 95% and 99% (left to right). The change of the PWA of PW with smaller wavenumbers is most significant, reaching more than 99% above about 35 km. The change of the PWA 1 and 2 is still significant in the upper stratosphere, but at a lower confidence level (>80–90%). Above 50 km significances decrease, except for PW 7–9. Legend as Fig. 3.

10.2.3 Variability of PW

Following equation (24), the variability of our PWA index is determined by more effects than just the linear trend. Particularly oscillations on different temporal scales can also impact the trend. Therefore, it is mandatory to extract such periodic oscillations from the time series. Spectral analysis in atmospheric sciences is often used to disassemble a time series into different spectral components, which means to quantify the spectrum of frequencies / periods. Some fundamental aspects related to the spectral analysis of our time series will be briefly outlined below.

Most spectral analysis tools assume statistical stationarity over the whole time series. This means that at least the first three statistical momentums mean (eq. 25), variance (eq. 26), skewness are constant over time.

$$Skew = \frac{1}{n} \sum_{i=1}^n \left[\frac{DAI_i - \overline{DAI}}{\sigma} \right]^3 \quad (28)$$

In the case of our time series of the PWA this would mean, that amplitude A_i , phase φ_i and period τ_i of the oscillation in equation 24 must be constant over the time series. In fact, time series of atmospheric parameters can hardly be treated as being stationary. For example Holm (2014) describes in great detail how delicate it can be to interpret spectral analysis results in terms of non-stationarity problems. Therefore, some analysis tools, as for example the wavelet analysis (Daubechies, 1992, Chui, 1992, Torrence & Compo 1998), were established. They assume stationarity only for short parts of the time series. Another method, the so-called empirical mode decomposition (EMD) method after Huang et al. (1998), does not assume stationarity at all. We made use of both methods and they are therefore briefly outlined below. A good overview about handling non-stationary time series is given in Pfaff (2008) and references therein.

To extract periodic oscillations of the DAI-time-series the so called "empirical mode decomposition method" (EMD), first introduced by Huang et al. (1998), is used. It evolves a time series into modes that are highly nonlinear and not stationary. That means amplitude and period of each mode can vary over time. The modes are called intrinsic mode functions (IMF).

The procedure of extracting an IMF is called "sifting". In a first step all local maxima are identified and connected by a cubic spline. The same is done for all minima. The area between the two splines covers all data points. The mean values are calculated for both splines for all locations of the x-axis. These means are subtracted from the original data. In a further step the same analysis is done until the mean values approximate zero and no further analysis run improves the result. The first IMF is defined. The IMF is then subtracted from the input data. The shifting procedure is repeated for the residuals until the next IMF is defined. After subtracting the last identified IMF the residuals describe a straight curve with no further fluctuations. This procedure implies that the first IMF has always the highest frequency. The modes are not sorted by amplitude as it is common with most spectral analysis tools.

Using the abovementioned EMD the time series of the DAI is deconvoluted into three until four modes and a residual. To get an idea of the typical periods and the uncertainty interval of each single mode, a wavelet analysis is applied. A wavelet analysis is especially useful for transient signals. It resolves a time series into the temporal occurrence and intensity of a signal with a specific period. The result of the analysis can be shown with a periodogram.

The idea is to slide a distinct function that quickly approximates zero in both directions along the time series. Thereby, the function must fit at least two times in the time series. The correlation of the function and the time series gives the intensity of the present signal for a specific date.

To use the wavelet technique a Morlet-mother wavelet originally proposed by Morlet et al. (1982) is used. The wavelet transform is given by

$$S(a, b) = \frac{1}{a} \int_{-\infty}^{\infty} f(t) h\left(\frac{t-b}{a}\right) dt \quad (29)$$

where $f(t)$ is the time series under study. h represents the Morlet mother wavelet

$$Sh(t) = \frac{1}{\pi^{\frac{1}{4}}} \left(e^{ikt} - e^{-\frac{k^2}{2}} \right) e^{-\frac{t^2}{2}}, \text{ where } k = \pi \left(\frac{2}{\ln 2} \right)^{\frac{1}{2}} \quad (30)$$

a is the dilation-scale factor determining the characteristic frequency, and b is the translation in time. This wavelet has proven to work very well in numerous applications (e. g. Bittner et al., 2010; Höppner & Bittner, 2007; Wüst & Bittner, 2006; Bittner et al., 2000; Chui 1992).

We analyzed the PWA in the UMLT with the EMD (see Fig. 7). The PWA, given in the top graph, is modulated on different temporal scales. The first mode varies with a periodicity around 2 to 3 years, the second mode (IMF2) is characterized by a very non-stationary signal. As the results of the DAI indicate (described later) we interpret this mode as a combination of two quiet well-known signals, the ENSO and solar radiation. We assume, that the time series of the PWA in the UMLT is not long enough yet, to clearly spate the two signals. The third mode has a periodicity of around 22 years. The overall course follows the solar magnet field cycle of the sun (also described later). The residues indicate an increase of the PWA in the UMLT, but it is so weak, that it is not significant.

We also analyzed the DAI of the Northern Hemisphere with the EMD. The analysis deconvolutes the PWA into four modes. Each mode turned out to be characterized by a typical period which is present over nearly all heights. The modes are characterized by mean periodicities around about 2.5, 6, 11 and 20 years (see Fig. 8). The first three modes are rather prominent and are often observed in the atmosphere.

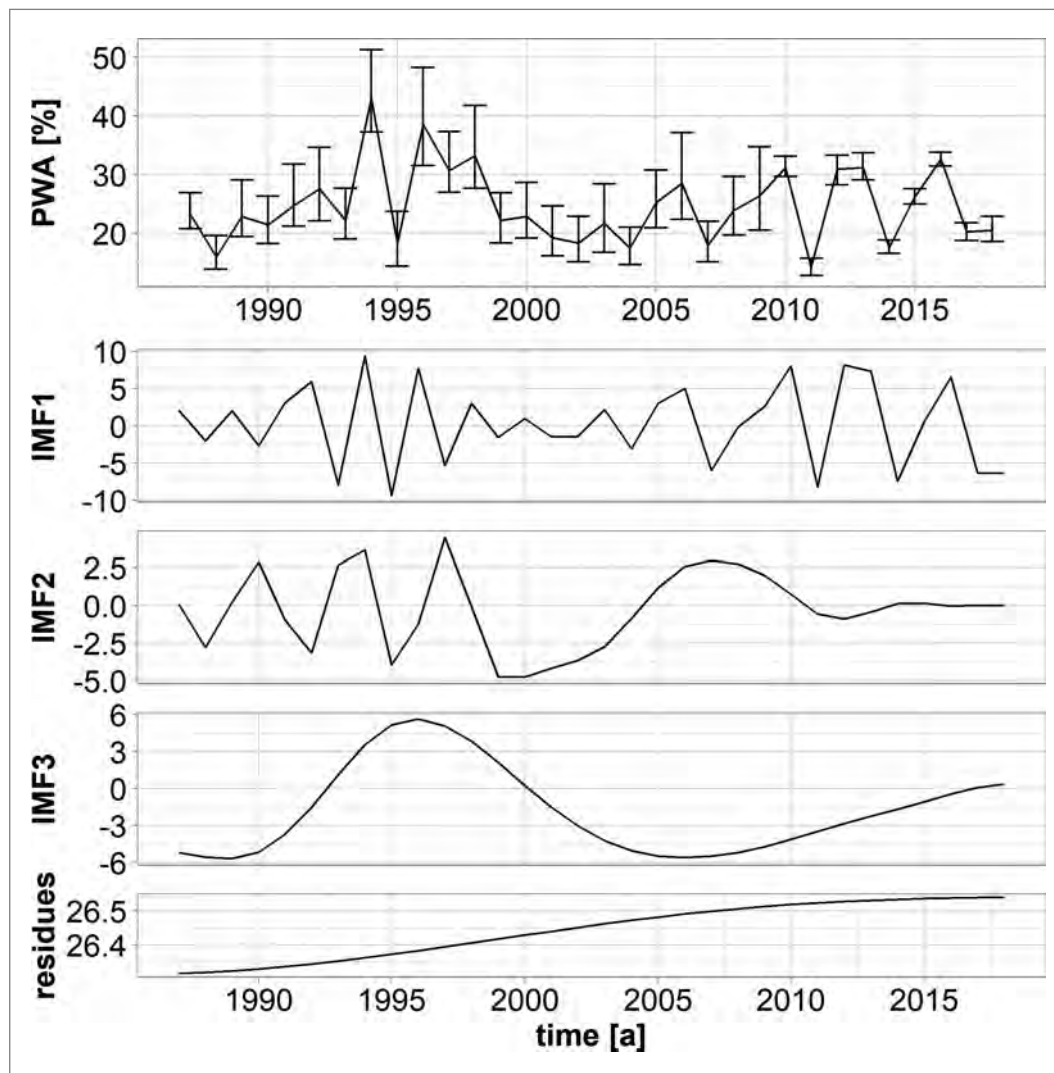


Fig. 7: PWA in the UMLT derived of GRIPS temperature measurements (top). The PWA is deconvoluted with the EMD into three modes (IMF1–3) and a residual. The units of all y-axis are all referred to the figure at the top.

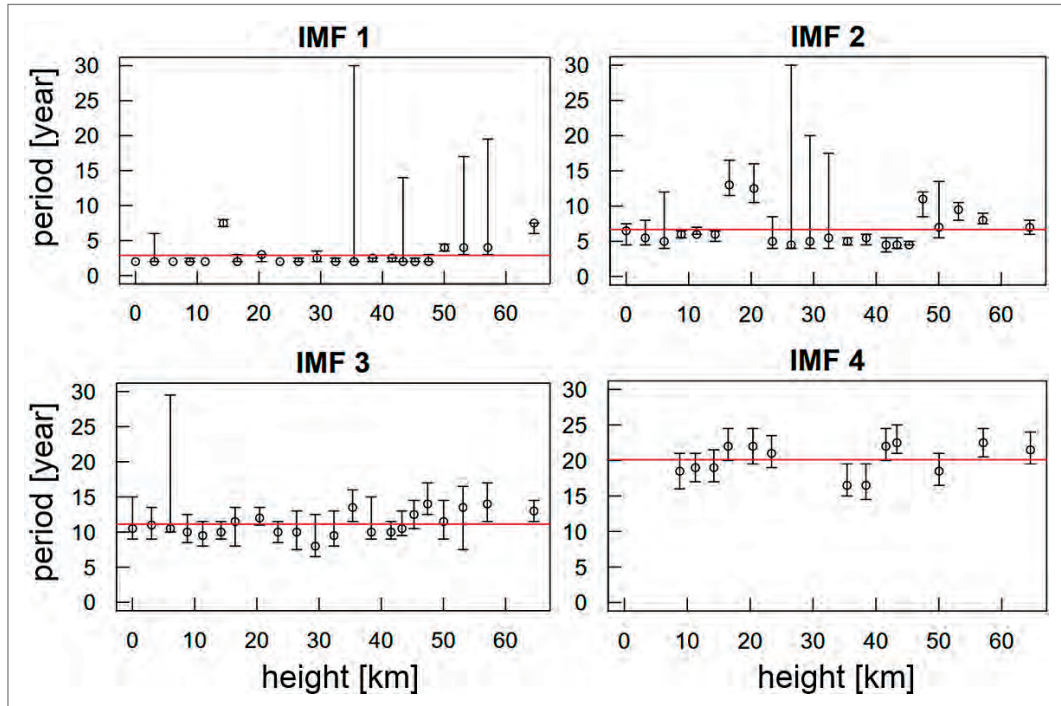


Fig. 8: Average periodicity of the extracted PWA signals as derived from station-based data with periods between 3 and 20 days from 10 m to 65 km high of the ERA interim temperature data set at grid point 11°E, 48°N.

The first mode is tentatively interpreted as being due to the so-called quasi biennial oscillation (QBO). The QBO is a rather prominent phenomenon in the atmosphere; numerous studies find the QBO to oscillate with a typical period round about 28 months (e.g. Naujokat 1986). The QBO describes the downward propagation of changing wind direction from easterlies to westerlies in the equatorial stratosphere. Although the QBO is originated at tropical latitudes, there is a significant impact onto the whole atmospheric dynamic (Baldwin et al., 2001). Holton & Tan (1980) found that an extratropical wave guide serves as a link between the easterly QBO phase, an increased stationary wave amplitude and therefore weaker polar vortex. One consequence of the link between the QBO and PW is that especially sudden stratospheric warmings occur more frequently during QBO-East phases (Labitzke 1982).

The second mode shows a typical period around about six years. We tentatively assign this signal being related to the so-called El Niño Southern Oscillation (ENSO) which is known to oscillate with a period of about six to eight years. ENSO is an oscillation located in the tropical to subtropical Pacific. It occurs due to a large-scale coupling mechanism between the atmosphere and the ocean, as described in Trenberth (1997) or Philander (1983). The temperature of the pacific varies between anomalously cold (La Niña) and anomalously warm (El Niño). ENSO seems to have direct influences on the PWA (Garfinkel & Hartmann 2008). On the one hand, Bell et al. (2009) show that general circulation models indicate a relation between El Niño events and a weak polar vortex, but only if the stratosphere is considered. PW seem to serve here as the linking mechanism. Iza et al. (2016) reported about a reduced upward PWA into the stratosphere and therefore stronger polar vortex based on reanalysis data. Li et al. (2013) were able to show the ENSO-signal even in the mesopause temperature. Although linking mechanisms are not completely understood, it is obviously not unusual that the signal of ENSO can be found in the PWA.

The modulation of the third mode shows a periodicity of eleven years as so does the intensity of the solar radiation (10.7 cm flux). There are several studies that report about the solar radiation cycle in various atmospheric parameters, as given in the review of Tsiropoula (2003). Lu et al. (2017) and references therein report that the total amount of incoming solar radiation varies only less than 0.1% in total, but some percentages in the UV spectrum. The authors point out that this leads to variations in the ozone concentration (which they quantify with about 2–4%) which then impacts the solar heating rates leading to temperature fluctuations of about 1 Kelvin. Lu et al. (2017) describe a classic mechanism for the relation between solar radiation and PW: As the tem-

perature is higher in the solar maximum, a stronger meridional temperature gradient evolves in the upper stratosphere. The equation of thermal wind (equation (22)) implies that stronger westerlies result, what leads to increased poleward wave breaking. As momentum and energy is lead to the polar the region, the polar jet stream is less disturbed and even increases. The opposite is expected during solar minimum. Moreover, also studies dealing with the temperatures in the UMLT report about the presence of this cycle (Beig 2011, 2008). It becomes clear, that the variability of solar radiation influences PW, but nevertheless, it remains still unclear, to what extent.

The period of the fourth mode is roundabout 21 years. Even though such periodicities are reported in the literature, the physical origin of this signal still remains unclear (e. g. Kalicinsky et al. 2016). Höppner & Bittner (2007) found a clear correlation between the PWA in mesopause temperatures, the solar magnetic cycle and the length of the day. In our study we updated this early analysis of Höppner & Bittner (2007) and can confirm their result on the basis of a time series which is now eleven years longer. We find a correlation between the DAI and the Hale Cycle larger than 0.7 in the UMLT. We also applied the analysis to other heights based on ERA-Interim data. The correlation remains high and statistically significant in the upper (40–50 km) and lower (20–30 km) stratosphere as well as in the troposphere. This finding therefore has to be taken serious. The question, if there is a physical mechanism that relates the Hale-cycle to the PWA needs to be addressed. If so, to what extend impacts the natural Hale-cycle the PWA? It is obvious that understanding (especially long-term) solar influences is indispensable in order to interpret the physical meaning of longer term changes or trends in PWA. Only then, longer term planetary wave variability can be adequately implemented into atmospheric and climate modelling.

Finally, we take the remark that it cannot be ensured that all oscillations are extracted yet. As the atmosphere is a highly complex system, a lot of interactions and mask effects distort signals. As soon as the time series become longer, longer oscillations can appear in the time series. This is one of the fundamental problems in climate research. The question if a trend, as a significant deviation of a certain mean state, is truly a trend is hardly to answer. Against this background, the trends introduced above should be rather regarded as tendencies. Moreover, the apparent non-stationarity of the oscillations of QBO and ENSO itself is so far unclear; it cannot be ruled out that these themselves could – at least in part – be a result of climate change; distinguishing between internal and external drives remains a very complex matter.

10.4 Summary

Of particular interest in the context of climate change is the question of whether and if so how and why the large-scale flow systems in the atmosphere change. Due to the comparatively strong temperature increase at the North Pole, a lot of studies have speculated how PW and therewith extreme weather events in the mid-latitudes might be affected.

PW are horizontal, transversal waves that contribute to the atmospheric circulation from ground level up to ~90 km height. They have their origin in the conservation of the angular momentum and can be described as meridional disturbances of the theoretical circumpolar Jetstream with the fundamental equations of fluid dynamics. PW are excited by vertical movements in the troposphere, propagate vertically and have their maximum amplitudes in the stratosphere where they lead to the meridional transport of ozone during winter. But still in the UMLT region at approximately 90 km height, signatures of PW can be found in temperature fluctuations, measured by GRIPS instruments at UFS, Schneefernerhaus.

Next to the classical approach addressing mainly the troposphere, it becomes clear, why the stratosphere and even the UMLT should be included into climate discussions. DAI shows an increase of the overall PWA during the last almost four decades, especially in the stratosphere. Not only because the atmosphere is a highly complex system, but also because it behaves non-linear. Special analysis methods are needed to deconvolute time series into non-stationary signals that can be interpreted in a further step. It turns out that the signal of the PWA is superimposed by different oscillations on different temporal scales. They can be attributed to the QBO, ENSO and solar radiation cycle. Moreover, a fourth mode with the period of about 21 years reminds strongly to the magnetic field cycle of the sun, but the physical mechanism behind is not understood yet.

References

- Andrews, D. G. (2010). *An introduction to atmospheric physics*. Cambridge University Press.
- Baldwin, M. P., Gray, L. J., Dunkerton, T. J., Hamilton, K., Haynes, P. H., Randel, W. J., ... & Jones, D. B. A. (2001). The quasi-biennial oscillation. *Reviews of Geophysics*, 39(2), 179–229.
- Barnes, E. A. (2013). Revisiting the evidence linking Arctic amplification to extreme weather in mid-latitudes. *Geophysical research letters*, 40(17), 4734–4739.
- Barnes, E. A., & Screen, J. A. (2015). The impact of Arctic warming on the midlatitude jet-stream: Can it? Has it? Will it?. *Wiley Interdisciplinary Reviews: Climate Change*, 6(3), 277–286.
- Beig, G. (2011). Long-term trends in the temperature of the mesosphere/lower thermosphere region: 2. Solar response. *Journal of Geophysical Research: Space Physics*, 116(A2).
- Beig, G., Scheer, J., Mlynczak, M. G., & Keckhut, P. (2008). Overview of the temperature response in the mesosphere and lower thermosphere to solar activity. *Reviews of Geophysics*, 46(3).
- Bell, C. J., Gray, L. J., Charlton-Perez, A. J., Joshi, M. M., & Scaife, A. A. (2009). Stratospheric communication of El Niño teleconnections to European winter. *Journal of Climate*, 22(15), 4083–4096.
- Bittner, M., Dech, S. W., & Loyola, D. (1997). Planetary scale waves in total ozone from ERS-2-GOME data. *ESA SP (Print)*, 703–706.
- Bittner, M., Offermann, D., & Graef, H. H. (2000). Mesopause temperature variability above a midlatitude station in Europe. *Journal of Geophysical Research: Atmospheres*, 105(D2), 2045–2058.
- Bittner, M., Offermann, D., Bugaeva, I. V., Kokin, G. A., Koshelkov, J. P., Krivolutsky, A., ... & De La Morena, B. A. (1994). Long period/large scale oscillations of temperature during the DYANA campaign. *Journal of Atmospheric and Terrestrial Physics*, 56(13–14), 1675–1700.
- Brasseur, G. P., & Solomon, S. (2006). *Aeronomy of the middle atmosphere: Chemistry and physics of the stratosphere and mesosphere* (Vol. 32). Springer Science & Business Media.
- Charney, J. G., & Drazin, P. G. (1961). Propagation of planetary scale waves from the lower atmosphere to the upper atmosphere. *J Geophys Res*, 66, 83–109.
- Chui, C. K., *An introduction to wavelets*, Academic Press, Inc., 1992.
- Cohen, J., Screen, J. A., Furtado, J. C., Barlow, M., Whittleston, D., Coumou, D., ... & Jones, J. (2014). Recent Arctic amplification and extreme mid-latitude weather. *Nature geoscience*, 7(9), 627–637.
- Coumou, D., Petoukhov, V., Rahmstorf, S., Petri, S., & Schellnhuber, H. J. (2014). Quasi-resonant circulation regimes and hemispheric synchronization of extreme weather in boreal summer. *Proceedings of the National Academy of Sciences*, 111(34), 12331–12336.
- Daubechies, I. (1992). *Ten lectures on wavelets* (Vol. 61). Siam.
- Dee, D. P., Uppala, S. M., Simmons, A. J., Berrisford, P., Poli, P., Kobayashi, S., ... & Bechtold, P. (2011). The ERA-Interim reanalysis: Configuration and performance of the data assimilation system. *Quarterly Journal of the royal meteorological society*, 137(656), 553–597. Edmon et al (1980)
- Erbetseder, T., Eyring, V., Bittner, M., Dameris, M., & Grewe, V. (2006). Hemispheric ozone variability indices derived from satellite observations and comparison to a coupled chemistry-climate model. *Fortrak* (1971)
- Francis, J. A., & Vavrus, S. J. (2012). Evidence linking Arctic amplification to extreme weather in mid-latitudes. *Geophysical research letters*, 39(6).
- Garfinkel, C. I., & Hartmann, D. L. (2008). Different ENSO teleconnections and their effects on the stratospheric polar vortex. *Journal of Geophysical Research: Atmospheres*, 113(D18).
- Godske, C. L., & Bjerknes, V. (1957). *Dynamic meteorology and weather forecasting* (Vol. 605). American Meteorological Society.
- Grotjahn, R., Black, R., Leung, R., Wehner, M. F., Barlow, M., Bosilovich, M., ... & Lee, Y. Y. (2016). North American extreme temperature events and related large scale meteorological patterns: a review of statistical methods, dynamics, modeling, and trends. *Climate Dynamics*, 46(3–4), 1151–1184.
- Holton (1980): The Influence of the Equatorial Quasi-Biennial Oscillation on the Global Circulation at 50 mb. *J. Atmos- Sci.* 37. 2200–2208.
- Holton, J. R. (1979). An introduction to dynamic meteorology. *Int. Geophys. Series*, 23.
- Höppner, K., & Bittner, M. (2007). Evidence for solar signals in the mesopause temperature variability?. *Journal of Atmospheric and Solar-Terrestrial Physics*, 69(4–5), 431–448.
- Huang, N. E., Shen, Z., Long, S. R., Wu, M. C., Shih, H. H., Zheng, Q., ... & Liu, H. H. (1998). The empirical mode decomposition and the Hilbert spectrum for nonlinear and non-stationary time series analysis. *Proceedings of the Royal Society of London. Series A: mathematical, physical and engineering sciences*, 454(1971), 903–995.
- Iza, M., Calvo, N., & Manzini, E. (2016). The stratospheric pathway of La Niña. *Journal of Climate*, 29(24), 8899–8914.
- Julian, P. R., & Labitzke, K. B. (1965). A study of atmospheric energetics during the January–February 1963 stratospheric warming. *Journal of the Atmospheric Sciences*, 22(6), 597–610.
- Kalicinsky, C., Knieling, P., Koppmann, R., Offermann, D., Steinbrecht, W., Wintel, J., & Laštovicka, J. (2016). Long-term dynamics of OH⁺ temperatures over central Europe: trends and solar correlations. *Atmospheric Chemistry & Physics*, 16(23).

- Küchelbacher, L. (2016). Variabilität und Trends planetarer Wellen der mittleren Atmosphäre der Nordhalbkugel. Master thesis, University Augsburg.
- Küchelbacher, L. (2021). Charakterisierung der Änderungen der planetaren Wellenaktivität vor dem Hintergrund des Klimawandels. Dissertation. University Augsburg.
- Kidston, J., Scaife, A.A., Hardiman, S.C., Mitchell, D.M., Butchart, N., Baldwin, M.P., & Gray, L.J. (2015). Stratospheric influence on tropospheric jet streams, storm tracks and surface weather. *Nature Geoscience*, 8(6), 433–440.
- Kodera, K., Eguchi, N., Lee, J.N., Kuroda, Y., & Yukimoto, S. (2011). Sudden changes in the tropical stratospheric and tropospheric circulation during January 2009. *Journal of the Meteorological Society of Japan. Ser. II*, 89(3), 283–290.
- Kornhuber, K., Petoukhov, V., Karoly, D., Petri, S., Rahmstorf, S., & Coumou, D. (2017). Summertime planetary wave resonance in the Northern and Southern Hemispheres. *Journal of Climate*, 30(16), 6133–6150.
- Kozubek, M., Krizan, P., & Lastovicka, J. (2017). Comparison of the long-term trends in stratospheric dynamics of four reanalyses. *Annales Geophysicae (09927689)*, 35(2).
- Labitzke, K. (1982). On the interannual variability of the middle stratosphere during the northern winters. *Journal of the Meteorological Society of Japan. Ser. II*, 60(1), 124–139.
- Li, T., Calvo, N., Yue, J., Dou, X., Russell III, J.M., Mlynczak, M.G., ... & Xue, X. (2013). Influence of El Niño–Southern Oscillation in the mesosphere. *Geophysical Research Letters*, 40(12), 3292–3296.
- Lu, H., Scaife, A.A., Marshall, G.J., Turner, J., & Gray, L.J. (2017). Downward wave reflection as a mechanism for the stratosphere–troposphere response to the 11-yr solar cycle. *Journal of Climate*, 30(7), 2395–2414.
- Mann, M.E., Rahmstorf, S., Kornhuber, K., Steinman, B.A., Miller, S.K., & Coumou, D. (2017). Influence of anthropogenic climate change on planetary wave resonance and extreme weather events. *Scientific Reports*, 7, 45242.
- Mitchell, D.M., Gray, L.J., Anstey, J., Baldwin, M.P., & Charlton-Perez, A.J. (2013). The influence of stratospheric vortex displacements and splits on surface climate. *Journal of Climate*, 26(8), 2668–2682.
- Morlet, J., Arens, G., Fourgeau, E., & Giard, D. (1982). Wave propagation and sampling theory—Part II: Sampling theory and complex waves. *Geophysics*, 47(2), 222–236.
- Nakamura, T., Yamazaki, K., Iwamoto, K., Honda, M., Miyoshi, Y., Ogawa, Y., ... & Ukita, J. (2016). The stratospheric pathway for Arctic impacts on midlatitude climate. *Geophysical Research Letters*, 43(7), 3494–3501.
- Naujokat, B. (1986). An update of the observed quasi-biennial oscillation of the stratospheric winds over the tropics. *Journal of the Atmospheric Sciences*, 43(17), 1873–1877.
- Petoukhov, V., Rahmstorf, S., Petri, S., & Schellnhuber, H.J. (2013). Quasiresonant amplification of planetary waves and recent Northern Hemisphere weather extremes. *Proceedings of the National Academy of Sciences*, 110(14), 5336–5341.
- Pfaff, B. (2008). *Analysis of integrated and cointegrated time series with R*. Springer Science & Business Media.
- Philander, S.G. H. (1983). El Niño southern oscillation phenomena. *Nature*, 302(5906), 295–301.
- Pichler, H. (1997). Dynamik der Atmosphäre, Spektrum.
- Rossby, C.G. (1939). Planetary flow patterns in the atmosphere. *Quart. J. Roy. Met. Soc*, 66, 68.
- Runde, T., Dameris, M., Garny, H., & Kinnison, D.E. (2016). Classification of stratospheric extreme events according to their downward propagation to the troposphere. *Geophysical Research Letters*, 43(12), 6665–6672.
- Scherhag, R. (1958). Das “Berliner Phänomen” und das Geophysikalische Jahr. *Beilage zur Berliner Wetterkarte*, 137.
- Schoeberl, M.R., & Geller, M.A. (1976). The structure of stationary planetary waves in winter in relation to the polar night jet intensity. *Geophysical Research Letters*, 3(3), 177–180.
- Screen, J.A., & Simmonds, I. (2013). Caution needed when linking weather extremes to amplified planetary waves. *Proceedings of the National Academy of Sciences*, 110(26), E2327–E2327.
- Screen, J.A., & Simmonds, I. (2014). Amplified mid-latitude planetary waves favour particular regional weather extremes. *Nature Climate Change*, 4(8), 704.
- Serreze, M.C., Barrett, A.P., Stroeve, J.C., Kindig, D.N., & Holland, M.M. (2009). The emergence of surface-based Arctic amplification. *The Cryosphere*, 3(1), 11.
- Sherwood, S.C., Meyer, C.L., Allen, R.J., & Titchner, H.A. (2008). Robust tropospheric warming revealed by iteratively homogenized radiosonde data. *Journal of Climate*, 21(20), 5336–5352.
- Torrence, C., & Compo, G.P. (1998). A practical guide to wavelet analysis. *Bulletin of the American Meteorological Society*, 79(1), 61–78.
- Trenberth, K.E. (1997). *The definition of El Niño*. *Bull. Am. Meteorol. Soc.* 78, 2771–2777.
- Tsiropoula, G. (2003). Signatures of solar activity variability in meteorological parameters. *Journal of Atmospheric and Solar-Terrestrial Physics*, 65(4), 469–482.
- Wüst, S., & Bittner, M. (2006). Non-linear resonant wave–wave interaction (triad): Case studies based on rocket data and first application to satellite data. *Journal of atmospheric and solar-terrestrial physics*, 68(9), 959–976.
- Wüst, S., Bittner, M., Yee, J.H., Mlynczak, M.G., & Russel III, J.M. (2017). Variability of the Brunt-Väisälä frequency at the OH* layer height. *Atmospheric Measurement Techniques*, 10, 4895–4903.

11 Statistical downscaling of future global climate change scenarios for Alpine high mountain regions

Andreas Philipp, Christoph Beck, Severin Kaspar, Stefanie Seubert and Jucundus Jacobeit

Institute for Geography, University of Augsburg

Keywords: Climate change, Statistical Downscaling, High mountain climate

Abstract

Global climate change is expected to show considerable impacts on the European Alpine high mountain region. However, global climate models show limitations concerning regional and local scales. Therefore, dynamical downscaling and statistical downscaling techniques have to be applied. Exemplarily for an especially simple method of statistical downscaling the Reference Class Forecast (RCF) method is explained and applied to the climatic time series at Zugspitze and Sonnblick. As a very different method, the technique of Artificial Neural Network (ANN) for downscaling is introduced. An important step is to find out an optimal set of predictors. However, if predictor screening is done appropriately, remarkably high skill scores can be achieved, which allow for confidence on the projected future assessments. The results of the downscaling approach applied for future scenarios are discussed concerning the degree of warming at the presented example stations and the changes in precipitation which not only show reduced rainfall in future summers, how it is assumed widely in the literature, but partly suggest the possibility of future increases in summer rainfall for the Zugspitze at the northern edge of the Alps in contrast to the Sonnblick in the center of the Alps. Reasons are probably higher transport rates for humidity in warmer air masses which are more relevant at the edge of the Alpine ridge, while the interior might be affected more by increased anticyclonicity.

11.1 Intro: Alpine regions exposed to climate change

Climate change in the Alps has wide-ranged implications due to strong interrelations between the different spheres (atmosphere, hydrosphere, cryosphere, lithosphere, pedosphere and biosphere) additionally intensified by distinct spatial complexity. The following short overview aims to give an idea about the broad potential effects of possible future temperature and precipitation changes and thus outlines the significance of the subsequently presented downscaling efforts and results.

With an observed increase of +2 °C (total annual mean temperature) since the late 19th century, air temperature in the Alps rises twice as much as the Northern hemisphere average (Auer et al. 2007). Since 1980 the recent warming has further accelerated and a faster increase of annual mean temperature (+0.5 °C per decade) is observed (European Environment Agency 2009). Alpine glacier retreat follows that trend and also increased in speed from 1980 onward (European Environment Agency 2017a). Since the beginning of the 20th century Alpine glaciers have lost nearly half of their ice masses (European Environment Agency 2017a, Huss 2012), an almost complete loss of their current volume is estimated until 2100 (84 and 90 % under RCP 4.5 and 8.5, Radić et al. 2013).

While increasing summer temperatures are regarded most important for this development, further future warming is expected for all seasons and the whole Alpine region. Until the end of the 21st century air temperature is projected to rise to +3,3 °C on annual average (Gobiet et al. 2014). Models agree on the sign of the expected change and emphasize the robustness of the warming signal (Heinrich et al. 2013).

Precipitation changes at present vary stronger concerning seasonal and regional distributions as well as the observed period (Gobiet et al. 2014). Regarding the spatial distribution of annual means a north-west to south-east gradient from slight increases to significant decreases during

the 20th century is shown (Brunetti et al. 2006). This north-south oriented distribution is expected to sharpen until the end of the 20th century with more precipitation in the northern Alps in winter, according to the Northern Europe pattern of change, and reduced precipitation in the southern Alps in summer, following the climate change signal in Southern Europe (Gobiet et al. 2014).

However, not only the enhanced warming or mean precipitation changes alone are critical, but also their implications for other meteorological and hydrological variables, mainly air humidity, precipitation variability and above all the resulting impacts on the hydrological storage terms, i.e. duration and depth of snowcover and glacier mass balance. Slight warming of just a few centidegrees can produce strong changes in the water budget e.g. if the melting point is reached for certain areas. The above mentioned accelerated glacier melting since 1980 for example has increased the glacier contribution to late summer runoff of four main European rivers originating in the Alps, namely Danube, Rhine, Rhone and Po (by around 13%, Huss 2011). Thus also the lowland parts, especially of catchments with high portions of glacial melt water in late summer, will be affected by future glacier retreat and lacking runoff contributions on the long-term. Lowered ground water levels, restricted water availability for agriculture or limitations of ship traffic along the main European streams are mentioned as potential risks of the future warming-induced glacier retreat in the Alps (Huss 2011).

With the consequences for the local economic sectors in mind, strong implications are expected from future changes of snow cover, entailing limitations for hydrological power generation (Kobierska et al. 2012) or especially the winter tourism (Steiger et al. 2010). For the entire Alps a dramatic decrease of snow cover duration and amount is projected until the end of 21st century, mainly for altitudes below 1500–2000 m (Gobiet et al. 2014, Steiger et al. 2013). Above, gains are expected (due to potentially increasing heavy precipitation), which leads amongst others to an increased avalanche activity, e.g. in the Western Alps in winter (Castebrunet et al. 2014).

Higher temperatures as well as less solid but more liquid precipitation during the winter half year have particular strong effects in high altitude regions with high relief energy: wet winters e.g. can reinforce the landslide activity in spring (Stoffel 2014). Being identified as one of the European “susceptibility hotspots for weather-induced landslides” (European Environment Agency 2017a), shallow landslides like rock falls, debris flows/avalanches but also ice falls and snow avalanches are expected to rise with future temperature and precipitation changes (Stoffel 2014). This gives rise not only to remarkable risks for summer tourism or transhumance but possibly endangers settling in the Alps in general.

In conclusion mountain landscapes are characterized by an exceptional complexity of geofactors, enhancing the vulnerability to climate change. The above mentioned complex structure of interrelations is responsible for amplifying even small irregularities in the input variables, in this context temperature and precipitation. To know their future changes and associated temporal and regional variations as exactly as possible is an essential base for accurate assessments of adaptation strategies.

All the consequences for the inanimate parts of nature are more dramatic due to the high relief. Thus, retreating glaciers and permafrost regions change the hydrological cycle and cause land and rock slides, to mention only a few aspects which can affect also human society directly and harder than in low lands. The Alps besides the Pyrenees are identified as hotspots.

11.2 Global Climate Change and Modelling

Global climate models allow to estimate the reaction of the climate system of the earth to climate forcing factors in a quantitative way. However, in order to be able to use the information provided by climate models, it is absolute essential to understand in principle how they work and to know about the strength and weakness of this scientific tool. The core of each climate model is a general circulation scheme including physical laws of i) conservation of energy, ii) conservation of momentum and iii) conservation of mass. These three laws can be connected by the equation of state and transformed into a system of prognostic equations, which allows to calculate the state of the climate system based on its state at a time step before. In a strong-

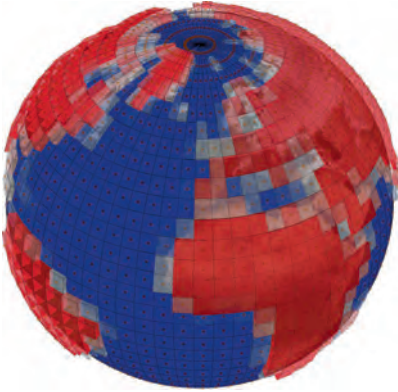


Fig. 1: Grid cells in T21 horizontal resolution used to describe the global land-sea-mask for GCMs. Values vary between 0.0 (blue) for grid cells completely covering ocean areas and 1.0 (red) for cells completely on land. Note that pixels covering coast lines as for western Africa are mixture pixels, half sea half land, indicating the low level of detail for such a low resolution.

ly simplified way it could be said, that e.g. the distribution of airmasses (measured as air pressure) is causing winds which itself redistribute air and change the pressure field in a second time step, which itself causes – now modified – winds causing a newly modified pressure field in a third time step and so on and so on. However, beside wind and pressure, it is of course necessary to include density, heat, moisture, heat capacity etc., in order to represent all dependencies of the system. The resulting set of non-linear partial differential prognostic equations can be resolved not analytically but only by extensive numerical methods (which is the real reason for calling them numerical models). However, even if all processes of the atmosphere are included, there remains a fundamental problem for all models: the spatial, and depending on this, the temporal resolution of the calculations. In order to get a realistic description of the distribution of a certain variable, let's say air pressure, over the globe, a regular network of grid points, e.g. on 32 latitudes and 64 longitudes what was state of the art in 1990ies, is defined.

However, with a limited number of discrete grid points for describing e.g. a low pressure system, only a limited degree of detail or only systems of a certain minimum size can be described. Although there is the possibility to represent the pressure changes over space by a set of overlaid continuous sinus functions, following the scheme of Fourier series, which is called the spectral representation and is used for some effective calculations in numerical models, only a limited number of functions can be used which also allows only for a limited degree of detail. In order to increase the detail level, the number of grid points or, equivalently, the number of wave functions, most often described by the so called triangular truncation number (e.g. T21), must be increased.

Tab. 1: model resolutions

Truncation	lat × lon	km at Equator	deg at Equator
T21	32x64	625	5.625
T42	64x128	310	2.8125
T62	94x192	210	1.875
T63	96x192	210	1.875
T85	128x256	155	1.4
T106	160x320	125	1.125
T255	256x512	60	0.703125
T382	576x1152	38	0.313
T799	800x1600	25	0.225

Table 1 shows a set of most commonly used horizontal spatial resolutions for numerical circulation models. It is apparent, that decreasing the distance between two grid points by a half, at the same time the number of grid points quadruplicates. If an increase of the number of levels in the vertical direction is considered additionally, it is clear that the computational effort increases dramatically, when the spatial resolution and thus the number of calculations for all grid points or spectral functions is increased. (National Center for Atmospheric Research Staff 2017).

However, the situation is even more difficult, because of the so called Courant-Friedrich-Levy (CFL) criteria.

$$|u \cdot dt/dx| \leq 0$$

This criterion is saying that the time step dt for the prognostic computations must be smaller than the distance between two grid points dx divided by the speed of flow in the model, e.g. wind u . Since the speed of flow in the model is something which is given by the physical circumstances, e.g. the subtropical jet stream in the upper troposphere, only the spatial (dx) and

temporal resolution (dt) can be changed by the modeller. If a certain spatial resolution is chosen, it subsequently demands for a certain maximum time step length with which the set of prognostic equations is solved repeatedly. The principle of the CFL criterion is saying nothing else than that a flow of mass, impulse or energy should not be faster, than that it reaches a distance not more than one grid point far within one time step, or in other words, no transport process within the model should skip a grid point along its way. What happens, when this criterion is violated can be seen in Fig. 2: the variables show a totally unrealistic pattern and extreme values outside the physically plausible range. The model „crashes“

Essentially it is the CFL criterion which prevents the model resolution becoming much more increased, while a limited capacity of compute power is available, even though, it is numerical modelling for which the most extensive compute clusters are build. However, when the spatial (and accordingly the temporal) resolution is limited, small and short term phenomena in the atmosphere, like thunderstorm cells or showers of rain, may be missed because they happen on the sub grid scale.

Another problem which is limiting the detail level of general circulation models, is just the complexity of certain phenomena in the atmosphere, which cannot be expressed by a reasonably small set of equations. One prominent example is precipitation. The process of generating precipitation is such complex that, apart from its high spatial variability, it is virtually impracticable to simulate it with the necessary precision directly. Especially the initiation and growth of cloud and later rain droplets interacting with condensation nuclei or its changes between ice and liquid phase is a highly complex subject of microphysics which has to consider effects down to the molecular scale. Calculation of all these effects, if they are understood at all, for the whole globe is simply impossible. In order to still include those processes, rough, empirical estimations of their quantitative dependence on its most important influences, described by certain parameters are used. Without these so called parametrisations, a climate model which should include most of the relevant processes is unimaginable and impracticable.

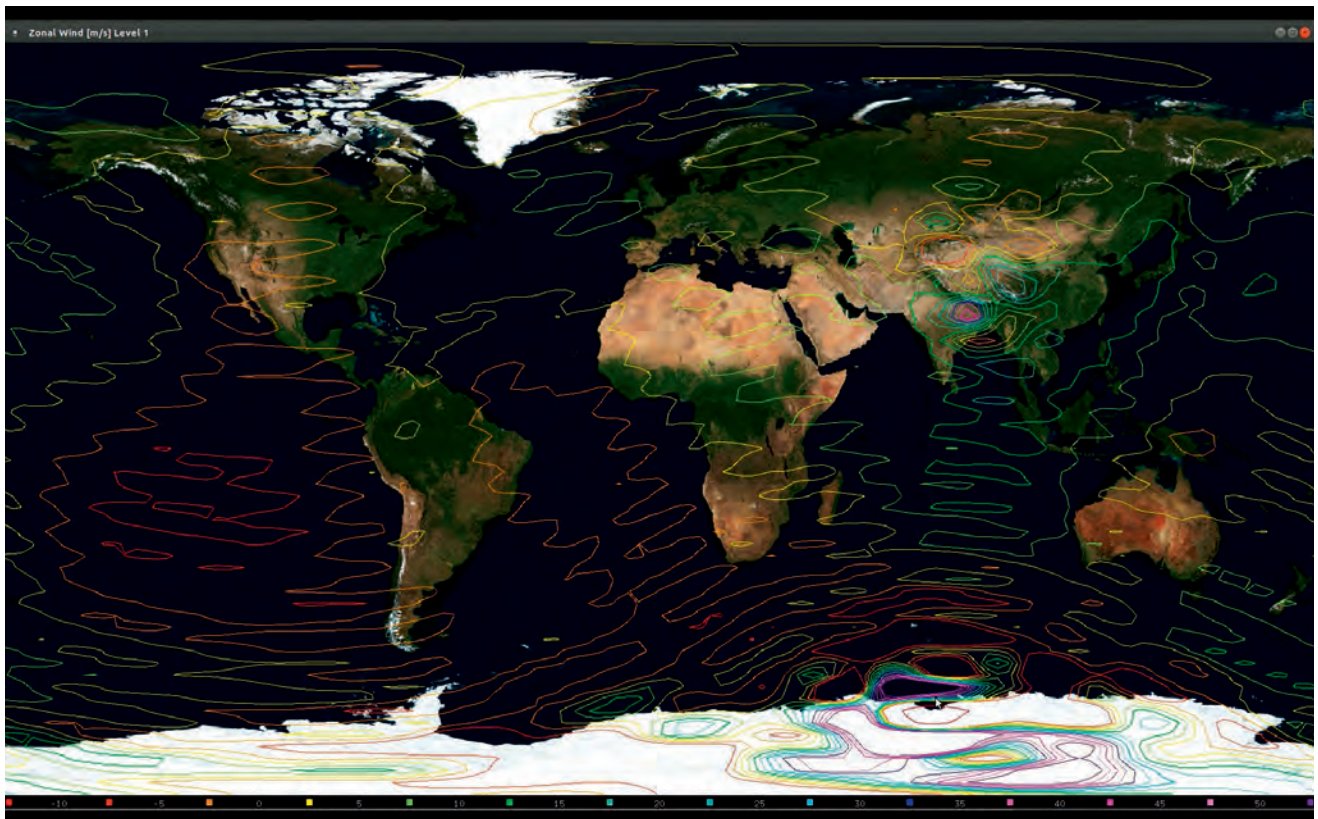


Fig. 2: Zonal wind component at surface level as displayed by the PLASIM interactive model environment (Fraedrich et al. 2005) immediately before a model crash due to violation of the Courant-Friedrichs-Lewy criterium (see text). Negative values (easterly wind) is colored orange to red (-15 m/s), positive values (westerly wind) yellow to violet (55 m/s). Model resolution was T21, time step intervall was 60 minutes. Note the unrealistic wave like pattern of alternating easterly and westerly winds extending from a center at the Antarctic coast with common high wind speeds, where the CFL-criterium was violated first.

However, both the spatial and the processual limited resolution obstructs a high level of detail of the model output, concerning the spatial details but also the processual details. This problem is not the same for all variables, thus, the global pressure field is much less affected than the temperature or the precipitation field (Raisanen 2007), since the complexity of the relevant processes is lower. Additionally the vertical level is important, thus, temperature in the mid and high troposphere can be modelled much more precisely than directly above the surface in the planetary boundary layer because there the influences are much more divers.

To conclude this, it can be said that general circulation models allow to simulate the global atmospheric state realistically on a rough level of detail. However the high demand for compute power, which is caused by the spatio-temporal and processual resolution, when simulating processes directly, prevents from a sufficient detail level of some variables especially near the surface, where applications of model output data mostly take place. In order to solve this problem several downscaling methods have been developed.

11.3 Downscaling methodology

Downscaling techniques try to close the gap between the low level of detail provided by general circulation models and the needed high level of detail for applications, which is caused mainly by the difference in spatial scale between global models and local applications.

In principle two main groups of downscaling techniques may be discerned: dynamical downscaling using regional climate models (RCM) on the one hand and statistical downscaling on the other. The latter using transfer functions to apply empirically determined dependencies between local variables of interest and global or large scale circulation data generated by GCMs for distinct scenarios. Other ways to categorize downscaling techniques are suggested by Maraun et al. (2010), however for the sake of clarity the two-fold distinction between dynamical and statistical methods is preferred here. Both ways have their advantages and disadvantages. For dynamical downscaling a highly resolved numerical simulation model, the RCM, is nested into a GCM. This means that only a certain area of the earth is simulated on a high resolution level, while the boundary conditions at the borders of the RCM are determined by the GCM output data. Regional climate models for dynamical downscaling need extensive compute power, usually not quite as much as GCMs do, since only a region of interest is simulated and not the full globe. However, the saved amount of computations is considerably reduced because of the increase in spatial resolution. Thus dynamical downscaling without parallelized high performance compute environments is not feasible. Another disadvantage for dynamical downscaling is the problem of discrepancies between spatial, temporal and processual detail at the boundary between highly resolved regional models and low resolution GCMs. Since at the border of the spatial domain of a RCM the highly resolved RCM data and the less resolved GCM data may show unrealistic steep gradients of the climate variables, this border has to be excluded from interpretation, leading to the necessity to configure a much larger RCM domain than actually needed. In order to achieve a smooth transition between GCM and RCM, usually a whole series of RCMs of successively increasing resolution are nested into a GCM and into itself by increasing the resolution slowly from step to step in order to reduce the inhomogeneities at the borders. This of course increases the demand of compute time additionally. RCMs also cannot avoid parametrisations, like GCMs do. However, RCM parametrisations can be tuned to a much higher level of detail than GCM ones. Thus e.g. precipitation can be much more realistically simulated concerning dynamical (e.g. orographic) or thermal convection. However, in areas of extreme relief energy, as it is the case for high mountain regions, simplifying assumptions may lead to unrealistic results. Even though the parametrisations of a RCM reflect empirical dependencies observed in the past, RCMs are able to simulate meteorological conditions that have not been observed before, because the driving circulation and most of the exchange processes are still simulated on basis of physical laws which are universally valid. However, remaining errors of RCM estimations are usually subject to so called model output statistics (MOS) for statistical correction of the results e.g. concerning the mean and distributions of the target variables, by shifting or scaling of the simulated values.

The full dependence on observations of the past is the most important disadvantage of statistical downscaling methods. Statistical downscaling is using significant relationships between the local target variable of interest, the so called predictand, and the large scale or synoptic

atmospheric conditions, described by so called predictor variables. If a certain manifestation of the variables of such a relationship was not observed in the past, it may lead to erroneous predictions of the state of the target variable for a scenario where new conditions of the predictors appear. If the relationship is a continuously linear function, the problem might be neglectable. However, unfortunately most relationships in the atmospheric sciences are non-linear. Using statistical methods which account for non-linear functions, which is shown below, therefore is of large importance. They also cannot extrapolate relationships beyond known parts of the spectra, but much better capture the links within the observed boundaries.

Sometimes only atmospheric circulation is used as predictor, usually described by the pressure field of the troposphere, since this is the variable which can be best simulated by GCMs and shows the highest spatial autocorrelation among all climate elements. However, other GCM variables are also used, and it is the main task of the so called calibration step in the statistical downscaling scheme to find optimal predictor combinations of variables in order to maximize the statistically explained fraction of variance of the predictand. However, the performance of statistical models not only depends on the kind of variables used (pressure, temperature, humidity etc.) but also on the size and position of the area from which the predictor is taken, the predictor domain. Additionally it is important which atmospheric level is used. Also building seasonal subsamples is of great relevance, since some processes are realized differently depending on the annual cycle. Many additional factors may be subject to the optimization of the statistical downscaling models.

The core of statistical downscaling is the method chosen as transfer function. As a basic method often multiple linear regression (LM) is used to model the predictand. In order to estimate a whole grid point field of predictands at once by linear regression, canonical correlation models may be used. However, LM rely on a normal distribution of the residuals, i.e. the unexplained variation of the target variable, which is often not fulfilled. Therefore it is often a better choice to use generalized linear models (GLM). Apart from these linear methods, several approaches exist to model non-linear functions of dependence between predictors and predictands. A much more simple method than regression techniques which actually is able to use non-linear relationships is the analog method (AM) presented e.g. by Zorita and von Storch (1990). The idea of this method is rather intuitive: for any situation of the circulation in the GCM where the state of a local target variable is of interest, choose the most similar situation from observation data in the past and use the referring value of the target variable from this analog situation as the downscaling result. It turns out that the performance of this method can be as good as that of regression models, while it can be applied without statistical prerequisites.

Exemplarily for the possible large bandwidth of the method spectrum used for downscaling, two selected methods, will be described more in detail below, since they have been applied recently in intensive downscaling studies in high mountain areas, i.e. for the Zugspitze and the Sonnblick. The first is the more simplistic reference class forecast method (RCF) based on circulation type classification (CTC), the second the more sophisticated technique of artificial neural networks (ANN).

11.4 Circulation Type Classification

A derivative of the analog method is the so called reference class forecast method (RCF) and its functional principle is described straightforwardly. This method is based on weather or circulation type classifications (CTC) of observed predictor fields (often pressure maps) from the past. Most prominent examples for often used weather type classifications are e.g. the Lamb classification for Great Britain (Lamb 1972) or the Hess-Brezowsky classification for central Europe (Hess and Brezowsky 1977) produced manually by assigning daily weather maps to subjectively defined weather types or the automatically produced classification of the German meteorological service DWD (Bissoli and Dittmann 2003). However many more classifications are available (see e.g. Huth et al. 2008).

In order to model a certain state, e.g. in the future, the expected predictor field for this situation, e.g. as simulated by a GCM, is assigned to its most similar class. The predictand value is then chosen as the mean of the target variable for this reference class in the past.

Even though this method is rather simple and easy to apply, it can show considerable good skill (see below). Its main limitations result from the fact, that this method assumes, that all relevant climatic changes in the (future) scenario are caused by changes in the frequencies of weather and circulation types. However, such actualistic principles are used for most of the downscaling methods based on known states of the large scale predictors. And even dynamical downscaling is affected by this problem, since many assumptions for setting up RCMs are based on observations of the past. Besides, the skill of RCF depends on several methodological technical factors, mainly concerning the underlying circulation type classification.

There are plenty of methods for weather and circulation type classifications that can be used for downscaling and the question arises which method is suited to achieve the best classification in order to maximize the downscaling skill, i.e. to minimize the model errors. A comprehensive comparison of classification methods was done within the COST Action 733 "Harmonisation and Applications of Weather Type Classifications for European regions" and the main results of these studies are also relevant for downscaling applications. First it has been found that the classifications resulting from 33 examined classification methods are surprisingly dissimilar among each other, i.e. they do not have significantly more in common than classifications based on purely randomly defined types, except for some methods based on non-hierarchical cluster analysis (Philipp et al. 2016). Second it has been found that there is no single method which can always provide the best skill in discriminating different states of a predictand variable, however methods based on cluster analysis (more generally spoken those using optimization algorithms) show a tendency to higher skills compared to others (Beck and Philipp 2010). This does not mean that cluster analysis is always the best, but it suggests that it is not the worst choice to consider them for downscaling.

Besides the classification method, the skill depends on the selection of the predictors, which is generally true for all statistical models. This includes the climatological variables used as predictors (e.g. pressure, wind components, large scale temperature, humidity etc.) as well as the location where they were measured. This includes the atmospheric level (near the surface or in the middle or upper troposphere) as well as the topographic region, i.e. the location, shape and size of the section of the grid point field used, what is usually called the model domain. The optimal model domain has been examined by Beck et al. (2013). It has been found that there are actually systematic preferences, e.g. for temperature the domain should be larger than for precipitation and west-east-elongated domains are often superior, however in order to achieve the optimal model for a certain predictand, it is necessary to empirically test potential configurations by a systematic predictor screening. An additional way to optimize a classification for a certain target is to include the target variable already during the classification process in the calibration step. Then the classification produces types with members that are not only similar concerning the pressure field e.g., but also concerning the target variable, like temperature e.g., which is called a conditional classification scheme. It could be shown that this method can improve classification based downscaling schemes in general if an optimal weighting between the predictor and the predictand variable is found (Lutz et al. 2011).

11.5 Artificial Neural Networks

Compared to RCF artificial neural networks (ANN) represent the other end of the scale of complexity of transfer functions for downscaling. As the name suggests this method tries to imitate the neural network of a brain consisting of neurons which receive a signal generated originally by a sensory organ at the one side and – depending on the result of an activation function – further transmit the signal to the next neurons on the other side. The strength of the forwarded signal depends on the transmitting neuron. Thus, after moving through the network, a signal can be filtered out completely or amplified leading to a corresponding reaction at the output of the system.

In statistics this principle is realized by defining an array of nodes connected by weighting factors. The array consists i) of an input layer, where the input neurons imitate the sensory organs and receive the values of the predictors, ii) the neurons responsible for the transport of the signals, which are called hidden neurons since they are not directly connected to external data and iii) the output layer where the output neurons (often only one) represent the predictands. In order to automatically get the desired result in the output layer in dependence from a certain

state of the predictors in the input layer, the weighting coefficients of the links between the layers have to be optimized by a learning algorithm. The most often used learning algorithm is the so called backward propagation (backprop) scheme, where the estimation error of the output neuron is propagated backwards through the net in order to optimize the weights of the links to the hidden neurons and then of the links to the input neurons. In order to reach optimal weights for all pairs of observed predictor and predictand data, this is done repeatedly for all elements (days) of the training data subset. Each time the network was shown all training data once (a so called training epoch) the weights are adjusted a bit better to learn the dependencies of the target variable. However the training has to be stopped before the absolute optimum is reached in order to keep a minimum level of abstraction in the net and avoid overfitting. Overfitting is given, when the network has memorized all single situations it was trained for but is not able to perform well for a new situation it hasn't seen before. Therefore, in order to decide for the stopping, an independent data subset (the validation subset) has to be kept aside the training data subset, which is only used to check the current network for its skill with unknown data. Otherwise the skill would not be representative for the application to the scenario GCM data.

11.6 Combination of ANN and CTC

Since CTC based downscaling is extremely fast compared to ANN training, it has been tested whether it is possible to combine both methods and still reach or even outperform the performance of ANNs. Therefore a non-hierarchical classification scheme is applied to the variables determined by predictor screening and the target variable in order to train an ANN for each class separately. The idea is, that it might be easier for a network to discern different factors for dry, normal and wet conditions and therefore reach a higher level of detail and model performance.

11.7 Skill

Before applying downscaling methods to GCM data in order to derive estimates of possible future regional or local scale climate change it is necessary to assess the confidence that can be attributed to the simulated future climate. This is typically done by determining the skill of the downscaling approaches via model validation experiments.

Such a model validation comprises firstly the derivation of estimates of the predictand variable (e.g. daily mean air temperature at a certain location) by applying the downscaling model to large-scale atmospheric predictor fields from available observational or reanalysis data sets and – secondly – the comparison of the downscaling model output to observed predictand data.

These comparisons utilize suitable performance measures which quantify the accordance or the mismatch between observed and modeled data. For continuous predictands commonly used measures are for instance the mean error, the mean absolute error, the mean squared error or the correlation coefficient. Furthermore, based on the comparison of these measures estimated for the downscaling model and for a reference model (e.g. utilizing the climatological mean of the predictand) respectively, skill scores can be calculated (e.g. the mean squared skill score based on the mean squared errors of the downscaling model and the reference) indicating in how far the downscaling model outperforms the reference model and thus is suitable to provide valuable future climate simulations.

Exemplary, the calculation of the mean squared skill score (MSSS) based on the mean squared error estimated for the downscaling model (MSE_{mod}) and for the climatological reference (MSE_{clim}) is illustrated in the following three equations (see also Wilks 2006).

$$MSE_{mod} = \frac{1}{n} \sum_{k=1}^n (y_k - a_k)^2$$

$$MSE_{clim} = \frac{1}{n} \sum_{k=1}^n (\bar{o} - o_k)^2$$

$$MSSS = 1 - \frac{MSE_{mod}}{MSE_{clim}}$$

With n being the number of observations, o being the observed values of the predictand, \bar{o} being the mean of the observed values and y being the simulated predictand values. Thus, an *MSSS* of 1 indicates a perfect model while an *MSSS* less or equal zero indicates a model performing equal or even worse than the climatological reference.

Those skill scores essentially describe the absolute errors of the model, i.e. the magnitude of the difference between o and y . However, it can happen, that there is a systematic error and the model values are always too high or too low compared to the observations by a certain amount, called bias. Then the model output can be corrected by subtracting the bias afterwards. Repeating the skill score calculation with bias corrected model results then increases the performance. The same might be true for the scaling, and dividing by a correction scale coefficient might improve the performance of the model.

In order to estimate the performance of the downscaling model directly, besides of any systematic bias or scale, i.e. just evaluating the coincidence of positive and negative anomalies relatively but not concerning the absolute values, correlation coefficients may be used. For that, the output values of the downscaling model for the historical reference period are correlated with the actually observed values of the target variable. Correlation coefficients can give information on how many percent of variance in the target variable is captured by the model if the squared correlation coefficient is considered: $r^2 = d$, where d is called the coefficient of determination.

However, as the skill estimate may be artificially high when calculated on the basis of the data that has been used to fit the downscaling model, it is necessary to validate the model on data that has not been used for model calibration. This is done by so called cross-validation. Here, the time period for which predictor data and observed predictand data are available is divided into two or more non-overlapping sub-intervals and the downscaling models are then in turn calibrated using all but one of these sub-intervals and validated in the remaining independent sub-interval. Variants of this cross validation approach include the use of varying lengths of the sub-intervals and varying methods for defining the sub-samples used for calibration and validation, including random sampling techniques.

For the overall performance of the regional to local scale future climate simulations beside the skill of the statistical downscaling approach it is in addition of crucial importance how well the GCMs simulate the large-scale input data for the statistical downscaling models. For instance, it is well known that many GCMs feature warm and as well cold biases in sea surface temperatures over different parts of the North Atlantic leading to an incorrect representation of the large-scale atmospheric circulation over Europe (Keeley et al. 2012). Such biases – model errors relative to observations – need to be considered utilizing varying approaches for bias correction (see for example Teutschbein and Seibert 2021 for a review of common approaches). For instance, one rather simple method – linear scaling (Lenderink et al. 2007) – uses the differences in the mean between GCM and observations (or reanalyses) for bias correction of the GCM output.

In addition, climate processes are partly differently represented in GCMs from different climate modelling groups leading to accordingly diverging future climate projections. To account for this source of uncertainty so called multi-model ensembles comprising projections from several GCMs are used to derive quantitative estimates of the range of uncertainty in future climate projections.

Furthermore, uncertainties may also arise from differences between projections of variants of the same GCM run with varying values of certain model parameters or run from varying start dates. So called perturbed physics ensembles are used to determine the range of uncertainty in future projections related to variants in model parameters whereas initial condition ensembles consider the effect of differing start dates.

Finally, uncertainties are also due to varying properties of the statistical downscaling models. For instance, using different techniques for cross validation or using different time periods for calibrating the final model which is then applied to GCM data may lead to differing statistical models and accordingly to varying future regional climate simulations. Thus, in addition to the above mentioned numerical ensembles as well statistical ensembles have been introduced to quantify uncertainty in climate projections.

11.8 Case study Zugspitze and Sonnblick

The success of developing a useful downscaling scheme for locations in high mountain areas is especially affected by two factors concerning the mountain relief. On the one hand high mountain places can be exposed to the free atmosphere, compared to the low land. This means that the large scale circulation and associated atmospheric parameters which can be simulated well by GCMs on the synoptic scale play a larger role for the variability of the local target variable than atmospheric processes working near the surface on the meso- and microscale, i. e. the subgrid scale for GCMs. This means that the downscaling models based on large scale GCM output as discussed above should perform especially well. On the other hand, the high relief energy of the mountains also includes areas affected strongly by GCM-subgrid processes, like luv/lee effects, channeling of wind, gradients in friction or radiation energy uptake, slope winds, mountain plane winds or increased turbulence which is mixing air from the boundary layer into the area up-stream of the measurement site (footprint area) etc. Thus, locations in high mountain areas which are less exposed to the free atmosphere but significantly affected by meso- and microscale processes, may be even less suitable for downscaling than low land stations.

A high mountain station especially suited for downscaling is the meteorological observatory at the Zugspitze (2962 m) maintained by the German weather service DWD. It offers a long time series of observation data (see Tab. 2) even though not all data can be used as explained below. Moreover, the location of the Zugspitze as a comparatively high peak, exposed at the northern edge of the high mountain range makes it a promising object for downscaling. Another high mountain observatory maintained with long records is the Sonnblick observatory at the Hoher Sonnblick (3106 m) operated by the Austrian meteorological service (ZAMG) and located in the Alpine main ridge. Compared to the Zugspitze the Hoher Sonnblick is surrounded by mountain ridges in all directions.

Tab. 2: Start time of daily records for the target variables precipitation and temperature at Zugspitze and Hoher Sonnblick

Station	Variable	Start of available records
Zugspitze	Precipitation	01.01.1901
	Temperature	01.08.1900
Hoher Sonnblick	Precipitation	01.08.1890
	Temperature	01.10.1886

In order to calibrate and validate the downscaling models, large scale circulation data have been obtained from the 20th century reanalysis dataset version 2 (Compo et al. 2011). They have been generated by a weather forecast model initiated by historical and recent station and radiosonde observations and are used as equivalent to large scale GCM output, however not for certain scenarios but for the past where also the target variables temperature and precipitation from Zugspitze and Hoher Sonnblick are known. The variables which have been examined as potential predictors include air pressure at sea level (slp), thickness of the layer between 850 hPa and 500 hPa (thi), geopotential height of several pressure levels (hgt), as a common way to describe air pressure distribution in upper levels, zonal wind speed (uwnd), meridional wind speed (vwnd), total horizontal wind speed (swnd), vertical wind speed (omega), air temperature (air), specific humidity (shum), relative humidity (rhum), zonal and meridional moisture flux (umf and vmf) as well as vorticity (vor) and divergence (div) of the wind field. In order to cover the whole vertical extent of the troposphere but at the same time restrict the number of variants, the variables have been extracted for the levels 850 hPa, 700 hPa, 500 hPa and 250 hPa.

In order to obtain useful and robust models, it is necessary to reduce the set of potential predictors to the most important ones. Even though the influence of less important variables is reduced by weighting in the classification scheme as well as during training of the neural network, it is much more effective and avoids to end up in less stable solutions of the model optimisation process if they are excluded and if the set of predictors is kept as small as possible. However, to obtain still a well-performing model it is very important to find out which variables

Tab 3: Optimal predictor combinations determined by screening through all possible configurations of variables (air pressure at sea level (slp), thickness of the layer between 850 hPa and 500 hPa (thi), geopotential height of several pressure levels (hgt), as a common way to describe air pressure distribution in upper levels, zonal wind speed (uwnd), meridional wind speed (vwnd), total horizontal wind speed (swnd), vertical wind speed (omega), air temperature (air), specific humidity (shum), relative humidity (rhum), zonal and meridional moisture flux (umf and vmf) as well as vorticity (vor) and divergence (div)), atmospheric pressure level (level), start and end of the domain given in degrees east (lon) and degrees north (lat) for each season (December, January, February (DJF), March, April, May (MAM), June, July, August (JJA) and September, October, November (SON)) and each target variable (precipitation (prc) and temperature (tmp) at Zugspitze (Zug) and Hoher Sonnblick (Son)).

			slp	thi	hgt	uwnd	vwnd	swnd	omega	air	shum	rhum	umf	vmf	vor	div		
Zug prc	DJF	level					0850		0700		0850	0700						
		lon					0:14		0:16		-2:14	4:14						
		lat					42:52		42:52		38:52	40:56						
	MAM	level				0850	0850				0700	0700						
		lon				-2:16	-4:16				-4:16	6:12						
		lat				40:50	38:50				40:52	44:52						
	JJA	level							0500		0850	0500				0850	0850	
		lon							-12:16		0:14	0:14				0:20	0:14	
		lat							44:52		42:52	42:52				42:52	40:54	
	SON	level				0850			0700		0850	0700				0850	0700	
		lon				2:12			6:20		2:12	6:16				-4:24	6:16	
		lat				44:48			44:52		42:52	42:52				38:52	40:50	
Zug tmp	DJF	level					0850			0700							0850	
		lon		6:16			2:20			6:16							2:14	
		lat		46:52			40:52			44:52							42:50	
	MAM	level								0850						0500		
		lon		4:14						0:14						4:18		
		lat		44:52						42:52						42:52		
	JJA	level								0850						0850	0850	
		lon		4:16						0:14						0:22	0:16	
		lat		46:52						44:52						40:52	42:52	
	SON	level					0850			0850						0500		
		lon					2:16			-4:14						0:18		
		lat					42:50			38:56						44:56		
Son prc	DJF	level							0700		0850	0700				0850	0700	
		lon								8:20		4:16	8:16			4:18	4:22	
		lat								46:52		44:52	44:52			36:50	40:52	
	MAM	level								0500		0700	0850			0850	0850	
		lon								2:18		6:14	4:16			-2:14	2:18	
		lat								42:50		44:52	44:50			38:56	40:50	
	JJA	level				0850				0700		0700	0700				0850	
		lon				-4:16				-4:20		2:16	6:16				-4:16	
		lat				36:50				40:54		44:54	44:52				40:52	
	SON	level									0850	0700				0850	0700	
		lon									0:16	4:18				-8:20	-4:22	
		lat									38:52	40:52				38:56	42:52	
Son tmp	DJF	level								0850					0850	0850		
		lon		8:18						6:14					-4:20	8:20		
		lat		44:52						42:50					38:50	42:50		
	MAM	level								0850					0500	0850		
		lon		4:18						4:16					4:20	8:16		
		lat		42:54						44:50					42:54	44:52		
	JJA	level								0850					0500			
		lon		6:18						4:18					8:24			
		lat		44:54						42:52					40:50			
	SON	level								0850					0850			
		lon								4:18					6:22			
		lat								42:50					36:50			

are the most important ones by a systematic predictor screening. This is done by applying a fast training algorithm (resilient backward propagation) iteratively to all possible predictor combinations including the different tropospheric levels and varying the domains defined by the sector latitudes and longitudes. Tab. 3 shows the results of the predictor screening. As is clearly apparent, precipitation can be predicted best by variables describing large scale humidity (shum, rhum), horizontal wind (uwnd, vwnd) and variables associated with vertical circulation (omega, div and vor) for both stations. Station temperature is best explained by the large scale temperature itself (thi, air) as well as vorticity and divergence, which are also associated with cyclonic activity.

The model calibration has been done not only once for the whole available period starting around the beginning of the 20th century but for 30-year subperiods, which are shifted by 1 year steps through the overall period in order to examine the eventually varying link between target

variable and predictors (see Tab. 3). In order to get robust results for each subperiod, the ANN for calibration was initialized 15 times. For each of these 15 ensemble members the spearman correlation coefficient between estimated and observed values for the target variable has been calculated and aggregated to an ensemble mean for the referring subperiod. The results in Fig. 3 reveal that in all cases there are so called non-stationarities (Hertig et al. 2015), i.e. the model performance is not constant. As expected, temperature estimation works generally better than the precipitation models. However, may be most striking is a drop in skill in the middle of the 20th century for precipitation at the Hoher Sonnblick. Such pronounced slumps are usually indicators for inhomogeneities, i.e. abrupt jumps in measurement time series, often caused by a change in the instrumentation or location of the instruments. However, another prominent feature, beside that, is a generally increase in skill over time for both variables in both places for all four seasons. A possible explanation is an increase in measurement and recording quality over time. In order to take this into account, the final calibration has been done for the period 1970 to 2000.

The skill of the final models, including circulation type classification, neural networks and their combination, is shown in Fig. 4. In order to compare the skill for the two main target variables precipitation and temperature to subordinated ones, the performance for specific humidity and wind at the station Zugspitze is included here. In some cases the RTF method based on circulation type classifications (triangles) is somewhat better than the ANN (circles). However, this is true only for the calibration skill (violet) and not for the real skill estimated with the validation data (green) which is the relevant one. Regarding the latter, i.e. looking only on the green symbols, the CTC based method is always the worst (except for the wind) and the ANN always the best. Further on it is striking that the skill for precipitation and temperature at the Zugspitze is always better than the skill for the Hoher Sonnblick throughout all seasons. A possible reason is assumed to be the topographical position of the Hoher Sonnblick within the Alpine main ridge and associated larger influence from the surface, modifying the direct forcing of the large scale predictors to some degree, although the skill for the Sonnblick is still remarkably high. Regarding the skill of the method combination ANN+CTC it turns out, that it is not as performant as

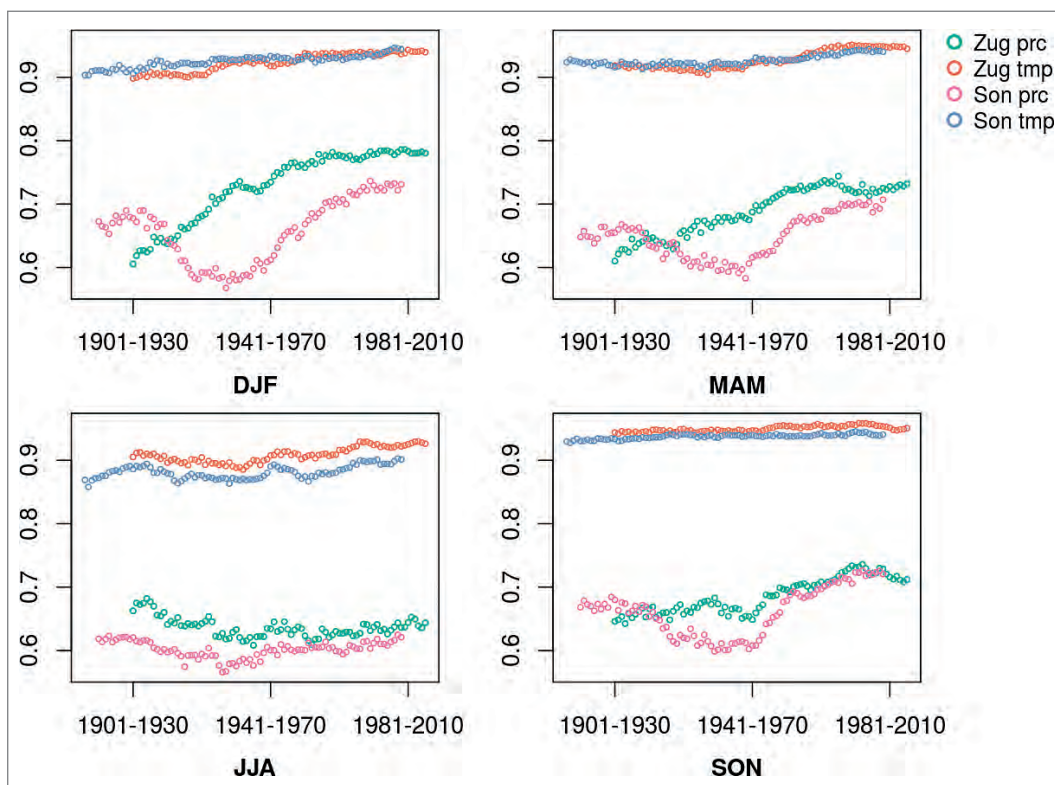


Fig. 3: Stationarity of the relation between predictors (see Tab. 3) and target variables: ensemble mean spearman correlation coefficients (ordinate) between observed values of the target variable and those estimated by artificial neural networks in shifting 30-year subperiods between 1901 to 2010 (abscissa) for winter (DJF), spring (MAM), summer (JJA) and autumn (SON).

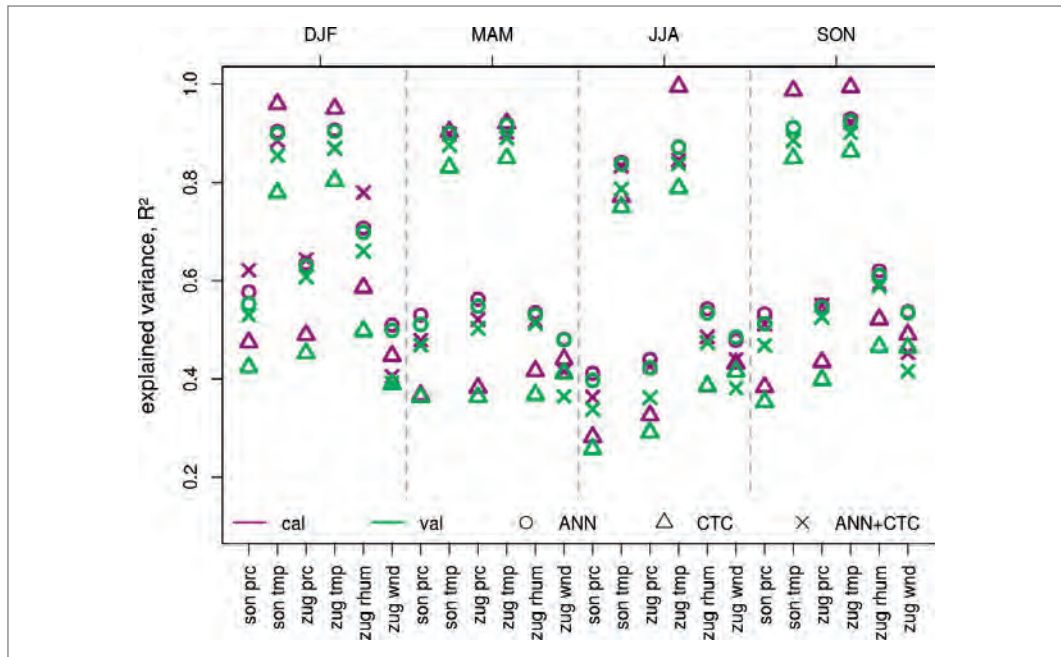


Fig. 4: Comparison of skill of ANN-, CTC- and combined downscaling models for various target variables (prc: precipitation, tmp: temperature, rhum: relative humidity and wnd: wind speed), station (zug: Zugspitze, son: Hoher Sonnblick) and season (DJF: winter, MAM: spring, JJA: summer, SON: autumn). Circles show the result of artificial neural networks (ANN), triangles those for circulation types (CTC) and crosses for the combined method (see text). Violet symbols denote the mean coefficients for 15 calibration subsamples, green symbols those for 15 validation subsamples in the period 1970 to 2000.

ANN alone. The networks in fact do learn faster within the classes, however finally they do not reach the skill level of single neural networks trained for a long time (several days up to weeks of compute time).

Even though the variance fraction of the target variables that can be explained by the downscaling models, as apparent from Fig. 4, is extraordinary high for temperature (ca. 90%) it is rather limited for precipitation, where only roughly 50% of the variability can be simulated, which is still high compared to other studies where 30% or 40% are reached (e.g. Cavazos and Hewitson 2005). However, it is still possible to estimate the precipitation changes that are caused by changes of the large scale predictors only, even if there might be other tendencies due to other factors. Thus the precipitation estimation must not be interpreted as the expected real change but only as one impulse for changes among others.

Keeping this in mind, the models are applied by feeding them with GCM output data for several scenarios. A common collection of GCM simulations is available by the Coupled Model Intercomparison Project Phase 5 (CMIP5) framework. Tab. 4 contains the models and their realisations for the scenarios. The first scenario is called "historical" (hist) and includes the boundary conditions for the global climate system since 1850 up to now. Since GCMs, even if they have reached high performance in the last few decades, can not simulate the observed climate absolutely perfect but sometimes show systematic discrepancies, the historical run of a GCM can serve as a reference run in order to determine the relative changes of any other scenario. Thus it is assumed, that the difference between the reference and the scenario runs can be transferred to the real world climate system, even if there is a general bias which is found in all model runs, but not relevant if the changes are of interest. This method is sometimes called the delta approach, and should be considered for all model interpretations. The future scenarios used in this study are the so called RCP4.5 and the RCP8.5 scenarios, the former assuming a global increase of radiative forcing by 4.5 W/m^2 and the latter by 8.5 W/m^2 in the year 2100 relative to the pre-industrial year 1850. RCP means representative concentration pathway and points out that it reflects not the emissions of radiation-relevant trace gases, but their actual concentration and its effect on the radiation budget. For the MPI model three realisations were available which helps to increase the robustness of the results by running the downscaling models with data from more than one GCM run, thus building an ensemble of runs, and calculating the ensemble mean result.

Tab. 4: Overview of the general circulation models and their scenarios used for driving the downscaling models. All model datasets offer a historical run (hist) and those for representative concentration pathways (RCP) for radiation-relevant trace gases leading to an increase of 4.5 respectively 8.5 W/m² in the radiative forcing of the climate system. For the German model three ensemble members are available for the RCP scenarios.

GCM model	Responsible Institute	Realisations/Scenarios
MPI-ESM-LR	Max-Planck-Institute, Germany	Hist, RCP4.5 (3 ens. members), RCP8.5 (3 ens. members)
HadGEM2-CC	Met Office, United Kingdom	Hist, RCP4.5, RCP8.5
ACCESS1-0	CSIRO (Commonwealth Scientific and Industrial Research Organisation) und BOM (Bureau of Meteorology), Australia	Hist, RCP4.5, RCP8.5
CMCC-CMS	CMCC (Centro Euro-Mediterraneo per i Cambiamenti Climatici), Italy	Hist, RCP4.5, RCP8.5
IPSL-CM5A-LR	IPSL (Institut Pierre Simon Laplace), France	Hist, RCP4.5, RCP8.5

The time series of annual mean temperatures and annual precipitation sums produced by driving the downscaling models with the GCM scenario output data for the respective predictor variables is shown in Fig. 6. While the thin lines, representing the single ensemble members result, allow to estimate the spread of the simulated target variables, the ensemble means point out their long term evolution. The temperature time series (Fig. 6a and b) show a strong trend as expected, which has been positively tested for significance by the trend-noise-ratio using the 5% uncertainty level. According to these results the station annual mean temperatures at the Zugspitze summit will approach the freezing point in the year 2100 for the RCP8.5 scenario which will have dramatic consequences for the whole environment in this region. At the Sonnblick the absolute temperature is generally a bit lower, but the changes are also significant.

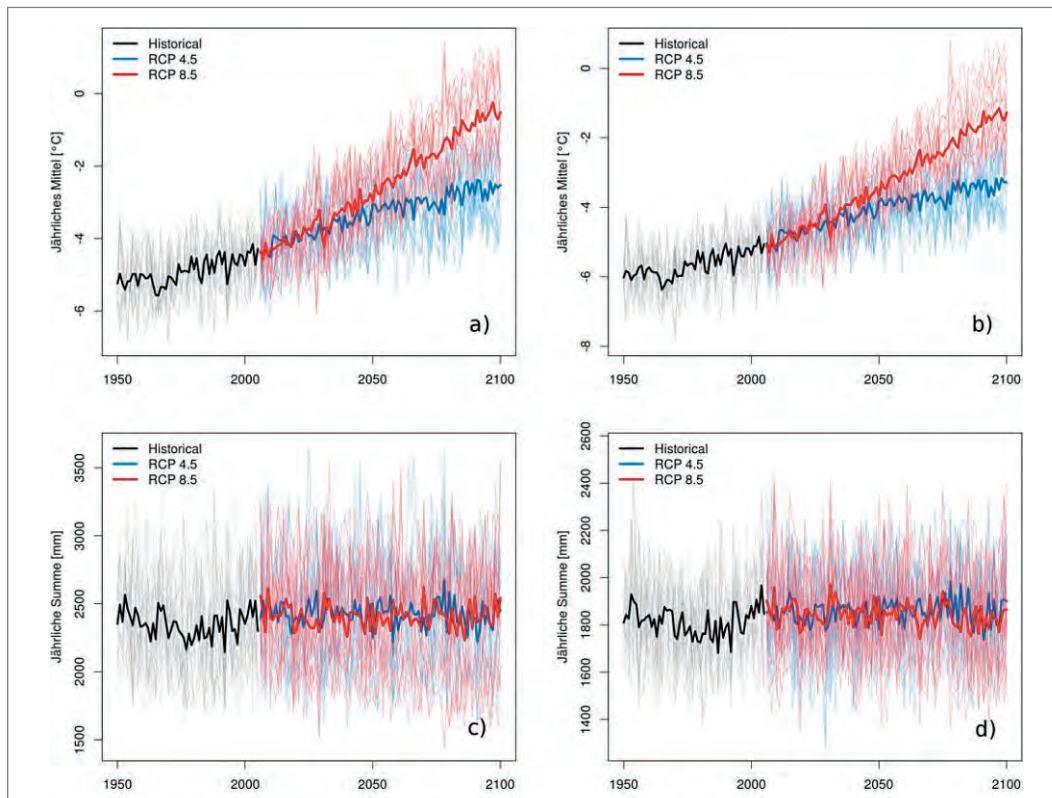


Fig. 5: Evolution of target variables temperature and precipitation simulated by downscaling models using circulation type classifications, artificial neural networks and their combination in the period 1970 to 2100 aggregated to annual values (means of temperature, sums for precipitation). Thin lines denote single time series of 15 cross validated model runs for each of the seven GCM runs, while the thick line represents the overall ensemble mean. a) Zugspitze temperature, b) Sonnblick temperature, c) Zugspitze precipitation, d) Sonnblick precipitation.

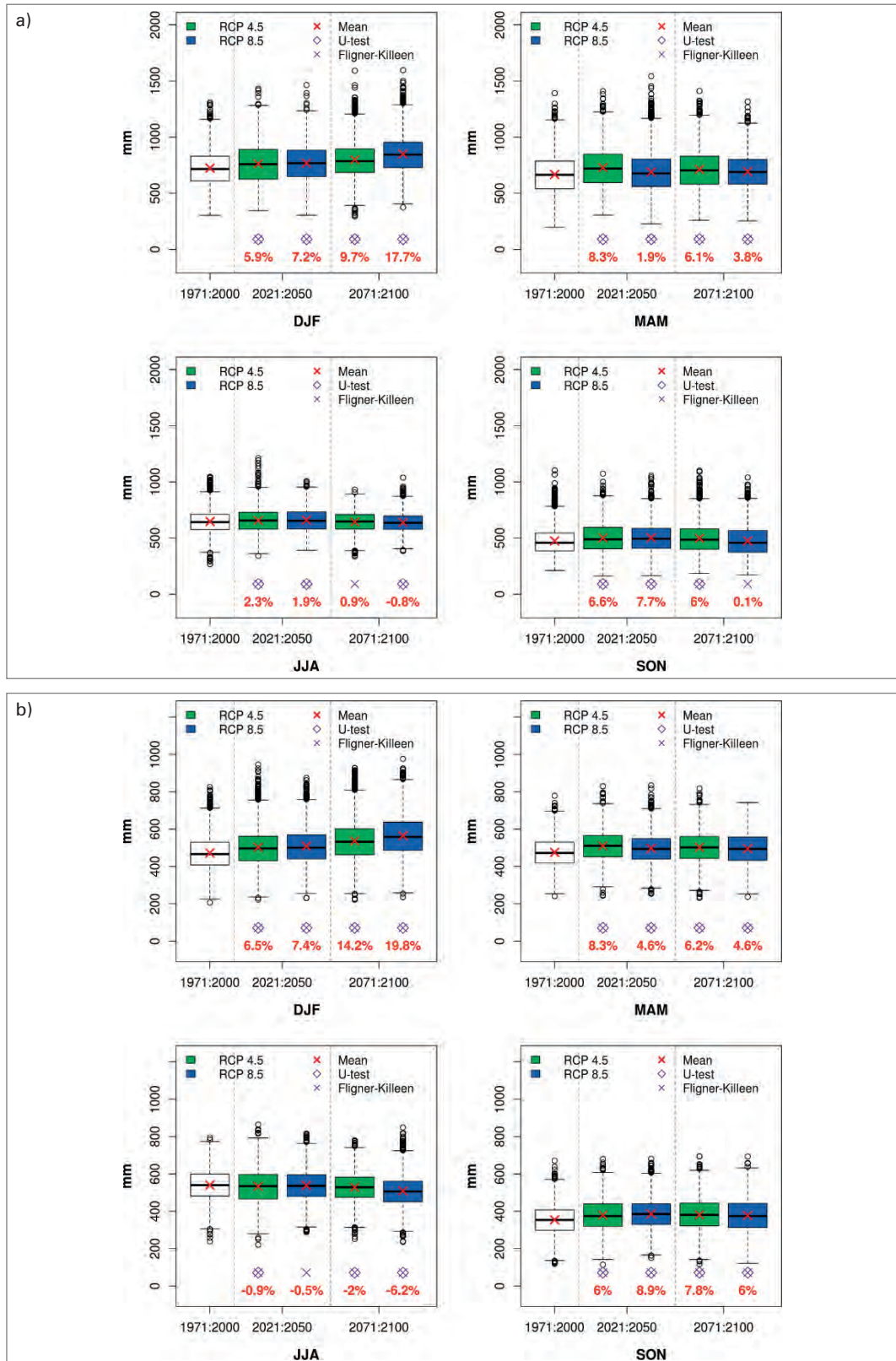


Fig. 6: Precipitation changes for a) Zugspitze and b) Hoher Sonnblick discerned by seasons: Red cross shows the mean and boxplots the distribution of seasonal precipitation sums estimated by 15 cross validation runs of neural network downscaling models driven by 7 GCM runs for the historical reference period 1971 to 2000 and the RCP4.5 (green) and RCP8.5 (blue) scenarios in the time range 2021 to 2050 and 2071 to 2100. Red numbers denote the changes in percent compared to the historical reference period. A violet circle indicates a significant difference in the central tendency according to the U-test, a violet cross a significant change in variability according to the Fligner-Killeen-test on the 5% uncertainty significance level.

Regarding precipitation, no significant trend can be observed for both RCP scenarios if the annual sum is considered at both stations (Fig. 6c and d).

However, if the precipitation is analysed separately for each season, different results are apparent. Fig. 6 shows the respective changes for seasonal precipitation sums for the 30-year periods 2021 to 2050 and 2071 to 2100 compared to the reference period 1971 to 2000 as obtained by the ANN models, which give the most reliable results compared to the other methods. According to the U-test there are significant changes for both stations in all seasons. In winter (DJF), spring (MAM) and autumn (SON) both, Zugspitze as well as Hoher Sonnblick show a similar tendency. In winter precipitation is constantly increasing, stronger for the RCP8.5, somewhat slower for the RCP4.5 scenario and somewhat stronger for the Hoher Sonnblick than for the Zugspitze. In spring (MAM) and autumn (SON) an initial strong increase in precipitation is followed by either constant or even decreasing rates of growth, except for RCP8.5 at the Zugspitze and RCP4.5 at Hoher Sonnblick with an accelerating increase. Regarding the summer (JJA) Hoher Sonnblick shows a growing decrease in precipitation for both scenarios. The Zugspitze, however, is characterized by an initial increase followed by conditions comparable to the historical period or even below.

Two antagonistic main processes forcing the moisture budget and precipitation are supposed to be responsible for such diverse climate change signals: i) increasing storage capacity for water vapor in a warmer troposphere and therefore increased moisture transport into the atmosphere with increased precipitation sums and ii) strengthening of the Mediterranean subtropical anticyclonic high pressure cell (Jacobeit et al. 2017) with increased subsidence and stable conditions suppressing precipitation. Thus it is fairly likely that at the beginning of a global warming period, the moisture storage effect dominates at the Zugspitze in summer until the effects of changing circulation dynamics prevail. The difference to Hoher Sonnblick, where increasing precipitation reduction prevails in summer, might be explained by its position in the interior of the Alpine ridge where air masses already have lost considerable amounts of their moisture content due to luv effects at the edge of the mountain ridge. Maybe the effect of increased moisture transport is therefore less important in the center of the Alps, a topic for further investigations. In any case, high mountain climate is indicated to be changed considerably according to the presented results with strong implications for the whole ecosystem of the Alps to be expected.

References

- Auer I., Böhm R., Jurkovic A., Lipa W., Orlik A., Potzmann R., Schöner W., Ungersböck M., Matulla C. Briffa K., Jones P.D., Efthymiadis D., Brunetti M., Nanni T., Maugeri M., Mercalli L., Mestre O., Moisselin J.-M., Begert M., Müller-Westermeier G., Kveton V., Bochnicek O., Stastny P., Lapin M., Szalai S., Szentimrey T., Cegnar T., Dolinar M., Gajic-Capka M., Zaninovic K., Majstorovic Z., Nieplova E. (2007): HISTALP – Historical instrumental climatological surface time series of the Greater Alpine Region 1760–2003. *International Journal of Climatology* 27, 17–46.
- Bavay M., Lehning M., Jonas T., Löwe H. (2009) Simulations of future snow cover and discharge in Alpine headwater catchments. *Hydrol Process* 23: 95–108. doi:10.1002/hyp.7195
- Beck C. and A. Philipp (2010): Evaluation and comparison of circulation type classifications for the European domain. *Physics and Chemistry of the Earth*, 35, 374–387. DOI: 10.1016/j.pce.2010.01.001
- Beck C., A. Philipp and F. Streicher (2016): The effect of domain size on the relationship between circulation type classifications and surface climate. *Int. J. Climatol.* 36: 2692–270.
- Bissolli, P., Dittmann, E., 2003. Objektive Wetterlagenklassen (Objective weather types). In: Klimastatusbericht 2003. DWD (Hrsg.). Offenbach 2004, Germany (in German).
- Brunetti, M., M. Maugeri, T. Nanni, I. Auer, R. Böhm & W. Schöner (2006): Precipitation variability and changes in the greater Alpine region over the 1800–2003 period. *Journal of Geophysical Research, Atmospheres*, D11107, 1–29.
- Castebrunet, H., N. Eckert, G. Giraud, Y. Durand & S. Morin (2014): Projected changes of snow conditions and avalanche activity in a warming climate: the French Alps over the 2020–2050 and 2070–2100 periods, *The Cryosphere*, 8(5), 1673–1697.
- Cavazos T. and B.C. Hewitson (2005): Performance of NCEP – NCAR reanalysis variables in statistical downscaling of daily precipitation. *Clim. Res.*, 28, 95–107.

- European Environment Agency (2017a): Climate change, impacts and vulnerability in Europe 2016. An indicator-based report. EEA Report 1/2017, Luxembourg.
- European Environment Agency (2017b): Climate change adaptation and disaster risk reduction in Europe. Enhancing coherence of the knowledge base, policies and practices. EEA Report 15/2017, Luxembourg.
- Fraedrich K., H. Jansen, E. Kirk, U. Luksch and F. Lunkeit (2005): The Planet Simulator: Towards a user friendly model. *Meteorologische Zeitschrift*, 14/3, 299–304.
- Gobiet, A., S. Kotlarski, M. Beniston, G. Heinrich, J. Rajczak, M. Stoffel (2014): Science of the Total Environment, 493, 1138–1151.
- Heinrich, G., A. Gobiet, H. Truhetz, T. Mendlik (2013): Expected climate change and its uncertainty in the Alpine region: extended uncertainty assessment of the reclip: century and ENSEMBLES multi-model dataset. *Wegener Center Scientific Report* 50.
- Hertig, E., C. Beck, H. Wanner and J. Jacobeit (2015): A review of non-stationarities in climate variability of the last century with focus on the North Atlantic-European sector. *Earth-Science Reviews*, doi:10.1016/j.earscirev.2015.04.009.
- Hess, P., and H. Brezowsky, 1977: Katalog der Großwetterlagen Europas 1881–1976, 3e verbesserte und ergänzte Auflage. *Berichte des Deutschen Wetterdienstes* 113, Offenbach, Germany, 70 pp.
- Huss, M. (2011): Present and future contribution of glacier storage change to runoff from macroscale drainage basins in Europe. *Water resources research*, 47, W07511.
- Huss, M. (2012): Extrapolating glacier mass balance to the mountain-range scale: the European Alps 1900–2100, *The Cryosphere*, 6(4), 713–727.
- Huth R., C. Beck, A. Philipp, M. Demuzere, Z. Ustrnul, M. Cahynová, J. Kyselý, and O.-E. Tveito (2008): Classifications of atmospheric circulation patterns: recent advances and applications. *Annals of the New York Academy of Sciences*. 1146, 105–152.
- Keeley, S., Sutton, R., Shaffrey, L., (2012), The impact of North Atlantic sea surface temperature errors on the simulation of North Atlantic European region climate. *Q.J. R. Meteorol. Soc.*, 138, 1774–783.
- Kobierska F, Jonas T, Zappa M, Bavay M, Magnusson J, Bernasconi SM (2012) Future runoff from a partly glacierized watershed in Central Switzerland: a two-model approach. *Adv Water Resour*, 55, 204–214.
- Lamb, H., 1972: *British Isles Weather Types and a Register of Daily Sequence of Circulation Patterns, 1861–1971*. *Geophysical Memoirs*, Vol. 116, Her Majesty's Stationery Office, 85 pp.
- Lenderink, G., Buishand, A., Van Deursen, W., (2007), Estimates of future discharges of the river Rhine using two scenario methodologies: direct versus delta approach. *Hydrol. Earth Syst. Sci.* 11 (3), 1145–1159.
- Lutz K., J. Jacobeit, A. Philipp, S. Seubert, H. Kunstmann & P. Laux (2011): Comparison and evaluation of statistical downscaling techniques for station-based precipitation in the Middle East (2011), *International Journal of Climatology*, 32, 1579–1595. DOI: 10.1002/joc.2381
- National Center for Atmospheric Research Staff (Eds), 2017: *The Climate Data Guide: Common Spectral Model Grid Resolutions*. Retrieved from <https://climatedataguide.ucar.edu/climate-model-evaluation/common-spectral-model-grid-resolutions>.
- Philipp A., C. Beck, R. Huth and J. Jacobeit (2016): Development and comparison of circulation type classifications using the COST 733 dataset and software. *Int. J. Climatol.* 36: 2673–2691.
- Räisänen J. (2007): How reliable are climate models? *Tellus*, 59A, 2–29.
- Rigling, A., C. Bigler, B. Eilmann, E. Feldmeyer-Christe, U. Gimmi, C. Ginzler, U. Graf, P. Mayer, G. Vacchiano, P. Weber, T. Wohlgemuth, R. Zweifel, and M. Dobbertin, 2013: Driving factors of a vegetation shift from Scots pine to pubescent oak in dry Alpine forests. *Global Change Biology*, 19, 229–240
- Steiger R (2010) The impact of climate change on ski season length and snowmaking requirements in Tyrol, Austria. *Clim Res* 43: 251–262. doi:10.3354/cr00941
- Stoffel, M., Tiranti, D. and Huggel, C., 2014, 'Climate change impacts on mass movements – Case studies from the European Alps', *Science of The Total Environment* 493, 1255–1266 (DOI: 10.1016/j.scitotenv.2014.02.102).
- Strasser U., T. Marke, L. Braun, H. Escher-Vetter, I. Juen, M. Kuhn, F. Maussion, C. Mayer, L. Nicholson, K. Niedertscheider, R. Sailer, J. Stötter, M. Weber and G. Kaser (2018): The Rofental: a high Alpine research basin (1890–3770 m a.s.l.) in the Ötztal Alps (Austria) with over 150 years of hydrometeorological and glaciological observations. *Earth Syst. Sci. Data*, 10, 151–171.
- Teutschbein, C., Seibert, J., (2012), Bias correction of regional climate model simulations for hydrological climate-change impact studies: Review and evaluation of different methods. *Journal of Hydrology*, 456–457, 12–29.
- Wilks, D. S., (2006), *Statistical Methods in the Atmospheric Sciences*, 2nd edn. Elsevier: Academic Press, 627 pp.
- Zorita E., H. von Storch (1990): The Analog Method as a Simple Statistical Downscaling Technique: Comparison with More Complicated Methods. *Journal of Climate*, 12, 2474–2489.

12 Evaluation of Measurement Series from high Mountain Stations

Ludwig Ries, Cedric Couret, German Environment Agency; Ye Yuan, Technical University of Munich; Esther Giemsa, Jucundus Jacobeit, Institute of Geography, University of Augsburg; Stephan Hachinger, Leibnitz Supercomputing Centre

12.1 Mountain Stations (Ludwig Ries)

12.1.1 The first alpine measurement stations and the present situation

The first high mountain stations were pioneers in atmospheric and climate research. In Central Europe, for example, important Alpine observation stations had been set up between the end of the 19th century and the first third of the 20th century. At a time when there were practically no methods of remote observation, these observatories enabled pioneering research to be carried out in the field of weather observation. Under very suitable visibility conditions, the radius of the observations could be extended to a range of more than 200 km. Apart from coastal areas, these weather stations were the first observatories for atmospheric remote sensing. As a result, it had become possible to detect weather changes at long distances and to transmit the results by telegraph to the central weather offices. In Austria, for example, the station Hoher Sonnblick was opened in 1886. The weather tower on the Zugspitze in Germany started in 1899 and the station Jungfrauoch in Switzerland in 1931. The station Puy de Dome in Auvergne, France, even had begun in 1876.

Since the mid-20th century, the number of high mountain stations worldwide has increased considerably. Today, a network of high mountain stations in Africa, Asia, North and South America supports atmospheric environmental monitoring and climate research. Even today, the great scientific advantage is the highly precise continuous measurement along the time axis.

12.1.2 Mountain stations in the Global Atmosphere Watch program

A prominent group of mountain stations supporting atmospheric research contributes to the station network of the Global Atmosphere Watch program (GAW). GAW started in 1989 as module for monitoring the physical and chemical state of the atmosphere within the Global Climate Observing System (GCOS) of UNO/WMO. From the very beginning the ground based, fixed station network had been the backbone of the Global Atmosphere Watch monitoring program. Presently GAW has evolved to an integrated network for atmospheric chemistry and physics observations, with additional ground based remote sensing measurements and measurements from ships, air planes and satellites.

The map (Fig. 1.1) provides the geographic distribution and the types of stations on mountains and selected high elevated sites, operating presently for atmospheric environmental research in GAW (cf. Tab. 1.1).

12.1.3 What is a mountain station?

In the sense of practical exploration, mountain stations provide platforms for atmospheric measurements at particularly representative locations on the mainland or on an island to allow drawing conclusions about the state of the atmosphere for a catchment area as large as possible. The amount of representative data in the measured time series should be as high as possible. This includes, that appropriate locations for mountain stations should be minimally influenced by pollution or other relevant anthropogenic influences.



Fig. 1.1: Map of GAW global observatories. GAW regional stations and contributing stations contribute for specialized atmospheric chemistry and physics monitoring supporting the worldwide Global Atmosphere Watch program. The selection includes stations which are in operational status and which measure aerosols and/or gases (greenhouse and reactive gases) and meteorological parameters. Data source: Gawsis station information system: <https://gawsis.meteoswiss.ch>

In contrary to the definitions of high mountain regions used in geography and geomorphology, we target an understanding, that applies worldwide across different climate zones and altitudes. In this way, for example, a comparable characteristic for lower altitude sites can be specified for moderate climates. However, this will not apply also to warmer climatic zones in South America or to highlands in largely uninhabited desert areas (e.g. Himalaya) or to areas in the Arctic and Antarctic. Considered worldwide, the characteristics cannot be understood as being constant over different climatic zones.

For a better comprehension of the whole phenomenon and because the characteristics for high mountain stations change fluently from higher to lower sites this text also refers partly to lower mountain sites. The overall objective of this chapter is, to identify the characteristics that high mountain stations and mountain stations in general have in common, to differentiate them and to be able to use these characteristics to analyze and understand measurement series from high mountain and mountain stations.

12.1.4 The objective of measurements at high altitude stations

The principal purpose for the measurement of high-altitude data is gaining representative information about the state of the atmosphere and the lower free troposphere. For example, for measurements for Global Atmosphere Watch, the main objective is to monitor the chemical and physical state of the atmosphere for detecting effects on climate change and to improve scientific understanding of the global climate system. This is different from the classical understanding of monitoring air quality which focuses on the adverse health effects on people from air pollution and which concentrates on ground-based sites in populated and additional at rural regions. Despite the very successful emergence of ground-based remote sensing programs measured time series from altitude mountain stations have the essential advantage to provide consecutive information along the time line. This enables a combined analysis. Remote sensing delivers data along the vertical altitude scale but mostly only for short times. Additionally, measuring the same parameter on a fixed mountain station, the monitoring data deliver a continuous time history along the time scale. A newer example for such a timeseries at Zugspitze station can be found in Yuan Y. and Ries L. et al., 2018. Together both kinds of data from both scales are essential for a better understanding and support validation and quality assurance of scientific results.

Tab. 1.1: Table of 45 GAW stations. It consists of global observatories, GAW regional stations and contributing stations working for additional monitoring activities supporting GAW. The selection includes stations which are in operational status and which measure aerosols and/or atmospheric gases (greenhouse and reactive) and meteorological parameters. Sites have been selected with altitudes starting from 950 meters a.s.l. or higher. Reference: Gawsis station information system: <https://gawsis.meteoswiss.ch>

WMO Region	Country	Station	Elevation (m a.s.l.)	GAW Station Type	Latitude (in °)	Longitude (in °)
Africa	Algeria	Assekrem	2710	GAW Global	23.26666641	5.633333206
Africa	Spain	Izana (Tenerife)	2373	GAW Global	28.30900002	-16.49939919
Africa	France	La Reunion	2160	GAW Regional	-21.0796	55.3841
Africa	Kenya	Mt. Kenya	3678	GAW Global	-0.0622	37.29719925
Antarctica	France	Concordia, Dome C	3233	GAW Other	-75.0998612	123.3334808
Antarctica	Belgium	Princess Elisabeth station	1350	GAW Regional	-71.95	23.35
Antarctica	United States	South Pole	2841	GAW Global	-89.9969482	-24.79999924
Asia	Taiwan, Province of China	Lulin	2862	GAW Other	23.46999931	120.8700027
Asia	China	Mt. Waliguan	3810	GAW Global	36.28749847	100.8963013
Asia	Nepal	Nepal Climate Observatory – Pyramid	5079	GAW Global	27.95779991	86.81490326
Asia	Viet Nam	Pha Din	1466	GAW Regional	21.5731	103.5157
Europe	Armenia	Amberd	2070	GAW Regional	40.38333511	44.25
Europe	Bulgaria	BEO Moussala	2925	GAW Regional	42.17919922	23.5855999
Europe	Slovakia	Chopok	2008	GAW Regional	48.96666718	19.60000038
Europe	Germany	Hohenpeissenberg	985	GAW Global	47.80149841	11.00961971
Europe	Switzerland	Jungfrauoch	3580	GAW Global	46.54748917	7.985089779
Europe	Russian Federation	Kislovodsk	2070	GAW Regional	43.72999954	42.65999985
Europe	Slovenia	Krvavec	1740	GAW Regional	46.29734948	14.53331438
Europe	Italy	Monte Cimone	2165	GAW Global	44.16666794	10.6833334
Europe	Italy	Monte Curcio	1796	GAW Regional	39.315972	16.42325
Europe	Spain	Montsec	1571	GAW Regional	42.051335	0.729564
Europe	Germany	Ochsenkopf	1185	GAW Other	50.0301	11.8084
Europe	Italy	Plateau Rosa	3480	GAW Regional	45.93534088	7.7073102
Europe	France	Puy de Dome	1465	GAW Global	45.7723	2.9658
Europe	Switzerland	Rigi	1031	GAW Regional	47.06739	8.46333
Europe	Germany	Schauinsland	1205	GAW Regional	47.90000153	7.916666508
Europe	Poland	Sniezka	1603	GAW Regional	50.73333359	15.73333359
Europe	Austria	Sonnblick	3106	GAW Global	47.05389023	12.95888901
Europe	Denmark	Summit	3238	GAW Regional	72.58000183	-38.47999954
Europe	Germany	Zugspitze-Gipfel	2962	GAW Global	47.421075	10.985896
Europe	Germany	Zugspitze-Schneefernerhaus	2671	GAW Global	47.4165	10.97964
North America	United States	Appalachian State University	1076	GAW Other	36.21300125	-81.69200134
North America	United States	Boulder Table Mountain (CO)	1689	GAW Other	40.125	-105.2369995
North America	United States)	Desert Rock (NV)	1007	GAW Other	36.61999893	-116.0179977
Central America	Mexico	Mex High Altitude Global Climate Observation Cente	4560	GAW Other	18.985842	-97.314433
North America	United States	Niwot Ridge – T-van (CO)	3523	GAW Regional	40.04999924	-105.5899963
North America	United States	Steamboat Springs (CO)	3220	GAW Regional	40.45500183	-106.7440033
North America	United States	Table Mountain (CA)	2286	GAW Regional	34.38233948	-117.688797
North America	United States	Wendover (UT)	1320	GAW Regional	39.90000153	-113.7200012
North America	Canada	Whistler Mountain	2182	GAW Regional	50.05929947	-122.9576035
South America	Bolivia	Chacaltaya	5340	GAW Regional	-16.2000008	-68.09999847
South America	Chile	El Tololo	2154	GAW Regional	-30.16833	-70.80361
South-West Pacific	United States	Mauna Kea (HI)	4204	GAW Other	19.82999992	-155.4799957
South-West Pacific	United States	Mauna Loa (HI)	3397	GAW Global	19.53623009	-155.5761566
South-West Pacific	Malaysia	Tanah Rata	1545	GAW Regional	4.484235	101.371606

12.1.5 What determines a site at high altitude?

12.1.5.1 Orography

For atmospheric research, it is not only the altitude above sea level that is relevant, but also the surface shape of the catchment area of the air masses which pass the station and whether the terrain is covered with vegetation and what the vegetation is like. It is also relevant how far away from the monitoring station there are settlement areas, how large the settlement areas are and what type and extent of air pollution is produced by the settlement areas. It is also crucial how the atmospheric circulation, which is determined by the climate zone and the surface shape in large, affects the transport of air masses to the measuring station, for example whether the station is situated on a coast or within a mountain chain or whether the mountain station is in the middle of a mainland or on an island, surrounded by the ocean.

Under special circumstances, an elevated station exceptionally may even not be located on a mountain. This is the case if the measuring station is located e.g., on an uninhabited plateau, which can be in a desert area or in a polar region. Examples for such stations are Assekrem (2710 m a.s.l.) in the Saharan region and South Pole (2841 m. a.s.l.). Despite the fact, that in this special situation the diurnal variation for determining representative periods of time and data must be interpreted principally different from sites on mountains, these stations were included also in this analysis. This was necessary, because on the one hand, the differences between the characteristics of the stations change fluently and it is relevant for a scientific understanding to analyze this situation correctly and to know the change of characteristics. And on the other hand, this knowledge is of fundamental importance when measurement series of elevated stations must be examined for their representativeness.

12.1.5.2 Meteorology

Apart from meteorological influences controlled by orography, mountain stations are exposed to continuously changing air masses from the atmospheric boundary layer and the lower free troposphere. This continuous change is controlled mainly by the diurnal variation and the seasonal variation. In moderate climates during the winter months from October to March mountain stations like site Zugspitze, are more frequently above the lower atmospheric boundary layer. Additionally, an existing snow cover then can prevent convective up wind transport. This results in a good separation from air within the atmospheric boundary layer (ABL) and clean air above. In contrast, during warmer summer and autumn a convective upwind system is formed, which transports during the day larger air masses from lower altitudes to the mountain station. Then often a maximum occurs in the midday and afternoon hours. In the evening hours the thermal upwind transport subsides again. The nightly cooling and collapse of the atmosphere causes that air masses with increased representativeness can be measured regularly at night. This thermal upwind phenomenon occurs when there is no snow cover under the influence of the sun on almost every mountain slope worldwide. In larger mountain regions, this intensive upward transport of air masses can lead also to an additional lateral horizontal transport of air. This phenomenon also is well known under the term alpine pumping. For further explanation see Winkler et. al. 2006.

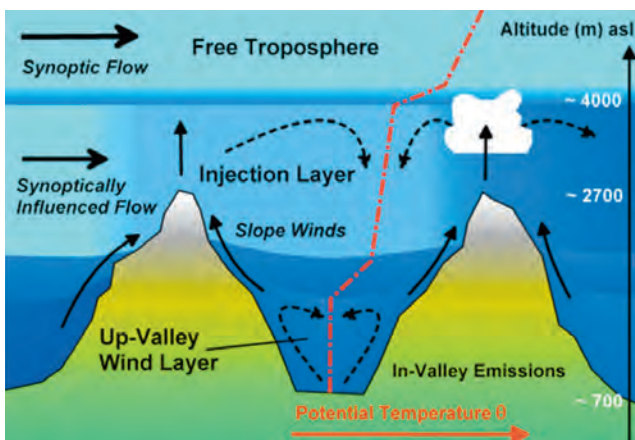


Fig. 1.2: Scheme of daytime air dynamics at mountain stations during summertime, according to Henne, 2004. For further explanation see the text.

This thermal upwind phenomenon occurs when there is no snow cover under the influence of the sun on almost every mountain slope worldwide. In larger mountain regions, this intensive upward transport of air masses can lead also to an additional lateral horizontal transport of air. This phenomenon also is well known under the term alpine pumping. For further explanation see Winkler et. al. 2006.

Figure 1.2 presents a schematic overview about the daytime dynamics of air flow at high mountain stations in Europe. It shows synoptic flow as well as the mainly summerly thermic upwind system as well as the injection layer above, which contains especially during the season with long radiation length rests from the upward wind injection from the last day.

12.1.6 Spatial representativeness of mountain stations

The spatial representativeness of a measuring station is of fundamental importance for the significance of the measurement data and their interpretation. In this section, a selection of different approaches is presented to determine the spatial representativeness of an individual mountain station.

12.1.6.1 Contribution of the topography to the influence of the atmospheric boundary layer

Mountain stations receive continuous influences from the underlying ground in combination with the ongoing air mass transport. The surface structure of the surrounding topography impacts significantly the dynamics and hence measurable frequency and direction of air mass transport to the station. Collaud, 2018, identifies topographical features which influence aerosol measurements at high altitude stations. Due to the dominant effect of the individually pronounced topography it becomes evident that the station height alone is not always a sufficient criterion for predicting correctly the proportion of measurements in the lower free troposphere (LFT). This approach can be used to compare the potential representativeness between stations or for the planning and selection of an optimal new site location between several opportunities.

12.1.6.2 Analysis of regions of ground influenced wind origin by sector classification

With meteorological data transport modelling can be used to gain quantitative information about the representativeness of a station. The presented approach uses a geometrical analysis of the flow frequencies, classified in direction and distance from the measurement station. The result gives a classification of regions of origin of wind transported to the measurement site. In the following example for site Zugspitze Schneefernerhaus the transport model FLEXPART with backward directed dispersion trajectories has been applied to a longer and hence representative 2-year data set of meteorological analysis data. Around the original grid point of the Environmental Research Station Schneefernerhaus a set of circles has been constructed with radii 300 km, 600 km and 900 km. Additionally in each of the four main directions NW, SW, SE and NE the circles have been subdivided in rectangular sectors. Thus, the whole area consists of 12 circular segments. For the analysis of the station ground influenced wind data have been selected from cases when the wind before arrival had passed an altitude of maximal 150 m a.s.l. or below. The relative ratio of frequency of arriving ground influenced wind is defined as footprint signal and thus can be quantified as a function of the cardinal direction. The resulting frequency statistic shows the possible ground influence from on-flowing wind which can affect measurements at the station. These frequency statistics explain the numerically complex results in a simpler and better communicable form. The analysis was only carried out with a maximum transport time of 5 days for European wide calculations. For each region, the percentage share of the total footprint sum was calculated in the model domain Europe. The area of this model domain ranged from 75 to 35 °N and from -10 °W to 34 °E (Fig. 2).

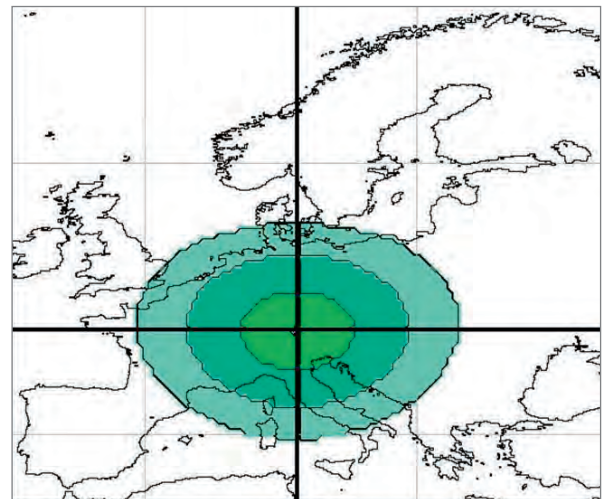


Fig. 1.3: Geometrical scheme of the 12 sectors around the site Environmental Research Station Zugspitze/Schneefernerhaus. Source: Birmili et. al. 2008.

Tab. 1.2: Relative transport frequency of on-streaming wind to the Environmental Research Station Schneefernerhaus with a maximum transport time of 5 days. The data are from 2005 and 2006. Applied Transport model was FLEXPART. All releases from 00:00 to 24:00hr have been used. Source: Birmili et. al. 2008.

Radius (km)	NW (in %)	SW (in %)	SE (in %)	NE (in %)	Total (%)
300	5.50	19.93	3.38	4.91	
600	5.18	10.62	2.41	2.27	
900	3.95	5.89	1.89	1.83	
Sum	14.63 (%)	36.44 (%)	7.68 (%)	9.01 (%)	67.76 (%)

12.1.6.3 Station footprints as quantifiable areas of influence from arriving ground-based winds.

The atmospheric dynamic produces very differentiated transport patterns of air arriving at a mountain station. Air mass transport is a result of the continuously measured and varying weather events. To gain quantifiable information about direction and frequency of transported air a series of backward directed dispersion trajectories (retro-plumes) can be used systematically. The following example for the site of Zugspitze-Schneefernerhaus is based on the meteorological analysis data of two consecutive years. The FLEXPART transport model was used to calculate series of backward trajectories. The results are values of a source-receptor relationship (QRB) as a function of latitude, and length for a release time t . This QRB is defined to the length of stay in a 150-m high layer above ground ("footprint") The unit of the Footprint QRB is ns/kg. This can be interpreted as empirical frequency from where ground influenced air has arrived at the Environmental Research Station Schneefernerhaus within the time which was described by the given input data. Because of known seasonal variations in the atmospheric transport the integrated results show different characteristics for the integrated seasonal data.

During *wintertime* the influence from ground reaches a minimum. Reason is the better separation from the ground as result of the frequently quite lower atmospheric boundary layer during wintertime. Also, the influence of eastern transported air is minimal. Simultaneously the air mass transport from NW and W is increased, compared to the other seasons. This also can be seen in wind rose statistics, where during wintertime the highest windspeed from western directions can be observed.

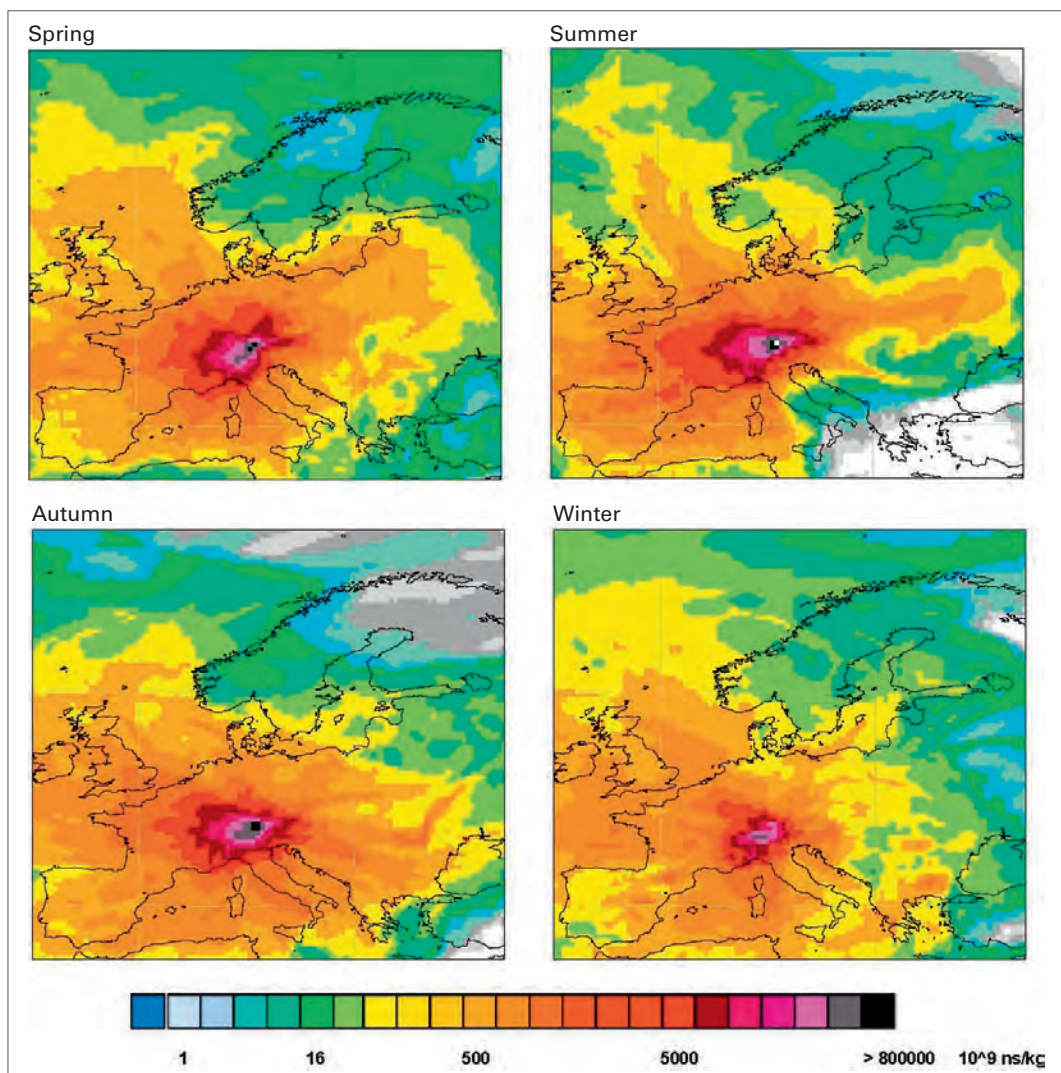


Fig. 1.4: Average seasonal transport frequency of air to station Zugspitze in the ground layer with a maximum transport time of five days for the duration of 2005 and 2006. Model: Flexpart, Source, Birmili et. al. 2008.

In *springtime*, the lateral wind transport and speed still is comparatively high. Like at wintertime conditions the lateral transport from western directions is enhanced. The convective upwind air mass transport starts and becomes gradually stronger with increasing day length.

At *summertime* the influence from ground-based air masses reaches a relative maximum. This can be understood as result of the intensive energy input from longer and more intensive sunshine duration and a resulting convective upwind system. This results in a more cellular weather regime and reduces long range lateral air mass transport mainly from western directions. During summer there is more eastern influence, whereas the western air mass transport changes from NW to W.

In *autumn*, the often-similar temperatures of the oceans and the continents create a more frequent stable air stratification. Because of relatively warm temperatures, compared to winter, the ground influence still is comparatively high.

12.2 Measurement series (Ludwig Ries, Cedric Couret)

Although the set of measurable variables in atmospheric chemistry and physics is much larger, in this section, we concentrate on selected measurement series examples from greenhouse gases, reactive gases and aerosols. The continuous measurement of parameters, relevant for the state of the Earth Atmosphere is a core issue in monitoring the changes in the climate system of the Earth's atmosphere. Within this section selected key measurement variables are presented being measured continuously by Global Atmosphere Watch for the Global Climate Observation System (GCOS).

12.2.1 Selected examples of measurement series and their role in atmospheric chemistry and physics

12.2.1.1 Carbon Dioxide

The most important cause of global warming are man-made greenhouse gases. Due to its high atmospheric concentrations, carbon dioxide is the most important greenhouse gas in addition to water vapor. The global concentrations of CO₂ have increased by 40 % since the beginning

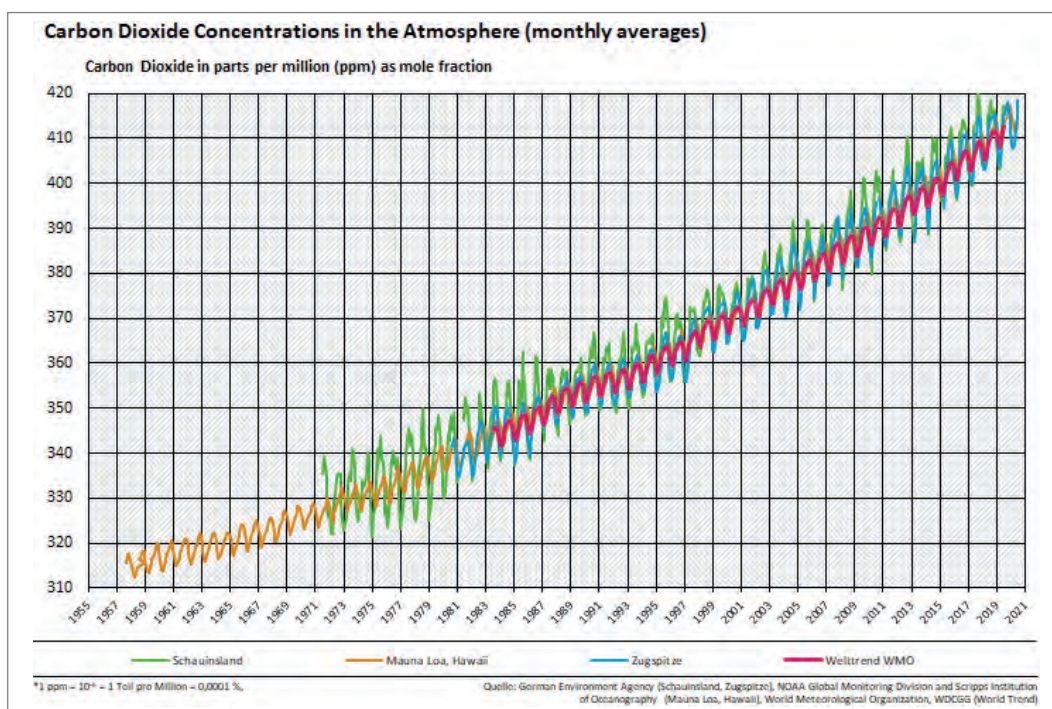


Fig. 2.1: Measured time series of carbon dioxide from Schauinsland GAW Regional station, Mauna Loa GAW global station and Zugspitze GAW global station, additionally compared with an average atmospheric CO₂ world trend. Source: website of Umweltbundesamt. www.uba.de

of industrialization in 1750. In contrast, CO₂ concentrations were almost constant in the previous 10000 years. The current increase in CO₂ is about 100 times faster than ever before in the past.

Long rows and their meaning

Long CO₂ measurement series provide a reliable measure of the global increase in CO₂ and continuously document the effect of fossil fuel combustion on the atmosphere. Thanks to their accuracy, they enable science to distinguish the effect of fossil fuel combustion from the seasonal fluctuation of the biosphere. This provides a reliable basis for analyzing long-term changes in the CO₂ reserves in the atmosphere with climate models and calculating future scenarios. Whereas in the 1950s the annual increase averaged 0.55 ppm CO₂ per year, differences in annual mean values over the past decade have shown an increase of about 1.9 ppm per year. Compared to the 1950s, global CO₂ production has thus more than tripled.

12.2.1.2 Methane

Since the pre-industrial age, the occurrence of methane (CH₄) in the atmosphere has risen by 270% due to anthropogenic activities. In the group of long-lived greenhouse gases, methane makes the second largest contribution to global warming after carbon dioxide. Never in the past 650,000 years has there been such high concentrations in the Earth's atmosphere. Despite a slower increase since 1990 and a stagnation of the concentration at a high level until 2005, climate models are predicting an accelerated increase in methane with increasing warming. Since 2007, global networks and satellites have been observing an increased increase in methane.

Long rows and their meaning

High-precision long time series provide a reliable picture of the methane concentrations, which ultimately result from the interaction of all sources and sinks. Although the sources for methane are known, the trends of the sources and their interaction with the sinks cannot always be adequately explained: With the methane trend as a whole still rising, the increase in methane has decreased continuously over the last two and a half decades and the reasons for this continuous decrease and the resulting consequences for the future warming of the atmosphere are not yet understood sufficiently. Long and reliable time series are of fundamental importance here so that the interaction of sources and sinks can be adequately explained in the future.

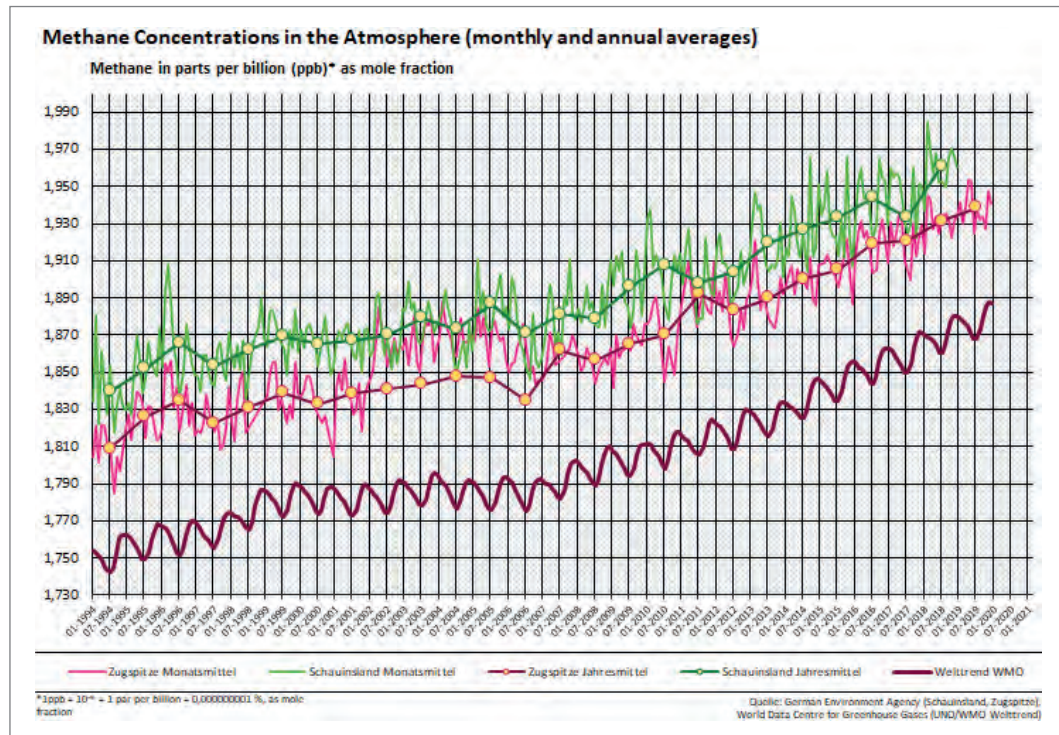


Fig. 2.2: Measured time series of methane from Schauinsland GAW Regional station and Zugspitze GAW global station, compared with the atmospheric WMO world trend, which shows lower concentrations, because it gives a more correct average over the whole earth surface (incl. oceans, which are no source area). Source: website of Umweltbundesamt. www.uba.de

12.2.1.3 Nitrous Oxide

Without their two most important representatives, CO_2 and CH_4 , the long-lived greenhouse gases (LLCG) still account for a remarkably high proportion of the greenhouse effect. The most important are nitrous oxide (N_2O), sulphur hexafluoride (SF_6) and halogenated, climate-effective trace substances. In this group there are some substances with extremely long lifespan, such as SF_6 at 3200 years or NF_3 at approx. 640 years, which will continue to have still long-lasting impact on the global climate.

Long time series and their importance

Nitrous oxide makes the third largest contribution to global warming by long-lived greenhouse gases. Compared to the pre-industrial era (1750), its occurrence in the atmosphere has only increased by 20%. But compared to CO_2 , its influence on the warming of the atmosphere is 300 times stronger over a period of 100 years! Approximately 40% of the N_2O emitted into the atmosphere comes from human activities. The rest comes from natural sources. The significantly higher percentage of land areas in the northern hemisphere and the use of artificial fertilizers in the mid-latitudes are the main reason for a small north-south gradient of nitrous oxide concentrations in the atmosphere. High-precision and long-time series in the northern and southern hemisphere are an important basis for a better understanding and forecasting of the temporal development of the sources. For this purpose, the in-situ measurement series must be measured with a very high accuracy of only 0.03%. This meets the limit of the current technical feasibility.

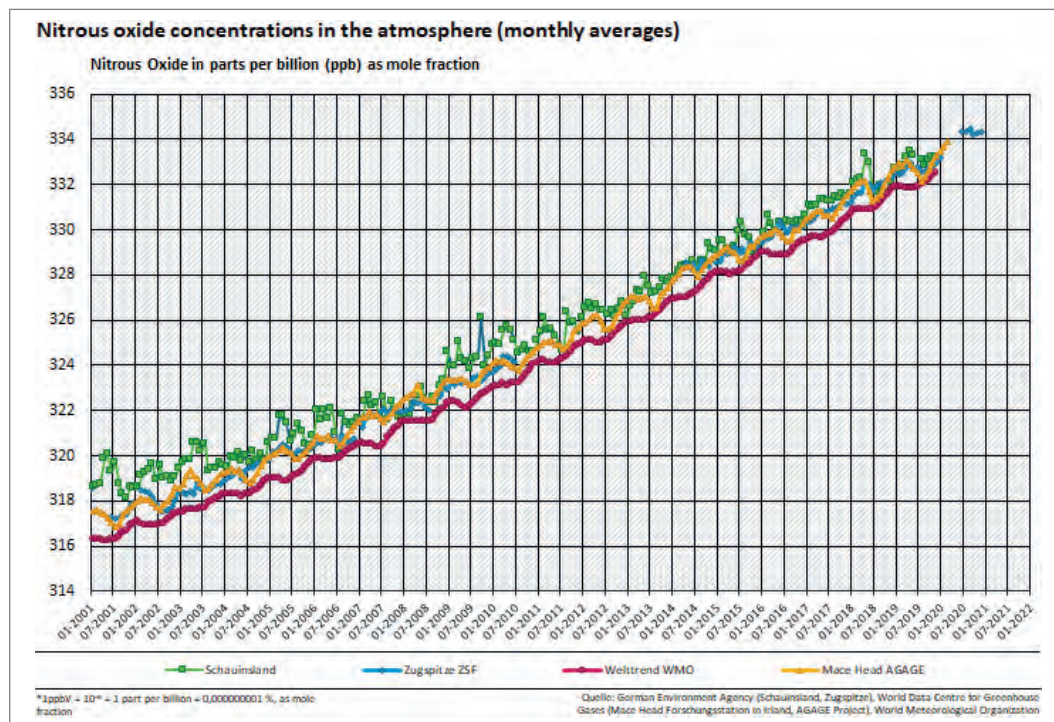


Fig. 2.3: Measured time series of nitrous oxide from Schauinsland GAW Regional station, Mace Head GAW global station and Zugspitze GAW global station and from WDCGG world trend.

12.2.1.4 Tropospheric Ozone

Ozone or trioxygen with chemical formula O_3 is a colorless gas, toxic for plants, animals, and humans. It plays a special role in the chemistry and physics of the Earth's atmosphere. Firstly, ozone is a greenhouse gas with a radiative forcing of approximately 0.4 W/m^2 (IPCC 5.th assessment report, 2013) which is approximately as large as the combined effect of all halogenated greenhouse trace gases. Then ozone is also a highly reactive gas, which plays an important role in the chemical transformation of likewise reactive nitrogen oxides in the troposphere. It should also be mentioned that the air layers above 10 kilometers contain over 90% of the gas and that this stratospheric ozone absorbs most of the harmful ultraviolet solar radiation, which is an important prerequisite for biological life on this planet. In the following, however, only the tropospheric ozone will be considered.

Unlike in conurbations and cities where the atmospheric lifetime of ozone is significantly less than one day, ozone can have a lifetime of up to 3½ weeks in the much cleaner air at 3000 m altitude. As a result, ozone can be transported from North America, for example, and in some cases as far as from Asia to Central Europe in higher layers of air. Furthermore, additional ozone is formed photo-chemically in the troposphere from natural and anthropogenic ozone precursors, such as various VOCs or nitrogen oxides such as NO_2 , by the action of sunlight.

Long continuous measurement series make it possible to combine short-term ozone measurements with a continuous history measured at a fixed location in the lower free troposphere. Thus they contribute to the plausibility check and quality control of remote sensing measurements. Several long measurement series of different measuring stations in a region enable parallel comparison and the validation of the temporal history of the development of atmospheric trends. This is also an important instrument for detecting errors in long-term measurement series. Furthermore, high-precision data representative of the lower free troposphere are an essential prerequisite for the ground calibration of satellite data over mainland. Only a highly time-resolved and highly precise measurement makes it possible to identify representative values that are unaffected locally and regionally.

The selected example of ozone measurements at the Zugspitze station shows at least the atmospheric result of two environmental protection measures. On the one hand, the discontinuation of the increase in ozone levels from 1983 shows the effect of the exhaust gas catalyst introduced in Germany and Central Europe at that time. The further decline in ozone background values from 2008 shows an effect of the success of the European environmental policy for the large-scale reduction of ozone precursors. See Bach H. et al. 2014, Ecorys.

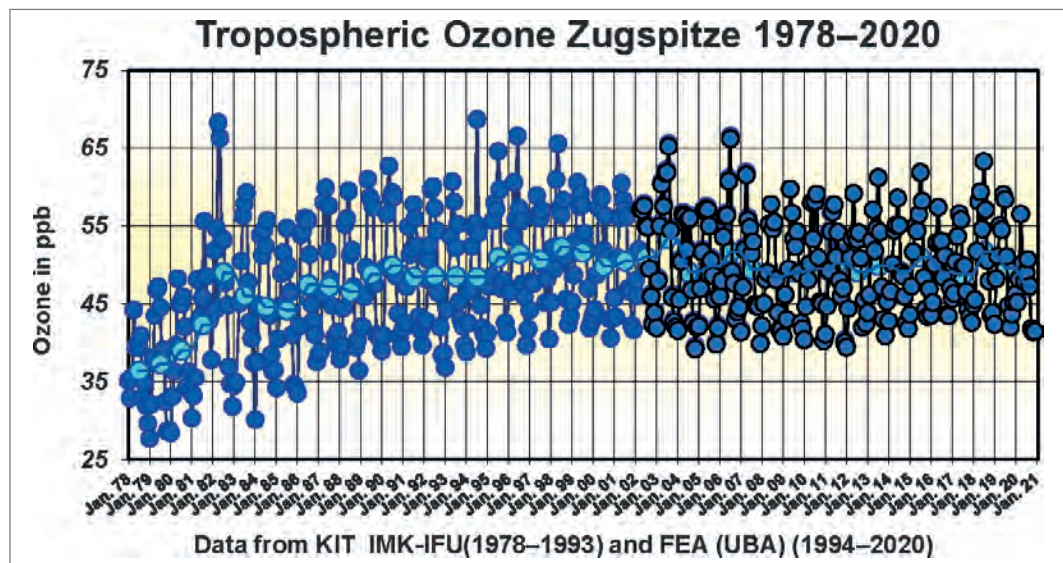


Fig. 2.4: Measured time series of ozone from Zugspitze GAW global station, measured with UV absorption photometer. From 1978 to 2000 data have been measured at Zugspitze summit station. Since 2001 the data are from Environmental Research Station Zugspitze Schneefernerhaus. The Schneefernerhaus data have been adjusted to the ozone level of the summit station. According to the + 0.82ppb O_3 long-time offset published with the station audit from 2011.

12.2.1.5 Aerosols

Aerosols have a largely cooling effect on the climate. Excluded from this is black carbon (BC) or soot, which belongs to the short-lived global warmers (SLCF). Situated on snow or ice, it reduces the backscattering up only to a few percent and thus has a strongly warming effect. However, black carbon in the atmosphere, heats the air masses but cools the underlying area on the ground. The mechanisms of climate warming effects of aerosols are not as well researched as with greenhouse gases. Also, the available measurement series of aerosols are significantly shorter than existing time series of greenhouse gases. An important known source of black carbon is traffic exhaust fumes, especially from diesel vehicles. Significant differences can be observed between high mountain sites (Zugspitze: $0.02 \mu\text{g}/\text{m}^3$ annual mean value), rural sites ($0.5 \mu\text{g}/\text{m}^3$ annual mean value) and traffic influenced measurement sites with mean values around $2\text{--}4 \mu\text{g}/\text{m}^3$.

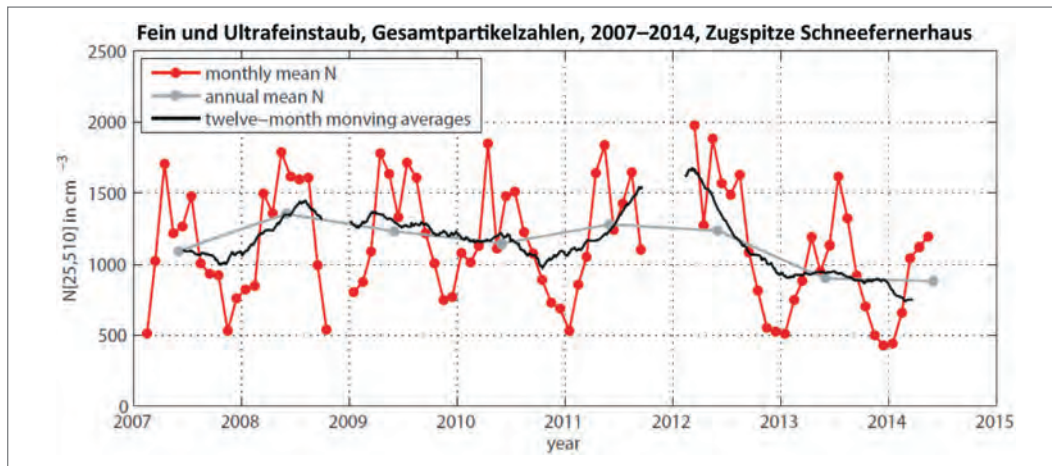


Fig. 2.5: Measured time series of fine and ultra-fine aerosols from Zugspitze GAW global station, measured with scanning mobility particle sizer (SMPS) and condensation particle counter.

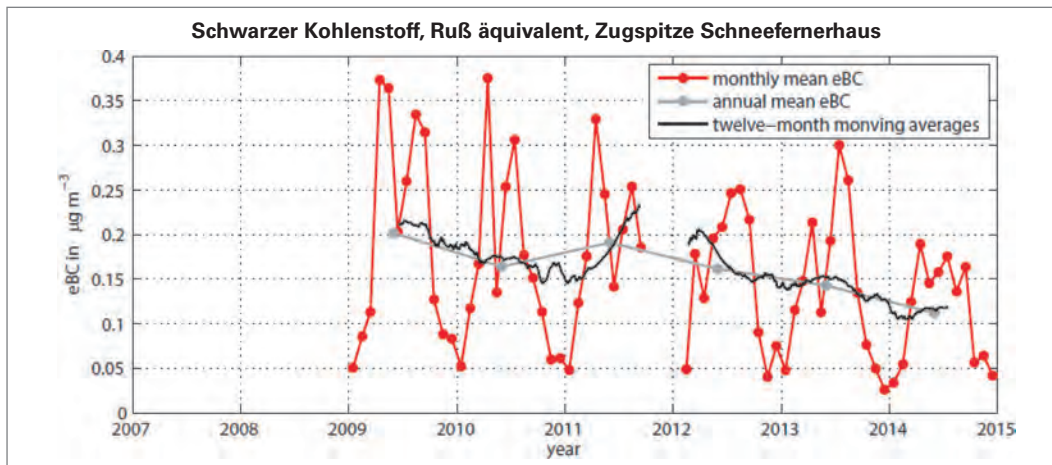


Fig. 2.6: Measured time series of atmospheric black carbon equivalent or soot (BC equiv.), measured with a multi angle absorption photometer (MAAP).

Like black carbon, ultrafine particles are a sensitive indicator of the influence of local combustion sources at a measurement site. A pronounced annual variation is observed for soot and fine and ultrafine particles. In winter, the highest readings occur in the lowlands. However, maximum concentrations are measured at the mountain stations in summer. The reason for this is the seasonal fluctuation of the mixing layer height. In summer the mixed layer is higher. In Central Europe, for example, its upper limit can be well over 3.5 km. This leads to good mixing during summer and relatively similar measured values of around $0.5 \mu\text{g}/\text{m}^3$ at all rural measuring points located within the mixing layer. But in winter inversion layers become effective, which reduce the dispersion and increase the concentrations in the lowlands. During wintertime, mountain stations often are above these inversion layers and therefore then detect significantly lower concentrations.

In central Europe and on Environmental Research Station Zugspitze a declining trend could be observed since the beginning of the black carbon measurements in 2008.

12.2.2 Measurement techniques and quality objectives

Over the past decades, measurement technology and quality assurance have been continuously developed further and have led to a high level of development in the present. Since a more detailed treatment of the measurement technology and quality assurance procedures currently applied according to the state of science is beyond the scope of this chapter, the official sources of measurement technology and quality assurance in GAW are only briefly discussed here. The state of knowledge in GAW with recommendations for measurement technology and measurement quality assurance is described in the GAW technical reports of WMO. It can be accessed from <https://library.wmo.int/>

Because the objective of GAW is to generate a world-wide database for global analysis using comparable high precision and high-quality data according to the state of science, the consideration of data quality objectives and a consistent data preparation as elementary prerequisite for a coherent data quality is absolutely essential for the evaluation of measurement series.

12.2.3 Assurance of data quality

This short section is intended to help the scientific user of measurement series to know the necessary prerequisites for data quality to ask the right questions when selecting the data.

Scientific analysis requires data quality that meets the specified data quality objectives. For example, for the compatibility of greenhouse gas measurements in the Global Atmosphere Watch Program of the UNO/WMO, the quality targets are specified in the GAW Report No. 229 on page three. These quality objectives are an integral part of the measurement program and must be considered, when selecting the measuring instruments, carrying out the calibrations and the scale connections, as well as during the comparison measurements and evaluation of the calibrations.

The user of measurement data series must be aware that the production process of the data corresponds to a quality chain that is only as good as the weakest link. Scientific evaluations require data obtained under correct and always controlled conditions. In practice, almost every measured variable has special requirements, which must then also be considered correctly in the measurement experiment. For scientific evaluation, series of measurements must be used which have been correctly calibrated and which do not show a sudden shift in the value level over time, whose values have been viewed and checked over time and whose values lie on the current measurement scale to be used for GAW. Incorrect data must be specially marked or flagged in the data of the measurement series. These include data failures, artifacts, calibrations, measurement comparisons and influences from known air pollutants. To maintain the principle of traceability, flagged data is not discarded, but only marked. The originally measured data series is thus retained. It is good scientific practice to flag the data in a differentiated way.

12.2.4 Availability of measurement series

For scientific analysis data on the GAW measurement series are available for free via the GAW World Data Centers on the following topics:

Tab. 2.1: Selected world data centers for Global Atmosphere Watch monitoring data for the physical and chemical state of the atmosphere. Source GAW website: <https://public.wmo.int/en/programmes/global-atmosphere-watch-programme>

Topic	Link
World Ozone and Ultraviolet Radiation Data Center	http://www.woudc.org/
World Radiation Data Center	http://wrdc.mgo.rssi.ru/
World Data Center for Greenhouse Gases	http://ds.data.jma.go.jp/gmd/wdceg/
World Data Center for Aerosols	http://www.gaw-wdca.org/
World Data Center for Aerosols	http://www.wdcpc.org/
World Data Center for Remote Sensing of the Atmosphere	http://wdc.dlr.de/

12.3 Analysis of the variation over time in measurement series (Ludwig Ries, Ye Yuan)

The central purpose for the measurement of high- altitude data is gaining more representative information about the state of the atmosphere in the lower free troposphere. Despite a systematically higher fraction of representative data at high altitude stations it is still a multifaceted scientific problem to differentiate less representative regional or locally influenced data from data which can be taken as representative.

On mountain sites atmospheric constituents show systematically different levels and variations in time, compared with other stations, situated in the lowlands or at conurbations. Often the levels of anthropogenic atmospheric pollutants are much lower at mountain stations. However, some other constituents like ozone show constantly higher levels.

No matter where and how the high-altitude measurements take place (continuous / discrete; in situ measurement/flask sampling), the measured data sets are usually treated as time series. Based on different measuring instruments and techniques, the measured time resolution could vary from seconds to days, weeks or even months.

For research and evaluation of data from measurement series from mountain stations the systematic analysis of the variation over time can be a very useful approach. Variations of data in time for example are diurnal, weekly, monthly, annual, or inter-annual variation. The following subsections explain some selected approaches more in detail.

12.3.1 Diurnal variation

Diurnal variation refers to the variation of data which had been measured during the day, by default from 0 a.m. local time (LT) this day to 0 a.m. local time the next day. The diurnal variation is very essential to understand and interpret short-term changes not only in atmospheric chemical constituents but also in physical and meteorological variables, such as temperature, aerosol concentration or solar radiation.

Practically at every measurement site a diurnal variation can be observed. But the characteristic of an individual diurnal variation is very specific for a site and hence decisive for the scientific interpretation and analysis of the measured data. In general, an analysis of diurnal variation requires data with 1 or ½ hr time resolution.

The figure 3.1 below presents four examples of the diurnal cycle from atmospheric CO₂ measured at high altitude site Zugspitze Schneefernerhaus. It shows a typical pattern for high elevated mountain stations during the four seasons. The CO₂ concentration levels remain relatively constant during a nightly time window, which is situated here at midnight. When the day starts with the morning hours, the CO₂ level increases by local influences and results in a diurnal peak by influence of air masses transported from local or regional sources.

Summertime: As the sun rises and starts with radiation, the lack of snow cover supports the development of anabatic winds, a daily thermal upwind system. Simultaneously, the upward transport of air with lower CO₂ levels caused by active photosynthesis reaches the measurement site. The up winds decrease until late night, when a nightly CO₂ level, more stable and with slightly higher values will be reached again. Then, after this minimum variation time window with especially well mixing the sun radiation of the next day starts again to build up the next thermic upwind system with upward transport of air masses. The intensity of this upwind system is driven by the duration of the sun radiation, which has its maximum on June 21st.

Wintertime: In wintertime generally, the nightly time window with especially well mixed air extends considerably longer. The driving factors then are the shorter length and weaker intensity of sun radiation and an existing snow cover, which suppresses the growth of a thermic

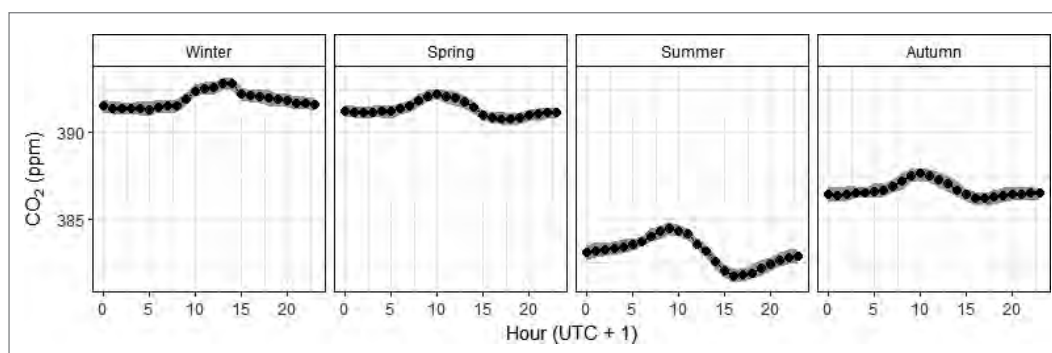


Fig. 3.1: CO₂ Mean CO₂ diurnal variations by season at measurement site Zugspitze Schneefernerhaus, Germany from 2002 to 2016. An explanation is given in the text.

upwind system. Often already at 21:00 h this nightly window starts and lasts considerably longer until to the morning hours of the next day at about 6:00 h. Under winter conditions at Zugspitze Schneefernerhaus a daily maximum builds up with a relative minimum during noon pause. In the average the wintery bimodal daily maximum follows the anthropogenic activity pattern on Zugspitze Platt.

At other mountain stations, the times of time windows can be different, being triggered by local orography and local to regional air mass transport, its current altitude and climate in connection with the geographic location.

12.3.2 Weekly variation

If the question is whether there is a regular systematic anthropogenic influence on the measurements in a time series, the investigation of the weekly variation can be a suitable approach to get to the root of this phenomenon. A week course of CO₂ measurements can hardly be explained by natural variability.

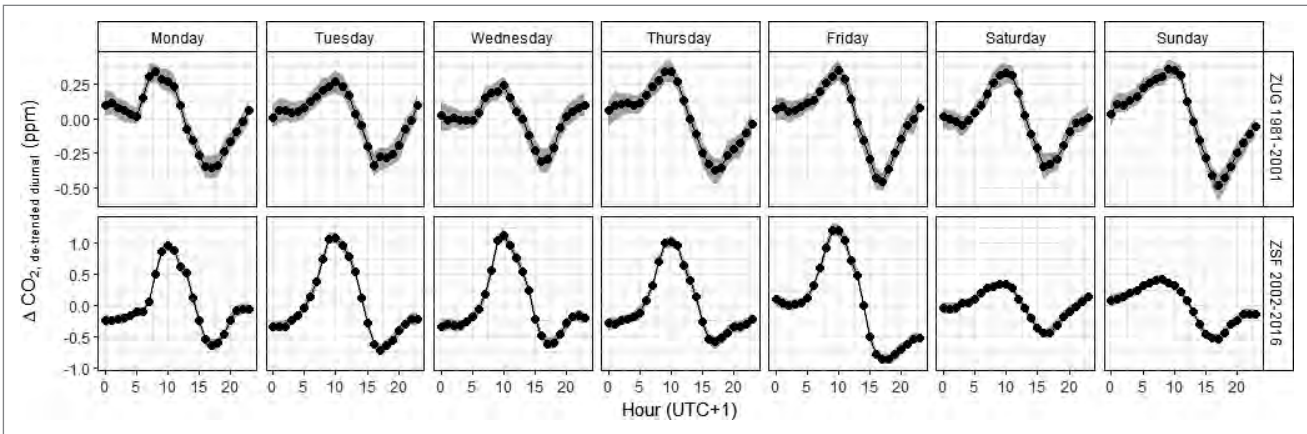


Fig. 3.2: Comparison of the weekly variation at two sites Zugspitze summit (ZUG, 1991–2001) and Zugspitze Schneefernerhaus (ZSF, 2002–2016). In contrary to the summit station at Environmental Research Station Schneefernerhaus a weekend minimum can be detected because the station is closed during weekends.

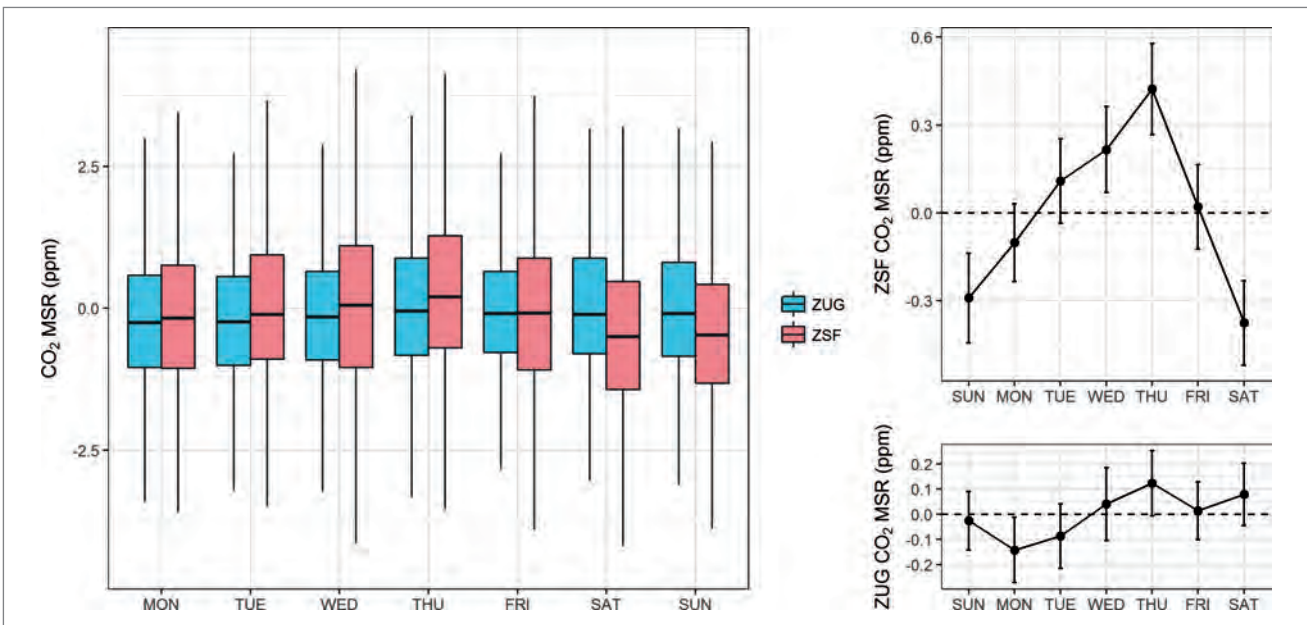


Fig. 3.3: Comparison of the weekly variation at two sites Zugspitze summit (ZUG) and Zugspitze Schneefernerhaus (ZSF). At Environmental Research Station Schneefernerhaus a weekend minimum can be detected in comparison to the weekly variation at Zugspitze summit. This is provided by the fact, that at weekends at site Schneefernerhaus there exists no anthropogenic activity, because of the closed station.

For example, the weekly variation between two sites can be displayed as a paired graphic comparison of seven mean daily courses, see Fig. 3.2. Depending on the problem, these daily courses can be averaged over the seasons of a year or several years, or they can be averaged over an entire year or over several years.

Another methodical approach for the analysis of weekly variations is the Mean Symmetrized Residual (MSR) statistic. The MSR can be regarded as a generalization of a residual over a weekly average. The calculation is described in Cervený and Coakley, 2002, which tested this approach with CO₂ data on the Mauna Loa Station. The MSR retains the units of the measured variable and is directly comparable to atmospheric measured values. Furthermore, the method is robust enough for long-term trends and seasonal trends to have only a negligible effect on MSR statistics.

In Fig 3.3 the weekly variations at the two measuring sites Zugspitze Gipfel (ZUG) and Zugspitze Schneefernerhaus (ZSF) are compared. This comparison is displayed graphically as a pair of box plots of the MSR values or as a linear approximated week course, in which for each week-day an MSR value is plotted together with a ± 1 -sigma uncertainty interval.

12.3.3 Annual variation

While the diurnal cycle itself can only provide information within relatively short time, an evaluation of the annual variation shows a more general view over the measured targets to track the seasonality and long-term trend. Annual variation can be calculated by differently aggregated data with interval length varying from hourly to monthly means. It is calculated by averaging the measured values into e.g. monthly averages to evaluate the variations between monthly values throughout the year. These variations are relevant due to biogenic activities which vary from season to season or the effect of the varying local transport dynamic during the different seasons.

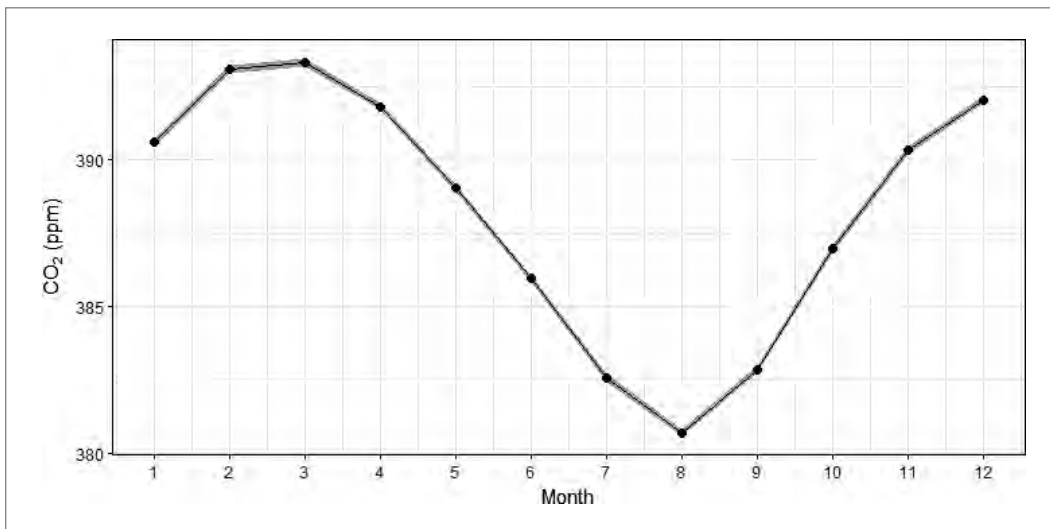


Fig. 3.4: Annual variation by monthly CO₂ averages from 2002 to 2016 at Zugspitze Schneefernerhaus, Germany.

From figure 3.4, we can see that there is a clear seasonal cycle of the atmospheric CO₂. The monthly maximum takes place in March and the minimum is in August. As the temperature rises from spring to summer, the effect of the photosynthesis of vegetation becomes increasingly stronger, causing the CO₂ levels to decline. When the vegetation growing season is over, the influence of photosynthesis to atmospheric CO₂ levels sinks and the CO₂ concentrations rise again. This explains the major cause for such seasonality in atmospheric CO₂ at high altitude measurement sites.

12.3.4 Case study example with Ozone, Carbon Monoxide and Nitrous Oxide

Gilge et al. (2010) compared long-term in situ measurements of atmospheric ozone, CO, and NO₂ at four alpine mountain stations in central Europe, which comprised Hohenpeissenberg and Zugspitze (Germany), Sonnblick (Austria), and Jungfraujoch (Switzerland). To give a general idea of the measurement results over time, the time series plots of all three components were represented by monthly mean values. The mean annual variations were plotted to explain the annual variation of the pollutants. The time series plots were also divided into four seasons with annual values for the comparison of different measurement sites in each season. Moreover, weekly variations (weekdays vs. weekend) were used to study whether there are working patterns during the week how they differ with data from weekend.

Regarding data analysis techniques, besides calculating the mean values, percentile was calculated for data analysis as well. By showing different range of percentiles (1st/99th; 5th/95th; 25th/75th) and minimum and maximum, the data quality and distribution with information of the outliers could be detected clearly. For trend estimation/approximation, linear regression with t-test, as one of the commonly used methods, was applied. In the following section, exemplary data analysis methods for evaluation of air mass transports and detection of pollution sources will be introduced.

12.4 Selection of representative data (Ye Yuan, Ludwig Ries)

12.4.1 Minimum diurnal variation

Atmospheric measurements are largely characterized by measurement sites. Within the Global Atmosphere Watch (GAW) network, two types of stations are defined with different research focuses as regional and global stations. One of the most essential goals at global stations is to detect the background level of atmospheric measurements. However, even though the global stations are mostly situated at remote areas, the measurements are still influenced by local to regional activities to certain extent. Therefore, to improve the data quality of the atmospheric measurements as well as the compatibility of measured data at different measurement sites, selection of the most representative is elementary.

Data selection is usually performed after data are obtained from measurement and have been validated. Data selection can be made based on various properties, such as meteorological parameters (wind speed, wind direction), chemical tracers (CO₂ vs. CO, CH₄) and statistical properties (data variability). The selected data represent the site-specific background values that form the basis for further analyses such as long-term trends, seasonality, influences of local sources and sinks, and comparison with satellite-based measurements.

In the following a newer statistical data selection method ADVS (Adaptive Diurnal Minimum Variation Selection) is presented in short. It was tested with atmospheric CO₂ measurements from 2010 to 2015 at six European elevated mountain stations (Yuan et al., 2018). The underlying automated algorithm selects data under best possible baseline conditions. It is based on the evaluation of the statistical structure of the given diurnal variation. As mentioned in Section 3.1, the diurnal variation alters seasonally, showing patterns resulting from different meteorological conditions, which are either from the lower free troposphere, or are influenced from local to regional sources. ADVS first detects a contiguous time window that has the least variation during the course of the day. Thereafter, the method starts the data selection based on the specified daily time window and examines the selection from the rest of the daily data based on statistical criteria. The figure 4.1 shows an example of selected atmospheric CO₂ data at measurement site Zugspitze Schneesfernerhaus from 2002 to 2016. The advantage of the ADVS method is, that the selected data are remarkably close to the conditions of the lower free troposphere and that for central European stations the correlation between the stations is better than with several other compared selection methods. The disadvantage is, that the percentage of data, which have been detected is comparatively small. Practical experience has shown that the method also can be applied to atmospheric ozone and aerosol data.

12.4.1.1 Analysis of a 36-year time CO₂ measurement time series at mount Zugspitze

After initial standardization, the ADVS data selection could be applied subsequently to the entire existing measurement series. This was possible because the selection methodology exploits the inherent structural properties of the measured time series. In that way a selection of representative data also can be applied to past data time series. The resulting CO₂ trend and seasonality after the data selection and a decomposition of the long-term time series into trend and seasonal components resulted in a mean CO₂ annual growth rate over the 36-year period at Zugspitze is $1.8 \pm 0.4 \text{ ppm yr}^{-1}$, which was in good agreement with the US-American Mauna Loa station and global means from UNO/WMO.

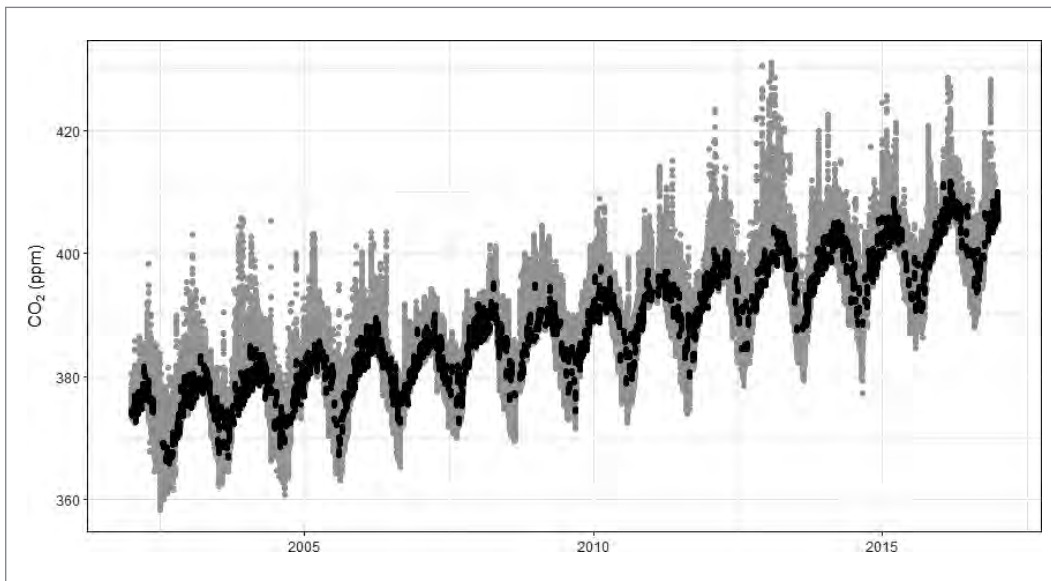


Fig. 4.1: Atmospheric CO₂ (in grey) from 2002 to 2016 at measurement site Zugspitze Schneefernerhaus with selected data (in black) by ADVS selection method.

12.4.1.2 Comparing selected CO₂ station measurement data with remote sensing and satellite data

The comparison of representative in-situ ground data with satellite data is of essential necessity for calibration of satellite measurements and required retrieval methods, especially over the continent. In 2019, Yuan et. al. showed a local comparison of in-situ CO₂ measurements at the Zugspitze site with co-located TCCON column measurements and results from satellite observations.

Based on the fact, that the application of consistent data processing routines to these CO₂ data with appropriate data preparation (retrieval and gap interpolation) is essential for a correct comparison of measurement results, trend and seasonality can be well extracted from all measurement datasets.

While the mean annual growth rates agreed well with about 2.2 ppm yr^{-1} over a 17-year period (2002–2018), the mean seasonal amplitudes showed significant differences (surface: 11.7 ppm /column-averaged: 6.6 ppm), which could be attributed to different air masses.

The applicability of consistent data processing routines remains challenging, yet at the same time it is an essential necessity to ensure global comparability of highly accurate and high-quality atmospheric measurement data.

12.4.2 Ambient Radon concentrations as tracer for ground-based air

When ^{222}Rn is measured additionally at a measuring station, such data can be used for a selection of representative data. Radon provides a good approximation of ground influence. ^{222}Rn is an indirect decay product of the radioactive decay series of uranium or thorium and is produced in the bedrock below the mountain massif. The gas has a radioactive half-life of 3.8 days. In combination with meteorological data, radon measurements support the classification of air masses and are therefore also an essential prerequisite for more precise dispersion calculations and source allocations of gases and aerosols. Increased radon concentrations are an important criterion for distinguishing between ground-level, unrepresentative air masses and mountain air of the lower free troposphere, which is defined by low radon concentrations. Previous investigations show that a maximum atmospheric concentration of $1\text{--}2\text{ Bq/m}^3$ ^{222}Rn at standard temperature and pressure is suitable as a criterion for unaffected mountain air. See also the work of Griffiths et al. 2014.

Compared to data selection with the minimum diurnal variation in 4.1, this method has the disadvantage that an additional measured variable must be measured but has the advantage of greater data yield. However, there is a possible restriction that the data selected as representative can nevertheless be influenced by regional or local sources from altitude sources, which may have to be additionally excluded.

References

- Birmili, W., et al., Determining the northern hemispheric background at the GAW station Zugspitze under consideration of remote transport of fine airborne particulates. Research Report from UFOPLAN 204 42 202/01 (in German), 2008
- Cerveny, R. S., Coakley, K. J., A weekly cycle in atmospheric carbon dioxide, (2002), *Geophysical Research Letters*, Vol 29, No. 2, pp. 15-1–15-4, doi = 10.1029/2001GL013952
- Hanne Bach, Jørgen Brandt, Jesper H. Christensen, Thomas Ellermann, Camilla Geels, Ole Hertel, Andreas Massling, Helle Ørsted Nielsen, Ole-Kenneth Nielsen, Claus Nordstrøm, Jacob K. Nøjgaard, and Henrik Skov, *DCE – Danish Centre for Environment and Energy, Aarhus University (AU), Denmark*, Tim Chatterton, Enda Hayes, Jo Barnes, Duncan Laxen, Jimi Irwin and Jim Longhurst, *University of the West of England (UWE), Bristol*, Florent Pelsy and Tony Zamparutti, *Milieu, Belgium*. Services to assess the reasons for non-compliance of ozone target value set by Directive 2008/50/EC and potential for air quality improvements in relation to ozone pollution (Final report) assess the), Ecorys, Rotterdam, NL, 21. January 2014, for client: DG Environment. [www.ecorys.nl](http://ec.europa.eu/environment/air/pdf/Final_ozone_report.pdf), http://ec.europa.eu/environment/air/pdf/Final_ozone_report.pdf
(Quelle: Ufoplan Bericht des IFT Leipzig 3703 43 200 vom September 2011).
- Henne S., Furger, M. Nyeki, S. Steinbacher, M., Neininger, B., De Wekker, S. F. J., et al. (2004). Quantification of topographic venting of boundary layer air to the free troposphere. *Atmos. Chem. Phys.* 4, 497–509. Doi: 10.5194/acp-4-497-2004
- Hermann, W., Sun, J., Birmili, W. (2017) VA0II Projekt, Teilprojekt: TP I/02 Trends klimawirksamer Gase und Aerosole und raumzeitliche Deposition persistenter organischer Umweltschadstoffe – Unterteilprojekt 3: Erweiterte Untersuchungen zu klimawirksamen Aerosolen, Leibniz-Institut für Troposphärenforschung (TROPOS), 2017, Leipzig, 28 S.
- Kürbis I. Fuzzy-Logic Filter für das Global Atmosphere Watch Programm. Entwicklung von datenbankgestützten Filterfunktionen zur Kennzeichnung der Luftmassen-Einflüsse in den Messreihen der Globalstation Zugspitze, Dissertation, Fakultät für Geowissenschaften der Ruhr-Universität Bochum, 2004 (Fuzzy Logic Filter for the Global Atmosphere Watch Programme. Development of database-supported filter functions for labelling the air mass influences in the measurement series of the Zugspitze Global Station, Dissertation, Faculty of Geosciences, Ruhr University Bochum, 2004. In German)
- Collaud C., Andrews E., Aliaga D., et al. Identification of topographic features influencing aerosol observations at high altitude stations, August 2018, *Atmospheric Chemistry and Physics* 18(16): 12289–12313, DOI: 10.5194/acp-18-122892018
- GAW Report No. 229, 18th WMO/IAEA Meeting on Carbon Dioxide, Other Greenhouse Gases and Related Tracers Measurement Techniques (GGMT-2015), La Jolla, CA, USA, 13–17 September 2015, Page 3. https://library.wmo.int/opac/doc_num.php?explnum_id=3074
- Griffiths, A. D., Conen, F., Weingartner, E., Zimmermann, L., Chambers, S. D., Williams, A. G., and Steinbacher, M.: Surface-to-mountaintop transport characterised by radon observations at the Jungfraujoch, *Atmos. Chem. Phys.*, 14, 12763–12779, <https://doi.org/10.5194/acp-14-12763-2014>, 2014.

- IPCC, 2013: Climate Change 2013: The Physical Science Basis. Contribution of Working Group I to the Fifth Assessment Report of the Intergovernmental Panel on Climate Change [Stocker, T.F., D. Qin, G.-K. Plattner, M. Tignor, S.K. Allen, J. Boschung, A. Nauels, Y. Xia, V. Bex and P.M. Midgley (eds.)]. Cambridge University Press, Cambridge, United Kingdom and New York, NY, USA, 1535 pp,
- Gilge S., Plass-Duelmer C., Fricke W., Kaiser A., Ries L., Buchmann B., Steinbacher M., 2010. Ozone, carbon monoxide and nitrogen oxides time series at four alpine GAW mountain stations in central Europe. *Atmos. Chem. Phys.* 10 (24), 12295–12316. 10.5194/acp-10-12295-2010.
- Sigmund A., Freier K., Rehm T., Ries I., Schunk C., Menzel A., Thomas C. K., Multivariate statistical air mass discrimination for the high-alpine observatory at the Zugspitze mountain, Germany. April 2019, *Atmospheric Chemistry and Physics*, DOI: 10.5194/acp-2019-211
- Winkler P., Lugauer M., Reitebuch O., Alpine Pumping, in *Promet*, Vol 32, Nr. 1/2, pp. 34–32 (in German), German Weather Service, 2006.
- Yuan Y., Ries L., Petermeier H., Steinbacher M., Gómez-Peláez A. J., Leuenberger M. C., Schumacher M., Trickl T., Couret C., Meinhardt F., and Menzel A.: Adaptive selection of diurnal minimum variation: a statistical strategy to obtain representative atmospheric CO₂ data and its application to European elevated mountain stations, *Atmospheric Measurement Techniques*, 11, 1501–1514, <https://doi.org/10.5194/amt-11-1501-2018>, 2018. <https://www.atmos-meas-tech.net/11/1501/2018/>
- Yuan Y., Ries L., Petermeier H., Trickl T., Leuchner M., Couret C., Sohmer R., Meinhard F., Menzel A. On the diurnal, weekly, seasonal cycles and annual trends in atmospheric CO₂ at Mount Zugspitze, Germany during 1981–2016, August 2018, *Atmospheric Chemistry and Physics*, DOI: 10.5194/acp2018-850
- Yuan Y., Sussmann R., Rettinger M., Ries L., Petermeier H., Menzel A., Comparison of Continuous In-Situ CO₂ Measurements with Co-Located Column-Averaged XCO₂ TCCON/Satellite Observations and CarbonTracker Model Over the Zugspitze Region, *Remote Sensing*. 2019, 11, 2981; doi:10.3390/rs11242981

12.5 Analysis of transport and source contributions based on back trajectories (Esther Giemsa, Jucundus Jacobeit, Stephan Hachinger)

The chemical characteristics of an air mass are often closely related to the amount of time it has spent in close contact with surface-based sources and sinks in its recent history. To examine the contribution of emission sources and sinks to measured concentration levels, the pathways on which air masses have travelled can be recalculated using a Lagrangian particle and dispersion model and further analysed by so called receptor models. Receptor modelling approaches proceed from concentrations at a receptor site backward to responsible emission sources and sinks by relating the on-site arriving paths of air mass back trajectories to the simultaneously measured concentrations. Thus, the back-trajectory receptor models assess the air mass history to infer geographic regions with influence on the concentration levels at a particular measuring site (Hopke 2016, Cheng et al. 2015). Two of these source apportionment tools based on back trajectories are presented together with examples for their application to the CO₂ concentration measurements at the Environment Research Station Schneefernerhaus.

12.5.1 Back Trajectories

Air mass back trajectories as a result of dispersion and transport models provide an approximation of the path air parcels have recently covered thereby acquiring their observed characteristics (Crawford et al. 2009). Therefore, back trajectories act as a dependable tool for investigating dynamical processes in the atmosphere on synoptic time scales (Hopke 2016). Since they offer the possibility to identify the location of major emission sources and sinks, they have been widely used to infer geographic regions that contribute to pollution events, enabling detailed insights into source-receptor relationships within the catchment area of a given station (Cheng et al. 2015). Especially if many back trajectories (over months to years) are analysed in specific ways as described below, they identify the geographic origins mostly associated with concentration anomalies. With enough (dissimilar) trajectories, those locations leading to the measured concentration levels are revealed (Carslaw 2015).

To represent the chaotic pathways of air masses especially during their residence time in the turbulent planetary boundary layer as realistically as possible, Lagrangian Particle Dispersion Models (LPDM) compute trajectories of a large number of so-called particles (not necessarily

representing real particles, but infinitesimally small air parcels) to describe the transport and diffusion of tracers in the atmosphere (Fleming et al. 2012). The main advantage of Lagrangian models is that, unlike in Eulerian models, there is no numerical diffusion. Furthermore, in Eulerian models a tracer released from a point source is instantaneously mixed within a grid box, whereas Lagrangian models are independent of a computational grid and have, in principle, infinitesimally small spatial units (Stohl et al. 2002). Consequently, the Lagrangian box is assumed to behave like a point identically following the wind patterns (Seinfeld & Pandis 2016).

In our exemplary study carried out to investigate the contribution from emission sources and sinks to CO₂ concentrations measured at the Environment Research Station Schneefernerhaus, the LPDM FLEXPART (Stohl et al. 2005) was employed. For the traceability of the impact from sources and sinks through atmospheric transport and mixing conditions, a large ensemble of four-dimensional (three space dimensions plus time) ten-day back trajectories from the receptor site Schneefernerhaus every two hours over the entire study period 2000–2015 is calculated with the LPDM FLEXPART driven by the ERA-Interim analysis fields of the European Centre for Medium-Range Weather Forecasts (ECMWF) with 0.2° resolution. Based on the ECMWF meteorology fields, a total of 10 000 particles carrying the traits of CO₂ molecules were released every two hours over the entire study period and followed backward in time for ten days. The positions of the dispersing particles were stored with a 2-hourly time step. To reduce intrinsic model uncertainties such as the restricted resolution of the meteorological ECMWF fields and the parameterisations of the LPDM itself, the backward FLEXPART simulations of the particle dispersions are aggregated to their centroid tracks (red dashed line in Fig. 5.1) resulting in the cancelling-out of errors. As for the assumption that the uncertainties are equally distributed, the coordinates of the centroid tracks represent the mean, and thereby least erroneous, air mass transport path. The resulting centroid tracks of the particle dispersion form the basis for the further described back trajectory receptor models that relate variability in chemical observations – in our case: CO₂ concentrations measured at Schneefernerhaus – to variations in synoptic-scale circulations.

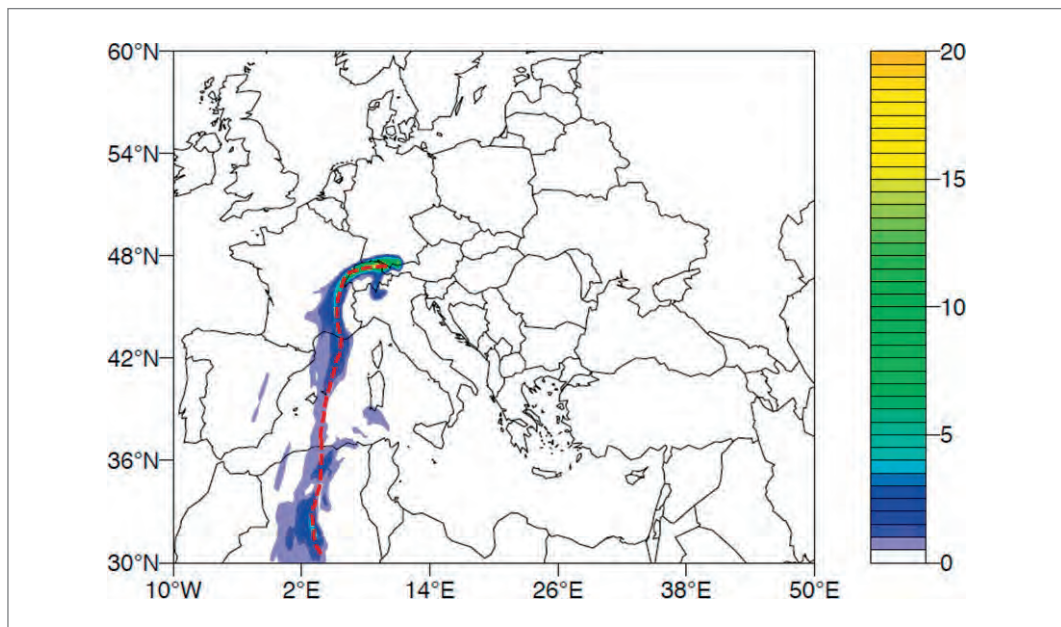


Fig. 5.1: Exemplary FLEXPART dispersion modelling [emission sensitivity in $\log(\text{s}/\text{m}^3/\text{kg})$] for 10 000 CO₂ particles released at the receptor site Schneefernerhaus backward in time together with the centroid track (red dashed line) corresponding to the mean transport locations of the particle tracing

12.5.2 Potential Source Contribution Function (PSCF)

The identification of geographic regions with impact on the CO₂ deviations at a particular site is performed by gridded receptor models based on air mass back trajectories. A well-known receptor model is the Potential Source Contribution Function (PSCF), originally developed by Ashbaugh et al. (1985), which calculates the probability that a source is located at latitude i and longitude j . The basic assumption of PSCF is that if a source is located at a specific spot, an air parcel back trajectory passing over that location can collect the material from the source and transports it along the trajectory to the receptor site (Carslaw 2015).

Air parcel back trajectories ending at a receptor site are represented by segment endpoints. Each endpoint has three coordinates (latitude, longitude and height) representing the central location of an air parcel at a particular time. To calculate the PSCF, the whole geographic region covered by the trajectories is divided into an array of grid cells whose size is dependent on the geographical scale of the problem so that the PSCF will be a function of locations as defined by the cell indices i and j . Air parcel backward trajectories were related to the composition of measured concentrations by matching the time of arrival of each trajectory at the receptor site. PSCF values for each grid cell were calculated by counting the trajectory segment endpoints that terminate within the grid cells. The number of endpoints that fall in the ij^{th} cell is $n(i, j)$. The number of endpoints for the same cell when the corresponding samples show concentrations higher than a certain criterion value – by default the 90th percentile – is defined to be $m(i, j)$. The PSCF value for the ij^{th} cell is defined as (Hopke 2016):

$$PSCF(i, j) = \frac{m(i, j)}{n(i, j)}$$

Thus, the potential source contribution function can be interpreted as a conditional probability describing the spatial distribution of probable geographical source locations inferred by using trajectories arriving at the sampling site. Cells related to the high values of the potential source contribution function are the potential source areas (Polissar et al. 1999).

In the PSCF analysis, it is likely that the small values of $n(i, j)$ produce high PSCF_{ij} values with high uncertainties. For large values of n , there is more statistical stability in the calculated value. In order to minimize this artefact, an empirical weight function $W(n_{ij})$ is multiplied into the PSCF value to better reflect the uncertainty in the values for these cells (Polissar et al. 1999):

$$W(n_{ij}) = \begin{cases} 1.00 & n_{ij} \geq 4 \\ 0.85 & n_{ij} = 3 \\ 0.65 & n_{ij} = 2 \\ 0.50 & n_{ij} = 1. \end{cases}$$

Although the trajectory segment endpoints are subject to uncertainty, a sufficient number of endpoints should provide accurate estimates of the source locations if the location errors are random and not systematic. Cells containing emission sources would be identified with conditional probabilities close to 1 assuming that trajectories that have crossed the cells effectively transport the emitted contaminant to the receptor site. The PSCF model thus provides a means to map the source potentials of geographical areas, though it does not apportion the contribution of the identified source area to the measured receptor data (Hopke 2016).

Calculated on basis of the previously described back trajectories together with the simultaneously measured de-seasonalised and de-trended CO₂ concentrations of the years 2000–2015 at the Schneefernerhaus, the PSCF-map of Fig. 5.2 refers to probable source regions especially Northeast of the receptor site (East of Germany and Poland), whereas the probability of emission sources within the central alpine region is zero even though this is the highest frequented area due to an alpine station as receptor site.

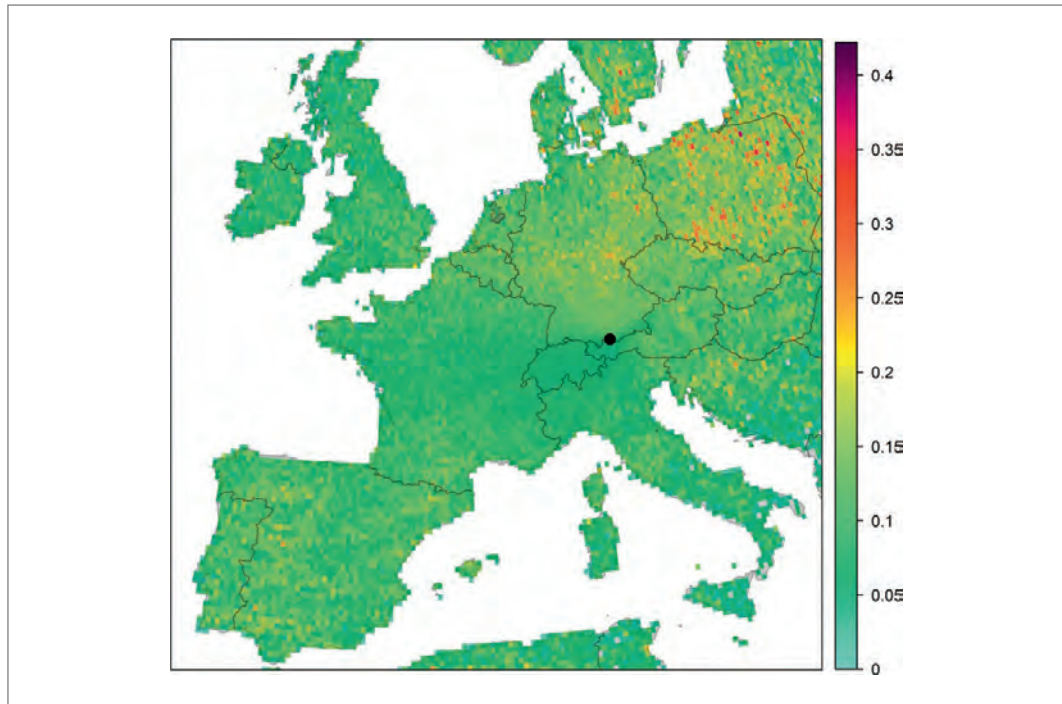


Fig. 5.2: Potential Source Contribution Function providing the probability (in %) that a source for high de-seasonalised and de-trended CO₂ concentrations (> 90th percentile) measured during the study period 2000–2015 at the receptor site Schneefernerhaus is located at the colour-coded grid cells of the map.

12.5.3 Concentration Weighted Trajectory fields (CWT)

A limitation of the PSCF method is that grid cells can have the same PSCF value when sample concentrations are either only slightly higher or much higher than the criterion (Hsu et al. 2003). As a result, it can be difficult to distinguish moderate sources from strong ones. Therefore, an advanced approach called the Concentration Weighted Trajectory fields (CWT) has been derived by Seibert et al. (1994) based on a grid domain as in the PSCF method. In analogue to the preceding PSCF, this second receptor modelling approach connects the on-site arriving paths of air masses to the contemporaneously measured short-term fluctuations in the CO₂ concentrations. In addition to the method of PSCF, however, the CWT approach also considers the residence time of the air parcels over geographic areas prior to their arrival at the observatory. Beyond that, the CWT methodology is able to distinguish between moderate sources/sinks and intense ones (Begum et al. 2005).

For CWT, a grid domain forms again the basis to identify contributing regions within the catchment area of the site. For each grid cell of the domain, Seibert et al. (1994) computed the mean concentration of the investigated species or chemical compound as follows:

$$\ln(\bar{C}_{ij}) = \frac{1}{\sum_{k=1}^N \tau_{ijk}} \sum_{k=1}^N \ln(c_k) \tau_{ijk}$$

where i and j are the indices of the grid, k the index of trajectory, N the total number of trajectories used in analysis, c_k the pollutant concentration measured upon arrival of trajectory k , and τ_{ijk} the residence time of trajectory k in grid cell (i, j) . A high value of τ_{ij} means that air parcels passing over cell (i, j) would, on average, cause high concentrations at the receptor site and vice versa (Carslaw 2015).

All gridded receptor models based on air mass pathways are founded on the basic assumption that air parcel back trajectories crossing a grid cell (i, j) where a source or sink is located, transport the entailed alterations of the atmospheric trace gas concentration effectively to the receptor (Hopke, 2003). The grid cells are colour-coded according to their probability to act as emission sources or sinks and, taken in their entirety, constitute a complete map (Cheng et al. 2015).

These maps representing the relevant areas affecting the concentrations at the measuring site are quite reliable, as comparisons with known emitters have shown (Begum et al. 2005). For the receptor site Schneefernerhaus, CO₂ released from forest fires in the Mediterranean area during summer (especially during hot years, e.g. 2003) as well as wood and coal combustion during winter (particularly in cold years, e.g. 2005/2013) are recognised as major emitters for CO₂ (see Fig. 5.3).

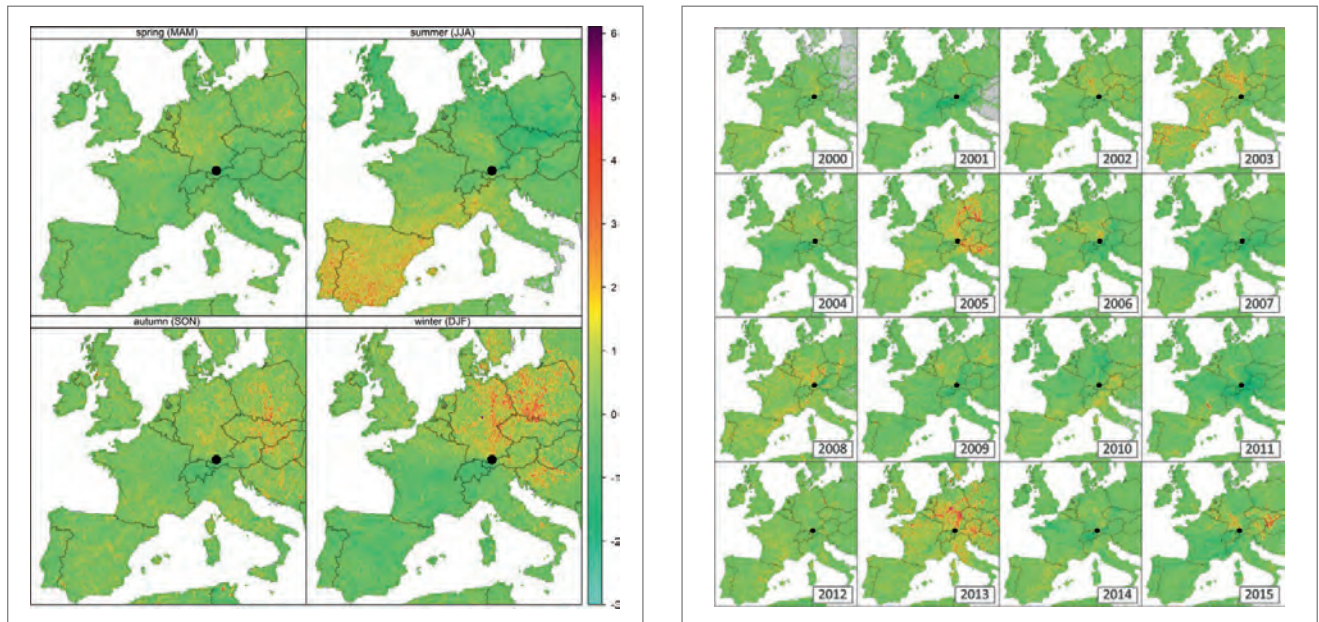


Fig. 5.3: Concentration Weighted Trajectory fields quantifying the influence of source and sink areas to the deviations of the de-seasonalised and de-trended CO₂ concentrations [in ppm] at the receptor site Schneefernerhaus, seasonally averaged (left) for the entire study period 2000–2015 and for individual years (right – same scale as the seasonal pendant).

References

- Ashbaugh, L. L., Malm, W. C., Sadeh, W. Z. (1985): A residence time probability analysis of sulfur concentrations at Grand Canyon National Park. *Atmospheric Environment*, 19, 1263–1270.
- Begum, B. A., Kim, E., Jeong, C.-H., Lee, D.-W., Hopke, P. K. (2005): Evaluation of the potential source contribution function using the 2002 Quebec forest fire episode. *Atmospheric Environment*, 39, 3719–3724.
- Carslaw, D. C. (2015): The openair manual – open-source tools for analyzing air pollution data. Manual for version 1.1–4., King's College London. 287 p.
- Cheng, I., Xu, X., Zhang, L. (2015): Overview of receptor-based source apportionment studies for speciated atmospheric mercury. *Atmospheric Chemistry and Physics*, 15, 7877–7895.
- Crawford, J., Zahorowski, W., Cohen, D. D. (2009): A new metric space incorporating radon-222 for generation of back trajectory clusters in atmospheric pollution studies. *Atmospheric Environment*, 43, 371–381.
- Fleming, Z. L., Monks, P. S., Manning, A. J. (2012): Review: Untangling the influence of air-mass history in interpreting observed atmospheric composition. *Atmospheric Research*, 104–105, 1–39.
- Hopke, P. K. (2003): Recent developments in receptor modeling. *Journal of Chemometrics*, 17, 255–265.
- Hopke, P. K. (2016): Review of receptor modeling methods for source apportionment. *Journal of the Air & Waste Management Association*, 66, 237–259.
- Hsu, Y. K., Holsen, T. M., Hopke, P. K. (2003): Comparison of hybrid receptor models to locate PCB sources in Chicago. *Atmospheric Environment*, 37, 545–562.
- Polissar, A. V., Hopke, P. K., Paatero, P., Kaufmann, Y. J., Hall, D. K., Bodhaine, B. A., Dutton, E. G., Harris, J. M. (1999): The aerosol at Barrow, Alaska: long-term trends and source locations. *Atmospheric Environment*, 33, 2441–2458.
- Seibert, P., Kromp-Kolb, H., Baltensperger, U., Jost, D. (1994): Trajectory analysis of high-alpine air pollution data. In: Gryning, S.-E., Millán M. M. (eds): *Air Pollution Modeling and Its Application X. NATO – Challenges of Modern Society*, 18, 595–596.

- Seinfeld, J. H. & Pandis S. N. (2016): *Atmospheric Chemistry and Physics – From Air Pollution to Climate Change*. 3. Ed., Wiley, 1152 p.
- Stohl, A., Eckhardt, S., Forster, C., James, P., Spichtinger, N., Seibert, P. (2002): A replacement for simple back trajectory calculations in the interpretation of atmospheric trace substance measurements. *Atmospheric Environment*, 36, 4635–4648.
- Stohl, A., Forster, C., Frank, A., Seibert, P., Wotawa, G. (2005): Technical note – The Lagrangian particle dispersion model FLEXPART version 6.2, *Atmospheric Chemistry and Physics*, 5, 2461–2474.

13 Cosmic Rays and the Earth

Vladimir Mares, Werner Rühm, Helmholtz Center Munich, Institute of Radiation Medicine

Abstract

The Earth is constantly being bombarded with particles from the galactic space and from the Sun with energies that are sufficiently high to penetrate the geomagnetic shielding of the Earth. These high-energy particles, also called primary cosmic rays (CRs), do not reach ground level because they interact with atoms in the atmosphere and initiate air showers producing many secondary particles. Some of these particles, also called secondary CRs, reach the ground and can be detected. An important contribution of secondary CRs to radiation-induced health risks comes from neutrons, because they contribute up to about 60% to the ambient dose equivalent, $H^*(10)$, from CRs at mountain regions.

The history of CR measurements can be traced back to the beginning of the 1910's, when an Austrian-American physicist, Victor Franz Hess, started series of measurements with ionization chambers onboard balloons. Since the 1950's, neutron monitors are considered as the best ground-based detectors for recording any variations of the primary CR intensity. However, a single neutron monitor does not provide any information on the energy distribution of detected neutrons. This knowledge is important, however, because it can help scientists to understand the nature of CRs. In 1997, major efforts have been made at the Helmholtz Zentrum München (former GSF) when the first ground-based measurement of the energy distribution of neutrons from secondary CRs with an extended-range Bonner sphere spectrometer were performed at the summit of Zugspitze mountain (2,963 m a.s.l.), Germany. Since 2005, the neutrons from secondary CRs have been continuously monitored with such a spectrometer at the Environmental Research Station Schneefernerhaus at Zugspitze (2,650 m a.s.l.).

The following section of this chapter summarizes general characteristics of CRs, and the three main kinds of shields protecting the Earth from CRs, namely the interplanetary magnetic field, the geomagnetic field, and the Earth's atmosphere.

The next section deals with the definition of effective dose as a protection dose quantity used for the implementation of dose limits. Because effective dose cannot be measured in practice, ambient dose equivalent, $H^*(10)$, is described as an operational dose quantity used to quantify external radiation exposures.

The third section describes detection principles of the extended-range Bonner sphere spectrometer installed in an instrument shed at the Environmental Research Station Schneefernerhaus at Zugspitze. All steps necessary for the data evaluation process in terms of detector counts and neutron spectrometry are explained. Special consideration is given to air pressure correction of measured count rates, and to the unfolding process used to derive neutron fluence energy spectra from measured count rates.

In the last section, two examples of long-term measurements of neutrons from secondary CRs with one-hour time resolution are shown. First, a rapid decrease within a few hours in measured intensity of secondary CR neutrons, a so-called Forbush decrease, was recognized in the count rates measured in September 2005. Second, the effect of snow cover on the neutron fluence energy spectra at ground level was observed between January 2010 and June 2014. The hypothesis that the snow cover might influence the number of neutrons absorbed or backscattered from soil (so-called albedo neutrons) was tested with Monte Carlo simulations. Finally, seasonal oscillations in neutron fluence due to the presence of a snow cover in winter and its absence in summer are described.

Keywords: Primary cosmic rays, secondary cosmic rays, neutron spectrometry, dose rate from cosmic rays

13.1 Cosmic Rays at the Surface of the Earth

The Earth is continuously exposed to high-energy particles from the galactic space (“galactic cosmic rays” – GCRs) and occasionally also from the Sun (“solar cosmic rays” – SCRs). These cosmic ray particles travel with almost the speed of light. When these particles, often called “primary cosmic rays”, enter the Earth’s atmosphere they interact with the atoms there. From the interactions with the atmospheric nuclei, a complex field of secondary particles is formed which are often called “secondary cosmic rays”. In general, cosmic rays contribute to the radiation exposure of the population. A general introduction on cosmic rays can be found in (Grieder 2001).

13.1.1 Primary Cosmic Rays

13.1.1.1 Galactic Cosmic Rays and Shielding by the Interplanetary Magnetic Field

Galactic Cosmic Rays consist mainly (i. e., about 98%) of hydrogen and helium nuclei (protons and alpha particles), but heavier nuclei, electrons, positrons and other components can also be found. When charged particles enter the solar system (heliosphere), they are deflected by the interplanetary magnetic field of the Sun (Lorentz force¹). Therefore, the intensity of the GCR particles entering into the inner heliosphere is attenuated. As the magnetic field of the Sun is correlated with the activity of the Sun, the attenuation of the GCR intensity is not constant with time. During periods of higher solar activity the GCR intensity near Earth is lower, and higher during periods of lower solar activity, i. e. the intensity of GCR particles close to the Earth’s orbit is anti-correlated with the 11-years cycle of the solar activity, which can be quantified by the Sunspot number.

Except for this 11-years cycle, the intensity of GCR particles entering the solar system is fairly constant with time. As a further exception, their intensity near the Earth may decrease for hours or days (“Forbush decrease”²), following a large coronal mass ejection (CME) from the Sun’s corona which causes changes in the interplanetary magnetic field.

Particles of GCR can have energies up to 10^{20} eV³, but lower-energy particles are the most frequent. After the GCR particles have penetrated the interplanetary magnetic field of the solar system, they approach the Earth rather isotropically. The peak of their energy spectrum close to the Earth’s orbit is at a few hundred MeV to 1 GeV per nucleon.

13.1.1.2 Solar Cosmic Rays

The Earth is occasionally also exposed to energetic protons and heavier particles that are accelerated in high-energy processes at or near the Sun (reconnection of magnetic field lines, shock waves from CMEs). When a CME is directed towards the Earth, it can disturb the geomagnetic field (geomagnetic storm) a few days after its release from the Sun. The energy spectrum of solar particle events (sometimes also called “solar proton events”, both abbreviated by “SPEs”) is less energetic than the GCR energy spectrum. Generally, the maximum energy of solar particles is below 100 MeV and only rarely above 10 GeV. SPEs are of short duration, a few hours to a few days, and highly variable in intensity. The frequency of SPEs is roughly correlated with the 11-year solar activity cycle. SPEs are most prevalent during the years around solar maximum (Shea and Smart, 2000; Feynman et al., 1993, Shea and Smart, 1990, 1999), but significant solar particle events have also occurred during solar minimum. Only a small fraction of SPEs, on average one per year, includes particles with energies high enough to produce secondary particles in the atmosphere that are able to reach the surface of the Earth. Such events are called ground level enhancements (GLEs).

Additionally, there is the solar wind, a stream of charged particles (called solar-wind plasma) released from the Sun’s corona. This plasma consists mostly of electrons, protons, and alpha

¹ Hendrik A. Lorentz (1853–1928), Dutch physicist, Nobel Prize in 1902.

² Scott E. Forbush (1904–1984), American astronomer, physicist and geophysicist.

³ eV is a physical unit of energy; in SI units it corresponds approximately to 1.6×10^{-19} joule (J). One eV is the energy gained or lost by an electron (having the elementary charge of 1.6×10^{-19} C) moving along an electric potential difference of 1 volt (V).

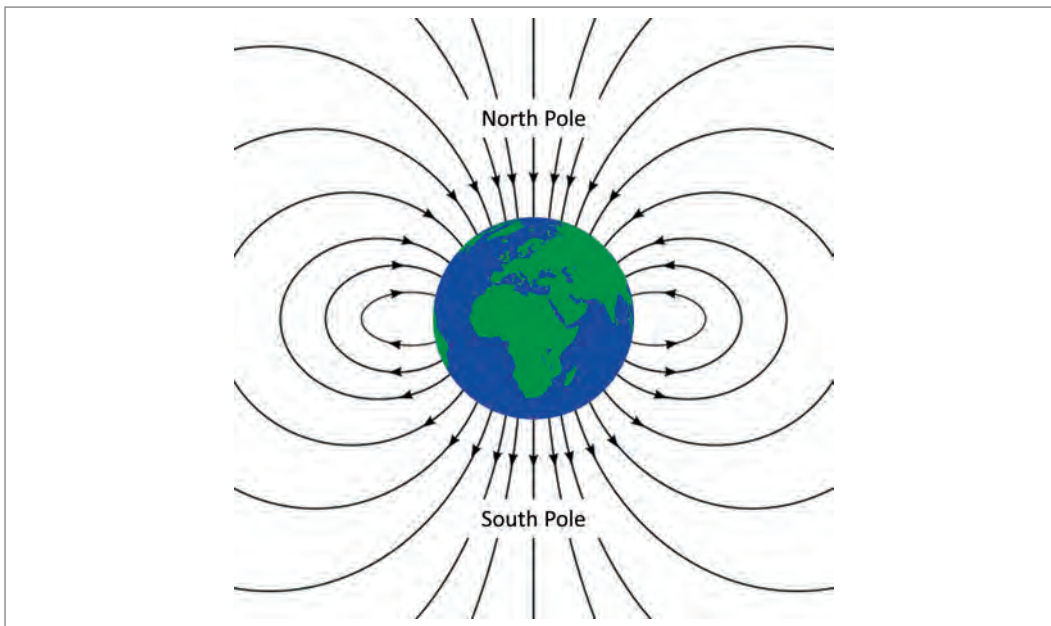


Fig. 1: Sketch of the geomagnetic field

particles. The interplanetary magnetic field is embedded within the solar-wind plasma. The solar wind varies in density, temperature and speed over time and depends on solar latitude and longitude. Its particles can escape the Sun's gravity because of their high energy resulting from the high temperature of the corona.

The Earth is protected against the solar wind by the geo-magnetic field, which deflects the charged particles of the solar wind (see below). Some of the charged particles are, however, trapped in the Van Allen radiation belts, and a smaller number of particles can travel to the Earth's upper atmosphere and ionosphere in the aurora zone. The solar wind is observable on the Earth when it is strong enough to produce phenomena such as the "Aurora borealis" above the north magnetic pole and "Aurora australis" above the south magnetic pole.

13.1.1.3 Geomagnetic Shielding

The Earth is shielded against the galactic and the solar cosmic rays by the Earth's magnetic field ("geomagnetic field"), as charged particles are deflected in a magnetic field by the Lorentz force. The shielding by the geomagnetic field is most effective at low geomagnetic latitudes (i. e., close to the geomagnetic equator), and less effective at high geomagnetic latitudes (i. e., close to the geomagnetic poles). This is so because near the equator the trajectories of cosmic ray particles are mainly perpendicular to the geo-magnetic field lines resulting in a strong Lorentz force. In contrast, the trajectories close to the magnetic poles are rather parallel to the magnetic field lines and, accordingly, the Lorentz force becomes weaker.

13.1.2 Secondary Cosmic Rays

Particles of the primary cosmic rays may interact with the atomic nuclei of atmospheric elements (e. g., oxygen, nitrogen), and the number of interactions depends on energy and intensity of the primary particles. These interactions lead to a variety of secondary particles including for example protons, neutrons, electrons, positrons, photons, muons (positive and negative), and pions (positive and negative). The energy of these particles covers many orders of magnitude and depends on the particle type. For example, the energy of secondary neutrons ranges from thermal energies (several meV or tens of meV) up to about 10 GeV. Due to the competing processes of secondary particle production and absorption in the atmosphere, the number of SCR particles is increasing with increasing height above the Earth's surface up to the Pfotzer Maximum at an altitude of about 15–20 km.

13.1.3 Surface and Near-Surface Observations of Cosmic Rays

Because the intensity of the GCR depends on the interplanetary solar magnetic field which in turn depends on the solar activity (see chapter 13.1.1), the production of secondary cosmic rays in the atmosphere also depends on the solar activity. Fig. 2 shows the number of counts measured at the surface of the Earth by a so-called neutron monitor, due to neutrons from secondary cosmic rays. Clearly, during the measurement period of 50 years corresponding to about five cycles of solar activity, the reading of this instrument showed an anti-correlation with Sunspot number, which in turn is a measure for solar activity.

As also mentioned in Chapter 13.1.1, the magnetic field of the Earth also shields against impinging charged particles. For this reason, the production of SCR particles in the atmosphere depends on geomagnetic latitude and, consequently, the dose rate from cosmic rays at any point of interest in the atmosphere also depends on geomagnetic coordinates (for definition of dose quantities see chapter 13.2). This is demonstrated in Fig. 3 where the calculated effective dose rate due to GCRs at an altitude of 11.3 km above sea level in 2005 is shown. Due to the geomagnetic field, the effective dose rate is only about $2 \mu\text{Sv}$ per hour close to the equator, while it is about $7 \mu\text{Sv}$ per hour close to the magnetic North and South poles of the Earth.

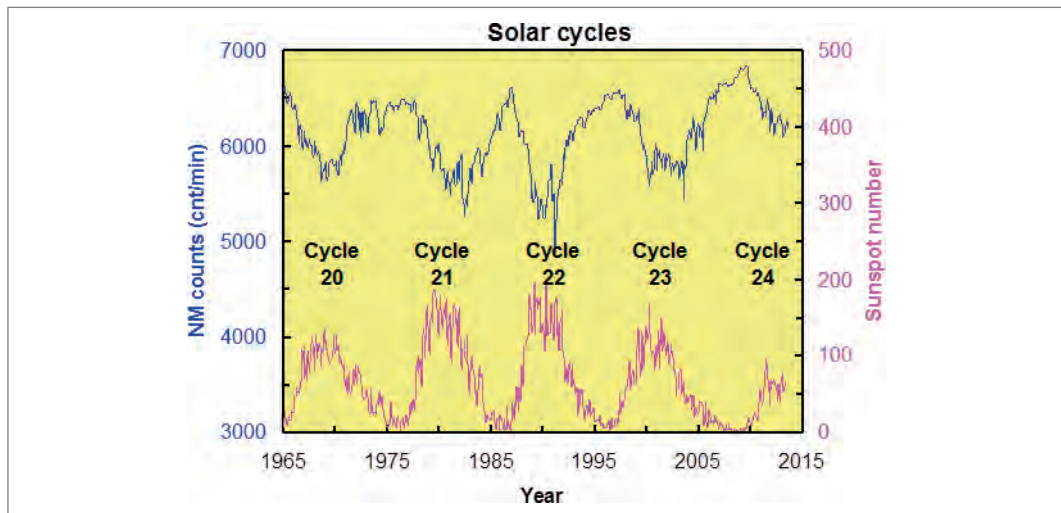


Fig. 2: Monthly averaged sunspot numbers (lower magenta curve) and counts measured by the Oulu Neutron Monitor (upper blue curve), for solar cycles 20 through 24 (Sunspots: from WDC-SILSO, Royal Observatory of Belgium, Brussels; Neutron monitor counts: from I. G. Usoskin and co-workers, <http://cosmicrays.oulu.fi/>)

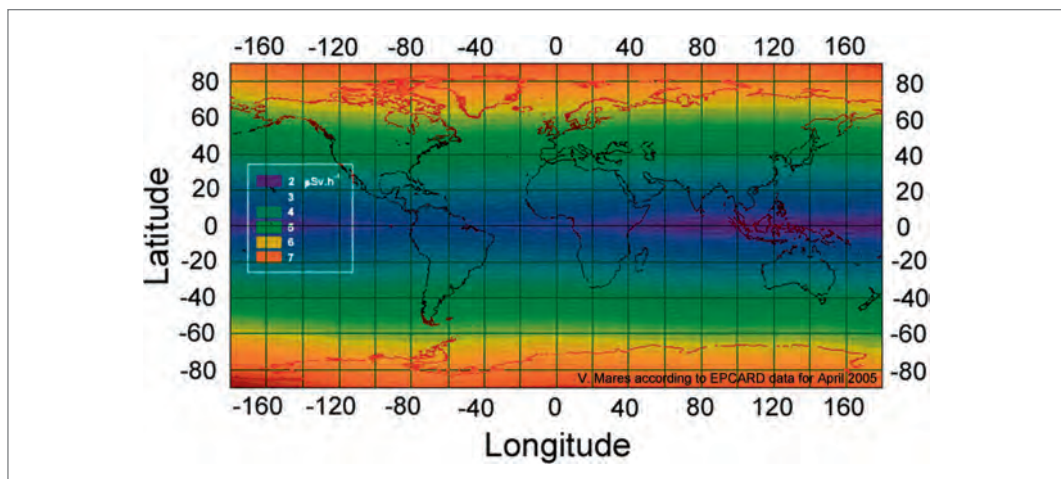


Fig. 3: World map of effective dose rate calculated with the EPCARD code for an altitude of 11.3 km above sea level and for April 2005 (Mares et al. 2009).

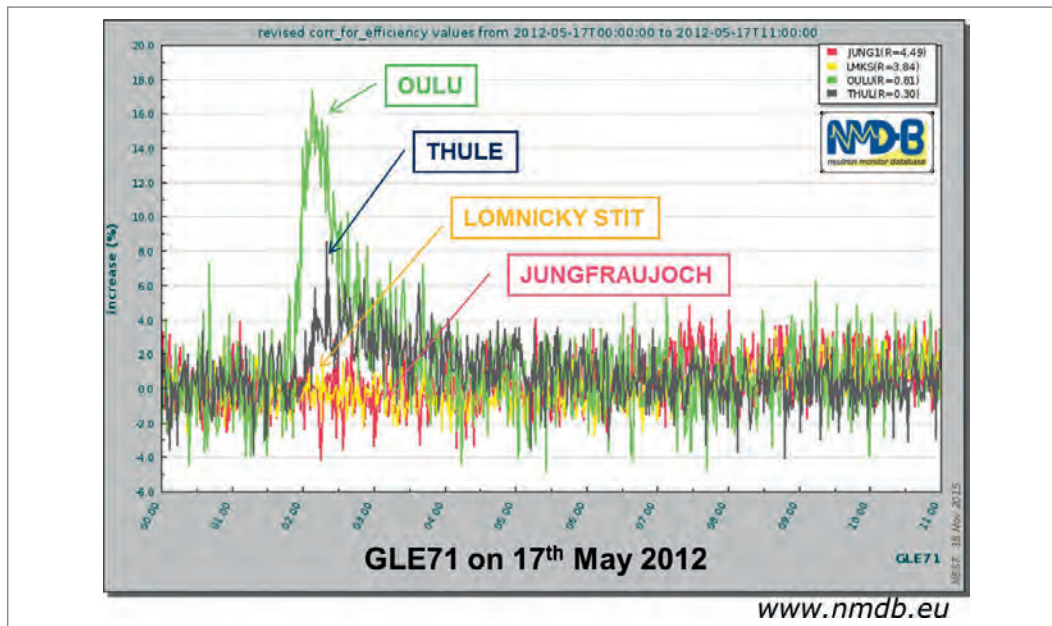


Fig. 4: Relative count rate increases as detected by several Neutron Monitors (at Oulu, Finland; Thule, Greenland; Junfrauoch, Switzerland, und Lomnický Stit, Slovakia) during GLE71 on May 17, 2012 (Source: Neutron Monitor Data Base, www.nmdb.eu).

Ground level enhancements (GLEs, see above) can also be detected by ground based neutron monitors. Fig. 4 shows as an example, short-term increases in neutrons from secondary cosmic rays as detected by a number of neutron monitors during GLE71 which occurred on May 17, 2012. Due to the anisotropic nature of this event, and due to the different geo-magnetic shielding at the locations of the neutron monitors, the count rates measured by these neutron monitors are rather different.

13.2 Radiation Dose Quantities

In general terms, interaction of ionizing radiation with matter (either inorganic or organic in nature) may give rise to the absorption of energy in the irradiated material. This is often quantified in terms of absorbed dose per unit mass, D , which is expressed in SI units of J/kg, and the special name “gray”⁴ was proposed by the International Commission on Radiological Protection, and the International Commission on Radiation Units and Measurements (ICRP 2007, ICRU 1993).

Although the absorbed dose might be a first indicator of radiation damage, for biological effects on organic materials additional factors are also important. For example, even for the same absorbed dose, different types of radiation (e. g., alpha, beta, gamma radiation, neutrons) can cause different biological effects. More specifically, neutrons, protons and alpha particles can cause 5–20 times more damage (e. g., chromosome aberrations in the cell nucleus) than the same absorbed dose of beta or gamma radiation. This is due to differences in the spatial distribution of the radiation-induced damage. In fact, ionizing events induced by neutrons or alpha particles of a certain energy in tissue are located much closer together than those induced by gamma radiation, resulting in more complex radiation damage which is more difficult for cells to repair.

13.2.1 Operational Dose Quantities

For this reason, in operational radiation protection the dose equivalent H defined by the product of the absorbed dose D at a point of interest in tissue and the radiation quality factor Q at this point was introduced by ICRU (Eq. 1):

⁴ Lois H. Gray (1905–1965), English physicist

$$H = QD \quad (1)$$

where Q describes the biological effects depending on radiation type based on physical considerations by taking into account different ionisation densities. Because Q is without dimension, the unit of H is J/kg and the special name is sievert (Sv)⁵.

The ambient dose equivalent, $H^*(10)$, is the operational quantity for area monitoring. It is the dose equivalent at a point in a radiation field that would be produced by the corresponding expanded and aligned field in a 30-cm-diameter sphere of unit density tissue (ICRU-sphere) at a depth of 10 mm on the radius vector opposing the direction of the aligned field (ICRU 1993).

13.2.2 Radiation Protection Dose Quantities

In contrast to ICRU, the ICRP has introduced the radiation weighting factor w_R based on experimental biological evidence (e.g., based on cellular and animal experiments) which, multiplied with absorbed dose, gives the equivalent dose, to account for the differences in biological effects induced by different radiation types. In addition, because it is well known that different human tissues (i.e., organs) react differently to radiation, ICRP has introduced tissue weighting factors, w_T . Accordingly, for routine radiation protection purposes ICRP recommends the use of the effective dose E , which is a rough indicator of the risk of stochastic effects (e.g., cancer, leukemia, hereditary effects) from ionizing radiation (ICRP 2007). E is defined as the tissue-weighted sum of the equivalent doses in all specified tissues and organs of the body, given by Eq. 2:

$$E = \sum_T w_T H_T = \sum_T w_T \sum_R w_R D_{T,R} \quad (2)$$

where H_T is the equivalent dose in a tissue or organ T given by $\sum_R w_R D_{T,R}$; $D_{T,R}$ is the mean absorbed dose from radiation type R in a tissue or organ T , and w_R and w_T are the radiation and tissue weighting factors, respectively. The SI unit for the effective dose is joule per kilogram ($J\ kg^{-1}$) and its special name is sievert (Sv).

13.3 Measurement of Neutrons from Secondary Cosmic Rays – the Extended-Range Bonner Sphere Spectrometer

13.3.1 Detection Principle

The original Bonner sphere spectrometer (BSS) was first described in 1960 by Bramblett, Ewing and Bonner (Bramblett et al., 1960). It is a device used to determine the energy spectrum of neutrons from thermal energies up to about 20 MeV. It employs thermal neutron detectors embedded in polyethylene (PE) moderating spheres of different sizes. In an effort to increase the BSS response for high-energy neutrons above 20 MeV up to 1 GeV, the HMGU BSS has been modified by adding two 9 inch spheres that include lead shells of different thickness (0.5 and 1 inch) [Mares et al., 1998a]. This device is called here Extended-Range Bonner Sphere Spectrometer (ERBSS). The HMGU ERBSS with 16 measuring channels uses 16 ^3He gas-filled spherical proportional counters of 3.3 cm diameter with partial pressure of 172 kPa (type SP9, Centronic Ltd.) and 13 PE spheres of different diameters (2.5, 3, 4, 5, 5.5, 6, 7, 8, 9, 10, 11, 12, 15 inch). One ^3He proportional counter without any PE sphere is used to measure thermal neutrons (Fig. 5). The SP9 ^3He detectors operate within the proportional region at a voltage of +800 V. The signals from these SP9 detectors are amplified in AChem7E charge sensitive preamplifiers and a Multiport II, both produced by Canberra Industries Inc. After that a built-in ADC (analog-to-digital converter) converts the amplified analog signals into digital signals.

⁵ Rolf M. Sievert (1896–1966), Swedish medical physicist

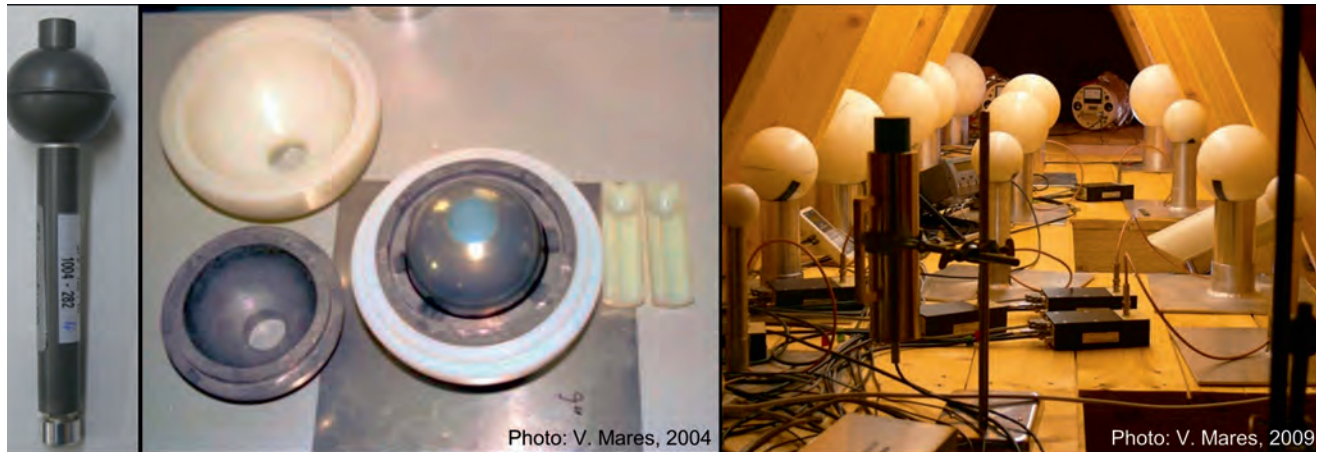


Fig. 5: The HMGU Extended-Range Bonner Spheres Spectrometer (ERBSS): left – ^3He gas-filled spherical proportional counter; middle – polyethylene sphere with lead shell; right – ERBSS at the UFS – PE spheres of various sizes surround the ^3He counters.

^3He filled proportional counters are most suitable for the detection of thermal neutrons because of their high neutron capture cross-section ($\sigma_{n,th} = 5.330 \text{ b}$) for the (n, p) nuclear reaction: after capture of a neutron by a ^3He nucleus, a proton is emitted and a ^3H (triton) nucleus is left. The kinetic energies of proton and triton are 573 and 192 keV, respectively, sharing the reaction energy of 764 keV plus the kinetic energy of the incident neutron. Both the proton and the triton are charged ions that lose their energy in the ^3He counter gas, producing ionizations along the proton and triton tracks and creating pulses with amplitudes that are proportional to the proton and triton energies.

The pulse-height spectrum measured by a ^3He proportional counter is quite complex. Depending on the counter dimension and ^3He pressure, the maximum track lengths of the proton and triton ions may be larger than the geometric dimensions of the counter. This results in pulses with reduced amplitudes and generates a continuous spectrum with two steps at 192 keV and 573 keV, respectively. It is only when both particles are stopped within the sensitive volume of the counter, that the height of the resulting current pulse is proportional to 764 keV. An example of a pulse-height distribution from an SP9 operating at a partial pressure of 172 kPa is shown in Fig. 6.

For each of the SP9 counters used, the counts between the left and right boundaries of region of interest (ROI) are added up (see Fig. 6) and divided by the measurement time (in seconds) to get the counts per second (“count rate”) shown in Fig. 7.

Once the count rates obtained by the measurement channels are known, conversion factors are needed to calculate neutron fluences from the count rates. For this, the fluence response functions HEMA99 of all spheres with a ^3He proportional counter in their center were calculated.

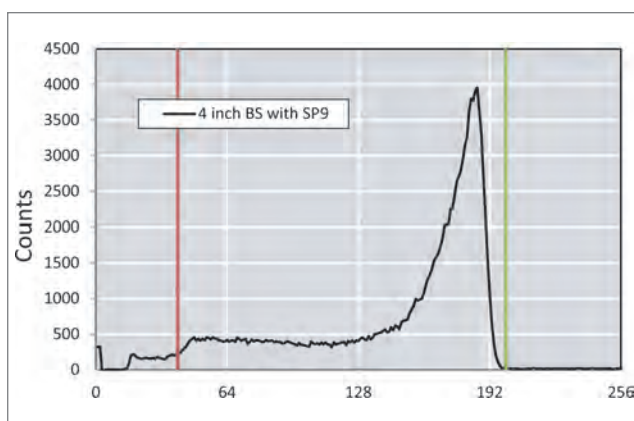


Fig. 6: Pulse height spectrum obtained with an SP9 ^3He proportional counter placed inside of 4 inch Bonner sphere: red and green vertical lines – define the region of interest (ROI). x-axis: channel numbers

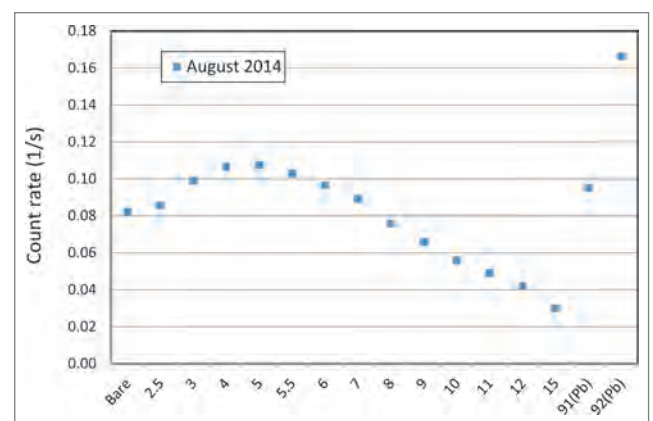


Fig. 7: Mean count rates measured in August 2014 on the UFS by means of the ERBSS. Data are corrected for a reference air pressure of 740 mbar.

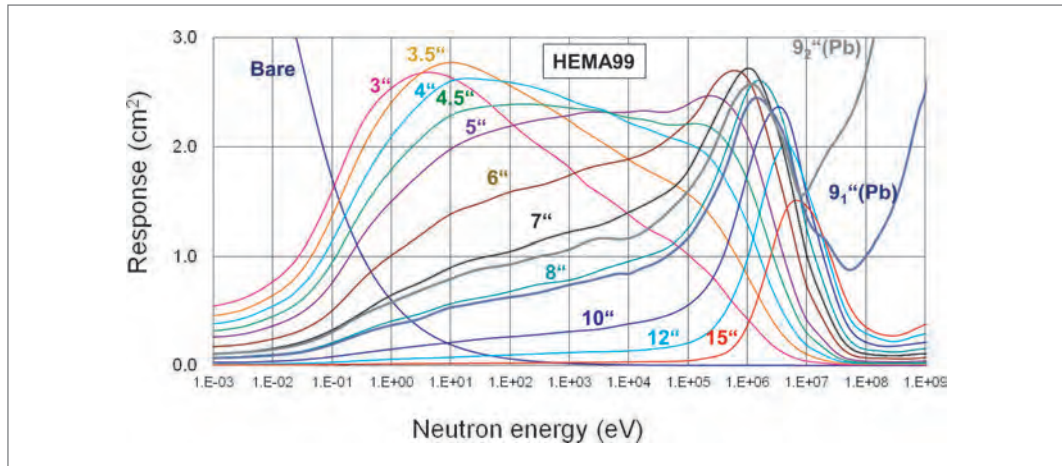


Fig. 8: Response functions of HMGU ERBSS calculated by Monte Carlo simulations as a function of neutron energy (Mares et al. 1991, 1998b).

ed by means of Monte Carlo (MC) simulations (Mares et al. 1991, 1998b) and experimentally validated at 13 mono-energetic neutron energies between thermal energies and 14.8 MeV (Alevra et al. 1992; Thomas et al. 1994), as well as at quasi-mono-energetic neutron fields with peak energies at 244 MeV and 387 MeV (Mares et al. 2013) (see Fig. 8). In the figure, response denotes the number of counts detected relative to the number of impinging neutrons per cm^2 .

13.3.2 Unfolding

The most complex part of neutron spectrometry is the unfolding process. Neutron energy spectra can be derived by unfolding the ERBSS neutron detector readout, i. e., the count rates provided by M ^3He proportional counters of the ERBSS. The count rate measured by the j_{th} detector, C_j , is given by a Fredholm integral equation of the first kind, where $R_j(E)$ is the response function of the j_{th} detector and $\Phi(E)$ the neutron fluence to which the system is exposed (Eq. 3).

$$C_j = \int_{E_{\min}}^{E_{\max}} R_j(E) \Phi(E) dE \quad j = 1, 2, \dots, M \quad (3)$$

To obtain a numerical solution, the system of Eqs. 3 is usually rewritten in terms of a discrete system of equations, described by Eq. 4, where $R_j(E_k)$ is the response function of the j_{th} sphere to neutrons of the energy that corresponds to the k_{th} energy bin, N the number of energy bins and $\Phi(E_k)$ the fluence in the k_{th} energy bin. However, Eq. 4 has no unique solution, because the number of unknowns ($N = 130$ energy bins of fluence $\Phi(E)$) is usually much larger than the number of equations ($M = 16$ measuring channels), i. e., $N \gg M$.

$$C_j = \sum_{k=1}^N R_j(E_k) \Phi(E_k) \quad j = 1, 2, \dots, M \quad (4)$$

For this reason, the unfolding process must necessarily include some physical pre-information in addition to the simulated response functions, the measured count rates and their uncertainties. An initial (guess, *a priori*) neutron fluence spectrum containing physical information about the neutron field is a way to provide such a pre-information.

There are a number of unfolding codes based on different approaches that can be used to determine $\Phi(E)$ values that satisfy the system of equations formulated in Eq 4. For example, methods based on linear and non-linear least-squares methods, Bayesian methods, maximum entropy and artificial neural networks methods, among others, have been used (Reginatto et al. 2010). Typically, the UFS neutron spectra are unfolded from the ERBSS count rates by means of the MSANDB (Matzke 1987, 2002) unfolding code, which is based on the earlier SAND-II code (McElroy et al. 1967). MSANDB uses iterative procedures and requires an initial *a priori* spectrum. For more details see (Simmer et al. 2010).

13.3.3 Correction for Air Pressure

Because the absorption properties of the atmosphere with respect to cosmic rays depends on atmospheric density, air pressure is an important parameter that influences the intensity of secondary cosmic rays at the Earth's surface. Thus, the count rates measured by the ERBSS must be corrected for any changes in air pressure. Generally, data on meteorological parameters measured at the UFS are provided by the German Weather Service (DWD). Additionally, the air pressure and temperature are also measured continuously inside the HMGU measurement shed where the HMGU ERBSS is located (see Fig. 9).

Such data on air pressure were used to correct the count rates measured with the ERBSS, by means of Eq. 5. This is of particular importance if the influence of other environmental parameters are to be studied or if data of different research stations are to be compared.

$$N_{\text{cor}} = N \cdot \exp[-\beta \cdot (P_0 - P)] \quad (5)$$

Where N is the observed count rate at a particular pressure, P , and N_{cor} is the corrected value for a standard pressure, P_0 , of 740 mbar (Röhrs, 1995). The quantity β is a barometric coefficient and a value of 0.721 % per mbar was used.

Fig. 10 shows the un-corrected and pressure-corrected ERBSS count rates obtained from 24th March to 13th April 2015 for selected spheres. After pressure correction, the count rates are lower from 24th March to 4th April, because the air pressure during this period of time was below the reference pressure of 740 mbar (see Fig. 9). In contrast, because the air pressure values were close to 740 mbar during the period from 8th April to 13th April, the raw and corrected count rates are very similar for this time period.

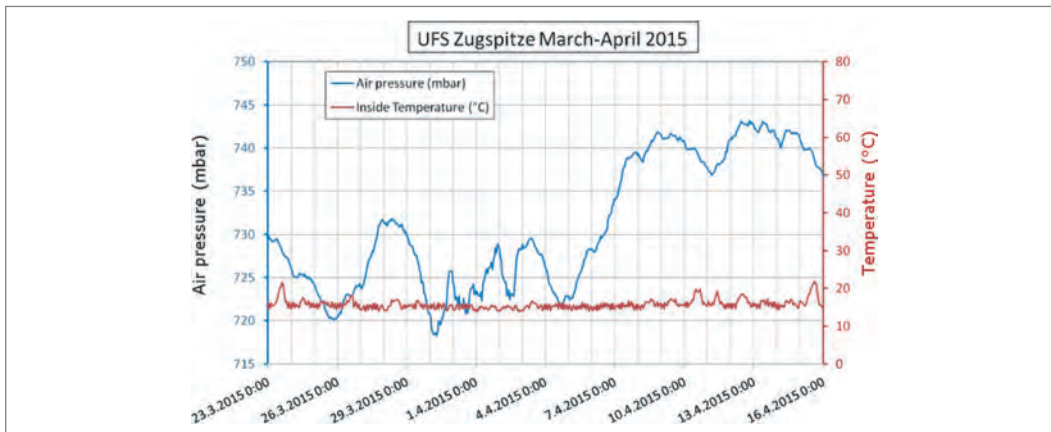


Fig. 9: Air pressure and temperature measured in March/April 2015 inside the HMGU instrument shed where the HMGU ERBSS is located.

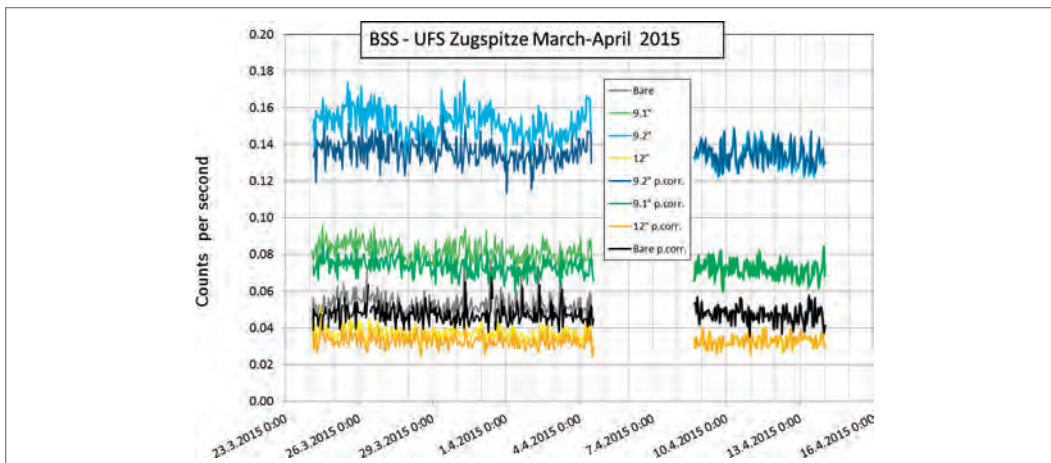


Fig. 10: Hourly un-corrected count rates as provided by selected ERBSS detectors in March/April 2015 (light colored lines), and pressure-corrected count rates at 740 mbar (dark-colored lines); the corresponding air pressure data are shown in Fig. 9.

13.3.4 The Extended-Range Bonner Sphere Spectrometer at the UFS



Fig. 11: Instrument shed on the measurement terrace of the UFS housing the Extended-Range Bonner Spheres Spectrometer of the HMGU (see also Fig. 5).

This HMGU ERBSS has been installed in 2004 at the Environmental Research Station “UFS Schneefernerhaus” (2,650 m above sea level) close to the summit of the Zugspitze Mountain, Germany, to measure continuously the energy spectrum of neutrons from secondary cosmic rays. Since October 2005, the system is running inside an instrument shed with slant roof on the terrace of the station (Figs. 5, 11) (Leuthold et al. 2009). The roof is tilted to avoid snow cover during winter times that could affect the measurements. Since then the ERBSS is providing routine data allowing the quantification of any variations in the intensity of neutrons from secondary cosmic rays, in the whole neutron energy range from a few meV up to GeV, larger than 10%. A similar system is operating at the Koldewey station of the Alfred Wegener Institute, the French-German arctic polar base (Rühm et al. 2009a, 2009b).

13.4 Results 1: Forbush Decrease on 11th September 2005

A Forbush decrease (FD), named after the American physicist Scott E. Forbush, is a rapid decrease in GCR intensity within a few hours, due to the magnetic field of the solar-wind plasma sweeping some of the GCR particles away from Earth, followed by a more gradual recovery phase typically lasting for several days. An FD occurs after a coronal mass ejection (CME). The magnitude of an FD varies from a few percent up to 25% in the decrease of GCR intensity. Such rapid changes in GCR intensity can for example be measured by neutron monitors (NMs).

Fig. 12 shows ERBSS count rates measured at the UFS Zugspitze in September 2005. The count rates obtained from all 16 ERBSS detectors were added, to reduce the statistical uncertainty, and compared to data from the neutron monitor on the Lomnický štít mountain (latitude: N 49° 20', longitude: E 20° 22', cutoff 3.84 GV, altitude 2,634 m), Slovakia. It is evident from Fig. 12 that a significant decrease was observed within a few hours in the morning of September 11th, which is attributed to a Forbush decrease. It is important to note that the second count rate decrease observed for a short period of time between the 17th and 20th of September was due to variations of environmental conditions (mainly snow cover; see below).

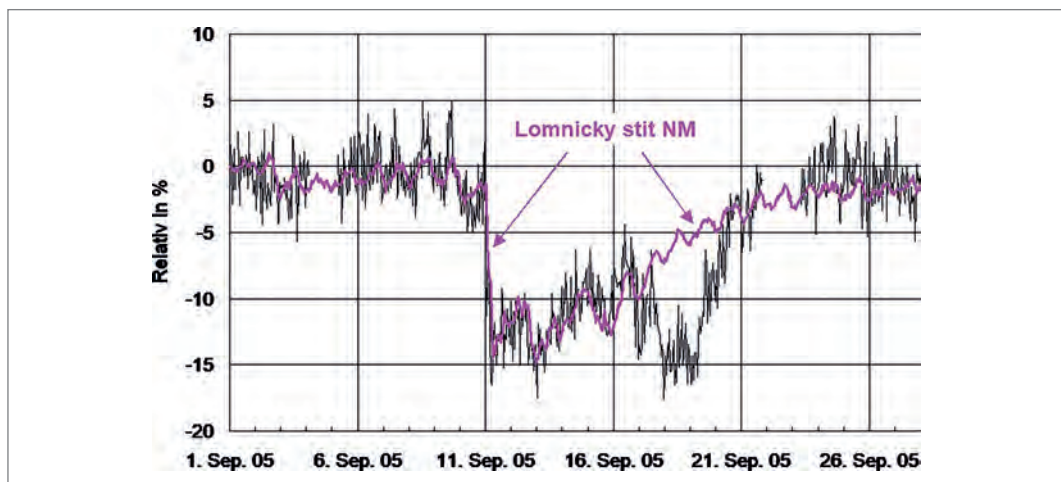


Fig. 12: Relative deviation of added hourly ERBSS count rates as measured in September 2005 (black line) compared to those measured by the Neutron Monitor at Lomnický štít, Slovakia (magenta line) (Leuthold et al., 2007).

13.5 Results 2: Influence of the Environment on Neutrons from Cosmic Rays

13.5.1 Effect of Snow – First Observations Based on Detector Count Rates

As already indicated earlier, the count rates obtained by the individual detectors of the ERBSS reflect the presence of neutrons from secondary cosmic rays, and the moderator thickness (i. e., radius of PE spheres) determines the energy range of these neutrons. For example, the count rates of the bare detector reflect the presence of thermal neutrons, while the count rates of the 9 inch spheres including lead mainly reflect the presence of high-energy neutrons. Fig. 13 shows, as an example, the monthly count rates of eight detectors (bare, 4", 5", 10", 12", 15", 9-1"(Pb), and 9-2"(Pb)) obtained between January 2010 and June 2014. In the figure all count rates are normalized to a reference pressure of 740 mbar. Clearly, seasonal variations are visible suggesting the presence of less neutrons during winter times and more neutrons during summer times, which could be due to variations in snow cover.

In order to investigate this hypothesis, let us first have a look at an obvious short-term decrease in count rates observed in Fig. 13 during autumn 2011 (marked in red in the figure). The period between May and December 2011 was rather dry, but was interrupted by a short period of heavy snow fall early October of that year (see Fig. 14). Obviously, the increase of snow cover thickness in the vicinity of the UFS early October led to a decrease in detector counts, while during the following snow melt later in October the count rates of all detectors recovered.

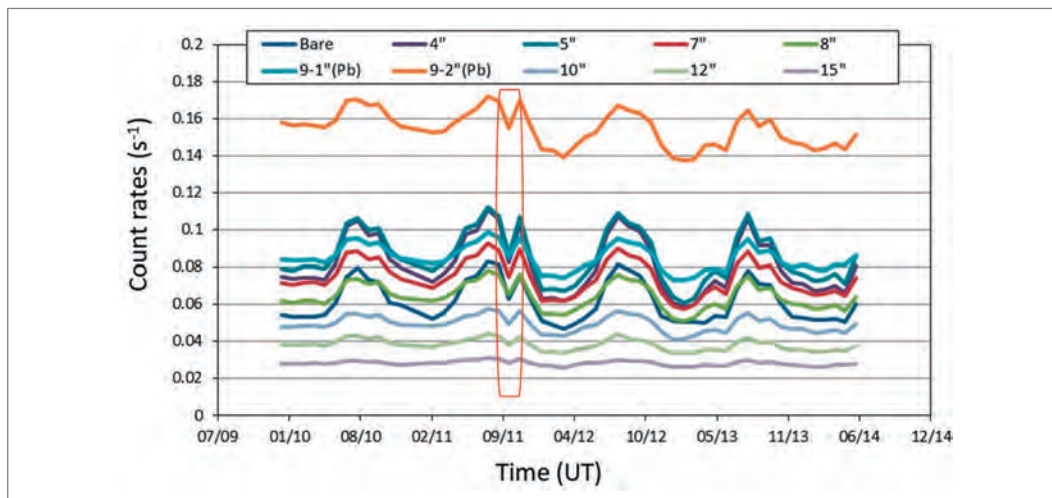


Fig. 13: Monthly count rates from eight detectors of the ERBSS, from Jan 2010 to June 2014, and normalized to a reference air pressure of 740 mbar. In autumn 2011 a short-term decrease in count rates can be observed (marked in red).



Fig. 14: UFS in September 2011 at dry conditions (left), and after heavy snow-fall in October 2011 (right).

13.5.2 Effect of Snow – Creation of a Hypothesis and First Simulations

The effect observed could be explained by the fact that a large part of the neutron spectrum measured at the UFS is from neutrons that were initially of very high energy, moderated in the ground towards lower energies, and then backscattered to the air where they were detected by the spectrometer. Any snow cover on top of the soil might absorb part of the backscattered neutrons (“albedo neutrons”), and the resulting neutron fluence above ground is reduced. Indeed, such an effect can be tested by Monte Carlo simulations.

Such simulations were performed by the GEANT4 code, which was initially developed at CERN to simulate the efficiency of various instruments to detect high-energy particles. In the present example, the code was used to simulate the transport of particles of secondary cosmic rays in an atmospheric volume of $100 \times 100 \times 317 \text{ m}^3$, allowing for moderation in and backscattering from soil. It was assumed that secondary neutrons impinge perpendicularly on that air volume (i.e., at a height of 317 m above ground) with an energy distribution as given by Roesler and co-workers (Roesler et al. 2002). Backscattered neutrons were scored at a height of 150 cm and averaged over an area of $20 \times 20 \text{ m}^2$. Although these assumptions represent only a simplified model of the real situation (for example, the angular distribution of impinging neutrons was neglected, the ground at the UFS is not horizontal but tilted, the UFS building and the measurement terrace with the ERBSS instrument was not modelled, etc.), they are useful to demonstrate the effect of snow cover on backscattered neutrons from secondary cosmic rays. Fig. 15 shows the energy distribution of neutrons backscattered from soil with a typical elemental composition without any snow or water on top. Dominating are neutrons between 20 and 500 MeV in energy (“cascade neutrons”) and those between 400 keV and 20 MeV (“evaporation neutrons”), and neutrons between 200 meV and 200 keV (“epithermal neutrons”). The presence of a water layer of 50 cm in the simulation covering the soil changes the situation: while almost no effect can be seen at high energies, the number of neutrons below 20 MeV is significantly reduced (a similar effect is seen for a water layer of 100 cm). Note that, for typical snow densities, a water layer of 50 cm might correspond to a snow layer of 100–150 cm thickness.

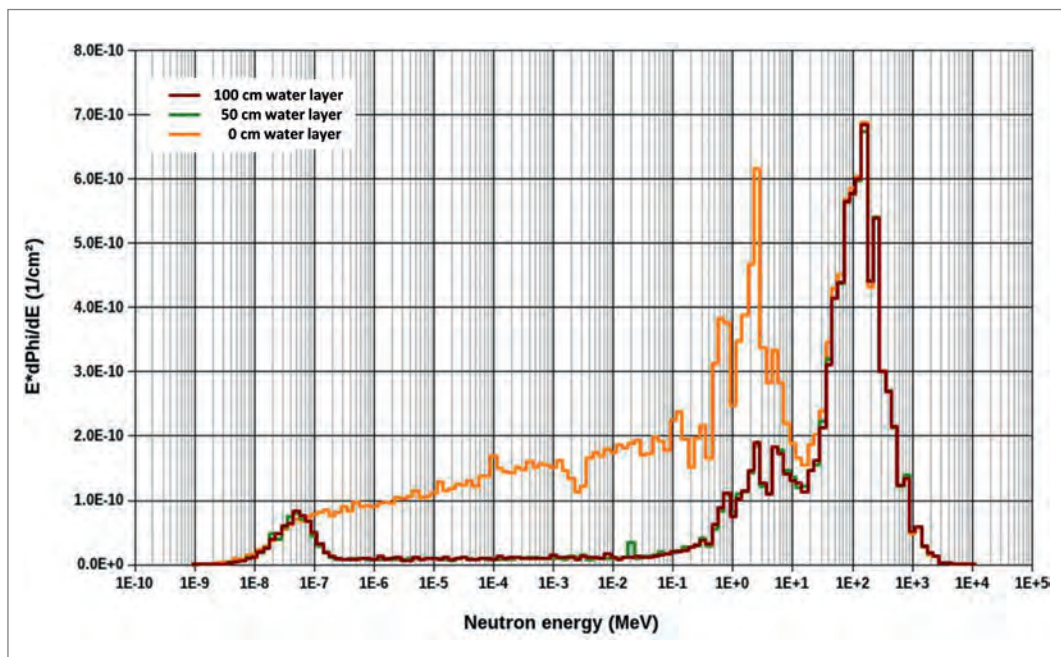


Fig. 15: Neutron spectra simulated with the Monte Carlo code GEANT4 at a height of 150 cm above ground, covered by water layers of various thickness (0 cm, 50 cm and 100 cm) (S. Trinkl, private communication, 2014).

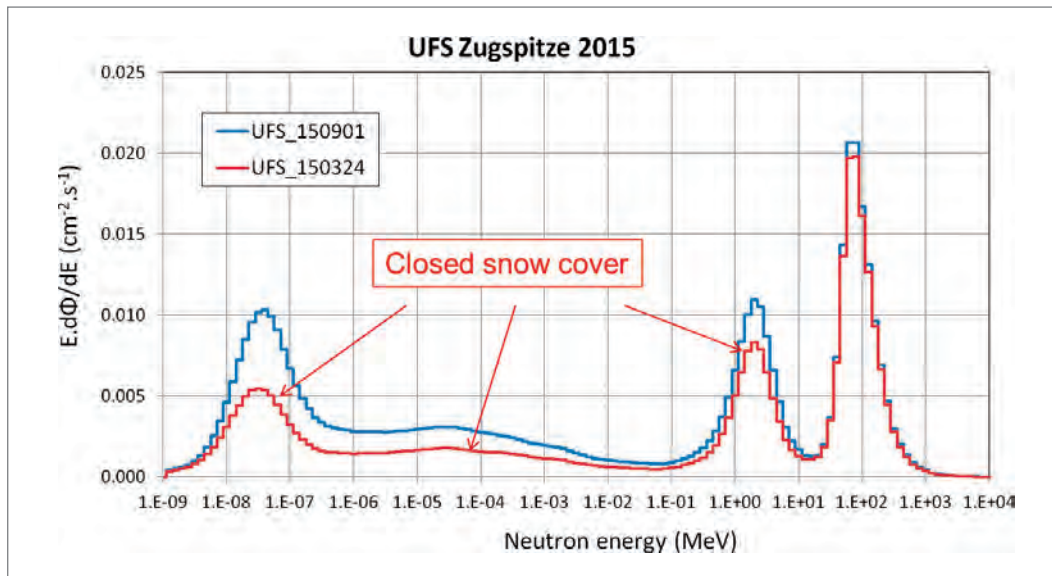


Fig. 16: Neutrons of secondary cosmic rays measured with the ERBSS on September 2015 (blue curve) and March 2015 (red curve).

13.5.3 Effect of Snow – Influence on Neutron Energy Distribution

In order to investigate the influence of environmental parameters under real conditions experimentally, we unfolded the count rates obtained by the ERBSS (see above) during dry periods and during periods with heavy snow cover. In Fig. 16 this was for example done for March 2015 (heavy snow cover) and September 2015 (no snow in the vicinity of the UFS). As expected, the high-energy cascade neutrons were not affected by the presence of snow. In contrast, neutrons with an energy of less than 20 MeV were reduced, as was predicted by the simulations (Fig. 15), due to absorption of neutrons scattered back from soil, by the snow.

13.5.4 Effect of Snow – Observation of Long-Term Seasonal Neutron Oscillations

The potential effects of snow cover on the number of neutrons of secondary cosmic rays close to the interface between lithosphere and atmosphere has been described above. If real, such effects should be responsible for a reproducible pattern of changes in seasonal neutron fluences with higher values during summer time and lower values during snowy winter time. Because the ERBSS at the UFS has been operative since 2005, the data obtained already cover a whole solar cycle. Consequently, the data can be used and any seasonal changes could be monitored for many years for the first time. More specifically, average monthly count rates obtained with the detectors of the ERBSS were calculated and, with the unfolding procedure described above, monthly neutron energy distributions were obtained. These distributions were then used and the number of neutrons was calculated by integrating the spectra over 4 energy ranges: less than 0.4 eV (“thermal neutrons”), 0.4 eV–0.1 MeV (“epithermal neutrons”), 0.1 MeV–20 MeV (“evaporation neutrons”), above 20 MeV (“cascade neutrons”). Figs. 17 (a–d) show the results (Rühm et al. 2012). Clearly, reproducible yearly oscillations are seen, which are more dominant at lower energies, and less dominant at higher energies, with almost no effect for the cascade neutrons.

In an attempt to quantify the measured oscillations, the following function was fitted to the data shown in Fig. 16 (Eq. 6):

$$y = a \cdot \sin[(2 \cdot \pi \cdot t \cdot b/365) + d] + c \cdot t + e \quad (6)$$

The function describes a sinodial behavior which is on top of a linear increase: a represents the amplitude of the oscillation, b the period, and c the slope of the linear increase (which might

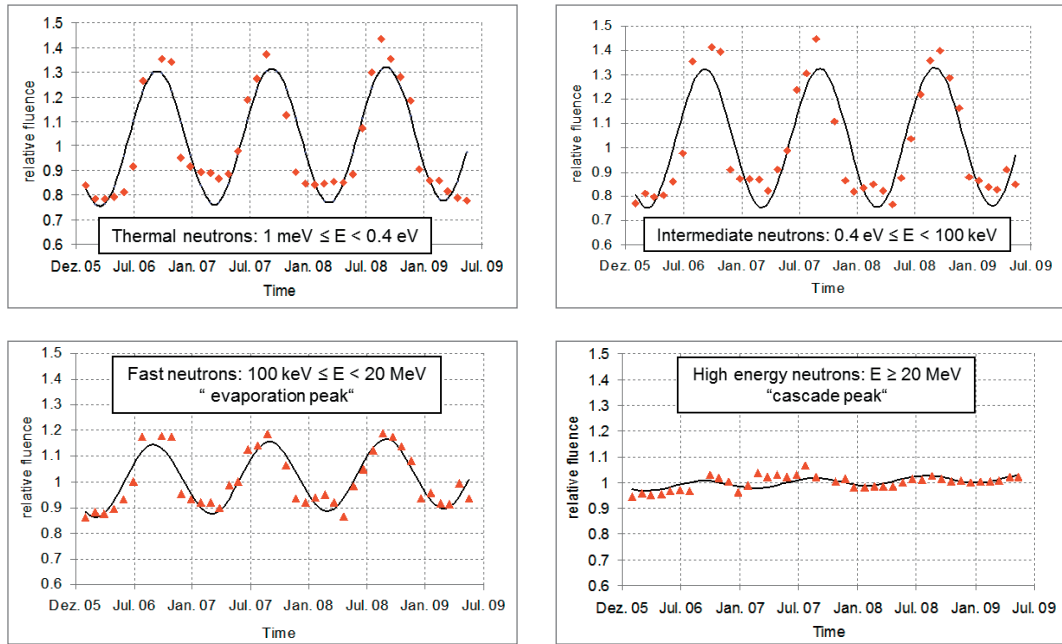


Fig. 17: Relative fluence of secondary fluences as obtained from the long-term ERBSS measurements at the UFS (closed symbols): a) thermal, b) epithermal, c) evaporation, d) cascade neutrons. Black solid line: fit through the data

be there due to the decrease in solar activity expected for the investigated period of time); d and e are additional fit parameters, t represents the time.

As a consequence of the observed oscillations, the radiation dose due to neutrons from secondary cosmic rays will also change and oscillate with time. Based on the results obtained, Fig. 18 shows the neutron doses, in terms of $H^*(10)$, at the UFS as a function of time, for the investigated period. Application of the fit function given above results in the following numerical parameters: $a = 0.068 \pm 0.006$, $b = 0.999 \pm 0.014$ und $c = (3.3 \pm 1.2) \times 10^{-5} d^{-1}$.

The fit parameters obtained suggest a duration of the oscillations of about 1 year (parameter b). The neutron dose varies between $\pm 7\%$. Finally, parameter c suggests a slight increase in neutron dose of about 1.2% per year, due to the decrease in solar activity during the measurement periods. Interestingly, neutron monitors suggest a similar increase in count rate during this period of time. Details of these results are given in Rühm et al. 2012.

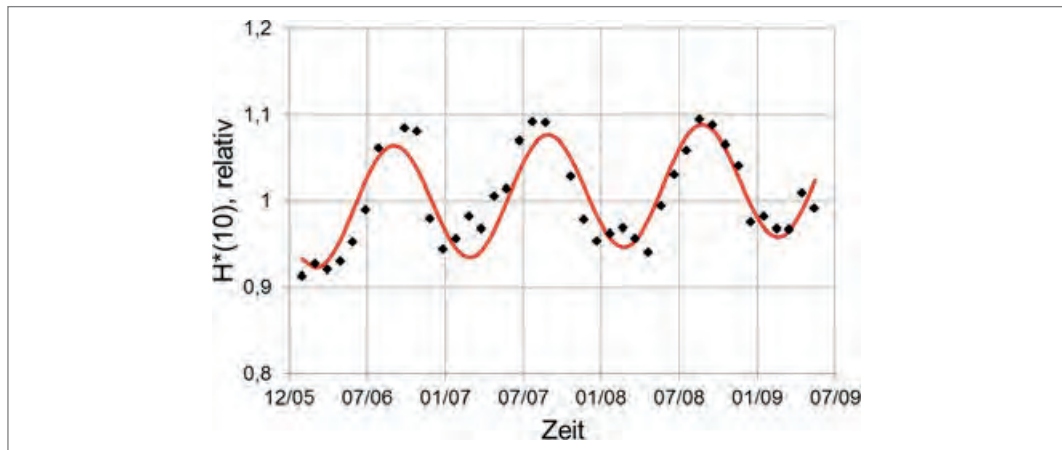


Fig. 18: Relative ambient dose equivalent from neutrons of secondary cosmic rays.

References

- Alevra AV, M. Cosack, J. B. Hunt, D. J. Thomas, H. Schraube, Experimental determination of the response of four Bonner sphere sets to monoenergetic neutrons (II) *Radiat. Prot. Dosim.* 40, 91–10 (1992).
- Bramblett, Richard L.; Ewing, Ronald I.; Bonner, T.W. (1960). "A new type of neutron spectrometer." *Nuclear Instruments and Methods.* 9 (1): 1–12.
- Feynman, J. G. Spitale, J. Wand, and S. Gabriel, Interplanetary Proton Fluence Model, *J. Geophys. Res.* 98, 13281–13294 (1993).
- Grieder, P. (2001) *Cosmic Rays at Earth: Researcher's Reference Manual and Data Book.* Elsevier, 1st edition
- International Commission on Radiation Units and Measurements (1993) *Quantities and Units in Radiation Protection Dosimetry.* ICRU Report 51.
- International Commission on Radiological Protection (2007) *Recommendations of the International Commission on Radiological Protection.* ICRP Publication 103, Ann. ICRP 37(2–4), Elsevier, 2007.
- Leuthold G, V. Mares, W. Rühm, E. Weitzenegger, H. G. Paretzke. Long-term measurements of cosmic ray neutrons by means of a Bonner spectrometer at mountain altitudes – first results. *Radiation Protection Dosimetry*, Vol. 126, No. 1–4, pp. 506–511, 2007.
- Mares, V., G. Schraube, H. Schraube, Calculated neutron response of a Bonner sphere spectrometer with ³He counter *Nucl. Instr. Meth. A* 307, 398–412 (1991).
- Mares V., H. Schraube, High energy neutron spectrometry with Bonner spheres, *Proceedings, The IRPA Regional Symposium on Radiation Protection in Neighbouring Countries of Central Europe, Prague, Czech Republic, September 1997, 543–547, (1998a)* http://www.iaea.org/inis/collection/NCLCollectionStore/_Public/30/031/30031466.pdf
- Mares, V., A. Sannikov, H. Schraube, The response functions of a ³He-Bonner spectrometer and their experimental verification in high energy neutron fields, *SATIF-3 Proceedings, Sendai, Japan, 237–248 (1998b)*
- Mares, V., Maczka, T., Leuthold, G. Rühm, W.: Air crew dosimetry with a new version of EPCARD, *Radiat. Prot. Dosim.* (2009), Vol. 136, No. 4, pp. 262–266.
- Mares, V., C. Pioch, W. Rühm, H. Iwase, Y. Iwamoto, M. Hagiwara, D. Satoh, H. Yashima, T. Itoga, T. Sato, Y. Nakane, H. Nakashima, Y. Sakamoto, T. Matsumoto, A. Masuda, H. Harano, J. Nishiyama, C. Theis, E. Feldbaumer, L. Jaegerhofer, A. Tamii, K. Hatanaka, T. Nakamura., Neutron dosimetry in quasi-monoenergetic fields of 244 and 387 MeV, *IEEE Trans. Nucl. Sc.* 60, 299–304 (2013).
- Mares, V.; Rühm, W., Computerprogramme zur Dosisberechnung beim Fliegen am Beispiel von EPCARD., *StrahlenschutzPRAXIS* 2, 18–21 (2014).
- Matzke, M. Private communication. Later Integrated into the Neutron2: Metrology File NMF-90, available from NEA Databank. <http://www.nea.fr/abs/html/iaea1279.html> (1987).
- Matzke, M. Propagation of uncertainties in unfolding procedures. *Nucl. Instrum. Methods Phys. Res. A* 476, 230–241 (2002).
- McElroy, W., Berg, S., Crockett, T. and Hawkins. R. Spectra Unfolding. Technical Report AFWL-TR-67-41, US Air Force Weapons Laboratory (1967).
- Reginato, M. Overview of spectral unfolding techniques and uncertainty estimation. *Rad. Meas.* 45, 1323–29 (2010).
- Röhrs, K. (1995) The neutron monitor at Kiel (Germany) operated by the Extraterrestrial Physics Department of the Institute for Experimental and Applied Physics of the Christian-Albrechts University of Kiel.
- Roesler, S., W. Heinrich, H. Schraube, Monte Carlo calculation of the radiation field at aircraft altitudes, *Radiat. Prot. Dosim.* 98, 4, 2002, 367–388.
- Rühm, W., V. Mares, C. Pioch, E. Weitzenegger, R. Vockenroth, and H. G. Paretzke (2009a), Measurements of Secondary Neutrons from Cosmic Radiation with a Bonner Sphere Spectrometer at 79°N, *Radiat. Environ. Biophys.*, 48, 125–133.
- Rühm, W., V. Mares, C. Pioch, G. Simmer, and E. Weitzenegger (2009b), Continuous measurement of secondary neutrons from cosmic radiation at mountain altitudes and close to the North Pole-A Discussion in terms of H*(10). *Radiat. Prot. Dosim.*, 136(4), 256–261.
- Rühm, W., U. Ackermann, C. Pioch, and V. Mares. Spectral neutron flux oscillations of cosmic radiation on the Earth's surface. *J Geophys Res* 117, A08309, 2012.
- Shea, M.A. and D.F. Smart, A Summary of Major Solar Proton Events, *Solar Phys.* 127, 297–320 (1990)
- Shea, M.A. and Smart, D.F., Cosmic Ray Implications for Human Health. *Space Science Reviews*, 93, 187–205 (2000).
- Shea, M.A. and D.F. Smart, Patterns of Solar Proton Events over Four solar Cycles, *Proc. 26th Int. Cosmic Ray Conf.* 6, 374–377 (1999).
- Simmer, G., Mares, V., Weitzenegger, E. and Rühm, W. Iterative unfolding for Bonner sphere spectrometers – sensitivity analysis and dose calculation. *Radiat. Meas.* 45, 1–9 (2010).
- Thomas, DH, A.V. Alevra, J. B. Hunt, H. Schraube Experimental determination of the response of four Bonner sphere sets to thermal neutrons *Radiat. Prot. Dosim.* 54, 25–31 (1994).

14 Observations of OH airglow at UFS "Schneefernerhaus"

Carsten Schmidt¹, Patrick Hannawald², René Sedlak², Stefan Noll², Sabine Wüst¹ and Michael Bittner^{1,2}

14.1 Introduction

14.1.1 Airglow

The term airglow describes a faint luminescence of the atmosphere in the visible to infrared part of the electromagnetic spectrum. The expressions airglow, nightglow, sky glow are often used synonymously in scientific literature, although to be scientifically correct they should not. Airglow is the most common expression. In a strict sense it comprises both the nightglow and the dayglow, which are different atmospheric emissions dominating through either night- or daytime. The sky glow on the other hand usually refers to the entire luminance of the night sky, including other sources, such as zodiacal light, starlight and even artificial light pollution (see Fig. 1). It is important to keep this ambiguity of expressions in mind, when studying literature on this topic.

Furthermore, airglow has to be distinguished from the well-known phenomenon of the aurora at high latitudes, despite the fact that some emissions can be identified in both, the aurora and the airglow. In contrast to aurora, generated by sporadically impacting high energetic particles accelerated in the Earth's magnetosphere, airglow emissions are due to exothermic chemical reactions exciting higher energetic states in both atomic and molecular species. These reactions happen all the time. Consequently, airglow is a so-called steady emission.

The primary source of energy for the chemical reactions is the solar ultraviolet (UV) radiation. This high energetic radiation is absorbed in the upper and middle atmosphere (above 50 km). Important mechanisms of absorption are ionization, photo dissociation of molecules and the generation of excited states in atoms and molecules. The primary energy provided by this electromagnetic radiation is thereby mainly stored in form of potential chemical energy. The dissociation of molecular oxygen is one of the most important mechanisms that lead to airglow emissions. Atomic oxygen takes up the main part of the primary energy and is involved in almost all reactions leading to airglow emissions (compare equations (1.1) to (1.14)). Depending on the wavelength of the solar radiation and on the height above ground, different reactions dominate, leading to the well-known so-called Herzberg- and Schumann-Runge absorption bands and continua of O₂ as well as to the Hartley bands of O₃ during daytime. Table 1 gives an overview of the most important reactions, describing how ultraviolet radiation creates chemical species during daytime, which later at night contribute to the nightglow; the shorter the wavelength is, the higher up in the atmosphere these reactions occur.

Table 1: Important reactions concerning the absorption of solar radiation during daylight, including the wavelength of the solar radiation being absorbed. The third column indicates the airglow emissions in which the species produced by these reactions are later involved (compare equations 1.1 to 1.14).

reaction	wavelength	relation to airglow
$O_2 + h\nu \rightarrow O_2^+ + e^-$	< 103 nm	OI red line
$H_2O + h\nu \rightarrow H + OH$	< 239 nm	OH
$O_2 + h\nu \rightarrow O + O$	< 242 nm	OH, O ₂ , Na, OI green line
$O_3 + h\nu \rightarrow O + O_2$	< 310 nm	OH, O ₂ , Na

Chemical reactions, including those causing the airglow, do not only depend on the abundance of the relevant species but also strongly on the surrounding pressure and temperature. Thus, different reactions take place at different heights of the atmosphere and the airglow phenom-

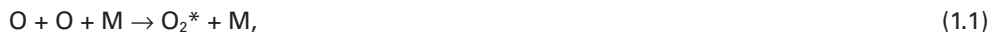
¹ German Aerospace Center (DLR-DFD), 82234 Weßling, Germany

² Augsburg University (UNA), 86135 Augsburg, Germany



Fig. 1: Airglow in the visible spectrum as seen from the international space station. The emissions of atomic oxygen at 95 km (green) and in the ionosphere between 160 km and 260 km (red) dominate. The faint yellow emission of sodium (Na) around 92 km is hardly recognizable. The infrared emissions of molecular oxygen (around 94 km) and hydroxyl (86–87 km) are closely below the pronounced green emission (image credit: NASA, ISS028-E-050184, 2011-09-15, contrast enhanced).

enon is confined to more or less well-defined layers, which typically span only a few kilometers in height. A prominent layer is given by the excited atomic oxygen in approximately 95 km to 100 km height, emitting at 557.7 nm, often simply called the “green line” (see also Fig. 1):



Here, M denotes an arbitrary species (mostly N_2), ensuring conservation of energy and momentum; ${}^1\text{S}$ and ${}^1\text{D}$ denote the respective states of atomic oxygen, whereas * represents an unspecified excited state (in contrast to the specific $b({}^1\Sigma)$ or ${}^3\Sigma$ states).

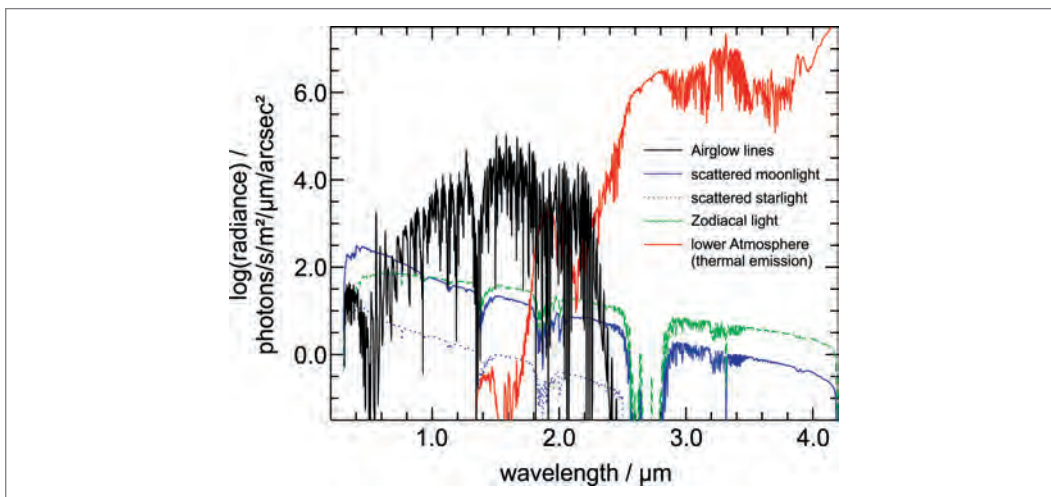
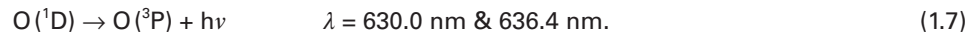


Fig. 2: Typical diffuse night sky brightness based on the Cerro Paranal Sky Model (Noll et al. (2012), Jones et al. (2013), Noll et al. (2014)). Airglow is the brightest phenomenon in the near-infrared spectral range between 700 nm and 2200 nm.

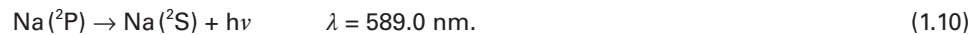
Instead of reactions (1.2) and (1.3) the following reactions can occur (amongst others), leading to the formation of a layer of excited molecular oxygen at approximately 94 km height:



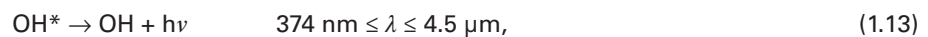
Both emissions shown in eq. (1.3) and (1.5) are limited in height by the three body reaction (1.1) becoming more likely deeper down in the denser atmosphere. In principal, $\text{O}(^1\text{D})$ could contribute to the airglow, but its lifetime of 110 s is too long, so it is deactivated by collisions with other species, the so-called “collisional quenching”. However, at greater (less dense) atmospheric heights, the dissociative recombination of O_2^+ also leads to the $\text{O}(^1\text{D})$ -state (reaction (1.6)). There, it results in the emission of the so-called “red line(s)” of atomic oxygen in a relatively broad layer (~100 km) at heights above 200 km (see Fig. 1):



The existence of a layer composed of metal atoms high up in the atmosphere may be surprising, but the yellow sodium doublet D-lines at 589.0 nm have been observed for a long time. The sodium originates from interplanetary dust which is deposited at these heights by meteoroids and it forms a narrow layer around 89 km and 92 km. The sodium is excited by the Chapman mechanism (Chapman (1939), here after Plane et al. (2007)):



Finally, the most important contribution to the nightglow is given by emissions of the hydroxyl (OH) molecule. These are excited during production of atomic hydrogen with ozone (Bates and Nicolet (1950)):



The excess energy of 3.32 eV is not enough to ionize OH or to put it into a higher electronic state. Rather vibrational and rotational levels of the molecule are excited. After formation according to reaction (1.12) OH will typically be in its 7th to 9th vibrational level. Transitions changing the vibrational quantum number ν by 2 are more likely than others, the transitions $\nu = 9$ to $\nu = 7$, $\nu = 8$ to $\nu = 6$, ... and $\nu = 2$ to $\nu = 0$ are the brightest. Since the formation of excited OH relies on the presence of both atomic hydrogen and ozone (the first one being more abundant higher up in the atmosphere and the second one exhibiting greater life times in lower parts of the atmosphere), the OH layer is confined to a height of approximately 86–87 km, with a half width of ± 4 km (Baker and Stair (1988)). Both, height and width of the OH layer can vary with latitude and season due to atmospheric dynamics. These properties of the OH layer can today be studied efficiently with satellite-based instruments (e.g., Wüst et al. (2020, 2017), Noll et al. (2017), von Savigny (2015), Marsh et al. (2006)).

As ozone is quickly destroyed by UV radiation (see Table 1), the OH airglow is a typical representative of the nightglow (although OH emissions can in principle be observed during daytime, but then they are orders of magnitude weaker than at night). Fig. 2 gives an overview of the airglow brightness (mainly OH) in comparison with other nocturnal light sources. In the spectral range between approximately 700 nm to 2.2 μm airglow emissions are the brightest phenomenon at the night sky.

14.1.2 Airglow temperatures

It takes the OH molecules several milliseconds to cascade down from their initial high vibrational states to the lower ones. These lower states can either be populated through radiative transitions from the initially populated higher levels or by collisional relaxation (and by a mix-

ture of both). In any case, the molecules will undergo many collisions with other atmospheric constituents until they have reached low vibrational states. Most of the (radiative) vibrational transitions will also change the rotational state of the molecule, which is the reason for the respective transitions being called rotational-vibrational transitions. In the emission spectrum one radiative vibrational transition will therefore split into dozens of individual lines, usually called branch or band.

The energy exchanged during the collisions is small compared to the vibrational energy, but it is sufficient to change the population distribution of their rotational levels: it becomes thermalized, which means it can be described by a Boltzmann distribution with the rotational temperature T_{rot} as essential parameter. In the following an arbitrary upper state is called "2" and the respective lower state "1" because there are actually ten thousands of possible transitions. The intensity $I_{i,v21,J21}$ of an emission line changing the vibrational state from v_2 to v_1 and the rotational level from $J_{i,v2}$ to $J_{i,v1}$ is then given by:

$$I_{i,v21,J21} = \frac{N_{i,v2}}{Q_{i,v2}} 2(2J_{i,v2} + 1) A_{i,v21,J21} \exp\left(\frac{-F_{i,v2,J21}}{k_B T_{\text{rot}}}\right). \quad (1.15)$$

Here, $J_{i,v2}$ denotes the initial quantum number of the angular momentum, i represents the doublet branch (1 or 2) of the transition, describing the two spin-orbit coupling possibilities, and k_B is the Boltzmann constant. $A_{i,v21,J21}$ and $F_{i,v2,J21}$ are the Einstein coefficient of the transition and the term value (energy) of the rotational level of the initial vibrational level v_2 . $N_{i,v2}$ and $Q_{i,v2}$ denote the population number and the state sum. The latter two are not easily accessible, but in local thermodynamic equilibrium (LTE) their ratio is supposed to be constant. Thus, a linear set of equations can be retrieved for the ratio of N/Q and T_{rot} if several lines of the same rotational-vibrational branch are observed:

$$\ln\left(\frac{I_{i,v21,J21}}{2(2J_{i,v2} + 1)A_{i,v21,J21}}\right) = \ln\left(\frac{N_{i,v2}}{Q_{i,v2}}\right) - \frac{F_{i,v2,J21}}{k_B T_{\text{rot}}}. \quad (1.16)$$

Mathematically, this results in a simple overdetermined set of equations (one equation for each line observed), which can be solved accordingly for any branch. Low vibrational levels are more likely to be in local thermodynamic equilibrium with the atmosphere, as the molecules have undergone more collisions with other atmospheric constituents before reaching a low vibrational state. Thus, their rotational temperature is more likely to equal the actual kinetic temperature of the atmosphere. Unfortunately, the lowest respective transition (2-0) cannot be observed from the ground due to absorption by H_2O in the lower atmosphere, thus the OH(3-1) transition is commonly used for the derivation of T_{rot} .

Fig. 3 shows the nightly mean OH(3-1) temperatures recorded from the Environmental Research Station "Schneefernerhaus" (UFS) between October 2008 and February 2021. One important characteristic of the temperatures at these heights is that they are higher in winter than in summer. At first glance, this is unexpected, since the primary solar energy input is greater in

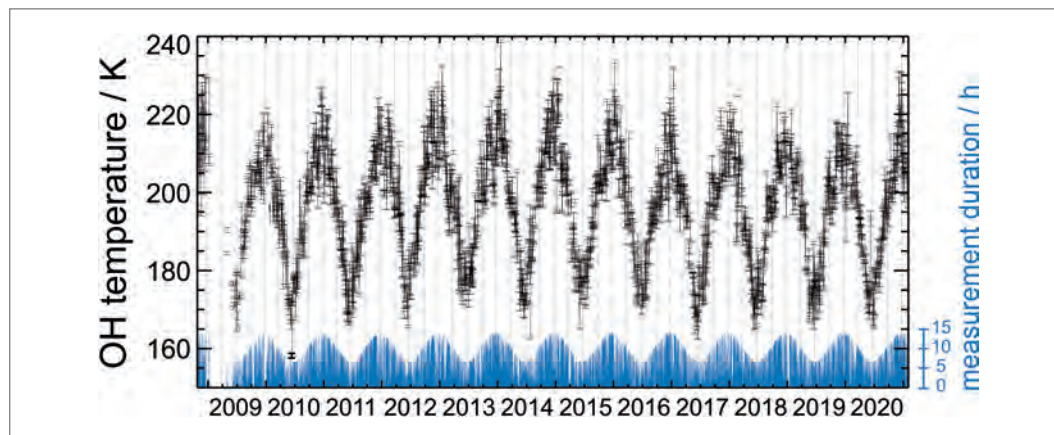


Fig. 3: The nightly mean OH temperatures above the Environmental Research Station "Schneefernerhaus" (black). The blue area denotes the effective observation time, the dashed vertical lines indicate equinoxes and solstices.

summer than in winter. For a long time this behavior was not well understood and airglow observations contributed a lot to the better understanding. Essentially, there is a meridional circulation from the summer pole to the winter pole. Vertical transport processes (summer pole: upward, winter pole: downward) then lead to the observed temperature features (due to adiabatic cooling/heating).

The formation of such a meridional circulation is not trivial, as in principle meridional atmospheric flows are supposed to be forced into a latitudinal flow by the Coriolis force. It is due to the so-called gravity waves, which propagate from lower to greater atmospheric heights and begin to break at heights above 70 km, depositing their momentum into the mean flow. Their breaking disturbs the balance between Coriolis force and pressure gradient (between lower and higher latitudes) and ultimately the so-called “residual” meridional circulation emerges. Wüst gives a more detailed description of gravity waves in chapter 20 of this book.

A closer inspection of Fig. 3 reveals a considerable amount of day-to-day variability in the temperatures. This variability is not due to noise as one might think at first, but rather it is mainly due to so-called planetary waves. These are large scale wave motions in the background flow. They exhibit wavelengths of several thousands of kilometers. As ground-based airglow observations are performed at a fixed location, these large scale waves show up as prominent temperature oscillations with periods from quasi two days to approximately three weeks. A detailed discussion of planetary waves is presented by Küchelbacher and Bittner in chapter 10 of this book.

14.2 Airglow observations at the Environmental Research Station “Schneefernerhaus”

All measurement techniques used to observe the airglow necessarily require optical instrumentation. However, there are several different measurement approaches, which can either be categorized by the parameter addressed (airglow intensity and/or related temperature) or by technical conversion as a single-point- or as a two-dimensional (imaging) observation. While temperature observations are usually performed with (single-point) spectroscopic or interferometric systems, intensity recordings are done with imagers (cameras) yielding two-dimensional information. The overall purpose of airglow observations is to study atmospheric dynamics on all time scales from mere seconds (e.g. infrasound) over minutes, hours (gravity waves and solar tides) and days (planetary waves) up to decadal changes, induced by climate change or solar forcing.

As was mentioned above, airglow features can be observed from the visible wavelength range up to well beyond 4 μm in the infrared spectral range. Certain spectral regions are favored for ground-based observation of those nightglow emissions distributed over a larger range. One lies in the visible range around 730 nm for the observation of OH(8-3), one around 860 nm for simultaneous observation of the OH(6-2) and O₂b(0-1) transitions and one between 1.5 μm and 1.7 μm for the observation of the bright OH(3-1) and OH(4-2)-bands, as well as sometimes O₂a(0-0) at 1.27 μm . Although intensities in the shorter wavelength region are lower, these transitions can be recorded with (common high-grade) silicon-based detectors or photomultipliers, which may even be sensitive enough to detect individual photons. But in the infrared spectral range beyond 1 μm rather sophisticated detectors based on Germanium, InGaAs (indium gallium arsenide) or MCT (mercury cadmium telluride) are required.

The Schneefernerhaus provides a unique place for observing the airglow. Being an alpine station it is practically in the middle of a “birthplace” of atmospheric gravity waves: the mountains serve as an obstacle to horizontal flows, forcing an uplift of air masses. Depending on the vertical temperature gradient, this vertical uplift can initiate atmospheric gravity waves (with buoyancy acting as the restoring force). Many of these waves can propagate all the way up into the mesosphere, where they start to break above 70 km height. In addition, the isolated place and altitude of 2650 m put the UFS above the atmospheric boundary layer, providing a better view through the clear air and less light pollution by big cities.

For this reason, the first airglow spectrometer installed at the UFS, GRIPS 3 (Ground-based Infrared P-branch Spectrometer) was deployed in 2005. At the beginning of the 2000s sensitive OH airglow spectrometers operated in the short-wave infrared, such as GRIPS 3, still relied on very deep cooling of their Germanium photodiodes, only possible with liquid nitrogen. So the

UFS with its nitrogen liquefying facility also provided yet another technical advantage for airglow studies. Fig. 4a shows a photograph of GRIPS 3 with a 120-l storage tank of liquid nitrogen attached to the spectrometer.

However, with a temporal resolution of three minutes and its bulky design requiring high maintenance efforts, a complete redesign of the instrument started in 2006. It resulted in a new generation of GRIPS instruments, starting with GRIPS 5. This prototype was operated for the first time in October 2008 and laid the foundation for a revolution in airglow spectroscopy. Today this type of instrument represents the most common type of airglow spectrometers in the global airglow community. It consists of a linear photodiode array with 512 pixels, placed behind a Czerny-Turner spectrograph in crossed-beam configuration. The photodiode array is thermoelectrically cooled down to $-60\text{ }^{\circ}\text{C}$. It acquires one spectrum between $1.5\text{ }\mu\text{m}$ and $1.6\text{ }\mu\text{m}$ every 15 seconds. Fig. 4b shows the GRIPS 8, being in operation at the UFS since 2010. An extensive overview of the new GRIPS design is given by Schmidt et al. (2013) and Schmidt (2016).

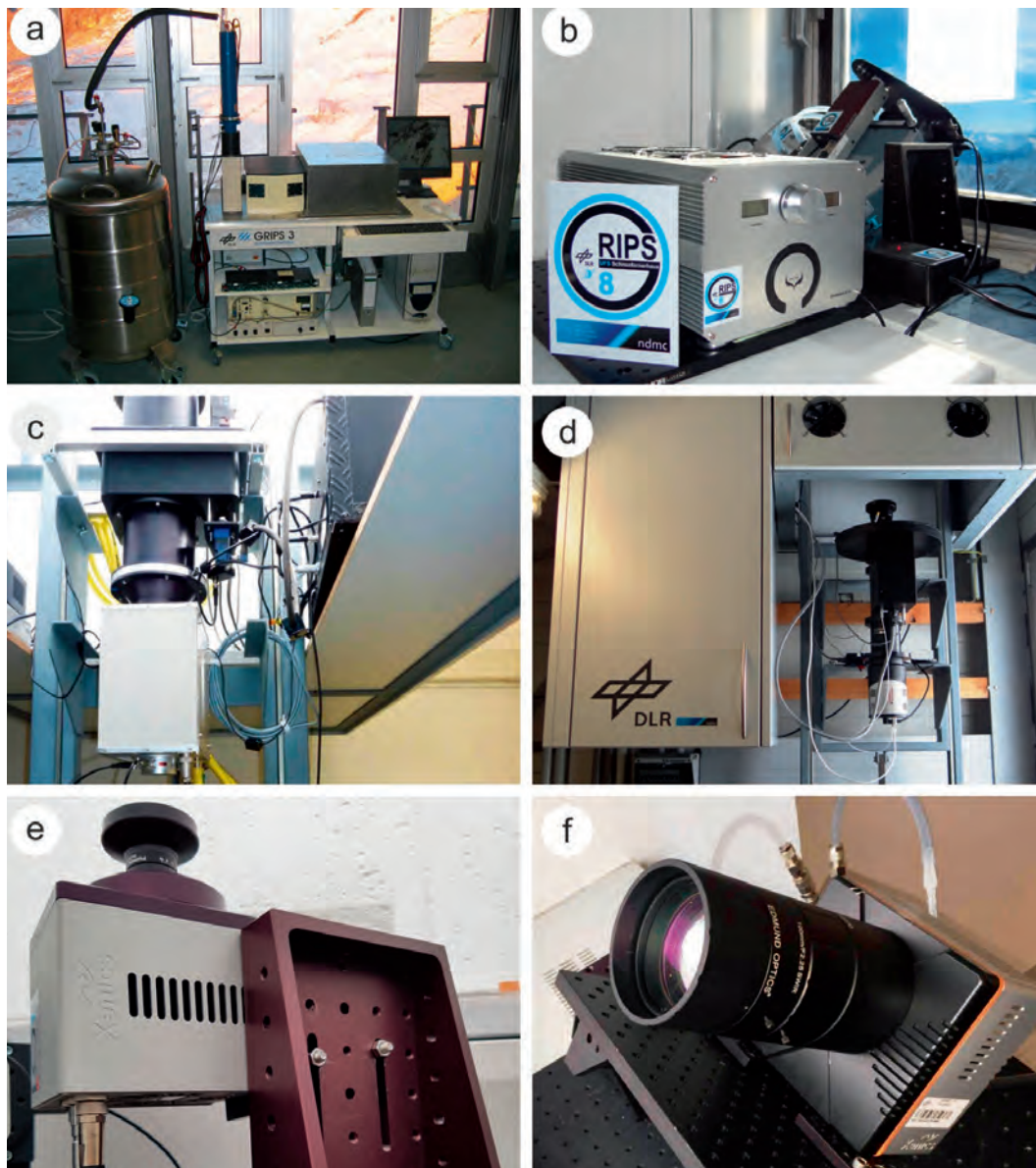


Fig. 4: Different airglow instruments; (a) the first airglow spectrometer GRIPS 3 at the UFS, in operation from 2005 until 2009; (b) the newly developed, compact GRIPS spectrometers in operation at the UFS since 2008; (c) the highly sensitive TANGOO instrument performed observations in a different spectral region for a time limited campaign in 2014/2015; (d) BAIER, Bavaria's first airglow imager, installed on top of the 9th floor acquires all-sky airglow images since 2012; (e) the newly developed FAIM 4 is significantly smaller and its temporal resolution has improved by an order of magnitude; (f) unlike the other imagers FAIM 3 does not observe in all-sky mode, but with a narrow aperture, allowing studies of small scale features (e.g. turbulent processes).

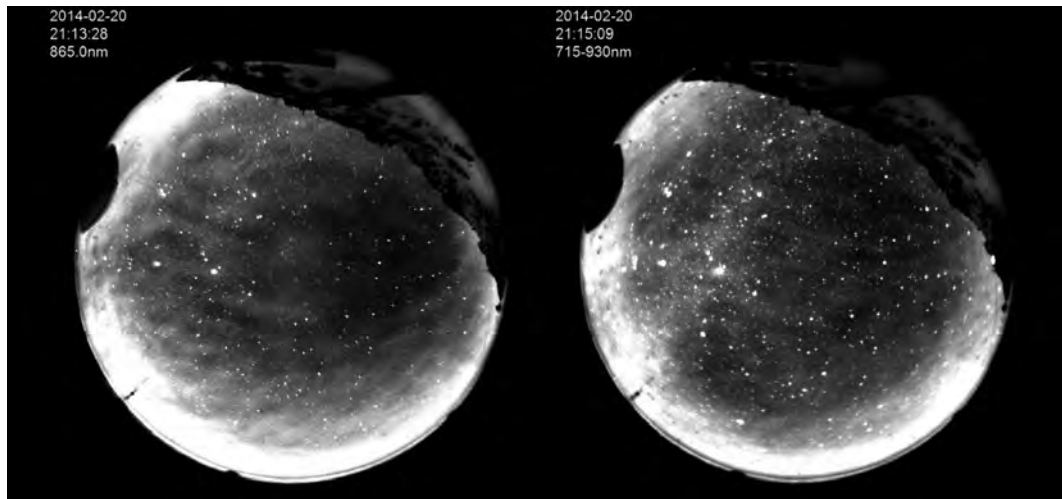


Fig. 5: All-sky images acquired with the BAIER instrument in two different spectral regions. The left panel ($865.0 \text{ nm} \pm 5 \text{ nm}$) shows O_2 emissions from 94 km and the right image depicts OH emissions between 715 nm and 930 nm, originating at approximately 87 km altitude. The patchy structures are actually wave-induced disturbances of the airglow emissions and show the dynamics at the respective airglow layer altitudes. The bright spots in the background are stars and the bright band from the lower left (near the antenna) to the top is the Milky Way, the summit of Zugspitze is at the right side of the images (top = north, right = east).

Due to the unique location, the observations performed at the UFS are of such importance that today they are performed with a twin system (GRIPS 7 and GRIPS 8). The temporal coverage of the observations amounts to approximately 80 percent, since this setup achieved full operability in September 2010. This means that for 80 percent of all nights a mean airglow temperature could be derived (compare Fig. 3). The remaining 20 percent are mainly lost due to unfortunate weather conditions (e. g., dense cloud coverage).

In addition to GRIPS, another sensitive spectrometer aimed at the simultaneous observation of OH and O_2 emission was developed and performed a time-limited observation campaign at the UFS from May 2014 until April 2015. This “Tilting-filter spectrometer for Atmospheric Nocturnal Ground-based Oxygen & hydrOxyl emission measurements” (TANGOO) is equipped with a highly sensitive photomultiplier operated in photon counting mode (see Fig. 4c). It observes the OH(6-2) and $\text{O}_2b(0-1)$ between 839 nm and 867 nm and allows for the derivation of rotational temperatures from both emissions or heights, respectively.

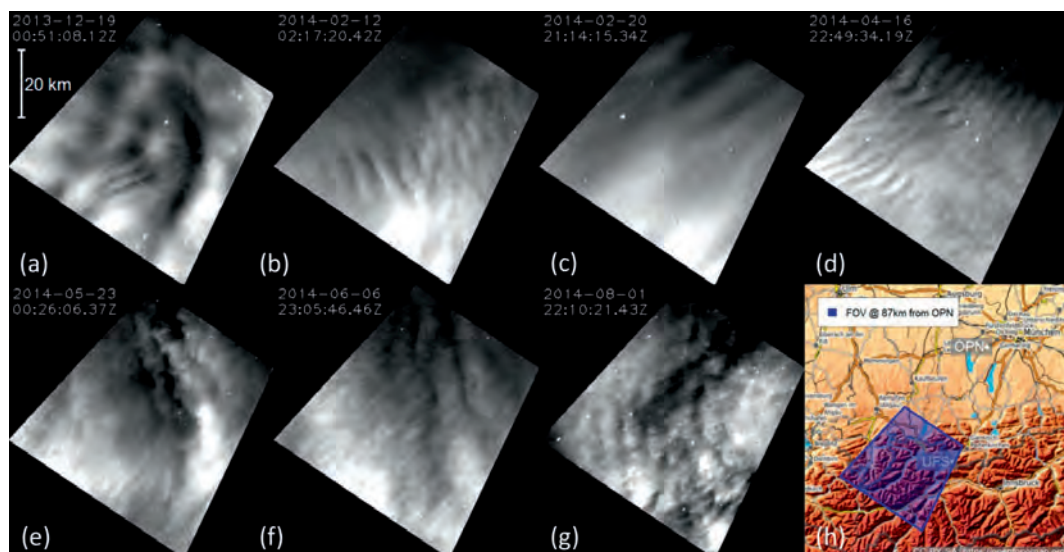


Fig. 6: OH images acquired with the FAIM 1 system in the spectral range between 850 nm to 1600 nm. In this setup the temporal (spatial) resolution is thirty (five) times higher than the resolution of BAIER, but it does not cover the entire sky. Panel (h) shows the geographical location of the field of view, based on the mean emission height of 87 km; panel (c) was acquired simultaneously with the BAIER all-sky images shown in Fig. 5 (map credit: <https://opentopomap.org>, license CC-BY-SA).

Although they provide airglow temperatures, spectroscopic observations are only single-point measurements and so the insight into wave motions is limited by the fact that the horizontal structures of waves cannot be resolved. Since December 2012 the observations are therefore complemented by the Bavarian Airglow ImagER (BAIER) shown in Fig. 4d. This instrument utilizes a high-performance, silicon-based camera system, sensitive in the spectral range from the visible to the near infrared up until approximately $1\ \mu\text{m}$ wavelength. It is capable of successively capturing all airglow emissions mentioned in section 1 by means of a filter wheel with six positions. These interference filters have narrow band passes of $589.0\ \text{nm} \pm 1\ \text{nm}$ for the observation of the yellow sodium lines, $557.7\ \text{nm} \pm 1\ \text{nm}$ and $630.0\ \text{nm} \pm 1\ \text{nm}$ for the green and red atomic oxygen lines, $572\ \text{nm} \pm 1\ \text{nm}$ for a background reference as well as two broader band passes of $865\ \text{nm} \pm 5\ \text{nm}$ for the observation of molecular oxygen emissions and $715\ \text{nm}$ to $930\ \text{nm}$ (with a notch at $865\ \text{nm} \pm 5\ \text{nm}$) for the observation of OH airglow.

Usually, only the latter two are addressed during routine observations, providing information on the horizontal structures of gravity waves in the respective heights of ca. $87\ \text{km}$ and $94\ \text{km}$ every two minutes (15 s exposure for OH and 90 s exposure for the fainter O_2). The (exchangeable) standard optics consists of a fisheye lens with 180° aperture angle, providing images of the entire sky: BAIER belongs to a type of so-called all-sky imagers. Fig. 5 shows two exemplary images of the O_2 and OH airglow acquired with BAIER. At both heights the patchy structures are caused by atmospheric gravity waves disturbing the emission intensity. However, the patterns are deviating slightly between the two images, indicating that the waves have already undergone changes between $87\ \text{km}$ (OH) and $94\ \text{km}$ (O_2).

While all-sky imagers can provide important information about the structures of propagating waves (e.g., wave amplitude, horizontal wavelength and propagation direction) across a huge portion of the sky, their spatio-temporal resolution is usually not high enough to gain detailed insight into the important process of wave breaking.

So in 2013 the development of a new type of infrared imager was started. This system, called Fast Airglow IMager (FAIM), is based on the experience with the new GRIPS, but unlike GRIPS (equipped with a linear InGaAs-photodiode array) it uses one of the first commercially available Peltier-cooled two-dimensional InGaAs-photodiode arrays. It is one of the few imaging systems worldwide, which can now observe the OH airglow in the spectral range of approximately $850\ \text{nm}$ to $1600\ \text{nm}$, the spectral region where the OH emissions are orders of magnitude brighter than in the visible or near infrared (see Fig. 2). This allows for a significant increase in both spatial and temporal resolution. Important details concerning the FAIM setup are given by Hannawald et al. (2016) and Sedlak et al. (2016).

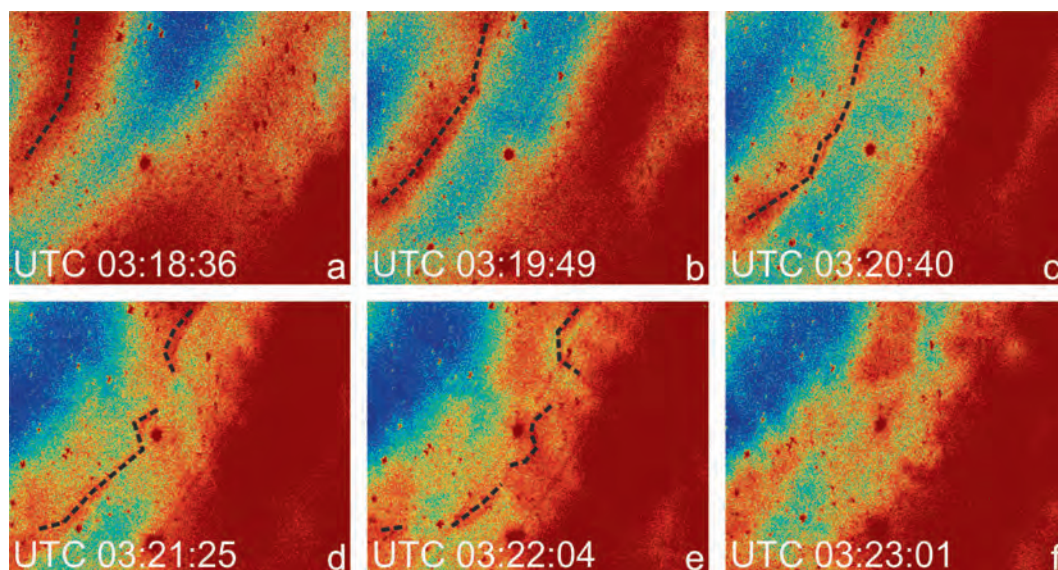


Fig. 7: False color images of high-resolution FAIM data showing the decay of a gravity wave front (dashed line) in OH airglow and its dissipation into turbulent structures; the horizontal scales of the images correspond to approximately $11\ \text{km}$ times $9\ \text{km}$ at $87\ \text{km}$ height.

During the development phase, FAIM 1 was first operated from Oberpfaffenhofen (OPN: 48.09°N, 11.28°E), approximately 70 km north of the Schneefernerhaus. In order to be able to observe wave motions above the Alps it was pointing Southwest with a zenith angle of 45°. Thus, its field of view in the mesopause region, in the nominal OH emission height of 87 km, was lying above the UFS. Thanks to its high spatial resolution of 200 m/pixel rather small scale structures are observable (compare panels 6 (a) to 6 (g)). The structure shown in Fig. 6 (d) exhibits a wavelength of only 3 km. These scales are hardly accessible for all-sky imagers, such as BAIER, which achieves a resolution of approximately 1 km in zenith direction. The appearance of wave events can vary from rather faint structures or show little contrast (e.g., Fig. 6 (c), acquired simultaneously with the BAIER images shown in Fig. 5) to clearly contoured patterns (shown in panels 6 (a), (e) and (g)). The patchy event in Fig. 6 (a) represents a typical example of several waves superimposing each other. An overview with comprehensive statistical results obtained from these FAIM observations can be found in Hannawald et al. (2019).

With a temporal resolution of up to 0.5 s, the FAIM instruments can now be used to study transient processes such as wave instabilities as well as their dissipation into turbulent structures (see the case study by Sedlak et al. (2016)). Fig. 7 shows one such case, utilizing false colors to enhance the contrast (red/blue corresponding to bright/dark regions). A gravity wave front enters the field of view at the upper left corner around 03:18 UTC and propagates further to the lower right corner. In less than five minutes the initially well-defined wave front (7a and 7b) breaks up and has completely dissolved into ‘granular’ structures at 03:23 UTC. During this process the wave deposits both, its momentum and its energy into the background mean flow. Details of the processes involved in wave dissipation are the focus of current research activities, because they are crucial for the understanding of the energy balance of the middle atmosphere and its long-term evolution.

14.3 Schneefernerhaus airglow observations in the global context

Long-term observations of OH temperatures are commonly used to study changes in the atmosphere and to quantify temperature changes at these heights. Routine observations of airglow intensities and rotational temperatures are performed since at least the late 1960s (e.g. Shefov (1969)). Unfortunately, a lot of the longer time series are subject to extensive data gaps and/or changes in instrumentation, consequently resulting in some criticism. Published results of, e.g., long-term trend estimates derived from OH rotational temperatures range from -10.8 ± 1.5 K/decade at 23°S over near zero trend at 51°N to $+3 \pm 2$ K/decade at 56.9°N (Clemesha et al. (2005), Bittner et al. (2002), Espy and Stegman (2002)).

Especially, these ambiguous long-term trend estimates for Mesosphere-Lower-Thermosphere (MLT)-region temperatures derived from airglow observations resulted in the foundation of the Network for the Detection of Mesospheric Change – NDMC in the year 2007. Since one of NDMC’s primary objectives is the identification and quantification of climate changes in the mesopause region, a major topic is the harmonization of measurement techniques as well as analysis methodologies and quality assurance efforts.

An overview of the European part of the NDMC observation sites is presented in Fig. 8. Obviously, the observations performed at the UFS play a prominent role: not only is the Schneefernerhaus placed in the Alps, a key site for the generation of gravity waves, but it is also more or less located in the centre of the European NDMC observations. Consequently, airglow observations at UFS are continuously being improved in order to further establish the UFS as NDMC’s reference station.

Currently, two major objectives are being pursued: the first objective is to increase precision and accuracy of the observations by providing traceability to national standards (hosted by the Physikalisch-Technische Bundesanstalt (PTB)). Elaborate calibrations and intercomparison campaigns were performed in 2016, 2017 and from 2018 until 2021. The respective measurements are currently thoroughly evaluated. A sophisticated redesign of GRIPS 13 was performed in close collaboration with PTB from 2014 to 2017, which resulted in a further improved version of GRIPS concerning not only its signal-to-noise ratio but also other important criteria, e.g. the



Fig. 8: European part of the NDMC network. Blue triangles denote stations, which are equipped with a standard GRIPS and/or FAIM instrument (as shown in Fig. 4 (b), (e), (f) for the UFS); red triangles show stations which in addition to a GRIPS or FAIM also host other independent instrumentation aimed at observations in the mesosphere; grey triangles denote stations with different airglow instrumentation; stations with temporary observations are marked by open triangles (background image credit: NASA Earth Observatory, excerpt from blue marble next generation (August), Reto Stöckli).

long-term stability and repeatability of the observations. While respective upgrades of the instruments GRIPS 6, GRIPS 7 and GRIPS 8 (OPN, UFS) will be installed soon, the prototype GRIPS 13 is becoming the mobile reference spectrometer of the entire NDMC. A respective calibration schedule is currently being developed with the GRIPS 13 first improving the calibration of the stations UFS and OPN, before it will successively travel to the other NDMC sites improving the calibration status of and providing traceability to the entire network.

The second objective concerns the density of the observations in the Alps. In order to gain further knowledge about the generation, propagation and dissipation of mountain-induced gravity waves, more sites in or near the Alps have been set up in recent years (e. g., at Sonnblick Observatory (SBO: 47.05°N, 12.95°E) in 2015 and Otlica Observatory (OTL: 45.93°N, 13.91°E) in 2017). Another site supposed to deliver comparative data at a certain distance from the Alps was put in operation in the Czech Republic in 2018 (Panská Ves (PAN: 50.53°N, 14.57°E)). Fig. 9 shows a close-up of the geographical positions of airglow observations above and around the Alps. The current layout permits studying airglow dynamics from the Observatoire de Haute-Provence (OHP: 44.69°N, 5.25°E), France in the West to Otlica Observatory (45.93°N, 13.91°E), Slovenia in the East. All these sites are associated with the Virtual Alpine Observatory (VAO) founded in 2012 and share their data with scientists across other disciplines via the Alpine Environmental Data Analysis Center (AlpEnDAC).

Fig. 10 represents one of the first events, which clearly shows the propagation of a wave from the Northwest (OPN, OHP: red/grey) to the South (UFS, black). Temperature amplitudes of 15 K to 20 K reached above the UFS are quite remarkable. The lower panel shows the variation of

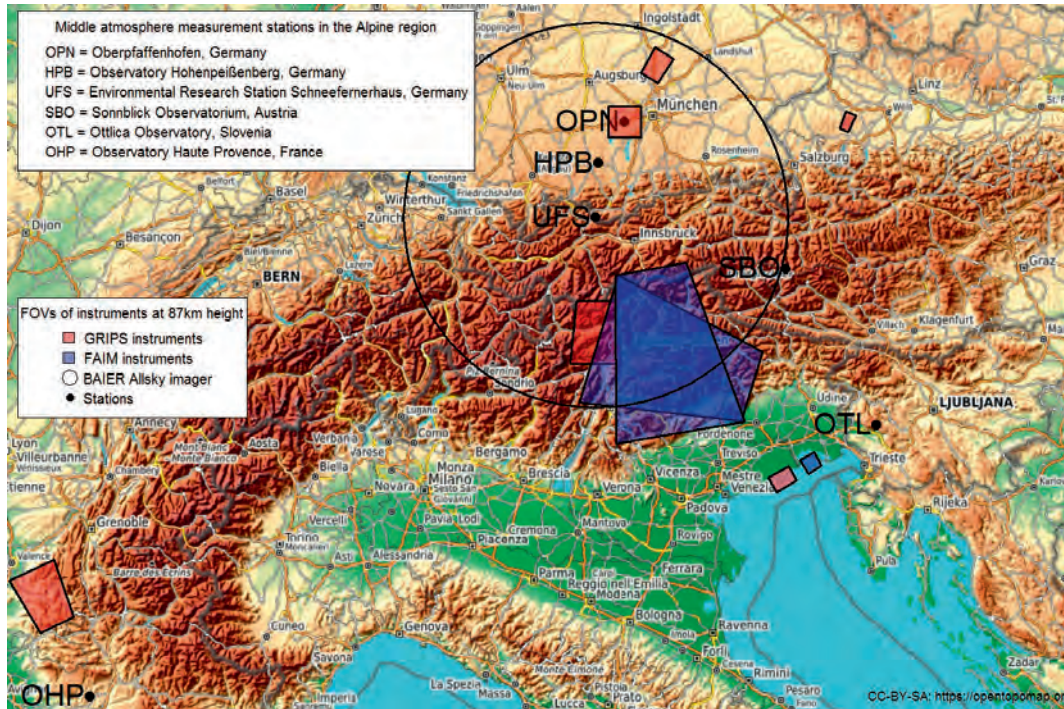


Fig. 9: Alpine observatories which are equipped with airglow instrumentation and their respective fields of view in the Mesopause region (state: 2018). The red areas show locations of spectrometric observations, the blue areas show areas observed with imagers, the large circle denotes the area, which is effectively observed by the BAIER all-sky imager from the UFS. FAIM 1 (OTL) and FAIM 4 (OPN) target the same area, thus allowing the study of dynamical features under different viewing geometries, so-called stereoscopic imaging (map credit: <https://opentopomap.org>, license CC-BY-SA).

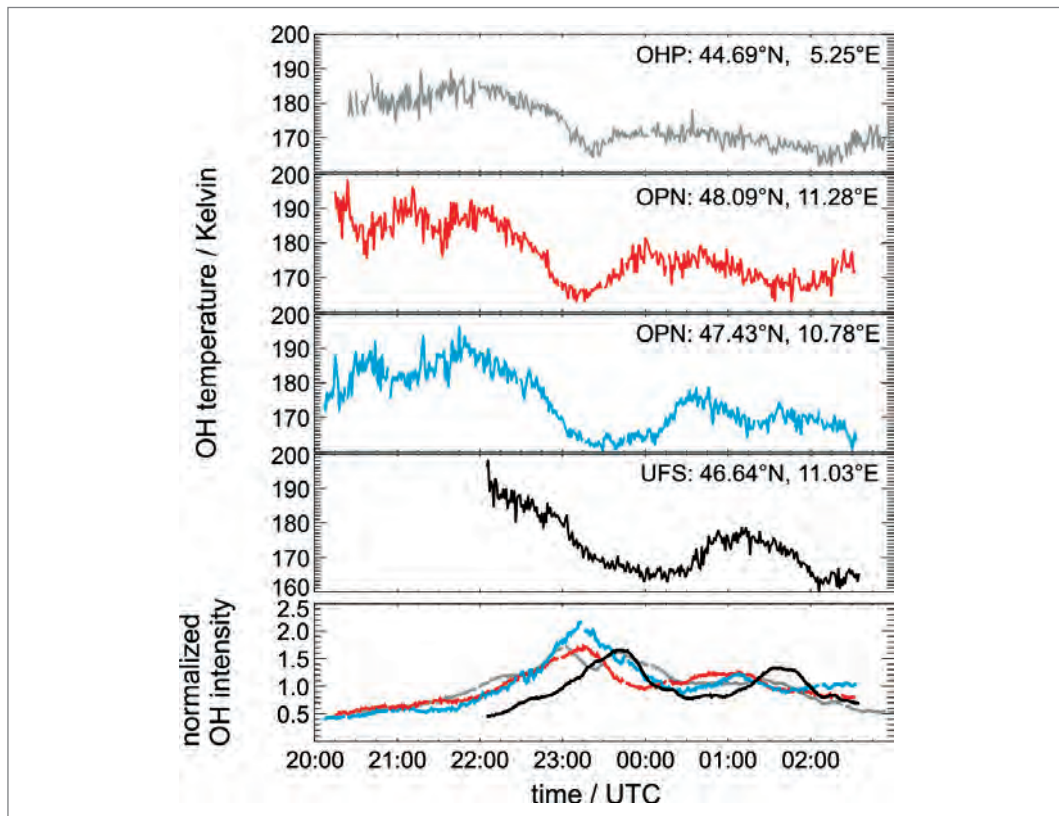


Fig. 10: Simultaneous airglow observations performed from June 24th to 25th, 2015, at the sites shown in Fig. 9 (note: the third panel shows data from an additional instrument located at OPN which pointed to SSW direction). The upper four panels show OH temperatures, the lower panel shows the evolution of the respective airglow intensities. A gravity wave moves southeastwards across the Alps.

airglow intensity for all four stations: clearly the oscillation observed from the UFS lags the other stations by more than half an hour. It is expected that such events will be studied more often and in greater detail with the data contributed by the new observing sites as well as new analysis approaches (see Sedlak et al. (2020), Schmidt et al. (2018), Wüst et al. (2016)).

The geographical distance of a few hundred kilometres between the individual observing sites is perfectly suited for setting up a measurement scheme, called stereoscopic imaging. In this setup two camera systems point at the same region of the sky, thus viewing the airglow under different angles, allowing for the retrieval of additional (vertical) wave parameters. The first camera system (FAIM 1) of the respective setup was installed at Otlica Observatory in October 2017 and it is joined by the second system (FAIM 4) in January 2018. Their fields of view meet above the Alps overlapping with the GRIPS field of view, which delivers additional temperature data for the same region (see Fig. 9).

Thus, ever new and important data on airglow variability are acquired on all time scales from a few seconds to decadal changes at the Schneefernerhaus and related stations in the Alps.

References

- Baker, D.J. and A.T. Stair, Jr., 1988. Rocket measurements of the altitude distributions of the hydroxyl airglow. *Physica Scripta*, 37, 611–622, <https://doi.org/10.1088/0031-8949/37/4/021>.
- Bates, D.R. and M. Nicolet, 1950. The Photochemistry of Atmospheric Water Vapor. *Journal of Geophysical Research*, 55, 301–327, <https://doi.org/10.1029/JZ055i003p00301>.
- Bittner, M., Offermann, D., Graef, H.-H., Donner, M. and K. Hamilton, K. 2002. An 18-year time series of OH rotational temperatures and middle atmosphere decadal variations. *Journal of Atmospheric and Solar-Terrestrial Physics* 64, 1147–1166, [https://doi.org/10.1016/S1364-6826\(02\)00065-2](https://doi.org/10.1016/S1364-6826(02)00065-2).
- Chapman, S., 1939. Notes on Atmospheric Sodium. *Astrophysical Journal*, 90, 390, <https://doi.org/10.1086/144109>.
- Clemesha, B., H. Takahashi, D. Simonich, D. Gobbi and P. Batista, 2005. Experimental evidence for solar cycle and long-term change in the low-latitude MLT region. *Journal of Atmospheric and Solar-Terrestrial Physics* 67, 191–196, <https://doi.org/10.1016/j.jastp.2004.07.027>.
- Espy, P.J. and J. Stegman, 2002. Trends and variability of mesospheric temperature at high-latitudes. *Physics and Chemistry of the Earth* 27, 543–553, [https://doi.org/10.1016/S1474-7065\(02\)00036-0](https://doi.org/10.1016/S1474-7065(02)00036-0).
- Hannawald, P., Schmidt, C., Wüst, S. and M. Bittner, 2016. A fast SWIR imager for observations of transient features in OH airglow. *Atmos. Meas. Tech.* 9 (4), 1461–1472, <https://doi.org/10.5194/amt-9-1461-2016>.
- Hannawald, P., Schmidt, C., Sedlak, R., Wüst, S. and M. Bittner, 2019. Seasonal and intra-diurnal variability of small-scale gravity waves in OH airglow at two Alpine stations. *Atmospheric Measurement Techniques* 12(1), 457–469, <https://doi.org/10.5194/amt-12-457-2019>.
- Jones, A., Noll, S., Kausch, W., Szyszka, C. and S. Kimeswenger, 2013. An advanced scattered moonlight model for Cerro Paranal. *Astronomy & Astrophysics*, 560, A91, <https://doi.org/10.1051/0004-6361/201322433>.
- Marsh, D.R., Smith, A.K., Mlynczak, M. G. and J.M. Russell III, 2006. SABER observations of the OH Meinel airglow variability near the mesopause. *Journal of Geophysical Research*, 111, A10S05, <https://doi.org/10.1029/2005JA011451>.
- Noll, S., Kausch, W., Barden, M., Jones, A. M., Szyszka, C., Kimeswenger, S. and J. Vinther, 2012. An atmospheric radiation model for Cerro Paranal-I. The optical spectral range. *Astronomy & Astrophysics*, 543, A92, <https://doi.org/10.1051/0004-6361/201219040>.
- Noll, S., Kausch, W., Kimeswenger, S., Barden, M., Jones, A. M., Modigliani, A., Szyszka, C. and J. Taylor, 2014. Skycorr: A general tool for spectroscopic sky subtraction. *Astronomy & Astrophysics*, 567, A25, <https://doi.org/10.1051/0004-6361/201423908>.
- Noll, S., Kimeswenger, S., Proxauf, B., Unterguggenberger, S., Kausch, W. and A. M. Jones, 2017. 15 years of VLT/UVES OH intensities and temperatures in comparison with TIMED/SABER data. *Journal of Atmospheric and Solar-Terrestrial Physics*, 163, 54–69, <https://doi.org/10.1016/j.jastp.2017.05.012>.
- Plane, J.M. C., Saiz-Lopez, A., Allan, B. J., Ashworth, S. H., and P. Jenniskens, 2007. Variability of the mesospheric nightglow during the 2002 Leonid storms. *Advances in Space Research*, 39, 562–566, <https://doi.org/10.1016/j.asr.2006.06.009>.
- Schmidt, C., 2016. Entwicklung eines bodengebundenen Infrarotspektrometers für die zeitlich hochaufgelöste Beobachtung des OH-Leuchtens aus der Mesopausenregion. Dissertation, Augsburg University. ISSN1434-8454, ISRN DLR-FB--2016-49, <https://elib.dlr.de/108415/>.
- Schmidt, C., K. Höppner, and M. Bittner, 2013. A ground-based spectrometer equipped with an InGaAs array for routine observations of OH(3-1) rotational temperatures in the mesopause region. *J. Atmos. Sol. Terr. Phys.* 102, 125–139, <https://doi.org/10.1016/j.jastp.2013.05.001>.

- Schmidt, C., Dunker, T., Lichtenstern, S., Scheer, J., Wüst, S., Hoppe, U.P. and M. Bittner, 2018. Derivation of vertical wavelengths of gravity waves in the MLT-region from multispectral airglow observations. *Journal of Atmospheric and Solar-Terrestrial Physics* 173, 119–127, <https://doi.org/10.1016/j.jastp.2018.03.002>.
- Sedlak, R., Hannawald, P., Schmidt, C., Wüst, S. and M. Bittner, 2016. High-resolution observations of small-scale gravity waves and turbulence features in the OH airglow layer. *Atmos. Meas. Tech.* 9 (12), 5955–5963, <https://doi.org/10.5194/amt-9-5955-2016>.
- Sedlak, R., Zuhr, A., Schmidt, C., Wüst, S., Bittner, M., Didebulidze, G.G. and C. Price, 2020. Intra-annual variations of spectrally resolved gravity wave activity in the upper mesosphere/lower thermosphere (UMLT) region. *Atmospheric Measurement Techniques*, 13(9), 5117–5128, <https://doi.org/10.5194/amt-13-5117-2020>.
- Shefov, N.N., 1969. Hydroxyl emission of the upper atmosphere—I. The behaviour during a solar cycle, seasons and geomagnetic disturbances. *Planetary and Space Science*, Vol. 17, No. 15, pp. 797–813, [https://doi.org/10.1016/0032-0633\(69\)90089-0](https://doi.org/10.1016/0032-0633(69)90089-0).
- von Savigny, C., 2015. Variability of OH(3–1) emission altitude from 2003 to 2011: Long-term stability and universality of the emission rate-altitude relationship. *Journal of Atmospheric and Solar-Terrestrial Physics* 155, 120–128, <https://doi.org/10.1016/j.jastp.2015.02.001>.
- Wüst, S., Bittner, M., Yee, J.-H., Mlynczak, M. G., and J. M. Russell III, 2020. Variability of the Brunt–Väisälä frequency at the OH*-airglow layer height at low and midlatitudes, *Atmos. Meas. Tech.* 13, 6067–6093, <https://doi.org/10.5194/amt-13-6067-2020>.
- Wüst, S., Schmidt, C., Bittner, M., Silber, I., Price, C., Yee, J.-H., Mlynczak, M. G. and J. M. Russell III, 2017. First ground-based observations of mesopause temperatures above the Eastern-Mediterranean Part II: OH*-climatology and gravity wave activity. *Journal of Atmospheric and Solar-Terrestrial Physics* 155, 104–111, <https://doi.org/10.1016/j.jastp.2017.01.003>.
- Wüst, S., Wendt, V., Schmidt, C., Lichtenstern, S., Bittner, M., Yee, J. H., Mlynczak, M. G. and J. M. Russell III, 2016. Derivation of gravity wave potential energy density from NDMC measurements. *Journal of Atmospheric and Solar-Terrestrial Physics* 138, 32–46, <https://doi.org/10.1016/j.jastp.2015.12.003>.

15 Passive sampling of POP and PAH with virtual organisms in alpine environments

Karl-Werner Schramm^{1,2}, Marchela Pandelova²

15.1 Introduction

Virtual Organisms (VO) are defined as an artificial property-tool, and are reflecting exposomic processes in compartments of real organisms (Schramm et al. 2013). For instance, VO containing fat or proteins such as albumin can be employed to investigate the exposure of chemicals against such compartments which are common for many species in the kingdom of animals. The duration of VO exposure can be well defined and does not depend on the lifetime (Schramm et al. 2013). To estimate ambient concentrations VO are exposed and Performance Reference Compounds (PRC) are in use to estimate the sampling rate of air over time. Qualitatively the VO mainly sequestered gas phase contaminants.

Exposomics is the study of the exposome and is related to genomics, metabonomics, lipidomics, transcriptomics, proteomics, and includes the study of exposures in the environment. Biomarkers of exposure and effect are targeted. The exposome of real organisms is defined as the measure of all the exposures of an individual in a lifetime and how those exposures relate to disease (CDC 2010). However, environmental exposomics has not been tackled so far although the definition can be extended to other organisms than humans. Further, molecular exposomics does not cover all exposomic aspects such as noise, radiation, pathogens but focuses only on the exposure of individuals to molecules or better chemicals and their effects within a lifetime. Individuals other than humans might have also advantages with respect to their observation due to their shorter lifetime or less transient exposure situation. If we look at the kingdom of molecules, resp. chemicals, the exposure to chemicals of transient behavior is difficult to quantify. In contrast, chemicals which are persistent and bioaccumulating are better and easier to investigate in exposomics due to their long lasting presence in compartments of individuals. In some cases the individuals even do not achieve equilibrium between their and environmental compartments during lifetime. Persistent Organic Pollutants (POP) once marketed are expected to remain in the environment and biota for a long time and might peak even years after their use in the following generations of individuals. Due to these POP properties the exposure can be accurately estimated. Thus molecular exposomics is reflecting time dependent exposure and effects of molecules with its intrinsic challenges and perspectives which are outlined besides for humans also for the environment and for VO of exposure sciences (Schramm et al. 2013).

15.2 Lipidome-VO

VO are artificially designed to simulate the specific biological compartment such as fat as a part of the lipidome of an organism. VO reflecting this fatty compartment and especially POP are accumulating to a large extent in fatty tissues as an important part of the long lasting storage compartment of persisting and very Persistent very Bioaccumulative Toxic compounds (vPvBT) of real organism's exposome. VO consists of Polyethylene (PE) lay-flat tubing enclosing a thin film of natural-like trioleine, a high molecular weight (MW = 885 g/mole) natural lipid. VO can develop a biofilm during exposure. Therefore stable isotope labelled Performance Reference Compounds (PRC) are added into the VO-trioleine to compensate environmental conditions at different sampling locations such as turbidity, temperature, biofouling etc. during exposure. PRC losses are then used to calculate the air volume sampled by the VO and thus to calculate the ambient mean concentrations of the PBT.

Several VO are placed in stainless steel container or Stevenson Huts which are usually deployed in air 2–12 weeks.

¹ TUM, Wissenschaftszentrum Weihenstephan für Ernährung und Landnutzung, Department für Biowissenschaften, Weihenstephaner Steig 23, 85350 Freising, Germany, schramm@wzw.tum.de

² Helmholtz Zentrum München (GmbH), Molecular EXposomics (MEX), Ingolstädter Landstr.1, D-85764 Neuherberg, Germany, schramm@helmholtz-muenchen.de

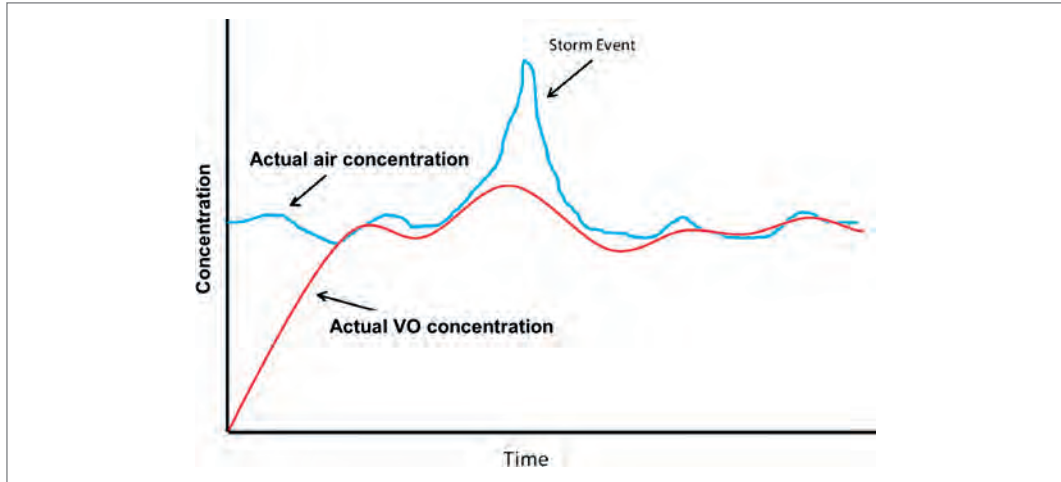


Fig. 1: Schematic representation of accumulation behavior for VO. The actual air concentration is integrated and averaged over time.

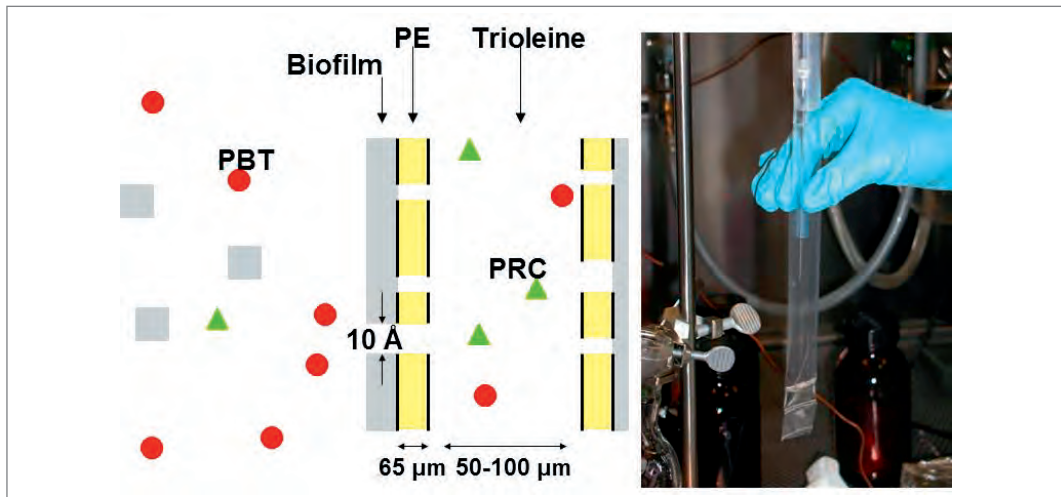


Fig. 2: Schematic representation of the uptake of the chemicals of interest and the elimination of the PRC into the environment as a measure of the air volume sampled by the VO (left). Right: picture of the lay-flat LPDE membrane filled with synthetic triolein similar to natural fat and representing the lipidome.

15.3 VO-theory

15.3.1 Kinetic Model

If the resistance to the mass transfer is controlled by the boundary layer, we can model the system considering the VO device as a one compartment as follows:

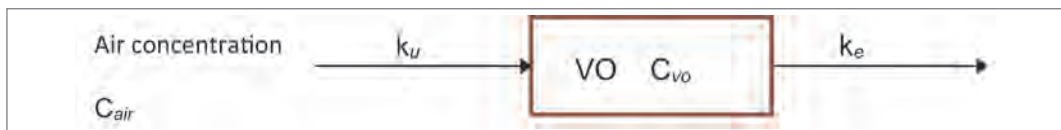


Fig. 3: Schematic representation of one compartment model for VO. C_{air} : compound concentration in air, k_u : uptake rate constant, C_{vo} : compound concentration within the VO, k_e : elimination rate constant.

Applying a mass balance in the VO compartment leads to:

$$\frac{\partial C_{vo}}{\partial t} = k_u C_{air} - k_e C_{vo} \tag{Equation 1}$$

Out of this mass balance, the relation between sampling time t , C_{vo} and C_{air} can be calculated. Regrouping and integrating equation 1 in a span of time t gives:

$$\frac{\partial C_{vo}}{(k_u C_{air} - k_e C_{vo})} = \partial t \Rightarrow \frac{-1}{k_e} \int_0^{c(t)} \frac{\partial C_{vo}}{\left(\frac{-k_u C_{air}}{k_e} + C_{vo}\right)} = \int_0^t \partial t \Rightarrow \text{Ln} \left(\frac{\frac{-k_u C_{air}}{k_e} + C_{vo}(t)}{\frac{-k_u C_{air}}{k_e}} \right) = -k_e t$$

Applying ex and regrouping: results in:

$$C_{vo}(t) = \frac{k_u C_{air}}{k_e} [1 - e^{-k_e t}] \Rightarrow C_{vo}(t) = K_{vo_a} C_{air} [1 - e^{-k_e t}] \quad \text{Equation 2}$$

where K_{vo_a} is the VO-air partition coefficient $\left(K_{vo_a} = \frac{k_u}{k_e}\right)$.

When the VO is still in the linear stage, the amount of compound released from the VO to the air compartment is negligible, thus from equation 1 $k_e C_{vo} \rightarrow 0$

$$\Rightarrow \partial C_{vo} / \partial t \cong k_u C_{air} \quad \text{Equation 3}$$

Integrating this approximation in a span of time t leads to:

$$C_{vo}(t) = k_u C_{air} t \quad \text{Linear uptake stage} \quad \text{Equation 4}$$

When the VO has reached equilibrium conditions, such that the concentrations do not change anymore, equation 1 leads to:

$$\partial C_{vo} / \partial t = 0 \Rightarrow k_u C_{air} = k_e C_{vo} \quad \text{Equation 5}$$

so the compound concentrations in the air and the VO are related through the uptake and elimination rate constants:

$$C_{air} = \frac{C_{vo} k_e}{k_u} = \frac{C_{vo}}{K_{vo_a}} \quad \text{Equilibrium conditions} \quad \text{Equation 6}$$

15.3.2 Mass Transfer Coefficient Model

The mass transfer in the system can be described by means of mass transfer coefficients as follows:

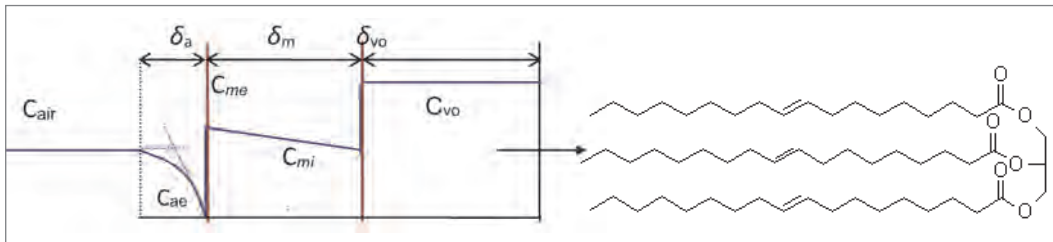


Fig. 4: Schematic overview of the concentration distribution air-VO. C_{air} : compound concentration in air, C_{ae} : compound concentration at the membrane outside boundary layer, C_{me} : compound concentration at the membrane inside boundary layer, C_{mi} : compound concentration at the membrane internal side, C_{vo} : compound concentration in VO, δ : effective thickness of each region and their associated subscripts.

Applying Fick's First law and assuming concentration homogeneity within the device, the flux F generated is

$$F = -DA \frac{\partial C}{\partial \delta}, \quad \text{Equation 7}$$

where D is the diffusivity of the compound and A is the sectional area where the compound is transferred (membrane surface area). Substituting the mass transfer coefficients $k_m = D_m / \delta_m$ and $k_a = D_a / \delta_a$ in the equation:

$$F = k_m A_{vo} (C_{me} - C_{mi}) = k_a A_{vo} (C_{air} - C_{ae}) = V_{vo} \frac{\partial C_{vo}}{\partial t} \quad \text{Equation 8}$$

Using the equilibrium partition coefficients defined as $K_{ms} = C_{mi}/C_{vo}$, $K_{ma} = C_{me}/C_{ae}$ and $K_{vo_a} = C_{vo}/C_{air}$ the equation is re-written as a function of the variables of interest C_{air} and C_{vo} , obtaining:

$$F = k_o A_{vo} (C_{air} K_{ma} - C_{vo} K_{ms}) = V_{vo} \frac{\partial C_{vo}}{\partial t} \quad \text{Equation 9}$$

where k_o is the total mass transfer coefficient:

$$\frac{1}{k_o} = \frac{1}{k_m} + \frac{K_{ma}}{k_a} \quad \text{Equation 10}$$

Assuming independence and additivity of the coefficients and regrouping and integrating the equation 3 we obtain:

$$C_{vo} = C_{air} \frac{K_{ma}}{K_{ms}} (1 - e^{-(k_o A_{vo} K_{ms} t / V_{vo})}) = C_{air} K_{vo_a} (1 - e^{-k_T t}) \quad \text{Equation 11}$$

In this equation the overall uptake rate constant is defined as $k_T = k_o A_{vo} K_{ms} / V_{vo}$ and K_{vo_a} is substituted by K_{ma} / K_{ms} .

Equation 1 and 5 describe the uptake stages depicted in Fig. 5. In short exposure periods (equation 5), for $t \rightarrow 0$ the limit of the exponential term tends to

$$\lim (1 - e^{-(k_o A_{vo} K_{ms} t / V_{vo})}) \rightarrow k_o A_{vo} K_{ms} t / V_{vo} \quad \text{Equation 12}$$

Substituting this term in equation 5 a linear time-dependent function is obtained:

$$C = C_{air} K_{vo_a} k_o A_{vo} K_{ms} t / V_{vo} = C_{air} K_{ma} k_o A_{vo} t / V_{vo} \quad \text{Equation 13}$$

In this linear stage, the uptake of compounds depends on the design of the device (volume and area) and the physical chemical properties of the chemical. The sampling rate R_s is defined as the volume of compound incorporated by the passive sampler per unit of time:

$$R_{vo} = K_{ma} k_o A_{vo} \quad \text{Equation 14}$$

and substituting equation 14 in equation 13 :

$$C = C_{air} R_{vo} t / V_{vo} \Rightarrow R_{vo} = C_{vo} V_{vo} / C_{air} t \quad \text{Equation 15}$$

In this way, in the linear uptake stage, the sampling rate of a compound can be calculated if the VO and air concentrations of the compound for a determined exposure time are known.

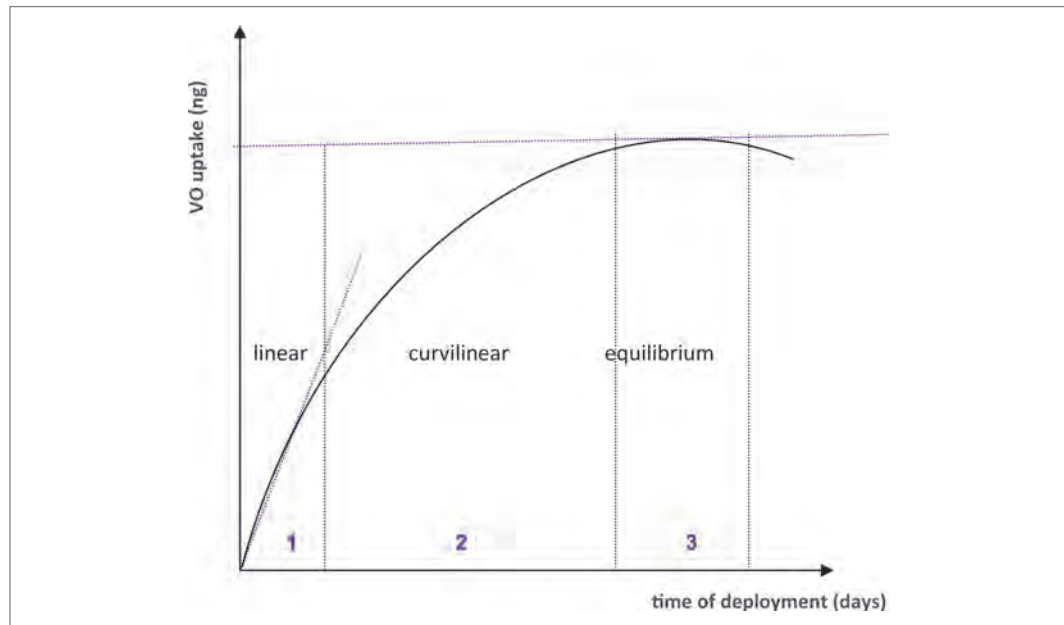


Fig. 5: Schematic overview of the concentration development in VO. If VO concentration is close to zero the accumulation proceeds in a pseudo-linear manner at times close to zero, followed by a curvilinear period and finally approaching constant concentrations at equilibrium with the air, provided that the air concentration remains nearly constant.

For the empirical calculation of sampling rates, $C_{vo}V_{vo}$ is equivalent to the amount of mass N_s sequestered in the VO. Substituting N_{vo} in the equation 15 leads to:

$$R_{vo} = N_{vo}/C_{air}t \quad \text{Equation 16}$$

Once sampling rates for compounds have been established for a determined sampling design using equation 16, these sampling rates can be used to estimate the air concentrations of a compound, from the compound uptake into the VO and the time of deployment.

In devices deployed enough time to reach steady state conditions the exponential term of equation 11 tends to zero and thus:

$$C_{vo} = C_{air}K_{vo_a} \quad \text{equilibrium conditions} \quad \text{Equation 17}$$

In the equilibrium stage the concentrations in air and VO_{fat} (triolein) are related exclusively through the $VO_{fat-air}$ partition coefficient K_{TA} (equation 29).

$$C_{vo_{fat}} = C_{air}K_{TA} \Rightarrow C_{air} = C_{vo_{fat}}/K_{TA} \quad \text{Equation 18}$$

The equation 18 allows the calculation of the compound air concentration just knowing the K_{TA} value and the amount of chemical accumulated in the triolein under steady state conditions.

Note that the two models presented above can be related through the constants; elimination rate constant k_e in the kinetic model (equation 8) and overall uptake rate constant k_T in the mass transfer coefficient model (equation 11).

15.3.3 Performance Reference Compounds

Performance reference compounds (PRC) are non-interfering organic chemicals with medium to high affinity for triolein which are added to it before the membrane enclosure and distributed homogeneously in the lipid phase (Huckins et al., 2002). In preference, PRC have to be compounds not exhibited in the environment and due to this, ^{13}C -PAH or ^{13}C -PCB compounds are adequate. The purpose of these compounds is to compensate the effect of environmental variables at the different sampling sites. The theory is based on the assumption that the elimination rate (k_e) of PRC is related to the uptake rate (k_u) of the corresponding native compounds. The release of PRC follows an exponential decay with the exposure time:

$$\frac{\partial C_{PRC}}{\partial t} = -k_e C_{PRC} \Rightarrow \int_{C_{PRC_0}}^{C_{PRC}} \frac{\partial C_{PRC}}{C_{PRC}} = -k_e \int_0^t \partial t \Rightarrow C_{PRC} = C_{PRC_0} e^{-k_e t} \quad \text{Equation 19}$$

The initial amount of PRC (C_{PRC_0}) and the remaining amount after the exposure time (C_{PRC}) are known, such that the elimination rate can be calculated by regrouping the equation 19:

$$k_e = \frac{\text{Ln}(C_{PRC_0}/C_{PRC})}{t} \quad \text{Equation 20}$$

The elimination rate constant k_e is assumed to be also identical to the overall uptake rate constant k_T in the mass transfer coefficient model for the native and labelled compound leading to:

$$k_e = k_{ma} k_o A_{vo}/V_{vo} K_{vo_a} \Rightarrow k_e = R_{vo}/V_{vo} K_{vo_a} \Rightarrow k_e V_{vo} K_{vo_a} = R_{vo} \quad \text{Equation 21}$$

where R_{vo} was substituted using the equation 14 from the mass transfer model. Equation 21 relates the sampling rate of the compound to the elimination rate obtained "in situ" for a determined compound with the PRC. In this way, the effects generated by differences in the exposure sampling conditions can be contemplated. Studies performed by Söderström and Bergqvist, (2004) with PRC demonstrated the influence of the wind speed in the sampling rate. As a consequence, the devices are sheltered in order to avoid differences due to wind effects affecting the turbulence and as a consequence the air-membrane boundary layer thickness (Ockenden et al., 2001). Additionally, the sheltering is also important to avoid photodegradation of compounds sensible to UV light. Some other environmental conditions, such as temperature, are also affecting the sampling rate. The use of PRC allows the R calculation regarding environmental conditions and even a posterior quantification of compounds in the environment.

15.3.4 VO data calculation

Sixteen 13C-PRC-PAH and three 13C-PRC-PCB retain in VO were used to calculate the sampling rates and polycyclic aromatic hydrocarbons (PAH), polychlorinated biphenyls (PCB) and organochlorine pesticides (OCP) water concentrations (Temoka et al., 2016). According to equation 21, the sampling rate of PRC $R_{vo,PRC}$ is estimated according to

$$R_{vo,PRC} = V_{vo}K_{vo,a}k_{e,PRC} \quad \text{Equation 22}$$

where V_{vo} is the VO volume (L), $K_{vo,a}$ the VO-air partition coefficient is the volume averaged partition coefficient (see below) of low density polyethylene (LPDE) and triolein ((mass/L)/(mass/L)) and $k_{e,PRC}$ is the elimination rate constant of PRCs per day (d^{-1}). Thus, $k_{e,PRC}$ is given by:

$$k_{e,PRC} = -\frac{\ln(N_{t,PRC}/N_{0,PRC})}{t} \quad \text{Equation 23}$$

where $N_{0,PRC}$ is the related PRC fraction at the beginning of the exposure period and $N_{t,PRC}$ is the related PRC fraction after the exposure period (t). For compounds with very low $k_{e,PRC}$ values a minimal sampling rate $R_{vo,min}$ is further established and used as corrector value of $R_{vo,PRC}$ (Temoka et al., 2017).

Subsequently, the obtained R_{vo} value was used to back-calculate the air concentrations (Ca) of the pollutants.

$$C_{air} = \frac{N}{V_{vo}K_{vo,a}(1 - \exp(-R_{vo,t}/V_{vo}K_{vo,a}))} \quad \text{Equation 24}$$

where N is the amount of analyte accumulated after a given exposure time.

However, PCB and OCP sampling rates (R_{vo}) were estimated on the base of resulted correlation coefficient $R^2 > 0.75$ regarding the relation between PRC-PAHs R_{sPRC} and the exponential product of octanol-water partition coefficient $\log K_{ow}$ and molecular weight MW (g/mole).

$$R_{vo,analyte}(N) = a e^{b \text{MW} \log K_{ow}} \quad \text{Equation 25}$$

where a and b are constants for a given exposure situation.

Triolein containing VO were utilized as passive samplers also for the three categories of substances PAH, PCB and OCP in air:

$$K_{VO-A} = \frac{K_{TA}V_T + K_{LPDEA}V_{LPDE}}{V_T + V_{LPDE}} \quad \text{Equation 26}$$

where V_T is the volume of the triolein (cm^3), V_{LPDE} the volume of LPDE (cm^3), K_{TA} is the triolein-air partitioning coefficient ($\text{mass}/\text{m}^3 / (\text{mass}/\text{m}^3)$) and K_{LPDEA} is the LPDE-air partitioning coefficient ($\text{mass}/\text{m}^3 / (\text{mass}/\text{m}^3)$).

$$\log K_{TW} = \log K_{ow} + 0.105 \quad \text{Chiou et al., 1985} \quad \text{Equation 27}$$

and

$$\log K_{LPDEA} = 1.05 \log K_{ow} - 0.59 \quad \text{Booij and Smedes, 2010} \quad \text{Equation 28}$$

$$K_{TA} = \frac{K_{TW}RT}{H} \quad \text{Equation 29}$$

$$K_{LPDEA} = \frac{K_{LPDEW}RT}{H} \quad \text{Equation 30}$$

where K_{ow} is the octanol-water partition coefficient, K_{TW} and K_{LPDEW} are the triolein- and LPDE-water partition coefficients, R is the ideal gas constant ($8.314 \text{ Pa m}^3 \text{ mol}^{-1} \text{ K}^{-1}$), T is the absolute temperature (293 K) and H is the Henry's law constant of the chemicals ($\text{Pa m}^3 \text{ mol}^{-1}$).

Finally, the gas-concentrations were estimated based on the performance of the reference compounds, which were used to estimate their sampling volume of the deployment period (Ockenden et al., 2001). The total concentrations were calculated on the basis of measured or estimated aerosol concentrations and by using $K_{aerosol-gas}$ (Mackay et al., 1986) partitioning followed by summing the gaseous and aerosol part per m^3 .

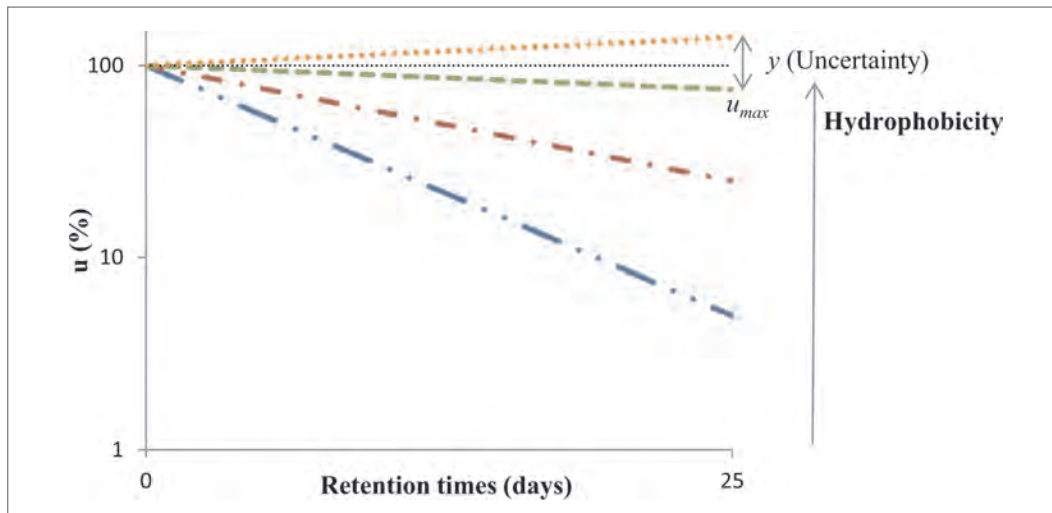


Fig. 6: Scheme representing uncertainty field of dissipated PRC values (u) during exposure times. u_{\max} is the largest possible deviation from the average dissipation \bar{u} of a PRC which does not exhibit significant dissipation after a certain sampling period. u_{\max} can be used to estimate the minimal possible sampling rate for such compounds.

The variability of k_e values can encompass about two orders of magnitude at high K_{oa} levels and within one order of magnitude at lower K_{oa} values. Even after 1 year substantial dissipation for some high K_{oa} compounds could not be determined or is scattering around zero in relation to the analytical precision possible for active as well as passive sampling (Fig. 6). In contrast to other theories the measurements show that at low k_e -values the R_{vo} values are increasing dramatically and are indicating very high R_{vo} and thus very low concentrations in the free gas phase. Therefore it must be concluded that air concentrations estimated for PAH based on a similar VO design and the theories of Huckins et al. can be overestimated by orders of magnitude – especially if the sampling volume of a PRC with dissipation in the 80–20% range is used to calculate gas-phase concentrations of compounds beyond 20%.

Therefore an alternative method, based on the use of all in situ PRC data, including those whose PRC concentration remaining are close to the limit of detection LOD and those whose PRCs are non-depleted. To allow this approach, uncertainties are modelled using PRC data of field blanks never exposed to the environment. The Student- t distribution is used to obtain confidence limits for measurement uncertainty. Replicated VO-field blanks were measured to obtain a standard deviation that could be used directly as the standard analytical uncertainty. The uncertainty values were used to estimate the minimal sample rate R_{\min} . Efforts to reduce bias and variability can be improved by increasing the number of blank samples. R_{\min} was applied as the new values of PRC sampling rate $R_{vo,PRC}(N)$ if a direct measurement was not obtainable.

The VO-field blanks consisted of loaded samplers taken to and from the field with other VOs but never removed from their airtight vials. These blanks were prepared and analyzed simultaneously in the same manner as the deployed samplers to determine whether contamination or losses occurred during the VO loading, transport or analysis. A normal distribution for the results can be assumed, because the PRC concentrations can be well determined in cases of minor or no losses.

For each PRC, the standard deviation was calculated from obtained retained PRC values of the blank samples. The obtained values u_o of blank sample were first normalized in percentage $\%u$ according to the expected values u_w , following this equation (Fig. 6):

$$\%u = \frac{u_o}{u_w} \cdot 100 \quad \text{Equation 32}$$

Then the standard deviation $Sn(\%)$ was obtained by following the equation:

$$Sn(\%) = \sqrt{\frac{\sum_{i=1}^n (\%u_i - \% \bar{u})^2}{n-1}} \quad \text{Equation 33}$$

$\%u_i$ are the obtained values in percent for the blank sample i , \bar{u} is the sample mean of the obtained values and n is the amount of blank samples used for the measurements.

The coefficient of variation CV (%) is calculated as following:

$$CV(\%) = \frac{S_n}{\% \bar{u}} \cdot 100 \quad \text{Equation 34}$$

The standard error S_{CV} of the coefficient of variation is calculated as:

$$S_{CV} = \frac{CV}{\sqrt{2n}} \quad \text{Equation 35}$$

The uncertainty (γ) of the VO-field blanks is then:

$$\gamma = CV + t_{a,v} S_{CV} \quad \text{Equation 36}$$

Where $t_{a,v}$ is the critical value of Student's t for the chosen α level and for $\nu = n - 1$ degrees of freedom. The analysis is based on the best measurement capability. The uncertainty value ($\gamma = CV + t_{a,v} S_{CV}$) is used to obtain the maximal retained PRC concentration after exposure time:

$$u_{\max} = 100 - \gamma, \quad \text{Equation 37}$$

u_{\max} is used to determinate the maximum possible elimination rate ke_{\max} based on analytical uncertainty.

$$ke_{\max} = -\frac{\ln(u_{\max}/u_0)}{t} \quad \text{Equation 38}$$

Thus the minimal expected sampling rate ($R_{s,\min}$) is thereby deduced.

$$R_{VO,\min} = V_{VO} K_{VO_a} ke_{\max} \quad \text{Equation 39}$$

$R_{VO,\min}$ is used to adjust $R_{vo,PRC}$ (Eq.1.3) to $R_{vo,PRC}(N)$. The *in situ* sampling rate of PRC $R_{vo,PRC}(N)$ represents the *in situ* sampling rate of target compound $R_{vo,analyte}(N)$ with similar physicochemical properties.

15.4 Chemicals sampled from the air compartment

PAH, PCB and OCP entering the natural ecosystems are distributed into the solid, liquid, or gaseous phases of environmental compartments. They release into the environment and stay persistent for many years because of their relatively low water solubilities and vapor pressures, and relatively large octanol-water and octanol-air partition coefficients. For instance, the spatial distribution of DDT and metabolites in Germany can clearly be attributed to historic application. Up to the 1980s, technical DDT was extensively used in the former Eastern Germany (GDR) and elevated concentrations are recently detected in wetland soil layers (Berger and Schwarzbauer, 2016). PAH are emitted into the atmosphere by various combustion sources including small wood stoves/boilers for domestic heating (Fernandes and Brooks, 2003; Bari et al., 2010) or released into the aquatic environment through the discharges from human activities such as industrial or domestic sewage effluents. In addition, it is well recognized that these contaminants are widely distributed all over the globe and atmospheric transport and temperature dependent partitioning between the atmosphere and environmental media is a leading pathway for their diffusion (Lohmann et al., 2007; Nizzetto et al., 2010). On the other hand, these persistent organic pollutants deposited in sinks such as water and ice are expected to revolatilize into the atmosphere, and there is evidence that this process may have already begun for volatile compounds (Ma et al., 2011).

Consequently, PAH, PCB and OCP may cause adverse human health effects even far away from their origin. In addition, it must be considered that the organisms may bioconcentrate low to relatively high levels of contaminants in their lipids. In the recent years, VO (Schramm et al., 2013) have been successfully used for determination of POPs in aquatic environment and sediments (Amdany et al., 2014; Temoka et al., 2016) due to their attractive qualities (i.e. their long-term stability, low cost, and ease of deployment). However, there are only limited published

data pertaining to the use of these passive sampling tools for the field of air monitoring. In this study, the level of PAH, PCB and OCP was determined in triolein containing VOs utilized as passive samplers for air and concentrations per cubic meter consisting of air + aerosols are estimated.

15.5 VO preparation

The procedure of VO sampler preparation in this study was similar to those described in Wang et al. 2009. In brief, low-density polyethylene lay flat tubing (LDPE, 2.5 cm wide, wall thickness 65 μm) supplied by VWR Ismaning, Germany was used. The LDPE tube was heat-sealed at a distance of 2.5 cm from one end. 700 μL of triolein (Sigma, Munich, Germany, 99%) which was spiked with performance reference compounds (sixteen ^{13}C -EPA-PAH, ^{13}C PCB: PCB60, PCB127, PCB159) were added as close as possible to the sealed bottom by using a capillary pipette. The length of the whole VO was 29 cm and the triolein-containing part of the sampler (i. e., excluding the mounting loops) had an area of 115 cm^2 . The sampler preparation was performed in a purified glovebox under nitrogen atmosphere to avoid contaminations. The prepared VO were stored in closely aluminium sealed heat cleaned 10 mL glass vials, further stored at $-28\text{ }^\circ\text{C}$ and kept cooled during transportation until deployment. The VO were transported in sealed flasks to and from the place of deployment. The VO were mounted in metal frames and placed in Stevenson screen boxes 2 m above the ground (Fig. 7). The VO were deployed at all the sampling sites from end of July 2015 till beginning of September 2015 for 43 days.

15.6 Sampling and locations

Three sampling locations at 270 m.a.s.l. (Bolzano city), 1700 m.a.s.l. (Ritten Station) and 2270 m.a.s.l. (the department for civil protection of Bolzano province, Rittner Horn) were arranged from the Italian Agency of Environment. In addition, a fourth sampling location was chosen in a private area of Mittelberg at 1100 m.a.s.l. (Pandelova et al. 2016)



Fig. 7: Picture of Stevenson hut and google map depicting the four locations of the altitude profile which was investigated in the framework of the Virtual Alpine Observatory (VAO)

15.7 Extraction, clean-up and analysis

The samples were spiked with a range of deuterated and ^{13}C -labeled compounds to monitor the extraction and cleanup procedures. VO were cut into small pieces and then extracted with 100 mL cyclohexane overnight at 200 rpm on a constant left-right shaker. The volume of generated extract for both sediment and VO samples was reduced to 1 mL and the residue was re-dissolved again with approximately 1–2 mL mixture of n-hexane:dichloromethane (1:1). Consequently, the sample underwent cleanup using a mixed column and C_{18} SPE cartridge (Wang et al., 2015). A recovery standard ($^{13}\text{C}_{12}$ -1,2,3,4-TCDD, Pentachlorotoluene, $^{13}\text{C}_{12}$ -1,2,3,7,8,9-HxCDD, PCB111) was added in the final eluate and the sample was concentrated with a gentle flow of nitrogen to 20 mL to be ready for analytical determination. The measurement was carried out with HRGC/HRMS. The parameters used for the isomer specific detection of PAH, PCB and OCP are given in (Temoka et al., 2016; Wang et al., 2015). All results were expressed on pg/VO, and those samples with contents less than the detection limit are reported as not detected (n.d.). The concentrations of the targeted analytes are then converted to concentrations per cubic meter air utilizing the PRC information to estimate the compound specific sampling rates of air.

15.8 Quality control/quality assurance

The accredited laboratory applies quality management system practices according to EN ISO/IEC 17025 standards. The applied analytical methods were regularly verified.

Laboratory blanks and field blanks were carried out. Laboratory blanks comprised the whole sample pre-treatment without VO in order to control the background levels of the studied compounds at the laboratory. All used solvents, silica, and alumina adsorbents were of trace analysis grade and supplied by LGC Standards (Wesel, Germany). The field VO blanks were carried to and from the place of deployment, and after being shortly opened at the deployment place, hermetically sealed again and then stored at $-28\text{ }^{\circ}\text{C}$ at the laboratory for the same period as the VO sampling deployment. The generated data was blank corrected by field blanks. Substances whose values after blank correction were lower than three times the standard deviation of the field blank value were considered as not detectable (n.d.) and the three times the standard deviation of the field blank value was provided in brackets. Analytes in samples that were not detected before field blank correction were given as not detectable (n.d.) with their limit of detection provided in brackets. The limit of detection of the instrumental methodology is considered as a signal/noise ratio 3:1. For VO samples, the recovery percentages for PCB, PAH, and OCP ranged from 40% to 125%.

15.9 Results of the altitude profile Bozen-Ritten

The PAH, PCB and OCP results (pg/m^3) in air (C_A) and air and aerosols (PM10) (C_{Total}) across the 4 sampling sides (270, 1100, 1700, and 2270 m.a.s.l.) are summarized in Table 1. Comparison of C_A and C_{Total} show that the portion of pollutant which can be attributed to the aerosol fraction is of minor relevance for those compounds which could be clearly identified and quantified in VO. The difference between C_A and C_{Total} increases only for compounds of very low vapor pressure such as 5-ring PAH, higher chlorinated PCB, and OCP of higher molecular weight eg. DDT. The main reason for this finding is the low concentration of aerosols in the remote alpine environment and proportions can be changed toward the aerosol fraction if the aerosol concentration increases substantially. The results show that the sampling of only aerosols is by far not sufficient to quantify the exposure of ambient air to living organisms.

Tab. 1: PAH, PCB and OCP results (pg/m³) in air (C_A) and air and aerosols (PM10) (C_{Total}) across the 4 sampling sides (270, 1100, 1700, and 2270 m.a.s.l.)

	270 m.a.s.l.		1100 m.a.s.l.		1700 m.a.s.l.		2270 m.a.s.l.	
PM10 (µg/m ³)	14.4*		10**		9.7*		10**	
	C _A	C _{Total}	C _A	C _{Total}	C _A	C _{Total}	C _A	C _{Total}
PAH (ng/m³)								
Naphthalene	29.55	29.55	n.d.	n.d.	n.d.	n.d.	n.d.	n.d.
Acenaphthylene	1.52	1.52	0.4566	0.4566	n.d.	n.d.	0.2808	0.2808
Acenaphthene	3.79	3.79	n.d.	n.d.	n.d.	n.d.	n.d.	n.d.
Fluorene	5.37	5.37	1.26	1.26	n.d.	n.d.	0.7145	0.7146
Phenanthrene	5.07	5.08	0.9635	0.9640	n.d.	n.d.	0.2886	0.2887
Anthracene	0.4318	0.4323	0.0446	0.0446	n.d.	n.d.	n.d.	n.d.
Fluoranthene	0.3461	0.3495	0.0527	0.0530	0.0087	0.0087	0.0120	0.0121
Pyrene	0.0392	0.0395	0.0031	0.0031	n.d.	n.d.	0.0020	0.0020
Benzo(a)anthracen	0.0003	0.0004	0.0001	0.0001	n.d.	n.d.	0.0001	0.0001
Chrysen	0.0010	0.0018	0.0001	0.0002	n.d.	n.d.	0.0001	0.0002
Benzo(b)fluoranthene	0.0027	0.0589	n.d.	n.d.	n.d.	n.d.	n.d.	n.d.
Benzo(k)fluoranthene	0.0092	0.2029	0.0032	0.0499	n.d.	n.d.	0.0022	0.0355
Benzo(a)pyrene	0.0032	0.0159	n.d.	n.d.	n.d.	n.d.	n.d.	n.d.
Indeno(1,2,3c,d)pyrene	n.d.	n.d.	n.d.	n.d.	n.d.	n.d.	n.d.	n.d.
Benzo(g,h,i)perylene	n.d.	n.d.	n.d.	n.d.	n.d.	n.d.	n.d.	n.d.
Dibenzo(a,h)anthracen	n.d.	n.d.	n.d.	n.d.	n.d.	n.d.	n.d.	n.d.
PCB (pg/m³)								
PCB #28	38.21	38.35	21.69	21.75	21.29	21.35	23.91	23.97
PCB #52	17.34	17.47	8.22	8.26	8.00	8.04	7.12	7.16
PCB #101	10.85	11.24	3.12	3.20	3.23	3.31	3.18	3.26
PCB #138	1.16	1.34	n.d.	n.d.	n.d.	n.d.	0.4466	0.4963
PCB #153	1.68	1.96	n.d.	n.d.	n.d.	n.d.	n.d.	n.d.
PCB #180	0.0902	0.1492	n.d.	n.d.	n.d.	n.d.	0.0483	0.0703
PCB #77	0.4549	0.4746	n.d.	n.d.	0.2105	0.2166	0.1263	0.1301
PCB #81	n.d.	n.d.	n.d.	n.d.	n.d.	n.d.	n.d.	n.d.
PCB #126	0.0152	0.0194	n.d.	n.d.	n.d.	n.d.	n.d.	n.d.
PCB #169	n.d.	n.d.	n.d.	n.d.	n.d.	n.d.	n.d.	n.d.
PCB #105	0.8174	0.9431	0.1675	0.1854	n.d.	n.d.	0.1360	0.1505
PCB #114	0.1218	0.1370	0.0348	0.0379	0.0480	0.0520	0.0441	0.0479
PCB #118	2.01	2.21	0.4476	0.4799	0.3949	0.4225	0.3943	0.4228
PCB #123	n.d.	n.d.	n.d.	n.d.	0.0592	0.0629	0.0397	0.0422
PCB #156	0.0424	0.0716	n.d.	n.d.	n.d.	n.d.	0.0353	0.0521
PCB #157	0.0152	0.0264	n.d.	n.d.	n.d.	n.d.	0.0071	0.0107
PCB #167	0.0346	0.0473	n.d.	n.d.	n.d.	n.d.	0.0133	0.0167
PCB #189	0.0031	0.0129	n.d.	n.d.	n.d.	n.d.	0.0019	0.0061

	270 m.a.s.l.		1 100 m.a.s.l.		1700 m.a.s.l.		2270 m.a.s.l.	
	C _A	C _{Total}	C _A	C _{Total}	C _A	C _{Total}	C _A	C _{Total}
OCP (pg/m³)								
α-HCH	9.20	9.21	11.10	11.11	13.07	13.07	12.51	12.51
β-HCH	0.2240	0.2247	0.0907	0.0909	0.1182	0.1185	0.0659	0.0660
γ-HCH	38.03	38.15	9.61	9.63	9.34	9.36	9.36	9.38
δ-HCH	0.0755	0.0758	n.d.	n.d.	0.0499	0.0500	0.0546	0.0548
ε-HCH	n.d.	n.d.	n.d.	n.d.	n.d.	n.d.	n.d.	n.d.
Hexachlorobutadiene	n.d.	n.d.	n.d.	n.d.	n.d.	n.d.	n.d.	n.d.
Pentachlorobenzene	36.59	36.60	55.863	55.866	68.346	68.350	106.3	106.3
Hexachlorobenzene	143.1	143.1	209.2	209.3	321.2	321.2	412.0	412.1
Pentachloroanisole	135.8	136.0	104.1	104.3	108.2	108.3	145.9	146.1
Octachlorostyrene	0.5376	0.5634	0.7840	0.8101	0.7565	0.7809	1.42	1.46
4.4'-DDT	2.10	3.45	0.5697	0.8229	0.3949	0.5651	0.5524	0.7979
2.4'-DDT	0.97	1.46	0.3031	0.4088	0.2193	0.2935	0.3570	0.4816
4.4'-DDD	n.d.	n.d.	n.d.	n.d.	n.d.	n.d.	n.d.	n.d.
2.4'-DDD	n.d.	n.d.	n.d.	n.d.	n.d.	n.d.	n.d.	n.d.
4.4'-DDE	8.29	8.48	1.86	1.89	1.22	1.24	1.26	1.28
2.4'-DDE	0.2389	0.2449	0.0389	0.0396	0.0370	0.0376	0.0436	0.0444
trans-Chlordane	n.d.	n.d.	n.d.	n.d.	0.4221	0.4292	n.d.	n.d.
cis-Chlordane	1.46	1.51	0.9274	0.9484	0.7681	0.7850	n.d.	n.d.
oxy-Chlordane	n.d.	n.d.	0.6298	0.6709	0.6506	0.6917	0.8670	0.9235
Heptachlor	0.4101	0.4102	n.d.	n.d.	n.d.	n.d.	n.d.	n.d.
cis-Heptachloroepoxide	3.93	3.93	3.20	3.20	3.96	3.96	3.95	3.95
trans-Heptachloroepoxide	n.d.	n.d.	n.d.	n.d.	n.d.	n.d.	n.d.	n.d.
Aldrin	n.d.	n.d.	n.d.	n.d.	n.d.	n.d.	n.d.	n.d.
Dieldrin	3.40	3.42	2.07	2.08	2.31	2.32	3.17	3.18
Endrin	1.30	1.39	0.2868	0.2999	n.d.	n.d.	0.3151	0.3294
Endosulfan-I	3.97	4.01	3.03	3.05	2.64	2.6633	2.87	2.89
Endosulfan-II	0.2276	0.2276	0.1365	0.1365	0.0936	0.0936	0.0823	0.0823
Endosulfan-sulfate	0.3570	0.3801	0.2856	0.2985	0.3215	0.3356	0.2488	0.2601
Methoxychlor	n.d.	n.d.	n.d.	n.d.	n.d.	n.d.	0.3791	0.4208
Mirex	n.d.	n.d.	0.0222	0.0222	n.d.	n.d.	0.0381	0.0381
Cypermethrine	n.d.	n.d.	n.d.	n.d.	n.d.	n.d.	n.d.	n.d.

* mean concentration during the sampling campaign measured on site.

** estimated concentration value

In practice the air concentration excl. particle contribution can be used to calculate the potential maximum concentration in the fat compartment (due to exposure to air without aerosols) of living organisms by using equation 18, 27 and 29 because the triolein is very similar to natural fat of organisms (data not shown). Values estimated like that can be also compared to existing limits for fatty feed and food.

15.10 Discussion

15.10.1 PAH distribution

A significant difference between the gas phase and the total concentration of gas and aerosol particle is not found in case of PAH of lower molecular weight. In general, the PAH concentrations decreased with altitude. No PAH except Fluoranthene were detectable at 1170 m.a.s.l. However, slight increase in concentrations was observed for the sampling location at 2270 m.a.s.l.

15.10.2 PCB distribution

Generally, the water solubility and volatility decrease as the degree of PCB chlorine substitution increases, and the lipid solubility increases with increasing chlorine substitution. Thus, PCB the levels in the aerosol compartment increased for higher chlorinated PCB. Regarding here investigated mountain profile a strong drop in PCB concentration was observed for the first three sampling sides. However, higher PCB concentrations were determined at Rittner Horn but the levels are far below those found in Bolzano city.

15.10.3 OCP distribution

Since the most OCP are volatile, these compounds are commonly found in the gas phase. Also, the difference between the total concentration (C_{Total}) and the gas phase (C_A) was in the range of 0–45%. Some OCP compounds decrease with altitude, while other compounds increase (Pentachlorobenzene, Hexachlorobenzene and Octachlorostyrene).

4,4'-DDE and 4,4'-DDT are the major components of DDTs in all samples and the most abundant area with these compounds is determined in the valley of 270 m.a.s.l. Since the province of Bolzano is an industrial as well as wine production site the main source of DDT may come from historical uses.

15.11 Source apportionment

For the DDT group of chemicals the following ratios (Tab. 2) are proposed for judging about possible sources and/or the age of the contamination (Zhu et al., 2015).

Tab. 2: Ratios of DDT-compounds and their interpretation

$(4,4'\text{-DDE}+4,4'\text{-DDD})/4,4'\text{DDT}<1$	fresh 4,4'-DDT, resp. input
$(4,4'\text{DDE}+4,4'\text{DDD})/4,4'\text{DDT}>1$	aged 4,4'-DDT
$(2,4'\text{-DDE}+2,4'\text{-DDD})/2,4'\text{DDT}<1$	fresh 2,4' DDT, resp. input
$(2,4'\text{DDE}+2,4'\text{DDD})/2,4'\text{DDT}>1$	aged 2,4'-DDT
$(4,4'\text{DDE}+4,4'\text{DDD})/4,4'\text{DDT}$ converging $(2,4'\text{DDE}+2,4'\text{DDD})/2,4'\text{DDT}$ dicofof input	

In our study, the ratios are calculated for the altitude profile and compared to the actual concentrations found (Fig. 8).

For Bolzano profile the estimated ratio decreased with altitude and suggested fresher DDT input despite of decreasing DDTs-concentrations with altitude.

15.12 Conclusions

Ratios between chemical identities still indicate release of some OCP-POP and help for source apportionment of chemicals. Passive sampling employing VO is cheap and powerful for altitude

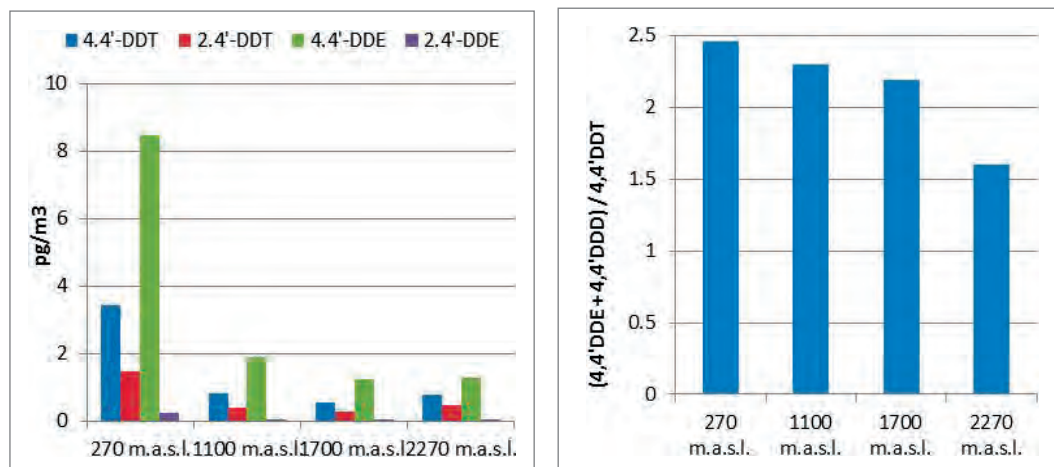


Fig. 8: Calculated $(4,4'\text{-DDE} + 4,4'\text{-DDD})/4,4'\text{-DDT}$ ratios (right) along Bolzano-Ritten altitude profile show that DDT is becoming 'fresher' with increasing altitude although the concentrations are decreasing with altitude (left)

profiling and indicative for long range transported POP. VO are suitable for the measurement of air quality of remote regions like the Alps with minor infrastructure. VO can also suit to estimate the exposure of the lipidome via air and compare the equilibrium concentrations of the natural fat like triolein to limits for fatty food and feed. Moreover it is possible to monitor also air and water in combination (Pandelova et.al. 2021) and conclude about the partitioning and exsomics of the chemicals between these two compartments.

Acknowledgments

The research was granted by the Bavarian State Ministry for Environment and Consumer protection within VA0II SP I/02 Trends of climate forcing gases and aerosols and spatio-temporal deposition of persistent organic pollutants (POPs).

References

- Amdany, R., Chimuka, L., Cukrowska, E., Kukučka, P., Kohoutek, J. and Vrana, B. (2014) Investigating the temporal trends in PAH, PCB and OCP concentrations in Hartbeespoort Dam, South Africa, using semi-permeable membrane devices (VOs). *Water SA*. 40, 425–436.
- Bari, M.A., Baumbach, G., Kuch, B., and Scheffknecht, G. (2010) Particle-phase concentrations of polycyclic aromatic hydrocarbons in ambient air of rural residential areas in southern Germany. *Air Qual Atmos Health* 3, 103–116.
- Berger, M. and Schwarzbauer, J. (2016) Historical deposition of riverine contamination on terrestrial floodplains as revealed by organic indicators from an industrial point source. *Water Air Soil Pollut* 227: 20, 1–14.
- Booij, K. and Smedes, F. (2010) An improved method for estimating in situ sampling rates of nonpolar passive samplers. *Environ Sci Technol*, 44, 6789–6794.
- CDC 2010: <http://www.cdc.gov/niosh/topics/exposome/>
- Chiou, C.T. (1985). Partition coefficients of organic compounds in lipid-water systems and correlations with fish bioconcentration factors. *Environ Sci Technol* 19, 57–62.
- Fernandes, M. and Brooks, P. (2003) Characterization of carbonaceous combustion residues: II. Nonpolar organic compounds. *Chemosphere* 53, 447–458.
- Huckins, J.N., Petty, J.D., Lebo, J.A., Almeida, F.V., Booij, K., Alvarez, D.A., Clark, R.C. and Mogensen, B.B. (2002). Development of the permeability/performance reference compound approach for in situ calibration of semipermeable membrane devices. *Environ Sci Technol* 36, 85–91.
- Huckins, J.N., Petty, J.D., and Booij, K. (2006). *Monitors of organic chemicals in the environment: Semi-permeable membrane devices*. Springer, New York.
- Lohmann, R., Breivik, K., Dachs, J., and Muir, D. (2007) Global fate of POPs: Current and future research directions. *Environ Pollut* 150, 150–165.

- Ma, J., Hung, H., Tian, C., and Kallenborn, R. (2011). Revolatilization of persistent organic pollutants in the Arctic induced by climate change. *Nature Climate Change* 1, 255–260.
- Mackay, D., Paterson, S. and Schroeder, W.H. (1986) Model Describing the Rates of Transfer Processes of Organic Chemicals Between Atmosphere and Water, *Environ Sci Technol* 20, 810–816.
- Nizzetto, L., Lohmann, R., Gioia, R., Dachs, J., and Jones, K. (2010) Atlantic Ocean surface waters buffer declining atmospheric concentrations of persistent organic pollutants. *Environ Sci Technol* 44, 6978–6984.
- Ockenden, W., Corrigan, B. Howsan, M. and Jones, K. (2001) Further developments in the use of semipermeable membrane devices as passive air samplers: Application to PCBs. *Environ Sci Technol* 35, 4536–4543.
- Pandelova, M., Anritter, F., Feicht, E., Kirchner, M., Henkelmann, B., Corsten, C., Bernhöft, S., Verdi, L., Bachmann, C., Schramm, K.-W., 2016. Ambient air altitude profile of PAH, PCB and OCP near Bolzano determined by Virtual Organisms (VO). In: 36th Intl. Symposium on Halogenated Persistent Organic Pollutants <http://www.dioxin20xx.org/index.html>
- Pandelova, M., Henkelmann, B., Lalah, J.O., Norf, H., Schramm, K.-W., 2021 Spatial, temporal, and inter-compartmental environmental monitoring of lipophilic pollutants by virtual organisms. *Chemosphere* 264, 128546
- Schramm, K.-W., Wang, J., Bi, Y., Temoka, C., Pfister, G., Henkelmann, B. and Scherb, H. (2013) Chemical- and effect-oriented exposomics: Three Gorges Reservoir (TGR). *Environ Sci Pollut Res* 20, 7057–7062.
- Söderström H S, Bergqvist P A. Passive air sampling using semipermeable membrane devices at different wind-speeds in situ calibrated by performance reference compounds. *Environmental Science and Technology*, 38: 4828–4834.
- Temoka, C., Wang, J., Bi, Y., Deyerling, D., Pfister, G., Henkelmann, B. and Schramm, K.-W. (2016) Concentrations and mass fluxes estimation of organochlorine pesticides in Three Gorges Reservoir with virtual organisms using in situ PRC-based sampling rate. *Chemosphere* 144, 1521–1529.
- Temoka, P., Pfister, G., Henkelmann, B., Schramm, K.-W. (2017) Adapting current model with field data of related performance reference compounds in passive samplers to accurately monitor hydrophobic organic compounds in aqueous media. *Environ. Monit. Assess.* 189:543
- Wang, J., Bi, Y., Pfister, G., Henkelmann, B., Zhu, K., and Schramm, K.-W. (2009). Determination of PAH, PCB, and OCP in water from the Three Gorges Reservoir accumulated by semipermeable membrane devices (VO). *Chemosphere* 75, 1119–1127.
- Wang, J., Liang, W., Henkelmann, B., Pfister, G., and Schramm, K.-W. (2015). Organochlorine pesticides accumulated by VO-based virtual organisms and feral fish in Three Gorges Reservoir, China. *Environ Pollut* 202, 160–167.
- Zhu N., Schramm K.-W., Wang T., Henkelmann B., Fu J., Gao Y., Wang Y. and Jiang G. (2015). Lichen, moss and soil in resolving the occurrence of semi-volatile organic compounds on the southeastern Tibetan Plateau, China. *Sci Total Environ*, 518–519, 328–336.

16 Introduction to solar FTIR spectrometry of the atmosphere and research highlights from the Zugspitze summit

Ralf Sussmann and Petra Hausmann

Karlsruhe Institute of Technology, IMK-IFU, Garmisch-Partenkirchen, Germany

16.1 Introduction

Solar Fourier-transform infrared (FTIR) spectrometry is a ground-based remote sounding technique, which allows to infer total column abundances and vertical concentration profiles of more than three dozens of atmospheric trace gases simultaneously. Thereby a snap shot of the chemical state of the atmosphere can be attained within typically 10 minutes: climate gases, ozone-relevant gases, and air quality gases. During the last 20 years this technique has become wide spread around the world and is today the dominant science-driven ground-based remote sounding technique in atmospheric research, while other activities, e. g., using microwave techniques have declined on international level. Section 16.2 gives a basic introduction to this powerful technique, which is operated by Karlsruhe Institute of Technology (KIT), e. g., at the Zugspitze summit since 1995 (Sussmann and Schäfer, 1997; Fig. 1.1).

As an example science application for solar FTIR spectrometry, we look at measurements of atmospheric methane (CH_4) in Section 16.3. Currently, there is a load of ≈ 400 ppm carbon dioxide (CO_2) in the atmosphere and only ≈ 2 ppm CH_4 . So why is research on atmospheric CH_4 necessary? Exactly this lower atmospheric concentration of CH_4 leads to the fact that CH_4 causes a factor of 84 higher radiative forcing compared to CO_2 on a per-kilogram-emissions basis and on a time scale of 20 years (IPCC, 2013): Today's high CO_2 levels cause CO_2 absorptions to already saturate in some spectral regions (so additional molecules have less impact on forcing), whereas there are still nearly no saturated CH_4 lines at all. Therefore, increasing atmospheric CH_4 concentrations matter much more than increases in CO_2 , and here we are currently witnessing a critical development: Since 2007 instruments like the Zugspitze solar FTIR have been detecting a persistent strong renewed global CH_4 increase. A crucial question for designing effective mitigation measures is, which sources of emissions are driving this renewed methane increase: biogenic, thermogenic, food production, fossil fuels or biomass burning? Based on solar FTIR spectrometry, we have derived for the first time reliable numbers on the (strong) relative contribution of the oil and natural gas sector to the renewed post-2006 CH_4 increase in the atmosphere (Hausmann et al., 2016; Section 16.3).



Fig. 1.1: The solar FTIR observatory at the Zugspitze summit (2964 m.a.s.l.) as a contribution to the international networks NDACC and TCCON. The optics dome opens during clear sky conditions and a computer controlled solar tracker redirects the solar beam into the FTIR spectrometer inside the building.

Another research focus of this article is on atmospheric water vapor (H_2O) which acts as dominant contributor to the global greenhouse effect (Kiehl and Trenberth, 1997). In Section 16.4 we will present newest solar FTIR-based decadal trend results from the Zugspitze summit. Furthermore, valuable information on tropospheric moisture pathways and associated transport of other tracers can be provided by measurements of water vapor and its isotopes (Schneider et al., 2016). This is of relevance to the question of intercontinental transport of air pollution which lead to the 1979 Geneva Convention on Long-Range Transboundary Air Pollution (CLRTAP, <http://www.unece.org/env/lrtap/welcome.html>). In this context, we will demonstrate in Section 16.4 that consistent H_2O - δD observations by solar FTIR can serve as a valuable new transport tracer to study atmospheric transport to the Central European free troposphere (Hausmann et al., 2017). This finding is relevant for the currently reinforcing research on how environmental parameters like atmospheric humidity and temperature, aeroallergens, or aerosols impact upon human health.

16.2 Introduction to solar FTIR spectrometry

The principle of solar FTIR spectrometry exploits the fact that solar radiation is a spectrally continuous broad-band source of electromagnetic radiation which penetrates the terrestrial atmosphere where it is attenuated by molecular absorption at distinct resonance frequencies in the infrared. These absorption features are typical for different atmospheric trace gases. The width and depth of these spectral “fingerprints” contain information on the vertical columns and concentration profiles of the absorbing molecular trace species at the moment of observation.

There are two international measurement networks based on this technique, i. e., the Network for the Detection of Atmospheric Composition Change (NDACC, <http://www.ndsc.ncep.noaa.gov/>) and the Total Carbon Column Observing Network (TCCON, <http://www.tcon.caltech.edu/>). While TCCON performs near-infrared measurements focusing on high-accuracy-and-precision soundings of greenhouse gases (CO_2 , CH_4 , N_2O , CO), NDACC-type FTIR measurements are performed in the mid infrared. This allows for CH_4 and CO_2 retrievals with slightly lower accuracy, but many additional species can be retrieved, e. g., O_3 , HF , HCl , ClONO_2 , HNO_3 , NO_2 , C_2H_6 , H_2CO , H_2O , HDO , and others. Furthermore, from mid-infrared soundings, profile information can be attained up to higher altitudes. This is due to the lower Doppler width compared to the near infrared, which may be understood along with Sect. 16.2.1.

16.2.1 Solar radiation and molecular infrared absorption

Solar radiation. The spectral solar irradiance at the top of the atmosphere (Fig. 2.1) can be approximated by Planck’s radiation law using a temperature of ≈ 6000 K. The resulting spectral distribution is modulated during radiative transfer through the atmosphere by a variety of processes, e. g., Rayleigh scattering by nitrogen molecules, Mie scattering by aerosols, thermal emission from the air or from clouds, or UV absorption by O_3 (Fig. 2.1). In the infrared, molecular absorption via vibration-rotation excitation of a variety of atmospheric trace gases is the dominant process.

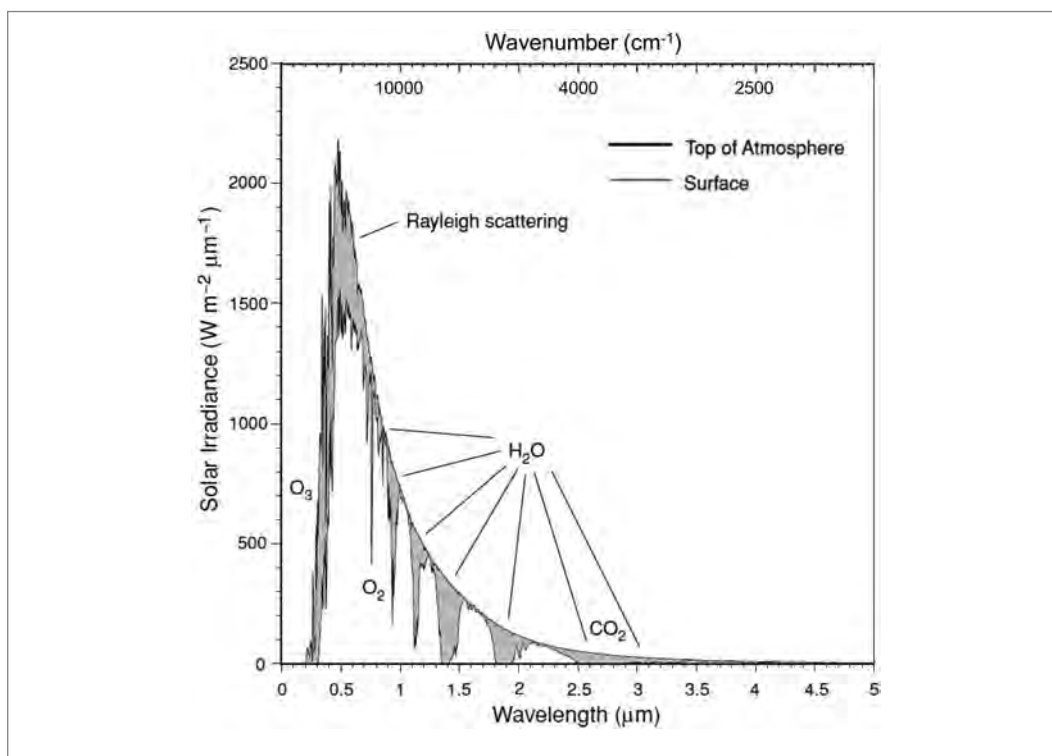


Fig. 2.1: Solar spectral irradiance at the top of atmosphere and at the surface for a solar zenith angle of 60° under cloud- and aerosol-free conditions. Spectral regions affected by molecular absorption are indicated for most important species (adapted from Liou, 2002).

The fundamental equation in solar absorption spectrometry is Lambert Beer's law which describes the exponential decay of spectral radiance passing through an absorbing medium, i. e.,

$$I_{\lambda}(s) = I_{\lambda}(\text{toa}) \exp \left(- \int_{\text{toa}}^s \sigma_{\text{abs},\lambda}(s') n_{\text{abs}}(s') ds' \right), \quad (2.1)$$

where $I_{\lambda}(s)$ is the solar spectral radiance observed at an optical path length s , $I_{\lambda}(\text{toa})$ is the solar radiance incident at top of the atmosphere (toa), $\sigma_{\text{abs},\lambda}$ is the spectral absorption cross section of the medium, and n_{abs} is the number density of the absorbing species (units of m^{-3}). The absorption cross section (in units of m^2) depends on temperature and pressure along the optical path. Considering a gas mixture, the integrand in Eq. (2.1) becomes a sum over different absorbing species. For ground-based solar absorption measurements, integration is performed along the optical path of direct sunlight from the top of the atmosphere to the surface.

Molecular absorption. Each atmospheric molecular species exhibits a characteristic absorption spectral line signature, which can be understood as follows. The energy content of radiation is proportional to its wavenumber and the number of photons. The energy of a single photon is described by $E_{\text{ph}} = hc\nu$ with the Planck constant $h = 6.626 \times 10^{-34}$ J s. A specific photon may only be absorbed by a molecule, if the photon energy corresponds to the discrete energy difference ΔE between two molecular energy levels, i. e.,

$$\Delta E = hc\nu. \quad (2.2)$$

The total energy E of a molecule is composed of its continuous translational energy (E_{tra}) and quantized energy levels of its electronic configuration (E_{ele}), its vibrational state (E_{vib}), and its rotational state (E_{rot}). It can be written as

$$E = E_{\text{tra}} + E_{\text{ele}} + E_{\text{vib}} + E_{\text{rot}}. \quad (2.3)$$

Focusing on absorption of mid-infrared radiation, only transitions between vibrational and rotational states have to be considered.

Rotational energy levels. Under typical atmospheric conditions many rotational modes of molecules are activated. Rotations of diatomic molecules can be described by the model of a linear rigid rotator. Based on quantum mechanics, only discrete levels of rotational energy are possible given by

$$E_{\text{rot}}(J) = hcBJ(J+1), \quad (2.4)$$

where J is the rotational quantum number ($J = 0, 1, 2, \dots$) and $B = h/8\pi^2 cI_{\text{rot}}$ is the rotational constant with the moment of inertia I_{rot} of the rigid rotator. The magnetic quantum number m_J can take on values of $-J \leq m_J \leq +J$. Therefore, in absence of external fields, each rotational energy level is $(2J+1)$ -fold degenerated.

Absorption of radiation requires the coupling of the absorbing molecule with an electromagnetic wave. Molecular rotations can only be activated by infrared absorption if the molecule has a permanent electric dipole moment. Energy differences between rotational states are relatively small, i. e., pure rotational absorption lines are located in the far-infrared and microwave spectral region.

Vibrational energy levels. Vibrations of a diatomic molecule can be described by means of the quantum-mechanical analog of a harmonic oscillator, i. e., two atoms oscillating around their equilibrium position with a restoring force proportional to the displacement. Vibrational energy levels are given by

$$E_{\text{vib}}(\nu) = hc\nu_0(\nu + 1/2), \quad (2.5)$$

where ν_0 is the vibrational wavenumber and ν is the vibrational quantum number ($\nu = 0, 1, 2, \dots$). The selection rule for vibrational transitions is $\Delta\nu = \pm 1$. Most atmospheric molecules populate the vibrational ground state ($\nu = 0$) and absorption activates the first excited state ($\nu = 1$). A vibrational mode can only be activated by infrared radiation if a change in the molecular dipole moment is induced. Vibrational energy transitions require photons with higher energies than rotational energy transitions and vibrational absorption lines occur in the mid-infrared spectral region.

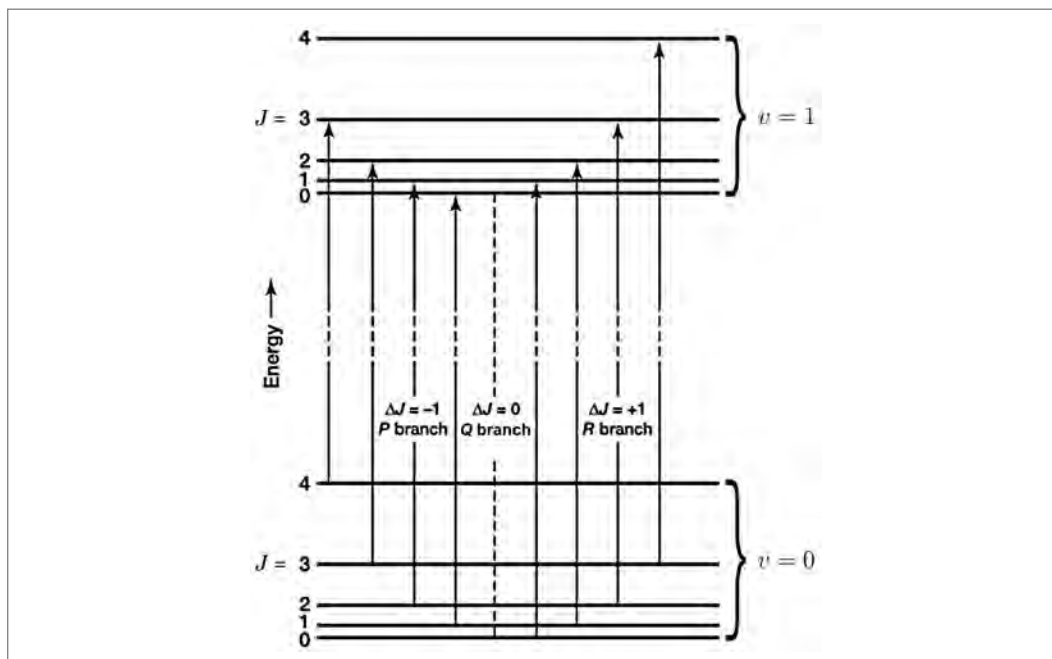


Fig. 2.2: Schematic representation of molecular energy levels and allowed vibration-rotation transitions (adapted from Brasseur and Solomon, 2005, with permission of Springer).

Deviations from the idealized harmonic oscillator and rigid rotator models give rise to overtone bands ($\Delta v = \pm 2, \pm 3, \dots$) and differences between vibrational wavenumbers of ground-state and upper-state transitions. Molecules with more than two atoms have higher degrees of freedom resulting in additional vibrational modes, e.g., the deformation of bond angles. Isotopes of a molecular species can be distinguished by their distinct spectral fingerprints, as their absorption line positions deviate from each other in consequence of their differing masses determined by the number of neutrons ("isotopic shift").

Vibration-rotation bands. As molecular vibrations result in an oscillating dipole moment, simultaneous molecular rotations can be activated – even for molecules without a permanent dipole moment. Combined vibration-rotation transitions generate complex vibration-rotation bands, which are composed of many individual absorption lines in the vicinity of the fundamental vibrational wavenumber. Fig. 2.2 illustrates such a vibration-rotation transition from the vibrational ground-state ($v = 0$) to the first excited state ($v = 1$) superimposed by various rotational transitions. The P-branch of the absorption band corresponds to rotational transitions with selection rule $\Delta J = -1$, while the R-branch corresponds to $\Delta J = +1$. The Q-branch of $\Delta J = 0$ is forbidden for linear diatomic molecules. In contrast, for linear (e.g., CO_2) or bent (e.g., H_2O) triatomic molecules the transition $\Delta J = 0$ is allowed, which results in the formation of a Q-branch at the vibrational wavenumber itself.

Line broadening. Molecular absorption lines are characterized by line intensity and line shape. Line intensity depends on the quantum-mechanical probability of the transition to an excited state and on the population of the ground-state, which is a function of temperature. Absorption line shapes observed are not infinitely narrow spectral lines but extend over finite wavenumber regions. This broadening of spectral absorption lines is caused by different line broadening mechanisms, which are introduced in the following.

First, the natural line width is a direct consequence of Heisenberg's uncertainty principle which states that the energy E of an excited molecular state and its lifetime τ cannot be simultaneously determined with unlimited high precision, i. e.,

$$\Delta E \cdot \Delta \tau \geq h/2\pi. \quad (2.6)$$

Hence, the finite natural lifetime of an excited molecular state implies a finite uncertainty in its energy. The corresponding spectral line is distributed over a narrow wavenumber interval. Natural line broadening is small compared to the following broadening effects and is therefore negligible under atmospheric conditions.

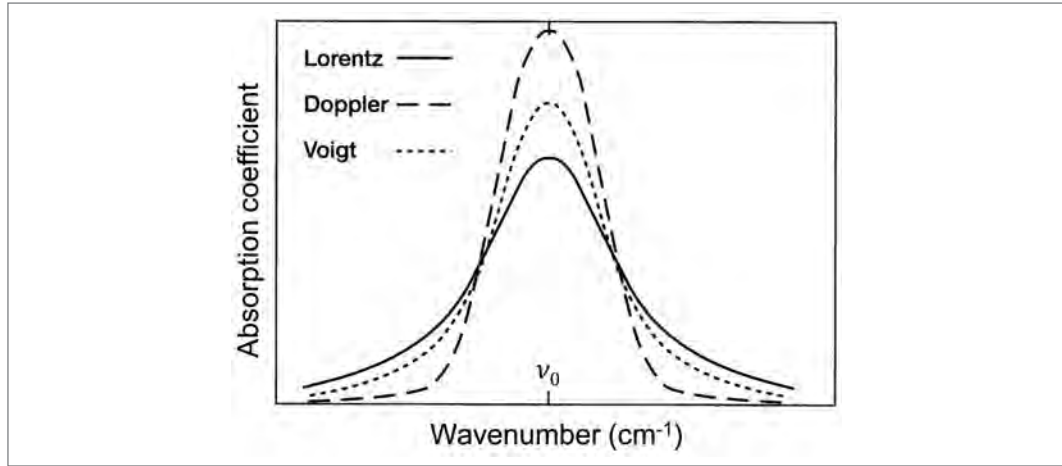


Fig. 2.3: Lorentz, Doppler, and Voigt line shapes of molecular absorption lines with equal line widths and intensities (from Brasseur and Solomon, 2005, with permission of Springer).

The second mechanism is pressure broadening. Molecular collisions diminish the lifetime of an excited molecular state and therefore increase its energy uncertainty (see Eq. (2.6)). As collision frequency increases with pressure, pressure broadening dominates at altitudes below 20 km. It can be described by a Lorentz line shape, i. e.,

$$f_L(\nu - \nu_0) = \frac{1}{\pi} \cdot \frac{\alpha_L}{\alpha_L^2 + (\nu - \nu_0)^2} \quad (2.7)$$

where ν_0 is the wavenumber of the line center and α_L is the half-width at half-maximum. The half-width is a function of pressure and, to a lesser extent, of temperature and can be written as

$$\alpha_L(p, T) = \alpha_L(p_0, T_0) \frac{p}{p_0} \sqrt{\frac{T_0}{T}} \quad (2.8)$$

with standard pressure p_0 and temperature T_0 .

Above 40 km altitude where pressure broadening is negligible, a third line broadening mechanism becomes dominant. Thermal broadening results from the Doppler effect, caused by different velocity components of absorbing molecules relative to the radiation direction. The velocity distribution depends on molecular mass and is determined by gas temperature. Doppler broadening yields a Gaussian line shape given by

$$f_D(\nu - \nu_0) = \frac{1}{\alpha_D \sqrt{\pi}} \exp\left(-\frac{(\nu - \nu_0)^2}{\alpha_D^2}\right) \quad (2.9)$$

where α_D is the Doppler width of the line, i. e.,

$$\alpha_D(T) = \frac{\nu_0}{c} \sqrt{\frac{2kT}{M}} \quad (2.10)$$

with the Boltzmann constant k and the mass M of the absorbing molecule. The corresponding half-width at half-maximum may be calculated as $(\alpha_D \sqrt{\ln 2})$. Consequently, Doppler line width is independent of pressure but depends on temperature.

Finally, in the intermediate altitude region (20–40 km), both pressure and Doppler broadening need to be taken into account. The resulting line shape can be obtained by convolution of Doppler and Lorentz line shapes and is referred to as Voigt profile, i. e.,

$$f_V(\nu - \nu_0) = \frac{\alpha_L}{\alpha_D \pi^{3/2}} \int_0^{\infty} \frac{1}{\alpha_L^2 + (v' - \nu_0)^2} \exp\left(-\frac{(\nu - v')^2}{\alpha_D^2}\right) dv'. \quad (2.11)$$

The line shapes of the different line broadening mechanisms are illustrated in Fig. 2.3. As different line broadening effects are dominant in distinct altitude regions (due to altitude-dependent pressure and temperature), absorption lines contain information on the vertical concentration distribution of absorbing molecules. This is utilized by solar absorption spectrometry.

16.2.2 Instrumental basis for solar FTIR measurements

Ground-based solar absorption FTIR spectrometry is a passive remote sensing method using the sun as light source and the atmosphere as absorbing medium. Such measurements require an optical device to track the exact position of the sun (Fig. 2.4) and a spectrometer to record the absorption signal. The core of an FTIR instrument is a Michelson interferometer (Fig. 2.5). The incoming beam of solar radiation is split into two parts by a beam splitter. Subsequently, one of these beams is reflected at a fixed mirror, while the other beam hits a mirror moving at constant velocity. Both individually reflected beams are recombined after passing the beam splitter once more. Finally, the resulting interference pattern is recorded by the detector. Interference arises due to the optical path difference between the fixed mirror path and the moving mirror path. An interferogram is generated by recording the signal at many discrete positions of the moving mirror.

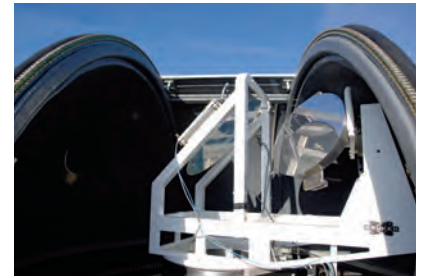


Fig. 2.4: Solar tracker optics of the FTIR spectrometer system at the Zugspitze summit.

To gain the spectral information of interest, the interferogram $I(\Delta x)$, i. e., intensity as function of mirror displacement Δx , has to be converted to a spectrum $I(\nu)$, i. e., intensity as function of wavenumber. This can be achieved by means of an inverse Fourier transformation. A Fourier transformation translates from the domain of wavenumbers to the domain of mirror displacement and can be written as

$$I(\Delta x) = \int_{-\infty}^{+\infty} I(\nu) \cos(2\pi\nu\Delta x) d\nu \quad (2.12)$$

We are interested in the inverse Fourier transformation given by

$$I(\nu) = \int_{-\infty}^{+\infty} I(\Delta x) \cos(2\pi\nu\Delta x) d\Delta x \quad (2.13)$$

The interferogram of an ideal monochromatic source is an infinite cosine wave and inverse Fourier transformation would result in a delta function at the respective wavenumber.

In reality, the interferogram is truncated at a finite maximum mirror displacement. Therefore, the FTIR spectrum of a monochromatic source yields a broadened spectral line with additional side lobes. The spectral resolution of an FTIR spectrometer depends on its maximum optical path difference OPD_{\max} (i. e., twice the maximum moving mirror displacement). With increasing maximum optical path difference spectral resolution is improved, i. e., $\Delta\nu = 1/OPD_{\max}$. Consequently, the FTIR absorption line shape is a combination of the physical line shape of the atmospheric spectrum (see Fig. 2.3) and the instrumental line shape (ILS). This characteristic line shape of an FTIR instrument resembles a cardinal sine function. The width of the ILS has to be small compared to the width of spectral lines that are to be observed. In practice, a trade-off needs to be found between optimizing spectral resolution, measurement duration, and signal-to-noise ratio.

Compared to dispersive spectrometers, the FTIR technique has several advantages. First, all wavenumbers are simultaneously recorded (“ Fellgett advantage”) and, consequently, FTIR

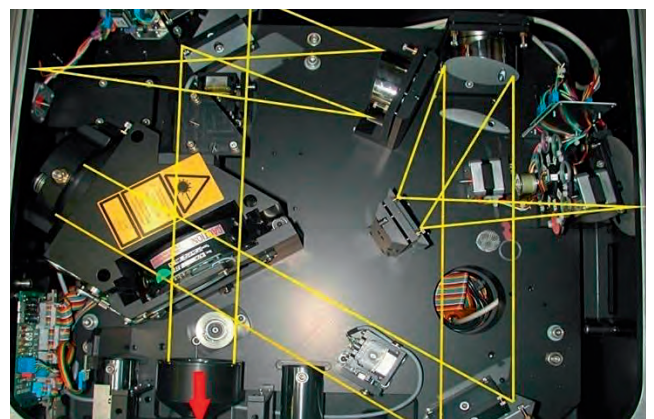
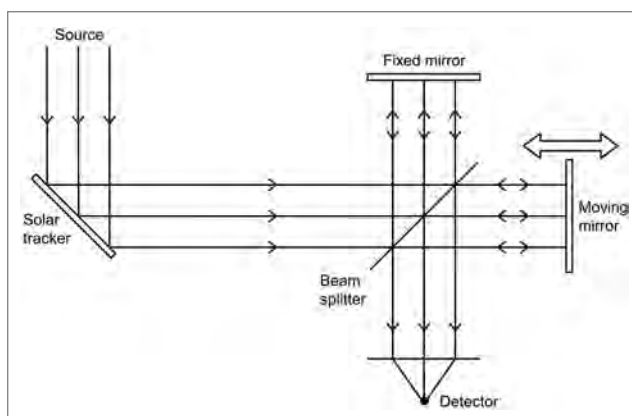


Fig. 2.5: Schematics of an FTIR spectrometer and photograph of interior of the Zugspitze instrument.

measurements are significantly faster than grating spectrometers which record each wavenumber separately. Second, FTIR spectra exhibit a higher signal-to-noise ratio for same resolution and measurement duration (“Jacquinot advantage”), as the throughput is not diminished by slits or apertures as narrow as applied in grating spectrometers. Third, FTIR uses a reference laser for permanent control of the optical path difference, which results in a built-in wavenumber calibration (“Connes advantage”).

FTIR measurements analyzed within the scope of this article are primarily obtained at the high-altitude observatory Zugspitze (47.42 °N, 10.98 °E; 2964 m a.s.l.). As part of the Network for the Detection of Atmospheric Composition Change, a Bruker IFS 125HR FTIR spectrometer has been in operation since 1995 (Sussmann and Schäfer, 1997). Mid-infrared FTIR spectra are recorded by cooled InSb detectors with a typical spectral resolution of 0.005 cm^{-1} ($\text{OPD}_{\text{max}} = 175 \text{ cm}$). Six individual scans are averaged which results in an integration time of about seven minutes. Recently, the Zugspitze instrument has been extended to perform also near-infrared measurements in alternating mode as a contribution to TCCON.

16.2.3 Retrieval of trace gas profiles

Vertical trace gas concentration profiles (atmospheric state vector \mathbf{x}) can be inferred from measured mid-infrared spectra (measurement vector \mathbf{y}), which are connected via the forward model F

$$\mathbf{y} = F(\mathbf{x}) + \varepsilon \quad (2.14)$$

where ε denotes the measurement noise. In general, F is a complex non-linear function which simulates a measured spectrum by modeling the propagation of light through the atmosphere. For this purpose, the model atmosphere is divided into discrete levels and \mathbf{x} becomes a discrete representation of the continuous atmospheric state at the moment of measurement. A synthetic spectrum can be computed using the forward model and a priori knowledge on the profiles of pressure, temperature.

While F maps from the state space \mathbf{x} into the measurement space \mathbf{y} , we are interested in the inverse mapping, which is ill posed and can be formulated as a least squares problem. Due to the non-linearity of F , a Newtonian iteration is applied and a regularization term $\mathbf{R} \in \mathfrak{R}^{n \times n}$ is used that allows to constrain the ill-posed solution and thereby avoid oscillating profiles

$$\mathbf{x}_{i+1} = \mathbf{x}_i + (\mathbf{K}_i^T \mathbf{S}_\varepsilon^{-1} \mathbf{K}_i + \mathbf{R})^{-1} \times (\mathbf{K}_i^T \mathbf{S}_\varepsilon^{-1} (\mathbf{y} - F(\mathbf{x}_i)) - \mathbf{R}(\mathbf{x}_i - \mathbf{x}_a)), \quad (2.15)$$

where the subscript i denotes the iteration index and \mathbf{x}_a is the a priori profile. Here $\mathbf{K} = F/\partial\mathbf{x}$ are the Jacobians and \mathbf{S}_ε is the measurement covariance (assumed to be diagonal).

Using first-order Tikhonov regularization (Tikhonov, 1963), \mathbf{R} is set up by the relation

$$\mathbf{R} = \alpha \mathbf{L}_1^T \mathbf{L}_1 \in \mathfrak{R}^{n \times n}, \quad (2.16)$$

where α is the regularization strength and \mathbf{L}_1 is the discrete first derivative operator

$$\mathbf{L}_1 = \begin{pmatrix} -1 & 1 & 0 & \dots & 0 \\ 0 & -1 & 1 & \dots & \vdots \\ \vdots & \dots & \dots & \dots & 0 \\ 0 & \dots & 0 & -1 & 1 \end{pmatrix} \in \mathfrak{R}^{(n-1) \times n}, \quad (2.17)$$

which constrains \mathbf{x} in a way such that a constant profile is favored for the difference $\mathbf{x} - \mathbf{x}_a$.

Convergence of the iterative inversion is reached if calculated and measured spectra deviate less than a defined convergence threshold. The solution is not the true profile \mathbf{x}_{true} but the optimal estimate \mathbf{x} of the atmospheric state given the measurement \mathbf{y} and the a priori knowledge \mathbf{x}_a along with the constraint \mathbf{R} . The retrieval result can be characterized by means of the averaging kernel matrix \mathbf{A} which relates the variability of the true state \mathbf{x}_{true} at measurement time to the retrieved state variability relative to the a priori state vector, i. e.,

$$\mathbf{x} - \mathbf{x}_a = \mathbf{A}(\mathbf{x}_{\text{true}} - \mathbf{x}_a). \quad (2.18)$$

For an ideal remote sensing system, \mathbf{A} is a unity matrix representing perfect sensitivity at each model level without inter-correlations between the levels. In practice, the vertical resolution of an FTIR system is limited. It can be determined by the full width at half maximum of the averaging kernels (i. e., the rows of \mathbf{A}).

Retrieval strategy for water vapor and its isotopes. In the context of this article, two stable water vapor isotopes are of particular interest: H₂O (¹H₂¹⁶O) and HDO (¹H²H¹⁶O) with average abundances of 99.7% and 0.03%, respectively. Variations in the HDO-H₂O ratio of atmospheric water vapor are typically expressed in terms of δD , i. e.,

$$\delta D = \left(\frac{\text{VMR}_{\text{HDO}}/\text{VMR}_{\text{H}_2\text{O}}}{R_{\text{SMOW}}} \right) - 1 \times 1000\text{‰} \quad (2.19)$$

where VMR_{HDO} and $\text{VMR}_{\text{H}_2\text{O}}$ are volume mixing ratios of HDO and H₂O and $R_{\text{SMOW}} = 3.1152 \times 10^{-4}$ is the HDO-H₂O ratio of Standard Mean Ocean Water (Craig, 1961).

A retrieval method for tropospheric profiles of water vapor and δD from mid-infrared FTIR measurements has been published by Schneider et al. (2016). As water vapor volume mixing ratios are log-normally distributed, the retrieval is performed on logarithmic scale. A priori profiles are derived from LMDZ model runs and an inter-species constraint between H₂O and HDO is applied. Absorption line data from the high-resolution transmission molecular absorption database (HITRAN, version 2012; Rothman et al., 2013) are optimized for speed-dependent Voigt line shape parameterization. The retrieval comprises the analysis of 12 microwindows and a simultaneous fit of several interfering species (CO₂, O₃, N₂O, CH₄, HCl, and temperature). The model atmosphere is discretized in 22 altitude levels covering the range from observer altitude to about 60 km altitude.

Retrieval strategy for methane and ethane. In this work, methane column abundances are retrieved from mid-infrared FTIR spectra using the strategy developed by Sussmann et al. (2011) which has been shown to agree very well with near-infrared retrievals (Sussmann et al., 2013). This retrieval method optimizes methane total column precision, while minimizing water vapor interference errors. Three spectral microwindows are analyzed (Fig. 2.6). Beside the target species, three interfering species (i. e., H₂O, HDO, and NO₂) are fitted by scaling of the respective first guess profile. Additionally, five species (CO₂, O₃, N₂O, HCl, and OCS) are considered in the model atmosphere without fitting. Absorption line data are taken from HITRAN 2000. A priori profiles are derived from a 40-year model run of the Whole Atmosphere Community Climate Model (WACCM version 6; Garcia et al., 2007).

Beside the retrieval of methane, atmospheric ethane time series are derived and utilized for the source attribution of methane trends in Chapter 3. The ethane retrieval strategy applied in this thesis follows the method described in Vigouroux et al. (2012). Two microwindows are analyzed covering the wavenumber regions of 2976.66–2976.95 cm⁻¹ and 2983.20–2983.55 cm⁻¹. For methane and ethane retrievals, the atmosphere is discretized in 43 model levels covering an altitude region up to 120 km. Pressure and temperature data are compiled from hourly ground pressure measurements and four times daily temperature profiles provided by the National Center for Environmental Prediction (NCEP).

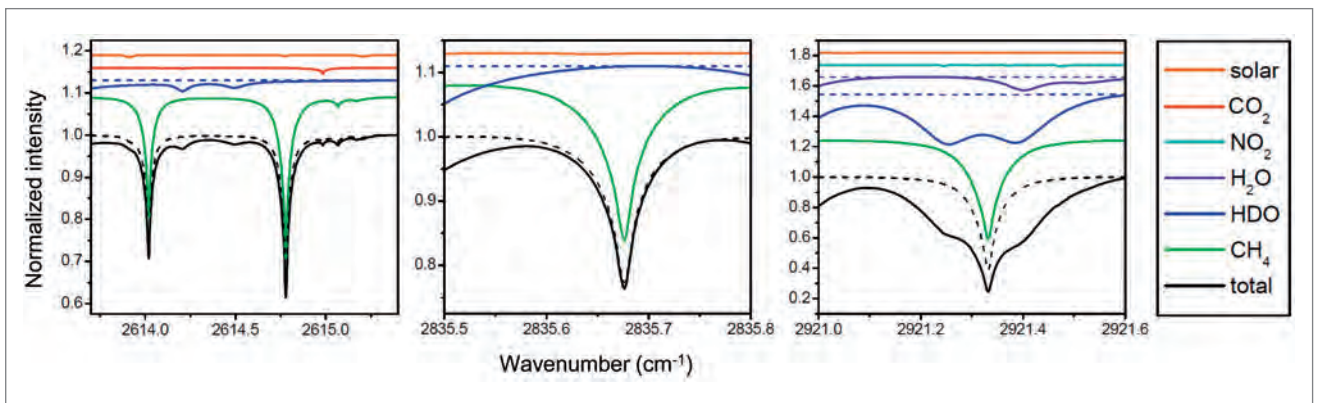


Fig. 2.6: Spectral microwindows applied in the methane retrieval: spectral contributions from target and interfering species under moist (solid lines) and dry conditions (dashed lines) at a solar zenith angle of 65° (adapted from Sussmann et al., 2011).

16.3 Renewed methane increase after 2006

Like carbon dioxide, methane is one of the most important greenhouse gases. After a period of stagnation around the year 2000, atmospheric methane concentrations started to rise again in 2007 (e.g., Sussmann et al., 2012). So far, the causes have been unknown. According to our recent solar FTIR based study, at least 40% of this increase result from the growing production of oil and natural gas in the northern hemisphere (Hausmann et al., 2016).

16.3.1 Quantifying oil and gas contribution

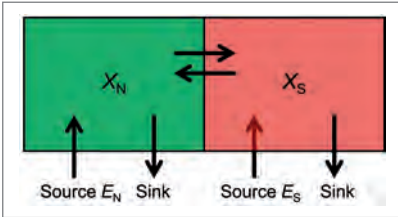


Fig. 3.1: Schematics of the atmospheric two-box model: two well-mixed hemispheres with methane and ethane sources and sinks and interhemispheric exchange.

The attribution to thermogenic methane from the oil and natural gas industry is based on our solar FTIR measurements of vertically column averaged methane and ethane (X_{CH_4} and $X_{C_2H_6}$). Apart from thermogenic methane formed within deep rock layers at high temperatures and emitted into the atmosphere as a result of oil and gas production, growing biogenic emissions by anaerobic processes are another cause. The corresponding contributions from e.g. wetlands or animal husbandry have been analyzed in parallel by other research teams. Ethane is essential for quantifying the contribution of thermogenic methane. Like methane, it is a hydrocarbon compound and one of the main components of natural gas. In case of biogenic methane sources, no simultaneous ethane emissions occur.

To investigate which kind of emissions have driven the renewed methane increase since 2007, long-term observations of methane are combined with observations of ethane, i.e., a tracer of thermogenic methane emissions. An atmospheric two-box model is applied to simulate hemispheric time series of column-averaged methane and ethane and link them to corresponding emission histories (Aydin et al., 2011; Kai et al., 2011). Two well-mixed hemispheres, each with distinct methane and ethane sources and sinks, are interconnected by interhemispheric exchange with a timescale of about 1 year (Fig. 3.1). Annual growth rates of hemispheric mean column-averaged mole fractions are determined by hemispheric emissions, chemical loss, and interhemispheric exchange, as expressed in the following equations for the Northern and the Southern Hemisphere:

$$\frac{dX_N}{dt} = E_N - \frac{X_N}{\lambda^*} - \frac{X_N - X_S}{\tau_{ex}} \quad (3.1)$$

$$\frac{dX_S}{dt} = E_S - \frac{X_S}{\lambda^*} - \frac{X_N - X_S}{\tau_{ex}} \quad (3.2)$$

Here, X_N and X_S are annual mean column-averaged mole fractions in the Northern and Southern Hemisphere, λ^* is the tracer atmospheric lifetime, and τ_{ex} is the interhemispheric exchange time. E_N and E_S are total hemispheric tracer emissions (in units of ppb yr⁻¹). The latter can be determined from global emissions (E_{glob} in Tg yr⁻¹) according to $E_N = f_N \cdot E_{glob} \cdot 2/c_{em}$ and $E_S = (1 - f_N) \cdot E_{glob} \cdot 2/c_{em}$ (with the fraction f_N of global emissions in the Northern Hemisphere and the emission unit conversion factor c_{em} in Tg ppb⁻¹).

Further analysis is based on our long-term measurements at the Zugspitze summit and from colleagues of the National Institute of Water and Atmospheric Research in Lauder, New Zealand. The solar FTIR measurements of X_{CH_4} and $X_{C_2H_6}$ are representative of the background concentration of methane and ethane in both hemispheres of the Earth. This is an advantage of total column measurements versus surface (in situ) measurements which are much more impacted by local sources. While the column measurements at the Zugspitze show a significant correlation between ethane and methane, i.e., a sudden increase of the column concentrations of both trace gases from 2007 onwards, the Lauder time series show a similar renewed increase for methane only (red and green dots in Fig. 3.2; time series have been de-seasonalized via a seasonal model, i.e., a 3rd-order Fourier series). From iterative re-calculation of X_{CH_4} and $X_{C_2H_6}$ (lines in Fig. 3.2) from assumed emissions for both hemispheres via the two-box model and performing a fit to the column measurements, we find that i) since 2007 there is at least a 40-per cent contribution from the oil- and gas sector to the global methane increase since 2007, and ii) that these observed emissions have originated from the northern hemisphere.

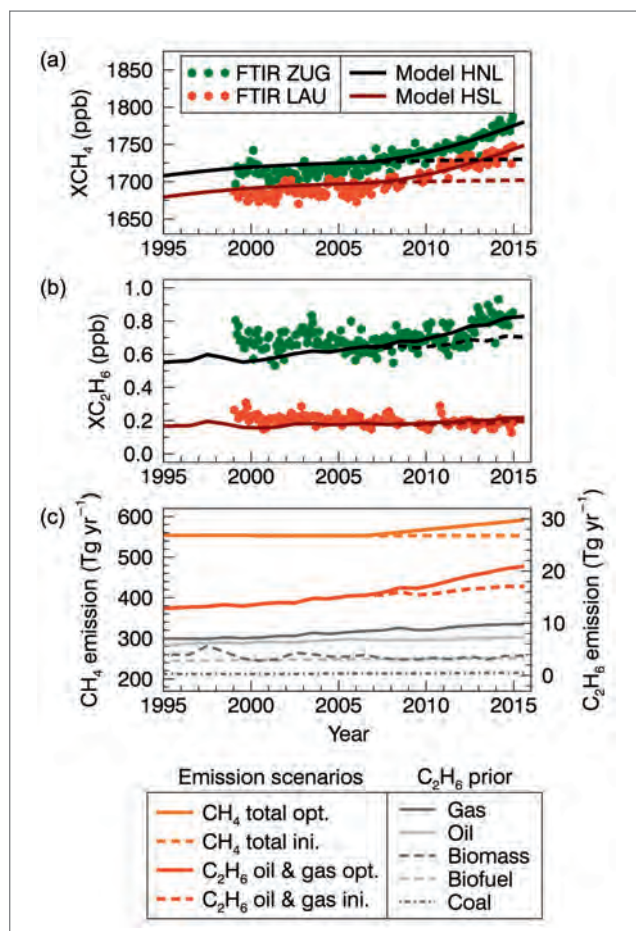


Fig. 3.2: Methane and ethane two-box model: (a) monthly mean column-averaged methane and (b) ethane from Zugspitze and Lauder FTIR observations (de-seasonalized). Modeled annual means of XCH_4 and XC_2H_6 are shown for high northern and southern latitudes (HNL, HSL) after emission optimization (solid lines) and with prior emissions (dashed lines). An overall offset is applied to the modeled time series to fit the observed average for 2007–2014. (c) Emission scenario for 2007–2014: optimized global emissions of methane (“ CH_4 total opt.,” left y axis) and ethane from oil and natural gas sources (“ C_2H_6 oil & gas opt.,” right y axis). For comparison, the corresponding initial emission histories are displayed along with prior ethane emissions of all considered source categories (taken from Hausmann et al., 2016).

16.3.2 Discussion of other methane trend contributions and synthesis

Other trend contributions. Other studies show that we cannot rule out inter-annual variations in the hydroxyl radical (OH) chemical methane sink as the cause for renewed methane increase (Rigby et al., 2017; Turner et al., 2017). However, these studies do not directly show changes in atmospheric OH or provide a mechanistic reason for a change.

In parallel to our ethane based study giving proof for increasing emissions from the oil- and gas sector, another team found a concurrent decrease in the heavy isotope content of methane ($^{13}CH_4$) which points toward an increasing biogenic source (Schaefer et al., 2016). According to their analysis, the main contribution to the renewed methane concentration increase since 2007 would be of biogenic origin, i. e., from microbial production related to animal husbandry or wet tropical environments like marshes and rice paddies. However, when their estimates plus the oil-gas-estimate from our ethane-based study (Hausmann et al., 2016) were added to estimates of other sources, the sum was considerably more than the observed increase. In fact, each estimate was large enough to explain the whole increase by itself.

Another team from California focused on fires which are also a source of methane (Worden et al., 2017). They showed that biomass burning emissions of methane decreased by $3.7 (\pm 1.4)$ Tg CH_4 per year from the 2001–2007 to the 2008–2014 time periods using satellite measurements of CO and CH_4 , nearly twice the decrease expected from prior estimates based on measurements of burnt area reduction.

Synthesis. After updating both the total and isotopic budgets for atmospheric methane with these revised biomass burning emissions (and assuming no change to the chemical sink via OH), finally our actual understanding per today is that fossil fuels contribute between 12–19 Tg CH_4 per year to the recent atmospheric methane increase, thus reconciling the isotopic- and ethane-based results (Schaefer et al., 2016; Hausmann et al., 2016; Worden et al., 2017).

16.4 Water vapor and its isotopes as transport tracer

So far, research on atmospheric long-range transport to Central Europe has mainly been based on investigations or field campaigns of special transport events combining observations of conventional tracers (such as ozone, aerosols, and humidity) at few sites. This classical approach is not sufficient to fully capture complex transport mechanisms within the global hydrological cycle.

Valuable information on tropospheric moisture pathways and associated transport of other tracers is provided by measurements of water vapor and its isotopes (Schneider et al., 2016). The isotopic composition of atmospheric water vapor is modified during phase transitions (evaporation, condensation, and sublimation) due to fractionation processes caused by isotopic mass differences (Dansgaard, 1964). The main source of water vapor in the atmosphere is evaporation from the oceans. Subsequently, air masses are transported to regions of lower temperatures, where condensation or sublimation occurs together with associated rainout. These processes cause the air mass to become increasingly dehydrated and depleted in the heavier isotope HDO. Resulting large-scale isotope effects (e.g., Worden et al., 2007) include increasing HDO depletion with higher latitudes (latitude effect), with higher altitudes (altitude effect), and with increasing distance from oceans (continental effect).

The goal of the investigations presented in this section is to evaluate new possibilities in transport research, which are provided by long-term consistent H_2O - δD observations via solar FTIR spectrometry. The results were published in Hausmann et al. (2017). A combined H_2O - δD retrieval (Sect. 16.2.3) is applied to an exemplary midlatitude FTIR site (i. e., Mt. Zugspitze). The resulting Zugspitze water vapor time series is an update of Sussmann et al. (2009) including isotopic information (Sect. 16.4.1). Our main subsequent goal is to identify distinct H_2O - δD signatures for long-range transport patterns (Sect. 16.4.2).

16.4.1 Long-term H_2O - δD time series at Zugspitze

Time series of daily mean integrated water vapor (IWV) and column-based δD above Mt. Zugspitze are presented in Fig. 4.1 for the period 2005–2015. For column-based δD , a statistically insignificant trend of 0.8 [−3.1, 4.7] % per decade is inferred (relative to the overall $\delta\text{D}_{\text{col}}$ mean). The IWV time series yields a weakly positive but also insignificant trend of 2.4 [−5.8, 10.6] % per decade (relative to the overall IWV mean). Over the same time period, temperature increas-

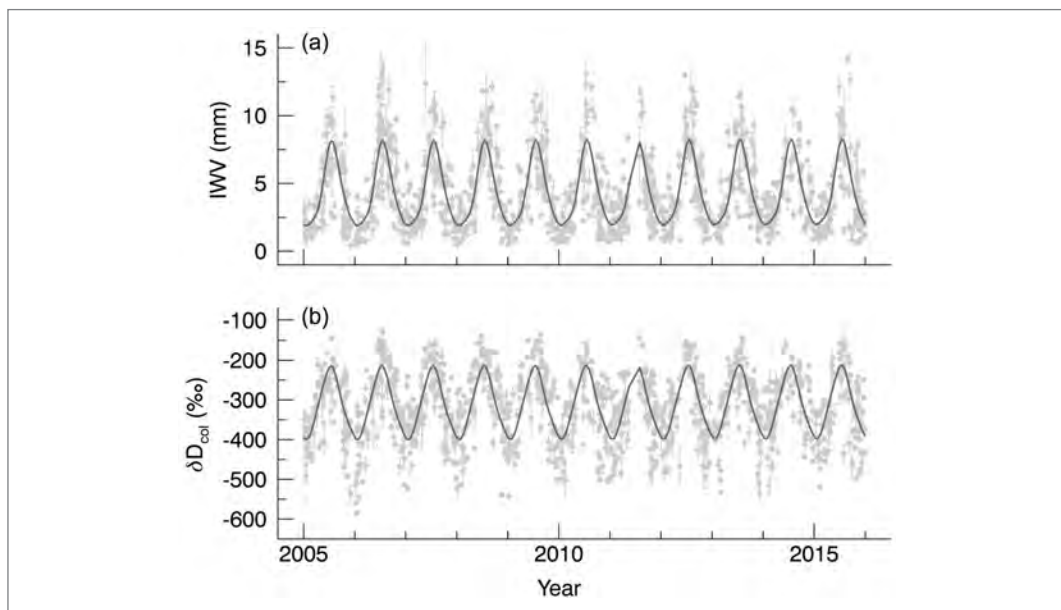


Fig. 4.1: Daily mean time series of (a) integrated water vapor and (b) column-based δD retrieved from Zugspitze FTIR measurements. Error bars indicate ± 2 standard errors of daily means and grey lines show seasonal cycles determined by fitting a third-order Fourier series (taken from Hausmann et al., 2017).

es significantly (1.3 [0.5, 2.1] K per decade) at Mt. Zugspitze. This has been derived from daily mean temperature data based on hourly in situ measurements, which are coincident with FTIR data (coincidence interval ± 30 min). Assuming constant relative humidity (RH) and following the Clausius-Clapeyron equation, the observed temperature increase translates to a positive IWW trend of 9.2 [3.7, 14.7] % per decade. This calculated IWW trend agrees with the observed IWW trend within uncertainties. The assumption of constant RH is valid on large spatial scales, while over specific land regions RH might have slightly decreased (IPCC, 2013), which would explain the relatively large calculated IWW trend compared to observations.

16.4.2 H₂O- δ D signatures of long-range transport events

Here we examine to what extent H₂O- δ D observations can provide information on long-range transport events. We investigate three distinct long-range transport patterns to the Central European free troposphere, defined as follows.

Intercontinental transport from North America (TUS). This transport pattern may carry anthropogenic pollution plumes (e. g., ozone or aerosols) to Central Europe within typically 3–10 days (Stohl and Trickl, 1999; Huntrieser et al., 2005). Consequently, North American emissions strongly contribute to the European total column tracer mass (i. e., 43% for a tracer with 10 days lifetime; Stohl et al., 2002). The typical pathway of polluted boundary layer air from North America is uplift in a warm conveyor belt (WCB, i. e., an ascending air stream ahead of a surface cold front in an extratropical cyclone) and subsequent transport by strong westerly flows in the middle-upper troposphere. The North American tracer enters Europe typically in altitudes of 5–8 km and at high latitudes (> 60 °N). Here, the circulation frequently turns anticyclonic and tracers eventually reach Northern Alps (Huntrieser and Schlager, 2004). WCB climatologies reveal a major inflow region at the southeastern coast of North America (Madonna et al., 2014). In the following, Zugspitze backward trajectories passing this source region (25–45 °N, 70–110 °W, 0–2 km altitude) are assigned to the TUS category.

Intercontinental transport from Northern Africa (TNA). This second transport category leads to associated transport of Saharan mineral dust influences air quality, soil fertility, radiative budget, and atmospheric oxidation capacity in the receptor region (Ravishankara, 1997). Saharan mineral dust import to Central Europe occurs 5–15 times per year and each event lasts 1–3 days (Flentje et al., 2015). In the following, Zugspitze backward trajectories passing the Saharan boundary layer region (15–30 °N, 15 °W–35 °E, 0–2 km altitude; Engelstaedter et al., 2006) are assigned to the TNA category.

Extratropical stratospheric intrusions (STI). The third transport class accounts for events, which occur mainly in synoptic-scale processes such as tropopause folds and cutoff lows near the polar or subtropical jet stream (Stohl et al., 2003). Filaments of ozone-rich stratospheric air descend from the lowermost stratosphere and proceed to the Central European free troposphere via several pathways (Škerlak et al., 2014). Mixing with tropospheric air might exhibit relatively long time scales and little modification is reported even after several days of transport (Trickl et al., 2014). In the following, Zugspitze backward trajectories originating above the zonal mean tropopause (TP) taken from ECMWF data (Eckhardt et al., 2004) at latitudes above 20 °N are assigned to the STI category (required minimum residence time of five hours above TP, which is penetrated at least once by more than 1 km).

H₂O- δ D signatures of transport events. The described long-range transport categories (TUS, TNA, STI) are expected to have characteristic imprints on H₂O- δ D pairs observed at Mt. Zugspitze. Stratospheric intrusions originate in the lowest few kilometers of the stratosphere, where moisture content is extremely low and the mean δ D profile exhibits a minimum before increasing above due to growing influence of isotopically heavier water vapor from methane oxidation (Zahn et al., 2006). Consequently, STI events potentially import relatively dry and HDO depleted air masses to the Central European troposphere. In contrast, TUS and TNA air masses originate in the moist boundary layer and may transport relatively moist and less depleted air masses. However, strong WCB updraft during TUS events may cause air mass dehydration and HDO depletion through rainout (Rayleigh process). Criteria for long-range transport events described above are applied to categorize Zugspitze backward trajectories as shown in Fig. 4.2. Distributions of de-seasonalized VMR_{H₂O} and δ D for the corresponding classes of free tropo-

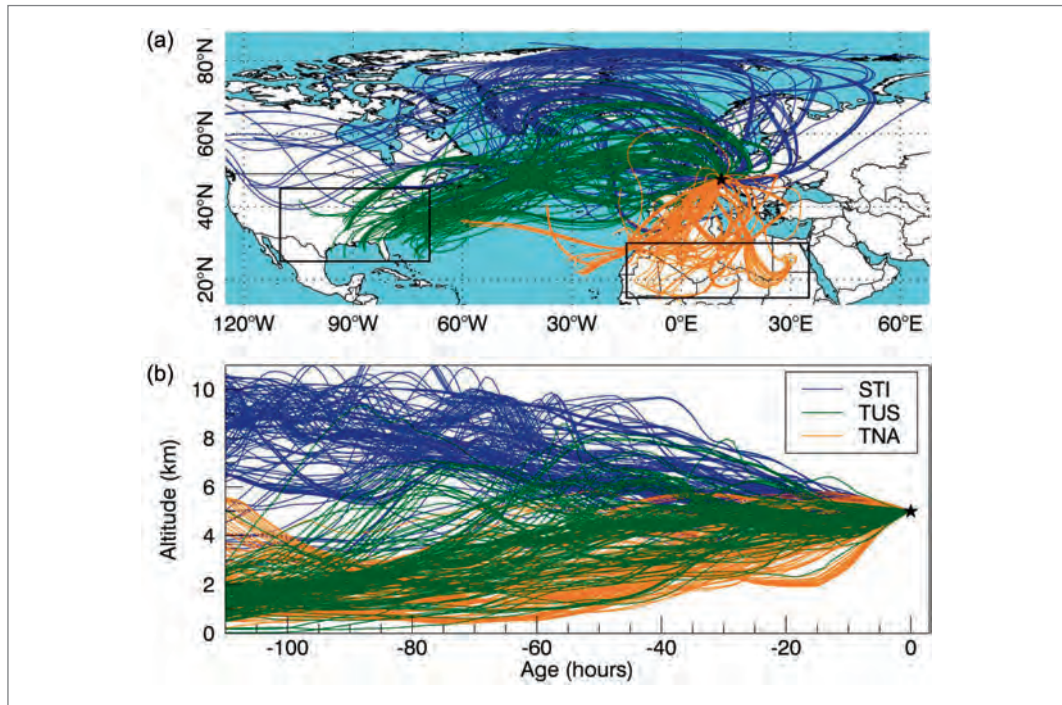


Fig. 4.2: Categorization of backward trajectories for long-range transport events: (a) map projection and (b) vertical cross section for stratospheric intrusions (STI), transport from North America (TUS), and from Northern Africa (TNA). Black boxes indicate source regions used to classify TUS and TNA (Table 4.1), black star marks Mt. Zugspitze (taken from Hausmann et al., 2017).

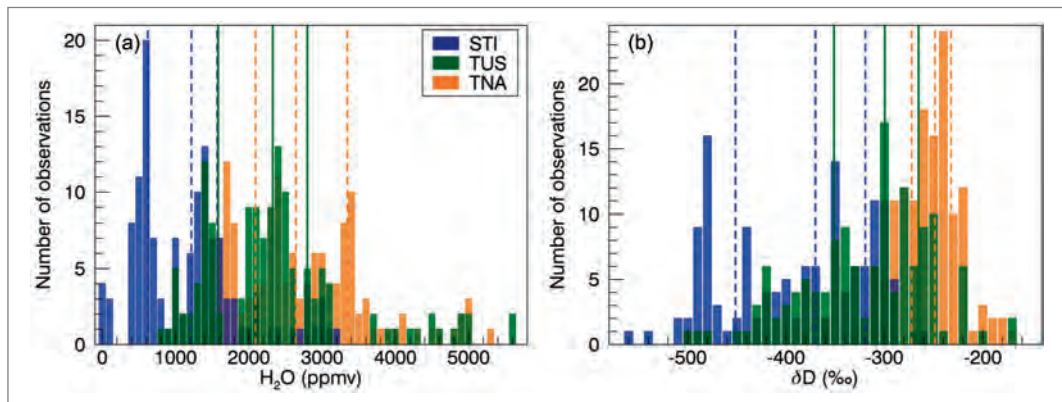


Fig. 4.3: H_2O - δD signatures of long-range transport events: distribution of deseasonalized (a) $\text{VMR}_{\text{H}_2\text{O}}$ and (b) δD in the free troposphere above Zugspitze (5 km a.s.l.) for trajectory classes shown in Fig. 4.2. Vertical lines mark corresponding 25th, 50th, and 75th percentiles of the distributions while mean and standard errors are given in Table 4.1 (taken from Hausmann et al., 2017).

spheric Zugspitze FTIR data (5 km a.s.l.) are depicted in Fig. 4.3. Considering uncertainty of two standard errors, mean $\text{VMR}_{\text{H}_2\text{O}}$ and δD values are significantly different for all three transport classes (Table 4.1).

As expected, STI is associated with the driest and most HDO depleted air masses. TNA is connected to moister and less depleted air, while TUS exhibits intermediate $\text{VMR}_{\text{H}_2\text{O}}$ and δD values. The standard deviation of $\text{VMR}_{\text{H}_2\text{O}}$ distributions is similar for all transport classes ($\text{SD} \approx 1000$ ppmv). In the case of δD distributions, TNA shows less scatter ($\text{SD} = 34\%$) compared to TUS ($\text{SD} = 65\%$) and STI ($\text{SD} = 73\%$). This indicates a quite homogeneous source region and transport regime for TNA. Larger scatter for TUS might result from variable strengths of WCB uplift causing various levels of dehydration and HDO depletion. Relatively large scatter in the δD distribution for STI events implies that also weakly depleted air masses are observed during STI events. This could have several reasons: First, stratospheric intrusions with depths ranging from few hundreds to several thousands of meters are not necessarily resolved by the vertical resolution

	STI	TUS	TNA
Trajectory source region:			
Latitude	> 20° N	25–45° N	15–30° N
Longitude	–	70–110° W	15° W–35° E
Altitude	> zonal mean TP	0–2 km	0–2 km
H ₂ O- δ D signature (mean \pm 2 SE):			
VMR _{H₂O} (10 ³ ppmv)	1.21 [1.07, 1.34]	2.42 [2.25, 2.59]	2.78 [2.63, 2.93]
δ D (‰)	–384 [–397, –372]	–315 [–326, –303]	–251 [–257, –246]

Table 4.1: Backward trajectory classification for long-range transport patterns of stratospheric intrusions (STI), transport from North America (TUS), and from Northern Africa (TNA) along with the resulting distribution of deseasonalized VMR_{H₂O} and δ D.

of the FTIR. Second, as a climatological tropopause altitude is applied to identify STI events, local and seasonal TP variations are not accounted for, i. e., also (upper) tropospheric trajectories might be included in the STI class. Third, mixing with tropospheric air might occur during transport from the stratosphere, which however was found to be very slow in the free troposphere (Trickl et al., 2014). Fourth, δ D values in the lower stratosphere might be less depleted than predicted from Rayleigh processes, which is probably caused by extratropical troposphere–stratosphere transport, e. g., by convectively lofted ice (Randel et al., 2012). All these mechanisms would yield higher δ D observations at Zugspitze than expected for STI events from the δ D minimum in the lower stratosphere.

A first order interpretation of the H₂O- δ D data pairs can be obtained by their comparison to theoretical Rayleigh and mixing lines (Schneider et al., 2015; González et al., 2016). Such a comparison is illustrated in Fig. 4.4, which shows Zugspitze H₂O- δ D data at 5 km altitude along with simulated Rayleigh and mixing processes. An idealized Rayleigh process simulates the gradual dehydration of an air parcel during adiabatic cooling with immediate removal of the condensate. During this process, the remaining water vapor becomes depleted in HDO. Rayleigh dehydration processes (black lines in Fig. 4.4) are simulated using a mean midlatitude profile of pressure and temperature (Christner, 2015, Table 13) and initial evaporation conditions which are characteristic for midlatitude oceanic or continental moisture sources ($T = 15^\circ\text{C}$, $\text{RH} = 80\%$, and δD values of -60% , -130% , and -160%). Furthermore, mixing processes are simulated (dark red lines in Fig. 4.4) for moist lower-middle tropospheric air masses with dry, HDO depleted upper tropospheric air ($\text{VMR}_{\text{H}_2\text{O}} = 200$ ppmv, $\delta\text{D} = -585\%$). The δD value of the mixture is mainly determined by the δD value of the mixing partner with higher water vapor content (Noone et al., 2012). Three moist mixing partners are considered here: (i) boundary layer air with $\text{VMR}_{\text{H}_2\text{O}} = 13500$ ppmv and $\delta\text{D} = -130\%$, (ii) moderately dehydrated and depleted air with $\text{VMR}_{\text{H}_2\text{O}} = 6100$ ppmv and $\delta\text{D} = -200\%$, and (iii) even more dehydrated air with $\text{VMR}_{\text{H}_2\text{O}} = 3000$ ppmv and $\delta\text{D} = -270\%$.

A comparison of such simulations of Rayleigh and mixing lines with H₂O- δ D data pairs for the 3 long-range transport patterns is depicted in Fig. 4.4: For TNA events, it can be derived from this analysis that moist boundary layer air is imported to the free troposphere by means of dry convection without significant condensation and cloud formation (González et al., 2016). Therefore, TNA air masses are less depleted

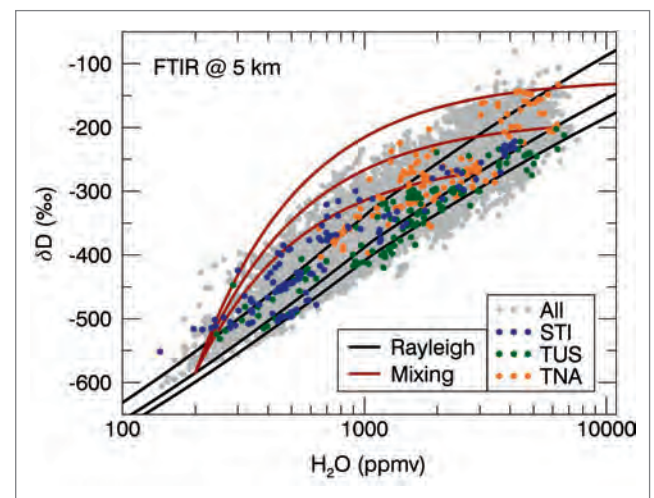


Fig. 4.4: H₂O- δ D distribution of free tropospheric measurements above Zugspitze (5 km a.s.l.) for all 2005–2015 data and for long-range transport categories shown in Fig. 4.2. Simulated Rayleigh and mixing processes are shown for comparison (taken from Hausmann et al., 2017).

in HDO (higher δD values). In case of TUS events, either dry or moist air masses can be imported to Central Europe. TUS transport is generally in line with agrees with Rayleigh models. In case of dry STI events, air masses seem to be partially influenced by mixing processes of dry upper tropospheric or lower stratospheric air with free tropospheric air masses.

16.5 Conclusions

Solar FTIR spectrometry is a powerful technique to obtain atmospheric columns and vertical concentration profiles from more than three dozens of trace gases. This technique has become the dominant science-driven ground-based remote sounding technique in atmospheric research. NDACC-type network solar FTIR measurements in the mid-infrared allow to measure more species and attain more information on vertical profiles, while TCCON-type near-infrared FTIR measurements enable higher accuracy for greenhouse gases (GHG). TCCON has thereby become the reference for satellite measurements of GHG and contributes to the global inverse modelling of sources and sinks of GHG.

The advantage of solar FTIR spectrometry compared to surface in situ techniques is that it measures the total column and thereby is less sensitive to local sources. E. g., Zugspitze methane column soundings are representative for the whole high northern hemisphere. Additionally, solar FTIR provides the same quantity (total columns) as satellites and can thereby be used as ground reference. In the near future new generation multi-spectral channel solar FTIR spectrometers will allow for simultaneous NDACC- and TCCON-type measurements, which enables to exploit the advantages of both techniques within one instrument. Small mobile solar FTIRs have become available recently and this opens a variety of new applications, e. g., differential column soundings at multiple locations around a large city allow to infer the total GHG emission rate.

After a period of stagnation around the year 2000, atmospheric methane concentrations started to rise again in 2007. We have shown that at least 40% of this increase during 2007–2014 resulted from the growing production of oil and natural gas in the northern hemisphere. Our result suggests a connection to the North American oil and natural gas boom that started in 2007. Given that most of the oil and gas boom of the last decade has occurred in the US this would contradict official estimates of the US Environmental Protection Agency (EPA) that reported constantly low or even decreasing methane emissions from the oil and natural gas sector in the US during the last ten years.

These inconsistencies might be explained by assuming too small leakage rates from the production and use of oil and natural gas. While EPA uses extrapolations of random samples (bottom-up estimate), our study uses representative atmospheric background measurements (top-down method). There is need for further research to explain discrepancies between bottom-up and top-down estimates.

Finally, distinct H_2O - δD fingerprints were found in Zugspitze FTIR data for three categories of long-range transport patterns, namely intercontinental transport from North America (TUS), intercontinental transport from Northern Africa (TNA), and extratropical stratospheric intrusions (STI). Consequently, we have demonstrated that combined consistent H_2O - δD observations can serve as a valuable new transport tracer to study atmospheric transport to the Central European free troposphere.

This finding is relevant for forecasting parameters like aeroallergens, and aerosols which impact human health. In case critical thresholds are exceeded, the question is whether this situation will persist in the days to follow. The answer is often related to long-range atmospheric transport events. E. g., in case of polar air intrusions to mid-latitudes extremely cold and dry conditions will persist, while during subtropical intrusions moist and humid air with an elevated aerosol load will prevail for several days. However, a forecast of such persisting situations is not possible via now casting of the environmental health parameters. A future solution to this problem could be the operational monitoring and analysis of atmospheric transport indicators as the H_2O - δD observations investigated here.

Acknowledgments

Our work has been performed as part of the ESA GHG-cci project. In addition we acknowledge funding by the EC within the INGOS project and by the Bavarian State Ministry of the Environment and Consumer Protection via grant VAO-IITPI/01.

References

- Aydin, M. et al.: Recent decreases in fossil-fuel emissions of ethane and methane derived from firm air, *Nature*, 476, 198–201, doi:10.1038/nature10352, 2011.
- Alvarez, R.A. et al.: Greater focus needed on methane leakage from natural gas infrastructure, *Proc. Natl. Acad. Sci. USA*, 109, 6435–6440, doi:10.1073/pnas.1202407109, 2012.
- Brasseur, G.P. and Solomon, S.: *Aeronomy of the Middle Atmosphere: Chemistry and Physics of the Stratosphere and Mesosphere*, vol. 32 of *Atmospheric and Oceanographic Sciences Library*, Springer, Dordrecht, The Netherlands, 3rd edn., 2005.
- Christner, E.: Messungen von Wasserisotopologen von der planetaren Grenzschicht bis zur oberen Troposphäre zur Untersuchung des hydrologischen Kreislaufs, Ph.D. thesis, Karlsruhe Institute of Technology, Germany, available at: <https://publikationen.bibliothek.kit.edu/1000046021> (last access: 3 October 2016), 2015.
- Craig, H.: Standard for reporting concentrations of deuterium and oxygen-18 in natural waters, *Science*, 133, 1833–1834, doi:10.1126/science.133.3467.1833, 1961.
- Dansgaard, W.: Stable isotopes in precipitation, *Tellus*, 16, 436–468, doi:10.1111/j.2153-3490.1964.tb00181.x, 1964.
- Eckhardt, S. et al.: A 15-year climatology of warm conveyor belts, *J. Clim.*, 17, 218–237, doi:10.1175/1520-0442(2004)017<0218:AYCOWC>2.0.CO;2, 2004.
- Flentje, H. et al.: Identification and monitoring of Saharan dust: An inventory representative for south Germany since 1997, *Atmos. Environ.*, 109, 87–96, doi:10.1016/j.atmosenv.2015.02.023, 2015.
- García, R., Marsh, D., Kinnison, D., Boville, B., and Sassi, F.: Simulation of secular trends in the middle atmosphere, 1950–2003, *J. Geophys. Res.*, 112, 2156–2202, doi:10.1029/2006JD007485, 2007.
- González, Y. et al.: Detecting moisture transport pathways to the subtropical North Atlantic free troposphere using paired H₂O- δ D in situ measurements, *Atmos. Chem. Phys.*, 16, 4251–4269, doi:10.5194/acp-16-4251-2016, 2016.
- Hausmann, P., Sussmann, R., and Smale, D.: Contribution of oil and natural gas production to renewed increase in atmospheric methane (2007–2014): top-down estimate from ethane and methane column observations, *Atmos. Chem. Phys.*, 16, 3227–3244, doi:10.5194/acp-16-3227-2016, 2016.
- Hausmann, P., Sussmann, R., Trickl, T., and Schneider, M.: A decadal time series of water vapor and D / H isotope ratios above Zugspitze: transport patterns to central Europe, *Atmos. Chem. Phys.*, 17, 7635–7651, doi:10.5194/acp-17-7635-2017, 2017.
- Huntrieser, H. and Schlager, H.: Air pollution export from and import to Europe: Experimental evidence, in: *Intercontinental Transport of Air Pollution*, edited by Stohl, A., pp. 69–98, Springer, Berlin, Germany, doi:10.1007/b10681, 2004.
- Huntrieser, H. et al.: Intercontinental air pollution transport from North America to Europe: Experimental evidence from airborne measurements and surface observations, *J. Geophys. Res.*, 110, D01 305, doi:10.1029/2004jd005045, 2005.
- IPCC: *Climate Change 2013: The Physical Science Basis. Contribution of Working Group I to the Fifth Assessment Report of the Intergovernmental Panel on Climate Change*, edited by: Stocker, T.F. et al., Cambridge University Press, Cambridge, United Kingdom and New York, NY, USA, 2013.
- Kai, F.M. et al.: Reduced methane growth rate explained by decreased Northern Hemisphere microbial sources, *Nature*, 476, 194–197, doi:10.1038/nature10259, 2011.
- Kiehl, J.T. and Trenberth, K. E.: Earth's annual global mean energy budget, *Bull. Am. Meteorol. Soc.*, 78, 197–208, doi:10.1175/1520-0477(1997)078<0197:EAGMEB>2.0.CO;2, 1997.
- Liou, K. N.: An Introduction to Atmospheric Radiation, vol. 84 of *International Geophysics Series*, Elsevier Science, San Diego, USA, 2nd edn., 2002.
- Madonna, E. et al.: Warm Conveyor Belts in the ERA-Interim Dataset (1979–2010). Part I: Climatology and Potential Vorticity Evolution, *J. Clim.*, 27, 3–26, doi:10.1175/jcli-d-12-00720.1, 2014.
- Noone, D.: Pairing Measurements of the Water Vapor Isotope Ratio with Humidity to Deduce Atmospheric Moistening and Dehydration in the Tropical Midtroposphere, *J. Clim.*, 25, 4476–4494, doi:10.1175/jcli-d-11-00582.1, 2012.
- Randel, W.J., Moyer, E., Park, M., Jensen, E., Bernath, P., Walker, K., and Boone, C.: Global variations of HDO and HDO/H₂O ratios in the upper troposphere and lower stratosphere derived from ACE-FTS satellite measurements, *J. Geophys. Res.*, 117, D06 303, doi:10.1029/2011jd016632, 2012.

- Ravishankara, A. R.: Heterogeneous and multiphase chemistry in the troposphere, *Science*, 276, 1058–1065, doi:10.1126/science.276.5315.1058, 1997.
- Rigby, M. et al.: Role of atmospheric oxidation in recent methane growth, *Proc. Natl. Acad. Sci. USA* 114, 5373–5377, doi:10.1073/pnas.1616426114, 2017.
- Rothman, L. et al.: The HITRAN2012 molecular spectroscopic database, *J. Quant. Spectrosc. Radiat. Transfer*, 130, 4–50, doi:10.1016/j.jqsrt.2013.07.002, 2013.
- Schaefer, H. et al.: A 21st century shift from fossil-fuel to biogenic methane emissions indicated by $^{13}\text{CH}_4$, *Science*, 352, 80–84, doi:10.1126/science.aad2705, 2016.
- Schneider, M. et al.: Empirical validation and proof of added value of MUSICA's tropospheric δD remote sensing products, *Atmos. Meas. Tech.*, 8, 483–503, doi:10.5194/amt-8-483-2015, 2015.
- Škerlak, B., Sprenger, M., and Wernli, H.: A global climatology of stratosphere–troposphere exchange using the ERA-Interim data set from 1979 to 2011, *Atmos. Chem. Phys.*, 14, 913–937, doi:10.5194/acp-14-913-2014, 2014.
- Stohl, A. and Trickl, T.: A textbook example of long-range transport: Simultaneous observation of ozone maxima of stratospheric and North American origin in the free troposphere over Europe, *J. Geophys. Res.*, 104, 30 445–30 462, doi:10.1029/1999JD900803, 1999.
- Stohl, A. et al.: On the pathways and timescales of intercontinental air pollution transport, *J. Geophys. Res.*, 107, 4684, doi:10.1029/2001jd001396, 2002.
- Stohl, A. et al.: Stratosphere-troposphere exchange: A review, and what we have learned from STACCATO, *J. Geophys. Res.*, 108, 8516, doi:10.1029/2002jd002490, 2003.
- Sussmann, R. and Schäfer, K.: Infrared spectroscopy of tropospheric trace gases: combined analysis of horizontal and vertical column abundances, *Appl. Opt.*, 36, 735–741, doi:10.1364/AO.36.000735, 1997.
- Sussmann, R. et al.: Harmonized retrieval of column-integrated atmospheric water vapor from the FTIR network – first examples for long-term records and station trends, *Atmos. Chem. Phys.*, 9, 8987–8999, doi:10.5194/acp-9-8987-2009, 2009.
- Sussmann, R., Forster, F., Rettinger, M., and Bousquet, P.: Renewed methane increase for five years (2007–2011) observed by solar FTIR spectrometry, *Atmos. Chem. Phys.*, 12, 4885–4891, doi:10.5194/acp-12-4885-2012, 2012.
- Sussmann, R., Forster, F., Rettinger, M., and Jones, N.: Strategy for high-accuracy-and precision retrieval of atmospheric methane from the mid-infrared FTIR network, *Atmos. Meas. Tech.*, 4, 1943–1964, doi:10.5194/amt-4-1943-2011, 2011.
- Sussmann, R., Ostler, A., Forster, F., Rettinger, M., Deutscher, N. M., Griffith, D. W. T., Hannigan, J. W., Jones, N., and Patra, P. K.: First intercalibration of column-averaged methane from the Total Carbon Column Observing Network and the Network for the Detection of Atmospheric Composition Change, *Atmos. Meas. Tech.*, 6, 397–418, doi:10.5194/amt-6-397-2013, 2013.
- Tikhonov, A.: On the solution of incorrectly stated problems and a method of regularization, *Dokl. Acad. Nauk SSSR*, 151, 501–504, 1963.
- Trickl, T., et al.: How stratospheric are deep stratospheric intrusions?, *Atmos. Chem. Phys.*, 14, 9941–9961, doi:10.5194/acp-14-9941-2014, 2014.
- Turner, A. J. et al.: Ambiguity in the causes for decadal trends in atmospheric methane and hydroxyl, *Proc. Natl. Acad. Sci. USA*, 114, 5367–5372, doi:10.1073/pnas.1616020114, 2017.
- Vigouroux, C. et al.: FTIR time-series of biomass burning products (HCN, C_2H_6 , C_2H_2 , CH_3OH , and HCOOH) at Reunion Island (21 °S, 55 °E) and comparisons with model data, *Atmos. Chem. Phys.*, 12, 10 367–10 385, doi:10.5194/acp-12-10367-2012, 2012.
- Worden, J., et al.: Importance of rain evaporation and continental convection in the tropical water cycle, *Nature*, 445, 528–532, doi:10.1038/nature05508, 2007.
- Worden, J. R., Bloom, A. A., Pandey, S., Jiang, Z., Worden, H. M., Walker, T. W., Houweling, S., Röckmann, T.: Reduced biomass burning emissions reconcile conflicting estimates of the post-2006 atmospheric methane budget, *Nature Comm.*, 8, 2227, doi:10.1038/s41467-017-02246-0, 2017.
- Zahn, A. et al.: Modelling the budget of middle atmospheric water vapour isotopes, *Atmos. Chem. Phys.*, 6, 2073–2090, doi:10.5194/acp-6-2073-2006, 2006.

17 Environmental Medicine in the Alpine Region

Claudia Traidl-Hoffmann and Volker Schiller
University of Augsburg, Institute for Environmental Medicine

17.1 Introduction

17.1.1 Environmental health sciences and environmental medicine

Until the turn from the second to the third millennium, our standpoint as medical researchers had been mainly defined [1, 2] by the science of the physical response, especially immune mechanisms, in case of disease. With the start of the 21st century, however, **the interactions between the body and its exposome** has become more and more the focus of health sciences. The exposome is either of biogenic origin, such as pollen and UV irradiation, or anthropogenic origin, such as air pollutants from traffic. Today, plenty of newly classified environments define various interactions. One exemplary environment are microbe populations that co-exist on the surfaces of bodies likewise from men and animals as well as on elementary materials such as soil and water or even on more abstract objects like industrial dust or pollen. Another environment comprises natural factors such as geographic characteristics or soil properties but also plant diversity and air conditions. (Psycho-)Social relations constitute another environment, with discernible effects on people's well-being and care. Many more environments have been and will be defined. All the environments interact with each other and with the body. Environmental medicine explores all possible environments and consequent interactions on a molecular level and in their full reciprocity with the body system.

17.1.2 Environmental medicine in the alpine region

At different altitudes exist alternating climatic, floristic, and faunal conditions. Some alpine regions feature less harmful and less numerous environmental factors and additionally provide lower noise and stress levels. Patients with severe diseases who retreat to the alpine region often report a decrease in symptoms and a general uplift of mood and physical strength [3]. Now, **our research mission is to investigate the interactions and molecular mechanisms** that cause these benefits – with a focus on allergic diseases – and to make them applicable **for diagnosis, therapy, and prevention** of allergies and allergy related, chronic inflammatory skin diseases. Therefore, we as scientists and physicians perform patient monitoring and treatment together with a minute documentation of clinical parameters. We also precisely observe and measure environmental factors. As a co-benefit, this research delivers results about health effects caused by climate change and environmental pollution. Research in the alpine region, moreover, helps us to develop a set of educational measures: how to avoid risk factors, how to treat and prevent properly, and how to improve the quality of life for patients and relatives in rural and urban regions.

17.2 Basic information

17.2.1 Biology of pollen

Pollen grains primarily bear a natural mission: Pollen is produced for matters of reproduction by flowering plants such as deciduous trees, conifers, and weeds. This natural mission is an unitary adaptive function to reach a receptive stigma and to deliver two haploid nuclei to the recipient ovary in order to transmit genetic information from the male parent to the offspring. For fertilisation to be achieved, pollen must establish molecular congruity or compatibility with the stigma. Thus, there must be a continuous exchange of both physical and chemical signals between pollen and pistil from the moment a pollen grain arrives on the stigma to the moment the pollen tube enters the ovule (reviewed in [4]). Allergists and immunologists have neglected the view about the "natural mission" of pollen grains for the last decades. Instead, they have focused basically on the allergen alone. However, the immune system is not necessarily ex-

posed to the allergen in pure manner, but rather in particulate form, either by pollen or by their starch granules. Most probably, a pollen grain that lands on the mucosal surface tries to find out whether it is on the right germination surface. Consequently, a cross talk similar to the natural process will start with the release of an array of substances from the pollen to become recognised – however, without success on men. Nevertheless, the nasal mucosa is exposed to all the substances responsible for the pollen-stigma intercourse. In summary, pollen resemble complex biological packages that deliver a composition in myriads of substances which – as discussed in detail below – do indeed have a biological function on the human immune system.

17.2.2 Pollen monitoring

Pollen monitoring is the basis to detect the number, localisation, prevalence, and variety of airborne allergens in different altitudes and under consideration of varying environmental factors [5, 6]. Concomitant measures of air pollutants, like nitric oxides, and environmental factors, such as ozone, can be correlated to the microbial load and allergenicity of pollen [7]. Together, sites for pollen observation deliver comprehensive data that is a prerequisite to compare the effect between aeroallergens and air pollutants on health at moderate to high altitudes and between urban versus non-urban environments.

The **personal pollen trap** is of special interest to environmental medicine as it enables the researchers, first of all, to receive information about indoor airborne particles. Secondly, this sampler is of interest to physicians because the obtained results give a clue about each patient's personal exposure to allergens. The portable pollen sampler has a steady draught of 10 litres of air per minute, which equals an average human breath. The **volumetric pollen and spore trap** operates on the principle of Hirst. Again, 10 litres of air is ducted within one draught of the sampler to an adhesive tape where fine air particles stick on it. The tape is placed in a cylinder that rotates by clockwork for the duration of one week. After its removal, the ready tape is prepared on microscope slides and thus becomes analyzable for several decades. By the use of a microscope, scientists can identify the pollen types and count their number with statistical methods. A volumetric pollen trap gives evidence about pollen flight in two-hour intervals. Theoretically speaking, it was possible to count other airborne particles on the slides, too. The **fully automated pollen sampler** has a draught of 1000 litres air per minute. The air particles tap to an object carrier which is then directly analyzed in the pollen monitor. Inside the monitor, the particles become digitalized by a high-resolution camera. The individual pollen are further identified and counted by an image recognition software as well as by the help of a neuronal network. Finally, the collected data becomes available in a file. This file can be immediately sent to a server and graphically depicted on screen.

A combined analysis of data from different pollen samplers and data from weather and climate stations [5, 6, 8] makes a detailed and accurate pollen forecast possible. However, solely the automatic pollen sampler allows an online information service about real-time pollen concen-

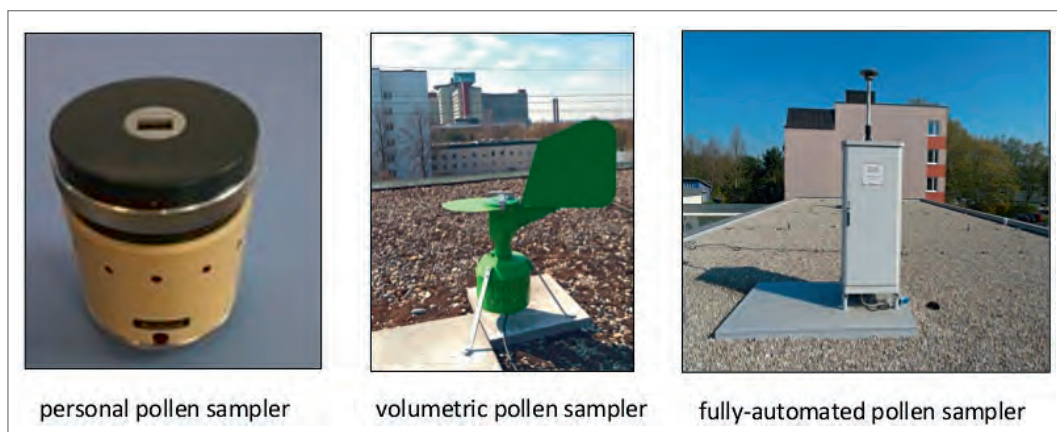


Fig. 1. The current three methods for pollen data collection: personal pollen sampler, volumetric pollen sampler, and an automatic pollen sampler. The Klinikum Augsburg und the UNIKA-T office premises are visible in the background of the latter two photos.

tration [9]. The combination of forecast and live data empowers allergic patients to correctly adjust their medication and to carefully plan leisure activities. The pollen data, moreover, contributes to political decisions, for example to the sensible construction of green areas in urban regions or the reduction of climate pollutants in air and soil. The primary objective of pollen observation is an increase in the quality of life for allergic patients. As a secondary consequence, the financial and organisational burdens for likewise health systems and employers could be lowered because of less sick reports caused by allergic diseases.

17.2.3 Allergies and skin diseases

The basis for a focus on therapy and prevention in the alpine region with regards to allergies and allergy-related, chronic inflammatory (epithelial) diseases stems from the fact that these diseases recordably rise in incidence and prevalence, notably among children and foremost in highly industrialized regions. **Allergic diseases pose the most hazardous epidemiological threat** worldwide at the start point of the 21st century. Allergies are non-communicable diseases (NCDs) and further characterized by their tendency for chronicity, their suggestibility to environmental factors, and their potential to trigger comorbidities such as atopic eczema [10].

17.2.3.1 Pathogenesis of allergic diseases

An allergen is per se a harmless protein to which the immune system normally develops a tolerogenic (immune) response [11, 12]. Importantly, allergen carriers like pollen release not only the (allergenic) proteins but also low molecular substances such as lipid mediators or adenosine that function as danger signals [11, 13–15]. These adjuvant factors pave the way in susceptible individuals towards an Th2-dominated immune response. According to Coombs and Gell, four different types of allergic responses exist. The allergies of type I (immediate reaction) and type IV (delayed type reaction) are of immediate relevance for environmental medicine because their pathogenesis is largely associated with environmental factors such as pollen, house dust mite, food (type I allergy), and fragrances or nickel (type IV allergy). An allergic disease begins with a **sensitisation phase** and can lead over to an **inflammation phase** after subsequent exposure to the allergen. During sensitisation, i. e. on first contact with an allergen, allergen-specific antibodies (IgE for type I allergy) are produced by B-cells and bound to mast cells, basophils, eosinophils, dendritic cells, and many more. The phase of the allergic cascade does not come along with symptoms. This “phase” of sensitisation can persist for many years. After a certain time – and it has not become clear yet when and why someone is susceptible, not even the someone – the re-exposure to the allergen results in the induction of an allergic inflammation with clinical symptoms. Note that only the presence of allergic symptoms legitimates for the diagnosis “allergy”, not the mere existence of antibodies.

17.2.3.2 Disease progression in allergies

Allergy designates not one disease but acts as an umbrella term for various diseases [1, 2, 16]. The cascade often starts with children from six months onwards, who develop an atopic eczema – a severe inflammation of the skin. The second stage is frequently a food allergy. Whereas children show an allergic reaction towards new food substances such as fish, wheat, soy, egg, or milk products, adults often suffer from pollen-associated cross reactions with pre-existing food allergies. Further stages are asthma or rhinitis. Children regularly lose their food allergies which means that they develop tolerance. If we come to understand the respective mechanisms of “natural” tolerance development, we could be able to actively induce tolerance at other ages. The latter is relevant because the elderly often (re-)develop atopic eczema.

17.2.3.3 Skin structure and epithelial barrier

Environmental factors and pollutants first impinge on the epithelia of skin, lung, or gut. An epithelium is a multi-layer surface that works like an organ on its own, senses harm, and induces defence. First of all, we need to investigate the epithelial barriers’ structure and function before we can holistically describe **the mechanisms of atopies**, i. e. the tendency to develop allergic symptoms on the skin or respiratory tract such as eczema, asthma, or rhinitis. Four barriers define the epithelial structure. Its main fabric consists either of skin cells or mucosal tissue. The following figure shows an epithelial barrier on the example of the skin.

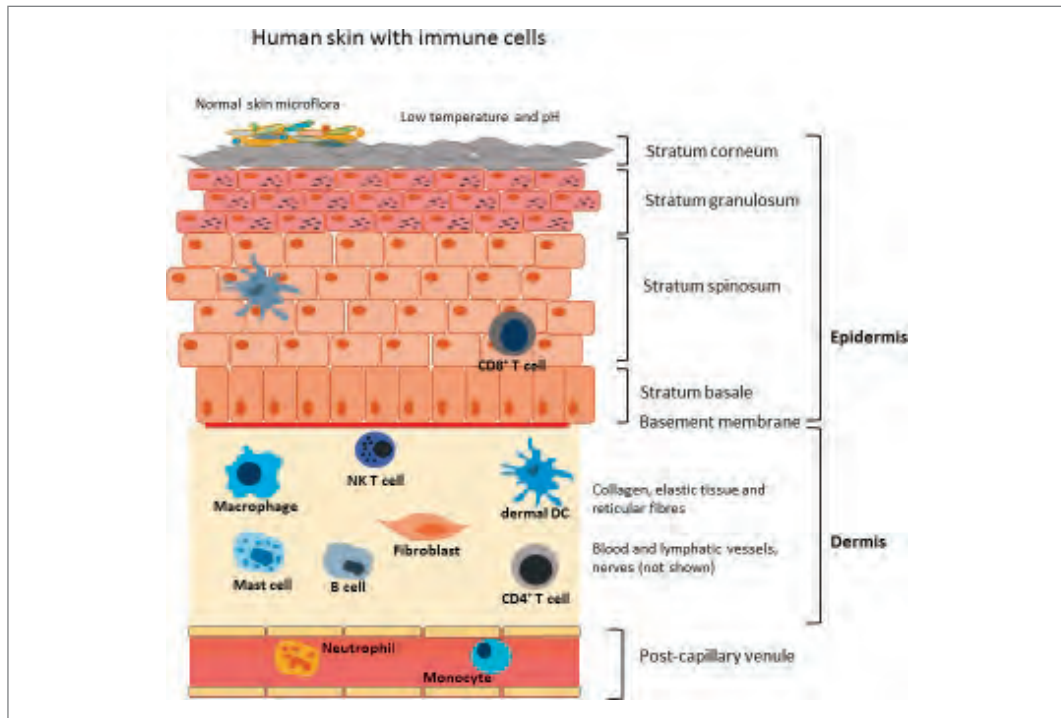


Fig. 2: The structure of the skin with its four barriers. The epidermal layers form the physical barrier. A chemical and microbial barrier are predominantly working on the skin's surface. The immune barrier consists of immune cells that work from the *Stratum spinosum* down to the lymph and blood vessels.

At the skin, two important markers of the **chemical barrier** are its pH value and the natural moisturizing factor (NMF). The **microbial barrier** consists of bacteria, viruses, and fungi. Together, they form an extensive ecosystem with a homeostasis as its healthy status. The **physical barrier** is structurally connected to with the chemical, microbial, and **immune barrier**. Furthermore, the physical barrier functionally interacts with the other three barriers in order to ensure a full protection from external assaults, like pathogens, xenobiotics, or UV irradiation, and to prevent the loss of water and solutes. Each epithelium's interactions are a pre-requisite for its functionality and defence mechanisms [17].

17.2.4 Clinical studies in the alpine region

A clinical study that examines the possible correlations between allergies, skin diseases, and the effect of a stay in the alpine region requires test persons that suffer from atopies plus urban and alpine test regions. Fig. 3 shows that the Umweltforschungsstation Schneesfernerhaus / Zugspitze, the Hochgebirgsklinik Davos, and the facilities of Environmental Medicine in Augsburg and Munich provide all the necessary clinical institutions and scientific facilities for such a study.

17.2.4.1 Clinical studies – structure, test persons, environmental factors

By the help of questionnaires and allergy specific biomarkers, the formation of a study group becomes possible that features exactly the allergic disease patterns of interest. As soon as the number of test persons fits a study design, the clinical part begins. At first, each study participant stays in the urban environment for several weeks and then retreats to the alpine region for several days or even weeks. The subjects undergoes regular visits by physicians who take blood, skin, and mucosal samples. Thereby, **the identification of specific environmental factors** becomes possible that are probable involved in the pathogenesis of each test person's disease. Follow-up studies address multiple environmental factors and compare the study results with the data from volumetric pollen traps and automatic pollen samplers, supplemented by meteorological and biological data. This study concept allows for a detailed description of alpine

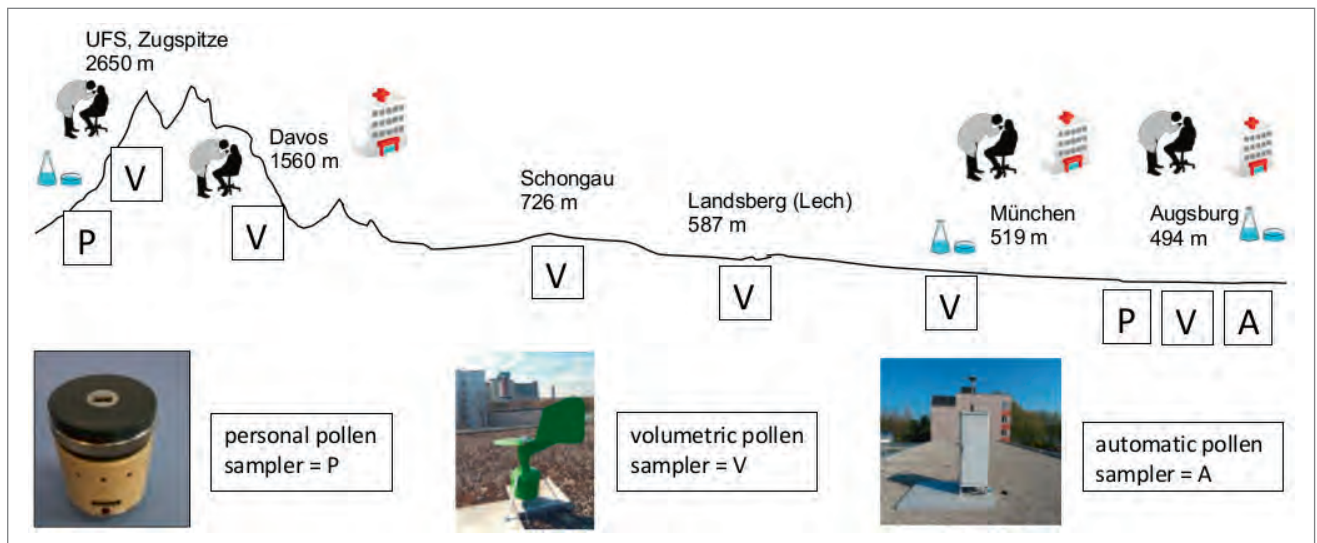


Fig. 3: (the elevation profile is illustrative not geographical): Six major pollen stations at lowland to high altitudes deliver pollen data. Several minor pollen stations function as supplement. The volumetric pollen sampler can be mounted at almost every subsurface and altitude (even the Weißfluhjoch and the Zugspitze). The personal pollen sampler was mainly designed for indoor air. The automated pollen sampler delivers the pollen data in real-time. In Munich and Augsburg, clinics and lab facilities allow for treatment, clinical tests, and research. The Hochgebirgsklinik in Davos provides space for treatment and clinical tests, and the Umweltforschungsstation Schneefernerhaus / Zugspitze has lab facilities and the possibility to conduct clinical trials.

effects on health. At the same time, the patient number can be reduced by the help of this study design since every patient is her or his own control for symptoms and immunological reactions both in alpine and urban regions.

17.2.4.2 Laboratory work and clinics

A number of high-end laboratory devices is set up to analyse **biomarkers**, i.e. biological parameters such as the IgE levels in blood serum, cell counts, or a change in microbial patterns from epithelial surfaces. Of special interest is the epidermal water loss, nasal secretion, and respiratory capacity. The results from the laboratory work become further analysed by physicians, technicians, and scientists (notably bioinformaticians). Alpine clinics are very suitable for the collection of specific data about the effect from a stay in the alpine region because they provide the necessary equipment and medical staff. Patients with severe chronic inflammation of skin or respiratory tract need intense medical care. Their sickrooms have to be largely free of environmental factors, such as pollen and house dust mite, or air pollutants, like ozone and nitric oxides. The test person's participation in a study is essential as they represent the patient group with severe symptoms. One exemplary alpine clinic is the **Hochgebirgsklinik in Davos**, which offers best standards and a very healthy environment.

17.3 Results

17.3.1 Patient recovery in the alpine region

Allergies can cause a permanent decrease in the quality of life. Therefore, a sustainable recovery is among the major goals when it comes to patient treatment in the alpine region [18–20]. But the Alps themselves face climate effects and undergo constant change. Scientific knowledge about the alpine region as a place for regeneration and therapy could also help to protect this region from substantial damage for now and for future generations.

17.3.1.1 Benefits of recovery in the alpine region

The less allergens, environmental pollutants, and stress factors are present in the environment, the better for the recreational value. Because patients are not distracted by their day-to-day life during recovery in the alpine region, their medication can be minutely adjusted and consumed

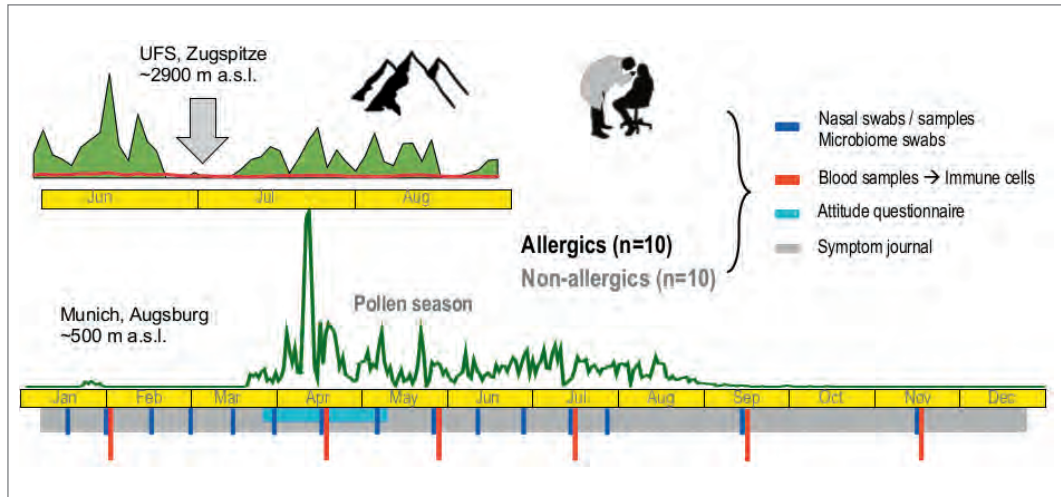


Fig. 4: By pollen monitoring, it is possible to match symptoms with pollen flight. Patients and controls had been clinically observed from January to December 2016 in Augsburg. During a multi-day stay at the Umweltforschungsstation Schneefernerhaus / Zugspitze in summer 2016, patients showed significantly less allergic symptoms due to a clearly reduced amount of pollen in the environment.

on schedule. A drug's effect can be clearly observed, and a prompt reaction to changes in health status becomes possible. Under alpine conditions, biomarkers are best suitable for both the exact assessment of the patient's status and for the research on the disease patterns. The pollen samplers at the alpine research stations (see Fig. 3) show that pollen, mites, or spores are variably less in number and variation in Davos or the Zugspitze. The Bavarian State Ministry of the Environment and Consumer Protection granted and funded a project at the University Center for Health Sciences at the Klinikum Augsburg, UNIKA-T, in order to compare symptoms from allergic individuals with the symptoms from non-allergic subjects in an alpine and urban environment.

One prerequisite for a general relaxation of the patient's mood and for a success in medical treatment is the reduction of symptom triggers, but also educational matters become much more effective if less symptoms strain the patient.

17.3.1.2 Short-term and long-term effects of recovery in the alpine region

Bersuch et al summarize in the publication "Lung function improvement and airways inflammation reduction in asthmatic children after a rehabilitation program at moderate altitude" results from a study at the Hochgebirgsklinik Davos [21]. The study shows **the regenerative effect of a stay in moderate alpine altitude**. Next to a reduced number of airborne allergens, the factor time is of particular significance for recovery. More than 14 days of stay delivered a better therapeutic effect of medicine and brought an increase for regenerative mechanisms like that of the lung. We can label this the "alpine effect" as Karin Fieten explains in her publication "Relation between regional exposure and allergic sensitisation in (pre-)school children in Davos"[19]. Besides allergen tests, the researchers in this study performed measures of dust particles. A comparison between the Davos group and the test group from the urban places Munich and Günzburg allows for further correlations. A third study "Perception of climate change in patients with chronic lung diseases"[22] indicates that more and more allergic patients lament about the effects of climate change. The fact that days with cloudless sky and high temperature mean an additional cardiovascular (and general) health risk has not raised the necessary awareness, yet. But especially those kind of days cause stronger symptoms due to dehydration, high UV irradiation, and aggressive pollen. Such factors harm the epithelium of the skin and respiratory tract and thus enforce pathogenic microbes and environmental pollutants to cause even more damage to the epithelial barriers.

17.3.2 Results from environmental medicine research in the alpine region

The formulation of correlations between the human health and climate effects, environmental factors, air pollutants, or microbial loads requires an interdisciplinary research network that consists of physicians, scientists, and technicians. From the hundredfold collection of pollen or blood samples, over to exact climate and weather observations, and up to the development of new laboratory methods and computer algorithms, environmental medicine unites distant research fields for the purpose of practical help to patients and relatives.

17.3.2.1 Health differences in urban, rural, and moderate to high altitude environments

Results from studies that investigated the recovery capacity in the alpine region prove that an industrially characterized environment usually contains more air pollutants. This circumstance, first of all, commonly results in a reduced barrier functionality at skin, gut, and lung. The barrier's inherent function was to stop environmental factors such as pathogenic microbes, pollen, or UV irradiation from causing a damage to cell structures, but **a disrupted barrier opens the doors way to the exposome**, i.e. the sum of external environmental factors and pollutants. Secondly, science hypothesizes that the immune system loses the capacity of tolerance development if sparse microbial exposition takes place. This circumstance is extremely relevant for atopy prevention at infancy [23, 24]. It partly explains why diversity is the key to health in many contexts. There seems to be a time window of a few years during early childhood that favours the preventive effect of life in non-urban environments with regards to atopy development in adolescence [25]. Whether the microbial homeostasis of adults benefits from a stay in a rural or alpine environment has still to be investigated. A follow-up study with the Amish people in the USA brought evidence that the contact to cattle seems to be of considerable advantage for prevention, besides that this study has further confirmed the positive effect of a diverse environment. A stay in an environment of moderate to high altitude and in a rural environment combines the beneficial effects of a non-urban environment with significantly less airborne allergens and pollutants.

17.3.2.2 Psycho-social factors and health improvement in the alpine region

One major benefit of recovery in the alpine region stems from the fact that patients avoid those psycho-social stress factors that are continually present in their usual environment. Some studies already showed that the factor "psycho-social stress" is clearly relevant and can be associated with allergic diseases in general and atopic diseases in particular. For example, Patterson et al investigated whether perceived stress can be linked to allergy flares [26]. Therefore, they analysed online diary entries on allergy flares, stressful events, perceived stress and mood. Moreover, they collected salivary cortisol levels in two blocks of 14 days. Before each fortnightly period, perceived stress and depressive symptoms were obtained. Finally, they could show that those subjects who reported allergy flares had higher perceived stress levels and lower mood levels than the subjects without allergic symptoms. The authors concluded that subjects with persistent psycho-social stress very likely have more frequent allergy flares. In another study, Rod et al investigated whether psychosocial stress can lead to adult-onset allergies or atopies [27]. Therefore, they analysed longitudinal data from the Copenhagen City Heart Study of 5,648 participants that had no allergies. At baseline (1981–1983), the participants were asked for perceived stress and ten years later they were asked for self-reported asthma, allergic rhinitis, and atopic eczema. The authors found out that **psycho-social stress can be strongly associated with asthma incidence, allergic rhinitis, and atopic eczema**. The results suggest that stress release might be an important first step towards the improvement of the quality of life for allergic individuals and towards the prevention of allergic diseases in adults.

17.3.3 Results from pollen research and pollen monitoring

Pollen research does not only comprise the observation of pollen flight and the phenological studies of allergenic plants but also includes the study of environmental pollutants such as ozone and nitric oxide. What is more, we observed that even pollen has an individual microbiome. This fact means that new correlations become observable and modes of interaction multiply [7].

17.3.3.1 Air pollutants and pollen allergenicity

Zhao et al discuss in recent publications the effect of nitric oxide on pollen. The respective studies prove the enhancing effect of nitric oxides on pollen amount and plant allergenicity of the neophyte ambrosia [28–30]. In grass pollen, the bioavailability of allergens may also be modulated by NO₂ [31]. NO_x in general belongs to the classical and most aggressive air pollutants. The main sources of NO₂ are combustion processes from energy production, industrial processes, and car traffic. NO₂ affects human health by irritating the bronchial tubes and thus influences the respiratory tract's functionality [32, 33]. With regards to the ecosystems, NO₂ concentrations of around 100 ppb substantially damage plants. This results in leaf necrosis, reduced growth, and premature senescence [34, 35]. But also growth promoting effects were described, however, at lower NO₂ concentrations of 50 ppb [36]. Another interesting result from pollen research reveals the nitrosylation and nitration of allergens by NO₂ that can enhance the allergenic responses of both pollen and food allergens [37–39]. Ozone [40, 41] and urbanisation [42] are correlating with changes in pollen's allergenicity, too. Therefore, future studies about environmental conditions in urban and alpine regions have to address the investigation of plants and pollen with respect to their allergenic potential.

17.3.3.2 Changes in pollen season

Airborne pollen measurement has been a research subject for a long period of time and are also among the most recent datasets of biological origin. In this respect, the data **represents a valuable proxy of climate effects**. Extensive research over the last decade has showcased that airborne pollen increase in abundance, but also that pollen seasons shift to an earlier start and different duration [8]. The average temperatures increase all over the planet: in lowlands, seas, riversides, and mountainous regions as well as in the troposphere. Next to temperature means, peaks of heat and frost continue to become more numerous [43]. Both phenomena change the sequences in pollen season of endemic plants. Hazel shrubs and trees for instance have started to flower much earlier in winter, sometimes even as soon as late autumn. Whether this outcome is a result of increased pollen production per floral unit and per individual plant or the output of changes in land usage has still to be researched. To date, the main causative factors for described shifts and changes have been considered as either **air pollutants** and higher **air temperatures**, associated with a global increase of average temperatures, or **urbanisation rates** and **changes in land usages** [44]. We know that air pollutants are responsible for a higher biomass production (including flower and pollen) but also for a higher allergenicity of pollen. Wan et al [45] and Wayne et al [46] experimentally found out that – specifically in combination with elevated air temperature – increased CO₂ does not alter pollen production per se but enhance plant biomass in *Ambrosia artemisiifolia*. That is one reason, consequently, why individual plants produce more pollen. Ziska et al [47] also studied the *Ambrosia* plant species, this time under realistic environmental conditions, or rather in a gradient that simulated distinct climatic scenarios. Again, they explored that plants exhibited higher biomass, pollen production, and earlier flowering dates. Ziska et al additionally concluded that plant expansion rates and regional abundance may increase, too. At a wider spatial scale, an escalation of allergenic pollen exposure rates becomes probable. An indirect consequence of the climate effect is the introduction of foreign plant species, often by means of international transport. They enter left growth niches because they put forward a better resistance to temperature shifts or peaks. Such plant species are often more allergenic. For example, seeds of *Ambrosia artemisiifolia* have entered the European continent presumably via transport boxes of international traded goods [6, 48]. *Ambrosia* seeds probably endure the transport distances more easily when the weather is warm and dry, preventing the seeds from germination. Besides the fact that *Ambrosia* produces a highly allergenic pollen, it survives temperature peaks and flimsily fills the empty-left niches of regressing endemic plants.

17.3.3.3 Variations in landmarks of airborne pollen

Pollen research by its nature contains the observation of allergen fractions in the air and in different altitudes as well as in terms of their landmarks. We observe that the climate effect resulting from warmer and drier days changes the pollen seasons towards earlier start points and towards a prolongation of bloom phases. Further results indicate differences in pollen flight at day and night. Now, measurements of pollen concentrations at different altitudes has shown two tendencies: pollen can travel over long distances, even cluster in pollen clouds and pass mountains and seas, i. e. very high and very low land surfaces [5]. Moreover, the air in areas which up to now have been considered as more or less free of pollen verifiably contains larger amounts of pollen. The reason for the latter is on the one hand that higher average temperatures allow plants to grow at altitudes other than their original habitat. On the other hand, changes in the pollen seasons' start and stop points together with a surplus in pollen amounts of plants necessarily increase the number of pollen in the air in general. As a consequence, **pollen shows higher numbers in moderate to high altitudes as well**. An interesting fact is that some alpine areas function like an air cavity that houses pollen and air pollutants like CO₂. In contrast, other alpine regions benefit from the surrounding walls of mountain peaks and crests that keep pollen or polluted air all around the outer edges.

17.3.4 Pollen information services and educational measures

Results from research on allergies and environmental factors can help the population to keep healthy, especially at times when the pollen season starts and symptoms appear or worsen. Knowledge about interactions between disease patterns and the climate, the weather, pollen flight, the microbiome, and immune mechanism, furthermore, essentially complement already formulated educational measures.

17.3.4.1 UNIKA-T pollen flight service and ePIN

At the University Center for Health Sciences at the Klinikum Augsburg, UNIKA-T, a very modern pollen super site has been operating since 2016. The site consists of two automatic and two volumetric pollen samplers. In an attached pilot project, the UNIKA-T offers **real-time information about the current pollen flight** on its website (www.unika-t.de/pollenflug) which is of relevance to the population of Augsburg and its region. Every three hours, new pollen data is uploaded to a server and from there, an algorithm prepares the data for an optimal readability on the UNIKA-T website. For allergic patients, the direct access to actual pollen flight counts as vital information for a better quality of life. Pollen information includes the number of pollen, the time of flight, and the pollen species. The data from the volumetric pollen samplers helps the scientists to compare both the non-automated and the automatic pollen monitoring methods. Public institutions in Bavaria have initiated the network ePIN, which is the acronym for electronic pollen information network. For this network's implementation, a vast number of fully automated pollen monitors in addition to the many already existing volumetric ones has to be installed all over the country. The pollen sites make it possible to provide the (Bavarian) population permanently with regional pollen flight information.

17.3.4.2 CK-CARE

The CK-CARE foundation (Christine Kühne – Center for Allergy Research and Education; www.ck-care.ch) has initiated a platform for research, therapy, and prevention that directly addresses allergies and allergy-related skin diseases like atopic eczema. **Prevention works primarily by means of educational matters** both for physicians and care staff as well as for patients and their relatives. CK-CARE offers courses that are well-organized and teach the central aspects of allergic diseases. Often, life style is one of the reasons why allergies become so prevalent. Children are the least defensible and most vulnerable members of our society with regards to both environmental factors and air pollutants. Therefore, how to manage allergies properly and what strategies work to prevent allergy pathogenesis make up two major aspects of the CK-CARE education program. The improvement in the quality of life is central to every allergic person. The courses of CK-CARE teach how to improve quality of life by following certain rules such as

the careful planning of medication and leisure activity. Additionally, **patient care is essential for a successful medical treatment.** That is why physicians and nurse staff undergo courses at CK-CARE that tell them how to best adapt to a patient's situations and how to treat symptoms with the most modern techniques and medicine. In general, CK-CARE education methods rely on the research results that stem from various fields of science. The interdisciplinary approach of this foundation has led to a global initiative with the goal of addressing allergies as the most dangerous epidemic threat in the 21st century.

17.4 Conclusion

The performance of environmental medicine research in the alpine regions is an absolutely necessary pre-requisite for the formulation of plausible preventive and therapeutic options to people that suffer from atopies. Above the latter, environmental studies help to gain full knowledge about the interactions between climate, nature, man, and health. As a result, the protection of the alpine region becomes the basis for its use as a place of retreat to allergic patients. The observation of pollen flight and abundance at different altitudes together with the data from weather and climate stations allow, in addition, to identify exactly those environmental factors that are mainly present in urban environments and that are trigger factors for allergies. Finally, research in the alpine region is of real benefit to patients: stress relief, improvement in the quality of life – and above all, less symptoms.

References

1. Bieber, T., et al., *Global Allergy Forum and 3rd Davos Declaration 2015: Atopic dermatitis/Eczema: challenges and opportunities toward precision medicine.* Allergy, 2016. **71**(5): p. 588–92.
2. Ring, J., et al., *Davos declaration: allergy as a global problem.* Allergy, 2012. **67**(2): p. 141–3.
3. Schobersberger, W., et al., *Austrian Moderate Altitude Studies (AMAS): benefits of exposure to moderate altitudes (1,500–2,500 m).* Sleep Breath, 2010. **14**(3): p. 201–7.
4. Doucet, J., H. K. Lee, and D. R. Goring, *Pollen Acceptance or Rejection: A Tale of Two Pathways.* Trends Plant Sci, 2016. **21**(12): p. 1058–1067.
5. Damialis, A., et al., *Estimating the abundance of airborne pollen and fungal spores at variable elevations using an aircraft: how high can they fly?* Sci Rep, 2017. **7**: p. 44535.
6. Smith, M., et al., *Geographic and temporal variations in pollen exposure across Europe.* Allergy, 2014. **69**(7): p. 913–23.
7. Obersteiner, A., et al., *Pollen-Associated Microbiome Correlates with Pollution Parameters and the Allergenicity of Pollen.* PLoS One, 2016. **11**(2): p. e0149545.
8. Ziello, C., et al., *Changes to airborne pollen counts across Europe.* PLoS One, 2012. **7**(4): p. e34076.
9. Oteros, J., et al., *Automatic and Online Pollen Monitoring.* Int Arch Allergy Immunol, 2015. **167**(3): p. 158–66.
10. Traidl-Hoffmann, C., *[Allergy – an environmental disease].* Bundesgesundheitsblatt Gesundheitsforschung Gesundheitsschutz, 2017. **60**(6): p. 584–591.
11. Gilles, S., et al., *The pollen enigma: modulation of the allergic immune response by non-allergenic, pollen-derived compounds.* Curr Pharm Des, 2012. **18**(16): p. 2314–9.
12. Traidl-Hoffmann, C., T. Jakob, and H. Behrendt, *Determinants of allergenicity.* J Allergy Clin Immunol, 2009. **123**(3): p. 558–66.
13. Gilles-Stein, S., et al., *Pollen derived low molecular compounds enhance the human allergen specific immune response in vivo.* Clin Exp Allergy, 2016. **46**(10): p. 1355–65.
14. Wimmer, M., et al., *Pollen-derived adenosine is a necessary cofactor for ragweed allergy.* Allergy, 2015. **70**(8): p. 944–54.
15. Gilles, S., et al., *Non-allergenic factors from pollen modulate T helper cell instructing notch ligands on dendritic cells.* World Allergy Organ J, 2015. **8**(1): p. 2.
16. Ring, J., et al., *Global Allergy Forum and Second Davos Declaration 2013 Allergy: Barriers to cure-challenges and actions to be taken.* Allergy, 2014. **69**(8): p. 978–82.
17. Eyerich, S., et al., *Cutaneous Barriers and Skin Immunity: Differentiating A Connected Network.* Trends Immunol, 2018. **39**(4): p. 315–327.
18. Heeringa, J. J., et al., *Treatment for moderate to severe atopic dermatitis in alpine and moderate maritime climates differentially affects helper T cells and memory B cells in children.* Clin Exp Allergy, 2018.
19. Fieten, K. B., et al., *Effectiveness of alpine climate treatment for children with difficult to treat atopic dermatitis: Results of a pragmatic randomized controlled trial (DAVOS trial).* Clin Exp Allergy, 2018. **48**(2): p. 186–195.

20. Fieten, K. B., et al., *Alpine climate treatment of atopic dermatitis: a systematic review*. *Allergy*, 2015. **70**(1): p. 12–25.
21. Bersuch, E., et al., *Lung function improvement and airways inflammation reduction in asthmatic children after a rehabilitation program at moderate altitude*. *Pediatr Allergy Immunol*, 2017. **28**(8): p. 768–775.
22. Gotschke, J., et al., *Perception of climate change in patients with chronic lung disease*. *PLoS One*, 2017. **12**(10): p. e0186632.
23. Stein, M. M., et al., *Innate Immunity and Asthma Risk in Amish and Hutterite Farm Children*. *N Engl J Med*, 2016. **375**(5): p. 411–421.
24. Renz, H., et al., *The neonatal window of opportunity-early priming for life*. *J Allergy Clin Immunol*, 2018. **141**(4): p. 1212–1214.
25. Kutzora, S., et al., *Asthmatic/wheezing phenotypes in preschool children: Influential factors, health care and urban-rural differences*. *Int J Hyg Environ Health*, 2018. **221**(2): p. 293–299.
26. Patterson, A. M., et al., *Perceived stress predicts allergy flares*. *Ann Allergy Asthma Immunol*, 2014. **112**(4): p. 317–21.
27. Rod, N. H., et al., *Perceived stress and risk of adult-onset asthma and other atopic disorders: a longitudinal cohort study*. *Allergy*, 2012. **67**(11): p. 1408–14.
28. Zhao, F., et al., *Pollen of common ragweed (*Ambrosia artemisiifolia* L.): Illumina-based de novo sequencing and differential transcript expression upon elevated NO₂/O₃*. *Environ Pollut*, 2017. **224**: p. 503–514.
29. Zhao, F., et al., *Common ragweed (*Ambrosia artemisiifolia* L.): allergenicity and molecular characterization of pollen after plant exposure to elevated NO₂*. *Plant Cell Environ*, 2016. **39**(1): p. 147–64.
30. El Kelish, A., et al., *Ragweed (*Ambrosia artemisiifolia*) pollen allergenicity: SuperSAGE transcriptomic analysis upon elevated CO₂ and drought stress*. *BMC Plant Biol*, 2014. **14**: p. 176.
31. Behrendt, H., et al., *Air pollution and allergy: Experimental studies on modulation of allergen release from pollen by air pollutants*. *International Archives of Allergy and Immunology*, 1997. **113**: p. 69–74.
32. Jacquemin, B., et al., *Home outdoor NO₂ and new onset of self-reported asthma in adults*. *Epidemiology*, 2009. **20**: p. 119–126.
33. Takenoue, Y., et al., *Influence of outdoor NO₂ exposure on asthma in childhood: Meta-analysis*. *Pediatrics International*, 2012. **54**: p. 762–769.
34. Kress, L.W. and J.M. Skelly, *Response of several eastern forest tree species to chronic doses of ozone and nitrogen dioxide*. *Plant Disease*, 1982. **66**: p. 1149–1152.
35. Honour, S. L., et al., *Responses of herbaceous plants to urban air pollution: Effects on growth, phenology and leaf surface characteristics*. *Environmental Pollution*, 2009. **157**: p. 1279–1286.
36. Takahashi, M., et al., *Nitrogen dioxide regulates organ growth by controlling cell proliferation and enlargement in *Arabidopsis**. *New Phytologist*, 2014. **201**(4): p. 1304–1315.
37. Gruijthuisen, Y.K., et al., *Nitration enhances the allergenic potential of proteins*. *International Archives of Allergy and Immunology*, 2006. **141**: p. 265–275.
38. Untersmayr, E., et al., *Nitration of the egg-allergen ovalbumin enhances protein allergenicity but reduces the risk for oral sensitization in a murine model of food allergy*. *Plos One*, 2010. **5**: p. e14210.
39. Reinmuth-Selzle, K., et al., *Nitration of the birch pollen allergen Bet v 1.0101: Efficiency and site-selectivity of liquid and gaseous nitrating agents*. *Journal of Proteome Research*, 2014. **13**: p. 1570–1577.
40. Jochner, S., et al., *Nutrient status: a missing factor in phenological and pollen research?* *J Exp Bot*, 2013. **64**(7): p. 2081–92.
41. Beck, I., et al., *High environmental ozone levels lead to enhanced allergenicity of birch pollen*. *PLoS One*, 2013. **8**(11): p. e80147.
42. Bryce, M., et al., *Impact of urbanization on the proteome of birch pollen and its chemotactic activity on human granulocytes*. *Int Arch Allergy Immunol*, 2010. **151**(1): p. 46–55.
43. Jochner SC, B. I., Behrendt H, Traidl-Hoffmann C, Menzel A., *Effects of extreme spring temperatures on urban phenology and pollen production: a case study in Munich and Ingolstadt*. *Climate Research*, 2011. **13**.
44. Voltolini S, M. P., Troise C, Bignardi D, Modena P, Arobba D, Negrini AC., *Trend of herbaceous pollen diffusion and allergic sensitisation in Genoa, Italy*. *Aerobiologia*, 2000. **16**: p. 245–249.
45. Wan, S., et al., *Response of an allergenic species, *Ambrosia psilostachya* (Asteraceae), to experimental warming and clipping: implications for public health*. *Am J Bot*, 2002. **89**(11): p. 1843–6.
46. Wayne, P., et al., *Production of allergenic pollen by ragweed (*Ambrosia artemisiifolia* L.) is increased in CO₂-enriched atmospheres*. *Ann Allergy Asthma Immunol*, 2002. **88**(3): p. 279–82.
47. Ziska, L. H., et al., *Cities as harbingers of climate change: common ragweed, urbanization, and public health*. *J Allergy Clin Immunol*, 2003. **111**(2): p. 290–5.
48. Hoflich, C., et al., *Potential health risk of allergenic pollen with climate change associated spreading capacity: Ragweed and olive sensitization in two German federal states*. *Int J Hyg Environ Health*, 2016. **219**(3): p. 252–60.

18 Lidar remote sensing of water vapor with DIAL

Hannes Vogelmann and Thomas Trickl

IMK-IFU, Karlsruhe Institute of Technology, Garmisch, Germany

18.1 Introduction

Lidar (for “light detection and ranging”) is a remote sensing measurement technique using the scattering properties of light by gases, liquids, and solids to infer some of their physical properties. This technique has many applications from the ground, aircraft or space such as atmospheric sensing, oceanography, and topography. The earliest records of using the lidar technique for atmospheric remote sensing date back to the 1930s when searchlight projectors were used to determine atmospheric density (Hulburt, 1937; Elterman, 1951). Following the emergence of lasers in the 1960s, lidar instruments typically in use today for atmospheric remote sensing are based on the emission of essentially monochromatic laser light. The best-known properties of the atmosphere that can be measured by lidar are air density, wind speed and direction, air temperature, the concentrations of ozone, carbon dioxide, and water vapor, and the density, basic shape and size of aerosols, ice crystals, and water droplets. Comprehensive reviews of the various existing lidar techniques for atmospheric remote sensing can be found, for example, in (Hinkley, 1976); Measures, 1992-; Weitkamp, 2005; Fiorani and Mitev, 2010).

In this chapter we focus on the characterization of a lidar method called differential absorption lidar (DIAL) for the measurement of water vapor which is exemplary implemented at the Schneefernerhaus research station (UFS) at Mt. Zugspitze (2675 m a.s.l., Germany). Reaching the Upper Troposphere and Lower Stratosphere (UT/LS), a region of the Earth’s atmosphere that is particularly relevant to climate change in respect to the most important greenhouse gas water vapor (Oltmans and Hofmann, 94; Forster and Shine, 2002; Solomon et al., 2010), was one major goal when installing the water vapor lidar systems at this high altitude station. Profiling temperature, which is the most important parameter for the radiative balance, up to the meso-pause region (roughly 80 km) was an additional goal when setting up the Raman lidar at UFS.

18.2 Lidar Principle and Equation

As for many other lidar applications, the lidar equation is the starting point for the retrieval of water vapor using both the DIAL (Wulfmeyer and Bösenberg, 2005) and the Raman lidar (Weitkamp, 2005) techniques. DIAL exploits the wavelength dependence of light absorption by water vapor. The Raman method using inelastic backscattering of light by water vapor with respect to a reference well-mixed gas.

The lidar principle underlying the lidar equation and the formation of lidar signals is presented in Fig. 1. A laser pulse at wavelength λ_L is emitted into the atmosphere. The light is scattered by the air molecules and particles, and a fraction is collected in the lidar receiver with a telescope of area AT . Knowing the speed of light, the distance r to scattering molecules or particles is deduced from the travel time of the photons on their way upward and then after the scattering back to the lidar. Since the lidar includes the light source itself, the lidar technique is known as an active remote sensing technique, in contrast to other remote sensing instruments such as radiometers and spectrometers which are passive. The precise timing of the lidar-measured samples and the high-speed electronics currently available yield a high vertical resolution (from a few meters to a few hundred meters) compared with most passive instruments which are sensitive to light reaching the instrument with no spatio-temporal information of its origin. The light collected by the lidar telescope is geometrically and spectrally separated in a polychromator (e.g., with optical filters and beam splitters) and detected with photosensitive devices (e.g., photomultipliers (PMTs) and avalanche photo-diodes (APDs)) where it is converted to

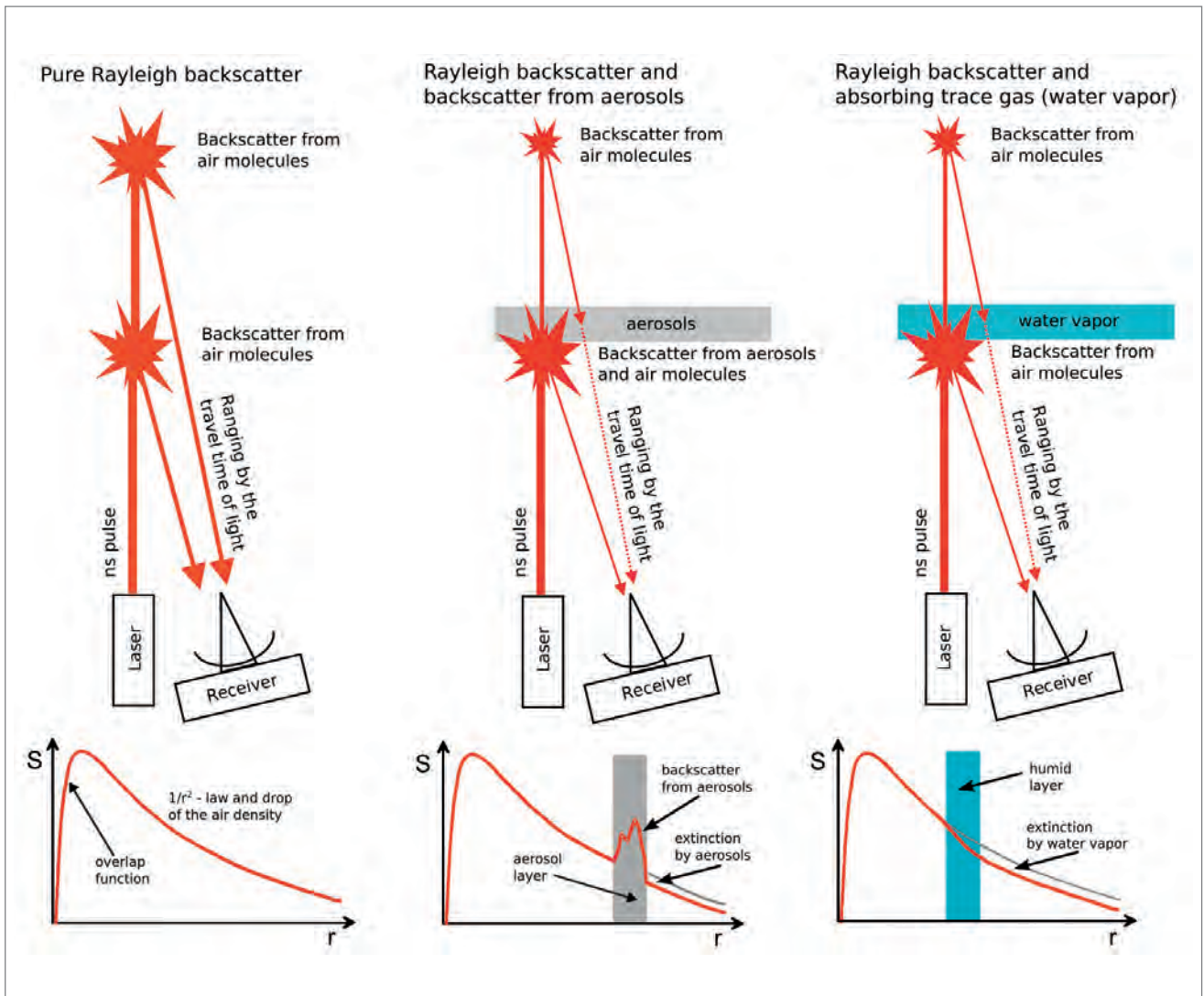


Fig. 1: Principal function of a lidar remote sensing.

electronic lidar signals. The signals are sampled in time (i.e., distance), and, within a certain range, they are proportional to the product of the number of photons backscattered at a certain altitude at a certain wavelength.

For a vertically pointing lidar system, one of the simplest and most general forms of the lidar equation expressing the lidar signal which is linear to the number of photons backscattered at distance r from the lidar by a volume element of thickness δr , and collected at the detection wavelength λ_D is:

$$S(r, \lambda_D) = \frac{1}{r^2} \cdot P_L(r, \lambda_L) \cdot \eta(\lambda_D) \cdot O(r) A_T \cdot \delta r \cdot \beta(r, \lambda_L \rightarrow \lambda_D) \cdot t_{\uparrow}(r, \lambda_L) \cdot t_{\downarrow}(r, \lambda_D) \quad (1)$$

P_L is the number of photons emitted, per laser shot, at emission wavelength λ_L ,
 S is the lidar signal detected, per laser shot, at the detection wavelength λ_D ,
 η is the overall optical transmittance and quantum efficiency of the receiver channel,
 O is the telescope field-of-view and laser beam overlap function (between 0 and 1),
 A_T is the area of the receiving telescope,
 β is the total backscatter coefficient for the type of scattering considered,
 t_{\uparrow} and t_{\downarrow} are the total atmospheric transmittances along the light path from the lidar to the scattering process (\uparrow) and back (\downarrow), respectively. These two terms represent the extinction by light scattering and absorption along the laser beam path (Beer-Lambert extinction law).

$$t_{\uparrow}(r, \lambda_L) t_{\downarrow}(r, \lambda_D) = e^{-\int_0^r a_{\uparrow}(r, \lambda_L) dr} \cdot e^{-\int_0^r a_{\downarrow}(r, \lambda_D) dr} \quad (2)$$

α_{\uparrow} and α_{\downarrow} are the total atmospheric extinction coefficients along the beam path from the lidar up to the scattering layer and back, respectively.

Eqs. 1 and 2 are valid for all detection wavelengths, all types of atmospheric scatterers, and all types of scattering process. The appropriate choice of the emission and detection wavelengths allows further development and simplification of these equations, which commonly refers to using a specific “lidar technique”; for example, DIAL or Raman lidar.

18.3 Remote sensing of water vapor with DIAL

Ground-based lidar sounding of water vapor up to the middle troposphere (i. e., 8 km altitude) has become rather mature. However, extending operation to the tropopause and beyond (typically above 12 km) is impeded by the drop, by more than five orders of magnitude, in the water vapor density from the ground to the lower stratosphere. At the same time the backscatter signal strongly diminishes as a function of distance. Hence, particularly powerful laser systems and large telescopes for receiving the backscattered radiation are needed for lidar measurements of water vapor extending to the UT/LS. The implementation of lidar systems that can measure water vapor up into this region is, therefore, a significant and contemporary challenge (Leblanc and McDermid, 2009). Both lidar techniques dedicated to the measurement of atmospheric water vapor, have advantages and drawbacks. For example, because of the high abundance of water vapor in the lower tropospheric layers, ground based routine measurements in the upper troposphere by a water vapor DIAL can only be achieved from a high mountain (e. g., Zugspitze). Airborne or spaceborne DIAL measurements even can access the lower stratosphere by using stronger absorption bands of H₂O (Browell et al., 1998; Ehret et al., 1999), but, are practically prohibited for routine monitoring by its high operating costs. For this reason and because of a less demanding laser technology, the Raman lidar technique is usually preferred for measurements of UT/LS water vapor. However, the vibrational Raman scattering process is several orders of magnitude weaker than the elastic Rayleigh scattering involved in the DIAL technique (Hinkley, 1976). This allows for distant water vapor profiling with the Raman lidar only during the nighttime darkness while DIAL provides tropospheric water vapor profiles also during daytime (Vogelmann and Trickl, 2008) and with rather short integration times.

18.3.1 The DIAL method

The development of differential-absorption lidar (DIAL) systems to measure the vertical distribution of water vapor has a history of more than three decades (Schotland, 1966; Murray et al., 1976; Browell et al., 1979; Zuev et al., 1983; Grant et al., 1987; Bösenberg, 1991; Ehret et al., 1993; Higdon et al., 1994; Senff et al., 1994; Sachse et al., 1995; Moore et al., 1996; Browell et al., 1996; Wulfmeyer, 1998; Ehret et al., 1999; Bruneau et al., 2001; Little and Papen, 2001; Nagasawa et al., 2001; Poberaj et al., 2002; Ertel, 2004; Machol et al., 2004; Vogelmann and Trickl, 2008). The only ground-based DIAL system so far fulfilling the important goal of reaching the upper troposphere (Vogelmann and Trickl, 2008) because it is installed at 2675 m in the high altitude observatory Schneefernerhaus. where major light losses caused by absorption in the moist boundary layer are avoided.

In this section we explain the DIAL method ground-based measurements throughout the free troposphere and use examples from the Zugspitze DIAL system in order to characterize the potential of this method. In the case of the Differential Absorption Lidar (DIAL) technique, usually elastic backscatter from air molecules and aerosols is detected by the receiver which means that emission and detection wavelengths are equal. But, the wavelengths can be chosen in a way that the emitted and backscattered light undergoes a specific molecular absorption by the trace gas of interest (i. e. water vapor, right panel in Fig. 1). Then, the extinction coefficients in Eq. 1 α_{\uparrow} and α_{\downarrow} as a function of the distance r become essential and can directly be used to retrieve the number density N of the absorbing trace gas at the distance r .

The extinction coefficient can be further expanded by separating the total extinction along the laser beam path into molecular extinction and particulate extinction terms: ($\alpha = \alpha_M + \alpha_P$), then

by separating the molecular extinction into molecular (Rayleigh) scattering and molecular absorption coefficients ($\alpha_M = \alpha_R + \alpha_A$). Finally, the molecular absorption coefficient can be separated into individual contributions of each absorbing species. Each of these contributions can be expressed as the product of the number density N_i of the absorber by its absorption cross-section σ_i :

$$\alpha(r, \lambda) = \alpha_P(r, \lambda) + \alpha_R(r, \lambda) + \sum_i \sigma_i(r, \lambda) N_i(r) \quad (3)$$

If only one absorbing species is of interest (i. e. water vapor), it is an obvious advantage to use a wavelength showing a significant and specific absorption by this species and no interference with other absorbing species. Then, $\sum \sigma_i N_i$ reduces to σN . This is fulfilled by single absorption lines of the 815 nm band of water vapor which is typically used by ground based water vapor DIALs like the system at UFS.

Only as a very first approximation the total extinction along the laser beam path on the way up is basically equal to that on its way back for a detection wavelength identical to the emission wavelength ($\lambda_D = \lambda_L = \lambda$). In the case of dominating Rayleigh backscatter in a clean air (e. g., free troposphere) and narrow single molecular absorption lines (e. g. 815 nm band of water vapor), the extinction along the laser beam path on the way up significantly differs from the extinction on its way down because of the Doppler broadening of the Rayleigh backscatter (Ansmann and Bösenberg, 1987). Thus, we get different cross sections $\sigma_\uparrow(r, \lambda)$ and $\sigma_\downarrow(r, \lambda)$ for the way up and back down while α_R and α_P do not change significantly. Assuming the detection of only elastic backscatter at the certain wavelength λ we get the following simplified lidar equation:

$$S(r) = P_L O(r) A_T \eta \frac{\beta(r) \delta r}{r^2} \cdot e^{-\int_0^r [N(r')(\sigma_\uparrow(r') + \sigma_\downarrow(r')) + 2(\alpha_R(r') + \alpha_P(r'))] dr'} \quad (4)$$

We have to keep in mind that, of course, η , β , α_R , α_P and σ depend on the wavelength. And we must be aware, that the effective absorption cross sections σ_\uparrow and σ_\downarrow are as well functions of r , because the line shape of molecular absorption lines is a function of pressure and temperature and the spectral distribution of the backscattered light is also a function of temperature (Doppler broadening) and the backscatter ratio from aerosols (see below, Fig. 3). The total backscatter coefficient β can be expressed as the sum of molecular (Rayleigh) and particulate backscatter $\beta = \beta_R + \beta_P$. Due to a spectrum with well-resolved absorption lines the H₂O molecule is particularly well suited for DIAL measurements, the only disadvantage being the moderate atmospheric backscatter coefficient β_R in the near infrared (IR). As an example Fig. 2 shows the section of the absorption spectrum of H₂O around 817.2 nm, within the preferred absorption band in several DIAL systems. This approach is highly substance-specific since other trace constituents with sharp spectral signatures are easily separated by an appropriate line selection. For a water-vapor DIAL the wavelengths are selected closely spaced so that the absorption differential between two laser wavelengths is reduced to that of water vapor only which is represented by $N(r)[\sigma_\uparrow(\lambda, r) + \sigma_\downarrow(\lambda, r)]$.

In order to retrieve the number density of atmospheric species such as water vapor, we use a certain laser wavelength which shows a significant molecular absorption by the species of interest and call it λ_{on} because it is somewhere "on" a molecular absorption line of the species' molecular spectrum. Then, we just invert Eq. 4 with respect to $N(r)[\sigma_\uparrow(r) + \sigma_\downarrow(r)]$:

$$N(r)[\sigma_\uparrow(r) + \sigma_\downarrow(r)] = \frac{-d}{dr} \ln \frac{r^2 S(r)}{P_L O(r) A_T \eta \beta(r) \delta r} - 2[\alpha_R(r) + \alpha_P(r)] \quad (5)$$

Principally, the number density of the species of interest (i. e. water vapor) could be retrieved with Eq. 5, but only, if the other terms depending on the distance r are well known which, unfortunately, is usually not the case. Particularly, the presence of aerosols can dominate the backscatter coefficient $\beta(r) = \beta_R + \beta_P$ indeterminably and can also cause undefined additional extinction by α_P (Fig.1, middle).

At this point the quintessence of DIAL method comes into play: A second measurement with a slightly different wavelength is performed, just in a way that the only significant change of the terms in Eq. 5 strikes the molecular absorption coefficients σ_\uparrow and σ_\downarrow while all the other terms remain unaffected. Practically, this means the second wavelength is chosen just somewhere beside the absorption line on which λ_{on} is placed, so that σ_\uparrow and σ_\downarrow have significantly smaller

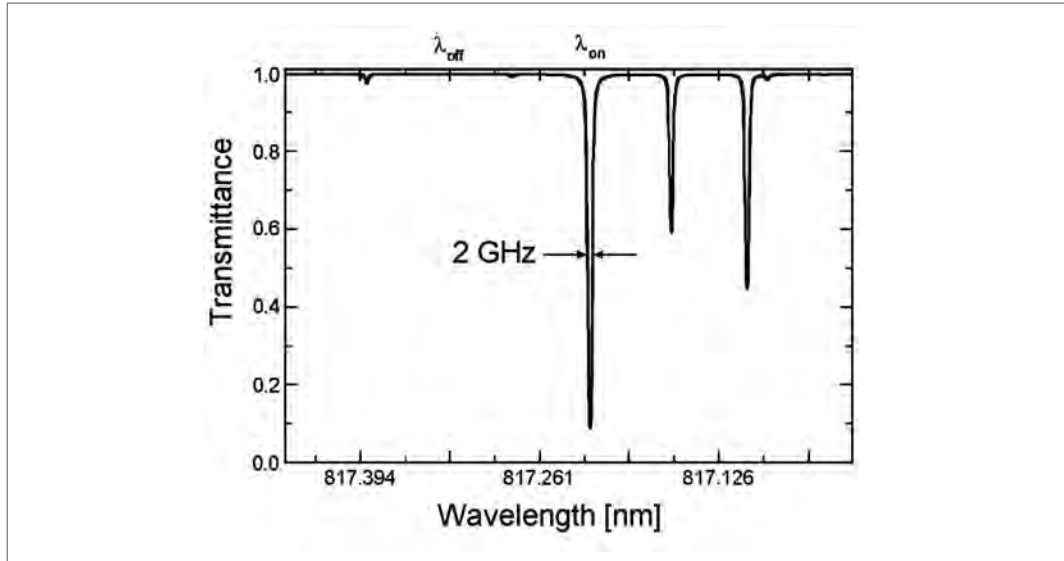


Fig. 2: Spectrum of H₂O near 817 nm calculated for 0.1 bar air at 230 K, a H₂O volume mixing ratio of 1% and a path length of 1 km using HITRAN (Rothman et al., 2003; Rothman et al., 2009); the “on” and “off” wavelength positions are indicated.

values (Fig. 2). We call this wavelength λ_{off} , because it is “off” the line. Thus, we get two equations of Eq. 5, one each for λ_{on} and λ_{off} . From this point we use the indices “on” and “off” to indicate to which wavelength a term refers. For an appropriate optical design and laser beam alignment the quotient of the overlap functions O_{on}/O_{off} is independent of the distance r .

By subtracting these two equations from each other all terms equal for λ_{on} and λ_{off} cancel out and we get the so-called DIAL equation for the number density of water-vapor as a function of distance, which is surprisingly simple:

$$N_{H_2O}(r) = \frac{-1}{\Delta\sigma_{\uparrow}(r) + \Delta\sigma_{\downarrow}(r)} \frac{d}{dr} \left[\ln \left(\frac{S_{on}(r)}{S_{off}(r)} \right) \right] \quad (6)$$

where $\Delta\sigma_{\uparrow}(r) = \sigma_{\uparrow on}(r) - \sigma_{\uparrow off}(r)$ and $\Delta\sigma_{\downarrow}(r) = \sigma_{\downarrow on}(r) - \sigma_{\downarrow off}(r)$.

It is remarkable, that obviously all physical parameters of the lidar device have canceled out, even the number of photons per laser shot. Also the backscatter coefficient β undetermined by aerosols and the undetermined particulate extinction α_p have canceled out. Only σ_{\uparrow} and σ_{\downarrow} being potentially very different for the wavelengths λ_{on} and λ_{off} and quotient of the two detected signals (S_{on}/S_{off}) determine the number density of water vapor. This means that neither a cali-

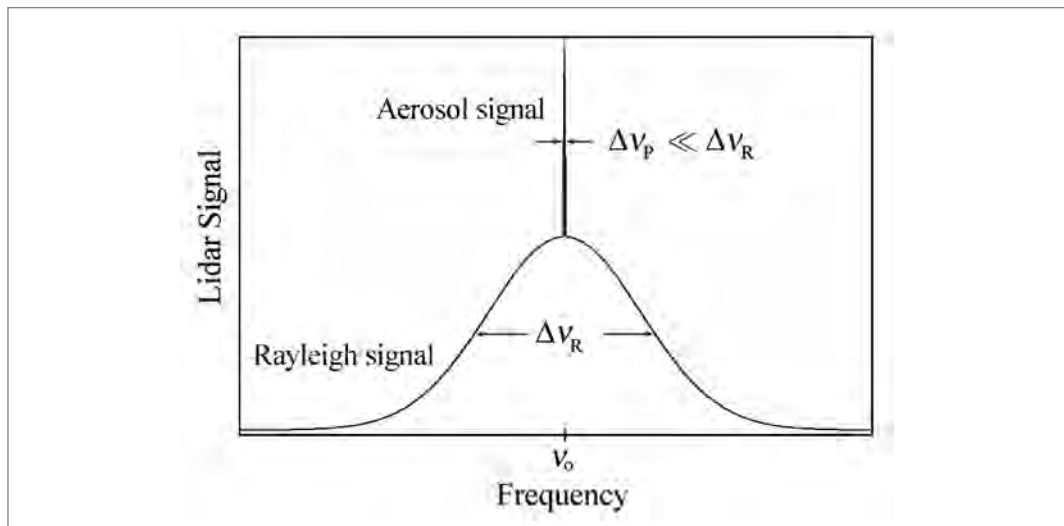


Fig. 3: Spectrum of narrow-band laser light backscattered from the atmosphere.

bration to physical parameters of the lidar device nor a calibration to the optical properties of the atmosphere, as a first approximation, is necessary for which reason the DIAL method is known as “self calibrated”.

Although the DIAL method is advantageous regarding calibration issues, it is sophisticated regarding the laser technique which is required for measuring differential absorption of single molecular spectral lines of water vapor. A spectral purity of more than 99.8%, a wavelength stability better than 100 MHz and a laser bandwidth of less than 200 MHz is demanded (Vogelmann and Trickl, 2008, and references therein). Another elaborate issue is the precise determination of the absorption cross sections σ_{\uparrow} and σ_{\downarrow} with the laser line shape and the line shape of the returning backscattered light as a function of altitude. The shape of molecular spectral lines is determined by Doppler broadening (temperature) and by broadening by molecular collisions (pressure). The result is a so-called Voigt profile which is a convolution of a Gaussian and a Lorentz profile respectively (Demtröder, 1993). The line shape of the laser emission is ideally a Gaussian whose width is determined by the length of the laser pulse due to the uncertainty principle ($\Delta f = 0.4413/\Delta t$). The variation of line shapes under different atmospheric conditions is illustrated in Fig. 4.

As mentioned above, the differences in the upward and downward coefficients are caused by the Rayleigh-Doppler-Brillouin broadening of the backscattered narrow-band laser light (Fiocco and De Wolf, 1968; Fiocco et al., 1971). The bandwidth of the spectral distribution becomes comparable with the atmospheric absorption line width of H₂O. As a consequence, the absorption cross sections σ_{\uparrow} and σ_{\downarrow} for the upward and downward path of the light are different (Ansmann and Bösenberg, 1987) and must be calculated by a convolution integral of the molecular spectrum and the line shape of the light on the way up and on the way down, respectively. Doing this for all altitudes within the lidar range means a tremendous computing effort. In practice this can be accomplished by calculating look-up tables with values for σ_{\uparrow} and σ_{\downarrow} for certain altitudes and certain atmospheric conditions (temperature, pressure) and interpolation between the nodes (Vogelmann, 2006).

The effect of the varying line shape of the backscattered light is moderate in the case of pure Rayleigh scattering almost negligible for cases dominated by light scattering by aerosols, because backscatter from aerosols undergoes no significant broadening due to their big weight and low thermal motion compared to air molecules. But, in cases of mixed backscatter from molecules and aerosols and complex aerosol distributions, H₂O-density errors of more than 20% may be reached in vertical sections with significant aerosol gradients, because σ_{\downarrow} from a

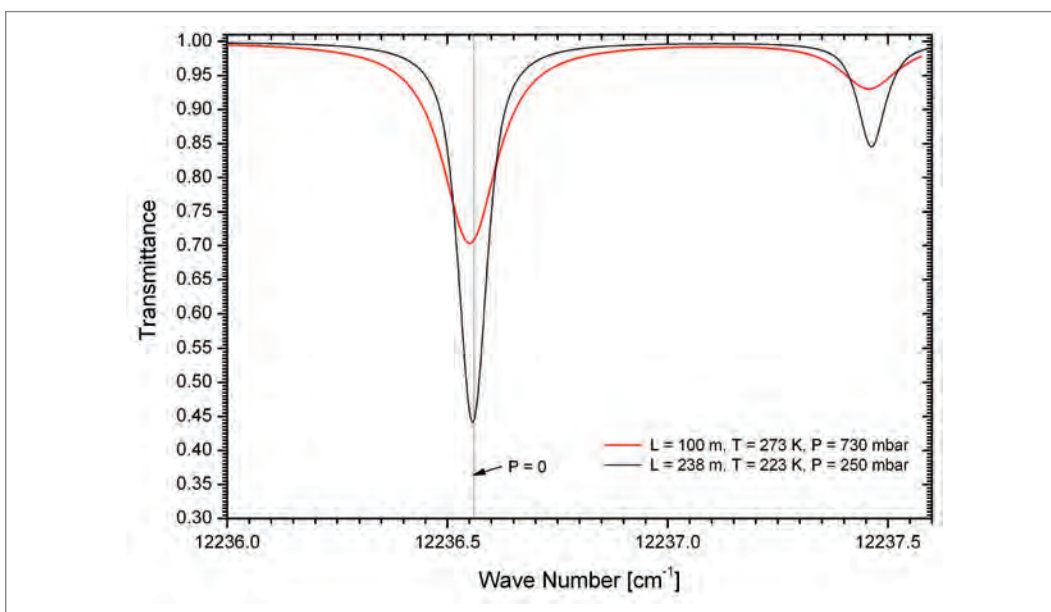


Fig. 4: Atmospheric transmittances in water vapor in the vicinity of 817 nm calculated with HITRAN data for conditions typical of the Schneefernerhaus research station (lidar: 2675 m a.s.l.) and roughly 10 km and approximately equivalent absorption paths. The pressure shifts were taken from (Ponsardin and Browell, 1997).

look-up table may be deficient. For understanding this, we must be aware that the spectral distribution of the backscattered light varies also in the case of large aerosol gradients. The spectral line-shape functions must be included in the lidar equation which makes the DIAL equation much more complex by convoluted integration over different line shapes and the extinction terms, both varying as a function of altitude. At this point, the aerosol contribution that we have cancelled down before by performing a second measurement with λ_{off} re-enters the DIAL equation, because the ratio of backscatter from molecules and aerosols affects the effective molecular absorption cross sections.

The method is described in detail by Bösenberg (1998) and one example of a practical solution suitable for free-tropospheric measurements with slightly elevated aerosol is given by (Vogelmann and Trickl, 2008). The DIAL Eq. 6 is modified by introducing an additional Term $G(r)$:

$$N_{\text{H}_2\text{O}}(r) = \frac{1}{\Delta\sigma_{\uparrow}(r) + \Delta\sigma_{\downarrow}(r)} \left(G(r) - \frac{d}{dr} \left[\ln \left(\frac{S_{\text{on}}(r)}{S_{\text{off}}(r)} \right) \right] \right) \quad (7)$$

For this approach two important assumptions were made: First, the laser bandwidth is almost negligible and second, the term G for λ_{off} is negligible due to an appropriate wavelength choice in a range with minimum absorption. The term G becomes important only in the presence of significant backscatter from aerosols, in particular in the region of pronounced concentration gradients. The calculation of G is described in detail in Vogelmann and Trickl (2008) and we note, that $G(r)$ is dependent on the aerosol backscatter and the water-vapor density itself. This means that for complex aerosol distributions and rather humid conditions some iterations of the retrieval may be necessary.

18.3.2 Numerical retrieval of water vapor

In practice, the derivative in the DIAL equation (Eq.7) is, e.g., calculated by a linear regression line (least-squares) with a certain number of data points arranged symmetrically around the data point of interest. We calculate

$$\frac{d}{dr} \ln \left(\frac{S_{\text{on}}(r)}{S_{\text{off}}(r)} \right) = \frac{S_{\text{off}}(r)}{S_{\text{on}}(r)} \cdot \frac{d}{dr} \left(\frac{S_{\text{on}}(r)}{S_{\text{off}}(r)} \right) \quad (8)$$

in order to avoid the density bias caused by the asymmetric noise distribution for the logarithm. For equidistant data points the result of the fits may be expressed in a rather simple formula, resulting in the following solution of the DIAL equation for the i th data point (Vogelmann and Trickl, 2008):

$$N_{\text{H}_2\text{O}, i} = \frac{1}{\Delta\sigma_{\uparrow i} + \Delta\sigma_{\downarrow i}} \left(G_i - \frac{1}{q_i \cdot \delta} \frac{\sum_{j=i-k}^{i+k} (j-i) q_j}{\sum_{j=i-k}^{i+k} (j-i)^2} \right) \quad (9)$$

with $q_i = S_{\text{on}}(r_i)/S_{\text{off}}(r_i)$ and δr being the size of the altitude bin of the transient digitizer. The transient digitizers of the Zugspitze-DIAL provide a sample rate of 20 MHz which corresponds to a physical vertical resolution of $\delta r = 7.5$ m. For each single least square fit, $2k + 1$ data points are symmetrically arranged around r_i . The denominator may be further simplified by considering that $\sum_{j=i-k}^{i+k} (j-i)^2 = k(k+1)(2k+1)/3$.

It has turned out that a quadratically growing number of data points ($2k + 1$) as a function of the distance r provides sufficient smoothing for keeping the signal to noise ratio in a reasonable range. E.g., we start with 11 data points and increase the number to 101 at the 1000th data point which marks a distance of 7.5 km (roughly 10 km a.s.l. at Zugspitze). The method of calculating the derivative in the DIAL equation by linear least square fits for each data point as in Eq. 9 leads to a vertical resolution of the water vapor profile of roughly $2k\delta/3$.

18.3.3 Uncertainties

We have to distinguish between two types of uncertainties. Random uncertainties, induced by the signal to noise ratio (SNR) and systematic uncertainties. We must keep in mind, that the SNR is determined by the quotient of the two lidar signals, $q_i = S_{\text{on}}/S_{\text{off}}$. As q_i is part of the denominator in Eq. 9, the noise of S_{on} dominates the statistical error propagation. Thus, it is important to find a proper selection of absorption cross sections and wavelengths for λ_{on} and λ_{off}

for certain atmospheric conditions. The extinction for λ_{on} needs to be sufficiently small to avoid a vast light loss in the targeted measurement range, but, at the same time, it needs to be sufficiently large to be measured. This balancing act is illustrated in Fig. 5 for average winter and summer humidity. Noise-induced errors can usually be calculated from scratch by Gaussian error propagation in the DIAL equation (Eq. 9).

$$\sigma_{N_{wv}} = \frac{1}{\Delta\sigma_{\uparrow i} + \Delta\sigma_{\downarrow i}} \cdot \frac{1}{q_i} \cdot \sqrt{\frac{a_i^2}{q_i^2} \sigma_{q_i}^2 + \sigma_{a_i}^2} \quad \text{with} \quad a_i = \frac{d}{dr} q_i \quad (10)$$

a_i is the slope of the regression line within the $2k + 1$ data points q_j (r_j) symmetrically arranged around q_i (r_i). σ_{q_i} and σ_{a_i} calculate to:

$$\sigma_{q_i} = \sqrt{\frac{1}{(2k+1)-2} \sum (a_i r_j + b_i - q_j)^2} \quad \text{and} \quad \sigma_{a_i} = \frac{\sigma_{q_i}}{\delta_i \sqrt{\sum (j-i)^2}} \quad (11)$$

This uncertainty depends on the noise level which is mostly induced by electronic noise and disturbing stray light from the atmosphere. Latter can become dominant, in particular during daytime and in the presence of cirrus clouds. Because of the diminishing backscatter signal with growing distance, in particular at the specifically absorbed λ_{on} wavelength, the statistical uncertainty is a function of altitude which limits the altitude range of a DIAL. This type of uncertainty is practically reduced by enlarging the regression interval $2k + 1$ as mentioned above. Doing so, for the water vapor DIAL at Mt. Zugspitze we calculated a 5% uncertainty to a mean vertical water vapor profile throughout the free troposphere. Because of the drop of water vapor concentration at the tropopause level and above (typically varying between 8 km and 12 km) the noise induced measurement error cannot be controlled by further enlarging the regression interval $2k + 1$ with a reasonable vertical resolution. In this altitude range we reach the sensitivity limit of the DIAL system which correspond to a water vapor mixing ratio of 18 ppm at 10 km a.s.l.. Fig. 6 shows the relative measurement errors for a given regression interval of $2k + 1 = 67$ which corresponds to a vertical resolution of 150 m and optimal cross-sections for different conditions and additional stray light.

Although the DIAL method is known to be self calibrated, there remains a high potential for systematic errors from very different sources. Here we discuss only the two most important error sources of this type.

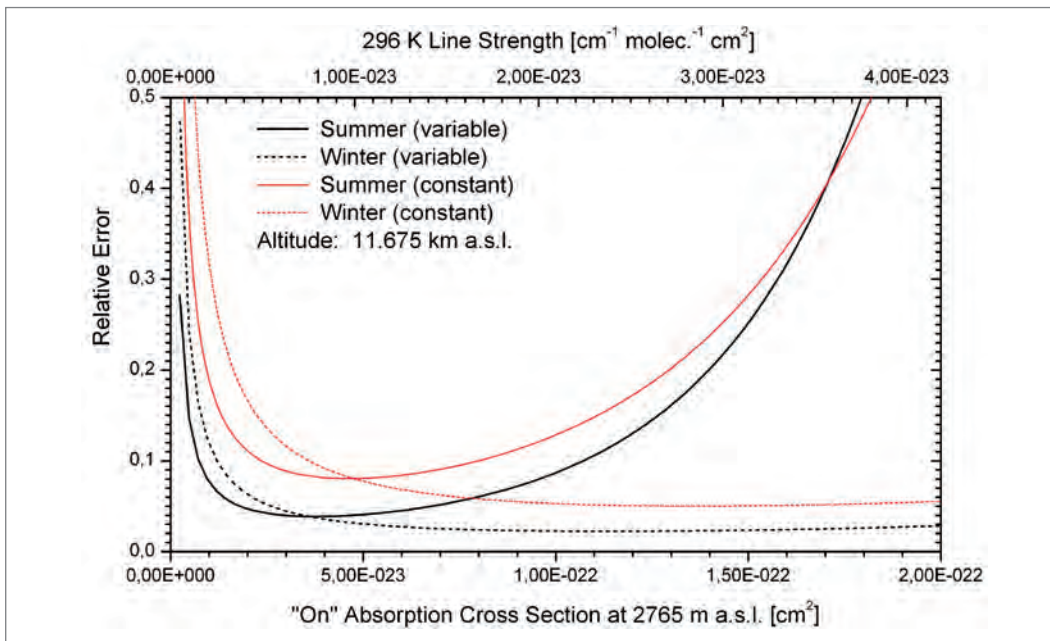


Fig. 5: Relative uncertainty of the water-vapor density at 817 nm as a function of the absorption cross section at an altitude of 11.675 m a.s.l. (i.e., 9 km above the lidar laboratory) for the LOWTRAN 7 seasonal models "mid latitude summer" and "mid latitude winter" LOWTRAN 7 model (1989); the results are shown for line widths variable and constant as a function of altitude. Top scale: 296 K line strength. The strongest line ($4.98 \times 10^{-23} \text{ cm}^{-1} \text{ molecule}^{-1} \text{ cm}^2$) (Ponsardin and Browell, 1997) above) is highly suitable under dry conditions.

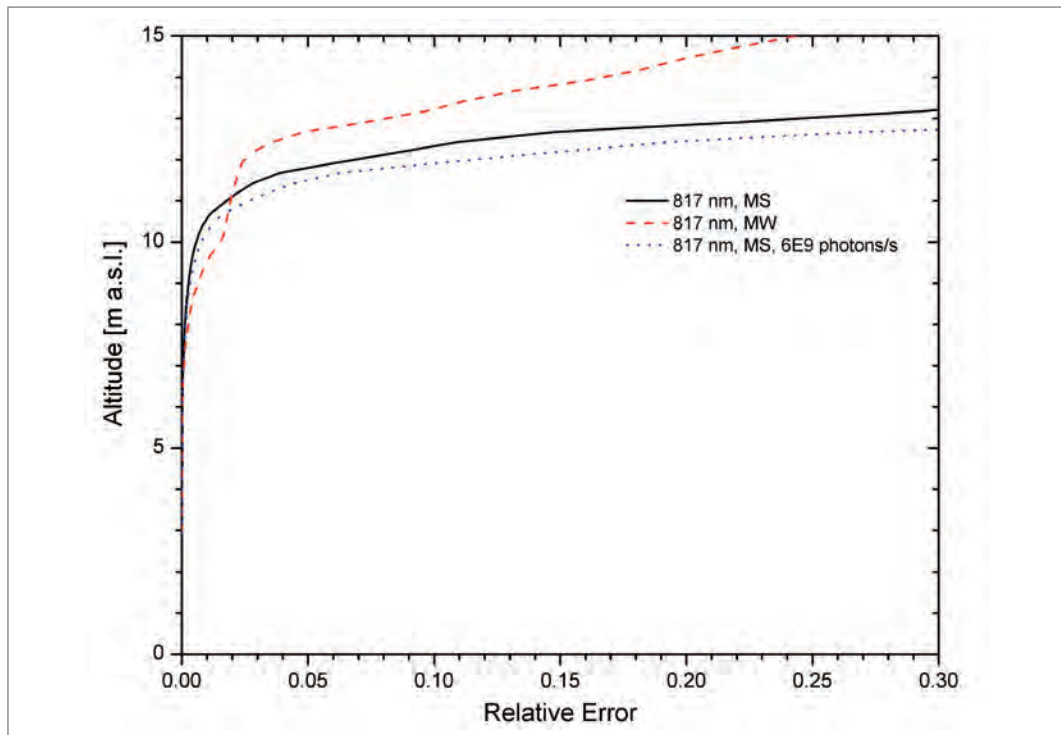


Fig. 6: Relative uncertainty of the water-vapor density at 817 nm as a function of altitude for optimally selected absorption cross sections; the range reduction during daytime is rather small (Vogelmann and Trickl, 2008). MS and MW refer to the LOWTRAN 7 seasonal models “midlatitude summer” and “midlatitude winter” respectively. For the dotted line, a typical daylight photon flux reaching the detector was estimated.

Nonlinearity of the detection system can become a severe problem, if it is not a static behavior but caused by the lidar signals itself in relation to the huge dynamic of the lidar signals of typically more than 5 orders of magnitude. In most cases this signal induced “noise” can be described as a function of the integrated lidar signal and behaves similar to the discharging of a capacitor after the main pulse has passed and a numerical correction should be applied before the signals are further processed. The shape of signal induced noise is dependent on both the detector type and the connected electronics. One method of characterization is the detection of signals from a hard and non transparent target, such as a dense cloud, a distant building or a mountain face. If nonlinearity is a static phenomena, it usually can be numerically corrected before data processing. A common method to identify static nonlinearities is the execution of a reference measurement with a blocked laser beam, but with the laser turned on.

Uncertainties about absorption cross sections result in linear errors in the retrieval algorithm, which can be easily corrected a-posteriori if it is possible to acquire corrected values for the cross sections. Wrong information about cross sections have three causes. Firstly, wrong assumptions about atmospheric conditions (temperature, pressure). This leads only to moderate errors, because temperature and pressure are mainly a function of altitude with only moderate variations due to weather conditions. In most cases, sufficiently precise information is available from weather services and their data products (e. g., NCEP). Secondly, wrong assumptions about the spectral distribution of the transmitted laser radiation. This can cause severe errors, if the spectral distribution is not reproducible, i. e., if a malfunction of the laser (e. g., resulting in insufficient spectral purity) or the wavelength control occurred. In this case, only a calibration with a third-party instrument will be helpful. Thirdly, assumptions about line-strengths and line-shapes are wrong. This causes only moderate linear errors in the retrieval, but, a correction is only possible if correct line parameters are available, which is not always the case. Therefore, it is important to choose absorption lines from the H_2O spectrum carefully. In particular, pressure-shifts, temperature-dependency of line strengths, should be well known and should have been characterized by laboratory experiments. For this reason, the Zugspitze-DIAL uses only a small set of spectral lines which have been well characterized by Ponsardin and Browell (1997). An example is given in Fig. 4. The cross sections of the spectral lines used at the Zugspitze DIAL may differ by up to about 10% from the values taken from the HITRAN database (Rothman et al., 2009).

18.4 Technical implementation

The technical implementation of a water vapor DIAL system at the Schneefernerhaus at Mt. Zugspitze is exemplary. Because this system was designed to record water vapor profiles throughout the entire free troposphere, a large and powerful system is needed. For boundary layer applications a water vapor DIAL with much less laser power and a smaller receiving telescope also would be suitable.

18.4.1 Laser systems

Due to a particularly wide tuning range in the near IR, covering the three band systems of H₂O mentioned in the preceding subsection, its high output power and its reasonable thermal performance the Ti:sapphire laser has become the preferred laser source for DIAL sounding (Moore et al., 1996; Browell et al., 1996; Nagasawa et al., 2001; Ertel, 2004; Ertel et al., 2005; Vogelmann and Trickl, 2008), although also alexandrite lasers and optical parametric oscillators (OPOs) have been used (Wulfmeyer and Bösenberg, 1998 and Poberaj et al., 2002).

In order to avoid line-shape corrections the laser bandwidth must be reduced to about one tenth of the absorption line width (≥ 2 GHz) or less. This requires single-longitudinal mode (SLM) operation of the laser. Different approaches to achieve single-mode operation of these systems have been reported. In most systems continuous-wave diode lasers directly seed the Ti:sapphire crystals. This, although limiting the wavelength tuning range, is particularly important in mobile or air-borne systems where an efficient active feedback control of the laser frequencies is needed. The master oscillators of the Zugspitze DIAL are two pulsed single-longitudinal mode (SLM) Optical Parametric Oscillators (OPOs) in Littman cavity configuration pumped by a frequency doubled Nd:YAG laser. This approach combines the advantages of very wide tunability and of reducing the number of expensive seed lasers, in particular laser-pumped continuous Ti:sapphire lasers that could also provide a large tuning range. On the other hand the use of sensitive pulsed oscillators requires higher passive (mechanical and thermal) stability. The OPOs were modified for a more stable single-mode operation (Vogelmann and Trickl, 2008). Pulses next to the Fourier-transform limit were obtained, e. g., for near-Gaussian pulses 4.0 ns long 130 ± 15 MHz (Fourier limit: 110 MHz). Active frequency locking to a precise interferometer system is used to stabilize the laser frequency.

The layout of the complete laser system, including the OPOs and the Ti:sapphire laser, is shown in Fig. 7 (see Table 1 for specifications). The Ti:sapphire laser is set up in ring configuration with a ring circumference of 4.8 m. This size allows for storing laser pulses up to a pulse length of 10 ns without interfering with themselves. Radiation is coupled into or out from the ring by high-speed polarization switching. The flashlamp-pumped Ti:sapphire ring laser emitted up to 250 mJ per pulse at a repetition rate of 20 Hz. This setup is currently changed to a transversely laser pumped design with a repetition rate of at least 100 Hz, but with a lower pulse energy of about 100 mJ. This promises a more reliable operation far from damage thresholds with even a higher average output.

Transmission measurements in a absorption cell filled with Cs vapor verified a spectral purity of the generated IR radiation at least 99.9%. This is a consequence of the large resonator size (Fig. 7) and spatial filtering, which remove the divergent broadband contributions.

18.4.2 Receiver

In order to collect as much of the backscattered light as possible, a large telescope in the lidar receiver must be used. Therefore, for the Zugspitze system the principal component of the receiver (Fig. 8; specifications: Table 1) is a Newtonian telescope with an 0.65 m-diameter parabolic mirror ($f = 2$ m), more or less limited by the dimensions of the slit of the costly astronomical dome above the laboratory. The light entering the telescope is collimated and fed through a 5 nm interference filter, separated into near- and far-field channels with a 1-% beam splitter, and finally detected with avalanche photo diodes (APDs). In the far-field channel an additional 0.5 nm-bandwidth interference filter is installed during daytime in order to reduce further the solar background.

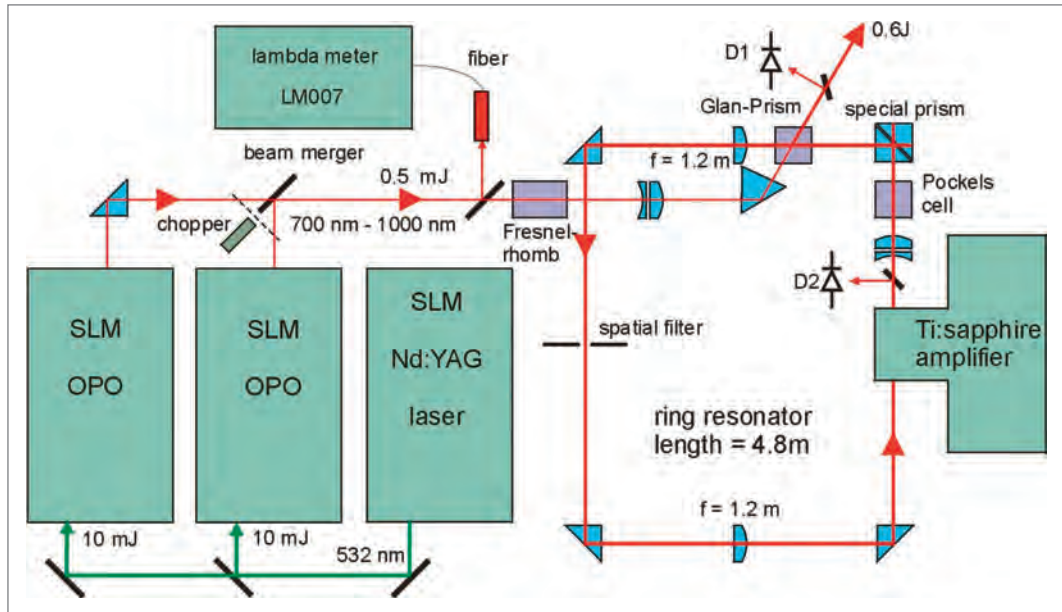


Fig. 7: Layout of the laser system of the Zugspitze DIAL; abbreviations: D1, D2 ... fast photo diodes (Vogelmann and Trickl, 2008).

The laser beam is sent into the atmosphere at a distance of not more than 0.7 m from the telescope axis, which ensures a full beam overlap (beginning of the operating range) at a distance of 300 m. This allows for comparisons with the FTIR spectrometer and the in-situ measurements at the Zugspitze summit. The telescope axis, the laser beam, and the optical axis of the ocular are aligned in a common plane. The near-field contribution in the far-field channel is cut off by an adjustable-slit aperture. This aperture also rejects a major part of the solar background, outside the useful rectangular field of view. The signals for the "on" and "off" wavelengths are separated by sequential detection. Optionally, a second far-field channel can be added (as indicated in the figure) if the detection spectral bandwidth must be further reduced with at least one Fabry-Perot etalon in the future.

The pre-amplified signal from each APD is recorded by a 12-bit transient digitizer with 16384 registers and a sample rate of 20 MHz, which provides a spatial resolution of 7.5 m.

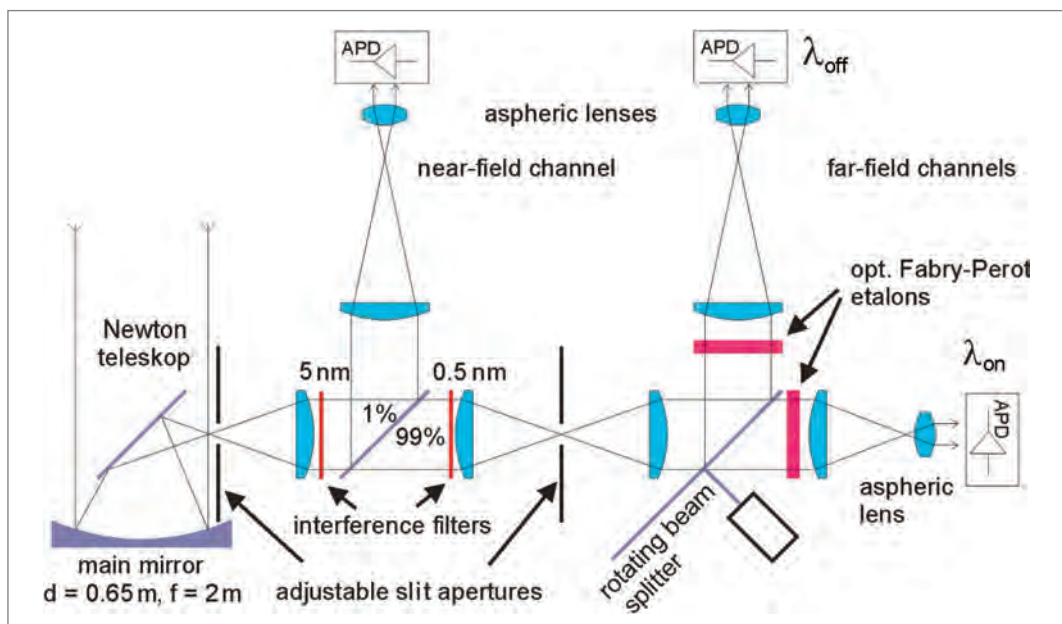


Fig. 8: Layout of the receiver of the Zugspitze DIAL; the λ_{off} far-field channel is optional and not yet installed. Abbreviation: APD ... avalanche photo diode (Vogelmann and Trickl, 2008).

Table 1: The most important specifications of the Zugspitze DIAL

<i>Laser System</i>	
Laser oscillators	2 KTP Littman OPOs, pumped at 532 nm
Number of wavelengths	2, both next to 817 nm
Pulse repetition rate	20 s ⁻¹ (10 s ⁻¹ for each wavelength)
Pulse length	2 ns - 4 ns
Pulse energy	0.25 J around 800 nm
Tuning range	700 nm - 950 nm
Single-shot bandwidth	130 MHz - 250 MHz
Frequency noise	±35 MHz
Spectral purity	>99.9%
Beam pointing stability	≈30 μrad
Beam diameter	7 mm
Beam divergence	≈0.25 mrad
<i>Receiver</i>	
Main-mirror diameter	0.65 m
Focal length	2 m
Number of channel	2 (optionally 3)
Far-field field of view	1.25 mrad x 3 mrad
Near-field field of view	2.5 mrad x 8 mrad
Detectors	Si APD (3 mm diameter)
APD detection efficiency	77%
APD noise (after amplification)	200 μV (peak to peak, 10 ⁴ shots averaged)
Typical peak signal	300 μV
Spectral filtering near field	5 nm
Spectral filtering far field	0.5 nm
Sample rate of transient digitizer	20 MHz
Digital resolution	12 bit
Number of shots	10 ⁴
Vertical resolution for H ₂ O	varied from 50 m to 260 m (VDI-Richtlinie 4210, 1999)

18.4.3 System performance

In this and the following subsection we discuss the performance so far achieved for the wide-range Zugspitze DIAL. The system has been thoroughly tested since the summer of 2004. In 2007 routine operation was started, with typically two measurement days per week, if the weather conditions are favorable. A number of examples of measurements, obtained under different conditions, are shown in (Vogelmann and Trickl, 2008). Here, just two of them are presented to illustrate the capabilities of the Zugspitze DIAL (Figs. 9 and 10). Further examples are given in the parallel contribution by Trickl and Vogelmann (this volume) and the references cited therein.

For a first validation, several RS80 radiosondes were launched in Garmisch-Partenkirchen by the Meteorological Institute of the University of Munich in autumn 2005. Although the distance of the launch site to the lidar is just 10 km the influence of the differences in time and space was mostly not negligible. In Fig. 9 the results of a successful comparison are shown. Apart from some vertical displacement, rather likely caused by the sonde drifting outside the Alps, the agreement is very good up to 8 km.

A very good agreement was also achieved when intercomparing integrated water vapor profiles with the integrated water vapor measurements from the solar Fourier transform mid infrared spectrometer at the Zugspitze summit (Vogelmann et al., 2011).

Fig. 10 shows an example of a narrow stratospheric air intrusion at 3.2 km a.s.l.. This narrow layer arrived approximately from the east. Thus, the Munich radiosonde, which ascended almost at the time of the lidar measurement, probed roughly the same phase of the air mass. The agreement of the two measurements is quite astonishing, both showing as little as 1% relative humidity in the dry layer. This indicates the absence of significant mixing with the air surrounding this

thin dry tongue in the middle and lower troposphere. When the intrusion had descended to the Zugspitze summit (2962 m a.s.l.) three hours later the relative humidity had grown to 13%, which is about three times the error specified for the *in-situ* measurement. In a systematic study we found that the minimum humidity in intrusion layers can be even much lower and frequently match values in the lowermost stratosphere (Trickl et al., 2014). This demonstrates that a water-vapor DIAL is capable of resolving these extreme values at least in the lower free troposphere.

The example in Fig. 10 shows a principal agreement between the measurements above UFS and Munich, but also clear differences. This underlines the difficulty of a validation of humidity profiles with instruments not sharing the observational volume. This could be avoided in a comparison of the Zugspitze DIAL with the air-borne DIAL-system DLR-WALES (935 nm) on-board the FALCON aircraft within the LUAMI campaign (Wirth et al., 2009; Trickl et al., 2016). Both systems showed a remarkable agreement (deviation < 3%) in a major part of the altitude range during the FALCON overpass. The result of the comparison is shown in Fig. 6 of our parallel contribution (Trickl and Vogelmann, 2022). No bias between the two lidar systems could be resolved at an uncertainty level of about 1%. Finally, three optical remote sounders (2 DIALs, 1 FTIR) operating in three different regions of the water vapor molecular spectrum demonstrated their precision by direct intercomparison for the first time.

Routine measurements with the DIAL were carried out from 2007 to 2015. The measurements have revealed a considerable variability of the free-tropospheric water-vapor densities over the year by roughly a factor of thirty. By using different wavelength pairs there is rarely a problem in reaching altitudes of more than 10 km.

The current sensitivity limit of the lidar in the upper troposphere is chosen as the amplitude of the density noise, which is roughly $1.5 \times 10^{22} \text{ m}^{-3}$ (and sometimes even better), corresponding to about 18 ppm of H_2O for an altitude of 10 km. Anticipating a substantial increase in laser pulse energy and an order-of-magnitude reduction in signal-processing noise the sensitivity limit of the Zugspitze DIAL could be improved to about 2.5 ppm, i.e., below the stratospheric H_2O mixing ratio of typically 4 to 5 ppm.

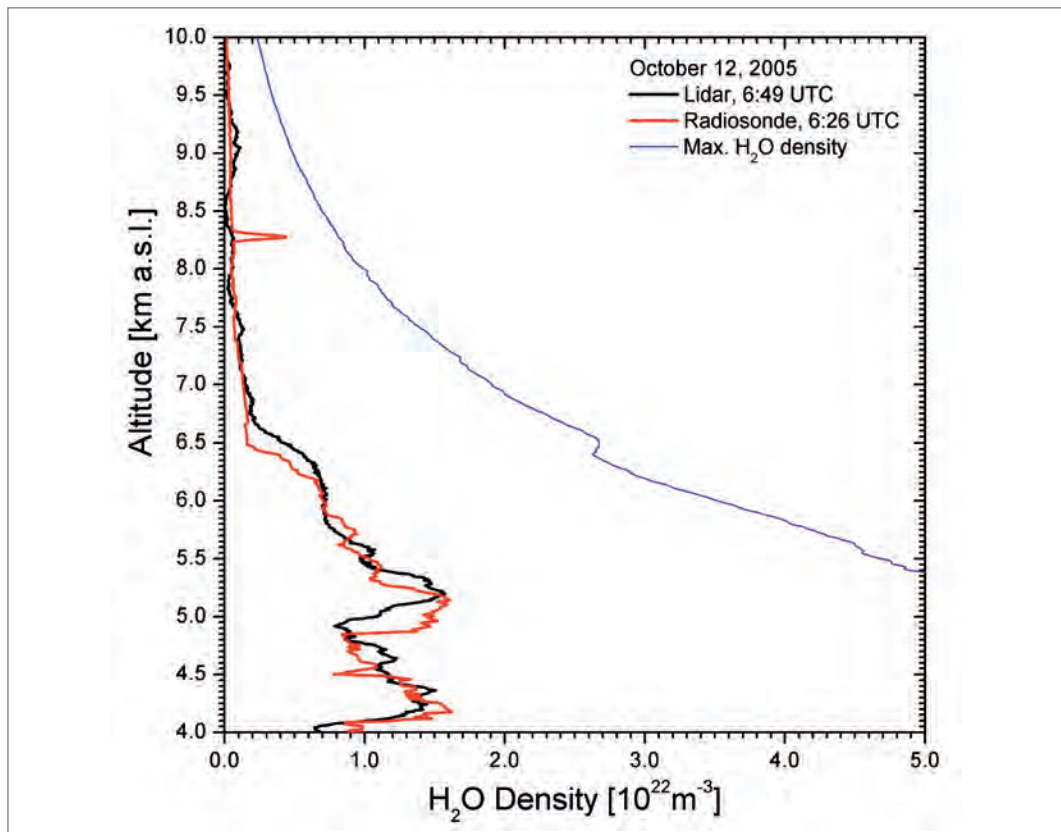


Fig. 9: Comparison of an almost simultaneous measurement of the Zugspitze DIAL and with a RS80 radiosonde launched at Garmisch-Partenkirchen on October 12, the maximum possible water-vapor density (100% relative humidity) is derived from the sonde temperature profile (Vogelmann and Trickl, 2008).

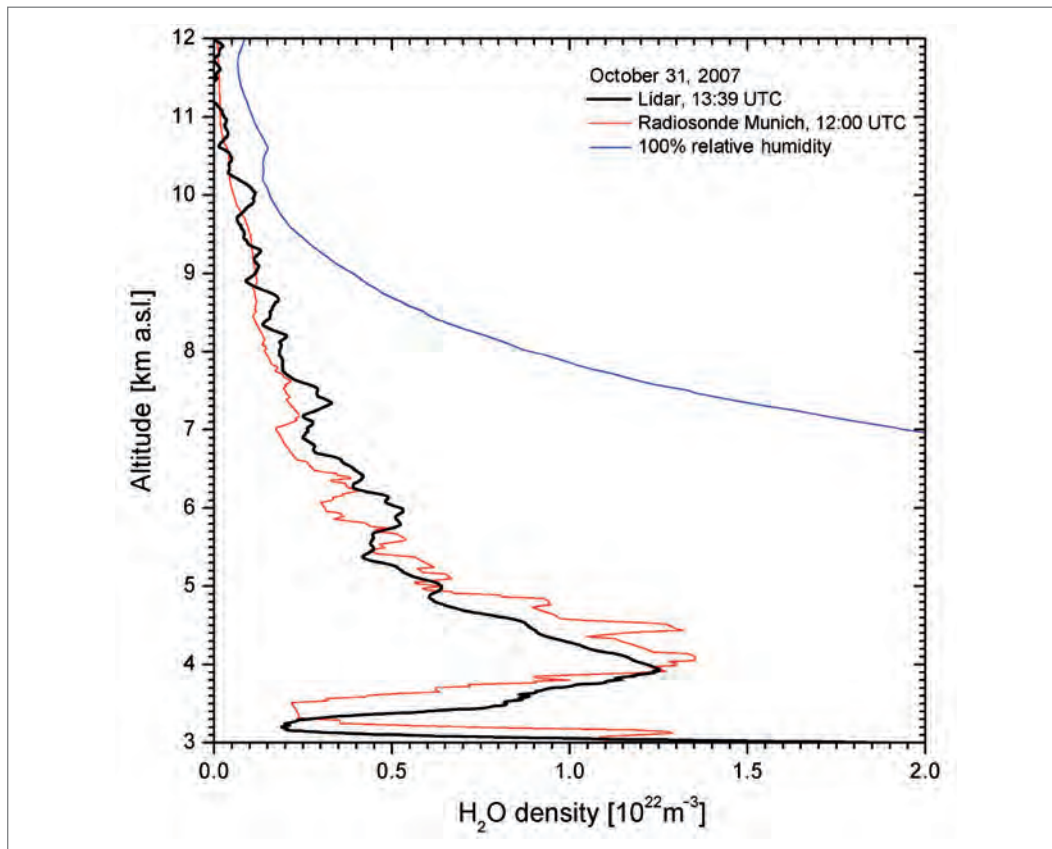


Fig. 10: Measurements of Zugspitze DIAL and Munich radiosonde during a stratospheric intrusion event on October 31, 2007; the density for 100% relative humidity is derived from the sonde temperature profile. The lidar data were re-evaluated with higher vertical resolution than in Fig.15 of (Vogelmann and Trickl, 2008) in order to show the true system performance within the stratospheric air layer at 3.2 km.

18.5 Conclusions and outlook

Due to their good temporal and spatial resolution DIAL measurements are ideal for detailed studies of tropospheric trace gases. The DIAL technique is also highly suitable for routine measurements due to its stable calibration. The first ground-based DIAL system covering almost the entire free troposphere is the high-power lidar at the Schneefernerhaus research station in the Northern Alps. Excellent daytime performance has been demonstrated. Although a measurement error corresponding to 5% of the average seasonal humidity, as demanded by the climate-research community (e.g. Harries, 1997) and suggested by the performance simulations, is not yet proved above 9 km, the results indicate, that the final performance of the system could be close to this or even better. Cases in which upper-tropospheric measurements are not possible due to complete light absorption at lower altitudes are rare. This demonstrates the advantage of the high-altitude lidar laboratory. The Zugspitze DIAL was in successful routine operation from 2007 to 2015 until a major damage of the laser system, which is currently replaced. It contributed to important studies of atmospheric variability and long range transport as well as stratosphere to troposphere exchange (Trickl et al., 2013, 2014; Vogelmann et al., 2015; Trickl et al., 2015, 2016; 2020; Trickl and Vogelmann, 2022). Lidar remote sounding of water vapor and other atmospheric constituents and parameters is an ongoing development which is coupled to the performance and development of laser transmitters. As shown in this chapter, ground based DIAL measurements of water vapor are limited to the troposphere because of light losses in lower altitudes and the drop of the water vapor concentration in the tropopause region. This gave us motivation for developing a Raman-Lidar for stratospheric water vapor measurements up to 25 km (Klanner et al., 2021). This technique, is based on directly measuring inelastic backscatter from H_2O molecules, that is smaller than Rayleigh backscatter at the same wavelength by more than three decades. On the other hand, this method is not limited by its principle to a certain altitude range and can be scaled up to any level by increasing the laser

power and the size of the receiver telescope. The new Raman lidar at UFS has a laser power of 180 W (308 nm) and a main telescope with 1.5 m. The performance of the Raman lidar also allows for temperature measurements up to at 90 km by measuring the air density from inelastic and elastic backscatter from air molecules. As temperature being the most important parameter for radiation and an indicator for the propagation of atmospheric gravity waves, remote temperature profiling is also of great interest in atmospheric and climate research.

A Raman lidar has two main disadvantages. Wide-range operation is limited to the night because of the weak far-field signal is perturbed by the noise of solar background, a limitation that is much less severe for a DIAL (see Fig. 6). Secondly, a Raman lidar must be calibrated. At UFS we have the unique advantage of the parallel operation of the DIAL that ensures volume matching. A first positive comparison of the two UFS lidar systems in a highly complex situation is described in Klanner et al., 2010). Both reasons strongly motivate to provide a new high-power laser system for the DIAL. The development of a new laser is under way. A new concept has been chosen and the first version was successfully tested.

References

- Ansmann, A. and Bösenberg, J.: Correction scheme for spectral broadening by Rayleigh scattering in differential absorption lidar measurements of water vapor in the troposphere, *Appl. Opt.*, 26, 1987.
- Browell, E.V., Wilkerson, T.D., and McIlrath, T. J.: Water vapor differential absorption lidar development and evaluation, *Appl. Opt.*, 18, 3474–3483, 1979.
- Browell, E.V., Ismail, S., Hall, W.M., Moore, A.S., Kooi, S.A., Brackett, V.G., Clayton, M.B., Barrick, J.D.W., Schmidlin, F.J., Higdon, N.S., Melfi, S.H., and Whiteman, D. N.: LASE validation experiment, in: *Advances in Atmospheric Remote Sensing with Lidar*, edited by Ansmann, A., Neuber, R., Rairoux, P., and Wandinger, U., pp. 289–295, Springer-Verlag, selected Papers of the 18th International Laser Radar Conference (ILRC), Berlin, 22–26 July 1996, 1996.
- Browell, E.V., Ismail, S., and Grant, W. B.: Differential absorption lidar (DIAL) measurements from air and space, *Appl. Phys. B*, B 67, 399–410, 1998.
- Bruneau, D., Quaglia, P., Flament, C., Meissonnier, M., and Pelon, J.: Airborne lidar LEANDRE II for water-vapor profiling in the troposphere. I. System description, *Appl. Opt.*, 40, 3450–3460, 2001.
- Bösenberg, J.: A differential absorption lidar system for high resolution water vapor measurements in the troposphere, *Tech. Rep. 71*, Max-Planck-Istitut für Meteorologie, 1991.
- Bösenberg, J.: Ground-Based differential absorption lidar for water-vapor and temperature profiling: methodology, *Appl. Opt.*, 37, 3845–3860, 1998.
- Demtröder, W.: *Laser-Spektroskopie, Grundlagen und Techniken*, Springer-Verlag, 3 edn., 1993.
- Ehret, G., Kiemle, C., Renger, W., and Simmet, G.: Airborne remote sensing of tropospheric water vapor with a near-infrared differential absorption lidar system, *Appl. Opt.*, 32, 4534–4551, 1993.
- Ehret, G., Hoinka, K.P., Stein, J., Fix, A., Kiemle, C., and Poberaj, G.: Low stratospheric water vapor measured by an airborne DIAL, *J. Geophys. Res.*, 104, 31 351–31 360, doi:10.1029/1999JD900959, 1999.
- Elterman, L.: The measurement of stratospheric density distribution with the searchlight technique, *J. Geophys. Res.*, 58, 509–520, 1951.
- Ertel, K.: *Application and Development of Water Vapor DIAL Systems*, Dissertation (in English), Universität Hamburg, 2004.
- Ertel, K., Linné, H., and Bösenberg, J.: Injection-seeded pulsed Ti:sapphire laser with novel stabilization scheme and capability of dual-wavelength operation, *Appl. Opt.*, 44, 5120–5126, 2005.
- Fiocco, G. and De Wolf, J. B.: Frequency Spectrum of Laser Echoes from Atmospheric Constituents and Determination of the Aerosol Content of Air, *J. Atmos. Sci.*, 25, 488–496, 1968.
- Fiorani, L., and Mitev, V. (Eds.): *Series: Optoelectronic Materials and Devices*, Vol. 7: *Recent Advances in Atmospheric Lidars*, INOE, Bucharest (Romania), ISBN 978-973-88109-6-9, 407 pp., 2010.
- Fiocco, G., Benedetti-Michelangeli, G., Maischberger, K., and Madonna, E.: Measurement of the Temperature and Aerosol to Molecule Ratio in the Troposphere by Optical Radar, *Nature*, 229, 78–79, 1971.
- Forster, P. M. d. F. and Shine, K. P.: Assessing the climate impact of trends in stratospheric water vapor, *Geophys. Res. Lett.*, 29, 060 000–1, doi:10.1029/2001GL013909, 2002.
- Grant, W.B., Margolis, J. S., Brothers, A. M., and Tratt, D. M.: CO₂ DIAL measurements of water vapor, *Appl. Opt.*, 26, 3033–3042, 1987.
- Harries, J. E.: Atmospheric radiation and atmospheric humidity, *Q. J. R. Meteor. Soc.*, 123, 2173–2186, 1997.
- Higdon, N.S., Browell, E.V., Ponsardin, P., Grossman, B.E., Butler, C.F., Chyba, T.H., Mayo, M.N., Allen, R.J., Heuser, A.W., Grant, W.B., Ismail, S., Mayor, S.D., and Carter, A. F.: Airborne differential absorption lidar system for measurements of atmospheric water vapor and aerosols, *Appl. Opt.*, 33, 6422–6438, 1994.

- Hinkley, E. D. (Ed.): *Laser Monitoring of the Atmosphere*, vol. 14 of *Topics in Appl. Phys.*, Springer-Verlag, Berlin, ISBN 3-540-07743-X, 1976.
- Hulburt, E. O.: Observations of a searchlight beam to an altitude of 28 kilometers, *J. Opt. Soc. Am.*, 27, 377–382, 1937.
- Klanner, L., Höveler, K., Khordakova, D., Perfahl, M., Rolf, C., Trickl, T., and Vogelmann, H.: A powerful lidar system capable of one-hour measurements of water vapour in the troposphere and the lower stratosphere as well as the temperature in the upper stratosphere and mesosphere, *Atmos. Meas. Tech.*, 14, 531–555, 2021.
- Leblanc, T. and McDermid, I. S.: The TMF Water Vapor Raman Lidar, *Appl. Opt.*, manuscript in preparation, 2009.
- Little, L. M. and Papen, G. C.: Fiber-based lidar atmospheric water-vapor measurements, *Appl. Opt.*, 40, 3417–3427, 2001.
- LOWTRAN 7 model: ONTAR Corporation, Address: 9 Village Way, North Andover, MA 01845-2000 USA, 1989.
- Machol, J. L., Ayers, T., Schwenz, K. T., Koenig, K. W., Hardesty, R. M., Senff, C. J., Krainak, M. A., Abshire, J. B., Bravo, H. E., and Sandberg, S. P.: Preliminary Measurements with an Automated Compact Differential Absorption Lidar for the Profiling of Water Vapor, *Appl. Opt.*, 43, 3110–3121, 2004.
- Measures, R. M.: *Laser remote sensing: fundamentals and applications*, Krieger Pub. Co., Malabar, FL, 1992.
- Moore, A. S., Brown, K. E., Hall, W. M., Barnes, J. C., Edwards, W. C., Petway, L. B., Little, A. D., Luck, W. S., Jones, I. W., Antill, C. W., Browell, E. V., and Ismail, S.: Development of the Lidar Atmospheric Sensing Experiment (LASE) – An advanced airborne DIAL instrument, in: *Advances in Atmospheric Remote Sensing with Lidar*, edited by A. Ansmann, R. Neuber, P. R. and Wandinger, U., pp. 281–288, Springer-Verlag, selected Papers of the 18th International Laser Radar Conference (ILRC), Berlin, 22–26 July 1996, 1996.
- Murray, E. R., Hake, Jr., R. D., van der Laan, J. E., and Hawley, J. G.: Atmospheric water vapor measurements with an infrared (10- μ m) differential-absorption lidar system, *Appl. Phys. Lett.*, 28, 542–543, 1976.
- Nagasawa, C., Nagai, T., Abo, M., Shibata, Y., and Uchino, O.: Development of airborne DIAL for water vapor measurement, in: *Lidar Remote Sensing for Industry and Environment Monitoring – Proceedings of SPIE – The International Society for Optical Engineering*, edited by Singh, U. N., Itabe, T., and Sugimoto, N., vol. 4153, pp. 599–606, 2001.
- Oltmans, S. J. and Hofmann, D. J.: Increase in lower-stratospheric water vapor at a mid-latitude Northern Hemisphere site from, *Nature*, 347, 146–149, 1994.
- Poberaj, G., Fix, A., Assion, A., Wirth, M., Kiemle, C., and Ehret, G.: Airborne all-solid-state DIAL for water vapour measurements in the tropopause region: system description and assessment of accuracy, *Appl. Phys. B*, 75, 165–172, 2002.
- Ponsardin, P. L. and Browell, E. V.: Measurements of H₁₆ 2 O Linestrengths and Air-Induced Broadenings and Shifts in the 815 nm Spectral Region, *J. Mol. Spectrosc.*, 185, 58–70, 1997.
- Rothman, L. S., Barbe, A., Benner, D. C., Brown, L. R., Camy-Peyret, C., Carleer, M. R., Chance, K., Clerbaux, C., Dana, V., Devi, V. M., Fayt, A., Flaud, J. M., Gamache, R. R., Goldman, A., Jacquemart, D., Jucks, K. W., Lafferty, W. J., Mandin, J. Y., Massie, S. T., Nemtchinov, V., Newnham, D. A., Perrin, A., Rinsland, C. P., Schroeder, J., Smith, K. M., Smith, M. A. H., Tang, K., Toth, R. A., Vander Auwera, J., Varanasi, P., and Yoshino, K.: The HITRAN molecular spectroscopic database, edition of 2000 including updates through 2001, *J. Quant. Spectrosc. Radiat. Transfer*, 82, 5–44, 2003.
- Rothman, L. S., Gordon, I. e., Barbe, A., Benner, D. C., Bernath, P. F., Birk, M., Boudon, V., Brown, L. R., Campargue, A., Champion, J., Chance, K., Coudert, L. H., Dana, V., Devi, V. M., Fally, S., Flaud, J., Gamache, R. R., Goldman, A., Jacquemart, D., Kleiner, I., Lacome, N., Lafferty, W. J., Mandin, J., Massie, S. T., Mikhailenko, S. N., Miller, C. E., Moazzen-Ahmadi, N., Naumenko, O. V., Nikitin, A. V., Orphal, J., Perevalov, V. I., Perrin, A., Predoi-Cross, A., Rinsland, C. P., Rotger, M., Šimečková, M., Smith, M. A. H., Sung, K., Tashkun, S. A., Tennyson, J., Toth, R. A., Vandaele, A. C., and Vander Auwera, J.: The HITRAN 2008 molecular spectroscopic database, *J. Quant. Spectrosc. Radiat. Transfer*, 110, 533–572, doi:10.1016/j.jqsrt.2009.02.013, 2009.
- Sachse, G., Wang, L., Antill, C., Ismail, S., and Browell, E. V.: Line-center/side-line Diode Laser Seeding for DIAL Measurements of the Atmosphere, in: *Optical Remote Sensing of the Atmosphere*, pp. 289–295, OSA, Salt Lake City, UT, February 5–9, 1995, 1995.
- Schotland, R. M.: Some observations of the vertical profile of water vapor by a laser optical radar, in: *Proceedings of the Fourth Symposium on Remote Sensing of the Environment*, pp. 273–283, University of Michigan, Ann Arbor, Mich., 1966.
- Senff, C., Bösenberg, J., and Peters, G.: Measurement of Water Vapor Flux Profiles in the Convective Boundary Layer with Lidar and Radar-RASS, *J. Atmos. Oceanic Technol.*, 11, 85–93, 1994.
- Solomon, S., Rosenlof, K. H., Portmann, R. W., Daniel, J. S., Davis, S. M., Sanford, T. J., and Plattner, G.-K.: Contributions of Stratospheric Water Vapor to Decadal Changes in the Rate of Global Warming, *Science*, 327, 1219–1223, doi:10.1126/science.1182488, 2010.

- Trickl, T., and Vogelmann, H.: Simultaneous lidar measurements of ozone, water vapour, and particles: long-term investigation of atmospheric transport up to the hemispheric scale, chapter 21, this book, 2022.
- Trickl, T., Giehl, H., Jäger, H., and Vogelmann, H.: 35 yr of stratospheric aerosol measurements at Garmisch-Partenkirchen: from Fuego to Eyjafjallajökull, and beyond, *Atmos. Chem. Phys.*, 13, 5205–5225, doi:10.5194/acp-13-5205-2013, URL www.atmos-chem-phys.net/13/5205/2013/, 2013.
- Trickl, T., Vogelmann, H., Giehl, H., Scheel, H.-E., Sprenger, M., and Stohl, A.: How stratospheric are deep stratospheric intrusions?, *Atmos. Chem. Phys.*, 14, 9941–9961, doi:10.5194/acp-14-9941-2014, URL <http://www.atmos-chem-phys.net/14/9941/2014/>, 2014.
- Trickl, T., Vogelmann, H., Flentje, H., and Ries, L.: Stratospheric ozone in boreal fire plumes – the 2013 smoke season over central Europe, *Atmospheric Chemistry and Physics*, 15, 9631–9649, doi: 10.5194/acp-15-9631-2015, URL <https://www.atmos-chem-phys.net/15/9631/2015/>, 2015.
- Trickl, T., Vogelmann, H., Fix, A., Schäfler, A., Wirth, M., Calpini, B., Levrat, G., Romanens, G., Apituley, A., Wilson, K. M., Begbie, R., Reichardt, J., Vömel, H., and Sprenger, M.: How stratospheric are deep stratospheric intrusions? LUAMI 2008, *Atmospheric Chemistry and Physics*, 16, 8791–8815, doi:10.5194/acp-16-8791-2016, URL: <http://www.atmos-chem-phys.net/16/8791/2016/>, 2016.
- Trickl, T., Vogelmann, H., Ries, L., Scheel, H.-E., and Sprenger, M.: Very high stratospheric influence observed in the free troposphere over the Northern Alps – just a local phenomenon? *Atmos. Chem. Phys.*, 20, 243–266. 2020.
- VDI-Richtlinie 4210: Fernmessverfahren, Messungen nach dem LIDAR-Prinzip, Messen gasförmiger Luftverunreinigungen mit dem DAS-LIDAR, vol. 5, chap. 2.4.2 Tiefenauflösung, p. 8, Verein Deutscher Ingenieure, Beuth Verlag, Berlin, 1999.
- Vogelmann, H.: Entwicklung und Aufbau eines Hochleistungs-Wasserdampf- Lidar-Systems auf der Zugspitze, Dissertation (in German), Universität Augsburg, Garmisch-Partenkirchen, 2006.
- Vogelmann, H. and Trickl, T.: Wide Range Sounding of Free Tropospheric Water Vapor with a Differential Absorption Lidar (DIAL) at a High Altitude Station, *Appl. Opt.*, 47, 2116–2132, doi: 10.1364/AO.47.002116, 2008.
- Vogelmann, H., Sussmann, R., Trickl, T., and Borsdorff, T.: Intercomparison of atmospheric water vapor soundings from the differential absorption lidar (DIAL) and the solar FTIR system on Mt. Zugspitze, *Atmos. Meas. Tech.*, 4, 835–841, doi:10.5194/amt-4-835-2011, URL <http://www.atmos-meas-tech.net/4/835/2011/>, 2011.
- Vogelmann, H., Sussmann, R., Trickl, T., and Reichert, A.: Spatiotemporal variability of water vapor investigated using lidar and FTIR vertical soundings above the Zugspitze, *Atmos. Chem. Phys.*, 15, 3135–3148, doi:10.5194/acp-15-3135-2015, URL <http://www.atmos-chem-phys.net/15/3135/2015/acp-15-3135-2015.html>, 2015.
- Weitkamp, C. (Ed.): Lidar, Range-Resolved Optical Remote Sensing of the Atmosphere, Springer, Berlin, Germany, 2005.
- Wirth, M., Fix, A., Ehret, G., Reichardt, J., Begie, R., Engelbart, D., Vömel, H., Calpini, B., Romanens, G., Apituley, A., Wilson, K. M., Vogelmann, H., and Trickl, T.: Intercomparison of Airborne Water Vapour DIAL Measurements with Ground Based Remote Sensing and Radiosondes within the Framework of LUAMI 2008, in: Proceedings of the 8th International Symposium on Tropospheric Profiling, edited by Apituley, A., Russchenberg, H., and Monna, W., Delft, The Netherlands, poster presentation, 2009.
- Wulfmeyer, V.: Ground-based differential absorption lidar for water-vapor temperature-profiling: development and specifications of a high-performance laser transmitter, *Appl. Opt.*, 37, 3804–3824, 1998.
- Wulfmeyer, V. and Bösenberg, J.: Ground-based differential absorption lidar for water-vapor profiling: assessment of accuracy, resolution, and meteorological applications, *Appl. Opt.*, 37, 3825–3844, 1998.
- Zuev, V.V., Zuev, V.E., Makushkin, Y.S., Marichev, V.N., and Mitsel, A. A.: Laser sounding of atmospheric humidity: experiment, *Appl. Opt.*, 22, 3742–3746, 1983.

19 Hydrological investigations in the Wetterstein Mountains at the UFS Schneefernerhaus (Bavarian Alps)

K.-F. Wetzel¹, M. Bernhardt², S. Weishaupt¹ & M. Weber³

19.1 Scientific background of hydrological research in high mountain regions

19.1.1 Why do we study high mountain hydrology?

High mountain regions of the world are receiving overproportioned amounts of precipitation in comparison with surrounding regions due to orographic effects. Simultaneously, evapotranspiration rates are low. Therefore, they have been termed as the global water towers by Viviroli et al. (2007). Above all, mountains in dry climate zones have a high significance for water availability for people living in the forelands and for agriculture purposes. In different publications Viviroli et al. (2007) depicted this fact by calculating an index for the contribution of mountain areas for the water supply in adjacent forelands. The regional distribution of this index (cf. Fig. 1) illustrates the hydrological significance of mountain regions on a global scale.

It is not only the total amount of precipitation why mountain areas are referred to as water towers. Besides, the temporal distribution of water availability plays an essential role. During the warm season, when solar radiation is high and primary production can be at its maximum rate, a sufficient water supply especially for agriculture is a prerequisite. In this context, the temporal storage of water by snow cover during the cold season and meltwater from snow and glaciers throughout the summer guarantee sufficient discharge of rivers and recharge of groundwater resources even in dry forelands of high mountain regions (e.g. Verbunt et al. 2003, Holko et al. 2011, Huss 2011).

Another fact, why research on mountain hydrology is necessary, is the ongoing climate change. Climate change affects high mountain regions stronger than lowlands, resulting in a change of regional water budgets, which may cause a shortening of water availability for human purposes (cf. Viviroli et al. 2011). In the European Alps for example, a shift of air temperatures of about 1.4 K has

¹ Institute of Geography, University of Augsburg

² Institute of Hydrology and Watermanagement, BOKU Wien

³ Department of Geography, LMU München

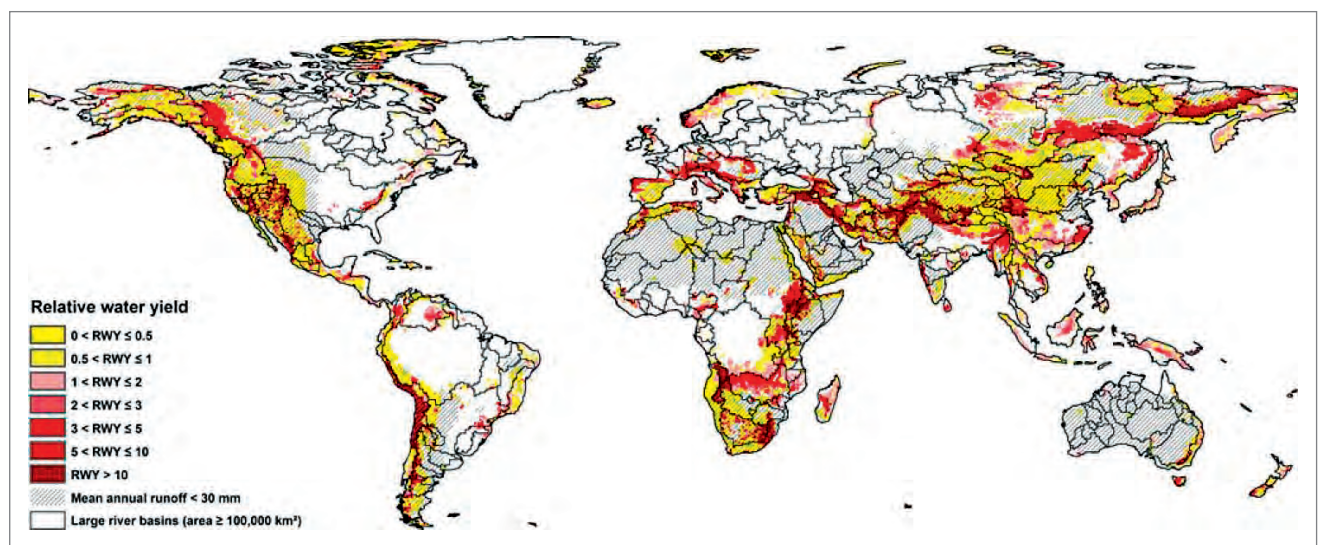


Fig. 1: Runoff formation of mountain areas relative to average lowland runoff given as a disproportionality factor RWY. Disproportionality in favour of runoff exists if RWY > 1, if RWY > 2 its remarkable and its essential if RWY > 5 (for details see Viviroli et al. 2007).

been observed for the last century (cf. Bunetti et al. 2009), which are as twice as high as the global trend (1901–2012) according to IPCC (2013). The rise of temperatures is accompanied by changes in the hydrological regime, mostly obvious in the retreat of glaciers in each part of the Alps and in other high mountain regions of the world (e.g. Hagg et al. 2012, Laghari et al. 2012, Hänggi & Weingartner 2013, Gobiet et al. 2014). The snow cover its areal extend as well as the duration and snow water equivalent are certainly affected by climate change in many upland regions of the world.

Despite the hydrological significance and the impact of climate change on water resources in mountain regions, there is still a gap in the knowledge of high mountain hydrology (e.g. Messerli et al. 2009, Pomeroy & Marks 2009). This gap in knowledge has many reasons. Above all, high mountain areas have harsh environmental conditions, a strong three-dimensional variability of all parameters relevant for hydrology and most areas are only accessible with strenuous efforts. These points will be stressed later in more detail.

19.1.2 Why do we study hydrology at UFS Schneefernerhaus in the Wetterstein Mountains?

There are many reasons why hydrological research is promising at UFS Schneefernerhaus in the Wetterstein Mountains inclusively the highest peak of Germany (Zugspitze, 2,962 m a.s.l.) (see Fig. 2). Important reasons are the special hydrogeological situation, long-term records of meteorological as well as glaciological data, the accessibility of the area, the infrastructure with hydro-meteorological stations and the network of different research institutions working at UFS Schneefernerhaus.

From the hydrological point of view, it is a precondition to have a catchment basin for quantifying the different fluxes of water and for solving the water balance on a regional scale. An ideal catchment basin should be closed and drainage of the basin should take place by only distinct watercourses. Then it is possible to quantify catchment runoff as a base for further analysis like recession behaviour, runoff component analysis or mass balances for environmental tracers as stable isotopes, dissolved carbon or micropollutants.

These hydrogeological preconditions of an ideal catchment basin can be found in the karstified research catchment Zugspitzplatt (RCZ), draining to the Partnach River karst spring (cf. Wetzel

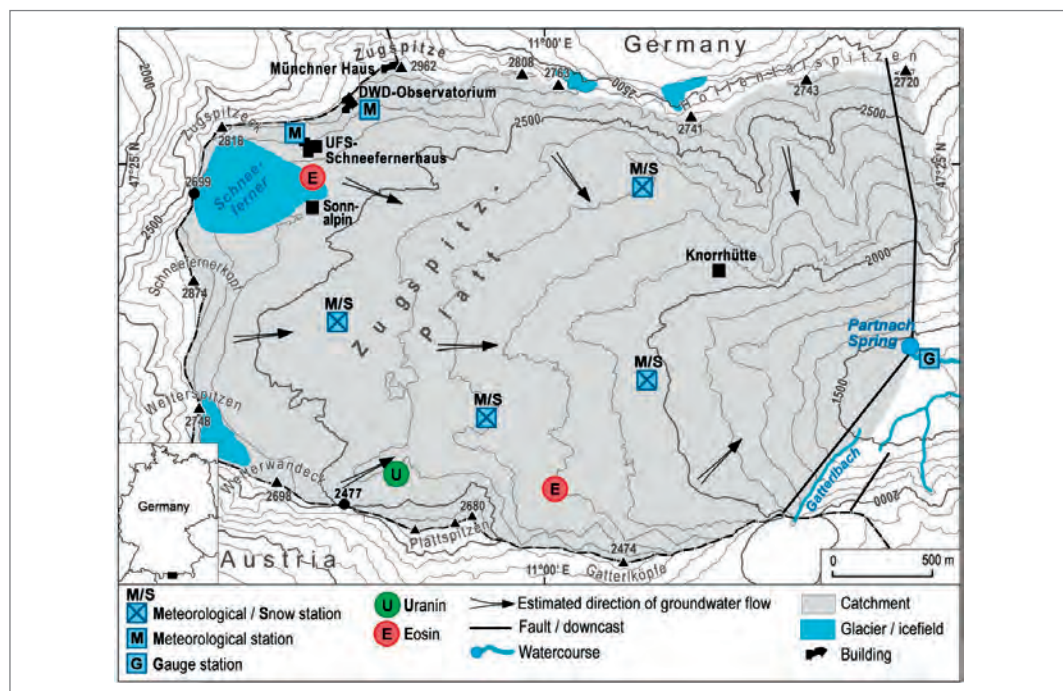


Fig. 2: Location and instrumentation of the research catchment Zugspitzplatt (RCZ). Arrows for the estimated direction of karst groundwater flow and the main fault lines forcing the groundwater for upwelling at Partnach Spring.

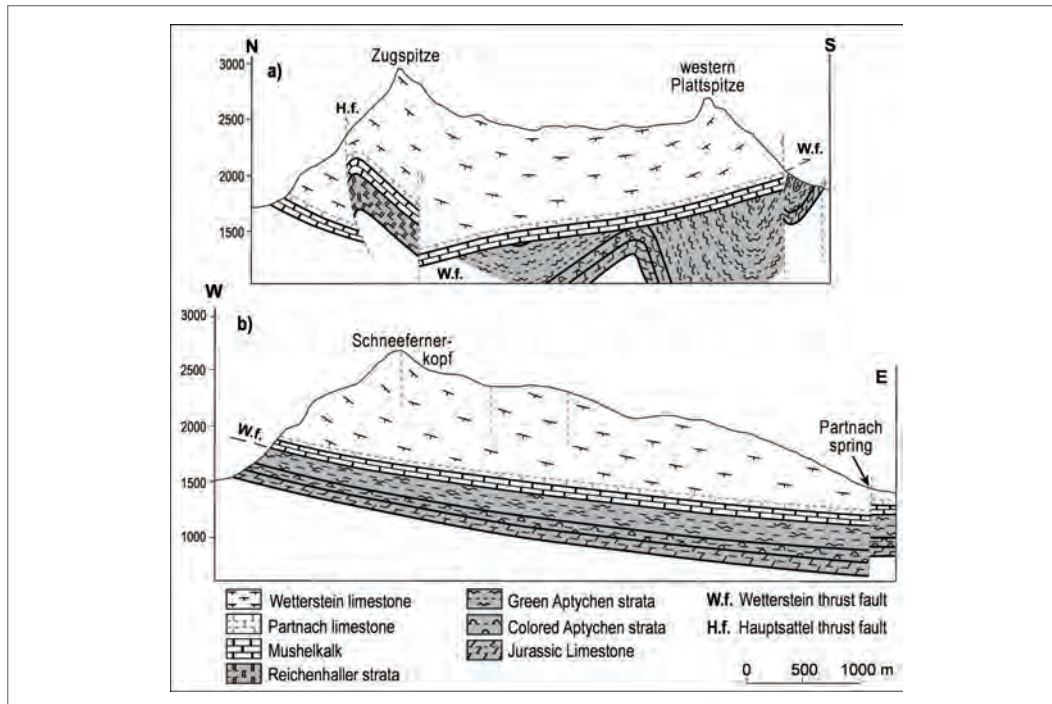


Fig. 3: Cross sections through RCZ according to Miller (1962) showing a) the syncline structure and b) the lowering of the western part of the syncline with RCZ. The marly Partnach limestone below Wetterstein limestone acts as an aquiclude.

2004). UFS Schneefernerhaus is situated within the 11.4 km² wide basin expanding from Partnach-Spring at 1,430 m a.s.l. to the summit of Zugspitze. As a result from tectonic stress from the south, the Zugspitze area is part of a westward rising geological syncline with circular stretching mountain ranges in the south, west and north (Hornung & Haas 2017) (cf. Fig. 2). The entire area is built up by the pure and heavily karstified Triassic Wetterstein Limestone with a thickness of about 600–800 m (Miller 1962, Hornung & Haas 2017). Underlying marly claystone (Partnach limestone, also Triassic) and other strata with an estimated thickness of around 300–600 m are acting as an aquiclude. According to Miller (1962) the higher western part of the Zugspitze area has been lowered geologically along two approximately north-south running fault lines by some tenth of meters (Fig. 3). At the crossing-point of these faults the spring is situated feeding the Partnach River by upwelling karst groundwater. The centre of the geological syncline has a quite smooth eastward dipping surface with a slope of about 13°, overtopped by surrounding mountain ranges by several hundred meters.

Due to high elevations and steep slopes with ongoing geomorphological processes (debris flows, rock fall) large parts of the area (ca. 40%) are not covered by vegetation. Typically for the northern Alps, in the lower part of the catchment up to an elevation of 2,000 m a.s.l. mountain forests with spruce, fir and pine are dominating. Above the tree line and below elevations of about 2,350 m a.s.l. patchy alpine grassland covers the ground where fine-grained moraine sediments can be found. A detailed map of vegetation cover of RCZ has been presented by Korch (2014).

For the region around Zugspitze a long-term meteorological record since 1900 AD of an observatory of the German weather service (DWD) exists. According to the data of the DWD observatory, the region has received little more than 2000 mm of precipitation per year for the period of 1961–1990 (Müller-Westermeier 1996). Because of the exposed position of the observatory, wind induced losses may lead to lower precipitation amounts as in the surrounding more sheltered areas. Mean temperature of this period according to data of DWD was –4.8 °C with extremes of 17.6 °C and –32.7 °C (Müller-Westermeier 1996). Snowfall can be observed throughout the year, but during winter season from October to the end of April, solid precipitation is dominating. At lower elevations snowmelt already starts in March and April, in May snowmelt can occur at the entire Zugspitzplatt usually having its maximum in middle of June and commonly lasting up to July. Typically, most parts of the catchment are snow free at

the end of July and hydrographs of the melting glaciated areas can be recorded at Partnach spring (cf. Wetzel 2004). During the summer season, heavy thunderstorms with high precipitation amounts may occur as well as long lasting intense rainfall events.

Beneath the mountain range in the northwest of RCZ, the remains of a formerly more than 3 km² wide glacier (beginning of 19th century) are situated. According to Hagg (2012) the glaciated area decreased to 32.6 ha in 2009 at the end of the mass balance period in September and for major glacier remain (Nördlicher Schneeferner) from 103.6 ha in 1892 over 27.8 ha (2009) to 23.9 ha in 2014 (cf. Wetzel & Bernhardt 2015). Observations and topographic data of the glacial retreat are available from 1892 AD on up to the recent.

Often accessibility of catchments can be a limiting factor for research in high mountain areas. Even fieldwork is hard in the RCZ because it has to be done by feet in a steep and rough terrain, the area can be reached easily all over the year by cable car or cogwheel train. In the centre of RCZ at an elevation of 2.580 m a.s.l. the main station for mountain tourists (skiing, sledding, hiking, etc.) is situated (see Fig. 2). From here, a cable car leads to the UFS Schneefernerhaus (2,650 m a.s.l.) where accommodation of about 30 researchers is possible. In the lower part of RCZ, two mountain huts of the "Deutscher Alpenverein" (DAV) are situated at an elevation of about 2,050 m and 1370 m a.s.l., respectively. They also offer accommodation during the summer season, making fieldwork more effective and easy.

The UFS Schneefernerhaus is a virtual institute consisting of ten partners organized in a consortium. As the consortia partners are representing different facets of environmental research from precipitable water in the atmosphere over raindrop formation processes to trace element analysis in the ecosystem, a scientific network exists at UFS Schneefernerhaus, stimulating interdisciplinary hydrological research. From the hydrological point of view, data of the DWD are of special interest as well as data from the LWD (Bavarian Avalanche Service) who maintains a climate station equipped with several devices specific for questions of snow hydrology. Additional climatological data from surrounding areas are recorded by the working group on bioclimatology and geosphere (TUM) of Prof. A. Menzel (see contribution XY in this book) in a special research on climatological gradients in a mountain environment (Klimagrad).

19.1.3 What are the problems constraining hydrological research in high mountain environments?

High mountain environments have harsh environmental conditions, constraining measurement of parameters relevant for hydrological research. Several international scientific commissions and working groups are engaged in the special task of cold regions hydrology, including hydrology of high mountains. Examples are the International Commission for Snow and Ice Hydrology (ICSIH) of the IAHS, the International Glaciological Society (IGC), the WMO Global Cryosphere Watch (GCW) mechanism or the International Network for Alpine Research Catchment Hydrology (INARCH) (Pomeroy et al. 2015).

Above all, it is the lower temperature leading to a high proportion of solid precipitation. Measurement of solid precipitation in a mountainous terrain and the estimation of water equivalent is a hard challenge due to the areal heterogeneity of snow properties, the redistribution of snow by wind as well as by avalanches and last but not least gaseous gains and losses. On the other hand, the three-dimensionality of the relief is causing a high variability in the wind field resulting in a heterogeneity of precipitation amounts even in short distances and other hydrological parameters as exposure or soil moisture.

A few examples shall illustrate the problems hydrological research is confronted with in mountain areas. Due to harsh climate conditions, measuring devices sometimes are failing. If snow cover is high for instance, measuring devices may be covered by snow. Therefore, instruments are often mounted higher as normally. Fig. 4 shows a typical weather station with instruments for temperature and humidity in 3 m and 5 m above the ground, respectively. The rain gauge for liquid and solid precipitation has also been mounted 5 m above ground, because of a thick snowpack during winter. Low temperatures can cause failures of electronic equipment as well as lightning strokes during thunderstorms in summer. Precipitation measurements have high wind induced losses in comparison to lowland stations because of stronger winds in high altitudes and since snow is prone to wind drift (cf. Sevruk 1996, Frei & Schär 1998).



Fig. 4: Summer and winter aspect of a meteorological station in the RCZ.

Runoff in mountain creeks is often extremely turbulent. Additionally, bedload transport is common during high flows resulting in difficulties determining discharge rates exactly. For runoff measurements, tracer techniques as the salt dilution method for instance are appropriate to turbulent flowing mountain waters, because traditional flow meters as well as acoustic devices may be damaged under these conditions. Otherwise, turbulent flowing water is a prerequisite for the use of tracer based runoff measurements. High concentrations of solids during storm runoff is a further item of mountain creeks leading to several problems at river gauges.

19.1.4 What is the design of our measuring approach?

The hydrogeological situation of RCZ with a westward rising syncline structure, circular stretching mountain ranges and a karst spring draining the entire catchment gives the idea of a big natural lysimeter (see Fig. 5). The idea of a natural lysimeter has been proven by dye tracer tests. A first dye tracer test was conducted in 1980. The Bavarian Geological Service injected about 10 kg of Uranine into the meltwater flow of the Nördlicher Schneeferner (Wrobel 1980). Because no information about flow velocities in the karst system existed, sampling procedure at the Partnach spring began about 18 hours after Uranine injection. At this time, the concentration peak of Uranine has just passed the spring in a distance of about 4.2 km and only the tailing of the dye experiment could be recorded. In August of 2005 again two dye tracers (5 kg Uranine and 10 kg Eosine) were inserted at two different points of the Zugspitzplatt (cf. Fig. 2) (Rappl et al. 2010). At well-developed sinkholes meltwater of a 20 cm snow cover flushed the dye tracers into the karst system. A dense network of sampling points round the Zugspitze area especially in the vicinity of the fault lines was set up. Over one year samples were taken in a decreasing temporal resolution of initially 30 min to monthly intervals. As a result no dye could be detected outside the Partnach River and recovery rates more than 90% for Uranine and around 50% for Eosine were calculated (Tab. 1). During a further dye tracer test in 2012, Eosine was injected in the southeaster part of Zugspitzplatt with the intention to verify the closed structure of the basin in the vicinity of the bordering fault line. Again, no emersion of tracer was observed and a recovery rate of about 50% could be determined (Strobl & Wetzel 2015) emphasising the closed character of RCZ and the idea of a natural lysimeter.

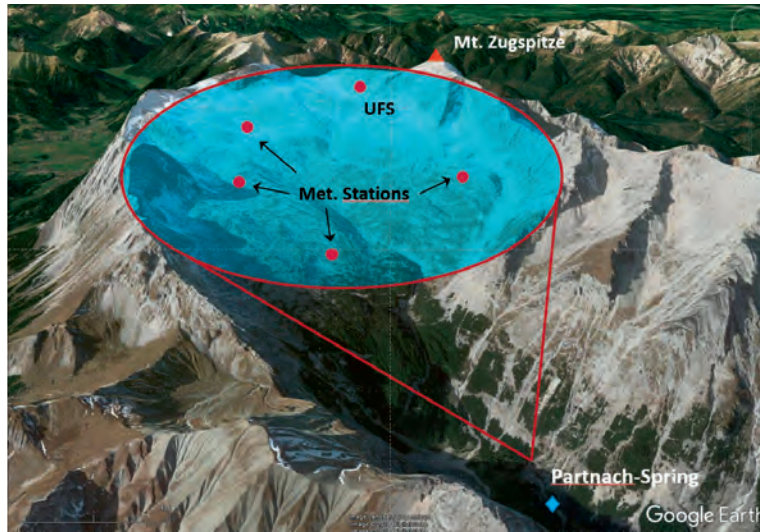


Fig. 5: The closed character of RCZ with a gauging station near Partnach-Spring provokes the idea of a natural lysimeter suitable for balancing the water budget of a high alpine catchment.

Tab. 1: Review of quantitative results of dye tracer experiments in the basin auf Partnach spring

	Experiment 2011	Experiment 2005		Experiment 1980
dye tracer	Eosine (4 kg)	Uranine (5 kg)	Eosine (10 kg)	Uranine (12 kg)
date of input	08-17, 12:00	08-16, 14:20	08-17, 11:00	08-05, 15:00
inclined distance to Partnach spring	2,907 m	4,155 m	3,510 m	about 3,500 m
first detection	53.5 h	32 h	20.5 h	< 18 h
max. velocity	54,3 m/h	130 m/h	171 m/h	> 200 m/h
mean velocity	14,3 m/h	67,8 m/h	104,2 m/h	-:-
mean longitudinal dispersivity α_1	50,3 m	41,4 m	189 m	-:-
recovery rate	ca. 53 %	> 90 %	> 52 %	ca. 20 %

To operate a natural lysimeter, it is necessary to quantify input and output fluxes as accurately as possible. This is especially problematic in mountain regions as relevant hydrological parameters show a high variability in space and would therefore require a dense measurement scheme (e. g. Strasser et al. 2013). The input term of the water balance equation is precipitation. Output of the hydrological system is generated by gaseous losses and by runoff. Because direct measurement of runoff is possible with a high accuracy, gaseous losses mostly are calculated by subtraction of precipitation and runoff (De Jong et al. 2005). Hence, our measurements are concentrating on solid and liquid precipitation on the input side and on registration of runoff for system output in a high temporal resolution.

Therefore, the research area is instrumented with meteorological stations extended by instruments for snow observation (Fig. 2). In 2013 three stations for meteorological and snow cover observations have been installed at about 2,320 m a.s.l. in the north and south of Zugspitzplatt as well as in eastern part at 2,000 m a.s.l. These stations are comparable to a meteorological station of the Bavarian Avalanche Warning Service (LWD), which is situated at about 2,420 m.a.s.l. in a central position of the Zugspitzplatt. Data of these stations are transmitted by GSM to a server, so permanent data access is possible. Tab. 2 gives an overview about the parameters measured at these four stations. A broad spectrum of meteorological data is available from the DWD observatory at Zugspitze. At UFS Schneesfernerhaus meteorological data as temperature, humidity and precipitation are recorded in addition to a multitude of remote sensing based measurements of the lower and middle atmosphere.

Tab. 2: The instrumentation of meteorological stations in the research area.

Sensor	Station East 2,015 m	Station North 2,295 m	Station South 2,300 m	LWD Station 2,420 m
Temperature 3 m	●	●	●	●
Temperature 5 m	●	●	●	–
Humidity 3 m	●	●	●	●
Humidity 5 m	●	●	●	–
Windspeed m/s	●	●	●	●
Wind direction	●	●	●	●
Snow hight	●	●	●	●
Surface temp.	●	●	●	–
Snow base temp.	●	●	●	–
Snow temp. 50 cm	●	●	●	–
Snow balance 6 m ²	–	–	–	●
Albedo global	●	●	●	●
Albedo shortw.	●	–	–	–
Albedo longw.	●	–	–	–
Prec. balance	●	–	–	●
Tippy bucket	●	●	●	●

Liquid precipitation is recorded by a network of tippy buckets and rain gauges at seven places distributed over the entire catchment and in the Partnach valley (Fig. 2). Tippy buckets are only working correctly while liquid precipitation occurs. Several thresholds for separating snow and rain by air temperatures were presented in the past (Kienzle 2008). In this study we use a threshold of 2 °C. When air temperatures are above plus 2 °C liquid precipitation is assumed. If temperatures are below this threshold data of the tippy buckets are not reliable and only data of

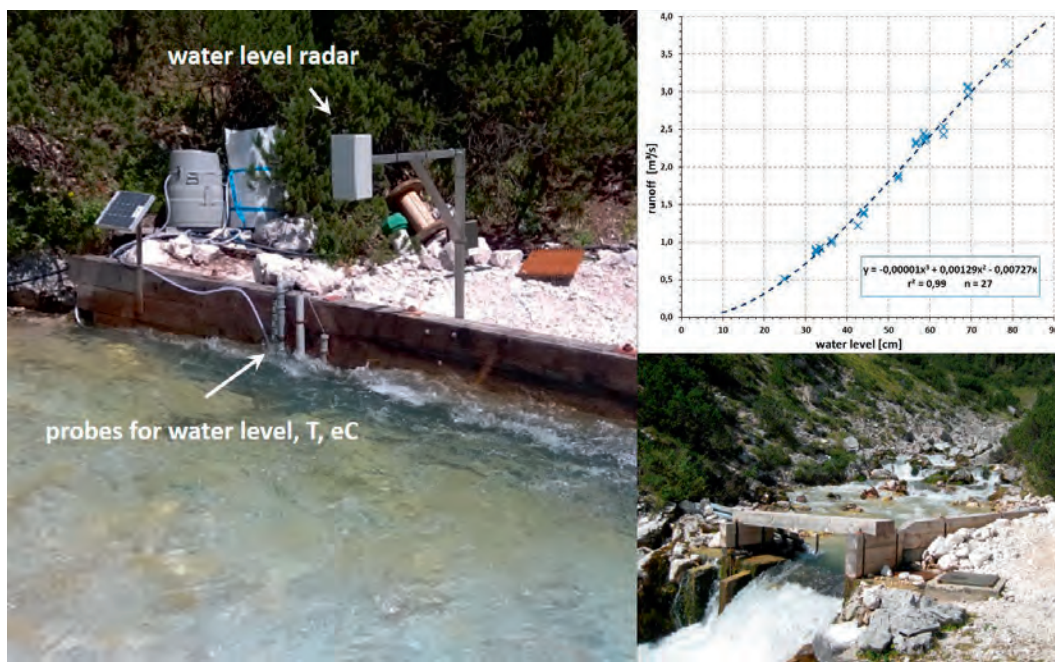


Fig. 6: Partnach River gauge with instruments for recording of water level, EC and water temperature as well as for automatic water sampling. The plot shows the relationship of water level and runoff derived from salt dilution measurements.

weighing rain gauges are used. The measurement of solid precipitation and above all the snow water equivalent is a challenging task, described later in a separate chapter.

System output is recorded at Partnach River gauge (see Fig. 6) nearly 250 m downstream of the Partnach spring. Due to the risk of avalanches during springtime, direct measurements at the spring are not possible. At Partnach River gauge water level is recorded every five minutes by a pressure probe and a radar system, additionally. Automatic water samplers are placed at the gauge station as well. The water level runoff relationship of Partnach River gauge has been computed by means of salt dilution runoff measurements. As Fig. 6 shows, we have a robust polynomial function for the calculation of runoff over a wide span of water levels.

Stable isotopes of the different runoff components (precipitation, meltwater and water from Partnach spring) are collected for mass balance calculations as well as for runoff separation and residence time estimations. For runoff separation by use of geochemical tracers, electric conductivity (EC) is recorded at Partnach River gauge.

19.2 Results of the hydrological research in the Wetterstein Mountains

19.2.1 Snow cover and its spatiotemporal distribution (M. Bernhardt & M. Weber)

It is a general challenge to describe the snow cover distribution in high mountain areas. This is because of the fact that the snow cover distribution is very much coupled on the local turbulence fields, which are influencing snow accumulation and snow redistribution. Hence, there was sceptics in the literature and it was nearly questioned if the prediction of the real snow distribution and of the steering factors might be possible at all. Klemes (1988) argued: *“Validating wind fields and snow transport processes in mountainous areas is a highly difficult and mostly impossible task”*. The main issues belonged to the limited accessibility of high alpine and crest regions, which are most interesting for model validation, which leads to a remarkable lack of validation data which can only be overcome if one has *“a team of Olympic skiing heroes available for the field campaign”* (Klemes 1988). But, it was also seen that there is a good chance to overcome at least some of these issues by using remotely sensed information, which should than balance the existing deficits at least to some degree (Klemes 1988, Hall et al. 1995). It can be stated that the mentioned issues are still existent and vast mountain areas, also of the research catchment Zugspitze (Bernhardt et al. 2014) do stay inaccessible at least during the winter season. Nevertheless, information about the amount of snow stored in the catchment is needed in different ways. Water from the alpine snow cover is buffering low flows in the summer, is used for energy production, can play a key role in course of flood generation and is important for the tourism industry. As many of the named topics are critical for the people which are living in the mountains or the forelands, highly precise information about the snow cover distribution in mountain catchments has to be delivered. It has become obvious that measurement campaigns are not an option because of the terrain characteristics. In addition, while today remotely sensed data can be very helpful for delineating the snow cover extent it is still impossible to derive the one value we are looking for in water resources management and that is the snow water equivalent. Snow water equivalent is describing the amount, which would be left if the snow pack would be completely unfreezed. The approach at the RCZ is to use scientific models to translate the available information from the meteorological stations into a spatially distributed snow cover. Different challenges have to be addressed here. First of all the point measurements of the meteorological variables have to be converted into a spatial field of these variables. This means for any point in the catchment has to be a temperature, a humidity, etc. information available for running the hydrological model at the respective point afterwards. This information can be produced by interpolation techniques of different complexity or by means of regional climate models (RCMs). Both is done at Zugspitze catchment. In case of an interpolation the methods included in micromet (Liston & Elder, 2006) or those included in meteoio (Bavay & Egger 2014) are used. Both are making more or less use of topographical characteristics in the catchment for distributing the meteorological variables. The

techniques reach thereby from simple gradient/lapse rate methods were the average increase/decrease of a meteorological variable with elevation is used for distributing the variable over the catchment with the help of a digital elevation model (DEM) (Bernhardt et al., 2010; Gao et al., 2012; Gao et al., 2014). Other more complex approaches as Kriging or Co-Kriging or other statistical approaches (Bavay & Egger 2014, Laux et al. 2009, Masson & Frei 2014) are used as well. Independent of the used scheme it has to be mentioned that meteorological information in high alpine areas might be extremely error prone and does have a limited spatial representativeness. This can be related to the harsh climatic conditions and the steep topography. It is not uncommon that a meteorological sensor freezes during the winter season and does therefore deliver none or false information. Beside of this high wind speeds in combination with solid precipitation usually leads to a robust underestimation of the precipitation. The limited spatial representativeness of the station measurements stems from the fact that the stations are usually located at flat and easily accessible locations which do only represent a small portion of the total catchment area. Knowing this is important for interpreting the results of the hydrological models in a proper way.

So, if the meteorological information is made available a certain type of hydrological model has to be selected. This is again a challenging task as there are numerous models with different complexity available. These reach from simple day degree models to complex multi-layer physically based model approaches. Temperature index models are not used at the research catchment Zugspitze as the scientific value of those models is questionable. Temperature index models are accumulating the snow at the ground if the air temperature during a precipitation event is below of a certain threshold temperature. This is also true for more complex models but those are usually using the wet bulb temperature as indicator for snow or rainy precipitation. If the temperature now reaches another threshold, the snow starts to melt again. This is under many aspects a huge oversimplification of the melting process which is in reality steered by the incoming short and longwave radiation, local turbulences in the windfield, internal energy budget of the snow pack, albedo of the snow surface, liquid water content within the snow pack and finally also by the air temperature. Hence, while temperature index models might be an adequate tool for applied approaches were a simple relationship between temperature and melt is needed or if extremely limited climatic inputs are available, there is no argument for using these models in a scientific context, by ignoring all of the relationships mentioned before. Zugspitze research catchment does deliver any key climatic parameter from numerous points in the catchments. The layout of the measurement network as described before is made for supporting the setup and the further development of sophisticated land surface models. This is why two advanced snow hydrological models are used here. The spatially distributed and raster based model Alpine3D developed at the SLF (Mott et al. 2014, Schlogl et al. 2016) and CRHM developed at the centre for hydrology of USASK (Fang & Pomeroy 2016, Lopez-Moreno et al. 2016, Weber et al. 2016). Main differences between these models are that the one has a spatial discretisation scheme which is raster based (Alpine3D) and do have a dynamic multi layer snow cover representation while the other one used hydrological response units (HRU) for a spatial discretisation and a three layer model for the snow pack description (CRHM). It could be shown that both models are very much able to reproduce the snow cover evolution when compare to the measurements at our measurement stations (cf. Fig. 7).

Also the spatial representation of the snow pack was very good when compared to satellite data (Fig. 8).

But, by saying this different other research questions appeared. First, how many HRUs do we need for sufficiently describe the hy-

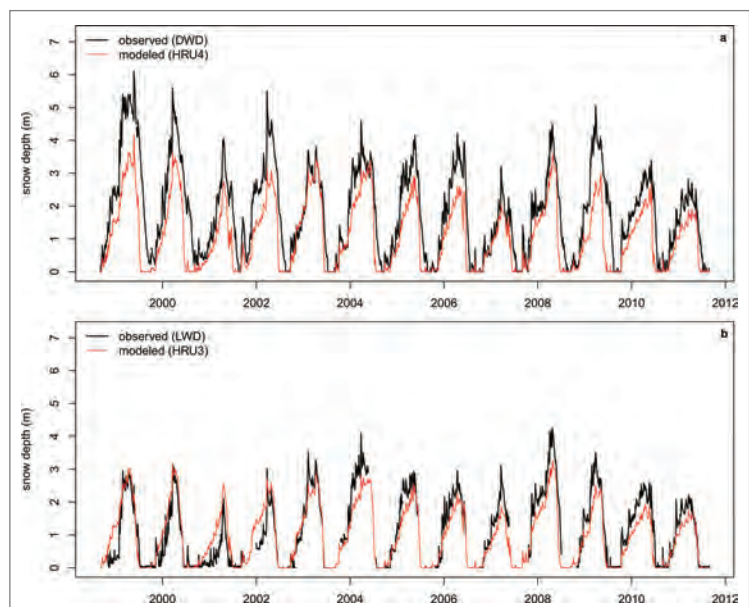


Fig. 7: Comparison of measured and modelled snow depth in RCZ.

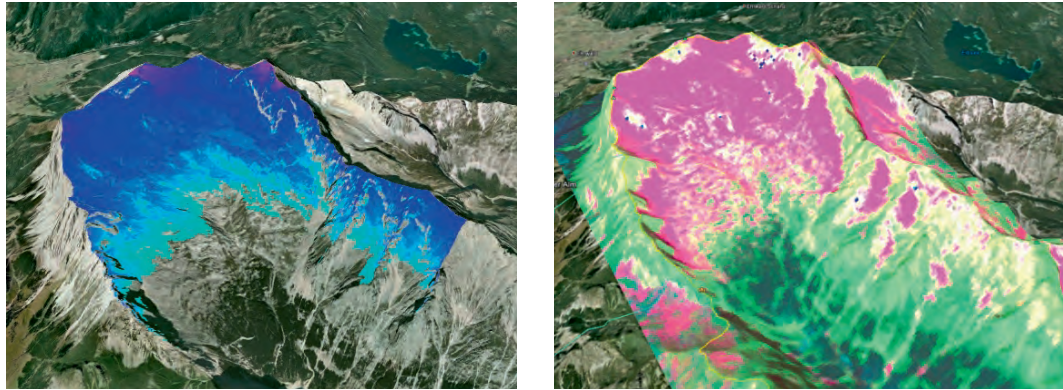


Fig. 8: The spatial representation of the snow packs by modelling and from satellite data.

drology of a catchment like the research catchment Zugspitze? Do the model modules and model schemes which are to some parts developed in other regions of the world really cover the dynamics at Zugspitze or are we right for the wrong reasons? Is our satellite evaluation data user independent and objective? Is the data we are using for future projections really covering all the processes we have identified as relevant with our long over a 100-year historical data series. All these questions were answered at Zugspitze during the last years. We have seen that the snow distribution in the catchment is mostly generated over snow redistribution of the still accumulated snow cover in our models. This behaviour can be observed in colder environments than Zugspitze is. These areas tend to have a very light and dry snow pack, which can be easily modified by local turbulences. The snow cover at Zugspitze instead is comparatively compacted

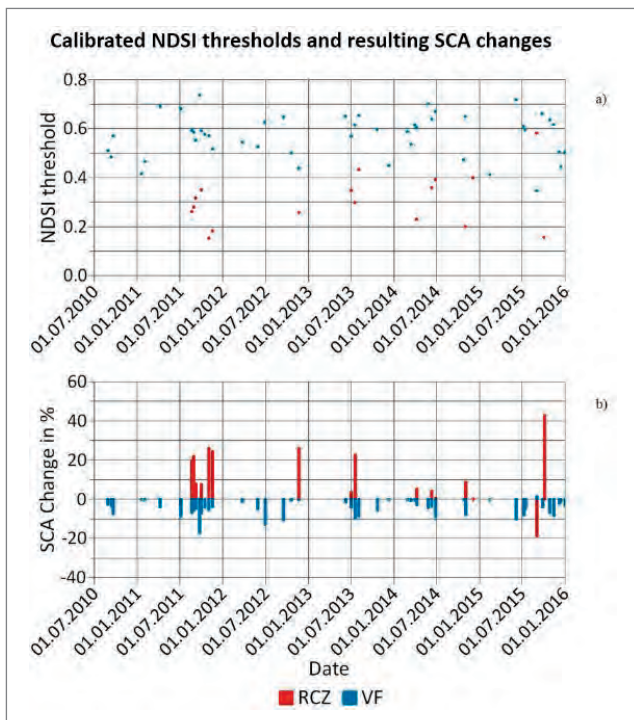


Fig. 9: Calibrated NDSI thresholds by PRACTISE for RCZ and the Vernagtferner area.

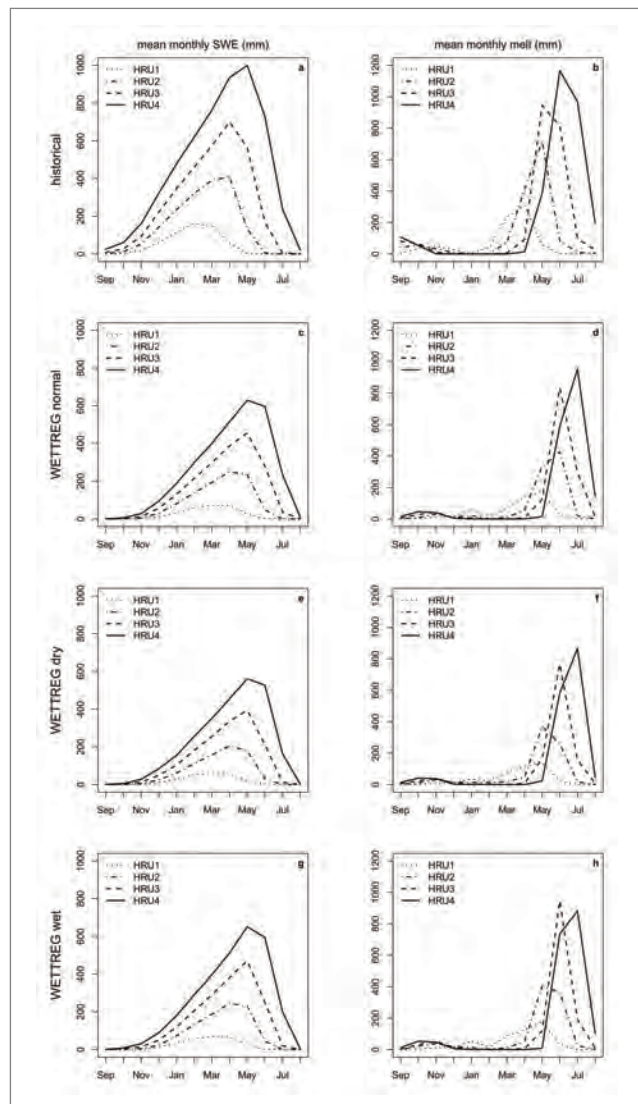


Fig. 10: Future projections of the time shift of snowmelt in the RCZ.

and denser. Hence, most of the observed spatial snow cover heterogeneity was generated during precipitation and in relation to the turbulence fields during precipitation. The resulting pattern is comparable but we have learned that the available model routines are not covering the process well here and they are adapted in the moment. In view of the satellite data the Normalized Difference Snow Index (NDSI) (Härer et al. 2016) is often used for snow mapping approaches. This index makes use of a threshold, which defines the NDSI value from which on snow is assumed to be present in the respective satellite pixel. The threshold is by standard 0.4. We could show that this threshold is not constant over the year. Many others assumed this and the threshold was very often adapted on basis of expert knowledge. However, the selection of the modified NDSI was therewith never intersubjective. This is why the software package PRACTISE was developed which allows for a calibration of the NDSI threshold on basis of local photography's (Härer et al. 2016). On basis of this package an explicit definition of the NDSI threshold for any satellite scene and any specific location has become possible. The example shows a derivation for the research catchment Zugspitze and another alpine catchment the Vernagtferner at Austria (Fig. 9).

Finally, future projections were made and it was clearly shown that the snow storage at Zugspitze will be strongly affected by the ongoing climate change (Weber et al. 2016).

The results are in line with other and comparable investigations and underline the sensitivity of the alpine space to rising temperatures. Additionally, the analysis of historical data shows a strong influence of the NAO on the snow cover development in the RCZ. However, the representation quality of the influence of large-scale climatic forcings like the NAO in future weather/climate scenarios is questionable and it could be therewith shown that one influencing factor on the snow cover development at Zugspitze might be neglected in the until now climate change studies.

19.2.2 The karst system contributing to the Partnach spring (K.-F. Wetzel & S. Weishaupt)

The RCZ is a heavily karstified high mountain catchment. Due to the pattern of tectonic structures in the bedrock the drainage pathways on the Zugspitzplatt run into an unknown system of karst channels to the reservoir in the phreatic zone, where the water is temporary stored und gradually drained at the Partnach-Spring. Precipitation water as well as snowmelt water infiltrates more or less directly into the karstic system meaning that no surface waters appear. As proven by dye tracer tests (cf. Wrobel 1980, Rappl et al. 2010 and Strobl & Wetzel 2015), a well-developed karst system with wide karst conduits must exist beneath RCZ resulting in mean travel times of some tenth of hours. Due to piston flow processes the hydrological reaction of Partnach-Spring is much faster than travel times. The size of the karst reservoir can be estimated roughly, as explained later.

Throughout the year, we observe a typical course of runoff (Fig. 11). By their characteristics, four periods can be distinguished. During the winter season (1) from the end of October to April no recharge of the karst system takes place and Partnach-Spring is falling dry (Morche 2010). At the end of April, melting processes are beginning in the lower parts of the catchment and first meltwater pulses can be observed running from the adjacent slopes into the Partnach River. The main melting period (2) in RCZ starts late in May lasting up to the beginning of July. During this period, the karst system of Zugspitzplatt is fed by meltwater and discharge at Partnach-Spring is continuously high. Rainfall induced runoff leads to pronounced peaks on top of this increased basal discharge level. Runoff at Partnach-Spring is a mixture of meltwater flowing off from areas in increasing elevations. After melting comes to an end, storm precipitation and long lasting events from advection are dominating runoff behaviour in the third period (3). Several distinct runoff events with steep rising and falling limbs can be detected (Fig. 11). The runoff reaction of Partnach-Spring is as fast as reactions of open watercourses again indicating the well-developed karst system. During autumn (4), when atmosphere is cooling down and storm precipitation is more seldom, recharge of karst groundwater is reduced. During this usual dry period often daily melting cycles of the glacier remain (Nördlicher Schneeferner) can be observed. This fourth period is leading over to the winter period. Cool temperatures and snowfall in higher elevations are terminating recharge and karst groundwater head is falling step by step beneath the level of Partnach-Spring.

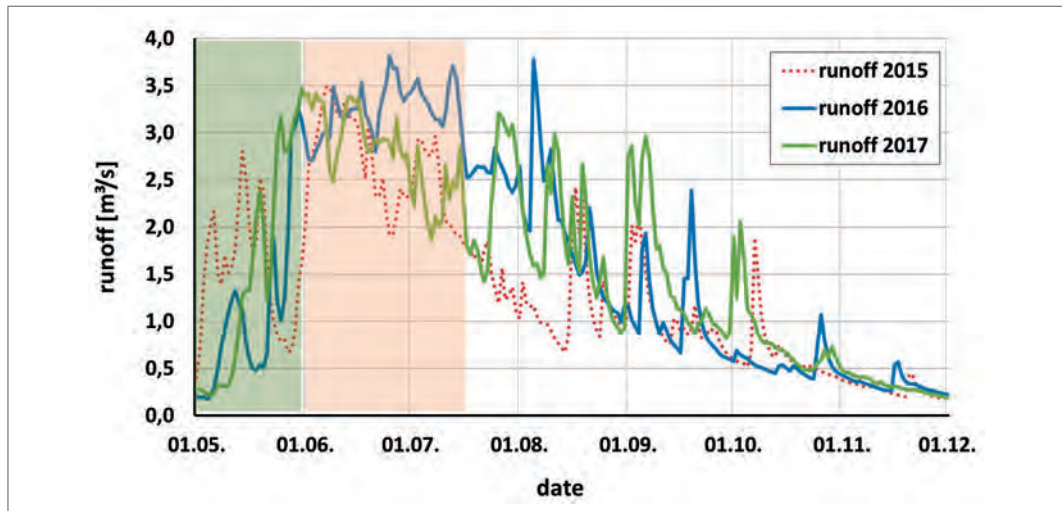


Fig. 11: The typical course of runoff at Partnach River gauge by examples of the years 2015 to 2017. Green (2): early melting period; light orange (3): main melting period; white (4): rainfall induced runoff and drying up of Partnach-Spring.

Especially for modelling purposes, information about storage behaviour of the karst system is necessary. Besides tracer based approaches recession analysis is a tool for investigating storage and depletion of groundwater bodies. In order to calculate time dependent recession curves and the recession constant “ α ”, pseudocontinuous depletion curves were constructed by splicing short falling hydrograph intervals together (e.g. Lamb & Beven 1997, Mattheß & Ubell 2003). For determining the recession constant “ α ” on a broad basis this procedure has been done for several years. The result was a surprise: the recession behaviour of the Partnach-Spring varies from year to year. The slowest decline of runoff with recession constants of around $\alpha = -0.02$ was calculated for the years 2003, 2005 and 2008 (Fig. 12). From 2008 on the absolute value of “ α ” increases to $\alpha = 0.06$ indicating a faster depletion of the karst groundwater. A distinct reason for that is not recognisable. Perhaps, flushing of debris into the karst system caused by heavy storm precipitation may have jammed water flow within karst conduits in some years. Anyway, the variability of recession behaviour makes runoff modelling in RCZ much more difficult.

By means of the depletion equation, an estimation of storage volumes of the vadose karst zone is possible. The time dependent depletion equation has the form

$$Q(t) = Q_0 \cdot e^{-\alpha t}$$

where $Q(t)$ is runoff at time t , Q_0 is runoff at the beginning of depletion and α is the recession constant. Since the recession constant is variable, storage volumes of the vadose zone are

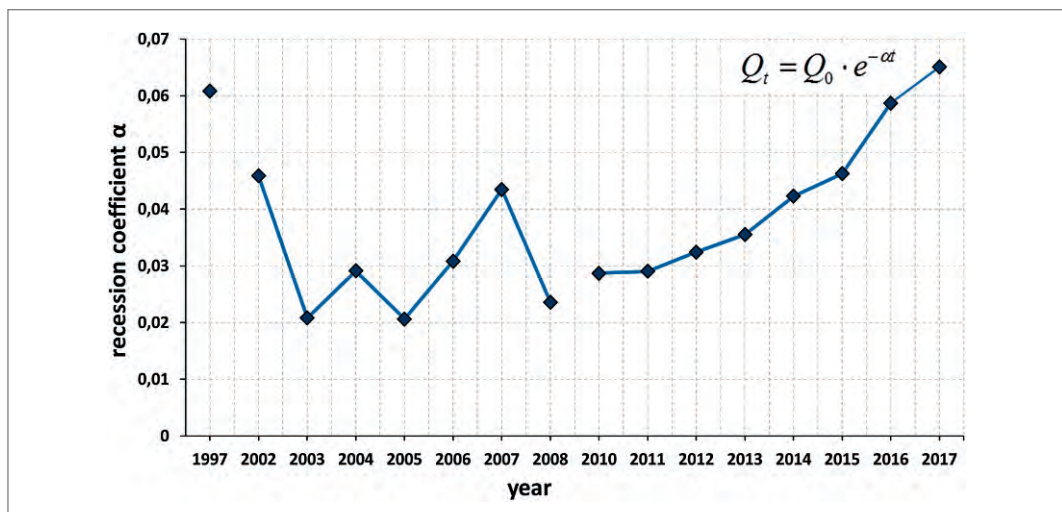


Fig. 12: The variability of the recession coefficient “ α ” of Partnach Spring over time.

varying, too. Assuming that runoff at t_0 is $1 \text{ m}^3/\text{s}$ and α is 0.06, a volume of water of about $1.39 \cdot 10^6 \text{ m}^3$ has been discharged until the spring dries up. If α is 0.02 or 0.04 this volume is around $4.0 \cdot 10^6 \text{ m}^3$ and $2.1 \cdot 10^6 \text{ m}^3$, respectively. Hence follows, that storage volume varies between $1.4 \cdot 10^6$ and $4.0 \cdot 10^6 \text{ m}^3$ in order to the status of the karst system, which corresponds approximately to 185–350 mm of precipitation.

19.2.3 Tracer based approaches for separating different components of runoff (S. Weishaupt & K.-F. Wetzel)

Different tracer approaches are existing to separate direct runoff, predominantly consisting of meltwater and rainwater, from deep karst water. In this study electric conductivity (EC) has been used as a tracer for the main dissolved cations (Mg^{++} and Ca^{++}) in the different components of runoff. In the stream flow of the Partnach River, EC varies with the amount of dissolved ions over the year. In spring, before melt-runoff occurs, the old water stored in the karstic system is highly mineralized and with the beginning of snowmelt and during strong precipitation events, the water of total runoff at the Partnach-Spring is gradually diluted and enriched again by the end of the year (see Fig. 13).

Even EC is a non-conservative tracer (e. g. Leibundgut et al. 2009), it was identified as suitable to perform two-component hydrograph separation, because of easy measuring and recording procedures in a high temporal resolution (cf. Wetzel 2003). From previous studies, it is known that melt and precipitation water solute ions within a short time after having contact with the rocks and these new waters infiltrate to the karstic system with an EC about $100 \mu\text{S}/\text{cm}$ (Hüttl 1999). Water, which lingers for long periods in cave formations, continues to dissolve minerals (predominantly Ca^{++}) and finally re-emerges with higher electric conductivity at the spring Partnach-Ursprung. Based on its typical concentration during low flow conditions, it can be concluded that the averaged EC of this old water is around $150 \mu\text{S}/\text{cm}$. Over the years of measurements of EC at the gauge station, it has been observed that the water is higher mineralized at the beginning of the melt in the spring. In the course of increasing melting processes moving up to higher elevations in the RCZ, the Partnach-water is gradually diluted until melting ceases. Due to the high flow rates in the karst system at this time, retention of the meltwater and thus the time of rock contact is reduced. Thereby the time required for a solute equilibrium is insufficient. Towards the end of the year in autumn, as soon as groundwater recharge decreases, the EC increases steadily until it reaches similar values as at the beginning of the year.

By means of a two-component mixing model (e. g. Wels et al. 1991), the two water sources, consisting of deep old karst water (Q_{old}) and the new event water (Q_{new}), can be separated.

$$Q_{\text{old}} = Q_{\text{total}} \cdot \left(\frac{EC_{\text{total}} - EL_{\text{new}}}{EC_{\text{old}} - EL_{\text{new}}} \right)$$

At the beginning of the melt, the water consists almost exclusively of old karst water from the phreatic zone (Fig. 13, purple line). The new melt water displaces this water in the reservoir stepwise and finally takes a share of about three quarters of the total runoff at the peak of the melt water runoff at the end of June. Depending on temperature changes on the Zugspitzplatt and precipitation rates of rain, which significantly influence the melting processes, the proportions of the respective runoff components can also change. At the end of the hydrological year, the total runoff is mainly influenced by high-mineralized old karst water. As Fig. 13 shows, a recovery of EC to a similar level as at the beginning of snowmelt can be observed. The total amount of separated new water until the end of melting phase in the middle of July 2016 was over 60 % of the total runoff which is around $6.5 \cdot 10^6 \text{ m}^3$.

By a simple EC-based mixing approach, it is possible to estimate the groundwater volume of the phreatic karst zone roughly. The EC of $110 \mu\text{S}/\text{cm}$ of spring discharge (EC_{total}) at the end of the melting phase in the middle of July results from mixing of deep karst water of $150 \mu\text{S}/\text{cm}$ (EC_{old}) and recharge water with an EC of about $100 \mu\text{S}/\text{cm}$ (EC_{new}). From this time on EC is rising again, because continuous recharge from low mineralized meltwater is decreasing. Considering, that EC is not a conservative tracer and dissolution processes are going on, the calculated volume of the phreatic zone may be overestimated. Otherwise, only a fraction of the total

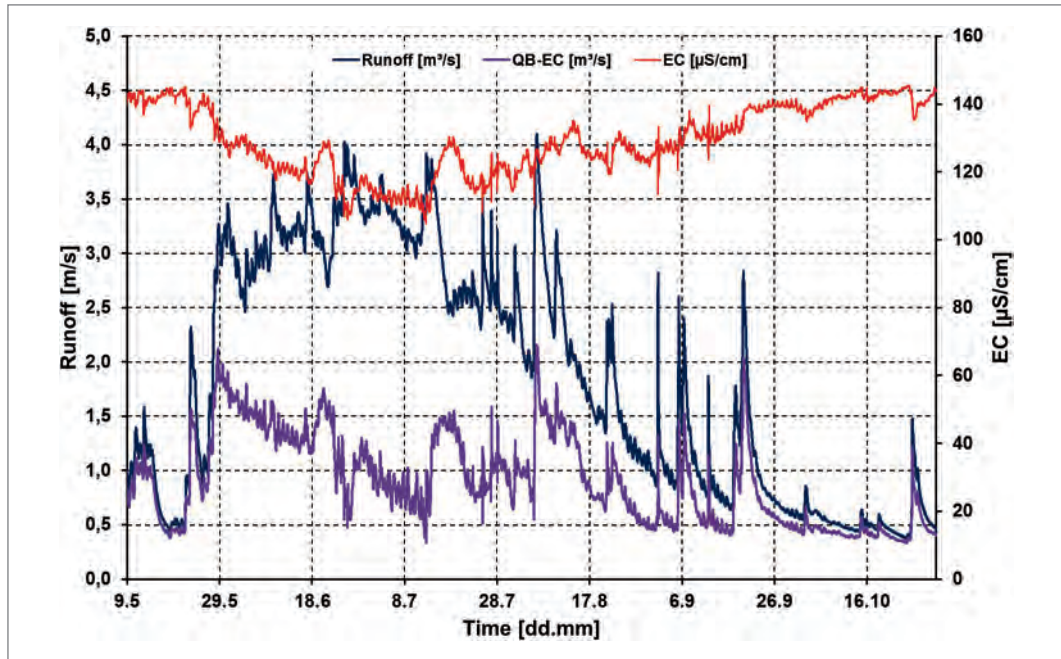


Fig. 13: Graphs of runoff, EC and runoff of deep karst water separated by means of EC (QB-EC) at Partnach River gauge throughout summer of 2016.

phreatic zone may be involved in runoff production and the effective volume of the phreatic zone is greater than calculated. However, the calculated volume has to be seen as a rough estimate.

Knowing the volume of recharge water (Vol_{new}) up to the middle of July, the volume of the phreatic zone has been estimated as follows:

$$EC_{total}(Vol_{old} + Vol_{new}) = EC_{old} \cdot Vol_{old} + EC_{new} \cdot Vol_{new}$$

The volume of recharge water has been taken from runoff data at Partnach River gauge. Solving the equation for Vol_{old} the volume of the phreatic zone of RCZ is about $10 \cdot 10^6 \text{ m}^3$. According to this, precipitation of nearly half a year is stored in the karst groundwater of RCZ.

Another frequently applied approach to separate runoff components is the use of stable isotopes ^2H and ^{18}O constituting the water molecule (overview in: Kendall & McDonnell 1998, Klaus & Mc Donnell 2013). Therefore, samples of inflow (rainfall, meltwater) and outflow waters at Partnach-Spring were taken for isotope analysis at Helmholtzzentrum München using laser spectroscopy (Picarro L2120-i). Results of isotope analysis are presented as the ratio of isotopes relative to a standard given in the delta notation as δ -value (‰), referenced to the VSMOW-SLAP scale (cf. Hürkamp et al. 2018 for further information). Together with the colleagues of Helmholtzzentrum, extensive investigations of the snowpack structure and its isotopic composition at different times throughout winter and spring were carried out (cf. Hürkamp et al. 2018). The results of the sampling have revealed a strong heterogeneity of the isotopic composition of the snow cover in spatial and temporal course especially during the degrading metamorphosis and the associated isotope fractionation processes (see Hürkamp et al. 2018). Therefore the isotopic composition of the snowmelt water can only be predicted to a limited extend by knowing the isotopic variation within the snow pack in different snow profile spots. Only the concentration of the stable isotopes ^2H and ^{18}O of the draining snowmelt water, the liquid precipitation and the glacier ice give exact knowledge about the input of stable isotopes into the karst system, which is the basis for separating melt water from total runoff.

The isotopic composition of meltwater and subsequently runoff changes strongly during the melting period (cf. Stichler 1987, Zhou et al. 2008, Hürkamp et al. 2018) (Fig. 14, green line). During the early melting phase up to the middle of May, snowmelt in the lower areas of RCZ releases meltwater with increasing content of ^2H and ^{18}O to the Partnach River. Partnach-Spring itself still does not flow in this period. Later, while the upper parts of the RCZ are melting, the content of the spring water initially is isotopic heavier deep karst water, which is continuously

replaced by the isotopic lighter meltwater (Fig. 14, after 22.5.). During the late melting phase the outflow of the spring is gradually altered to isotopic heavier water by summerlike precipitation events and the isotopic heavier meltwater at the end of the melting period due to fractionating processes (Zhou et al. 2008). Finally, the isotopic composition of runoff is primarily determined by the signal of precipitation events, which induces the content of stable isotopes of the karst water at the end of the hydrological year, before a new snow cover is formed by solid precipitation and recharge of the karst groundwater ceases.

Runoff separation by use of the stable Isotopes ^2H and ^{18}O is much more complex as by using EC as a geochemical tracer. This is, because the input signal of ^2H and ^{18}O varies in space as well as in time. Throughout snowmelt, the content of the heavy isotope species ^2H and ^{18}O in meltwater increases over time. On the other hand, snowmelt itself is a process with a high spatial variability, because the altitudinal belt of intense snowmelt is moving upward with increasing temperatures during May and June. Liquid precipitation additionally alters the isotopic composition of water entering the karst system and feeding Partnach-Spring. In this study isotope data of meltwater of an altitude between 2,350 m and 2,600 m a.s.l. throughout snowmelt were used. Doing so, is a simplification of the real situation and the results obtained have to be seen with some skepticism. For the future further investigations on the spatiotemporal distribution of stable isotopes in meltwater as well of liquid precipitation are necessary.

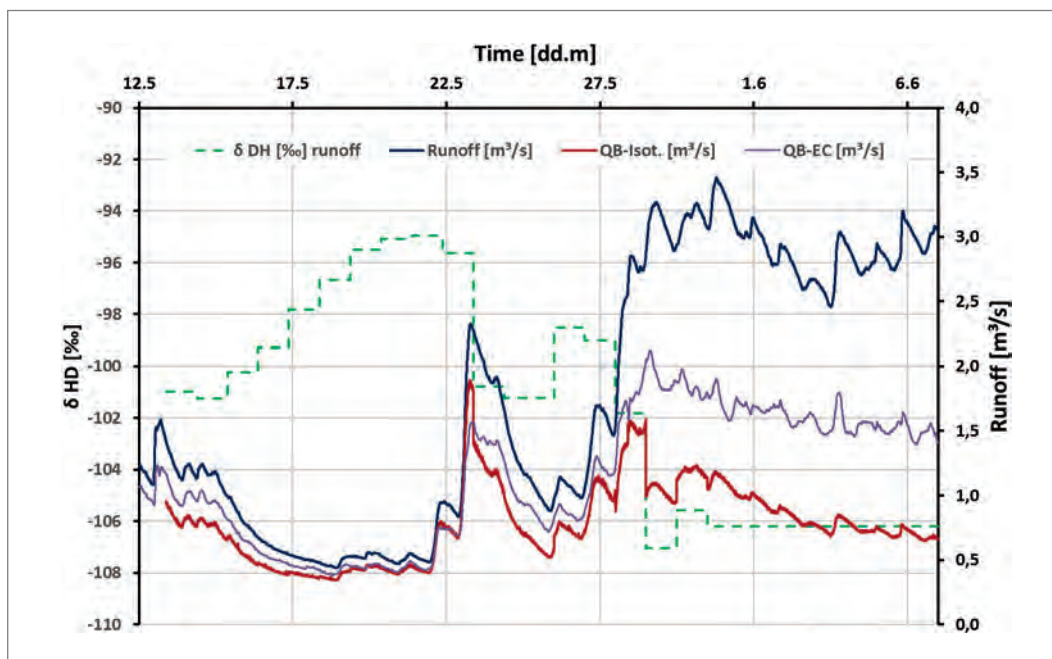


Fig. 14: Runoff and separated base flow by means of EC and $\delta^2\text{H}$ during early and main melting period of 2016 ($\delta^2\text{H}$ runoff: green dashed line, runoff at Partnach gauge: dark blue line, old deep karst water by means of $\delta^2\text{H}$: red line, old deep karst water by means of EC: purple line).

19.3 Conclusion

As a conclusion it can be said, that the tracer-based approach using stable isotopes and electrical conductivity for separation of the runoff components results in a better understanding of runoff generation processes. Including the monitoring of the hydro-meteorological input variables, a more detailed description of the water balance is possible. The collected and recorded data are important tools for the validation of snow hydrological models for the estimation of future conditions. The hydrological monitoring of a high alpine catchment becomes more valuable with both, an increasing volume of data and a growing period of hydrological monitoring. Only a long-term monitoring record gives the chance to estimate the influence of the current climatic change on the hydrological conditions in mountain regions and to future water management questions. They are therefore an indispensable component of the basic research of high mountain hydrology and as well of the environmental ecosystem research.

References

- Bavay, M. & T. Egger (2014): Meteolo 2.4.2: a preprocessing library for meteorological data. – *Geosci Model Dev*, 7(6), p. 3135–3151, doi:10.5194/gmd-7-3135-2014.
- Bernhardt, M., G.E. Liston, U. Strasser, G. Zangl & K. Schulz (2010), High resolution modelling of snow transport in complex terrain using downscaled MM5 wind fields. – *Cryosphere*, 4(1), 99–113.
- Bernhardt, M., S. Harer, J. Jacobeit, K.F. Wetzel & K. Schulz (2014), The Virtual Alpine Observatory – research focus Alpine hydrology, *Hydrol Wasserbewirts*, 58(4), 241–243.
- Brunetti, M., G. Lentini, M. Maugeri, T. Nanni, I. Auer, R. Böhm & W. Schöner (2009): Climate variability and change in the Greater Alpine Region over the last two centuries based on multi-variable analysis. – *Int J Climatol* 29: 2197–2225.
- De Jong, C., D. Collins & R. Ranzi (2005): *Climate and hydrology in mountain areas*. Wiley, 315 pp., Chichester.
- Fang, X. & J.W. Pomeroy (2016), Impact of antecedent conditions on simulations of a flood in a mountain headwater basin, *Hydrol Process*, 30(16), 2754–2772.
- Frei, C. & C. Schär (1998): A precipitation climatology of the Alps from high-resolution rain-gauge observations. *Int. J. Climatol.*, 18, 873–900.
- Gao, L., M. Bernhardt & K. Schulz (2012): Elevation correction of ERA-Interim temperature data in complex terrain. – *Hydrol. Earth Syst. Sc.*, 16(12), 4661–4673.
- Gao, L., K. Schulz & M. Bernhardt (2014): Statistical Downscaling of ERA-Interim Forecast Precipitation Data in Complex Terrain Using LASSO Algorithm – *Adv. Meteorol.*, Volume 2014 (2014), Article ID 472741, 16 pp.
- Gobiet, A., S. Kotlarski, M. Beniston, G. Heinrich, J. Rajczak & M. Stoffel (2014): 21st century climate change in the European Alps – A review. – *Science of the Total Environment*, 493, 1138–1151.
- Hagg, W., Mayer, C., Mayr, E. & A. Heilig (2012): Climate and glacier fluctuations in the Bavarian Alps during the past 120 years. *Erdkunde* 66: 121–142. DOI: 10.3112/erdkunde.2012.02.03.
- Hall, F., J. Townshend & T. Engman (1995): Status of remote sensing algorithms for estimation of land surface state parameters. – *Remote Sensing of Environment*, 51, p. 138–156.
- Hänggi, P. & R. Weingartner (2011): Inter-annual variability of runoff and climate within the Upper Rhine River basin, 1808–2007. – *Hydrol Sci J*, 56, 34–50.
- Härer, S., M. Bernhardt & K. Schulz (2016), PRACTISE – Photo Rectification And Classification Software (V.2.1), *Geosci. Model Dev.*, 9(1), 307–321.
- Holko, L., L. Gorbachova & Z. Kostka (2011): Snow Hydrology in Central Europe. – *Geography Compass* 5/4, 200–218.
- Hornung, T. & U. Haas (2017): Geologische Karte von Bayern 1:25000. Erläuterungen zu den Blättern 8531/8631 Zugspitze und 8532/8632 Garmisch-Patenkirchen. – LfU Bayern, 151 pp, Augsburg.
- Huss, M. (2011): Present and future contribution of glacier storage change to runoff from macroscale drainage basins in Europe. – *Water Resources Research* 47:W07511. doi:10.1029/2010WR010299, 2011.
- Hüttl, C. (1999): Steuerungsfaktoren und Quantifizierung der chemischen Verwitterung auf dem Zugspitzplatt (Wettersteingebirge, Deutschland). *Münchener Geographische Abhandlungen* 30, S. 215.
- Hürkamp, K., N. Zentner, A. Reckerth, S. Weishaupt, K.-F. Wetzel, J. Tschiersch & Chr. Stumpp (2018): Spatio-temporal variations of high alpine isotopic snow composition – Implications for mass transport and snowmelt runoff. – *Journal of Hydrology and Hydromechanics* (accepted). – *J. Hydrol. Hydromech.*, 67, 2019, 1, 49–58, DOI: 10.2478/johh-2018-0019
- IPCC (2013): *Climate Change 2013: The Physical Science Basis. Contribution of Working Group I to the Fifth Assessment Report of the Intergovernmental Panel on Climate Change* [Stocker, T.F., D. Qin, G.-K. Plattner, M. Tignor, S.K. Allen, J. Boschung, A. Nauels, Y. Xia, V. Bex and P.M. Midgley (eds.)]. Cambridge University Press, Cambridge, United Kingdom and New York, NY, USA, 1535 pp.
- Kendall, C & J. J. McDonnell (1998): *Isotope Tracers in Catchment Hydrology*. – Elsevier, 839 S., Amsterdam.
- Kienzle, S.W. (2008): A new temperature based method to separate rain and snow. – *Hydrological Processes*, 22(26), 5067–5085.
- Klaus, J. & J. J. McDonnell (2013): Hydrograph separation using stable isotopes: Review and evaluation. – *Journal of Hydrology*, 505, p. 47–64.
- Klemeš, V. (1988): Geophysical time series and climatic change – A skeptic's view, *Geophysical Time Series Workshop*, National Hydrology Research Centre, Environment Canada, Saskatoon, Saskatchewan, Canada, 1988.
- Korch, O. (2014): *Untersuchungen zu Flora und Vegetation des Zugspitzplatts (Wettersteingebirge, Bayerische Alpen)*. Dissertation, University of Augsburg, <http://opus.bibliothek.uni-augsburg.de/opus4/frontdoor/index/index/docId/2635>.
- Laux, P., S. Wagner, A. Wagner, J. Jacobeit, A. Bardossy & H. Kunstmann (2009), Modelling daily precipitation features in the Volta Basin of West Africa, *Int J Climatol*, 29(7), 937–954.
- Laghari, A. N., Vanham, D. & W. Rauch (2012): To what extent does climate change result in a shift in Alpine hydrology? A case study in the Austrian Alps. *Hydrological Sciences Journal*, 57, pp. 103–117.
- Lamb, R. & K. Beven (1997): Using interactive recession curve analysis to specify a general catchment storage model. – *Hydrol. Earth Syst. Sci.*, 1, 101–113.

- Leibundgut, Ch., P. Maloszewski & C. Külls (2009): Tracers in Hydrology. – Wiley-Blackwell, 415 S., Chichester.
- Liston, G.E., and K. Elder (2006), A meteorological distribution system for high-resolution terrestrial modeling (MicroMet), *J Hydrometeorol*, 7(2), 217–234.
- Lopez-Moreno, J. I., J. Boike, A. Sanchez-Lorenzo, and J.W. Pomeroy (2016), Impact of climate warming on snow processes in Ny-Alesund, a polar maritime site at Svalbard, *Global Planet Change*, 146, 10–21.
- Masson, D. & C. Frei (2014), Spatial analysis of precipitation in a high-mountain region: exploring methods with multi-scale topographic predictors and circulation types, *Hydrol Earth Syst Sc*, 18(11), 4543–4563.
- Matthess, G. & K. Ubell (2003): Allgemeine Hydrogeologie – Grundwasserhaushalt. Lehrbuch der Hydrogeologie Bd. 1. Gebr. Bornträger, 575 pp, Berlin / Stuttgart.
- Messerli, B., D. Viviroli & R. Weingartner (2009): Mountains of the world – water towers for the twenty-first century? In: Garrido, A. & A. Dinar (eds.): Managing water resources in a time of global change. – Routledge, London, New York, pp 11–31.
- Miller, H. (1962): Der Bau des westlichen Wettersteingebirges. Zeitschrift der deutschen geologischen Gesellschaft, 113, pp 161–203.
- Morche, D. (2010): Die fluviale Lösungsfracht und ihre Effektivität bei der rezenten geomorphologischen Formung in einem kalkalpinen Hochgebirgstal. – Salzburger Geographische Arbeiten 46, pp 95–112.
- Mott, R., D. Scipion, M. Schneebeli, N. Dawes, A. Berne, and M. Lehning (2014), Orographic effects on snow deposition patterns in mountainous terrain, *J Geophys Res-Atmos*, 119(3), 1419–1439.
- Müller-Westermeier, G. (1996): Klimadaten von Deutschland – Zeitraum 1961–1990. Deutscher Wetterdienst, Offenbach.
- Pomeroy, J. & D. Marks (2009): Hydrology in Mountain Regions: Observations, Processes and Dynamics – Preface. IAHS Publ. 326, Wallingford.
- Pomeroy, J., M. Bernhardt & D. Marks (2015): Research network to track alpine water. *Nature* 521(7550), 32–32.
- Rappl, A., K.-F. Wetzel, G. Büttner & M. Scholz (2010): Tracerhydrologische Untersuchungen am Partnach-Ursprung. – Hydrologie und Wasserbewirtschaftung, 54,4: 220–230.
- Schlögl, S., C. Marty, M. Bavay & M. Lehning (2016), Sensitivity of Alpine3D modeled snow cover to modifications in DEM resolution, station coverage and meteorological input quantities, *Environ Modell Softw*, 83, 387–396.
- Sevruk, B. (1996): Correcting precipitation measurements in Switzerland. – WMO (ed.): Proceedings of the workshop on the ACSYS solid precipitation climatology project, Reston, USA, 12–15. September 1995, p. 33–35.
- Stichler, W. (1987): Snowcover and snowmelt processes studied by means of environmental isotopes. In: Jones, H. G., Orville-Thomas, W. J. (Eds.): Seasonal Snowcovers: Physics, Chemistry, Hydrology. D. Reidel Publishing Company, Dordrecht, Holland, pp. 673–726.
- Strasser, U., T. Marke, O. Sass, S. Birk & G. Winkler (2013): John's creek valley: a mountainous catchment for long-term interdisziplinäre human-environment system research in Upper Styria (Austria). – *Environ Earth Sci* 69, p. 695–705.
- Strobl, G. & K.-F. Wetzel (2015): Virtuelles Alpenobservatorium – ein Statusbericht. – *Geographica Augustana Manuskripte* 17, 3–8, Augsburg.
- Verbunt, M., J. Gurtz, K. Jasper, H. Lang, P. Warmerdam & M. Zappa (2003): The hydrological role of snow and glaciers in alpine river basins and their distributed modeling. – *Journal of Hydrology* 282: 36–55.
- Viviroli, D., H. H. Dürr, B. Messerli, M. Meybeck & R. Weingartner (2007): Mountains of the world, water towers for humanity: Typology, mapping, and global significance. – *Water Resources Research*, Vol. 43, W07447, doi:10.1029/2006WR005653.
- Viviroli, D., D. R. Archer, W. Buytaert, H. Fowler, G. B. Greenwood, A. F. Hamlet, Y. Huang, G. Koboltschnig, M. I. Litaor, J. I. López-Moreno, S. Lorentz, B. Schädler, H. Schreier, K. Schwaiger, M. Vuille M & R. Woods (2011): Climate change and mountain water resources: overview and recommendations for research, management and policy. – *Hydrol. Earth Syst. Sci.* 15: 471–504.
- Weber, M., M. Bernhardt, J.W. Pomeroy, X. Fang, S. Harer, and K. Schulz (2016), Description of current and future snow processes in a small basin in the Bavarian Alps, *Environ Earth Sci*, 75(17).
- Wels, C., R. J. Cornett & B. D. Lazerte (1991): Hydrograph separation: A comparison of geochemical and isotopic tracers. In: *Journal of Hydrology*, 122, p. 253–274.
- Wetzel, K.-F. (2003): Runoff production processes in small alpine catchments within the unconsolidated Pleistocene sediments of the Lainbach area (upper Bavaria). – *Hydrol. Process.*, 17, pp. 2463–2483.
- Wetzel, K.-F. (2004): On the hydrology of the Partnach area in the Wetterstein mountains (Bavarian Alps). – In: *Erdkunde*, Vol. 58, pp 172–186.
- Wetzel, K.-F. & M. Bernhardt (2015): Gletscher, Klima und Wasserhaushalt. Klimareport Bayern 2015, 170–171.
- Wrobel, J.P. (1980): Bericht über den Markierungsversuch auf dem Zugspitzplatt im Sommer 1980. – Bayerisches Geologisches Landesamt, München.
- Zhou, S., Nakawo, M., Hashimoto, S. & A. Sakai (2008): The effect of refreezing on the isotopic composition of melting snowpack. – *Hydrol. Process.*, 22, 873–882.

20 Gravity waves

20.1 A brief summary of theory and data analysis results in the Alpine region

Sabine Wüst

German Aerospace Center, DLR, German Remote Sensing Data Center, Oberpfaffenhofen

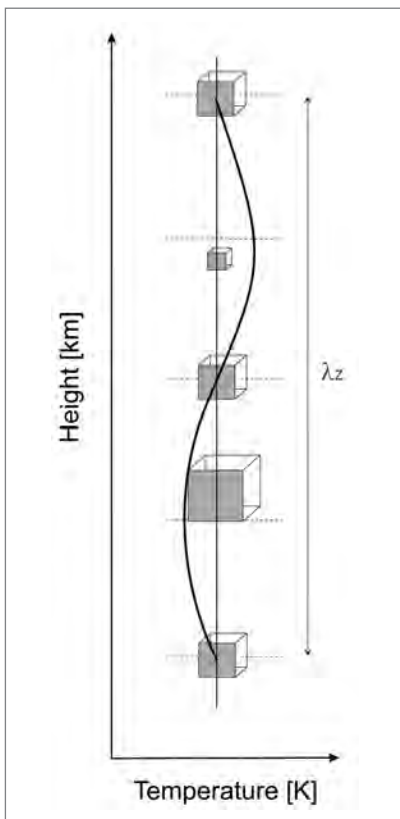


Fig. 1: Air parcels oscillate vertically and horizontally (not shown here) around their rest positions (horizontal dashed lines). This leads to temperature deviations (thick black line) from the assumed constant background (thin vertical black line).

Atmospheric waves are a distinct feature in atmospheric dynamics. In terms of wavelength and frequency, atmospheric waves range from relatively small-scale structures such as infrasonic waves via gravity waves to planetary or Rossby waves. Today, the extraordinary importance of atmospheric waves for the understanding of atmospheric dynamics is commonly recognized. In particular, this is because atmospheric waves re-distribute energy and momentum over wide spatio-temporal scales. Atmospheric waves thus allow “communication” (coupling) between different parts of the atmosphere. As one important consequence, these waves impact the atmospheric circulation and at least to some extent the spatio-temporal distribution of atmospheric constituents throughout the whole altitude regime from the troposphere up to the stratosphere, mesosphere, and thermosphere. Noteworthy, that the effect of dynamics on a constituent is not limited to advection; chemical and dynamical processes influence each other since temperature controls chemical reaction rates while, in turn, chemical reactions can alter the atmospheric temperature (see, for example, Marsh, 2011 and references therein).

The focus of this article is on internal gravity waves, i. e., on gravity waves which exist inside a medium like the atmosphere or the ocean and not at a boundary layer such as the sea surface.

Gravity waves are often described as vertically oscillating air parcels. A vertical oscillation can only exist in a stably stratified atmosphere. In an unstably stratified atmosphere a vertical impulse on an air parcel will lead to convection. The air parcel which is affected by the initial impulse moves, for example, upward and cools adiabatically if no heat exchange with the surrounding atmosphere takes place. So, the air parcel becomes colder (more dense) than the surrounding atmosphere. The upward movement stops and the air parcel starts to sink. Ideally, it warms adiabatically and moves through its original rest position. Now, it becomes warmer (less dense) than the surrounding atmosphere, stops sinking, moves again upward through its rest position, and so on.

Imagining the atmosphere as a set of coupled air parcels, it becomes clear that the initially oscillating air parcel deflects surrounding ones from their rest position which also start to oscillate. The vertical and/or horizontal distance between two air parcels which are both at maximum (minimum) deflection position is the vertical and/or horizontal wavelength (see Fig 1). The time which passes until one air parcel reaches its maximum (minimum) deflection position again, is the period. The maximal frequency of this oscillation is the buoyancy or Brunt-Väisälä frequency N , which is a resonant frequency of the atmosphere (Andrews, 2000; Nappo, 2013). Even if an oscillation with a frequency different than N is generated by some process, its amplitude will decay rapidly with distance from the forcing point (Nappo, 2013). Lower frequencies are observed for air parcels which oscillate not only vertically but also horizontally.

Gravity waves are transversal waves: the air parcels oscillate perpendicular to the propagation of the wave fronts (e. g., Holton, 2004). Air parcels which oscillate exclusively in the vertical lead to strictly horizontally propagating waves and vice versa even though these are idealized cases and therefore not observed in reality (Nappo, 2013).

Atmospheric waves in general result from an equilibrium of the pressure gradient, the gravity and the Coriolis force. Depending on the dominating forces, different wave types—planetary,

gravity and sound waves—can evolve. In the following, the most important characteristics of gravity waves are deduced. Unless stated otherwise, we mainly follow here Fritts and Alexander (2003).

The fundamental fluid equations in Cartesian coordinates result from the conservation of momentum (Navier-Stokes equation here in its approximated spherical version, equations 1–3), mass (continuity equation, equation 4) and energy (first law of thermodynamics, thermodynamic energy equation, equation 5). The derivation of the equations can be found in chapter 4 of Andrews (2000), for example.

$$\frac{du}{dt} - fv + \frac{1}{\rho} \frac{\partial p}{\partial x} = X \quad (1)$$

$$\frac{dv}{dt} + fu + \frac{1}{\rho} \frac{\partial p}{\partial y} = Y \quad (2)$$

$$\frac{dw}{dt} + g + \frac{1}{\rho} \frac{\partial p}{\partial z} = 0 \quad (3)$$

$$\frac{1}{\rho} \frac{\partial \rho}{\partial t} + \frac{\partial u}{\partial x} + \frac{\partial v}{\partial y} + \frac{\partial w}{\partial z} = 0 \quad (4)$$

$$\frac{\partial \theta}{\partial t} = Q \quad (5)$$

with

density ρ ($\rho = \rho_0 e^{-(z-z_0)/H}$ with $\rho_0 = \rho(z_0)$ the density at a reference level z_0 and H the scale height, which is typically ca. 7 km in the middle atmosphere),

pressure p ,

Coriolis parameter $f = 2\Omega \sin \phi$ (Ω = Earth rotation rate, ϕ = latitude),

potential temperature θ ,

fluid velocity vector (u, v, w) ,

unspecified forcings X, Y , and Q (e.g., frictional force), and

the total derivative $\frac{d}{dt}$.

Together with the definition of potential temperature

$$\theta = \frac{p}{\rho R} \left(\frac{\rho_0}{\rho} \right)^\kappa = T \left(\frac{\rho_0}{\rho} \right)^\kappa \quad (6)$$

where R = ideal gas constant,

$\kappa = \frac{R}{c_p}$ with c_p the specific heat at constant pressure, and

$\rho_0 = \rho(z_0)$ a reference pressure,

the equations (1)–(6) completely describe inviscid fluid motions.

This equation system is now linearized following the perturbation method by assuming

- a horizontally uniform hydrostatic basic state (with background wind $(\bar{u}, \bar{v}, 0)$, potential temperature $\bar{\theta}$, pressure \bar{p} and density $\bar{\rho}$) varying only in z , and
- superimposed small disturbances (primed variables).

This approach is applied to equations (1)–(6), and terms which consist of two primed variables are dismissed. Furthermore, unspecified forcings are neglected (X, Y , and Q equal to zero).

$$\frac{Du'}{Dt} + w' \frac{\partial \bar{u}}{\partial z} - fv' + \frac{\partial}{\partial x} \left(\frac{p'}{\bar{\rho}} \right) = 0 \quad (7)$$

$$\frac{Dv'}{Dt} + w' \frac{\partial \bar{v}}{\partial z} + fu' + \frac{\partial}{\partial y} \left(\frac{p'}{\bar{\rho}} \right) = 0 \quad (8)$$

$$\frac{Dw'}{Dt} + \frac{\partial}{\partial z} \left(\frac{p'}{\bar{\rho}} \right) - \frac{1}{H} \frac{p'}{\bar{\rho}} + g \frac{\rho'}{\bar{\rho}} = 0 \quad (9)$$

$$\frac{D}{Dt} \left(\frac{\theta'}{\bar{\theta}} \right) + w' \frac{N^2}{g} = 0 \quad (10)$$

$$\frac{D}{Dt} \left(\frac{p'}{\bar{\rho}} \right) + \frac{du'}{dx} + \frac{dv'}{dy} + \frac{dw'}{dz} - \frac{w'}{H} = 0 \quad (11)$$

$$\frac{\theta'}{\bar{\theta}} = \frac{1}{c_s^2} \frac{p'}{\bar{\rho}} - \frac{\bar{\rho}}{\bar{\rho}} \quad (12)$$

with

$$\frac{D}{Dt} = \frac{\partial}{\partial t} + \bar{u} \frac{\partial}{\partial x} + \bar{v} \frac{\partial}{\partial y},$$

the buoyancy or Brunt-Väisälä (angular) frequency¹ (Andrews, 2000)

$$N = \left(\frac{g}{\bar{\theta}} \frac{\partial \bar{\theta}}{\partial z} \right)^{1/2} = \left(\frac{g}{T} \left(\frac{dT}{dz} + \frac{g}{c_p} \right) \right)^{1/2} \quad (13)$$

(g/c_p is the dry-adiabatic lapse rate Γ , which has a value of ca. 9.8 K/km depending on the Earth radius and the height), and

the sound speed $c_s = \frac{c_p}{c_v} R \bar{T}$ (with c_v the specific heat at constant volume).

Now, one makes the following assumptions

- the horizontal background wind (\bar{u} , \bar{v}) and the buoyancy frequency N vary only slowly over a wave cycle in the vertical (WKB approximation), that means the shear terms in equation (7) and (8) can be neglected
- the systems consisting of the equations (7)–(12) can be solved by a monochromatic wave of the following form:

$$\left(u', v', w', \frac{\theta'}{\bar{\theta}}, \frac{p'}{\bar{p}}, \frac{\rho'}{\bar{\rho}} \right) = (\bar{u}, \bar{v}, \bar{w}, \bar{\theta}, \bar{p}, \bar{\rho}) \cdot e^{i(kx + ly + mz - \omega t) + \frac{z}{2H}} \quad (14)$$

with the wave vector (k, l, m) and the ground-relative (Eulerian) frequency ω .

Substituting equation (14) in equations (7)–(12) leads to the following six algebraic equations

for $\left(u', v', w', \frac{\theta'}{\bar{\theta}}, \frac{p'}{\bar{p}}, \frac{\rho'}{\bar{\rho}} \right)$:

$$-i\hat{\omega}\bar{u} - f\bar{v} + ik\bar{p} = 0, \quad (15)$$

$$-i\hat{\omega}\bar{v} + f\bar{u} + il\bar{p} = 0, \quad (16)$$

$$-i\hat{\omega}\bar{w} + \left(im - \frac{1}{2H} \right) \bar{p} = -g\bar{\rho}, \quad (17)$$

$$-i\hat{\omega}\bar{\theta} + \frac{N^2}{g} \bar{w} = 0, \quad (18)$$

$$-i\hat{\omega}\bar{\rho} + ik\bar{u} + il\bar{v} + \left(im - \frac{1}{2H} \right) \bar{w} = 0, \quad (19)$$

$$\bar{\theta} = \frac{\bar{p}}{c_s^2} - \bar{\rho} \quad (20)$$

where $\hat{\omega} = \omega - k \cdot \bar{u} - l \cdot \bar{v}$ is the intrinsic frequency, i. e., the frequency which is measured by an observer moving with the background wind (\bar{u} , \bar{v}). In contrast, ω is the apparent frequency measured by an observer in a fixed coordinate system (e. g., by a ground-based spectrometer). So, the intrinsic frequency is the frequency which is observed due to a change of the reference system. Chimonas and Hines (1986) denote $\hat{\omega}$ also the Doppler-shifted intrinsic wave frequency.

Most instruments such as spectrometers, radars, and lidars, are stationary. A time series derived by these instruments allows the derivation of the frequency ω and the phase speed

$c = \left(\frac{\omega}{k}, \frac{\omega}{l}, \frac{\omega}{m} \right)$. In order to calculate the intrinsic values, $\hat{\omega}$ and $\hat{c} = \left(\frac{\hat{\omega}}{k}, \frac{\hat{\omega}}{l}, \frac{\hat{\omega}}{m} \right)$, additional information about the wind velocity at the addressed height are necessary. If an instrument is travelling with the wind (e. g. long-duration stratospheric balloons), one derives the intrinsic frequency and the intrinsic phase speed that means the frequency and the phase speed relative to the background wind. The direction of phase propagation and its intrinsic equivalent do not necessarily need to agree.

The equation system (15)–(20) can also be used for the derivation of polarization relations (e. g., Andrews, 2000; Fritts and Alexander, 2003). They show how the perturbation amplitudes of the different variables are related to each other. This can be helpful, if, for example, meridional wind perturbations are needed but only zonal ones are measured.

The equation system (15)–(20) can also be used for the derivation of polarization relations (e. g., Andrews, 2000; Fritts and Alexander, 2003). They show how the perturbation amplitudes of the different variables are related to each other. This can be helpful, if, for example, meridional wind perturbations are needed but only zonal ones are measured.

¹ whose corresponding period $\frac{2\pi}{N}$ is a few minutes

The perturbation vertical velocity amplitude \tilde{w} can be expressed by a combination of the equations (7)–(12). Demanding \tilde{w} is a real number and not an imaginary one, leads to the following two equations:

$$\frac{g}{c_s^2} = \frac{1}{H} - \frac{N^2}{g}, \quad (21)$$

$$\hat{\omega}^2 \left(k^2 + l^2 + m^2 + \frac{1}{4H^2} - \frac{\hat{\omega}^2 - f^2}{c_s^2} \right) = N^2 (k^2 + l^2) + f^2 \left(m^2 + \frac{1}{4H^2} \right). \quad (22)$$

By letting the sound speed to infinity, one receives the dispersion relation for gravity waves:

$$\hat{\omega}^2 = \frac{N^2 (k^2 + l^2) + f^2 \left(m^2 + \frac{1}{4H^2} \right)}{k^2 + l^2 + m^2 + \frac{1}{4H^2}}. \quad (23)$$

Gravity waves can only propagate vertically, if $m^2 > 0$. Waves with $m^2 < 0$ are vertically damped (trapped or evanescent waves), and waves with $m^2 = 0$ can propagate only horizontally. It holds (see equation (23)):

$$\lim_{(k^2 + l^2) \rightarrow 0} \hat{\omega}^2 = f^2, \text{ and} \quad (24)$$

$$\lim_{(k^2 + l^2) \rightarrow \infty} \hat{\omega}^2 = N^2. \quad (25)$$

That means that the squared intrinsic frequency of gravity waves ranges between f^2 and N^2 .

If m^2 is zero, equation (23) simplifies to

$$\hat{\omega}^2 = \frac{N^2 (k^2 + l^2) + \frac{f^2}{4H^2}}{k^2 + l^2 + \frac{1}{4H^2}} = N^2 - \frac{N^2 - f^2}{4H^2 \cdot \left((k^2 + l^2) + \frac{1}{4H^2} \right)} \propto \frac{-1}{k^2 + l^2}. \quad (26)$$

Based on this information, the dispersion diagram can be sketched (Fig. 2).

An alternative formulation for the dispersion relation (equation 23) is

$$m^2 = \frac{(k^2 + l^2)(N^2 - \hat{\omega}^2)}{\hat{\omega} - f^2} - \frac{1}{4H^2} \quad (27)$$

It shows that the vertical wavelength and therefore also the ability of a wave to propagate vertically depends on the height since the the horizontal wind field and the Brunt-Väisälä frequency are height dependent (see Fig. 3 for an example).

Gravity waves transport energy and momentum through the atmosphere. The direction of energy transport is determined by the group velocity (c_{gx} , c_{gy} , c_{gz}) with

$$(c_{gx}, c_{gy}, c_{gz}) = \left(\frac{\partial \omega}{\partial k}, \frac{\partial \omega}{\partial l}, \frac{\partial \omega}{\partial m} \right). \quad (28)$$

Equation (23) provides an expression for ω . Please be aware of the fact that ω is assumed here to be positive:

$$\omega = k\bar{u} + l\bar{v} + \left(\frac{N^2 (k^2 + l^2) + f^2 \left(m^2 + \frac{1}{4H^2} \right)}{k^2 + l^2 + m^2 + \frac{1}{4H^2}} \right)^{1/2}. \quad (29)$$

Thus, it holds for (c_{gx} , c_{gy} , c_{gz}):

$$(c_{gx}, c_{gy}, c_{gz}) = \left(\frac{\partial \omega}{\partial k}, \frac{\partial \omega}{\partial l}, \frac{\partial \omega}{\partial m} \right) = (\bar{u}, \bar{v}, 0) + \frac{(k(N^2 - \hat{\omega}^2), l(N^2 - \hat{\omega}^2), -m(\hat{\omega}^2 - f^2))}{\hat{\omega} \left(k^2 + l^2 + m^2 + \frac{1}{4H^2} \right)} \quad (30)$$

A closer investigation of the vertical component c_{gz} shows for untrapped gravity waves that c_{gz} is negative (positive) if m is positive (negative) since $\hat{\omega}^2 - f^2$, $\hat{\omega}$, and $k^2 + l^2 + m^2 + \frac{1}{4H^2}$ are positive (see Fig. 2 and equation 23). That means a downward propagating gravity wave transports energy in upward direction and vice versa.

Depending on the intrinsic frequency of a wave, the dispersion relation (equation (23)) can be simplified.

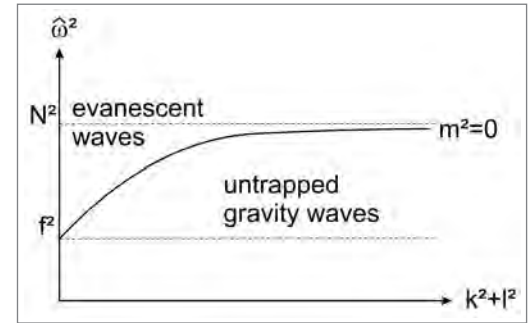


Fig. 2: Gravity waves exist and propagate vertically if their squared intrinsic frequency ranges between f^2 and the line denoted as $m^2 = 0$.

For high-frequency waves with $\hat{\omega} \gg f$ and $m^2 \gg \frac{1}{4H^2}$, the Coriolis force can be neglected, then equation (23) is approximated by

$$\begin{aligned}\hat{\omega}^2 &= \frac{N^2 - (k^2 + l^2)}{k^2 + l^2 + m^2} = N^2 \frac{(k^2 + l^2)}{(k^2 + l^2) + m^2} \cdot \frac{4\pi^2}{(k^2 + l^2) \cdot m^2} \\ &= N^2 \frac{\lambda_z^2}{\lambda_z^2 + \lambda_h^2} \\ &= N^2 \cos^2 \alpha\end{aligned}\quad (31)$$

where

$\lambda_h = \frac{2\pi}{\sqrt{k^2 + l^2}}$ is the horizontal wavelength, and α the angle between the wave fronts (lines of constant phase) and the vertical (see figure 4 for the x-z plane).

This simple result provides interesting insights into gravity wave orientation and propagation (Nappo, 2013).

If $\hat{\omega} \rightarrow N$, then $\alpha \rightarrow 0$, i.e., the wave fronts are nearly oriented vertically and tend to move only horizontally. The fluid parcels oscillate mainly vertically ($\lambda_z \rightarrow \infty$). In this case, a vertical transport of energy is very much reduced.

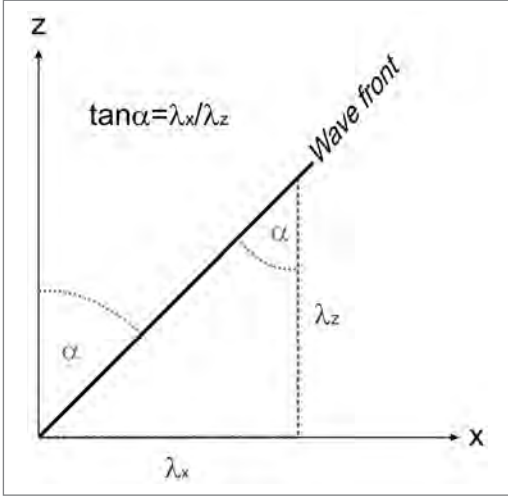


Fig. 4: α is determined by the horizontal and the vertical wavelength. In the three-dimensional case must be λ_x substituted by λ_h .

If one sets the background wind equal to zero, then the intrinsic frequency becomes equal to the frequency of the wave. From equation (31), it becomes clear that gravity waves will then move vertically along curved paths, since N is not constant with height (mainly indirectly proportional to the temperature).

For medium-frequency waves with $N \gg \hat{\omega} \gg f$ and $m^2 \gg \frac{1}{4H^2}$, equation (23) becomes fairly simple:

$$\hat{\omega}^2 \cdot \left(k_h^2 + m^2 + \frac{1}{4H^2} \right) = N^2 k_h^2 + f^2 \left(m^2 + \frac{1}{4H^2} \right) \quad (32)$$

$$\hat{\omega}^2 k_h^2 + \hat{\omega}^2 m^2 = N^2 k_h^2 + f^2 m^2 \quad (33)$$

$$k_h^2 (\hat{\omega}^2 - N^2) = m^2 (f^2 - \hat{\omega}^2) \quad (34)$$

$$k_h^2 N^2 = m^2 \hat{\omega}^2 \quad (35)$$

$$\hat{\omega}^2 = \frac{k_h^2}{m^2} N^2 \quad (36)$$

with $k_h = \sqrt{k^2 + l^2}$. This approximation is equivalent to

$$m^2 = \frac{k_h^2}{\hat{\omega}^2} N^2 = \frac{N^2}{\hat{c}_h^2} \quad (37)$$

and shows that the vertical wavelength is proportional to the intrinsic horizontal phase speed $\hat{c}_h = c_h - \sqrt{u^2 + v^2}$. If the horizontal phase speed becomes equal to the horizontal wind speed, the intrinsic horizontal phase speed and the vertical wavelength approach zero. The height where this holds is the critical level.

Low-frequency or inertia gravity wave are those, for which the rotation of the Earth and therefore the Coriolis force is important. An approximation for low- and medium-frequency waves ($\hat{\omega} \approx f$ that also means $N \gg \hat{\omega}$) can be derived starting with equation (34):

$$\begin{aligned}k_h^2 (\hat{\omega}^2 - N^2) &= m^2 (f^2 - \hat{\omega}^2) \\ k_h^2 (-N^2) &= m^2 (f^2 - \hat{\omega}^2) \\ \hat{\omega}^2 &= \frac{k_h^2}{m^2} N^2 + f^2\end{aligned}\quad (38)$$

If $\hat{\omega} \rightarrow f$, then $\frac{k_h^2}{m^2} \rightarrow 0$. In contrast to the high-frequency case, here, the wave fronts are oriented nearly horizontally, the wave propagates energy almost totally vertically, and the fluid parcels

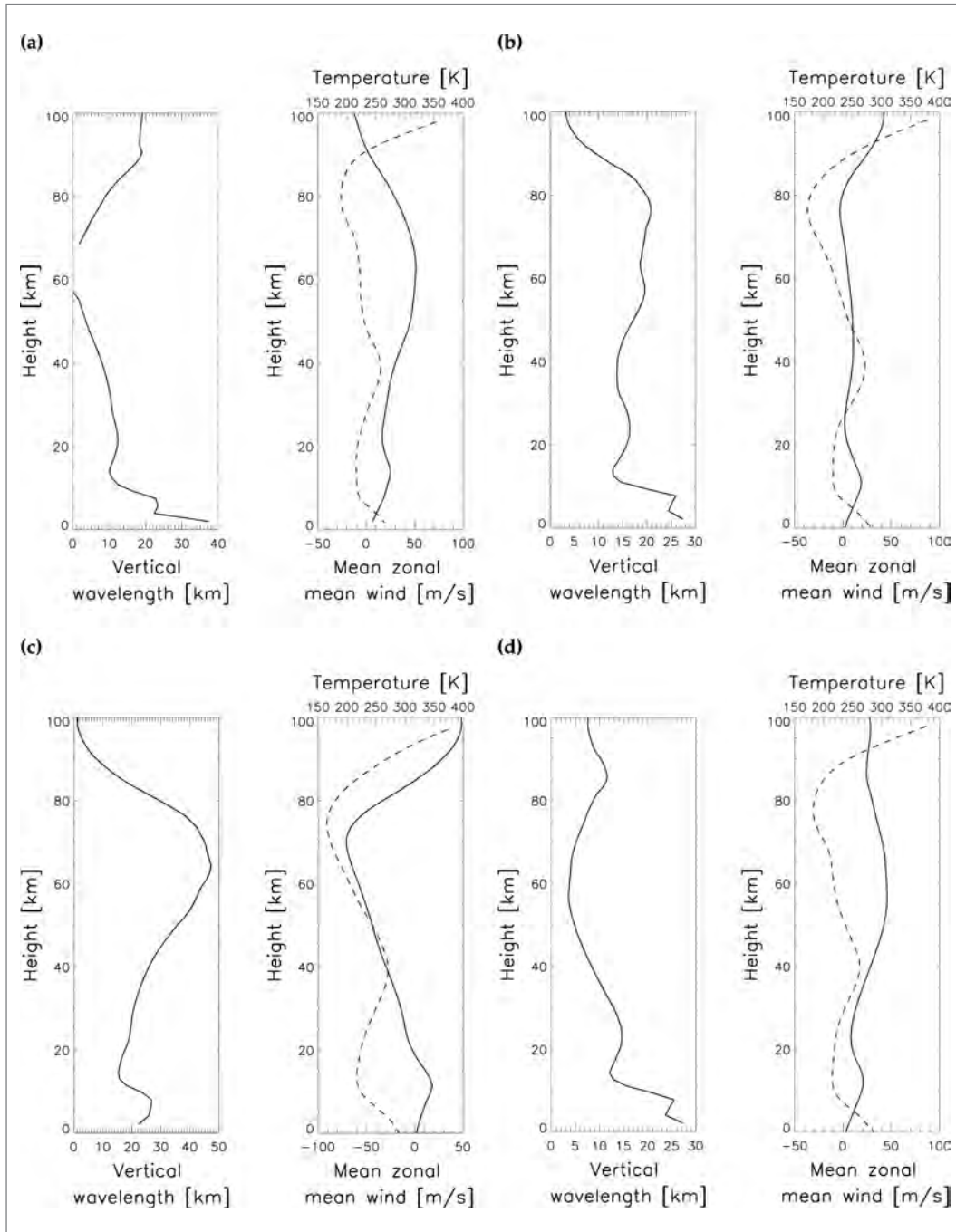


Fig. 3: Shown is the height-dependent vertical wavelength for a wave with a period of 3 h and a zonal wavelength of 650 km for (a) January, (b) April, (c) July, and (d) October. The right-hand side of each sub-figure shows the vertical monthly mean profiles of temperature (grey) and zonal wind (black). The data are taken from CIRA-86 (Download: 19th September 2017). The scale height is assumed to be 7 km.

tend to oscillate horizontally (see figure 5). So, the more the intrinsic frequency $\hat{\omega}$ approaches the Coriolis frequency f of the atmosphere, the more horizontally oriented the wave fronts are. The more the intrinsic frequency $\hat{\omega}$ nears the resonance frequency N of the atmosphere, the more vertically oriented the wave fronts are (Nappo, 2013).

The dispersion relation links the temporal to the spatial wave parameters, but also to the Brunt-Väisälä and the Coriolis frequency, to the scale height, and to the horizontal wind field. The latter is highly variable with height, and therefore strongly influences the intrinsic wave frequency. According to the different approximations of the dispersion relation shown above, $|m|$ goes to infinity, if the following holds:

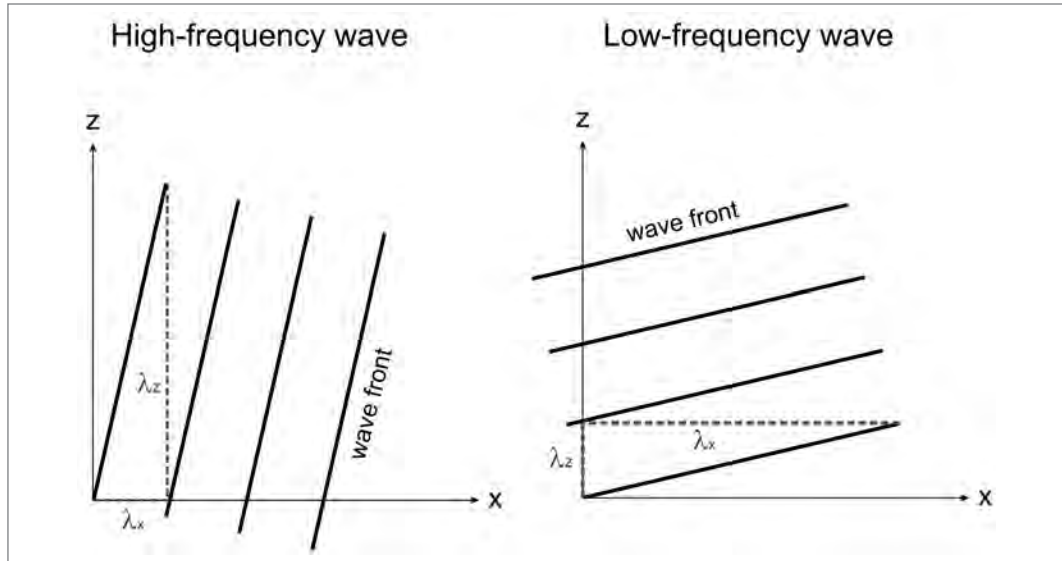


Fig. 5: The left (right) side depicts zonal and vertical wavelengths (dashed grey lines) as well as phase fronts (thick black lines) of a typical high-frequency (low-frequency) wave for the two-dimensional (x-z) case.

- High-frequency waves:

$$\begin{aligned}\hat{\omega}^2 &= \frac{N^2 k_h^2}{k_h^2 + m^2} \\ \Leftrightarrow k_h^2 + m^2 &= \frac{N^2}{\hat{\omega}^2} k_h^2 = \frac{N^2}{\hat{c}_h^2} = \frac{N^2}{\hat{c}_x^2 + \hat{c}_y^2} = \frac{N^2}{(c_x - u)^2 + (c_y - v)^2}\end{aligned}\quad (39)$$

That means $|m|$ goes to infinity, if the zonal (meridional) phase velocity c_x (c_y) approaches the zonal (meridional) wind speed u (v).

- Medium-frequency waves:

The same relation holds here (mentioned before).

- Low-frequency waves:

If $m^2 \rightarrow \infty$, the intrinsic frequency $\hat{\omega}^2$ approaches the Coriolis frequency f^2 , and vice versa. If $\hat{\omega}^2 \rightarrow f^2$, then the vertical wave number (wavelength) goes to infinity (zero).

As mentioned above, gravity waves transport energy through the atmosphere. They do this without transporting mass. Kinetic and potential energy are often provided as energy densities, i. e., energy per unit mass (in J/kg) or per unit volume (in J/m^3) in order to be independent of mass or density measurements. Kinetic and potential energy densities per unit mass, E_{kin} and E_{pot} , can be derived according to

$$E_{kin} = \frac{1}{2} (\overline{u'^2} + \overline{v'^2} + \overline{w'^2}), \quad (40)$$

$$E_{pot} = \frac{1}{2} \left(\frac{g}{N} \right)^2 \overline{\left(\frac{T'}{T} \right)^2}, \quad (41)$$

the horizontal bar denotes a temporal average (see, for example, Tsuda et al., 2000). Sometimes, the kinetic energy density is divided into its horizontal and vertical components. Then, the term kinetic energy density is used for the horizontal component (see, e. g., Placke et al., 2013; Geller and Gong, 2010). Multiplying equation (40) and (41) with the background density $\bar{\rho}$ and adding both together gives the total amount of energy per unit volume E_V (Nappo, 2013).

Thinking back to simple harmonic motions like a pendulum, it is not surprising that the ratio of kinetic and potential energy is reported to be constant (e. g., Placke et al., 2013; Torre et al., 2012; Tsuda et al., 2000; VanZandt, 1985). Mesoscale fluctuations which are measured in wind velocity or temperature are often due to a superposition of gravity waves, not to a single wave event. Therefore, it makes sense to describe the behaviour of gravity waves in terms of a spectrum as a function of ω , m , k , and l . The frequency spectrum $B(\omega)$ is represented by $B_0 \omega^{-p}$ with the

normalization constant B_0 . Following linear wave theory, it is expected that the ratio of kinetic (including the vertical component) and potential energy is equal to ρ (Tsuda et al., 2000). MST radar observations, for example, show ρ -values of 5/3–2.0 (e.g., Fritts et al., 1990). Geller and Gong (2010) provide the following ratios for the horizontal (vertical) kinetic and potential energy density, $E_{\text{kin},h}$ ($E_{\text{kin},v}$) and E_{pot} :

$$\frac{\overline{E_{\text{kin},h}}}{\overline{E_{\text{pot}}}} = \frac{1 + \left(\frac{f}{\hat{\omega}}\right)^2}{1 - \left(\frac{f}{\hat{\omega}}\right)^2} \quad (42)$$

$$\frac{\overline{E_{\text{kin},v}}}{\overline{E_{\text{pot}}}} = \frac{\hat{\omega}^2}{N^2} \quad (43)$$

The authors also show that $E_{\text{kin},h}$ is most sensitive to low-frequency gravity waves. $E_{\text{kin},v}$ has the most sensitivity to higher-frequency gravity waves and E_{pot} has its sensitivity maximum in between.

In the absence of a background wind, wave energy is a conserved quantity (e.g., Nappo, 2013). If this is the case, the density of wave potential energy per mass E_{pot} should increase exponentially with altitude (Lu et al., 2015). This is due to the exponential decrease of density with height. E_{pot} refers to the temperature variation of the oscillating air parcels. Due to the lower air density with height, the same amount of energy leads to a greater deflection of an air parcel with a certain mass from its rest position at greater heights compared to lower altitudes. This results in temperature variations and wave amplitudes which increase with height.

In contrast, the potential energy per volume $E_{\text{pot},v}$ should decrease exponentially with height since the volume of an oscillating air parcel increases exponentially with height (Lu et al., 2015). When wave dissipation occurs at the observed height range, the increase (decrease) of E_{pot} ($E_{\text{pot},v}$) with height is not exponentially any more, E_{pot} can even decrease (see, e.g., Lu et al., 2015; Lu et al., 2009).

In the presence of a background wind, wave action $\frac{\overline{E_v}}{\hat{\omega}}$, pseudo-energy $\frac{\overline{E_v}}{\hat{\omega}}$ ω and pseudo-momentum $\frac{\overline{E_v}}{\hat{\omega}}$ (k, l, m) are conserved quantities where the bar denotes the averaging over 2π (Nappo, 2013).

Therefore, the vertical fluxes of pseudo-energy (energy per time and area) and pseudo-momentum (momentum per time and area) are often considered rather than the vertical fluxes of wave energy and momentum. In order to derive the vertical fluxes, pseudo-energy and pseudo-momentum need to be multiplied by c_{gz} .

Departures from conservative propagation will lead to dissipation. Dissipation can be due to different processes like radiative damping, wave-wave and wave-mean flow interactions, wave breaking and instability processes. At heights below the thermosphere, viscosity and molecular diffusion are generally not important dissipation mechanisms. In the thermosphere, exponentially decreasing density and growth of kinematic viscosity with altitude allow these processes to dominate over the other ones. This growth of kinematic viscosity with height leads to the turbopause, typically at ca. 110 km. The dissipation of pseudo-momentum results in a force with direction and sign equal to the direction and sign of the horizontal phase propagation in the frame of reference moving with the wind (i.e., the horizontal intrinsic phase speed of the wave). Energy dissipation leads to local heating of the atmosphere (Fritts and Alexander, 2003).

Since many years, gravity waves in the (pre-)Alpine stratosphere and mesosphere are investigated by means of LIDAR (Light Detecting And Ranging) and airglow spectroscopy.

LIDAR temperature measurements at the Haute-Provence Observatory (43.93°N, 5.71°E), France, are performed since 1978 until today (e.g., Hauchecorne et al., 1991 and Hauchecorne and Chanin, 1980). Based on 16 years (1996–2012) of these measurements, Mzé et al. (2014) published a climatology of gravity wave potential energy density for the height range of 30–85 km. The results refer to periods of 52 min at minimum.

The authors observe night-to-night variations and also intra-annual variability, i.e., an annual cycle with a maximum in winter and a minimum in summer in the upper stratosphere and lower mesosphere. In the upper mesosphere (ca. 75 km height), they identified a semi-annual

cycle with global maximum in summer and a local one in winter. The summer maximum is probably due to oblique propagation. At the lower edge of their observations, the median of the potential energy density reaches ca. 10^0 J/kg. At 80–85 km height, it varies around 10^2 J/kg. The increase per height is not linear.

Since 2003, the temperature of the upper mesosphere and lower thermosphere (MLT) is derived operationally by means of OH-airglow spectroscopy at different stations in the (pre-)Alpine region. The instruments used are called GRIPS (GRound based Infrared P-branch Spectrometer, for further information see Bittner et al., 2000, Schmidt et al., 2013, and references therein). The (pre-)Alpine GRIPS-measurements started at the observatory Hohenpeißenberg (47.80°N, 11.00°E), Germany. This instrument based on the original design of GRIPS is not working any more today. The longest time series (2009–today) relying on a new version of GRIPS is available at Oberpfaffenhofen (48.09°N, 11.28°E), Germany. The measurements at Schneefernerhaus (47.42°N, 10.98°E), Germany, at Haute-Provence, France, at Sonnblick (47.05°N, 12.95°E), Austria, and at Otlica (45.93°N, 13.91°E), Slovenia, began later (2010, 2012, 2015, and 2017, for a map of stations see figure 6). These stations form the most dense sub-network equipped with identical instruments of the Network for the Detection of Mesospheric Change (NDMC, <https://ndmc.dlr.de/>). For further information on NDMC see also Schmidt et al. (2022).

The measurements refer to heights of ca. 84–88 km depending on the time of the year (Wüst et al., 2017). Wüst et al. (2016) estimated the density of potential energy density at the stations Oberpfaffenhofen, Schneefernerhaus, and Haute-Provence separately for periods shorter and longer than 60 min. A clear winter maximum is present for longer periods; also a summer maximum at Haute-Provence and Schneefernerhaus (zenith angle ca. 60°) can be observed around May and/or June. The findings are less clear for short-periodic waves. A minimum can be seen during June and/or July for the stations Schneefernerhaus (zenith angles 45° and 60°) and Oberpfaffenhofen. The instruments which look directly into zenith and are characterized by a smaller FoV, observe stronger activity in most cases.

Compared to Mzé et al. (2014), the values of wave potential energy density (wave periods longer than 60 min) derived at Haute-Provence differ only slightly when taking the error bars into account. The spectrometer-based values are a little bit lower, which is probably due to the different observational filters. The wave potential energy density for periods shorter than 60 min is in the range of 10^0 J/kg.

Satellite-based long-term investigations referring to the stratosphere and mesosphere and focused on the Alpine region are not available. In most cases, such analyses are provided on a

global basis. There, the Alpine region is covered only by a few pixels. For the global (satellite-based) investigation of gravity wave squared temperature amplitudes, vertical and horizontal wavelengths as well as absolute values of gravity wave momentum flux, the reader is referred to Ern et al. (2011), for example, and references therein.

Offermann et al. (2009) published a climatology of a proxy for temperature fluctuations caused by gravity waves for 20°N, 50°N, and 70°N (zonally averaged) at 70–100 km height. The results are based on analyses of Krebsbach and Preusse (2007) and Preusse et al. (2009) who made use of more than four years of TIMED-SABER² data (2002–2006, version 1.06). At 80–90 km height and 50°N, two maxima are

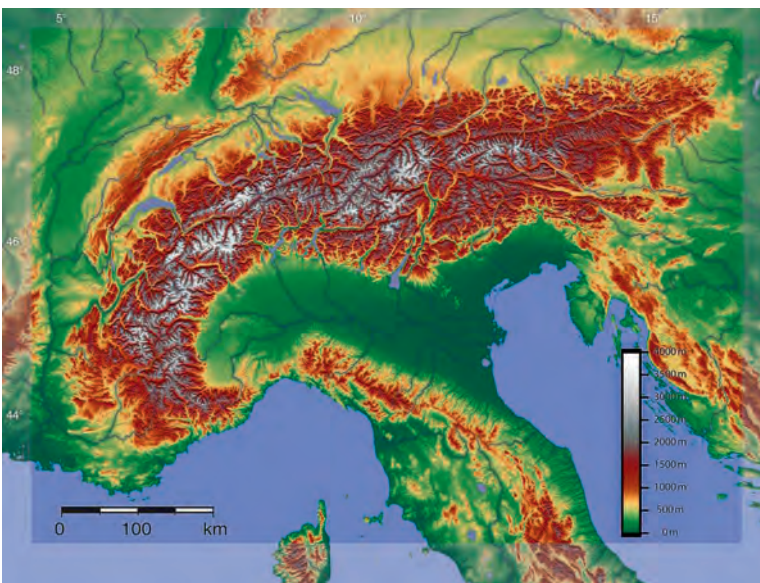


Fig. 6: Map of (pre-)alpine stations where GRIPS instruments (new version) are deployed (as of 20th October 2017). (Map based on SRTM data: CC some rights reserved, file: https://upload.wikimedia.org/wikipedia/commons/d/d9/Alpenrelief_01.jpg, author: Perconte, Download: 20.10.2017.)

² Thermosphere Ionosphere Mesosphere Energetics Dynamics, Sounding of the Atmosphere using Broadband Emission Radiometry

apparent: one in summer (July), which is in parts characterized by a double-peak structure (May and July), and one in winter (January and December). These values cannot be compared directly to the density of wave potential energy, however, they are closely related to this parameter. The results of Offermann et al. (2009) show that the semi-annual variation is not a specific characteristic of the Alpine region. However, whether there exists an annual or a semiannual cycle at a specific height depends also on latitude.

In literature, different possible explanations for the strong winter maximum can be found:

Allen and Vincent (1995) mention that weather conditions during winter (e. g., winter cold fronts) lead to more pronounced gravity wave generation. In contrast, Eckermann et al. (1995) and Alexander (1998) explain the winter maximum with enhanced growth of the wave amplitude due to the colder and more dense background atmosphere. Preusse et al. (2004) think that the stratospheric zonal wind field, which is oriented opposite with respect to the tropospheric zonal jet in summer (but not in winter), results in stronger gravity wave filtering during this season.

So, concerning the overall course of gravity wave activity or potential energy density during the year, the Alpine region is not extraordinary. However, compared to non-orographic regions, higher potential energy density can be observed especially during winter as shown by Wilson et al. (1991) based on LIDAR measurements (at Haute-Provence and at Biscarosse (44.40°N, 1.17°W), the latter a station at the west coast of France), for the upper stratosphere. Additionally, those authors report that energy and momentum dissipation happen at all heights levels between 30 km and 75 km. Nevertheless, they vary depending on height and season: the vertical growth of potential energy density is smaller in the upper stratosphere than in the mesosphere; it is larger in the mesosphere during summer than during winter. Mzé et al. (2014) who extended the analysed data set with respect to the covered height range and measurement period compared to Wilson et al. (1991) found out that the dissipation of gravity waves is most pronounced above 70 km height. This encourages the analysis of NDMC measurements regarding turbulent effects. Since 2014, more and more GRIPS stations in the (pre-)Alpine region are equipped additionally with FAIM systems (Fast Airglow IMager, Hannawald et al., 2016 and Sedlak et al., 2016). As pointed out by Schmidt et al. (2022), these instruments are suitable for the analysis of small-scale features such as turbulence.

In the following years, the growing amount of measurements in the Alpine region characterized in parts by an improved temporal and/or spatial resolution will foster further analyses of small-scale and non-linear processes.

References

- Alexander, M. (1998). Interpretations of observed climatological patterns in stratospheric gravity wave variance. *Journal of Geophysical Research: Atmospheres*, 103(D8):8627–8640.
- Allen, S. J. and Vincent, R. A. (1995). Gravity wave activity in the lower atmosphere: Seasonal and latitudinal variations. *Journal of Geophysical Research: Atmospheres*, 100(D1):1327–1350.
- Andrews, D. G. (2000). *An introduction to atmospheric physics*. Cambridge University Press.
- Bittner, M., Offermann, D., and Graef, H. H. (2000). Mesopause temperature variability above a midlatitude station in Europe. *Journal of Geophysical Research*, 105:2045–2058.
- Chimonas, G. and Hines, C. (1986). Doppler ducting of atmospheric gravity waves. *Journal of Geophysical Research: Atmospheres*, 91(D1):1219–1230.
- Eckermann, S. D., Hirota, I., and Hocking, W. K. (1995). Gravity wave and equatorial wave morphology of the stratosphere derived from long-term rocket soundings. *Quarterly Journal of the Royal Meteorological Society*, 121:149–186.
- Ern, M., Preusse, P., Gille, J., Hepplewhite, C., Mlynczak, M., Russell, J., and Riese, M. (2011). Implications for atmospheric dynamics derived from global observations of gravity wave momentum flux in stratosphere and mesosphere. *Journal of Geophysical Research: Atmospheres*, 116(D19).
- Fritts, D. C. and Alexander, M. J. (2003). Gravity wave dynamics and effects in the middle atmosphere. *Reviews of Geophysics*, 41:3–1–3–64. DOI:10.1029/2001RG000106.
- Fritts, D. C., Tsuda, T., VanZandt, T. E., Smith, S. A., Sato, T., Fukao, S., and Kato, S. (1990). Studies of velocity fluctuations in the lower atmosphere using the MU radar. Part II: Momentum fluxes and energy densities. *Journal of the Atmospheric Sciences*, 47(1):51–66.
- Geller, M. A. and Gong, J. (2010). Gravity wave kinetic, potential, and vertical fluctuation energies as indicators of different frequency gravity waves. *Journal of Geophysical Research: Atmospheres*, 115(D11).

- Hannawald, P., Schmidt, C., Wüst, S., and Bittner, M. (2016). A fast SWIR imager for observations of transient features in OH airglow. *Atmospheric Measurement Techniques*, 9(4):1461–1472.
- Hauchecorne, A. and Chanin, M.-L. (1980). Density and temperature profiles obtained by lidar between 35 and 70 km. *Geophysical Research Letters*, 7(8):565–568.
- Hauchecorne, A., Chanin, M.-L., and Keckhut, P. (1991). Climatology and trends of the middle atmospheric temperature (33–87 km) as seen by Rayleigh lidar over the south of France. *Journal of Geophysical Research: Atmospheres*, 96(D8):15297–15309.
- Holton, J.R. (2004). *An introduction to dynamic meteorology*. Academic Press.
- Krebsbach, M. and Preusse, P. (2007). Spectral analysis of gravity wave activity in SABER temperature data. *Geophysical Research Letters*, 34:L03814.
- Lu, X., Chu, X., Fong, W., Chen, C., Yu, Z., Roberts, B.R., and McDonald, A.J. (2015). Vertical evolution of potential energy density and vertical wave number spectrum of antarctic gravity waves from 35 to 105 km at mcmurdo (77.8°S, 166.7°E). *Journal of Geophysical Research: Atmospheres*, 120(7):2719–2737.
- Lu, X., Liu, A.Z., Swenson, G.R., Li, T., Leblanc, T., and McDermid, I.S. (2009). Gravity wave propagation and dissipation from the stratosphere to the lower thermosphere. *Journal of Geophysical Research: Atmospheres*, 114(D11).
- Marsh, D.R. (2011). Chemical–dynamical coupling in the mesosphere and lower thermosphere. In *Aeronomy of the Earth's Atmosphere and Ionosphere*, pages 3–17. Springer.
- Mzé, N., Hauchecorne, A., Keckhut, P., and Thétis, M. (2014). Vertical distribution of gravity wave potential energy from long-term Rayleigh lidar data at a northern middle-latitude site. *Journal of Geophysical Research*, 119:12,069–12,083.
- Nappo, C.J. (2013). *An introduction to atmospheric gravity waves*. Academic Press.
- Offermann, D., Gusev, O., Donner, M., Forbes, J.M., Hagan, M., Mlynczak, M.G., Oberheide, J., Preusse, P., Schmidt, H., and Russell III, J.M. (2009). Relative intensities of middle atmosphere waves. *Journal of Geophysical Research*, 114:D06110.
- Placke, M., Hoffmann, P., Gerding, M., Becker, E., and Rapp, M. (2013). Testing linear gravity wave theory with simultaneous wind and temperature data from the mesosphere. *Journal of Atmospheric and Solar-Terrestrial Physics*, 93:57–69.
- Preusse, P., Eckermann, S.D., Ern, M., Oberheide, J., Picard, R.H., Roble, R.G., Riese, M., Russell, J.M., and Mlynczak, M.G. (2009). Global ray tracing simulations of the SABER gravity wave climatology. *Journal of Geophysical Research: Atmospheres*, 114(D8).
- Preusse, P., Ern, M., Grossmann, K.U., and Mergenthaler, J.L. (2004). Seasonal variations of gravity wave variance inferred from CLAES. In *Remote Sensing of Clouds and the Atmosphere VIII*, volume 5235, pages 288–298. International Society for Optics and Photonics.
- Schmidt, C., Hannawald, P., Sedlak, R., Noll, S., Wüst, S., and Bittner, M. (2022). *Observations of OH airglow at the UFS "Schneefernerhaus"* in Bittner, M. (Editor), 2022. Science at the UFS "Schneefernerhaus", chapter 14, this book
- Schmidt, C., Höppner, K., and Bittner, M. (2013). A ground-based spectrometer equipped with an InGaAs array for routine observations of OH(3-1) rotational temperatures in the mesopause region. *Journal of Atmospheric and Solar-Terrestrial Physics*, 102:125–139.
- Sedlak, R., Hannawald, P., Schmidt, C., Wüst, S., and Bittner, M. (2016). High-resolution observations of small-scale gravity waves and turbulence features in the OH airglow layer. *Atmospheric Measurement Techniques*, 9(12):5955–5963.
- Torre, A., Alexander, P., Hierro, R., Llamedo, P., Rolla, A., Schmidt, T., and Wickert, J. (2012). Large amplitude gravity waves above the southern Andes, the Drake Passage, and the Antarctic Peninsula. *Journal of Geophysical Research: Atmospheres*, 117(D2).
- Tsuda, T., Nishida, M., Rocken, C., and Ware, R.H. (2000). A global morphology of gravity wave activity in the stratosphere revealed by the GPS occultation data (GPS/MET). *Journal of Geophysical Research: Atmospheres*, 105(D6):7257–7273.
- VanZandt, T.E. (1985). A model for gravity wave spectra observed by doppler sounding systems. *Radio Science*, 20(6):1323–1330.
- Wilson, R., Chanin, M., and Hauchecorne, A. (1991). Gravity waves in the middle atmosphere observed by rayleigh lidar: 2. climatology. *Journal of Geophysical Research: Atmospheres*, 96(D3):5169–5183.
- Wüst, S., Bittner, M., Yee, J.-H., Mlynczak, M.G., and Russell III, J.M. (2017). Variability of the Brunt-Väisälä frequency at the OH*-layer height. *Atmospheric Measurement Techniques*, 10(12):4895–4903.
- Wüst, S., Wendt, V., Schmidt, C., Lichtenstern, S., Bittner, M., Yee, J.-H., Mlynczak, M.G., and Russell III, J.M. (2016). Derivation of gravity wave potential energy density from NDMC measurements. *Journal of Atmospheric and Solar-Terrestrial Physics*, 138:32–46.

21 Simultaneous lidar measurements of ozone, water vapour, and particles: long-term investigation of atmospheric transport up to the hemispheric scale

Thomas Trickl, Hannes Vogelmann

Karlsruher Institut für Technologie, IMK-IFU, Kreuzeckbahnstr. 19, 82467 Garmisch-Partenkirchen, E Mail: thomas.trickl@kit.edu, hannes.vogelmann@kit.edu

Abstract

The vertical distribution of ozone, water vapour and aerosol in the troposphere has been routinely measured at UFS (Umweltforschungsstation Schneefernerhaus) and at Garmisch-Partenkirchen for more than a decade. These data are important factors for understanding the impact of air-mass transport on the chemical composition of the atmosphere. The source regions have been identified by state-of-the-art transport modelling by partner groups. Focus has been on intercontinental transport of pollutants, including biomass burning events, the influence of downward stratospheric air intrusions on the tropospheric ozone budget as well as Saharan or Asian dust outbreaks. Recent highlights have been the discovery that stratospheric influence in the free troposphere existed on 84 % of the measurement days and that long-range transport in the free troposphere undergoes substantially less turbulent mixing than previously thought. In fact, the water-vapour measurements with the UFS differential-absorption lidar (DIAL) have demonstrated that air descending from the lowermost stratosphere reaches the Alps almost unchanged after many days of travel and over thousands of kilometres. The water-vapour measurements have recently been extended to the lower stratosphere with a high-power Raman lidar that is operated at UFS alongside with the DIAL. Thus, the most important greenhouse gas can now be measured in the entire particularly climate-sensitive altitude range around the tropopause. A spectacular example with extremely low water vapour (2 ppm) between 15 and 16 km was found, that had been advected from lower latitudes where freeze drying has been postulated to occur in the tropopause region.

21.1 Introduction

The chemical composition of the atmosphere has been subject to considerable modification since the 1970s. The main reasons for this have been changes of anthropogenic air pollution and changing atmospheric dynamics most likely as a result of the ongoing warming (e. g., Lin et al., 2015; Neu et al., 2014). Constituents of particular interest have been ozone, nitric oxides and hydrocarbons as the main ozone precursors, water vapour (as a source of the OH radical or a tracer for transport), aerosols and sulphur dioxide. The long-term measurement of these and several other species is an important task in order to determine the reaction of the atmosphere to emission reductions or to detect unexpected new phenomena for example related to changing transport patterns. The observations reflect the air quality not only here in Europe, but also in the entire northern hemisphere. The air quality in Europe and North America has been improving (e. g., Jonson et al., 2006; Vautard et al., 2006; Simon et al., 2015), but in East Asia the rapidly growing industrialization has led to a strong increase of pollutants (e. g., Ding et al., 2017).

Mountain-top observations of atmospheric trace constituents are an important tool for identifying the chemical composition of the lower free troposphere. With growing altitude the contributions change from more regional to more hemispheric ("background"). In Central Europe particularly renowned stations are Mte. Cimone (Italy, 2165 m), Zugspitze (2962 m), Sonnblick (Austria, 3106 m) and Jungfrauoch (Switzerland, 3560 m). As early as the 1970s the Institute for Atmospheric Environmental Research (Institut für Atmosphärische Umweltforschung, IAU,

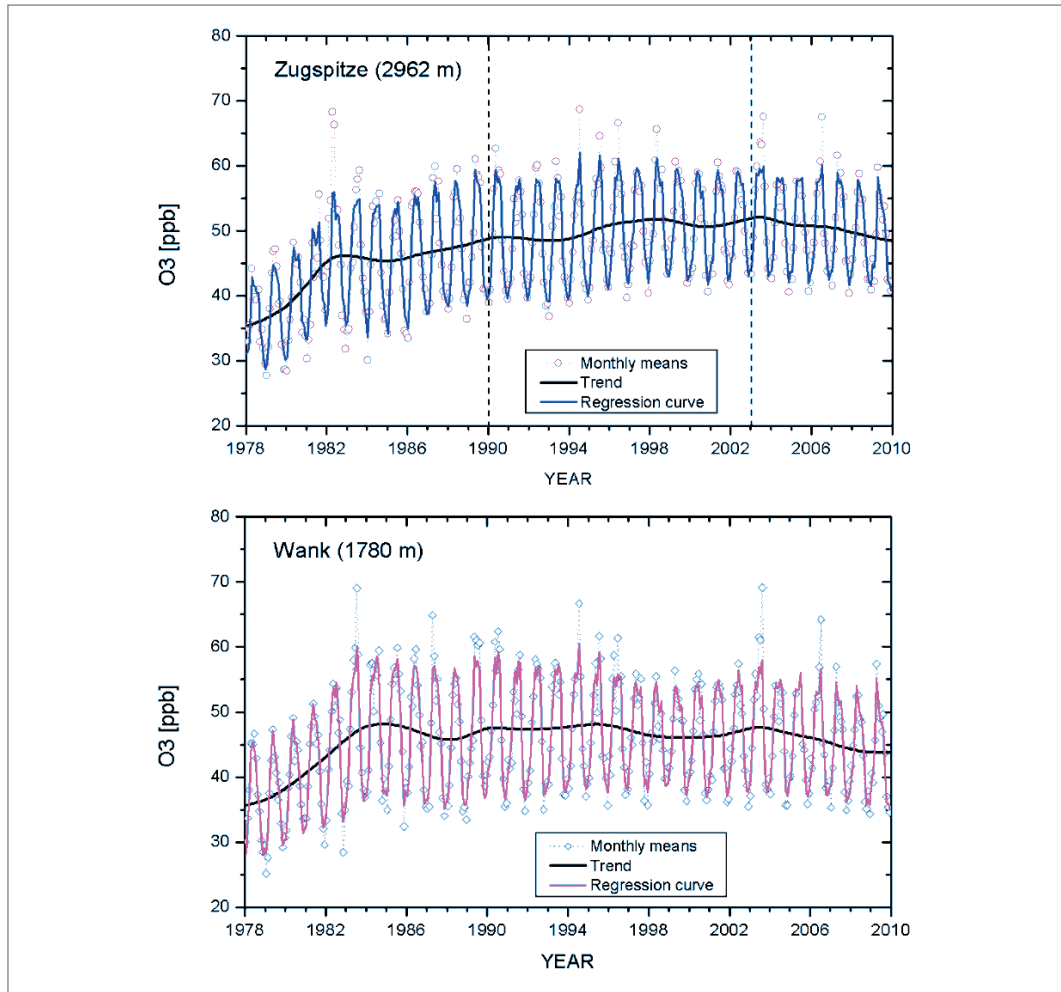


Fig. 1: Monthly mean ozone values of ozone from the measurements at the Zugspitze and Wank summits between 1978 and 2010 (from H. E. Scheel who deceased in 2013); the trends are visualized by black lines. The seasonal cycles with a summer maximum and a winter minimum are caused by the photochemical production of ozone in the presence of sunshine.

later IFU, now IMK-IFU) at Garmisch-Partenkirchen established monitoring stations at several altitudes, most importantly the sites at the Wank and Zugspitze summits (at 1780 m and 2962 m, respectively). The altitudes of these sites are representative for a quite different air-mass composition. What is unique is their co-location within just about 15 km. In 1978 precision in-situ measurements of ozone started (Fig. 1) and have found strong international interest (Logan et al., 2012; Parrish et al., 2012; Gaudel et al., 2018; Parrish et al., 2020) because of the strong positive trend that continued at the Zugspitze summit even after the emissions of ozone precursors started to decline around 1990. This positive trend is missing in the Wank ozone (Fig. 1), and the amplitude of the seasonal cycle at this station started to diminish in 1990. This behaviour is in agreement with the idea that the lower-lying Wank station is more influenced by the regional and European background than the Zugspitze summit. The positive trend at the higher station is ascribed to the difference in stratospheric influence at the two mountains, a very remarkable finding (Scheel, 2003; Trickl et al., 2010; 2020). The stratospheric fraction at 2962 m roughly doubled between 1978 and 2003, to surprisingly high 40% of the mean annual ozone.

In 1998 the Federal Office of the Environment (Umweltbundesamt, UBA) started a full-size observational programme of more than 30 trace gases and of particles at the Schneefernerhaus research station (UFS; air inlet at 2670 m) at the southern face of Mt. Zugspitze, as a principal contributor to the Global Atmosphere Watch (GAW) programme of the World Meteorological Organization. The measurements here have meanwhile fully replaced the measurements at the summit, which had to be discontinued after 2012.

Despite the benefit of providing observations around the clock, a ground-based station network cannot cover the main part of free troposphere. This requires methods based on balloon-, air-borne sensors or optical remote sensing. The optical methods offer the advantage of much more frequent measurements. However, optical sounding is limited to cloud-free conditions. Although horizontally delivering “point” measurements vertical sounding with lidar (light detecting and ranging) is an optimum solution for ground-based sounding as it combines the advantages of excellent temporal and vertical resolution. Time series yield time-altitude sections of atmospheric constituents. In this way, the impact of atmospheric transport processes becomes visible.

Lidar is an active remote-sensing method based on a pulsed laser system, on backscattering of the intense nanosecond radiation pulses in the atmosphere and on collecting the scattered photons by one or more telescopes at the ground with a resolution in time (typically 50 ns). The range information is derived from the travel time of the photons. IFU was one of the first institutes worldwide to use a lidar system for routine atmospheric measurements. The first aerosol backscatter lidar was installed in 1973. Beyond the tropospheric measurements that started soon (e.g., Reiter et al., 1975) a long-term time series of the stratospheric aerosol was started in 1976 and has yielded insight into the impact of stratospheric transport (Trickl et al., 2013). Two more (mobile) aerosol lidar systems were contributed in 1978 and 1990, operated in a wavelength range between 355 and 1560 nm.

Tropospheric trace-gas measurements with lidar are most commonly based on absorption measurements. The radiation loss due to the specific absorption loss of the travelling laser pulse and during the return of the backscattered portion of the pulse are registered as a function of time. By comparing the difference in loss for two adjacent laser wavelengths artefacts from interfering species such as aerosols can be minimised. This “differential-absorption lidar” (DIAL) method can imply the application of two or more laser wavelengths (e.g., Trickl, 2010; see Sec. 4.1). The DIAL technique is applicable for a number of gases such as ozone, water vapour, nitric oxides, sulphur dioxide, and some hydrocarbons. Due to the low free-tropospheric concentrations of most species only ozone and water vapour can be measured with sufficient sensitivity. The IFU lidar team has developed DIAL systems for both constituents. The H₂O system was installed at UFS in 2004. In 2007 a programme of routine measurement of aerosol, ozone and water vapour was started with the two DIAL systems.

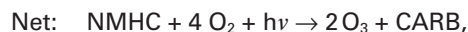
In order to extend accurate measurements of the key green-house gas water vapour into the lower stratosphere night-time measurements with a high-power Raman lidar have been started. This system also provides temperature measurements up to the mesosphere.

The rather comprehensive vertical sounding and in-situ instrumentation at UFS and the surrounding sites is unique and offers a considerable potential for atmospheric research. The activities are complemented by the activities at the nearby Hohenpeißenberg observatory of UFS partner German Weather Service (Deutscher Wetterdienst, DWD). The activities are integrated into international networks such as GAW, NDACC (Network for the Detection of Atmospheric Composition Change, <http://www.ndsc.ncep.noaa.gov/>) and EARLINET (European Aerosol Research Lidar Network, <https://www.earlinet.org/>, now a part of the European infrastructure ACTRIS).

This chapter gives examples for combining the lidar measurements in the study of atmospheric long-range transport, complemented by the local in-situ data. The research has been supported by high-quality transport modelling by partners at ETH Zürich and NILU (Norsk Institutt for Luftforskning) as well as on the internet (HYSPLIT model, <http://ready.arl.noaa.gov/HYSPLIT.php>), which is in detail described in the publications cited.

21.2 Tropospheric Ozone Chemistry

In areas with elevated pollutant emissions ozone is formed from precursors during daytime, mostly non-methane hydrocarbons (NMHC) and nitric oxides. Solar radiation decomposes ozone yielding electronically excited (¹D) oxygen atoms that subsequently react with water vapour. This mechanism is the most important source of OH radicals in the troposphere. The formation of ozone is described in the following simplified reaction scheme (Liu et al., 1987):



R denoting hydrocarbon radicals and CARB carbonyl compounds. Two ozone molecules are produced for every NMHC molecule oxidized. The cycle of NO and NO₂ (reactions R3 and R4) does not appear in the net equation. The carbonyl compounds may undergo further reactions that eventually also lead to ozone formation. The ozone production is highly nonlinear. Liu et al. (1987) estimate from model calculations that more than 40 ppb ozone can be generated per ppb NO per day under conditions up to 1 ppb NO. For high NO this rate gradually diminishes to 10 ppb per day and less.

21.3 Atmospheric Long-Range Transport

The concentrations of tropospheric trace constituents do not only depend on local or regional emissions and chemistry. The observations show clear signatures of rather remote sources up to the hemispheric scale. These signatures appear in lofted layers from Alpine summit heights to the upper troposphere. The most important remote sources are the stratosphere (ozone) and the boundary layers of North Africa (desert dust), North America (anthropogenic air pollution, fire plumes) and Asia (anthropogenic air pollution, desert dust, fire plumes).

21.3.1 Stratosphere-to-Troposphere transport

Stratosphere-to-Troposphere transport (STT; Holton et al., 1995; Stohl et al., 2003) is the most important natural source of tropospheric ozone. In the late 19th century, before the rise of anthropogenic air pollution, the related ozone mixing ratio was estimated to range around 10 ppb next to the ground (Volz and Kley, 1987). This low value has been questioned and a background twice as high as this is estimated (Tarasick et al., 2019). The reported mechanisms of STT are tropopause folding (e.g., Danielsen, 1968; Danielsen and Mohnen, 1977) in the vicinity of a jet stream, subsidence in cut-off lows (Price and Vaughan, 1993) and gravity-wave breaking (Lamarque et al., 1996).

The very dry stratospheric layers can descend down as far as to the top of the boundary layer. Penetration into the boundary layer seems to be strongly impeded, and Reiter (1990), based on several years of daytime observations on board the Zugspitze cable car, even concluded that stratospheric air does not reach altitudes below 1400 m. However, even the ground may be reached if the intrusion layer descends far enough during periods without daytime convection (Eisele et al., 1999; Cooper et al., 2005; Ott et al., 2016).

A region of particularly pronounced stratosphere-troposphere exchange are the regions along the subtropical jet stream (Sprenger et al., 2003; Škerlak et al., 2014). Despite a number of airborne measurements (e.g., Gouget et al., 1996; Cammas et al., 1998; Zachariasse, 2000; Zahn et al., 2002) this strong source of STT had long been underestimated. The subtropical jet stream is a rather persistent feature that caused downward transfer of stratospheric ozone over a major part of the year. Quite surprisingly, Langford et al. (1999) and Trickl et al. (2011) report strongly enhanced ozone from transport along the subtropical jet stream over the United States and Europe, respectively. Europe was reached after air-mass travel once around the northern hemisphere within 15 days.

STT is a very attractive topic for lidar research, because vertically confined concentration features (elevated O₃ and very low H₂O) can be conveniently traced in time. Lidar-based work in this field at our institute since 1996 (Eisele et al., 1999) has contributed considerable knowledge in this field.

21.3.2 Intercontinental Transport

Intercontinental transport of aerosols was first concluded for observations at the Wank summit (Reiter et al., 1984). Trans-Atlantic transport of ozone was first observed in lidar time series at IFU in May 1996 and also May 1997 (Eisele et al., 1999; Stohl and Trickl, 1999; Trickl et al., 2003). Trans-Pacific ozone transport was verified in 1997 for the Pacific Ocean (Jaffe et al., 1999). The benefit of lidar measurement is obvious since intercontinental ozone transport takes place mostly in the free troposphere (e.g., Fehsenfeld et al., 2006). This requires lifting of the polluted air masses from the boundary layer. Indeed, lofted layers have been observed downwind continents (e.g., Penkett et al., 1998; Myazaki et al., 2003; Parrish et al., 2004). Processes involved are warm-conveyor-belt (WCB) transport (e.g., Bethan et al., 1998; Stohl and Trickl, 1999; Cooper et al., 2002), convection (e.g., Dickerson et al., 1987; Lelieveld and Crutzen, 1994) and orographic lifting (e.g., Furger et al., 2000; Liu et al., 2003). WCB transport occurs ahead of frontal systems and has been seen as particularly important (Bey et al., 2001; Cooper, 2002; Hannan et al., 2003). The WCB occurrence maximizes to the east of the large continents, i.e., next to some of the most polluted areas in the northern hemisphere (Stohl, 2001), which suggests a severe role of these source regions.

The field of intercontinental transport studies quickly exploded after the first observations, implying numerous large field campaigns for assessing the changing chemical composition during the transport of the polluted continental air masses. A comprehensive summary can be found in (HTAP, 2010).

21.4 Lidar Systems in Garmisch-Partenkirchen and at UFS

21.4.1 Ozone DIAL at IMK-IFU

A tropospheric ozone DIAL has been operated in Garmisch-Partenkirchen, Germany, at IMK-IFU (formerly IFU; 47° 28' 37" N, 11° 3' 52" E, 740 m a.s.l.) since 1991 (Carnuth et al., 2002; Trickl et al., 2020b). The laser source is a narrow-band KrF laser set to 0.4 J/pulse at 100 Hz repetition rate, at a wavelength of 248.5 nm. Two separate receiving telescopes (diameters 0.13 and 0.5 m, respectively) are used to divide the dynamic range of the backscatter signal of roughly eight decades. The primary laser output is strongly absorbed by ozone and, thus, not used. Instead, it is shifted by stimulated Raman scattering in hydrogen and deuterium with conversion efficiencies of up to 40% (Kempfer et al., 1994). We use the radiation components at 277.1 nm ("on" wavelength), 291.8 nm ("on" wavelength) and 313.2 nm ("off" wavelength, i.e., minor absorption) for the DIAL measurements (Eisele and Trickl, 1999). The three-wavelength operation leads to a unique vertical range between roughly 0.25 km above the ground and 3 to 5 km above the tropopause, the measurement time interval being just 41 s. By comparing the ozone profiles retrieved from different wavelength combinations (277 nm–313 nm, 292 nm–313 nm, or 277 nm–292 nm) and for the two telescopes an internal quality check is possible. The DIAL features low uncertainties of about ± 3 ppb (parts per billion) in the lower free troposphere, the annual average Zugspitze ozone mixing ratio being about 55 ppb. The uncertainty roughly doubles in the upper troposphere. Comparisons with the nearby Zugspitze in-situ measurements (at 2962 m a.s.l.) show no relevant mutual bias. The uncertainty further diminished after another system upgrading in 2012 that reduced the noise level by roughly a factor of three. The vertical resolution is dynamically varied between 50 m in the lower troposphere and roughly 0.3 km below the tropopause.

Aerosol backscatter profiles with very good signal-to-noise ratio up to the lower stratosphere are obtained from the 313-nm "off" channel of the lidar (Eisele and Trickl, 2005). Examples demonstrating the high data quality achieved in recent years can be seen in (Trickl et al., 2015).

21.4.2 Water-Vapour Lidar Systems at UFS

The Zugspitze water-vapour DIAL is operated at UFS (47° 25' 00" N, 10° 58' 46" E) at 2675 m a.s.l., about 8.5 km to the south-west of IMK-IFU, and 0.5 km to the south-west of the Zugspitze summit. The full details of this lidar system were described by Vogelmann and Trickl (2008;

2022). It is based on a powerful tunable narrow-band Ti:sapphire laser system with up to 250 mJ energy per pulse operated at about 817 nm and a 0.65-m-diameter Newtonian receiver. Due to these specifications a vertical range up to about 12 km can be reached, almost unaffected by daylight. A separation of near-field and far-field signals is achieved by a combination of a beam splitter and a blade in the far-field channel. The operating range starts below the altitude of the Zugspitze summit station (2962 m a.s.l.). The electronics are almost identical to those of the ozone DIAL. However, at 817 nm avalanche photodiodes have been used that are noisier than the photomultiplier tubes preferred for shorter wavelengths. Improvements are planned.

The vertical resolution chosen in the data evaluation is dynamically varied between 50 m at low altitudes and roughly 350 m in the upper troposphere. Free-tropospheric measurements during dry conditions clearly benefit from the elevated site outside or just below the edge of the moist Alpine boundary layer (e.g., Carnuth and Trickl, 2000; Nyeki et al., 2000; Carnuth et al., 2002). After a fatal laser damage in winter 2015 a new Ti:sapphire laser system is under development.

The lidar has been validated in several intercomparisons, particularly with an airborne DIAL (Sec. 5.1.1). A noise level of 5% was determined up to more than 6 km, with no resolvable bias at an uncertainty level of 1%.

21.4.3 Raman Lidar at UFS

Because of the radiation loss in the absorption measurement the water-vapour measurements with the UFS DIAL are limited to the free troposphere, with somewhat degrading performance in the upper troposphere. Measurements at higher altitudes can be achieved by Raman scattering of short-wavelength laser radiation from the H₂O molecule due to much lower radiation loss in the troposphere. However, Raman scattering is more than three orders of magnitude weaker than Rayleigh scattering that is used for DIAL sounding. This disadvantage can, in principle, be compensated by upscaling power and size of the system, at least during nighttime, i.e., in the absence of the solar background. Also the use of ultraviolet (UV) wavelengths is highly advantageous because of the λ^{-4} wavelength dependence of Raman scattering. As a consequence, a high-power Raman lidar system has been developed at UFS, at the side of DIAL system (Höveler et al, 2016; Klanner et al., 2021). In the UV excimer lasers provide power levels exceeding laser sources so far used in water-vapour Raman lidars by more than one order of magnitude. We use a 180-W single-line XeCl laser, emitting at 308 nm, and a Newtonian receiver telescope for the backscattered radiation with a diameter as large as 1,5 m. In this way, a vertical range up to 20 km has been demonstrated for a measurement time of 1 h. In contrast to the DIAL the Raman lidar must be routinely calibrated. Due to the very high spatial and temporal variability of water vapour (Vogelmann et al., 2011; 2015) this is a demanding task. At UFS this issue will be solved in a unique way by the side-by-side operation of the highly accurate water-vapour DIAL system. One successful demonstration of this approach during a highly inhomogeneous situation was given before the interruption of the DIAL operation (Klanner et al., 2021).

21.5 Results of Long-Range transport studies (2007–2017)

Since 2007 routine measurements of ozone, water vapour and the aerosol have been conducted with the two DIAL systems at UFS and IFU. Due to the less complex laser technology of the ozone DIAL, allowing for automatic data acquisition, and the easier access to the station in the valley the number of measurements is dominated by the ozone soundings. Between 2007 and 2017, 2359 ozone measurements (on 625 days) have been evaluated, also yielding profiles of aerosol backscatter coefficients archived in the EARLINET data base. The water vapour measurements were made on typically two measurement days per week, but have been interrupted since 2015 (Sec. 4.2).

The interesting features in both the ozone and water-vapour profiles are mostly related to STT. In addition, about 90 days with air masses containing Saharan dust have been covered by observations. Long range transport of fires plumes was observed the most important source region being the United States, Canada, and Ukraine where continual burning occurs.

21.5.1 Results for Stratosphere-to-Troposphere Transport

21.5.1.1 Examples of measurements during Intrusion of Stratospheric Air into the Troposphere

As discussed by Trickl et al. (2010) stratospheric air intrusions passing over Garmisch-Partenkirchen arrive from almost all directions. Easterly directions mostly result from detours of the dry layers via Eastern Europe or curl formation over Central Europe potentially in cut-off lows. It is interesting that intrusion layers are observed under so many different conditions. We routinely observe pre-frontal and post-frontal intrusion layers, as well as very frequently intrusions slowly descending from the far west (Western Canada, Alaska, Siberia). Prefrontal ozone peaks are mainly associated with a descent of the stratospheric air masses from the Arctic to North Africa followed by some return to Central Europe, accompanied by Saharan dust. Postfrontal intrusions mostly reach low altitudes above Garmisch-Partenkirchen. They occur in “classical” case of beginning anti-cyclonic conditions (e.g., Stohl and Trickl, 1999; Trickl et al., 2003), but also between two fronts sometimes separated by not more than one day. In these cases the inclined descending layer can be sandwiched between the low-lying clouds of the preceding front and the high-lying clouds of the incoming new front.

Fig. 2 shows an ozone time series generated from measurements with the ozone DIAL system on December 30 and 31, 2013, at intervals of 1 to 2 h. The shape of the high-ozone areas in Fig. 2 indicates a tropopause fold that drifted through laser beam transversely to its main direction of postfrontal propagation from the Arctic south of Greenland to the Alps. What is very special here is that two descending high-ozone layers occur. The ozone DIAL is capable of resolving these very thin layers. The performance of the system also benefits from its outstandingly low noise level of about 1×10^{-6} of the full signal range after minor smoothing.

Peak mixing ozone ratios between 80 and 150 ppb in intrusion layers are normal. 200 ppb and more have only been observed three times in the history of the ozone DIAL system. In the lowest part of the layers in Fig. 2, reached on December 31, the mixing ratio dropped to about 60 ppb. Since the layer did not widen and the relative humidity was 1% or less throughout that period this low value cannot be due to mixing of the two layers with the surrounding tropospheric air during the long transport. It seems to be determined by the way of outflow from the lowermost Arctic stratosphere (Trickl et al., 2014; 2016).

The first simultaneous time series of both DIAL systems is shown in Fig. 3 (Trickl et al., 2014). The case was highly complex with three layers L1–L3 (with peak ozone mixing ratios of about 120 ppb, 180 ppb and 200 ppb, respectively) not behaving like the classical tropopause fold in Fig. 2. This is indicated by the trajectory bundle in Fig. 4: The intrusion was split into filaments confined in space that transversely drifted out of the observational area within rather short time. The four-day trajectories were calculated with the transport model LAGRANTO (Lagrangian Analysis Tool) model (Wernli and Davies, 1997) by our partners at ETH Zürich (Switzerland), run

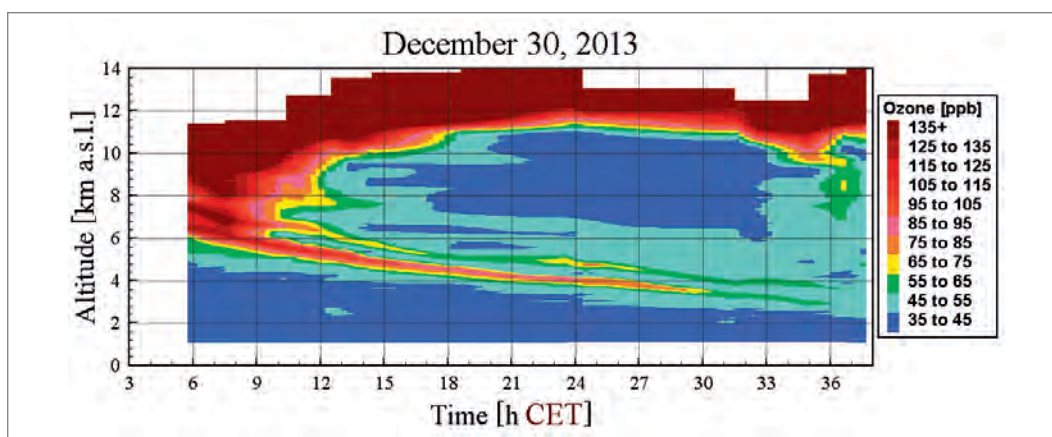


Fig. 2: Lidar time series of a stratospheric air intrusion cyclonically descending from 75 km a.s.l. south of Iceland: Two very thin layers subside for more than one day, the lower one to less than 3 km (for details see text).

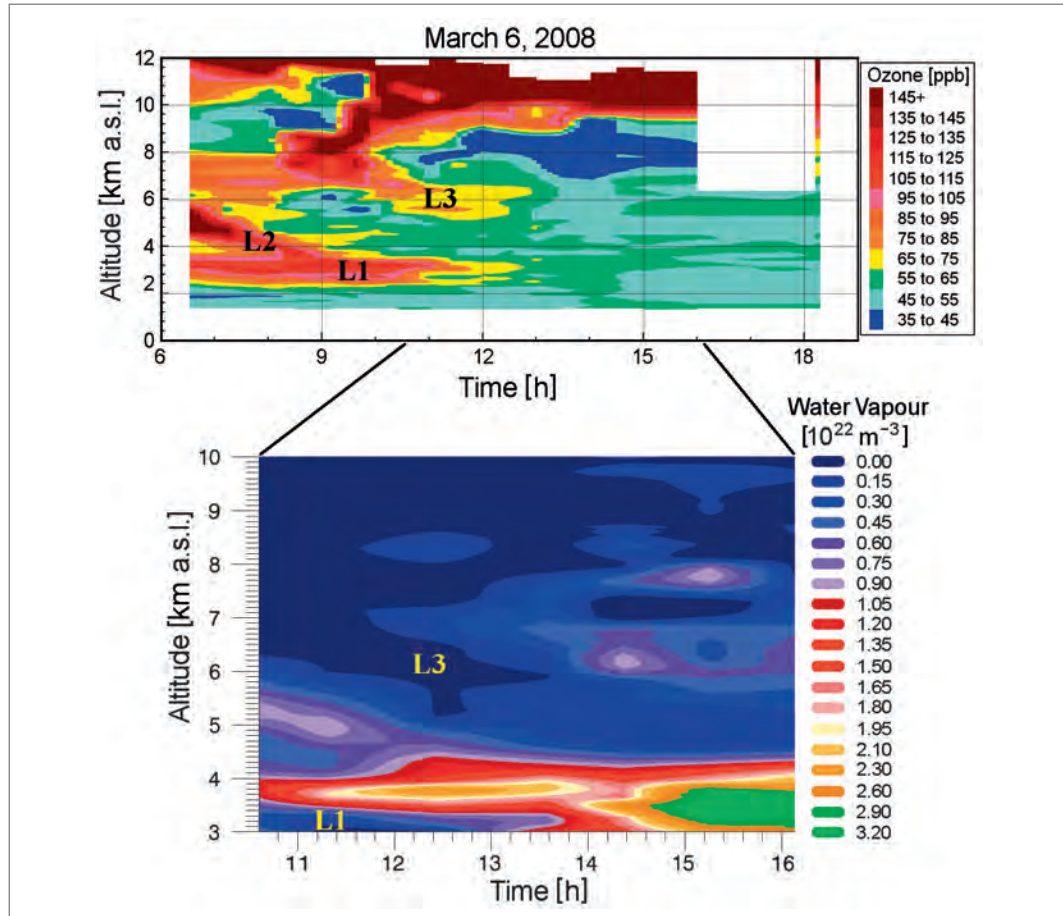


Fig. 3: First simultaneous time series of ozone and water vapour measured on March 6, 2008, (Trickl et al., 2014): Three layers (L1, L2, L3) with very high ozone mixing ratios (up to 200 ppb) were observed. High ozone corresponds to extremely low water-vapour density of less than $1.5 \times 10^{21} \text{ m}^{-3}$ (corresponding to a mixing ratio of, e. g., about 100 ppm at 4 km). The minimum humidity in Layer L1 is roughly zero (uncertainty: ± 25 ppm).

with re-analysis meteorological data from the European Centre for Medium-Range Weather Forecast. The re-analysis-based trajectories slightly differ from the operational forecast we receive every day (Zanis et al., 2003).

Again, the humidity was extremely low (almost negligible in Layer L1) suggesting the absence of major mixing on the way from Greenland to our site. Layer L3 started to become less dry after 13:00 CET. Since also ozone dropped considerably at the same time, this increase in humidity could mean a transition to an upper-tropospheric source in the Arctic.

On April 25, 2013, almost simultaneous nighttime measurements during the passage of three intrusion layers in the free troposphere were made with the Raman lidar and the water-vapour DIAL (Fig. 9 of Klanner et al., 2021). During nighttime the Raman lidar yields measurements without background and, thus, has a high sensitivity for low humidity. Two of the three STT layers were found to be extremely dry (relative humidity significantly below 1%) with both lidar systems.

In October 2008, for the first time the full tomography of a stratospheric intrusion layer was achieved that started to emerge from the stratosphere over Baffin Island (north-eastern Canada) and passed over Central Europe on October 17, 2008 (Trickl et al., 2016; Fig. 5). The observations were made during the LUAMI (Lindenberg Upper Air Methods Intercomparison) that had been planned for instrument validation purposes (Fig. 5). Vertical sounding of water vapour took place with the air-borne DIAL system WALES of UFS partner DLR and at the four observational sites Payerne (Switzerland), Bilthoven (The Netherlands), Lindenberg (Germany) and UFS. Transport modelling was, again, performed at ETH Zürich and yielded the trajectories in Fig. 5 and valuable transverse cross sections of the tropopause fold along its route (not shown here).

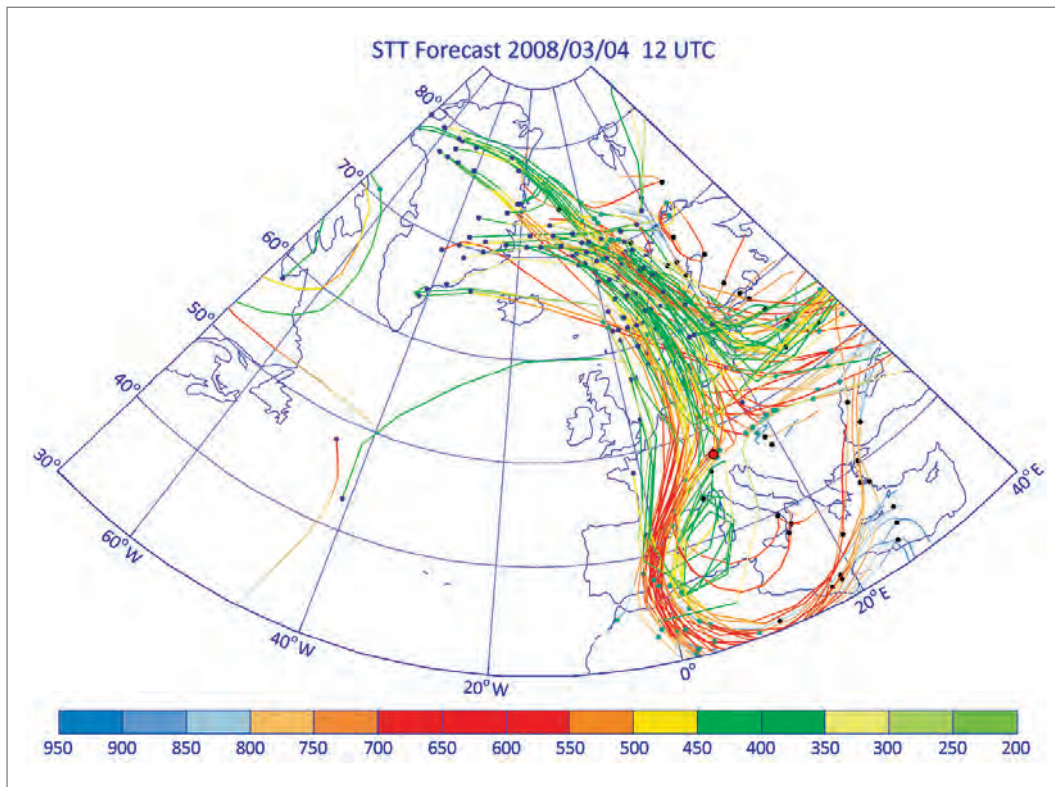


Fig. 4: Four-day forward trajectories with the LAGRANTO model based on ERA 40 meteorological re-analysis data from the European Centre for Medium-Range Weather Forecast (Trickl et al., 2014); the colour code is pressure in mbar, the red dot marks the position of Garmisch-Partenkirchen. The Zugspitze summit corresponds to a pressure of about 700 mbar. The trajectory positions for the times t_0 (12 UTC on March 4, 2008), $t_0 + 2$ d and $t_0 + 4$ d are given with dark blue, light blue and black dots, respectively.

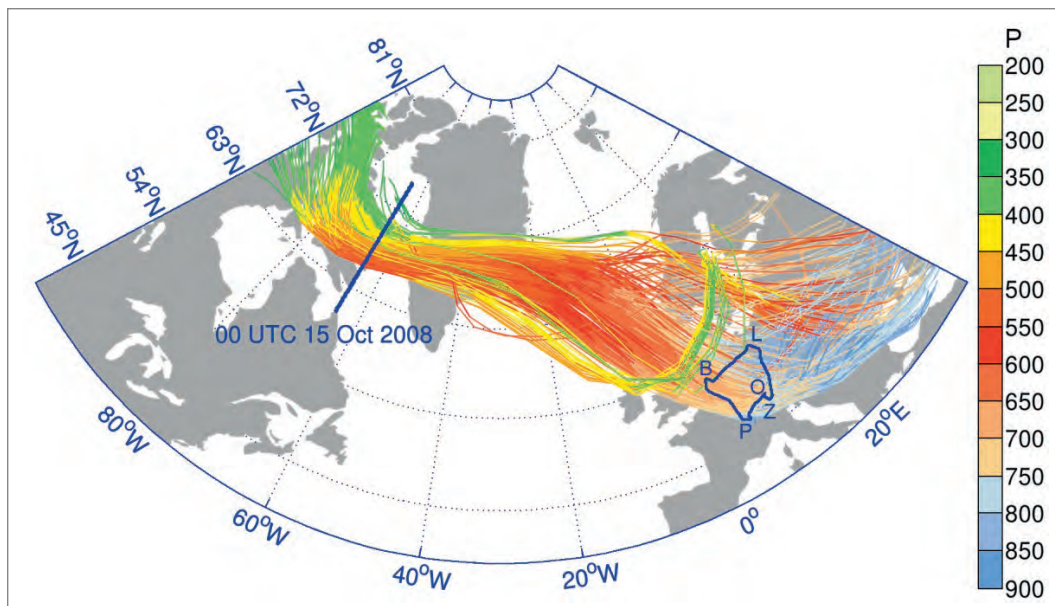


Fig. 5: Stratospheric Intrusion in October 2008 visualized with five-day LAGRANTO forward trajectories (Trickl et al., 2016): The dry layer started to emerge from the Stratosphere over Baffin Island as verified by a cross section along the blue line and to reach Central Europe on October 17 where air-borne and ground-based observations took place (blue curve). The flight passed over Payerne (P), Bilthoven (B), Lindenberg (L) and Mt. Zugspitze (Z).

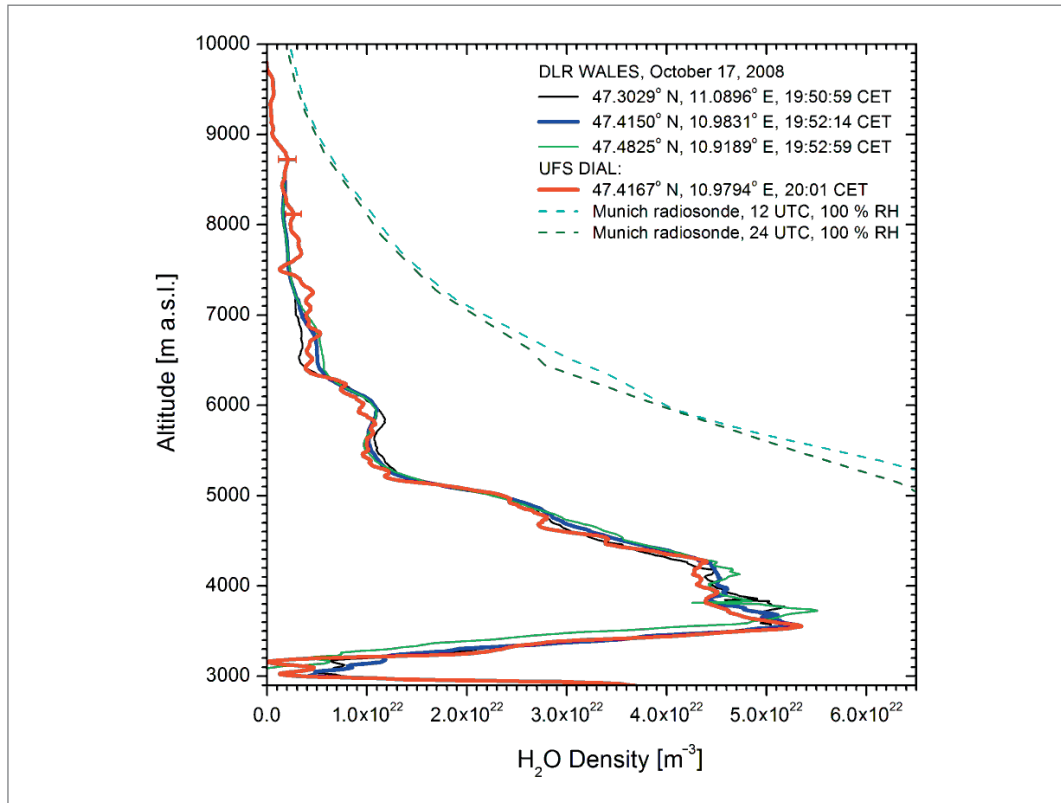


Fig. 6: Comparison of the UFS and WALES DIAL systems during LUAMI (Trickl et al., 2016); three WALES profiles are shown obtained during the approach (black), the passage over the Zugspitze summit (blue) and after the passage (green). The agreement was best for the best co-incidence.

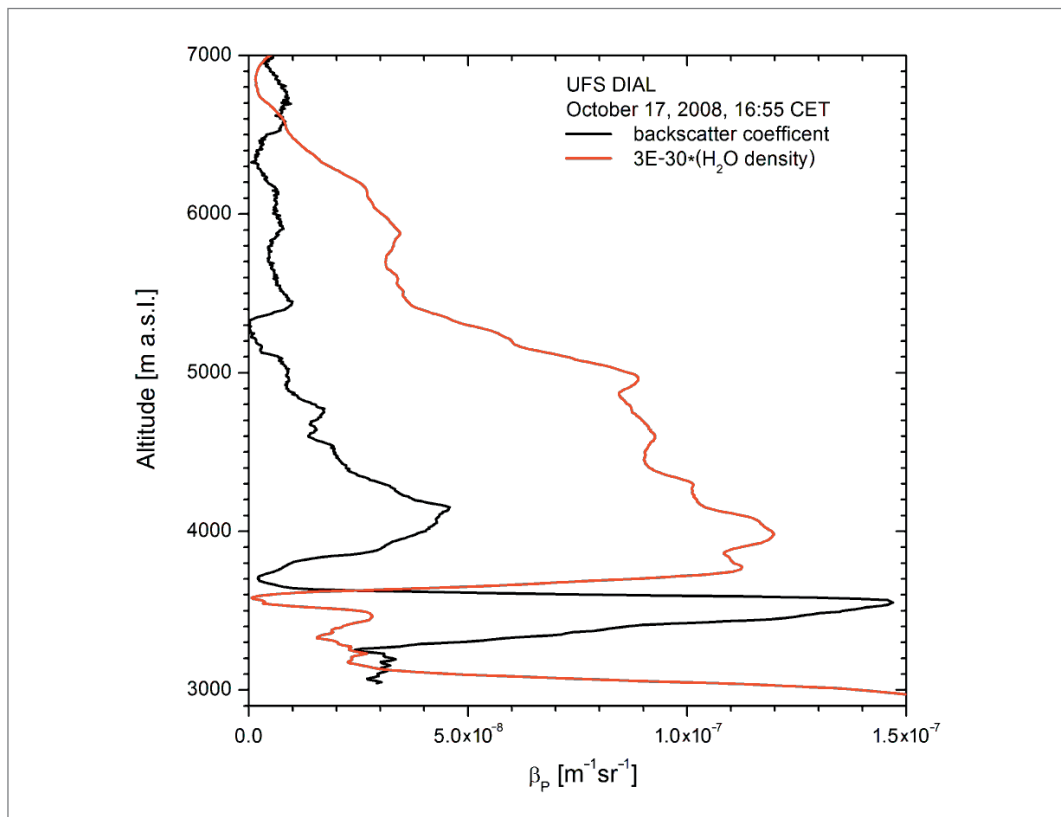


Fig. 7: Water vapour and 817-nm aerosol profile from the LUAMI measurements at UFS on October 17, 2008, showing volcanic particles descending in the stratospheric intrusion layer after the Okmok and Kasatochi eruptions in 2008 (Trickl et al., 2016)

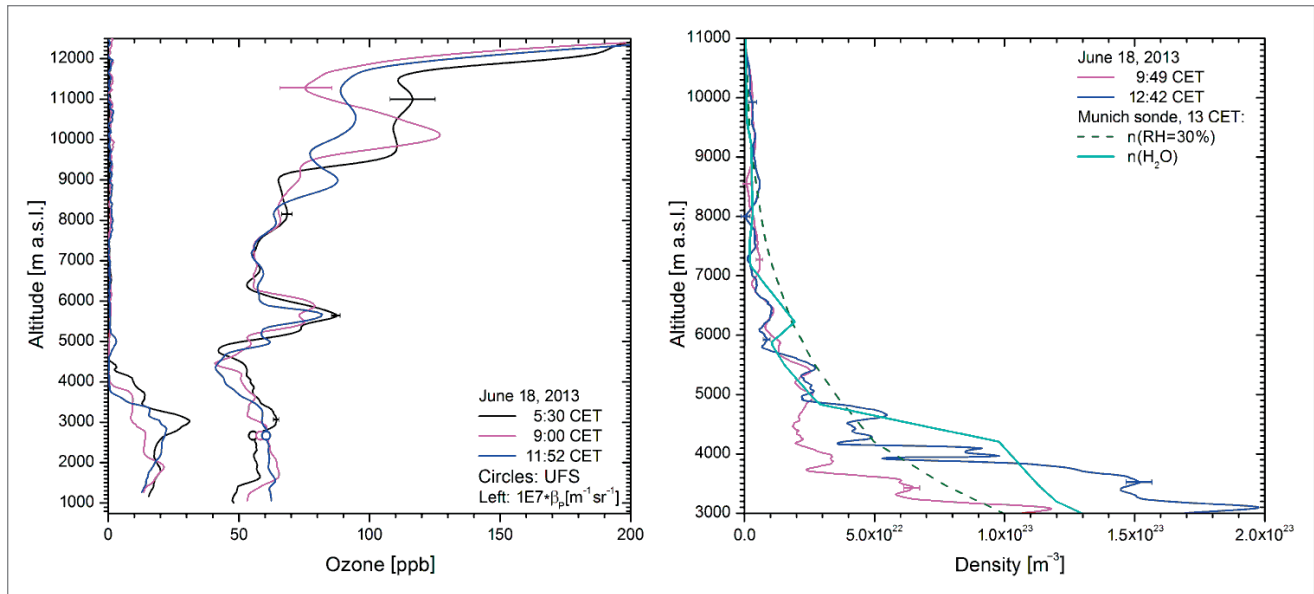


Fig. 8: Stratospheric intrusion on June 18, 2013, arriving over Garmisch-Partenkirchen at about 5.7 km a.s.l. ahead of a cold front also advecting rising dust-loaded air from the Sahara desert (left panel: ozone and aerosol backscatter coefficient; see Fig. 9); the UFS DIAL confirmed dry conditions to just below 6 km (right panel). Densities n from the Munich radiosonde are given for comparison.

At all four stations the H_2O mixing ratio was 100 ppm and less which is typical of the range just above the tropopause where fully stratospheric conditions with 5 ppm are not yet reached. It is interesting to note that the lowest mixing ratios (35 ppm and less) were registered at the south side of the layer, over Garmisch-Partenkirchen and Payerne. The comparison between the UFS DIAL and WALES is shown in Fig. 6 and demonstrates the excellent performance of both systems. The peak ozone mixing ratio was 70 ppb (not shown).

Over the entire observational area the intrusion layer also contained particles (see Fig. 7 for UFS). The particles are ascribed to the violent eruptions of the volcanoes Okmok and Kasatochi that reached the stratosphere (Trickl et al., 2013). Particles in intrusion layers were observed after all major mid-latitude eruptions since 2007. Downward transport in tropopause fold has been regarded as an important removal mechanism for stratospheric aerosol. In fact, aerosol from eruptions at middle and high latitudes, where tropopause folds maximize, is typically removed from the stratosphere with less than one year (Trickl et al., 2013).

Finally, we give an example of an intrusion with prefrontal arrival over Garmisch-Partenkirchen (Fig. 8) after merging with air from North Africa. The intrusion layer was centred at 5.7 km and featured peak ozone mix-

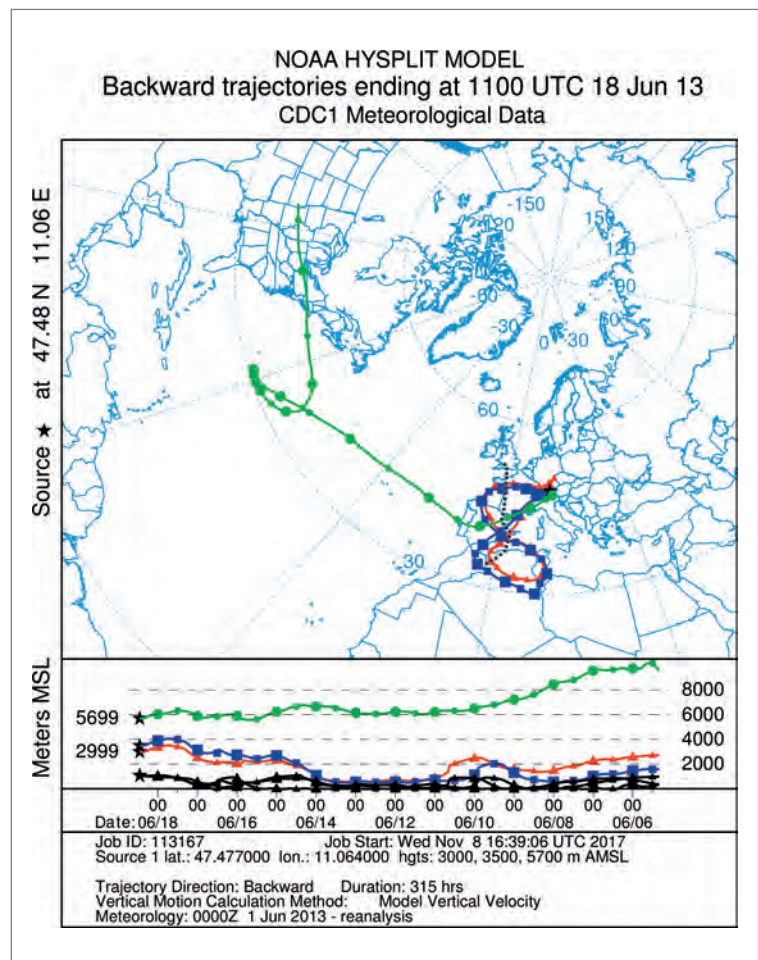


Fig. 9: HYSPLIT backward trajectories initiated above Garmisch-Partenkirchen at two altitudes within the aerosol layer (red and blue), passing over the central Sahara at low altitude, and at the centre of the intrusion layer (green). The dotted black line indicates the arriving cold front on June 18, 2013, 13 CET.

ing ratios of the order of 85 ppb. The minimum relative humidity was below 10% (right panel of Fig. 8), but did not reach the low values of the examples shown above, which indicates the occurrence of mixing during the long travel from the stratosphere over the northern U.S. to Garmisch-Partenkirchen as verified with 315-h HYSPLIT backward trajectories (<http://ready.arl.noaa.gov/HYSPLIT.php>). One example with a start altitude of about 10 km is shown in Fig. 9. Directly below the intrusion layer Saharan dust arrived above out site (left panel of Fig. 8; Fig. 9). The dust originated in the central Sahara. Obviously, the intrusion layer travelled faster than the cold front (dotted line in Fig. 9) and passed over it at an altitude of about 6 km. Since 2007 we have observed about 70 cases of simultaneous STT and Saharan dust.

21.5.2 Statistical Analyses of the STT Observations

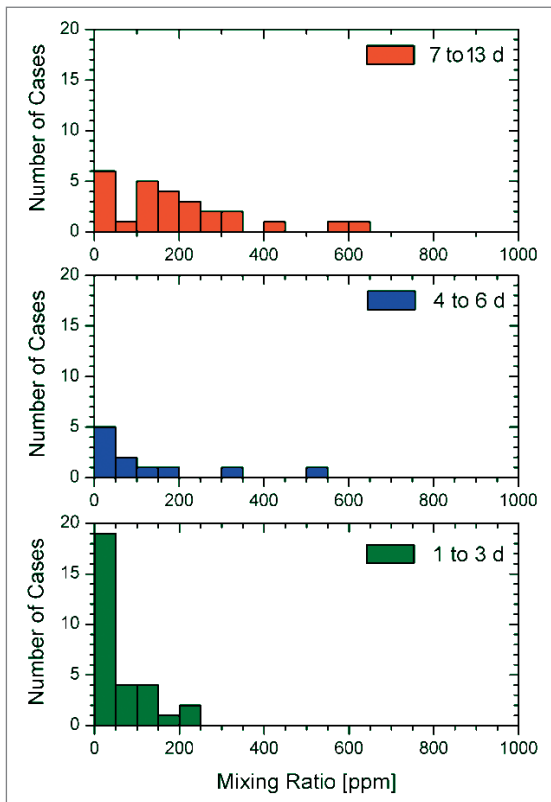


Fig. 10: Distribution of minimum water-vapour mixing ratio in deep stratospheric intrusion layers (reaching altitudes below roughly 4 km) for three different transport time ranges extracted from a total of more than 70 cases examined with the UFS DIAL

The observations have made possible rather fundamental statistical assessments for STT. The first one was based on the water vapour soundings at UFS alone. It was stimulated by the extremely low H_2O densities we found in intrusion layers already in the early phase of the measurements and documented in the previous section. By analysing more than 70 deep intrusions (to about 4 km and less) we found a clear general confirmation of this behaviour (Trickl et al., 2014). In Fig. 10, we show the distribution of the minimum water-vapour mixing ratio as a function of travel time downward from the tropopause estimated from ETH and HYSPLIT trajectory calculations. For subsidence times of three days less than 50 ppm and less were observed for 63% of the cases. The distribution widens for longer travel times, but unperturbed layers do exist even for the longest travel times (13 days for HYSPLIT). In one case negligible humidity was found in an intrusion layer even after more than 15 days of descent (Trickl et al., 2015, see Sec. 5.4).

These findings contradict the frequently read idea of quick erosion of the stratospheric nature of these descending stratospheric layers. Very likely, free-tropospheric mixing in atmospheric models is considerably overestimated and the corresponding parametrization must be revised accordingly. In Eulerian models, in addition, the problem of numerical diffusion exists which is caused by the finite grid size of the models (Roelofs et al., 2003; Eastham and Jacob, 2017).

The second great surprise was the very high number of days with observations of STT. Based on the large data set from the ozone DIAL, on the humidity measurements of the UFS H_2O DIAL, as well as of nearby radiosonde routine ascents we derived the seasonal cycle for 2007–2016 shown in Fig. 12

(Trickl et al., 2020a). The analysis with observational data were assisted by extensive trajectory calculations. Intrusions were observed on up to 94% of the monthly measurements days (annual average: 84%). This is substantially more than estimated in the assessment by Beekmann et al. (1997), but in some agreement with the recent study of Granados-Muñoz and Leblanc (2017) for California, at least in winter.

Our fractions maximize in summer whereas at the Alpine summit level a summer minimum is seen. In Fig. 12 both the analysis for the Zugspitze in-situ measurements (Trickl et al., 2010) and the cruder results from the lidar measurements for 3 km a.s.l. are shown.

An important question is: How much has the increase of STT contributed to the drying of the free troposphere reported by Paltridge et al. (2009)? The negative trend for water vapour during the past forty years would contradict expectations for the atmospheric warming.

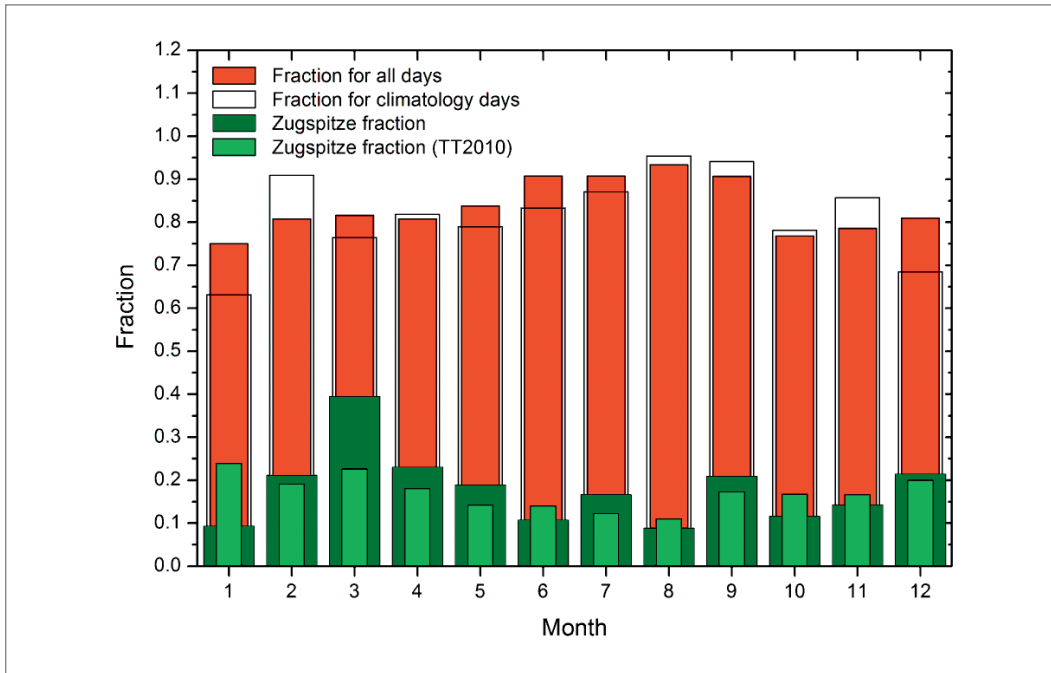


Fig. 11: Fractions of days with STT observations for the ozone DIAL measurements between 2007 and 2016

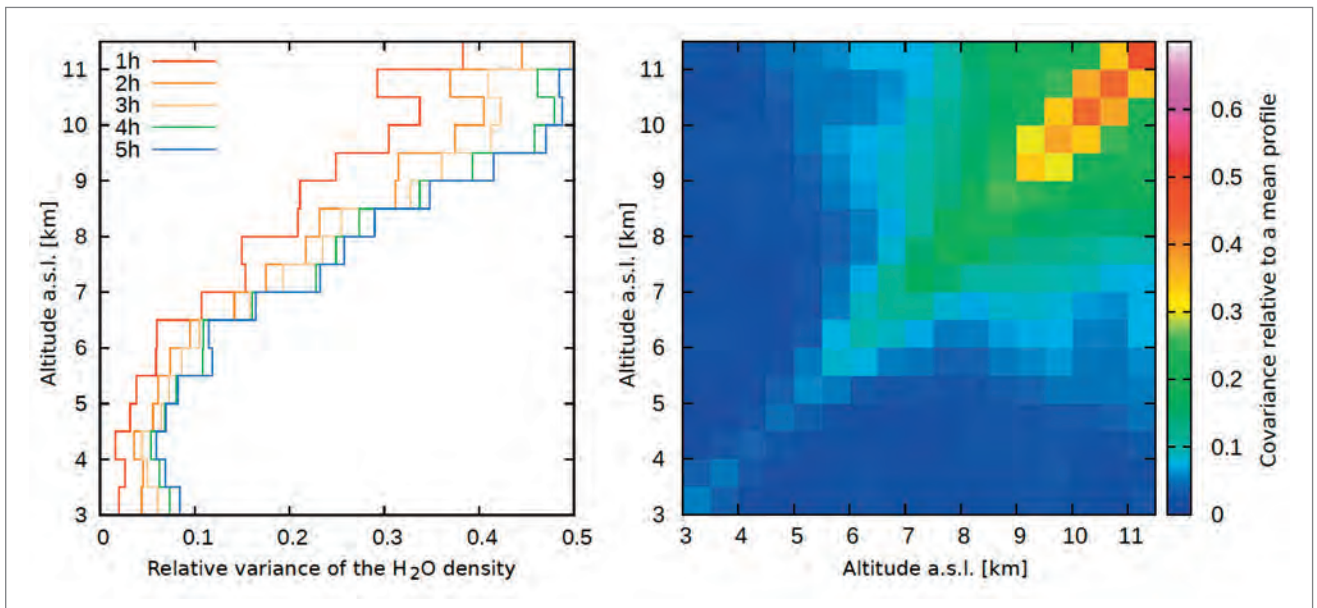


Fig. 12: The short-term variability of the vertical water-vapour profile is illustrated by the plot of the relative variance as a function of altitude within different time intervals (left plot). The covariance matrix (right plot) gives an idea of the interconnectivity of the variation between different altitudes.

21.5.3 Trans-Atlantic Transport

During the observational period most pronounced elevated-ozone features in the middle and upper troposphere were mainly related to the presence of strongly descending very dry air. However, a few clear examples of trans-Atlantic transport of high levels of ozone as during the observational period between 1996 and 2003 (e. g., Trickl et al., 2003) have been identified (Trickl et al., 2020a), but have been rare in recent years. The low occurrence of ozone peaks from across the Atlantic suggests an improved air quality over North America with respect to the 1990s.

21.5.4 Fire Plumes

Aerosol and ozone observations in the presence of fire plumes have been quite frequently made. The most important source regions have been the U.S., Canada, but occasionally also Europe, in particular Ukraine where almost persistently peat fires burn. The most spectacular period was July 2013 when smoke from a “road of fire” from Alaska to eastern Canada passed over Central Europe for several weeks (Trickl et al., 2015). On each day the combined lidar measurements, together with sonde data, revealed aerosol transport in stratospheric intrusion layers that descended from the remote west. The most interesting day was July 16, when a very thin but horizontally opaque layer hit the Zugspitze summit and, in part, UFS. This layer was extremely dry (< 25 ppm) despite subsiding from Siberia in as many as fifteen days, picking up soot-loaded air from a pyro-cumulonimbus (e.g., Fromm et al., 2010) event in eastern Canada.

In August 2017 strong pyro-cumulonimbus activity was reported for British Columbia (Baars et al., 2019). The plume from this event yielded the strongest stratospheric signature related to fires in our entire measurement series since 1976. The top of these aerosols gradually ascended to about 20 km.

21.5.5 Variability

The vertical distribution of tropospheric trace gases is subject to rapid change due to different layers advected from different source regions, sometimes at time scales of less than one hour. The resulting variability is particularly pronounced for water vapour. Our lidar measurements have revealed changes of integrated free-tropospheric water vapour by a factor of more than thirty and by far more than hundred. The extremes vary from very dry air from the upper troposphere and lower stratosphere and humid air from the tropical oceans.

The variability of free-tropospheric water vapour and its time scales was studied in great detail (Vogelmann et al., 2011; 2015). Fig. 12 shows in its left panel the variability (relative variance) of the vertical water vapour distribution from the UFS DIAL on time scales of 1 to 5 h. For the shortest time interval of this investigation (1 h), the relative variance starts with a value of as low as 0.02. Above 5 km, the variance continuously increases to more than 0.38 at an altitude of about 11 km a.s.l. This is the range where long-range transport maximizes, in particular STT. Due to the increasing wind speed in the upper troposphere (up to more than 100 m s^{-1} ; Riehl, 1962) layers from different source regions follow one another more rapidly.

For longer time intervals up to 5 h, the relative variance behaves quite similarly, but is shifted to higher values at all altitudes. In comparison to the 1 h profile, we see a more significant maximum at the lower edge at 3 km and a significant minimum at 4.5 km for longer time intervals. This enhanced increase between 3 and 4 km is, to our understanding, induced by the diurnally varying upper edge of the boundary layer during the warm season (Carnuth et al., 2002).

In the right panel of Fig. 12 we show the covariance matrix, calculated from all normalized profiles recorded from 2007 to 2011. There are no significant off-diagonal values below 6 km, which indicates absence of a coherent air flow in this range. This means that the horizontal flow at certain altitudes below 6 km is not or only weakly coupled to the flow above or below. The increase of off-diagonal values between 6 and 8 km indicates a partially coherent flow. The high off-diagonal values above 8 km indicate a large fraction of coherent flow of inhomogeneous air masses in this altitude region.

21.5.6 Water-Vapour Transport in the Lower Stratosphere

During the past few years the high-power Raman lidar at UFS system has been tested and optimized (Klanner et al., 2021). The system has been successfully validated up to 20 km in February 2019 with balloon-borne frost-point hygrometers of Forschungszentrum Jülich. In addition, a temperature retrieval yielded accurate temperature data up to almost 90 km as verified by sonde, NCEP, satellite and the mesospheric OH fluorescence measurements at UFS by DLR (Schmidt et al., 2013) from the same night.

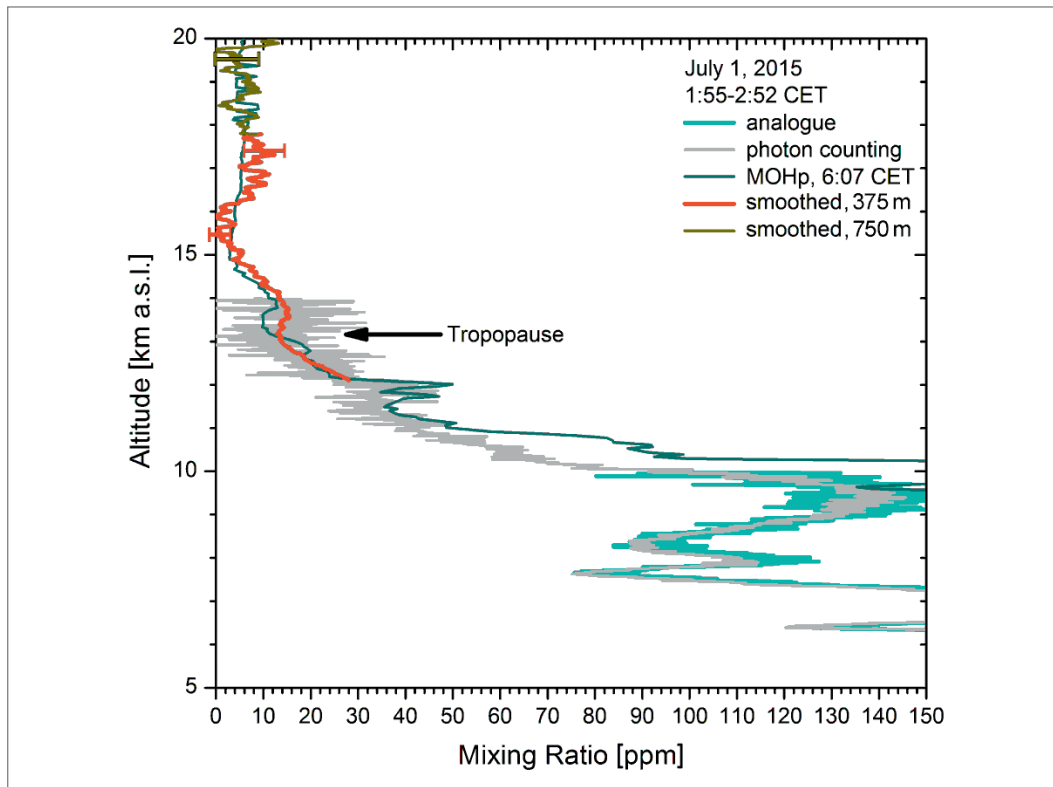


Fig. 13: Water-vapour profile obtained with the UFS Raman lidar system during the night hours on early July 1, 2015 showing very dry conditions above 6.3 km; the exceptional dryness between 15 and 16.3 km (1–2 ppm) is ascribed to the advection of air from the Caribbean Sea at high altitude, which indicates potential freeze-drying. The red and green curves were generated by sliding arithmetic averages corresponding to vertical resolutions of 375 m and 750 m, respectively. For comparison, the mixing ratio calculated from the data of the morning sonde ascent above the Meteorological Observatory Hohenpeißenberg (MOHp) is included

In Fig. 13 we show the water-vapour mixing ratio calculated by dividing the direct H_2O Raman vibrational backscatter signal at 347 nm by the nitrogen vibrational Raman backscatter signal. This measurement was the first demonstrating a range up to 20 km, but somewhat suffered at the highest altitudes from not perfect shielding background radiation from the full moon, which was greatly improved during the following years (Klanner et al., 2021). The mixing ratio was calibrated by comparison with that calculated from the midnight sonde data at Oberschleißheim (“Munich” sonde, 100 km roughly to the north) and the morning sonde launched at Hohenpeißenberg (about 40 km to the north) in the range around 5 km where the two sonde profiles agree best (around 3000 ppm). The mutual agreement of the three instruments at many altitudes is terrible, with local discrepancies of more than a factor of two. This reflects the strong inhomogeneity of the water vapour distribution in space and time that strongly suggests to apply the DIAL measurements at UFS for the calibration in the future. The Hohenpeißenberg humidity agrees best with that from the lidar in the tropopause region and was, therefore, included in Fig. 13.

What makes this measurement special is the very low mixing ratio of 2 ppm or less between 15.0 and 16.3 km, which is much less than the typical free-stratospheric values of about 5 ppm (e.g., Zahn et al., 2014). This humidity drop is confirmed by the Hohenpeißenberg sonde, which, nevertheless, becomes unreliable above the dry layer. Most importantly, HYSPLIT backward trajectories reveal high-altitude transport from the Caribbean Sea to our site just around 15.5 km. In the tropics convectively lifted moist air has been found to freeze-dry due to the very cold tropopause temperatures (e.g., Schiller et al., 2009).

We are also looking for elevated humidity due to prefrontal upward transport in warm conveyor belts entering the stratosphere in middle and high latitudes (Stohl, 2001). This could be a source of lower-stratospheric water vapour not discussed too frequently so far.

21.6 Conclusions

The routine DIAL measurements of ozone, water vapour and aerosol carried out at IFU and UFS since 2007 have yielded a rich data set that yields information on the impact of atmospheric transport. So far we have fully concentrated on a complete compilation of STT, fire and Saharan dust cases. But also signatures of anthropogenic air pollution from North America or Asian dust have been occasionally identified. A special event was the observation of the Eyjafjallajökull volcanic eruption plume in 2010 (Trickl et al., 2013).

STT is a particularly rewarding target for lidar work because of its high contrast in the ozone and water-vapour profiles. Our work confirms the findings for the Alpine summit stations that STT is a much higher source of tropospheric ozone than assumed by the “photochemical lobby” in the past. In addition, STT at the Zugspitze summit has grown since the mid-seventies. It will be interesting to follow the further development of the ozone concentrations in the entire free troposphere in a changing climate.

The results clearly demonstrate that Eulerian models must be thoroughly improved in order to quantify atmospheric long-range transport and, thus, the chemical composition of the troposphere. This holds in particular for coarse-grid climate models that even miss thin atmospheric layers. A key topic is a substantial lowering of free-tropospheric mixing in models.

Acknowledgements

The authors thank H.P. Schmid for his support. They emphasise the valuable contributions of L. Ries, H.E. Scheel, W. Steinbrecht, M. Sprenger, A. Stohl, M. Wirth and the other co-authors of the publications cited. An important contribution to the technical developments was made by S. Biggel, H. Giehl and M. Perfahl. In particular, we acknowledge the great support by the UFS team. The system development has been funded by the Bavarian State Government under numerous contracts.

References

- Bethan, S., Vaughan, G., Gerbig, C., Volz-Thomas, A., Richer, H., and Tiddeman, D. A.: Chemical air mass differences near fronts, *J. Geophys. Res.*, 103, 13413–13434, 1998.
- Baars, H., Ansmann, A., Ohneiser, K., Haarig, M., Engelmann, R., Althausen, D., Hanssen, I., Gausa, M., Pietruczuk, A., Szkop, A., Stachlewska, I., Wang, D., Reichardt, J., Skupin, A., Mattis, I., Trickl, T., Vogelmann, H., Navas-Guzmán, F., Haefele, S., Acheson, K., Ruth, A.A., Tatarov, B., Müller, D., Hu, Q., Podvin, T., Goloub, P., Vesselovski, I., Pietras, C., Haeffelin, M., Fréville, P., Sicard, M., Comerón, A., Fernández García, A.J., Molero Menéndez, F., Córdoba-Jabonero, C., Guerrero-Rascado, J.L., Alados-Arboledas, L., Bortoli, D., Costa, M.J., Dionisi, D., Liberti, G., Wang, X., Sannino, A., Papagiannopoulos, N., Boselli, A., Mona, L., D’Amico, G., Romano, S., Perrone, M.R., Belegante, L., Nicolae, D., Grigorov, I., Gialitaki, A., Amiridis, V., Soupiona, O., Papayannis, A., Mamouri, R.-E., Nisantzi, A., Heese, B., Hofer, J., Schechner, Y.Y., Wandinger, U., and Pappalardo, G.: The unprecedented 2017–2018 stratospheric smoke event: Decay phase and aerosol properties observed with the EARLINET, *Atmos. Chem. Phys.*, 19, 15183–15198, 2019.
- Bey, I., Jacob, D.J., Logan, J.A., and Yantosca, R. M.: Asian chemical outflow to the Pacific in spring: Origins, pathways, and budgets, *J. Geophys.-Res.*, 106, 23091–23113, 2001.
- Cammas, J.-P., Jacoby-Koaly, S., Suhre, K., Rosset, R., and Marenco, A.: Atlantic subtropical potential vorticity barrier of Ozone by Airbus In-Service Aircraft (MOZAIC) flights, *J. Geophys. Res.*, 103, 25681–25693, 1998.
- Carnuth, W. and Trickl, T.: Transport studies with the IFU three-wavelength aerosol lidar during the VOTALP Mesolcina experiment, *Atmos. Environ.*, 34, 1425–1434, 2000.
- Carnuth, W., Kempfer, U., and Trickl, T.: Highlights of the Tropospheric Lidar Studies at IFU within the TOR Project, *Tellus B*, 54, 163–185, 2002.
- Cooper, O.R., Moody, J.L., Parrish, D.D., Trainer, M., T.B. Ryerson, T.B., Holloway, J.S., Hübler, G., Fehsenfeld, F.C., and Evans, M. J.: Trace gas composition of midlatitude cyclones over the western North Atlantic Ocean: A conceptual model, *J. Geophys. Res.*, 107, 4056, doi: 10.1029/2001JD000901, 13 pp., 2002.

- Cooper, O.R., Stohl, A., Hübler, G., Hsie, E.Y., Parrish, D.D., Tuck, A.F., Kiladis, G.N., Oltmans, S.J., Johnson, B.J., Shapiro, M., Moody, J.L., and Lefohn, A. S.: Direct transport of midlatitude stratospheric ozone into the lower troposphere and marine boundary layer of the tropical Pacific Ocean, *J. Geophys. Res.*, 110, D23310, doi: 10.1029/JD005783, 15 pp., 2005.
- Danielsen, E. F.: Stratospheric-Tropospheric Exchange Based on Radioactivity, Ozone and Potential Vorticity, *J. Atmos. Sci.*, 25, 505–518, 1968.
- Danielsen, E. F., and Mohnen, V. A.: Project Dustorm Report: Ozone Transport, in Situ Measurements, and Meteorological Analyses of Tropopause Folding, *J. Geophys. Res.*, 82, 5867–5877, 1977
- Ding, J., Miyazaki, K., van der A, R.J., Mijling, B., Kurokawa, J., Cho, S.Y., Janssens-Maenhout, G. Zhang, Q., Liu, F., and Levelt, P. F.: Intercomparison of NO_x emission inventories over East Asia, *Atmos. Chem. Phys.*, 17, 10125–10141, 2017.
- Dickerson, R.R., Huffman, G.J., Luke, W.T., Nunnermacker, L.J., Pickering, K.E., Leslie, A.C. D., Lindsay, C.G., Slinn, W.G. N., Kelly, T.J., Daum, P.H., Delany, A.C., Greenberg, J.P., Zimmerman, P.R., Boatman, J.F., Ray, J.D., and Stedman, D. H.: Thunderstorms: An Important Mechanism in the Transport of Air Pollutants, *Science*, 235, 460–465, 1987.
- Eastham, S.D., and Jacob, D. J.: Limits on the ability of global Eulerian models to resolve intercontinental transport of chemical plumes, *Atmos. Chem. Phys.*, 17, 2543–2553, 2017.
- Eisele, H., and Trickl, T.: Improvements of the aerosol algorithm in ozone-lidar data processing by use of evolutionary strategies, *Appl. Opt.*, 44, 2638–2651, 2005.
- Eisele, H., Scheel, H.E., Sladkovic, R., and Trickl, T.: High-resolution Lidar Measurements of Stratosphere-troposphere Exchange, *J. Atmos. Sci.*, 56, 319–330, 1999.
- Fehsenfeld, F.C., Daum, P., Leatch, W.R., Trainer, M., Parrish, D. D., and Hübler, G.: Transport and processing of O₃ and O₃ precursors over the North Atlantic: An overview of the 1993 North Atlantic Regional Experiment (NARE) summer intensive, *J. Geophys. Res.*, 101, 28877–28891, 1996.
- Fromm, M., Lindsey, D.T., Servranckx, R., Yue, G., Trickl, T., Sica, R., Doucet, P., and Godin-Beekmann, S.: The Untold Story of Pyrocumulonimbus, *Bull. Am. Meteorol. Soc.*, 91, 1193–1209, 2010.
- Furger, M., Dommen, J., Graber, W.K., Pionngio, L., Prévôt, A., Emeis, S., Grell, G., Trickl, T., Gomiscek, B., Neininger, B. and Wotawa, G.: The VOTALP Mesolcina Valley Campaign 1996-concept, background and some highlights, *Atmos. Environ.*, 34, 1395–1412, 2000.
- Gaudel, A., Cooper, O.R., Ancellet, G., Barret, B., Boynard, A., Burrows, J.P., Clerbaux, C., Coheur, P.-F., Cuesta, J., Cuevas, E., Doniki, S., Dufour, G., Ebojje, F., Foret, G., Garcia, O., Granados-Muñoz, M.J., Hannigan, J., Hase, F., Hassler, B., Huang, G., Hurtmans, D., Jaffe, D., Jones, N., Kalabokas, P., Kerridge, B., Kulawik, S., Latter, B., Leblanc, T., Le Flochmoën, E., Lin, W., Liu, J., Liu, X., Mahieu, E., McClure-Begley, A., Neu, J., Osman, M., Palm, M., Petetin, H., Petropavlovskikh, I., Querel, R., Raupoe, N., Rozanov, A., Schultz, M. G., Schwab, J., Siddans, R., Smale, D., Steinbacher, M., Tanimoto, H., Tarasick, D., Thouret, V., Thompson, A.M., Trickl, T., Weatherhead, E., Wespes, C., Worden, H., Vigouroux, C., Xu, X., Zeng, G., and Ziemke, J.: Tropospheric Ozone Assessment Report: Present-day distribution and trends of tropospheric ozone relevant to climate and global atmospheric chemistry model evaluation, *Elem. Sci. Anth.*, 6, 39, DOI: <https://doi.org/10.1525/elementa.291>, 58 pp., 2018; 21-pp. supplement
- Gouget, H., Cammas, J.-P., Marenco, A., Rosset, R., and Jonquière, I.: Ozone peaks associated with a subtropical tropopause fold and with the trade wind inversion: A case study from the airborne campaign TROPOZ II over the Caribbean in winter, *J. Geophys. Res.*, 101, 25979–25993, 1996.
- Granados-Muñoz, M. J., and Leblanc, T.: Tropospheric ozone seasonal and long-term variability as seen by lidar and surface measurements at the JPL-Table Mountain Facility, California, *Atmos. Chem. Phys.*, 16, 9299–9319, 2016.
- Hannan, J.R., Fuelberg, H.E., Crawford, J.H., Sachse, G.W., and Blake, D. R.: Role of wave cyclones in transporting boundary layer air to the free troposphere during the spring 2001 NASA/TRACE-P experiment, *J. Geophys. Res.*, 108, 8785, doi: 10.1029/2002JD003105, 17 pp., 2003.
- Höveler, K., Klanner, L., Trickl, T., and Vogelmann, H.: The Zugspitze Raman Lidar: System Testing, 27th International Laser Radar Conference, New York City (U.S.A.), July 5 to 10, 2015, B. Gross, F. Moshairy, M. Arend, Eds., EPJ Web of Conferences, 199, 21004, DOI: 10.1051/epjconf/201611905008, http://www.epj-conferences.org/articles/epjconf/pdf/2016/14/epjconf_ilrc2016_05008.pdf, 4 pp., 2016.
- Holton, J.R., Douglass, A.R., Haynes, P.H., McIntyre, M.E., Rood, R.B., and Pfister, L.: Stratosphere-troposphere exchange, *Rev. Geophys.*, 33, 403–439, 1996.
- HTAP (2010), Hemispheric Transport of Air Pollution, Part A: Ozone and Particulate Matter, F. Dentener, T. Keating and H. Akimoto, Eds., United Nations (New York, Geneva), 278 pp., ISSN 1014-4625, ISBN 978-92-1-117043-6, http://www.htap.org/publications/2010_report/2010_Final_Report/HTAP%202010%20Part%20A%20110407.pdf
- Jaffe, D., Anderson, T., Covert, D., Kotchenruther, R., Trost, B., Danielson, J., Simpson, W., Berntsen, T., Karlsdottir, S., Blake, D., Harris, J., Carmichael, G., and Uno, I.: Transport of Asian Air Pollution to North America, *Geophys. Res. Lett.*, 26, 711–714, 1999.
- Jonson, J.E., Simpson, D., Fagerli, H., and Solberg, S.: Can we explain the trends in European ozone levels? *Atmos. Chem. Phys.*, 6, 51–66, 2006.

- Kempfer, U., Carnuth, W., Lotz, R., and Trickl, T.: A Wide-range UV Lidar System for Tropospheric Ozone Measurements: Development and Application, *Rev. Sci. Instrum.*, **65**, 3145–3164, 1994.
- Klanner, L., Höveler, K., Khordakova, D., Perfahl, M., Rolf, C., Trickl, T., and Vogelmann, H.: A powerful lidar system capable of one-hour measurements of water vapour in the troposphere and the lower stratosphere as well as the temperature in the upper stratosphere and mesosphere, *Atmos. Meas. Tech.*, **14**, 531–555, 2021.
- Lamarque, J.-F., Langford, A. O., and Proffitt, M. H.: Cross-tropopause mixing of ozone through gravity wave breaking: Observation and modeling, *J. Geophys. Res.*, **101**, 22969–22976, 1996.
- Langford, A. O., Stratosphere-troposphere exchange at the subtropical jet, contribution to the tropospheric ozone budget at midlatitudes, *Geophys. Res. Lett.*, **26**, 2449–2452, 1999.
- Lelieveld, J. and Crutzen, P. J.: Role of Deep Cloud Convection in the Ozone Budget of the Troposphere, *Science*, **264**, 1759–1761, 1994.
- Liu, H., Jacob, D. J., Bey, I., Yantosca, R. M., Duncan, B. N.: Transport pathways for Asian outflow over the Pacific: Interannual and seasonal variations, *J. Geophys. Res.*, **108**, 8786, doi: 10.1029/2002JD003102, 18 pp., 2003
- Logan, J. A., Staehelin, J., Megretskaia, I. A., Cammas, J.-P., Thouret, V., Claude, H., De Backer, H., Steinbacher, M., Scheel, H.-E., Stübi, R., Fröhlich, M., and Derwent, R.: Changes in ozone over Europe: Analysis of ozone measurements from sondes, regular aircraft (MOZAIC) and alpine surface sites, *J. Geophys. Res.*, **117**, D09301, doi: 10.1029/2011JD016952, 23 pp., 2012.
- Lin, M., Fiore, A. M., Horowitz, L. W., Langford, A. O., Oltmans, S. J., Tarasick, D., and Rieder, H. E.: Climate variability modulates western US ozone air quality in spring via deep stratospheric intrusions, *Nature Communications*, **6**:7105, doi: 10.1038/ncomms8105, 11 pp., 2015.
- Liu, S. C., Trainer, M., Fehsenfeld, F. C., Parrish, D. D., Williams, E. J., Fahey, D. W., Hübler, G., Murphy, P. C.: Ozone Production in the Rural Troposphere and the Implications for Regional and Global Ozone Distributions, *J. Geophys. Res.* **92**, 4191–4207, 1987.
- Y. Miyazaki, Y., Kondo, Y., Koike, M., Fuelberg, H. E., Kiley, C. M., Kita, K., Takegawa, N., Sachse, G. W., Flocke, F., Weinheimer, A. J., Singh, H. B., Eisele, F. L., Zondlo, M., Talbot, R. W., Sandholm, S. T., Avery, M. A., and Blake D. R.: Synoptic-scale transport of reactive nitrogen over the western Pacific in spring, *J. Geophys. Res.*, **108**, 8788, doi:10.1029/2002JD003248, 14 pp., 2003.
- Neu, J. L., Flury, T., Manney, G. L., Santee, M. L., Livesey, N. J., and Worden, J.: Tropospheric ozone variations governed by changes in stratospheric circulation, *Nature Geoscience*, **7**, 340–344, 2014.
- Nyeki, S., Kalberer, M., Kolbeck, I., De Wekker, S., Furger, M., Gäggeler, W., Kossmann M., Lugauer, M., Steyn, D., Weingartner, E., Wirth, M., and Baltensperger, U.: Convective Boundary Layer Evolution to 4 km asl over High-Alpine Terrain: Airborne Lidar Observations in the Alps, *Geophys. Res. Lett.*, **27**, 689–692, 2000.
- Oltmans, S. J., Lefohn, A. S., Shadwick, D., Harris, J. M., Scheel, H. E., Galbally, I., Tarasick, D. W., Johnson, B. J., Brunke, E.-G., Claude, H., Zeng, G., Nichol, S., Schmidlin, F., Davies, J., Cuevas, E., Redondas, A., Naoe, H., Nakano, T., and Kawasato, T.: Recent tropospheric ozone changes – A pattern dominated by slow or no growth, *Atmos. Environ.*, **67**, 331–351 (2012).
- Ott, L. E., Duncan, B. N., Thompson, A. M., Diskin, G., Fasnacht, Z., Langford, A. O., Lin, M., Molod, A. M., Nielsen, J. E., Pusede, S. E., Wargan, K., Weinheimer, A. J., and Yoshida, Y.: Frequency and impact of summertime stratospheric intrusions over Maryland during DISCOVER-AQ (2011): New evidence from NASA's GEOS-5 simulations, *J. Geophys. Res.*, **121**, 3687–3706, doi: 10.1002/2015JD024052, 2016.
- Paltridge, G., Arking, A., and Pook, M.: Trends in middle- and upper-level tropospheric humidity from NCEP reanalysis data, *Theor. Appl. Climatol.*, **98**, 351–359, 2009.
- Parrish, D. D., Ryerson, T. B., Holloway, J. S., Neuman, J. A., Roberts, J. M., Williams, J., Stroud, C. A., Frost, G. J., Trainer, M., Hübler, G., Flocke, F., and Weinheimer, A. J.: Fraction and composition of NO_y transported in air masses lofted from the North American continental boundary layer, *J. Geophys. Res.*, **109**, D09302, doi: 10.1029/2003JD004226, 18 pp., 2004.
- Parrish, D. D., Law, K. S., Staehelin, J., Derwent, R., Cooper, O. R., Tanimoto, H., Volz-Thomas, A., Gilge, S., Scheel, H.-E., Steinbacher, M., and Chan, E., Long-term changes in lower tropospheric baseline ozone concentrations at northern mid-latitudes, *Atmos. Chem. Phys.*, **12**, 11485–11504, 2012.
- Parrish, D. D., Derwent, R. G., Steinbrecht, W., Stübi, R., Van Malderen, R., Steinbacher, M., Trickl, T., Ries, L., and Xu, X.: Zonal Similarity of Long-term Changes and Seasonal Cycles of Baseline Ozone at Northern Mid-latitudes, *J. Geophys. Res.*, **125**, e2019JD031908, <https://doi.org/10.1029/2019JD031908>, 19 pp., 2020.
- Penkett, S. A., Reeves, C. E., Bandy, B. J., Kent, J. M., and Richer, H. R.: Comparison of calculated and measured peroxide data collected in marine air to investigate prominent features of the annual cycle of ozone in the troposphere, *J. Geophys. Res.*, **101**, 13377–13388, 1998.
- Price, J. D., and Vaughan, G.: The potential for stratosphere-troposphere exchange in cut-off-low systems, *Q. J. R. Meteorol. Soc.*, **119**, 343–365, 1993.
- Reiter, R.: The ozone trend in the layer of 2 to 3 km a.s.l. since 1978 and the typical time variations of the ozone profile between ground and 3 km a.s.l., *Meteor. Atmos. Phys.*, **42**, 91–104, 1990.

- Reiter, R., and Carnuth, W.: Comparing Lidar Reflectivity Profiles Against Measured Profiles of Vertical Aerosol Distribution between 1 and 3 km a.s.l., *Arch. Met. Geophys. Biocl. A*, 24, 69–92, 1975.
- Reiter, R., Pözl, K., and Sladkovic, R.: Determination of the Concentration of Chemical Main and Trace Elements (Chemical Matrix) in the Aerosol from 1972 to 1982 at a North-Alpine Pure Air Station at 1780 m a.s.l., Part II: Parametric Correlation Analysis of the Chemical Matrix with Consideration of Meteorological Quantities, *Arch. Met. Geophys. Biocl. B*, 35, 1–30, 1984.
- Riehl, H.: Jet Streams of the Atmosphere, Tech. Rep. 32, Department of Atmospheric Science Colorado State University Fort Collins, Colorado, 1962.
- Roelofs, G. J., Kentarchos, A. S., Trickl, T., Stohl, A., Collins, W. J., Crowther, R. A., Hauglustaine, D., Klonecki, A., Law, K. S., Lawrence, M. G., von Kuhlmann, R., and van Weele, M.: Intercomparison of tropospheric ozone models: Ozone transport in a complex tropopause folding event, *J. Geophys. Res.* 108, 8529, doi:10.1029/2003JD003462, *STA* 14, 13 pp., 2003.
- Scheel, H. E.: Ozone Climatology Studies for the Zugspitze and Neighbouring Sites in the German Alps, pp. 134–139 in: *Tropospheric Ozone Research 2, EUROTRAC-2 Subproject Final Report*, A. Lindskog, Co-ordinator, EUROTRAC International Scientific Secretariat (München, Germany, 2003); available at <http://www.trickl.de/scheel.pdf>.
- Schiller, C., Groß, J.-U., Konopka, P., Plöger, F., Silva dos Santos, F. H., and Spelten, N.: *Atmos. Chem. Phys.*, 9, 9647–9660, 2009.
- Schmidt, C., Höppner, K., and Bittner, M.: A ground-based spectrometer equipped with an InGaAs array for routine observations of OH(3-1) rotational temperatures in the mesopause region, *J. Atmos. Sol.-Terr. Ph.*, 102, 125–139, 2013.
- Škerlak, B., Sprenger, M., and Wernli, H.: A global climatology of stratosphere-troposphere exchange using the ERA-Interim data set from 1979 to 2011, *Atmos. Chem. Phys.*, 14, 913–937, 2014.
- Simon, H., Reff, A., Wells, B., Xing, J., and Frank, N.: Ozone Trends Across the United States over a Period of Decreasing NO_x and VOC Emissions, *Environ. Sci. Technol.*, 49, 186–195, 2015.
- Sprenger, M., Croci Maspoli, M., and Wernli, H.: Tropopause folds and cross-tropopause exchange: A global investigation based upon ECMWF analyses for the time period March 2000 to February 2001, *J. Geophys. Res.*, 108, 8518, doi: 10.1029/2002JD002587, *STA* 3, 11 pp., 2003.
- Stohl, A.: A 1-year Lagrangian “climatology” of airstreams in the Northern Hemisphere and lowermost stratosphere, *J. Geophys. Res.*, 106, 7263–7279, 2001.
- Stohl, A., and Trickl, T.: A textbook example of long-range transport: Simultaneous observation of ozone maxima of stratospheric and North American origin in the free troposphere over Europe, *J. Geophys. Res.*, 104, 30445–30462, 1999.
- Stohl, A., Bonasoni, P., Cristofanelli, P., Collins, W., Feichter, J., Frank, A., Forster, C., Gerasopoulos, E., Gäggeler, H., James, P., Kentarchos, T., Kromp-Kolb, H., Krüger, B., Land, C., Meloen, J., Papayannis, A., Priller, A., Seibert, P., Sprenger, M., Roelofs, G. J., Scheel, H. E., Schnabel, C., Siegmund, P., Tobler, L., Trickl, T., Wernli, H., Wirth, V., Zanis, P., and Zerefos, C.: Stratosphere-troposphere exchange – a review, and what we have learned from STACCATO, *J. Geophys. Res.*, 108, 8516, doi:10.1029/2002JD002490, *STA* 1, 15 pp, 2003.
- Tarasick, D., Galbally, I. e., Cooper, O. R., Schultz, M. G., Ancellet, G., Leblanc, T., Wallington, T. J., Ziemke, J., Liu, X., Steinbacher, M., Staehelin, J., Vigouroux, C., Hannigan, J., García, O., Foret, G., Zanis, P., Weatherhead, E., Petropavlovskikh, I., Worden, H., Osman, M., Liu, J., Chang, K.-L., Gaudel, A., Lin, M., Granados-Muñoz, M., Thompson, A. M., Oltmans, S. J., Cuesta, J., Dufour, G., Thouret, V., Hassler, B., Trickl, T., and Neu, J. L.: Tropospheric Ozone Assessment Report: Tropospheric ozone from 1877 to 2016, observed levels, trends and uncertainties, *Elem. Sci. Anth.*, 7, Article 39, DOI: <https://doi.org/10.1525/elementa.376>, 72 pp., 2019; 56 pp. supplemental material
- Trickl, T.: Tropospheric trace-gas measurements with the differential-absorption lidar technique, pp. 87–147 in: *Recent Advances in Atmospheric Lidars*, L. Fiorani, V. Mitev, Eds., INOE Publishing House, Bucharest (Romania), Series on Optoelectronic Materials and Devices, Vol. 7, version: <http://www.trickl.de/DIAL.pdf>, 2010.
- Trickl, T., Cooper, O. C., Eisele, H., James, P., Mücke, R., and Stohl, A.: Intercontinental transport and its influence on the ozone concentrations over central Europe: Three case studies. *J. Geophys. Res.*, 108, 8530, doi:10.1029/2002JD002735, *STA* 15, 23 pp., 2003.
- Trickl, T., Feldmann, H., Kanter, H.-J., Scheel, H. E., Sprenger, M., Stohl, A., and Wernli, H.: Forecasted Deep Stratospheric Intrusions over Central Europe: Case Studies and Climatologies, *Atmos. Chem. Phys.*, 10, 499–524, 2010.
- Trickl, T., Eisele, H., Bärtsch-Ritter, N., Furger, M., Mücke, R., Sprenger, M., and Stohl, A.: High-ozone layers in the middle and upper troposphere above Central Europe: potential import from the stratosphere along the subtropical jet stream, *Atmos. Chem. Phys.*, 11, 9343–9366, 2011.
- Trickl, T., Giehl, H., Jäger, H., and Vogelmann, H.: 35 years of stratospheric aerosol measurements at Garmisch-Partenkirchen: from Fuego to Eyjafjallajökull, and beyond, *Atmos. Chem. Phys.*, 13, 5205–5225, 2013.
- Trickl, T., Vogelmann, H., Giehl, H., Scheel, H. E., Sprenger, M., and Stohl, A.: How stratospheric are deep stratospheric intrusions? *Atmos. Chem. Phys.*, 14, 9941–9961, 2014.

- Trickl, T., Vogelmann, H., Flentje, H., and Ries, L.: Stratospheric ozone in boreal fire plumes – the 2013 smoke season over Central Europe, *Atmos. Chem. Phys.*, 15, 9631–9649, 2015.
- Trickl, T., Vogelmann, H., Fix, A., Schäfler, A., Wirth, M., Calpini, B., Levrat, G., Romanens, G., Apituley, A., Wilson, K. M., Begbie, R., Reichardt, J., Vömel, H. and Sprenger, M.: How stratospheric are deep stratospheric intrusions into the troposphere? LUAMI 2008, *Atmos. Chem. Phys.*, 16, 8791–8815, 2016.
- Trickl, T., Vogelmann, H., Ries, L., Scheel, H.E., and Sprenger, M.: Very high stratospheric influence observed in the free troposphere over the Northern Alps – just a local phenomenon? *Atmos. Chem. Phys.*, 20, 243–266. 2020a.
- Trickl, T., Giehl, H., Neidl, F., Perfahl, M., and Vogelmann, H.: Three decades of tropospheric ozone lidar development at Garmisch-Partenkirchen, Germany, *Atmos. Meas. Tech.*, 13, 6357–6390, <https://doi.org/10.5194/amt-13-6357-2020>, 2020b.
- Price, J.D., and Vaughan, G.: On the potential for stratosphere-troposphere exchange in cut-off-low systems, *Q. J. R. Meteorol. Soc.*, 119, 343–365, 1993.
- Vautard, R., Szopa, S., Beekmann, M., Menut, L., Hauglustaine, D.A., Rouil, L., and Roemer, M.: Are decadal anthropogenic emission reductions in Europe consistent with surface ozone observations? *Geophys. Res. Lett.*, 33, L13810, doi:10.1029/2006GL026080, 4 pp., 2006.
- Vogelmann, H. and Trickl, T.: Wide-Range Sounding of Free-Tropospheric Water Vapor with a Differential-Absorption Lidar (DIAL) at a High-Altitude Station, *Appl. Opt.*, 47, 2116–2132, 2008.
- Vogelmann, H. and Trickl, T.: Lidar remote sensing of water vapor with DIAL, chapter 18, this book, 2022
- Vogelmann, H., Sussmann, R., Trickl, T., and Borsdorff, T.: Intercomparison of atmospheric water vapor soundings from the differential absorption lidar (DIAL) and the solar FTIR system on Mt. Zugspitze, *Atmos. Meas. Technol.*, 4, 835–841, 2011.
- Vogelmann, H., Sussmann, R., Trickl, T., and Reichardt, A.: Spatiotemporal variability of water vapor investigated using lidar and FTIR vertical soundings above the Zugspitze, *Atmos. Chem. Phys.*, 14, 3135–3148, 2015.
- Volz, A., and Kley, D.: Evaluation of the Montsouris series of ozone measurements made in the nineteenth century, *Nature*, 332, 240–242, 1988.
- Wernli, H. and Davies, H. C.: A Lagrangian-based analysis of extratropical cyclones. I. The method and some applications, *Q. J. R. Meteorol. Soc.*, 123, 467–489, 1997.
- Zachariasse, M., van Velthoven, P.F. J., Smit, H. G. J., Lelieveld, J., Mandal, T.K., and Kelder, H.: Influence of stratosphere-troposphere exchange over the tropical Indian Ocean during the winter monsoon, *J. Geophys. Res.*, 105, 15403–15416, 2000.
- Zahn, A., Brenninkmeijer, C. A. M., Asman, W.A. H., Crutzen, P.J., Heinrich, G., Fischer, H., Cuijpers, J.W. M., and van Velthoven, P.F. J.: Budgets of O₃ and CO in the upper troposphere: CARIBIC passenger aircraft results 1997–2001, *J. Geophys. Res.*, 107, 4337, doi: 10.1029/2001JD001529, 19 pp., 2002.
- Zahn, A., Christner, E., van Velthoven, P.F. J., Rauthe-Schöch, A., and Brenninkmeijer, C.A. M.: Processes controlling water vapor in the upper troposphere/lowermost stratosphere: An analysis of 8 years of monthly measurements by the IAGOS-CARIBIC observatory, *J. Geophys. Res.*, 119, 11505–11525, doi: 10.1002/2014JD021687, 2014.
- Zanis, P., Trickl, T., Stohl, A., Wernli, H., Cooper, O., Zerefos, C., Gaeggeler, H., Priller, A., Schnabel, C., Scheel, H.E., Kanter, H.J., Tobler, L., Kubik, P.W., Cristofanelli, P., Forster, C., James, P., Gerasopoulos, E., Delcloo, A., Papayannis, A., and Claude, H.: Forecast, observation and modelling of a deep stratospheric intrusion event over Europe, *Atmos. Chem. Phys.*, 3, 763–777, 2003.

22 Impact of turbulence on cloud microphysics

Gholamhossein Bagheri¹, Eberhard Bodenschatz¹, John Lawson², Jan Moláček¹, Freja Nordsiek¹, Oliver Schlenczek¹

22.1 Introduction

Clouds consist of water droplets and ice particles that are dispersed within a highly non-stationary, inhomogeneous, and intermittent turbulent flow (Bodenschatz et al. 2010). Earth's atmosphere is dominated by the presence of clouds, which exert great control on the Earth's radiative balance, which strongly impacts weather and climate. Despite decades of research, a vast community of scientists and considerable measurement infrastructure (e.g. weather stations and satellites), insufficient understanding of cloud physics (moist convection and cloud evolution) is a primary source of uncertainty in weather and climate models (Stevens & Bony 2013). Why can't we reliably predict weather more than a few days ahead (and sometimes not even a few hours), let alone forecast the climate in 50 years?

Various factors can be blamed for the 'cloud challenge'. Two key factors are the enormous scale separations in cloud physics and turbulence (Bodenschatz et al. 2010). Physical phenomena related to formation and evolution of clouds span a wide range of scales from micrometres (scale of small cloud particles and aerosols) to hundreds of kilometres where clouds become part of global weather and climate. Additionally, there is a strong interplay and coupling with turbulence at all scales. In particular, the challenge is to incorporate the microphysical processes occurring at sub-metre scales, such as inertial clustering and entrainment of environmental air in clouds, into coarse-resolution weather and climate models. Even before that, we are yet to understand how such microphysical processes work (Stevens & Bony 2013; Bodenschatz 2015; Beals et al. 2015).

22.1.1 Rain initiation problem

"According to the Mt. Washington experiments, we should expect that droplets in summer cumulus clouds at +20C should grow to a diameter of about 26 microns in one minute and to about 72 microns in thirty minutes. ... Since cumulus clouds often develop rain within less than thirty minutes after their formation, we see that some mechanism other than that assumed in the evaporation-condensation theory must be involved in rain formation." Irving Langmuir (1948)

Seventy years after Langmuir's statement, we still don't understand the rapid growth of 30–80 μm diameter (d_p) drops in warm (ice-free) clouds (the growth of ice particles in mixed-phase clouds has been explained by the Wegener-Bergeron-Findeisen process since 1938, see Wallace & Hobbs, 2006). It is well understood that nucleation-condensation explains the rapid growth of d_p from sub-micron formation to 30 μm . At the same time, gravitational collisions explain the growth of drops with $d_p > 80 \mu\text{m}$ (section 7 in Pumir & Wilkinson, 2016). However, for 30–80 μm drops the growth process is still poorly understood (Grabowski & Wang 2013; Pumir & Wilkinson 2016). It is believed that these drops also grow by collision-coalescence, but the underlying mechanisms, and in particular the role of turbulence, need to be explained. In the following discussion, we will limit ourselves to the case of warm clouds – those consisting entirely of liquid water droplets, and thus talk only about rain.

22.1.2 The nature of turbulence in clouds

"The essential point is that fluid motion is almost always inherently unstable, and that incipient instabilities are suppressed only if the viscous dissipation is high enough. However, virtually all fluids have an extremely low viscosity. This is true of water, air, blood, the molten metal in the core of the earth, and the atmosphere of the sun. The implication is that turbulence is the natural state of things and indeed this is the case." Davidson (2015)

¹ Max Planck Institute for Dynamics and Self-Organization, Am Faßberg 17, 37077 Göttingen, Germany

² Aerodynamics and Flight Mechanics Research Group, University of Southampton, Southampton SO17 1BJ, UK

Atmospheric turbulence is characterized by its large separation of scales. One measure of this is the large-eddy Reynolds number:

$$Re_\ell = u' l / \nu \quad (1)$$

where u' is the fluctuating (root-mean-square) turbulent velocity, l is the integral length scale (i.e. the length scale of the flux carrying eddies $\sim 10^2$ – 10^3 m) and ν is the kinematic viscosity ($\sim 10^{-5}$ m²s⁻¹ for air). u' in clouds can vary over at least two orders of magnitude with a typical moderate cumulus cloud value of 1 m s⁻¹ (Shaw 2003). Since most turbulent kinetic energy is in the large eddies, we can safely replace u' by the fluctuating velocity of large eddies, i.e. $Re_\ell = u_\ell l / \nu$. For atmospheric clouds, Re_ℓ is typically $\sim 10^6$ – 10^8 .

According to Richardson's (1922) energy-cascade theory, the kinetic energy of velocity fluctuations in fully-developed turbulence cascades from large energy-containing scales (l) to smaller scales until it dissipates to heat. Dimensional analysis shows turbulence energy production scales as u_ℓ^3/l . Since a fully-developed turbulent flow cascade is a stationary state, the rate at which kinetic energy is transferred to the smaller scales is equal to the rate it is viscously dissipated ε :

$$\varepsilon \sim u_\ell^3/l, \quad (2)$$

which is one of the most important turbulence parameters. As an example in the spirit of the Kolmogorov (1941) hypotheses, knowing ε allows the estimate of various temporal and spatial scales of turbulence, scaling of the turbulence energy spectrum in intermediate length scales (inertial range), and statistics of low-order velocity increments. The cloud-average ε for moderate cumulus clouds is typically around 10^{-2} m²s⁻³. However, ε inside clouds can vary by several orders of magnitude with the highest values occurring typically around the cloud top (~ 0.1 m²s⁻³) and smaller values at the cloud base around $\sim 10^{-3}$ – 4×10^{-3} m²s⁻³ (Vaillancourt & Yau 2000; Shaw 2003).

The dissipation scales are called the Kolmogorov microscales of turbulence (Davidson 2015). The Kolmogorov length scale η is derived through dimensional analyses based on Kolmogorov's first similarity hypothesis (small-scale statistics in fully-developed turbulence should only depend on ν and ε)

$$\eta = (\nu^3/\varepsilon)^{1/4}. \quad (3)$$

Similarly, we can define Kolmogorov time τ_η and velocity u_η scales

$$\tau_\eta = (\nu/\varepsilon)^{1/2}, \quad (4)$$

$$u_\eta = (\nu\varepsilon)^{1/4}. \quad (5)$$

The Kolmogorov scale Reynolds number, $Re_\eta = \eta u_\eta / \nu$, is of order unity, which is consistent with the energy-cascade picture that viscous dissipation dominates at Kolmogorov scales. For atmospheric clouds, $\eta \sim 1$ mm, $\tau_\eta \sim 10$ ms, and $u_\eta \sim 1$ cm s⁻¹. Combining equations (1) to (5), one can see that the cloud scale separation l/η scales with $Re_\ell^{3/4}$. Considering that $Re_\ell \sim 10^6$ – 10^8 in clouds, the scale separation is $O(10^4)$ – $O(10^6)$.

The Taylor microscale Reynolds number, $Re_\lambda = u_\lambda l / \nu \sim (15 Re_\ell)^{1/2}$, is often used for quantifying turbulence strength. The Taylor length microscale, $\lambda \sim (u_\ell^2 \nu / \varepsilon)^{1/2}$, is the characteristic length scale of the mean spatial extension of velocity gradients, which lies between l and η (Vaillancourt & Yau 2000). Unlike Re_ℓ (which depends on the non-universal, flow-dependent, scales of large eddies) and Re_η (always of order unity), Re_λ is an appropriate dimensionless number for comparing universal statistics of different turbulent flows with each other since it is based on an intermediate length scale with universal characteristics. In clouds, $Re_\lambda \sim 10^4$.

The dispersion and interaction of cloud particles with turbulence is of great interest. The 30–80 μ m drops at the heart of the cloud problem are much smaller than η in typical clouds. Experimental measurements, such as the pioneering investigation of Snyder & Lumley (1971), have shown that the main parameters controlling dispersion of particles $d_p \ll \eta$ in a turbulent flow are the particle-to-fluid density ratio and Stokes number

$$St = \frac{\tau_p}{\tau_\eta} = \frac{\rho_p \varepsilon^{1/2} d_p^2}{18 \rho_f \nu^{3/2}} \quad (6)$$

where $\tau_p = \rho_p d_p^2 / 18 \rho_f \nu$ and ρ_p are the particle relaxation (or response) time and density, and ρ_f is the fluid density. St is a measure of particle inertia – $St \ll 1$ particles follow the fluid flow faithfully, while $St \gg 1$ particles are completely decoupled from the flow. Typical values of St for 10–100 μm cloud drops are 10^{-2} – 10^0 . Table 1 summarizes typical turbulence-cloud parameters.

Tab. 1: Ranges and values of important cloud-turbulence parameters typically encountered in free cumulus clouds and at the UFS.

Parameter	Typical range	Typical value	Meas. at UFS
ε [m^2s^{-3}]	10^{-3} – 10^{-1}	1×10^{-2}	8×10^{-2}
η [m]	10^{-4} – 10^{-3}	8×10^{-4}	4×10^{-4}
τ_η [s]	10^{-2} – 10^{-1}	4×10^{-2}	1×10^{-2}
u_η [ms^{-1}]	10^{-2} – 10^{-1}	2×10^{-2}	3×10^{-2}
Re_λ	10^3 – 10^4	8×10^3	3×10^3
St	10^{-3} – 10^{0*}	$3 \times 10^{-1*}$	$5 \times 10^{-2**}$

* considering cloud drops with diameters of 10–50 μm and mean of 30 μm .

** see Fig. 9 and 10 in Siebert et al. (2015).

22.1.3 Characteristics of clouds at the UFS

Measurements indicate that the microphysical and turbulent properties of clouds at the UFS are representative of free clouds, which makes the UFS a suitable site for investigating clouds. Easterly-westerly winds are dominant at the UFS as a result of the local topography (Fig. 1a). Warm clouds are dominant in the average 5°C summer. Wind speeds with and without clouds were usually $< 14 \text{ ms}^{-1}$ with a most probable value of $\sim 0.9 \text{ ms}^{-1}$ and an average of 1.2–2.6 ms^{-1} for 2000–2012 (Risius et al. 2015; Siebert et al. 2015), which can be seen in Figure 1b. The velocity energy spectrum measured by an ultrasonic anemometer and a hotwire at the UFS and the weather data from the DWD (Deutscher Wetterdienst) from the peak of the Zugspitze are shown together in Figure 1c (Risius et al. 2015).

Ultrasonic anemometry at the UFS indicates the RMS velocity is $u' \approx 1 \text{ ms}^{-1}$ (Risius 2012). Taking the approximate distance from the measurement point to the mountainside to be the large eddy scale of $l \sim 10 \text{ m}$, we obtain $\varepsilon \sim u'^3/l \approx 10^{-1} \text{ m}^2\text{s}^{-3}$, which is comparable to $\varepsilon = 8.5 \times 10^{-2} \text{ m}^2\text{s}^{-3}$ meas-

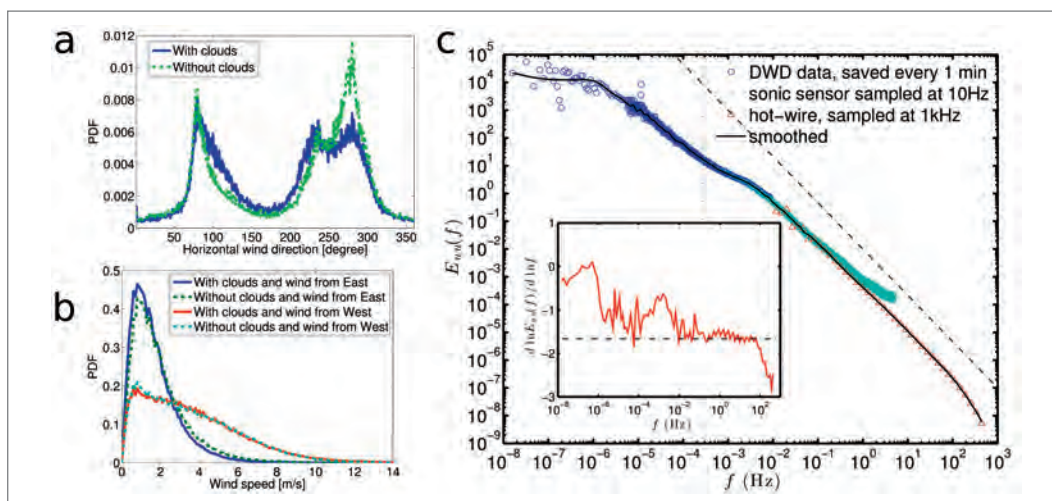


Fig. 1: Wind data from the Zugspitze (Risius et al. 2015). (a) Wind direction angle PDF and (b) speed PDF for the most common directions at the UFS measured by an ultrasonic anemometer (Fig. 4) in cloudy and non-cloudy conditions. (c) Turbulent energy spectrum of east-west wind on the Zugspitze. Hotwire and sonic data are from the UFS, and the DWD data is from the peak. The solid black line is the smoothed composite spectrum. The diagonal dash-dotted line is a Kolmogorov $f^{-5/3}$ spectrum line, and the vertical dashed line corresponds to 1 hr^{-1} . The inset shows the composite spectrum's local logarithmic slope compared to the Kolmogorov $-5/3$ spectrum (horizontal line).

ured by hot-wire anemometry (Siebert et al. 2015). $Re_1 \sim 10^6$, which is at the low end for free clouds in the atmospheric boundary layer (Siebert, Lehmann, Wendisch, et al. 2006). The maximum Re_λ is of the order of 10^4 with a most common value of ~ 3000 (Risius et al. 2015). These values are summarized in Table 1.

22.1.4 Physics of Rain Initiation

Every raindrop starts as a cloud condensation nucleus, a sub-micron aerosol particle (salt crystals, organic molecules, combustion residue, etc.) suspended in air. As the excess relative humidity greater than 100% (supersaturation) rises above a critical level, water vapor quickly condenses on the nucleus which acts as a catalyst. The droplet's radius grows over time proportionally to the local supersaturation level, which can be caused by adiabatic cooling such as what happens when an air mass flows up a mountain. At the same time, $dr/dt \sim r^{-1}$. Thus a period of rapid growth is followed by progressive slowdown, resulting in an increasingly narrow droplet size distribution where younger drops catch up with older ones.

Initially, the droplets have a settling speed much smaller than the typical updraft speeds effectively suspending them in the flow (a 20 μm diameter droplet has a settling speed of 2 cm/s whereas updrafts are typically several m/s). To reach sufficiently high settling speeds to overcome the updraft and fall to the ground, the droplets have to reach diameters of several hundred μm . Raindrop sizes typically follow an exponential distribution (Jameson & Kostinski 2001; Marshall & Palmer 1948) with the mean drop size increasing with increasing rain rate, and can reach up to and beyond the maximum stable diameter of about 6 mm (Gunn & Kinzer 1949).

For a droplet to reach millimetric raindrop size purely by condensational growth would take orders of magnitude longer than what is observed. This leaves only combining droplets together by various collision-coalescence processes. The simplest model for the evolution of droplet size distribution by collisions is

$$\frac{\partial n(r, t)}{\partial t} = \frac{1}{2} \int_0^r K(s, r') \left(\frac{\partial r'}{\partial r} \right)^{-1} n(s, t) n(r', t) ds - n(r, t) \int_0^\infty K(r, s) n(s, t) ds, \quad (7)$$

where $n(r, t)$ is the number density of droplets of radius r at time t , $K(s, r)$ is the coalescence kernel giving the rate of coalescence between drops of radius s and r , and $r' = (r^3 - s^3)^{1/3}$ is the required drop radius to form a drop of radius r when coalescing with a drop of radius s . The first integral is the rate of increase of $n(r, t)$ due to coalescence of smaller droplets, whereas the second term describes the decrease of $n(r, t)$ due to coalescence of droplets with radius r with other droplets.

In this simplest model, coalescence is assumed to happen whenever two droplets collide. In reality, this is only approximately true for large drops with small relative velocities. Large drops with large relative velocities tend to produce several droplets, and small droplets often move around each other due to the hydrodynamics of the gas between them. Henceforth we shall replace the coalescence kernel with the collision kernel. For drops moving in still air solely due to gravity where the typical time between collisions is larger than the relaxation time for droplets to reach terminal velocity, the collision kernel is simply

$$K_G(r, s) = \pi(r + s)^2 |V(r) - V(s)|, \quad (8)$$

where $V(r)$ is the settling speed of a drop with radius r , and $\pi(r + s)^2$ is the combined collision cross-section area.

While a modified version of (7)–(8) that accounts for the collision and coalescence efficiency describes the latest stages of large drop growth well, its fundamental weakness is that it depends on the differential settling speed, and hence differential size, to drive the collisions; so that it cannot explain how the initially narrow size distribution of small droplets produced by condensational can grow and broaden within a reasonable timeframe. This is where turbulence comes in. By creating shear down to η , turbulent flow makes it possible for even equally sized droplets to collide. Careful analysis (Saffman & Turner 1956) yields a turbulent shear collision kernel

$$K_{TS}(r, s) = 1.3(r + s)^3 \tau_\eta, \quad (9)$$

Unequally sized droplets respond differently to turbulent acceleration due to their different inertias, which enhances collision probability. The process' collision kernel is (Levich 1954)

$$K_{11}(r, s) = \pi(r + s)^2 |\tau_p(r) - \tau_p(s)| a_{\eta r} \quad (10)$$

where $a_{\eta} = \eta/\tau_{\eta}^2$ is the Kolmogorov acceleration. Even with these effects taken into account, the droplet growth rate at 20–100 μm diameter is still significantly underestimated.

These collision kernels have all been obtained under the assumption that the spatial distribution of droplets is uniformly random – that is, the likelihood of finding a given droplet at any location is the same. However, numerical simulations of particles in turbulent flows have shown that the particles actually cluster onto lower-dimensional fractal-like structures (Yoshimoto & Goto 2007). The level of clustering is dependent on the particle inertia. Particles with little inertia behave like passive tracers, faithfully following the surrounding flow, which, by virtue of its incompressibility do not cluster. Conversely, particles with large inertia cannot respond to the quick changes in the local flow conditions, effectively averaging flow structure over larger scales, which tends to lead to much weaker net effect on their trajectories. Thus, the uniform spatial distribution assumption holds for very small ($d_p < 10 \mu\text{m}$) and large ($d_p > 100 \mu\text{m}$); while for intermediate drop sizes, where the drop response time is comparable to τ_{η} , the clustering can produce structures with fractal dimension as low as 2.3 (Bec et al. 2007). The lower the fractal dimension, the more likely it is to find two drops very close to each other, which increases the collision rate.

The collision rate is also enhanced by caustics in the droplet velocity field due to the so-called sling effect (Falkovich et al. 2002) where the droplet velocity field becomes multivalued as droplet trajectories separating from regions of different air velocity cross. This allows droplets with significantly different velocities to come close to each other, which enhances not only their collision rate but also the collision efficiency. While the acceleration magnitudes required to create the sling effect for droplet size of interest are substantially higher than the typical accelerations encountered in the flow, turbulence is known to create these extreme events with a likelihood far larger than would be expected from a normal distribution (La Porta et al. 2001).

The approaches described up to now all start from some version of equation (7). This equation describes the droplet number density as if it were a continuous quantity evolving deterministically. In a real cloud, the droplet numbers are discrete and their collisions are a stochastic process – if we were to start from macroscopically identical initial conditions, the sequence of collisions would be different for each repetition. Since it takes about one million 10 μm diameter drops to produce a typical raindrop, one in a million droplets coalescing could be enough for a runaway process of growth by coalescence to start. Therefore, a relatively small number of discrete collision events can have a large impact on the total timescale of the rain initiation, which can lead to an underestimate of the droplet growth rate using the continuous model Eq. (7) compared to a stochastic approach (Kostinski & Shaw 2005). Furthermore, it highlights the need to understand the nature and likelihood of the rare events in which the first millionth of droplets collide. Such understanding necessitates collecting large amounts of data resolving the smallest spatial and time-scales at which these events occur.

22.1.5 Available methods

Turbulence-cloud interactions are analysed at various scales with theoretical analyses, numerical simulations, and laboratory and in-situ (field) measurements. Solving the Navier-Stokes equations (the equations of motion for fluids like air) by Direct Numerical Simulation (DNS) or Large Eddy Simulation (LES) are the two main computational approaches. With LES, the small scales are modelled indirectly while large scales are computed directly, which allows high Re_{λ} to be reasonably well simulated (Warhaft 2002) at the expense of fine-scale turbulent features (mixing, fluctuations, etc.) and particle-turbulent interaction. DNS, on the other hand, simulates all scales, but the computational cost increases rapidly as Re_{λ} and, therefore, l/η grows. Specifically, projecting the costs from $Re_{\lambda} \sim 10^3$ to 10^4 , yields 20–100 weeks on the fastest supercomputer available today³ for one eddy turnover time depending on the computational efficiency of the code (e.g. see Jimenez, 2003, for computational requirements), and that is without taking

³ <https://www.top500.org/>, November 2017 list

temperature, buoyancy, vapor, and particles into account. It will take years (if ever) before turbulent flows similar to clouds can be simulated. Nevertheless, DNS can provide detailed information on statistics of small-scale fluctuations in velocity, temperature, and water-vapour mixing ratio and droplet collision-coalescence (Balachandar & Eaton 2010; Grabowski & Wang 2013; Pumir & Wilkinson 2016).

Innovative experimental measurements are required to bridge the scales and develop validated sub-grid models for simulations and models.

Currently, creating real cloud conditions in laboratory experiments is very difficult. The difficulty is to reach cloud Re_λ with small cloud ε while ensuring that the gravitational settling is not negligible. Laboratory flows with low ε must either be very large or have Re_λ smaller than clouds. However, recently-developed turbulence wind tunnels, such as those developed by Bodenschatz et al. (2014), can produce decaying isotropic turbulence with $Re_\lambda \sim 6000$ and $\varepsilon \sim 0.1 \text{ m}^2\text{s}^{-3}$, which is promising.

Field observations in actual clouds are one of the most promising options. Most field observations are carried out with airborne campaigns that are flexible in picking clouds of interest away from ground topographical effects (Siebert, Lehmann, Wendisch, et al. 2006; Siebert et al. 2010; Malinowski et al. 2013; Beals et al. 2015). Aircraft-based measurements, however, are constrained by the resolution of flight speed and sampling frequency. A solution is to use blimps, aerostats, or kites; which are constrained by the wind speed instead of flight speed (Siebert, Lehmann & Wendisch 2006). Typical wind speeds encountered by aerostats are $\sim 1\text{--}10 \text{ m/s}$, which are an order of magnitude less than typical aircraft flight speed of $\sim 100 \text{ m/s}$. Another suitable field strategy is ground-based measurements, which are not constrained by the sampling time and provide the possibility to perform Lagrangian measurements, where droplets can be tracked in time. However, there is no freedom in selecting the cloud type and topographical effects must be considered.

22.2 Measuring flow and fluid properties

A very common method of measuring temperature is thermistors – resistors whose resistance has a significant temperature dependence. Resistance Temperature Detectors (RTD) are the most popular due to their linear resistance-temperature relationship. The measurement principles are largely independent of the kind of thermistor. The resistance is measured using a small current or voltage and measuring the other, while insuring that Ohmic heating of the thermistor is negligible. A thermistor is commonly mounted inside a metal body as shown in Figure 2a and 2b or used in the so-called cold-wire configuration (shown in Figure 2c and 2d) where a thin metal wire acting as the thermistor is held between two prongs and is immersed directly in the fluid. A good example is the T-NSTAP (Temperature – Nano Scale Thermal Anemometry Probe), which has a wire thickness of $100 \text{ nm} \times 2 \text{ }\mu\text{m}$ and a length of $200 \text{ }\mu\text{m}$ allowing it to measure temperature at very fine scales (Fan et al. 2015).

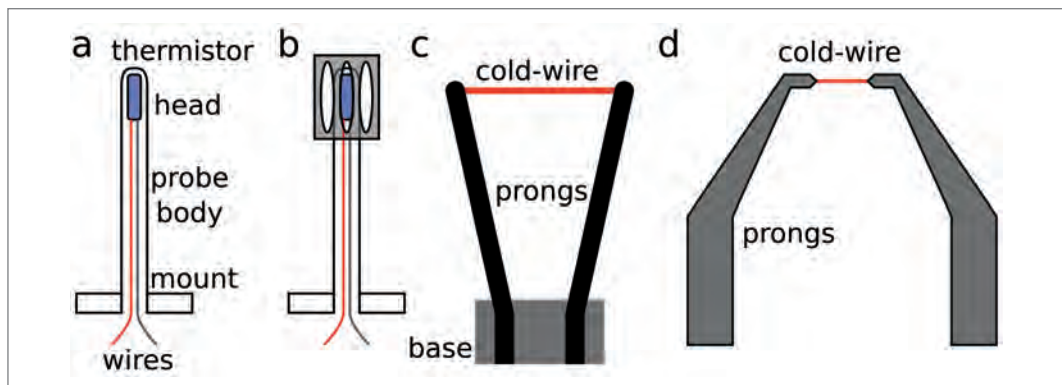


Fig. 2: (a) and (b) Diagram of two examples of thermistor probes with different housing styles. (c) and (d) Diagram of cold-wire thermistor probes, (c) being the larger conventional style and (d) being the smaller etched T-NSTAP style (Fan et al. 2015).

When Ohmic heating is not negligible, the thermistor will be significantly warmer than the surrounding fluid and exchange heat to the fluid. This is done deliberately to measure the fluid velocity. Such thermistors are known as hotwires and the technique as Hotwire Anemometry (HWA). The thermistor, almost always an RTD, is maintained at a temperature T which is greater than the fluid temperature T_f . Heat is conducted to the fluid which then diffuses and is advected away as shown in Figure 3. The heat loss P to the fluid can be approximately described by King's Law (King 1914) which is $P = (T - T_f)(A + B|u|^n)$ where n was originally derived to be $\frac{1}{2}$ (King 1914) but in practice typically deviates by a small amount, u is the fluid velocity, and A and B are coefficients that depend on the wire and fluid properties. Hotwire measurements are typically done by holding the hotwire at a fixed temperature/resistance much greater than the variation in T_f with a feedback circuit, known as Constant Temperature Anemometry (CTA). The electric potential V across the hotwire is measured. Then the heat loss is just $P = V^2/R$ and the fluid velocity then easily calculated.

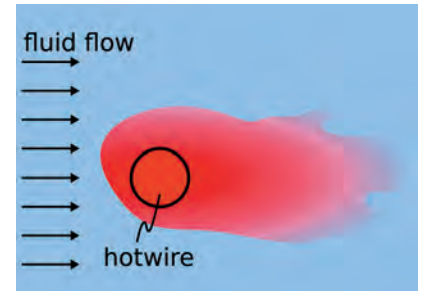


Fig. 3: Hotwire in a flowing colder fluid. The wire (seen edge on) heats the fluid which is diffused and advected away by the fluid. Elevated temperatures are shown in red.

Hotwire probes are typically used where there is a strong mean flow to measure the variation in u along the axis of the mean flow. By using the Taylor Frozen Field Hypothesis (Taylor 1938), the temporal measurements $u(t)$ can be translated to the spatial variation $u(x)$ along the mean flow direction ($U_{\text{mean}} \Delta t \approx \Delta x$). The kinetic energy spectrum can then be calculated, which allows the different scales of the fluid flow to be analysed and ε determined. Hotwires have been used to investigate the turbulent structures as well as turbulent intermittency (spatial variations in ε at small scales) in clouds (e.g. see H. Siebert et al. 2010).

Ultrasonic anemometers (sometimes called “sonics” or “sonic anemometers”) are another velocity measuring device, often found in weather stations. The sonics we have on the top deck of the UFS are shown in Fig. 4 along with some wind data from Risius et al. (2015) previously in Fig. 1. The sonics consist of two or more ultrasonic transducers, which gives the advantage of having no moving parts. For a pair of transducers that can hear each other, each alternately emits a short pulse whose time of flight, Δt_{12} and Δt_{21} , to the other transducer is measured. Because sound moves relative to its medium, the travel time will be reduced or increased depending on the fluid velocity component u along the axis between the two transducers. Δt_{12} and Δt_{21} can be used to eliminate the speed of sound and the other velocity components to get $u = \frac{1}{2}L(1/\Delta t_{12} - 1/\Delta t_{21})$, where L is the distance between them (McKeon et al. 2007). Typically, several transducers are used to form enough pairs so that two or three velocity components can be resolved, and to provide redundancy when the velocity is aligned with the axis between a transducer pair (transducers disrupt the measurement). Analysis can be done using Taylor's Frozen Field Hypothesis similar to hotwires, though sonics resolve only lower frequencies.

Another quantity of interest is the water vapor concentration of the air. To measure relative humidity, three main physical mechanisms can be used: (1) change in volume or length of a hygroscopic material (the principle used in hair hygrometers), (2) change in electrical properties due to absorption of water vapor on a surface (change in capacitance, used in capacitive hy-

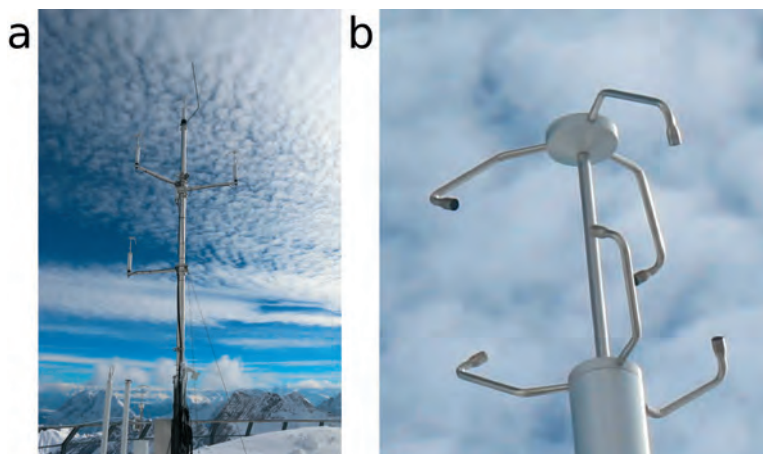


Fig. 4: (a) Picture of 6 ultrasonic anemometers, each with 6 transducers, at the UFS – 5 are on the mast and one is on the rail. (b) Picture of the rightmost ultrasonic anemometer on the mast, which has 6 transducers in an arrangement of 3 pairs.

grometers, and change in conductivity, used in lithium chloride hygrometers), and (3) spectroscopic methods (Lyman-alpha hygrometers, water vapor sensors in the near infrared) (see Harrison, 2014, for more details).

22.3 Particle Imaging Techniques

In this section, we summarise the operating principles and practical application of Particle Image Velocimetry (PIV) and Lagrangian Particle Tracking (LPT) techniques at UFS.

22.3.1 Particle Image Velocimetry

Thirty-five years since the first mention of its development in the literature, PIV capabilities have evolved from simple two-dimensional, two-component velocimetry to fully time-resolved, three-dimensional, three-component velocity, acceleration and pressure measurements (Scarano 2013). The ability to provide spatially detailed flow-field information, in comparison to single-point measurements like HWA, is perhaps why PIV has become the dominant approach to velocity measurement in experimental fluid mechanics (Westerweel et al. 2013). Several reviews and books have been dedicated to its principles and practice; in particular, Raffel (2007) and Adrian & Westerweel (2011) have become popular references amongst the fluid mechanics community.

The CloudKite PIV system, illustrated in Figure 5, has been developed to make measurements of the turbulence in clouds at UFS. The main advantages of PIV in this context are its ability to operate under variable imaging conditions and still provide comprehensive, spatial information about the turbulent flow. This allows fundamental turbulence quantities to be measured inside a cloud (turbulence intensity, structure functions, energy dissipation rate) without approximation. The basic setup is typical of 2D PIV. A dual-cavity laser is equipped with cylindrical lenses to generate a “light sheet”, which provides pulsed, planar illumination of seeding particles (droplets) embedded in the flow. A digital camera records pairs of images illuminated by sequential light pulses, separated by a time interval Δt . The velocity field is inferred from the displacement of particles over this interval.

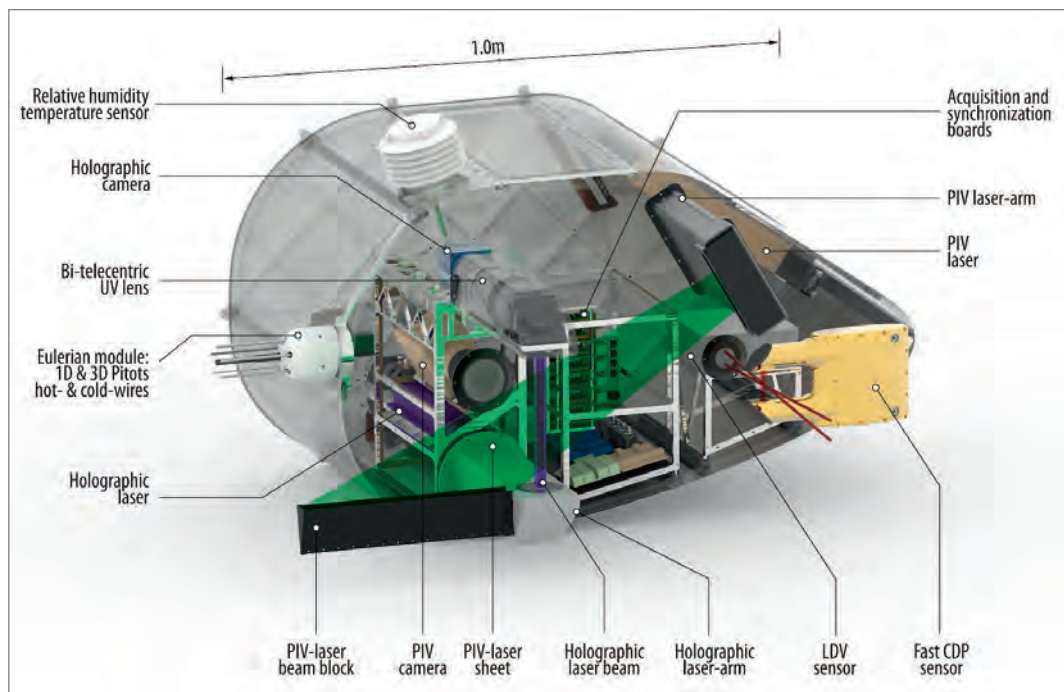


Fig. 5: CAD visualisation of the CloudKite instrument box, which can perform autonomous measurements in the air or on the deck of the UFS. The double-cavity Nd:YAG PIV laser illuminates cloud droplets within a thin laser sheet with double pulses at short time intervals. A high-speed digital camera captures image pairs of the illuminated droplets that can be used for PIV or PTV analysis.

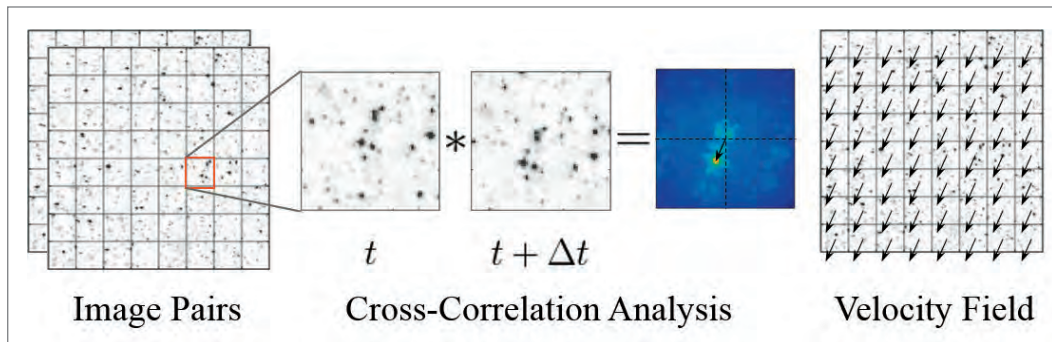


Fig. 6: Working principle of 2D PIV analysis: (a) start with image pairs divided into interrogation windows, (b) calculation of displacement, and (c) determination of velocity field.

Figure 6 illustrates the operating principle of 2D PIV. Before measurement, a calibration is performed to map camera images to a 2D plane coincident with the laser sheet. Pattern-matching between image pairs measures the displacement field Δx of particles in the plane. Since the particles follow the flow, the velocity field v is estimated as $v = \Delta x / \Delta t$. Image pairs are analysed piece-wise by subdividing them into Interrogation Windows or IWs (A). The spatial cross-correlation function is computed between IWs of image pairs (B). This correlation function has a maximum or “peak” at a location, which corresponds to the displacement Δx of the particle pattern and can be located to sub-pixel accuracy. Performing this procedure for all IWs yields 2D vector fields (C). Modern PIV algorithms iterate this procedure over multiple passes in a predictor-corrector scheme to enhance accuracy and dynamic range and incorporate additional steps to filter the result and reject obvious measurement errors. Several (tens of) open source and commercial software packages are available to perform this process.

Three basic rules of thumb inform the design of PIV measurements (Raffel 2007). Firstly, the seeding concentration should be sufficiently high to ensure around ten particles or more can be matched between IWs. Secondly, the maximum displacement should not exceed around one-quarter of the interrogation window size. Thirdly, the maximum displacement difference across each IW is limited to a fraction (3% or so) of the IW size. Violation of any of these criteria by even a factor of two substantially reduces the measurement reliability. Coupled with limits on displacement measurement accuracy, these constraints limit the measurement accuracy of PIV to about 1% of full range at best. For a given flow and spatial resolution, measurement accuracy is optimised by selecting the largest feasible Δt . In field measurements, the flow velocity and turbulence intensity can significantly vary over a timescale of seconds. The CloudKite incorporates a system to select an optimal Δt in real-time for each snapshot of the flow taken. This is accomplished using a pitot tube to estimate the bulk flow velocity at the time of the measurement, from which Δt is set.

22.3.2 Lagrangian Particle Tracking

Like PIV, Lagrangian Particle Tracking is an optical velocimetry technique capable of making two- or three-dimensional velocity and acceleration measurements of particles from recorded images of their motion. It can be combined with photogrammetric or holographic techniques to measure particle size. Extensive developments have been made over its five-decade history, summarised by (Dracos 1996) and (Raffel 2018). Owing to the simplicity of the technique, several groups within the fluid mechanics community have developed LPT codes, many of which are publicly available.

In contrast to PIV, which examines groups of particles, LPT involves the optical tracking of individual particles. Because of the requirement to unambiguously identify and follow particles, LPT is typically limited to simultaneously measuring an order of magnitude fewer particles than a comparable PIV measurement. This significantly reduces the spatial information simultaneously available. On the other hand, since flow information is localised to the position of individual particles rather than averaged over an interrogation window, very high spatial resolution can be achieved. The most significant benefit of LPT is the ability to examine the flow evolution from a Lagrangian perspective, moving with the flow. This makes it a natural tool for the study of turbulent transport and mixing (Yeung 2002) and droplet formation in clouds (Shaw 2003), which are problems most conveniently analysed in the Lagrangian frame.

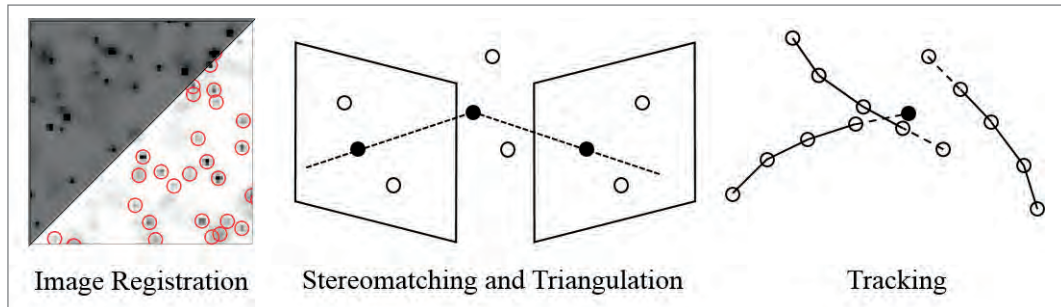


Fig. 7: The core steps of 3D Lagrangian Particle Tracking

Several variations on particle tracking methods exist (Maas et al. 1993; Dracos 1996; Ouellette et al. 2006; Schanz et al. 2016). Most operate on time-resolved videos of particle motion, captured from multiple perspectives. Although implementations differ, the core steps are illustrated in Figure 7. These are: image registration, where particle images are identified and their positions located on the image plane; stereo-matching and triangulation, where correspondences are made between particle images across cameras to reconstruct 3D particle positions; and tracking, where particles in one frame are associated with their trajectories through previous frames. This process is performed sequentially, building up tracks by stepping through each video frame. Particle velocity and acceleration are obtained by numerically differentiating its position measurement.

One exciting application of LPT at UFS is to explore the formation and collision of cloud droplets in situ. Figure 8 shows the setup of the Seesaw experiment at UFS, which implements a 3D LPT setup. Three cameras are mounted on a vibration damped camera box on a moving sled, sat amongst the clouds on the rooftop of UFS. Light from a fibre-coupled, pulsed laser is

used to provide volumetric illumination of a common field-of-view shared between cameras. This allows us to simultaneously record videos of ambient water droplets from three perspectives.

The Seesaw experiment at UFS has a number of unique features optimised for cloud measurements (Bertens et al. 2021). The most striking feature is the sled, which allows the cameras to follow particles as they are swept along by the prevailing wind. By doing so, the residence time of the particles within the measurement volume is extended to sample each particle hundreds of times on its passage through the volume. This is necessary to reliably measure each particle's motion and properties. Considerable technical effort has been expended in the design of the 3D LPT setup to minimise its weight, whilst maintaining enough stiffness to accelerate up to 5 m/s and stop again over a distance of only 5 m. Stringent requirements upon the temporal resolution, which oversamples the Kolmogorov timescale by a factor of 100, have been achieved. These are necessary to reliably measure the Lagrangian acceleration (Mordant et al. 2004), which exhibits rapid, extreme fluctuations hundreds of standard deviations in excess of the mean. Additional effort has been made in the automation of data acquisition systems, which can support

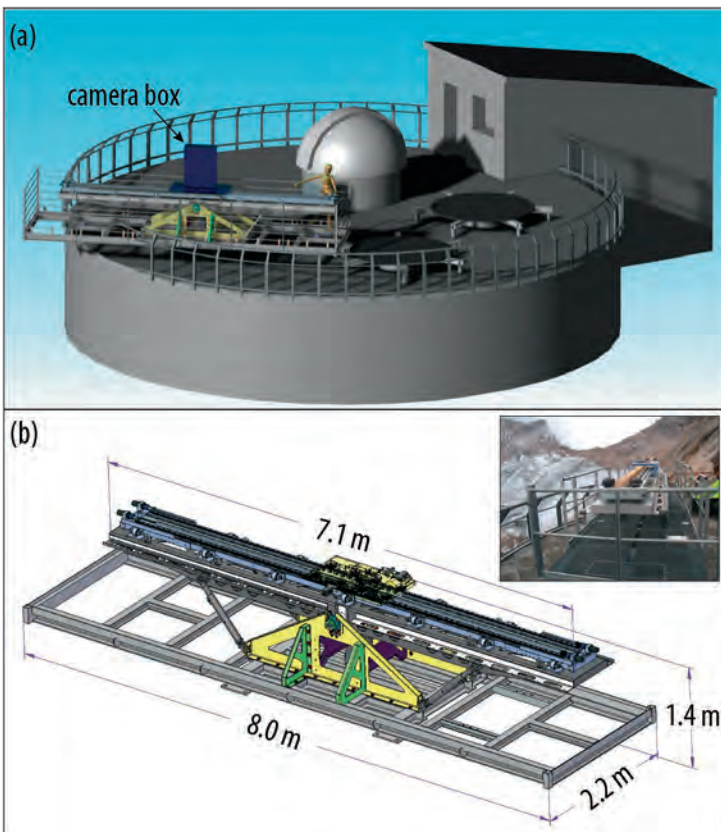


Fig. 8: Schematic (a) of Seesaw LPT experiment situated on the rooftop of UFS and (b) a detailed view of the camera box. Using angled mirrors, the three cameras are able to view droplets as they are illuminated by a laser beam from above.

a peak data acquisition rate of 4 TB of images per hour thanks to the direct integration of the experiment with a high performance computing and storage cluster. The high data throughput is necessary to acquire a statistically converged sampling of transient clouds, which have a typical duration of tens of minutes.

The experimental challenges of working in the field impact the particle tracking algorithms used to process the data. Despite moving with the flow, a large measurement volume is required to ensure sufficiently long residence times due to the unpredictability of the droplet's velocity. This results in a low illuminating power density, requiring the use of large apertures and shallow viewing angles and results in the majority of droplets' images being out-of-focus on the sensor. Extracting accurate position information under these circumstances requires state-of-the-art techniques, which we have developed building upon the ShakeThe Box algorithm (Schanz 2016). The approach is to improve the efficiency of the image registration and tracking steps (see Figure 7) by accurately modelling the images formed by droplets upon the camera sensor over an entire video sequence. By fitting this model to the observed images, the reliability and accuracy of image registration is improved enough to track over 10'000 droplets simultaneously.

22.4 Optical measurement of particle size and shape

Phase Doppler Interferometry (PDI), also known as Phase Doppler Particle Analyzer (PDPA), is a technique to measure one velocity component, size, and sometimes phase (Bachalo 1980; Chuang et al. 2008). A dual PDI probe in a cloud on the UFS and a diagram of its operation are shown in Figure 9. One laser beam is split into two equal beams which are crossed in a small volume with an angle 2α between them. The split beams $\vec{E}_{\pm} = \frac{1}{2}\vec{E}_0 \exp[i(kx \cos \alpha \pm k y \sin \alpha - \omega t)]$ interfere producing $\vec{E}_+ + \vec{E}_- = \vec{E}_0 \cos(ky \sin \alpha) \exp[i(kx \cos \alpha - \omega t)]$, which is a series of x-oriented interference fringes.

A particle in the overlap acts as a lens and mirror for the fringes. One or more photodetectors record the reflected or refracted fringes, which sweep past the detector/s as the particle moves in the y -direction. The detectors record so called Doppler bursts of the sweeping fringes. For approximately spherical particles (water and some ice), the Doppler burst frequency is related to velocity by $f_d = \frac{1}{\pi} k |v_y| \sin \alpha$, while the difference in phase between photodetectors is related to size (Bachalo 1980; Chuang et al. 2008). The special case of only one detector is Laser Doppler Velocimetry/Anemometry (LDV/A, see Foreman et al., 1965), which cannot obtain size.

In practice, however, three or more detectors are used to resolve particle diameter over a large range by resolving phase ambiguity and a small frequency shift is applied to one split beam to make sweeping fringes so that the sign of v_y can be determined and $v_y \approx 0$ can be resolved reliably. See Bachalo (1980), Sankar et al. (1991) and Chuang et al. (2008) for more details.

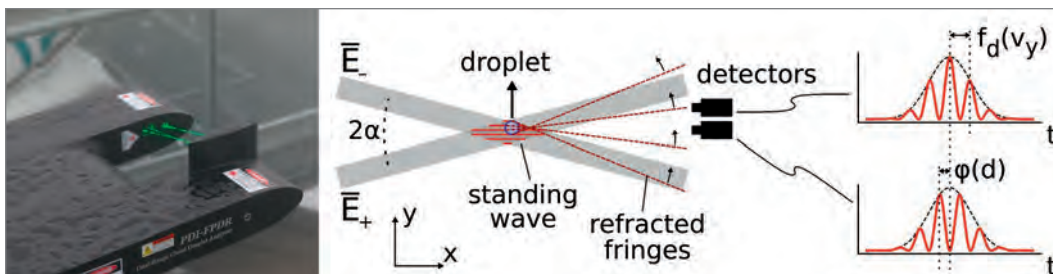


Fig. 9: (left) Dual PDI probe in a cloud at the UFS. (right) The working principle of Phase Doppler Interferometry (PDI). A laser beam is split and made to overlap producing fringes. A droplet passes through, causing refracted fringes to sweep, which are recorded as Doppler bursts by photodetectors. The frequency and phase differences between the Doppler bursts are related to the droplet y -velocity and diameter.

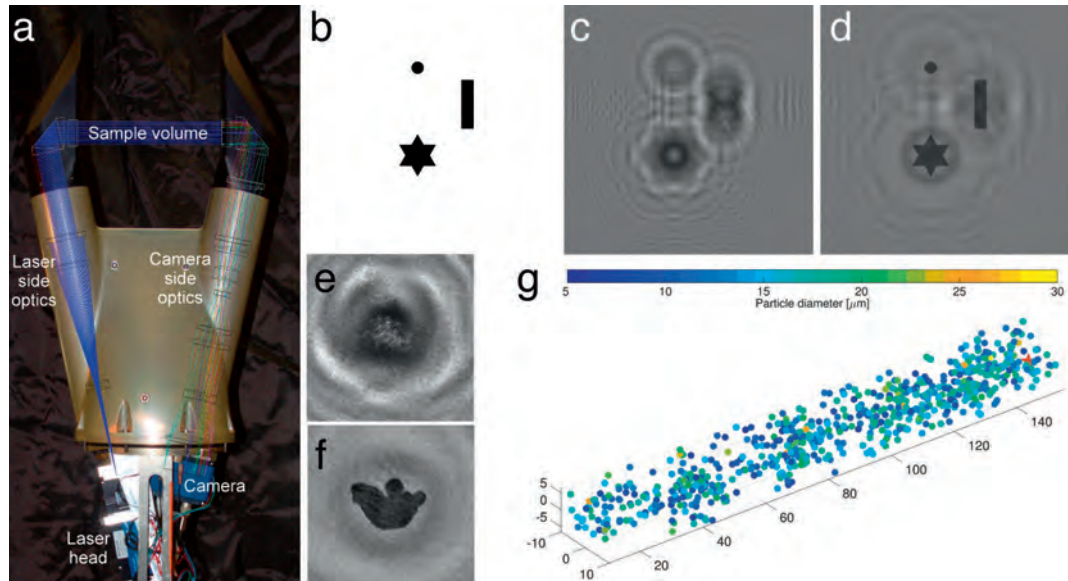


Fig. 10: (a) The HALOHolo instrument (Schlenczek 2018). (b) Mask of three obstructions used for the synthetic hologram in (c) which are a $100\ \mu\text{m}$ circle, a $100\ \mu\text{m} \times 400\ \mu\text{m}$ rectangle, and a $300\ \mu\text{m}$ wide six-pointed star. (c) Synthetic hologram for (b) 10 cm away from the mask for 355 nm light. (d) Reconstruction of (c) using the technique of Fugal et al. (2009). (e) Measured hologram of an ice particle. (f) Reconstruction of (e) using the technique of Fugal et al. (2009). (g) Positions (mm) and sizes of cloud droplets (color-coded) measured by 4 HALOHolo at UFS on 25 September 2019, 10:29:59 UTC. The position of the ice particle from (e) and (f) is shown as a red star.

Another interference technique is holography, which can measure many particle positions, sizes, and shapes simultaneously. The most common setup is in-line holography where a coherent light beam is sent through the volume and the diffraction pattern resulting from the beam and the light occluded and scattered by the particles is captured by a camera (Borrmann & Jaenicke 1993; Henneberger et al. 2013; Spuler & Fugal 2011). An example instrument, HALOHolo, is shown in Fig. 10a. The diffraction patterns cast by an obstruction in the beam (e.g. a particle) are a function of the distance from the obstruction to the camera, its size, and its shape. Fig. 10b shows a circle, a rectangle, and a six-pointed star obstructions. Their calculated diffraction patterns are shown in Fig. 10c. The interference patterns acquired by the camera must be reconstructed, which consists of diffracting the acquired image backwards (such as in Fig. 10d), to get the particle shapes, sizes, and positions which includes the distance from the camera. A hologram and its reconstruction from a measured ice particle are shown in Fig. 10e and 10f. The particle positions and sizes from a hologram obtained on 25 September 2019 from a long-lasting cloud at the UFS are shown in Fig. 10g.

The main advantages of holography are that it can be done with one camera and few optical elements, a weak laser, and a large depth of field. However, hologram reconstruction is very expensive in person hours (analog) or computation time (digital) (Schlenczek 2018). Depth resolution is limited, although a dual inline holography setup can mitigate this at the cost of added complexity and great difficulty in field use (Raupach et al. 2006). It is also difficult to distinguish the phase between small droplets and approximately spherical ice particles (Korolev et al. 2017). Notable results from holography in clouds include the observation of nonuniform droplet spatial distributions (Borrmann et al. 1993; Uhlig et al. 1998), partitioning of ice and droplets in mixed-phase clouds (Lohmann et al. 2016; Schlenczek 2018), size and spatial distributions in ice clouds (O'Shea et al. 2016; Schlenczek et al. 2017), and the analysis of mixing in convective clouds (Beals et al. 2015).

22.5 Outlook

With the Seesaw experiment at UFS, it will become possible for the first time to study the effect of gravity on the acceleration and velocity statistics of the drops in a high-Reynolds number turbulent flow with small ε . Since the accelerations and velocities involved are rather small, the shaking of the 3D LPT setup must be kept to a minimum in order not to introduce an artificial signal to the data. This is possible by carefully selecting the acceleration profile of the sled for each given velocity, isolating the vibrations of the sled from the setup via dampers and springs, and finally measuring and subtracting any remaining vibrations using a set of accelerometers.

We are also working on a way to use the existing LPT setup to measure the size of each individual droplet within our measurement volume, based on the amount of light it scatters onto the sensor. Given that we have data from 3 cameras available, each at a slightly different angle with respect to the incident laser beam, and that we track each droplet over substantial length of time, it should be possible to deduce the droplet size by reference to the known Mie scattering curves. This would allow conditioning droplet statistics on their size and yield more insight into the dynamics, as opposed to kinematics, of these objects.

We plan on eventually flying the Cloudkite (instrument diagram in Figure 5) from the Zugspitze to perform PIV (or 2-frame LPT when the particle concentration is low), holographic, hotwire, etc. measurements in clouds further from the mountainside (about 500 m) to reduce topographic effects. The Cloudkite will have a very high volumetric sample rate (~ 1 L/s) in order to get large statistics on the positions and sizes of cloud particles seen by its holography system, and cloud and particle velocities from its PIV system.

Combining the seesaw, the ultrasonic anemometers, and likely the HALOHolo instrument from Figure 10a on the deck of the UFS with the Cloudkite in the sky above; we hope to look at cloud microphysics at unprecedented detail including performing two point measurements from the ground and the Cloudkite at the same time which is important for looking at the spatial variation of particle dynamics within clouds. We hope these measurements will better elucidate the ‘cloud problem’. Eventually, we hope that the subgrid cloud modelling of clouds in weather and climate models will be improved so that we can better predict the weather and climate.

References

- Adrian, R. J., 1991. Particle-Imaging Techniques for Experimental Fluid Mechanics. *Annual Review of Fluid Mechanics*, 23(1), pp. 261–304. Available at: <http://www.annualreviews.org/doi/abs/10.1146/annurev.fl.23.010191.001401>.
- Adrian, R. J., 2005. Twenty years of particle image velocimetry. *Experiments in Fluids*, 39(2), pp.159–169.
- Adrian, R. J. & Westerweel, J., 2011. *Particle Image Velocimetry*,
- Bachalo, W. D., 1980. Method for measuring the size and velocity of spheres by dual-beam light-scatter interferometry. *Applied Optics*, 19(3), p.363. Available at: <https://www.osapublishing.org/abstract.cfm?URL=ao-19-3-363>.
- Balachandar, S. & Eaton, J. K., 2010. Turbulent Dispersed Multiphase Flow. *Annual Review of Fluid Mechanics*, 42(1), pp.111–133. Available at: <http://www.annualreviews.org/doi/10.1146/annurev.fluid.010908.165243>.
- Beals, M. J. et al., 2015. Holographic measurements of inhomogeneous cloud mixing at the centimeter scale. *Science*, 350(6256), pp.87–90. Available at: <http://www.sciencemag.org/cgi/doi/10.1126/science.aab0751>.
- Bec, J. et al., 2007. Heavy Particle Concentration in Turbulence at Dissipative and Inertial Scales. *Physical Review Letters*, 98(8), p.84502. Available at: <https://link.aps.org/doi/10.1103/PhysRevLett.98.084502>.
- Bertens, G., Bagheri, G., Xu, H., Bodenschatz, E. & Moláček, J., 2021. In situ particle tracking experiment. *Review of Scientific Instruments*, 92, p 125105
- Bodenschatz, E. et al., 2010. Can we understand clouds without turbulence? *Science*, 327(5968), pp. 970–971.
- Bodenschatz, E., 2015. Clouds resolved. *Science*, 350(6256), pp.40–41. Available at: <http://www.sciencemag.org/cgi/doi/10.1126/science.aad1386>.
- Bodenschatz, E. et al., 2014. Variable density turbulence tunnel facility. *Review of Scientific Instruments*, 85(9), p.93908. Available at: <http://scitation.aip.org/content/aip/journal/rsi/85/9/10.1063/1.4896138>.

- Borrmann, S. & Jaenicke, R., 1993. Application Of Microholography for Ground-based In Situ Measurements in Stratus Cloud Layers: A Case Study. *Journal of Atmospheric and Oceanic Technology*, 10(3), pp. 277–293. Available at: <http://journals.ametsoc.org/doi/abs/10.1175/1520-0426%281993%29010%3C0277%3AAOMFGB%3E2.0.CO%3B2>.
- Borrmann, S., Jaenicke, R. & Neumann, P., 1993. On spatial distributions and inter-droplet distances measured in stratus clouds with in-line holography. *Atmospheric Research*, 29(3–4), pp. 229–245. Available at: <http://linkinghub.elsevier.com/retrieve/pii/0169809593900059>.
- Celani, A., 2007. The frontiers of computing in turbulence: challenges and perspectives. *Journal of Turbulence*, 8 (October 2014), p. N34. Available at: <https://www.tandfonline.com/doi/full/10.1080/14685240601091668>.
- Chuang, P.Y. et al., 2008. Airborne Phase Doppler Interferometry for Cloud Microphysical Measurements. *Aerosol Science and Technology*, 42(8), pp. 685–703. Available at: <http://www.tandfonline.com/doi/abs/10.1080/02786820802232956>.
- Darcy, H., 1858. Note relative à quelques modifications à introduire dans le tube de Pitot. In *Annales des Ponts et Chaussées*. pp. 351–359.
- Davidson, P., 2015. *Turbulence: an introduction for scientists and engineers*, Oxford University Press, USA.
- DIN EN 60751 / IEC 60751, 2008. *Industrial platinum resistance thermometers and platinum temperature sensors*.
- Dracos, T., 1996. *Particle tracking in three-dimensional space*, Dordrecht: Kluwer.
- Falkovich, G., Fouxon, A. & Stepanov, M. G., 2002. Acceleration of rain initiation by cloud turbulence. *Nature*, 419(6903), pp.151–154.
- Fan, Y. et al., 2015. Nanoscale sensing devices for turbulence measurements. *Experiments in Fluids*, 56(7), p.138. Available at: <http://link.springer.com/10.1007/s00348-015-2000-0>.
- Foreman, J.W., George, E.W. & Lewis, R.D., 1965. MEASUREMENT OF LOCALIZED FLOW VELOCITIES IN GASES WITH A LASER DOPPLER FLOWMETER. *Applied Physics Letters*, 7(4), pp.77–78. Available at: <http://dx.doi.org/10.1063/1.1754319>.
- Fugal, J.P., Schulz, T.J. & Shaw, R.A., 2009. Practical methods for automated reconstruction and characterization of particles in digital in-line holograms. *Measurement Science and Technology*, 20(7), p. 75501. Available at: <http://stacks.iop.org/0957-0233/20/i=7/a=075501?key=crossref.faf5f591f6ae0efdc367574230506c8b8>.
- Grabowski, W.W. & Wang, L.-P., 2013. Growth of Cloud Droplets in a Turbulent Environment. *Annual Review of Fluid Mechanics*, 45(1), pp. 293–324. Available at: <http://www.annualreviews.org/doi/abs/10.1146/annurev-fluid-011212-140750>.
- Gunn, R. & Kinzer, G. D., 1949. THE TERMINAL VELOCITY OF FALL FOR WATER DROPLETS IN STAGNANT AIR. *Journal of Meteorology*, 6(4), pp.243–248. Available at: <http://journals.ametsoc.org/doi/abs/10.1175/1520-0469%281949%29006%3C0243%3ATTVOFF%3E2.0.CO%3B2>.
- Harrison, G., 2014. *Meteorological measurements and instrumentation*, Chichester, UK: Wiley Blackwell.
- Henneberger, J. et al., 2013. HOLIMO II: a digital holographic instrument for ground-based in situ observations of microphysical properties of mixed-phase clouds. *Atmospheric Measurement Techniques*, 6(11), pp.2975–2987. Available at: <http://www.atmos-meas-tech.net/6/2975/2013/>.
- Ishihara, T. et al., 2016. Energy spectrum in high-resolution direct numerical simulations of turbulence. *Physical Review Fluids*, 1(8), p.82403. Available at: <https://link.aps.org/doi/10.1103/PhysRevFluids.1.082403>.
- Jameson, A. R. & Kostinski, A. B., 2001. What is a Raindrop Size Distribution? *Bulletin of the American Meteorological Society*, 82(6), pp.1169–1177. Available at: [http://journals.ametsoc.org/doi/abs/10.1175/1520-0477\(2001\)082%3C1169:WIARSD%3E2.3.CO;2](http://journals.ametsoc.org/doi/abs/10.1175/1520-0477(2001)082%3C1169:WIARSD%3E2.3.CO;2).
- Jimenez, J., 2003. Computing high-Reynolds-number turbulence: will simulations ever replace experiments? *Journal of Turbulence*, 4(September 2002), pp.16–18. Available at: <http://www.informaworld.com/openurl?genre=article&doi=10.1088/1468-5248/4/1/022&magic=crossref%7C%7CD404A21C5BB-053405B1A640AFFD44AE3>.
- King, L. V., 1914. On the Convection of Heat from Small Cylinders in a Stream of Fluid: Determination of the Convection Constants of Small Platinum Wires, with Applications to Hot-Wire Anemometry. *Proceedings of the Royal Society A: Mathematical, Physical and Engineering Sciences*, 90(622), pp.563–570. Available at: <http://rspa.royalsocietypublishing.org/cgi/doi/10.1098/rspa.1914.0089>.
- Kolmogorov, A. N., 1941. The local structure of turbulence in incompressible viscous fluid for very large Reynolds numbers. In *Dokl. Akad. Nauk SSSR*. pp. 299–303.
- Korolev, A. et al., 2017. Mixed-Phase Clouds: Progress and Challenges. *Meteorological Monographs*, 58 (Fahrenheit 1724), p.5.1–5.50. Available at: <http://journals.ametsoc.org/doi/10.1175/AMSMONOGRAPHS-D-17-0001.1>.
- Kostinski, A. B. & Shaw, R.A., 2005. Fluctuations and Luck in Droplet Growth by Coalescence. *Bulletin of the American Meteorological Society*, 86(2), pp. 235–244. Available at: <http://journals.ametsoc.org/doi/abs/10.1175/BAMS-86-2-Kostinski>.
- Langmuir, I., 1948. THE PRODUCTION OF RAIN BY A CHAIN REACTION IN CUMULUS CLOUDS AT TEMPERATURES ABOVE FREEZING. *Journal of Meteorology*, 5(5), pp.175–192. Available at: <http://journals.ametsoc.org/doi/abs/10.1175/1520-0469%281948%29005%3C0175%3ATPORBA%3E2.0.CO%3B2>.

- Levich, V. G., 1954. The Theory of Coagulation of Colloids in Turbulent Liquid Stream. In *Dokl. Akad. Nauk SSSR*, pp. 809–812.
- Lohmann, U. et al., 2016. Persistence of orographic mixed-phase clouds. *Geophysical Research Letters*, 43(19), p.10,512–10,519. Available at: <http://doi.wiley.com/10.1002/2016GL071036>.
- Maas, H. G., Gruen, A. & Papantoniou, D., 1993. Particle tracking velocimetry in three-dimensional flows. *Experiments in Fluids*, 15(2), pp.133–146. Available at: <http://link.springer.com/10.1007/BF00190953>.
- Malinowski, S. P. et al., 2013. Physics of Stratocumulus Top (POST): turbulent mixing across capping inversion. *Atmospheric Chemistry and Physics*, 13(24), pp.12171–12186.
- Marshall, J. S. & Palmer, W. M. K., 1948. THE DISTRIBUTION OF RAINDROPS WITH SIZE. *Journal of Meteorology*, 5(4), pp.165–166. Available at: <http://doi.wiley.com/10.1002/qj.49707632704>.
- McKeon, B. et al., 2007. Velocity, vorticity, and Mach number. In *Springer Handbook of Experimental Fluid Mechanics*. Springer, pp. 215–471.
- Mordant, N., Crawford, A. M. M. & Bodenschatz, E., 2004. Experimental Lagrangian acceleration probability density function measurement. *Phys. D Nonlinear Phenom.*, 193(1–4), pp. 245–251. Available at: <http://linkinghub.elsevier.com/retrieve/pii/S0167278904000417>.
- O’Shea, S. J. et al., 2016. Airborne observations of the microphysical structure of two contrasting cirrus clouds. *Journal of Geophysical Research: Atmospheres*, 121(22), p.13,510–13,536. Available at: <http://doi.wiley.com/10.1002/2016JD025278>.
- Ouellette, N. T., Xu, H. & Bodenschatz, E., 2006. A quantitative study of three-dimensional Lagrangian particle tracking algorithms. *Exp. Fluids*, 40(2), pp.301–313. Available at: <http://link.springer.com/10.1007/s00348-005-0068-7>.
- Pitot, H. de, 1732. Description d’une machine pour mesurer la vitesse des eaux courantes et le sillage des vaisseaux. *Mémoires de L’Académie*.
- Pope, S. B., 2000. *Turbulent flows*, Cambridge university press.
- La Porta, A. et al., 2001. Fluid particle accelerations in fully developed turbulence. *Nature*, 409(6823), pp.1017–1019. Available at: <http://www.nature.com/doi/10.1038/35059027>.
- Pumir, A. & Wilkinson, M., 2016. Collisional Aggregation Due to Turbulence. *Annual Review of Condensed Matter Physics*, 7(1), pp.141–170. Available at: <http://arxiv.org/abs/1508.01538>.
- Raffel, M., 2007. *Particle image velocimetry a practical guide*, Heidelberg New York: Springer.
- Raupach, S. M. F. et al., 2006. Digital crossed-beam holography for in situ imaging of atmospheric ice particles. *J. Opt. A-Pure Appl. Op.*, 8(9), pp.796–806.
- Richardson, L. F., 1922. *Weather prediction by numerical process*, Cambridge University Press.
- Risius, S., 2012. *Investigation of turbulent flows at the Umweltforschungsstation Schneefernerhaus (Zugspitze)*. Institute for Nonlinear Dynamics, Emden.
- Risius, S. et al., 2015. Schneefernerhaus as a mountain research station for clouds and turbulence. *Atmospheric Measurement Techniques*, 8(8), pp. 3209–3218. Available at: <http://www.atmos-meas-tech-discuss.net/8/541/2015/>.
- Saffman, P. G. & Turner, J. S., 1956. On the collision of drops in turbulent clouds. *Journal of Fluid Mechanics*, 1(1), p.16. Available at: http://www.journals.cambridge.org/abstract_S0022112056000020.
- Sankar, S. V. et al., 1991. Sizing fine particles with the phase Doppler interferometric technique. *Applied Optics*, 30(33), p.4914. Available at: <https://www.osapublishing.org/abstract.cfm?URI=ao-30-33-4914>.
- Scarano, F., 2013. Tomographic PIV: principles and practice. *Measurement Science and Technology*, 24(1), p.12001. Available at: <http://stacks.iop.org/0957-0233/24/i=1/a=012001?key=crossref.06bb53d64ea6b5ebccdc8da58d8006e>.
- Schanz, D., Gesemann, S. & Schröder, A., 2016. Shake-The-Box: Lagrangian particle tracking at high particle image densities. *Experiments in Fluids*, 57(5), p.70. Available at: <http://link.springer.com/10.1007/s00348-016-2157-1>.
- Schlenczek, O., 2018. *Airborne and ground-based holographic measurement of hydrometeors in liquid-phase, mixed-phase and ice clouds*. University of Mainz.
- Schlenczek, O. et al., 2017. Microphysical Properties of Ice Crystal Precipitation and Surface-Generated Ice Crystals in a High Alpine Environment in Switzerland. *Journal of Applied Meteorology and Climatology*, 56(2), pp.433–453. Available at: <http://journals.ametsoc.org/doi/10.1175/JAMC-D-16-0060.1>.
- Shaw, R. a, 2003. Particle Turbulence Interactions in Atmospheric Clouds. *Annual Review of Fluid Mechanics*, 35(1), pp. 183–227. Available at: <http://www.annualreviews.org/doi/abs/10.1146/annurev.fluid.35.101101.161125>.
- Siebert, H. et al., 2015. High-resolution measurement of cloud microphysics and turbulence at a mountain-top station. *Atmospheric Measurement Techniques*, 8(8), pp.3219–3228. Available at: <http://www.atmos-meas-tech-discuss.net/8/569/2015/>.
- Siebert, H., Lehmann, K., Wendisch, M., et al., 2006. Probing Finescale Dynamics and Microphysics of Clouds with Helicopter-Borne Measurements. *Bulletin of the American Meteorological Society*, 87(12), pp.1727–1738. Available at: <http://journals.ametsoc.org/doi/abs/10.1175/BAMS-87-12-1727>.
- Siebert, H. et al., 2010. Towards understanding the role of turbulence on droplets in clouds: in situ and laboratory measurements. *Atmospheric Research*, 97(4), pp.426–437.

- Siebert, H., Lehmann, K. & Wendisch, M., 2006. Observations of Small-Scale Turbulence and Energy Dissipation Rates in the Cloudy Boundary Layer. *Journal of the Atmospheric Sciences*, 63(5), pp.1451–1466. Available at: <http://journals.ametsoc.org/doi/abs/10.1175/JAS3687.1>.
- Siebert, H., Shaw, R. a. & Warhaft, Z., 2010. Statistics of Small-Scale Velocity Fluctuations and Internal Intermittency in Marine Stratocumulus Clouds. *Journal of the Atmospheric Sciences*, 67(1), pp.262–273. Available at: <http://journals.ametsoc.org/doi/abs/10.1175/2009JAS3200.1>.
- Snyder, W.H. & Lumley, J.L., 1971. Some measurements of particle velocity autocorrelation functions in a turbulent flow. *Journal of Fluid Mechanics*, 48(1), pp. 41–71.
- Spuler, S.M. & Fugal, J., 2011. Design of an in-line, digital holographic imaging system for airborne measurement of clouds. *Applied Optics*, 50(10), p.1405. Available at: <https://www.osapublishing.org/abstract.cfm?URI=ao-50-10-1405>.
- Stevens, B. & Bony, S., 2013. What Are Climate Models Missing? *Science*, 340(6136), pp.1053–1054. Available at: <http://www.ncbi.nlm.nih.gov/pubmed/23723223>.
- Taylor, G.I., 1938. The Spectrum of Turbulence. *Proceedings of the Royal Society A: Mathematical, Physical and Engineering Sciences*, 164(919), pp. 476–490. Available at: <http://www.jstor.org/stable/97077>.
- Uhlig, E.-M., Borrmann, S. & Jaenicke, R., 1998. Holographic in-situ measurements of the spatial droplet distribution in stratiform clouds. *Tellus B*, 50(4), pp. 377–387. Available at: <http://www.tellusb.net/index.php/tellusb/article/view/16210>.
- Vaillancourt, P.A. & Yau, M.K., 2000. Review of Particle – Turbulence Interactions and Consequences for Cloud Physics. *Bulletin of the American Meteorological Society*, 81(2), pp. 285–298. Available at: <http://journals.ametsoc.org/doi/abs/10.1175/1520-0477%282000%29081%3C0285%3AROPAC%3E2.3.CO%3B2>.
- Voth, G.A., Satyanarayan, K. & Bodenschatz, E., 1998. Lagrangian acceleration measurements at large Reynolds numbers. *Phys. Fluids*, 10(9), pp. 2268–2280. Available at: <http://aip.scitation.org/doi/10.1063/1.869748>.
- Wallace, J.M. & Hobbs, P.V., 2006. Cloud Microphysics. In *Atmospheric Science*. Elsevier, pp. 209–269. Available at: <http://linkinghub.elsevier.com/retrieve/pii/B9780127329512500119>.
- Warhaft, Z., 2002. Turbulence in nature and in the laboratory. *Proceedings of the National Academy of Sciences of the United States of America*, 99 Suppl 1, pp. 2481–2486.
- Westerweel, J., Elsinga, G.E. & Adrian, R.J., 2013. Particle Image Velocimetry for Complex and Turbulent Flows. *Annual Review of Fluid Mechanics*, 45(1), pp. 409–436. Available at: <http://www.annualreviews.org/doi/10.1146/annurev-fluid-120710-101204>.
- Yeung, P.K., 2002. LAGRANGIAN INVESTIGATIONS OF TURBULENCE. *Annual Review of Fluid Mechanics*, 34(1), pp.115–142. Available at: <http://www.annualreviews.org/doi/10.1146/annurev.fluid.34.082101.170725>.
- Yeung, P.K., Zhai, X.M. & Sreenivasan, K.R., 2015. Extreme events in computational turbulence. *Proceedings of the National Academy of Sciences*, 112(41), pp.12633–12638. Available at: <http://www.pnas.org/lookup/doi/10.1073/pnas.1517368112>.
- Yoshimoto, H. & Goto, S., 2007. Self-similar clustering of inertial particles in homogeneous turbulence. *Journal of Fluid Mechanics*, 577, p.275. Available at: http://www.journals.cambridge.org/abstract_S0022112007004946.

List of Contributors

- V. Allertseeder** Technical University of Munich, Department of Dermatology and Allergy
Biederstein, Biedersteiner Str. 29, 80802 München
- Gholamhossein Bagheri** Max Planck Institute for Dynamics and Self-Organization, Am Faßberg
17, 37077 Göttingen, gholamhossein.bagheri@ds.mpg.de
- Christoph Beck** University of Augsburg, Institute of Geography, Universitätsstraße 2, 86159
Augsburg
- H. Behrendt**, Technical University of Munich and Helmholtz Center Munich, Center of Allergy
and Environment (ZAUM, Zentrum Allergie und Umwelt), Biedersteiner Str. 29, 80802
München
- M. Bernhardt** University of Natural Resources and Life Sciences (BOKU), Vienna, Institute of
Hydrology and Watermanagement
- Michael Bittner** German Aerospace Center, DLR, German Remote Sensing Data Center,
Oberpfaffenhofen, Münchener Straße 20, 82234 Weßling and University of Augsburg,
Institute of Physics, Universitätsstraße 2, 86159 Augsburg
- Eberhard Bodenschatz** Max Planck Institute for Dynamics and Self-Organization, Am Faßberg
17, 37077 Göttingen, eberhard.bodenschatz@ds.mpg.de
- Cedric Couret** German Environmental Agency, Wörlitzer Platz 1, 06844 Dessau-Roßlau
- Ulf Darsow** Technical University of Munich, Department of Dermatology and Allergy
Biederstein, Biedersteiner Str. 29, 80802 München
- B. Eberlein** Technical University of Munich, Department of Dermatology and Allergy Biederstein,
Biedersteiner Str. 29, 80802 München and Technical University of Munich and Helmholtz
Center Munich, Center of Allergy and Environment (ZAUM, Zentrum Allergie und Umwelt),
Biedersteiner Str. 29, 80802 München
- Cordula Ebner von Eschenbach** Technical University of Munich and Helmholtz Center Munich,
Center of Allergy and Environment (ZAUM, Zentrum Allergie und Umwelt), Biedersteiner
Str. 29, 80802 München
- R. Fischer** Ludwig-Maximilians-University Munich, Medical Hospital City, Department of
Pneumology, Ziemssenstraße 1, 80336 München
- R. Franz** Technical University of Munich, Department of Dermatology and Allergy Biederstein,
Biedersteiner Str. 29, 80802 München
- Korbinian P. Freier** Bavarian Environment Agency, Bürgermeister-Ulrich-Straße 160, 86179
Augsburg
- Arne Friedmann** University of Augsburg, Institute of Geography, Working Group Biogeography,
Alter Postweg 2, 86135 Augsburg
- Thomas Gallemann** Bavarian Environment Agency, Bürgermeister-Ulrich-Straße 160, 86179
Augsburg
- M. Garhammer** Ludwig-Maximilians-University Munich, Meteorological Institute, Theresienstr.
37, 80333 München
- Esther Giemsa** University of Augsburg, Institute of Geography, Universitätsstraße 2, 86159
Augsburg
- Thorsten Glauber** Bavarian State Ministry of the Environment und Consumer Protection,
Rosenkavalierplatz 2, 81925 München
- J. Gloning** Technical University of Munich, Department of Dermatology and Allergy Biederstein,
Biedersteiner Str. 29, 80802 München
- Stephan Hachinger** Leibniz Supercomputing Centre Boltzmannstraße 1, 85748 Garching
- Axel Häring**, German Aerospace Center, DLR, Oberpfaffenhofen – Institute of Atmospheric
Physics, Münchener Straße 20, 82234 Weßling
- Martin Hagen**, German Aerospace Center, DLR, Oberpfaffenhofen – Institute of Atmospheric
Physics, Münchener Straße 20, 82234 Weßling
- Patrick Hannawald** University of Augsburg, Institute of Physics, Universitätsstraße 2, 86159
Augsburg
- Petra Hausmann** Karlsruhe Institute of Technology, Institute of Meteorology and Climate
Research – Atmospheric Environmental Research (IMK-IFU), Kreuzeckbahnstraße 19, 82467
Garmisch-Partenkirchen
- Bernhard Henkelmann** Helmholtz Center Munich – Molecular EXposomics (MEX), Ingolstädter
Landstraße 1, 85764 Neuherberg

- R. Hennico** Technical University of Munich and Helmholtz Center Munich, Center of Allergy and Environment (ZAUM, Zentrum Allergie und Umwelt), Biedersteiner Str. 29, 80802 München
- P. Hoeppe** Ludwig-Maximilians-University Munich, Meteorological Institute, Theresienstr. 37, 80333 München
- Markus Homann** University of Augsburg, Institute of Geography, Universitätsstraße 2, 86159 Augsburg
- R. Huber** Ludwig-Maximilians-University Munich, Medical Hospital City, Department of Pneumology, Ziemssenstraße 1, 80336 München
- Kerstin Hürkamp** Helmholtz Center Munich, Institute of Radiation Medicine, Ingolstädter Landstraße 1, 85764 Neuherberg
- J. Huss-Marp** Technical University of Munich and Helmholtz Center Munich, Center of Allergy and Environment (ZAUM, Zentrum Allergie und Umwelt), Biedersteiner Str. 29, 80802 München
- Jucundus Jacobeit** University of Augsburg, Institute of Geography, Universitätsstraße 2, 86159 Augsburg
- Severin Kaspar** University of Augsburg, Institute of Geography, Universitätsstraße 2, 86159 Augsburg
- Manfred Kirchner** Helmholtz Center Munich – Molecular EXposomics (MEX), Ingolstädter Landstraße 1, 85764 Neuherberg
- B. Klotz** Medical University Innsbruck, Biomedical Physics, Christoph-Probst-Platz 1, Innrain 52, 6020 Innsbruck
- Stefan Kneifel** University of Cologne, Institute of Geophysics and Meteorology, Albertus-Magnus-Platz, 50923 Köln
- P. Koepke** Ludwig-Maximilians-University Munich, Meteorological Institute, Theresienstr. 37, 80333 München
- Wolfgang Körner** Bavarian Environment Agency, Bürgermeister-Ulrich-Straße 160, 86179 Augsburg
- Oliver Korch** University of Augsburg, Institute of Geography, Working Group Biogeography, Alter Postweg 2, 86135 Augsburg
- M. Kriegisch** Technical University of Munich and Helmholtz Center Munich, Center of Allergy and Environment (ZAUM, Zentrum Allergie und Umwelt), Biedersteiner Str. 29, 80802 München
- Lisa Küchelbacher** German Aerospace Center, DLR, German Remote Sensing Data Center, Oberpfaffenhofen, Münchener Straße 20, 82234 Weßling
- J. Latotski** Technical University of Munich and Helmholtz Center Munich, Center of Allergy and Environment (ZAUM, Zentrum Allergie und Umwelt), Biedersteiner Str. 29, 80802 München
- John Lawson** Aerodynamics and Flight Mechanics Research Group, University of Southampton, University Road, Southampton SO17 1BJ, United Kingdom, J.M.Lawson@soton.ac.uk
- M. Leibl** Technical University of Munich, Department of Dermatology and Allergy Biederstein, Biedersteiner Str. 29, 80802 München
- Michael Mahr** Ingenieurbüro, 82499 Wallgau
- Vladimir Mares** Helmholtz Center Munich, Institute of Radiation Medicine, Ingolstädter Landstraße 1, 85764 Neuherberg
- Wolfgang Moche** Environment Agency Austria, Spittelauer Lände 5, 1090 Wien
- Jan Moláček** Max Planck Institute for Dynamics and Self-Organization, Am Faßberg 17, 37077 Göttingen, jan.molacek@ds.mpg.de
- Stefan Noll** University of Augsburg, Institute of Physics, Universitätsstraße 2, 86159 Augsburg
- Freja Nordsiek** Max Planck Institute for Dynamics and Self-Organization, Am Faßberg 17, 37077 Göttingen, freja.nordsiek@ds.mpg.de
- Marchela Pandelova** Helmholtz Center Munich – Molecular EXposomics (MEX), Ingolstädter Landstraße 1, 85764 Neuherberg
- F. Pfab** Technical University of Munich and Helmholtz Center Munich, Center of Allergy and Environment (ZAUM, Zentrum Allergie und Umwelt), Biedersteiner Str. 29, 80802 München
- Andreas Philipp** University of Augsburg, Institute of Geography, Universitätsstraße 2, 86159 Augsburg
- Gabriela Ratz** Bavarian Environment Agency, Bürgermeister-Ulrich-Straße 160, 86179 Augsburg
- J. Reuder** Ludwig-Maximilians-University Munich, Meteorological Institute, Theresienstr. 37, 80333 München and University of Bergen, and Bjerknes Centre for Climate Research, Geophysical Institute, Jahnebakken 5, 5007 Bergen

- Ludwig Ries** German Environmental Agency, Wörlitzer Platz 1, 06844 Dessau-Roßlau
- J. Ring**, Technical University of Munich, Department of Dermatology and Allergy Biederstein, Biedersteiner Str. 29, 80802 München
- Werner Rühm** Helmholtz Center Munich, Institute of Radiation Medicine, Ingolstädter Landstraße 1, 85764 Neuherberg
- Volker Schiller** Institute for Environmental Medicine, Neusässer Straße 47, 86156 Augsburg
- Oliver Schlenczek** Max Planck Institute for Dynamics and Self-Organization, Am Faßberg 17, 37077 Göttingen, oliver.schlenczek@ds.mpg.de
- Carsten Schmidt** German Aerospace Center, DLR, German Remote Sensing Data Center, Oberpfaffenhofen, Münchener Straße 20, 82234 Weßling
- Kersten Schmidt** German Aerospace Center, DLR, Oberpfaffenhofen – Microwaves and Radar Institute, Münchener Straße 20, 82234 Weßling
- M. Schmitt** Technical University of Munich, Department of Dermatology and Allergy Biederstein, Biedersteiner Str. 29, 80802 München
- Karl-Werner Schramm** Technical University of Munich, School of Life Sciences, Alte Akademie 8, 85354 Freising and Helmholtz Center Munich – Molecular EXposomics (MEX), Ingolstädter Landstraße 1, 85764 Neuherberg
- René Sedlak** University of Augsburg, Institute of Physics, Universitätsstraße 2, 86159 Augsburg
- M. Seefeldner** Ludwig-Maximilians-University Munich, Meteorological Institute, Theresienstr. 37, 80333 München
- Stefanie Seubert** University of Augsburg, Institute of Geography, Universitätsstraße 2, 86159 Augsburg
- Siegfried Specht**, Bavarian State Ministry of the Environment und Consumer Protection, Rosenkavalierplatz 2, 81925 München
- Ralf Sussmann** Karlsruhe Institute of Technology, Institute of Meteorology and Climate Research – Atmospheric Environmental Research (IMK-IFU), Kreuzeckbahnstraße 19, 82467 Garmisch-Partenkirchen
- Jochen Tschiersch** Helmholtz Center Munich, Institute of Radiation Medicine, Ingolstädter Landstraße 1, 85764 Neuherberg
- Claudia Traidl-Hoffmann** Institute for Environmental Medicine, Neusässer Straße 47, 86156 Augsburg
- Thomas Trickl** Karlsruhe Institute of Technology, Institute of Meteorology and Climate Research – Atmospheric Environmental Research (IMK-IFU), Kreuzeckbahnstraße 19, 82467 Garmisch-Partenkirchen
- Hannes Vogelmann** Karlsruhe Institute of Technology, Institute of Meteorology and Climate Research – Atmospheric Environmental Research (IMK-IFU), Kreuzeckbahnstraße 19, 82467 Garmisch-Partenkirchen
- Andreas von Poschinger** Bavarian Environment Agency, Bürgermeister-Ulrich-Straße 160, 86179 Augsburg
- Bernhard Wagner** Bavarian Environment Agency, Bürgermeister-Ulrich-Straße 160, 86179 Augsburg
- M. Weber** Ludwig-Maximilians-Universität Munich, Department of Geography, Luisenstraße 37, 80333 München
- S. Weishaupt** University of Augsburg, Institute of Geography, Universitätsstraße 2, 86159 Augsburg
- Peter Weiss** Environment Agency Austria, Spittelauer Lände 5, 1090 Wien
- K.-F. Wetzel** University of Augsburg, Institute of Geography, Universitätsstraße 2, 86159 Augsburg, wetzel@geo.uni-augsburg.de
- Sabine Wüst** German Aerospace Center, DLR, German Remote Sensing Data Center, Oberpfaffenhofen, Münchener Straße 20, 82234 Weßling
- Ye Yuan** Technical University of Munich, School of Life Sciences, Hans-Carl-von-Carlowitz-Platz 2, 85354 Freising

www.klima.bayern.de

Herausgeber: Bayerisches Staatsministerium für
Umwelt und Verbraucherschutz (StMUV)
Rosenkavalierplatz 2
81925 München

Betriebsgesellschaft Umweltforschungsstation Schneefernerhaus
(UFS) GmbH
Kordinator Science-Team der UFS Prof. Dr. Michael Bittner
Zugspitze 5
82475 Zugspitze

Internet: www.stmuv.bayern.de
E-Mail: poststelle@stmuv.bayern.de
Druck: Druckerei Safner, Priesendorf
Gestaltung: CMS – Cross Media Solutions GmbH, Würzburg
Bildnachweis: Bilder und Abbildungen von den Autoren, Außer Kapitel 1: Abb. 1,
23, 26, 29 – 32: Markus Neumann; Abb. 2: European Space
Imaging Munich; Abb. 3, 4, 14, 18, 25, 28, 33: Siegfried Specht;
Abb. 5 bis 8: Bayerische Akademie der Wissenschaften (BAW);
Abb. 9: Österreichischer Alpenverein/Mu-seum – Archiv; Abb. 10,
11: Deutsches Museum München – Archiv; Abb. 12: Bayerische
Zugspitzbahn Berg-bahn AG (BZB) – Archiv; Abb. 13: Stiftung
Deutsches Technikmuseum Berlin – Hist. Archiv; Abb. 15 – 17: Dr.
Wolff & Tritschler, Historisches Bildarchiv, Offenburg; Abb. 19, 20:
Bayerische Zugspitzbahn Bergbahn AG – Max Prectel; Abb. 21,
22: Betriebsgesellschaft UFS GmbH; Abb. 24, 39 Georg Barth;
Abb. 27: Christoph Malin; Abb. 34 – 37 The Virtual Alpine
Observatory (VAO) (www.vao.bayern.de); Abb. 38: Michael Bittner,
Markus Leuenberger, Elke Ludewig

Stand: Mai 2022

© StMUV, alle Rechte vorbehalten

Gedruckt auf Papier aus 100% Altpapier

Diese Publikation wird kostenlos im Rahmen der Öffentlichkeitsarbeit der Bayerischen Staatsregierung herausgegeben. Jede entgeltliche Weitergabe ist untersagt. Sie darf weder von den Parteien noch von Wahlwerbern oder Wahlhelfern im Zeitraum von fünf Monaten vor einer Wahl zum Zweck der Wahlwerbung verwendet werden. Dies gilt für Landtags-, Bundestags-, Kommunal- und Europawahlen. Missbräuchlich ist während dieser Zeit insbesondere die Verteilung auf Wahlveranstaltungen, an Informationsständen der Parteien sowie das Einlegen, Aufdrucken und Aufkleben parteipolitischer Informationen oder Werbemittel. Untersagt ist gleichfalls die Weitergabe an Dritte zum Zweck der Wahlwerbung. Auch ohne zeitlichen Bezug zu einer bevorstehenden Wahl darf die Publikation nicht in einer Weise verwendet werden, die als Parteinahme der Staatsregierung zugunsten einzelner politischer Gruppen verstanden werden könnte. Den Parteien ist es gestattet, die Publikation zur Unterrichtung ihrer eigenen Mitglieder zu verwenden. Das Werk ist urheberrechtlich geschützt. Alle Rechte sind vorbehalten. Die publizistische Verwertung der Veröffentlichung – auch von Teilen – wird jedoch ausdrücklich begrüßt. Bitte nehmen Sie Kontakt mit dem Herausgeber auf, der Sie – wenn möglich – mit digitalen Daten der Inhalte und bei der Beschaffung der Wiedergaberechte unterstützt. Diese Publikation wurde mit großer Sorgfalt zusammengestellt. Eine Gewähr für die Richtigkeit und Vollständigkeit kann dennoch nicht übernommen werden. Für die Inhalte fremder Internetangebote sind wir nicht verantwortlich.



BAYERN|DIREKT ist Ihr direkter Draht zur Bayerischen Staatsregierung. Unter Tel. 089 122220 oder per E-Mail unter direkt@bayern.de erhalten Sie Informationsmaterial und Broschüren, Auskunft zu aktuellen Themen und Internetquellen sowie Hinweise zu Behörden, zuständigen Stellen und Ansprechpartnern bei der Bayerischen Staatsregierung.

www.klima.bayern.de



Umwelt
Forschungsstation
Schneefernerhaus